

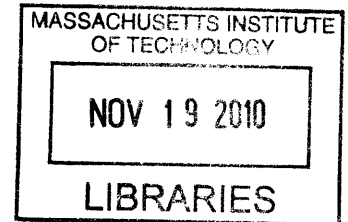
Life Extension of Structural Components via an Improved Nondestructive Testing Methodology

by

Brian P. Hohmann

S.M., Materials Science and Engineering
MIT, 2007

B.S., Ceramic Engineering
Rutgers University, 2004



ARCHIVES

SUBMITTED TO THE DEPARTMENT OF MATERIALS SCIENCE AND
ENGINEERING IN PARTIAL FULFILLMENT OF THE REQUIREMENTS FOR THE
DEGREE OF

DOCTOR OF SCIENCE IN MATERIALS SCIENCE AND ENGINEERING
AT THE
MASSACHUSETTS INSTITUTE OF TECHNOLOGY

September 2010

© 2010 Massachusetts Institute of Technology
All rights reserved

Signature of Author.....

Department of Materials Science and Engineering
August 12, 2010

Certified by.....

Thomas W. Eagar
Professor of Materials Engineering and Engineering Systems
Thesis Supervisor

Accepted by.....

Christopher Schuh
Chair, Departmental Committee on Graduate Students

This page intentionally left blank

Life Extension of Structural Components via an Improved Nondestructive Testing Methodology

by

Brian P. Hohmann

Submitted to the Department of Materials Science and Engineering on
August 12, 2010 in Partial Fulfillment of the Requirements for the
Degree of Doctor of Science in Materials Science and Engineering

Abstract

An experimental study was performed to determine the flaw detection sensitivity of advanced nondestructive testing (NDT) techniques with respect to structural applications. The techniques analyzed exemplify the incorporation of digital technology into NDT and includes the following: meandering winding magnetometer array (MWM-array®) eddy current, phased-array ultrasonic (PA-UT), three dimensional computed tomography (3D-CT), and digital radiography (DR). The three classes of samples inspected with these techniques consisted of alloy block specimens containing flat bottom hole (FBH) arrays, probability of detection (POD) wedding cake samples, and actual airplane engine components. Results from the sensitivity analyses were compared to current NDT techniques used industrially. An image analysis program called Cellprofiler was used to optimize the threshold correction factor for selected results. The Cellprofiler output was analyzed in conjunction with POD software, and the integration of digitally advanced NDT techniques with image analysis software resulted in approximately a threefold improvement in the minimum detectable flaw size at the 90/95 POD/CL level. An improved inspection methodology was presented which incorporated redundancy in the in-service inspection plan with the use of Bayesian updating techniques to forecast remnant life. Reliability block diagrams for structural disk and blade aircraft engine components were presented as examples of the methodology. Implementation of the proposed NDT methodology significantly increases the feasibility of a retirement-for-cause (RFC) approach to be applied to aging structural components in a cost-effective manner.

Thesis Supervisor: Thomas W. Eagar

Title: Professor of Materials Engineering and Engineering Systems

Acknowledgements

There are so many people who helped me over the course of this thesis project that I want to acknowledge. I would like to extend my gratitude to my thesis committee members, Professors Sam Allen and Joel Clark, for their time spent reviewing my writing and the insightful discussions we've had both in and out of the classroom over the years.

To the past and present members of the Welding Lab at MIT, including Harold Larson, Don Galler, Jeri Hill, Joel Williams, Chris Musso, and Yuttanant (Vee) Boonyongmaneerat, I'd like to thank you for all the guidance and for being there to listen when classes or research got tough. I'd like to especially thank my two main UROPS, Gene Settoon and Kevin Boehm, who provided a lot of assistance with my SM and ScD experiments and whom I now consider two close friends. Thanks also go out to Yu Watanabe, Josh Bodner, and Sergio Tavares for their invaluable assistance the past two years.

I would like to acknowledge the many amazing individuals who I have met at this institution since arriving in 2004 and am now lucky enough to call my friends, especially: Jay "Sonic" Trelewicz, Charles "Trey" Holzwarth, Dave "D\$" Fischer, Tim Rupert, Chris "CJ Betti" Bettinger, Tom Kollar, Sal Barriga, Andy Detor, Kevin McComber, Dave Bradwell, Yu "Albert" Bai, Biraja Kanungo, Gagan Saini, Vikram Mittal, Danielle Hinton, Kevin Lang, Jon Gibbs, and all of the undergraduates I came to know in my 3 years as a GRT at Simmons Hall. I'd also like to thank the many friends I met in Boston outside of MIT: Mary "Greek chick" Zachos, Bryan Betts, Tina Bullotta, Andrew Fischer, Dan Goikhman, Mike Mole, Lauren Trelewitz, Jocelyn Fary-Holzwarth, Ally Curtis, Charles Snow, Holly St. Peter, Jill Fineman, Lauren May, Ryan DeStefano, Scotty Petit, and Tom Cashman. I would also like to thank all the people at *Al Dente* and *Ricardo's Ristorante* in the North End for treating me like family the past 6 years.

Many companies and individuals helped to make this thesis possible. In particular, I'd like to thank Ravi Shankar and Dick Fenton of Chromalloy Gas Turbine Corp., Neil Goldfine and Dave Grundy of Jentek Sensors Inc., Rob Raimondi of Olympus NDT, Vicki Kramb of UDRI, Fettah Kosar of the Center for Nanoscale Systems at Harvard, Lisa Brasche of Iowa State Univ., Dr. Chi Chen of UMass Dartmouth, Charles Annis, Ray Jones of the Broad Institute, and the people at Baker Testing Services.

To my parents, Henry and Barbara Hohmann, thank you for always putting me and my sisters first. Without the family structure and discipline you provided I would have made the wrong life decisions and veered off course a long time ago. To my sisters Jennifer and Colleen, thanks for always believing in me and being there no matter what.

Finally, to my thesis advisor, Tom Eagar, words simply cannot describe how thankful I am that I had the privilege and honor of working with you the past 6 years. You have taught me so much not just by your words but by your actions and your approach to life. I am forever grateful for all you've done for me and only hope I can "pay it forward" to others in the future.

Table of Contents

ABSTRACT	3
ACKNOWLEDGEMENTS.....	4
TABLE OF CONTENTS.....	5
LIST OF FIGURES.....	7
LIST OF TABLES.....	16
CHAPTER 1 : INTRODUCTION	17
1.1 NDT/NDE PROCESSES	20
1.2 A DISCUSSION OF “TRADITIONAL” NDT PROCESSES APPLICABLE TO AEROSPACE APPLICATIONS	25
1.2.1 <i>Visual Inspection</i>	26
1.2.2 <i>FPI/LPI</i>	27
1.2.3 <i>Magnetic Particle Inspection</i>	30
1.2.4 <i>Eddy Current Inspection</i>	31
1.2.5 <i>X-ray Inspection</i>	36
1.2.6 <i>Ultrasonic Inspection</i>	40
1.3 THE LIMITATIONS OF THE TRADITIONAL NDT PROCESSES.....	46
1.3.1 <i>Sources of noise and variability in NDT methodologies</i>	46
1.3.2 <i>Embedded defects</i>	53
1.3.3 <i>Error Associated with Human Factors</i>	59
1.3.4 <i>Prior Catastrophic Failures</i>	62
1.4 ADVANCED NDT PROCESSES OF PROPOSED METHODOLOGY	67
1.4.1 <i>MWM®-Array Eddy Current Inspection</i>	67
1.4.2 <i>Phased Array Ultrasonic Inspection</i>	72
1.4.3 <i>Computed Tomography</i>	75
1.4.4 <i>Imaging Analysis and Process Automation</i>	81
1.5 BACKGROUND ON AIRPLANE ENGINE INSPECTION METHODOLOGY	83
1.5.1 <i>Safe Life/Damage Tolerant Approach</i>	84
1.5.2 <i>Structural Health Monitoring</i>	86
1.5.3 <i>Retirement for Cause Approach</i>	89
CHAPTER 2 : MWM-ARRAY® EDDY CURRENT INSPECTION.....	91
2.1 SAMPLE PREPARATION	91
2.1.1 <i>Alloy blocks</i>	92
2.1.2 <i>Wedding Cake Samples</i>	94
2.1.3 <i>Actual Engine Components</i>	101
2.2 EXPERIMENTAL PROCEDURE	102
2.3 RESULTS OF SENSITIVITY ANALYSIS	105
2.4 COMPARISON WITH TRADITIONAL EC TECHNIQUE.....	121
CHAPTER 3 : PHASED ARRAY ULTRASONIC INSPECTION.....	127
3.1 EXPERIMENTAL PROCEDURE	127
3.1.1 <i>Alloy Blocks</i>	128
3.1.2 <i>Wedding cake samples</i>	130
3.2 RESULTS OF SENSITIVITY ANALYSIS	135
3.3 COMPARISON WITH TRADITIONAL UT TECHNIQUE.....	155
CHAPTER 4 : COMPUTED TOMOGRAPHY INSPECTION.....	163
4.1 EXPERIMENTAL PROCEDURE	163
4.1.1 <i>Alloy Block Samples</i>	165

4.1.2 <i>Wedding Cake Samples</i>	167
4.1.3 <i>Actual Components</i>	169
4.2 RESULTS OF SENSITIVITY ANALYSIS	170
4.3 COMPARISON WITH TRADITIONAL X-RAY TECHNIQUE	176
CHAPTER 5 : IMAGE ANALYSIS AND POD MODELING	195
5.1 EXPERIMENTAL PROCEDURE FOR CELLPROFILER	195
5.2 IMAGE ANALYSIS RESULTS	201
5.3 POD MODEL	209
CHAPTER 6 : ADVANCED NDT METHODOLOGY	220
6.1 STATISTICAL APPROACH TO QUANTIFYING VARIABLES	220
6.1.1 <i>In-service Inspection</i>	228
6.2 METHODOLOGY APPLIED TO DISKS	238
6.3 METHODOLOGY APPLIED TO BLADES	243
6.4 DISCUSSION OF COST-BENEFIT ANALYSIS	247
6.5 OBSTACLES TO IMPLEMENTING METHODOLOGY	261
CONCLUSIONS	264
APPENDIX A : NOMENCLATURE	268
APPENDIX B : CRITICAL TURBINE ENGINE COMPONENTS	280
B.1 DISKS	285
B.2 BLADES	288
B.3 NON-HPT CRITICAL COMPONENTS	293
APPENDIX C : MATERIAL SELECTION FOR CRITICAL ENGINE COMPONENTS	296
C.1 NICKEL-BASE SUPERALLOYS: PROPERTIES AND PROCESSING EFFECTS	296
C.2 TI-ALLOYS: PROPERTIES AND PROCESSING EFFECTS	303
C.3 OTHER STRUCTURAL MATERIALS	311
APPENDIX D : TRADITIONAL UTI DATA FROM ALLOY BLOCK EXPERIMENTS AT UMASS DARTMOUTH	315
APPENDIX E : DIGITAL RADIOGRAPHIC IMAGES	333
REFERENCES	337

List of Figures

FIGURE 1.1: INDUSTRIAL TEST CELL USED TO SIMULATE ACTUAL TURBINE ENGINE SERVICE OPERATING CONDITIONS	24
FIGURE 1.2: IMAGE FROM A BORESCOPE INSPECTION REVEALING BLADE DAMAGE	27
FIGURE 1.3: SCHEMATIC SHOWING LIQUID PENETRANT INTO A SURFACE CRACK VIA CAPILLARY ACTION (ADAPTED FROM [44]).....	29
FIGURE 1.4: (A) VARIOUS STATIONS REQUIRED FOR FPI (B) DRY-DEVELOPER BIN WITH DUST CONTROL AND LIQUID RECLAMATION SYSTEM	30
FIGURE 1.5: THE UNDERLYING PRINCIPLE BEHIND EDDY CURRENT INSPECTION (REPRINTED FROM [50]).....	32
FIGURE 1.6: REFERENCE STANDARD USED IN THE CALIBRATION OF AN EDDY CURRENT PROBE FOR DETECTION OF CRACKS AND CORROSION IN AL-ALLOY AIRCRAFT COMPONENTS THAT CONTAIN FASTENER HOLES.	34
FIGURE 1.7: SCHEMATIC REPRESENTATION OF THE TRADE-OFF BETWEEN INSPECTION FREQUENCY AND SENSITIVITY AND THE AFFECT ON ECI DEPTH OF PENETRATION (REPRINTED FROM [50])	35
FIGURE 1.8: NDT TECHNIQUES BASED ON THE EM SPECTRUM. X-RAYS HAVE A MUCH SHORTER WAVELENGTH, AND THUS MORE ENERGY THAN OTHER TECHNIQUES INCLUDING VI, LPI, AND MPI. [59]	37
FIGURE 1.9: SCHEMATIC OF X-RAY TUBE (ADAPTED FROM [57]).....	37
FIGURE 1.10: (A) THE ACOUSTIC SPECTRUM SHOWING THE THREE SUB-SECTIONS OF THE ULTRASONIC FREQUENCY RANGE. (B) ILLUSTRATION OF THE DIRECTION OF PARTICLE MOTION VERSUS THE DIRECTION OF WAVE PROPAGATION FOR LONGITUDINAL AND SHEAR WAVES. (REPRINTED FROM [65])	42
FIGURE 1.11: X-Y RASTER SCANNING USED TO OBTAIN C-SCAN WITH TRADITIONAL ULTRASONIC SYSTEM (FIGURE PROVIDED BY PROF C.H. CHEN, UMASS DARTMOUTH)	45
FIGURE 1.12: S/N DENSITY DISTRIBUTION FOR (A) A LARGE FLAW (B) A SMALL FLAW AND (C) AN EXTREMELY SMALL FLAW WHOSE SIGNAL RESPONSE IS BELOW THE INHERENT MICROSTRUCTURAL (GRAIN) NOISE OF THE MATERIAL UNDER TEST. (ADAPTED FROM [84])	48
FIGURE 1.13: THE FOUR POTENTIAL OUTCOMES FOR AN NDT FLAW DETECTION PROCEDURE SHOWN IN A 2X2 MATRIX (ADAPTED FROM [84])	49
FIGURE 1.14: THE EFFECT OF DISCRIMINATION THRESHOLD LEVEL ON POD (A) CLEAR DISCRIMINATION (B) ACCEPT SOME FLAWS (C) REJECT SOME GOOD PARTS	50
FIGURE 1.15: FALSE POSITIVE (TYPE II) AND FALSE NEGATIVE (TYPE I) INSPECTION RESPONSES BASED ON PLACEMENT OF DISCRIMINATION THRESHOLD (ADAPTED FROM [84]).....	50
FIGURE 1.16: POD PLOTS FOR FOUR NDT METHODS ON THE SAME SET OF SPECIMENS. THE POD CURVES ARE ONLY APPLICABLE TO SURFACE FLAWS OF SPECIFIED SURFACE CONDITION A) PENETRANT INSPECTION B) ULTRASONIC INSPECTION C) EDDY CURRENT INSPECTION D) X-RAY INSPECTION (ADAPTED FROM [84])	52
FIGURE 1.17: (A) EFFECT OF RANDOM NOISE ON CT IMAGE (B) CT IMAGE QUALITY DETERIORATION DUE TO RING ARTIFACTS (REPRINTED FROM [57])	54
FIGURE 1.18: (A) TARGET LAYOUT IN DEFECT RING SPECIMEN (B) SCHEMATIC OF THE DIFFUSION BONDING PROCESS. (REPRINTED FROM [101] COURTESY OF V. KRAMB, UNIV. OF DAYTON RESEARCH INSTITUTE)	56
FIGURE 1.19: REJUVENATION HIP PROCESS FOR A BLADE SHOWING INTERNAL VOID COLLAPSE (ADAPTED FROM [106]).....	58
FIGURE 1.20: THE FULLY AUTOMATED TESI INSPECTION SYSTEM AT UDRI SHOWING THE ROBOT MANIPULATOR AND INSPECTION TANK (REPRINTED FROM [100])	60
FIGURE 1.21: SCHEMATIC OF THE BASIC STRUCTURE OF THE MWM SENSOR AS ORIGINALLY CONCEIVED (REPRINTED FROM [52]).....	68
FIGURE 1.22: PRECOMPUTED GRID CONTAINING ALL POTENTIAL SENSOR RESPONSES FOR THE CASE WHERE THE TWO UNKNOWN ARE CONDUCTIVITY AND LIFT-OFF. THE GRID IS FOR A PARTICULAR CHANNEL OF THE MWM-ARRAY SENSOR AT A PARTICULAR FREQUENCY.	71
FIGURE 1.23: MULTIPLE CHANNEL FA28 MWM-ARRAY SENSOR (REPRINTED FROM [52])	72
FIGURE 1.24: (A) SCHEMATIC OF BEAM SCANNING IN LONGITUDINAL E-SCAN (B) SCHEMATIC OF BEAM SWEEPING IN SECTORIAL S-SCAN (ADAPTED FROM [137]).....	74

FIGURE 1.25: SCHEMATIC OF THE GENERAL COMPONENTS IN A MODERN INDUSTRIAL 3D-CT SCAN (ADAPTED FROM [57]).....	75
FIGURE 1.26: (A) 2D SLICE OF A COMPLEX COMPONENT ACQUIRED DURING CT SCAN (B-C) 3D CT RECONSTRUCTION OF THE SAMPLE WITH VARIOUS CUTAWAY PLANES FOR INSPECTION OF INTERNAL DEFECTS.....	78
FIGURE 1.27: EFFECT OF BEAM HARDENING ON IMAGE QUALITY (REPRINTED FROM [57])	80
FIGURE 1.28: (A-B) TWO VIEWS FROM AN ATOS SCAN OF THE DISK COMPONENT IN FIGURE B.6(A)	82
FIGURE 1.29: ASPECTS OF THE ENHANCED LIFE MANAGEMENT PROCESS (REPRINTED FROM [8])	84
FIGURE 1.30: SHM ASPECTS OF THE CONVENTIONAL LIFE MANAGEMENT PROCESS (REPRINTED FROM [6])..	87
FIGURE 1.31: FATIGUE CRACK GROWTH UNDER A RFC INSPECTION APPROACH. PARTS ARE INSPECTED EVERY 1000 HRS. (REPRINTED FROM [183])	90
FIGURE 2.1: (A) SAMPLE H (B) SAMPLE L (C) SAMPLE U (D) SAMPLE R88.....	93
FIGURE 2.2: CLOSE UP VIEW OF 3X3 ARRAY OF #1FBH ON SAMPLE R88	93
FIGURE 2.3: CAD MODEL OF THE ORIGINAL WEDDING CAKE SAMPLE DESIGN.....	94
FIGURE 2.4: MACHINING PROCESSES PERFORMED IN THE WEDDING CAKE SAMPLE PREPARATION (A) CUTTING CYLINDRICAL ROD STOCK IN HALF ON BAND SAW (B) CLAMPING CUT STOCK IN CHUCK OF CNC LATHE (C) STABILIZING STOCK WITH CENTERING TAILSTOCK QUILL (D) TURNING DOWN THE LAYERS OF THE WEDDING CAKE SAMPLE	96
FIGURE 2.5: THE SPECIFIED HEIGHTS FOR THE FIVE LEVELS IN THE WEDDING CAKE SPECIMENS.....	96
FIGURE 2.6: (A) FRONT-SIDE TOP DOWN VIEW OF EMBEDDED DEFECT SAMPLE (B) BACK-SIDE VIEW OF THE EMBEDDED DRILL BIT DEFECT FROM THE REAR BASE OF LEVEL 1	97
FIGURE 2.7: (A) TOP-DOWN AND (B) BOTTOM-UP PERSPECTIVE OF THE SPECIFIED HOLE LAYOUT	98
FIGURE 2.8: COMPARISON OF THE HOLE LAYOUT FROM (A) SAMPLE CAD DESIGN AND (B) FABRICATED SAMPLE.....	98
FIGURE 2.9: (A-C) FRONT, BACK, AND TOP VIEW FROM ONE OF THE TURBINE BLADE SAMPLES	101
FIGURE 2.10: (A) FRONT AND (B) BACK SURFACE VIEW OF THE 1 ST STAGE DUCT SEGMENT.....	102
FIGURE 2.11: STEREOMICROSCOPE IMAGE OF THE DUCT SEGMENT SURFACE CRACKS. IMAGE SIZE IS 0.5 X 0.375 IN. (12.7X9.5MM)	102
FIGURE 2.12: (A) EARLY CAD CONCEPT DESIGN FOR THE AUTOMATED BLADE DOVETAIL INSPECTION SYSTEM (B) PHOTOGRAPH OF A FABRICATED SYSTEM CURRENTLY IN USE (ADAPTED FROM [112])	103
FIGURE 2.13: (A) X-Y ENCODER GANTRY SYSTEM TEST SETUP PRIOR TO INSPECTION (B) ENCODER SETUP DURING INSPECTION. A 2KG (4.4LB) WEIGHT WAS PLACED ON TOP OF THE SENSOR TO MINIMIZE LIFT-OFF VARIATION AND ENSURE INTIMATE CONTACT BETWEEN THE SENSOR AND THE TEST SAMPLE.	104
FIGURE 2.14: C-SCAN IMAGE OF R88 SAMPLE WITH A DESCRIPTION OF IMAGE FEATURES.....	106
FIGURE 2.15: (A) C-SCAN AND (B) B-SCAN DATA AT 15.84MHZ FOR INSPECTION SET 4 OF SAMPLE R88 ...	107
FIGURE 2.16: SIMPLE CRACK SIZING METHODS WITH THE GRIDSTATION® SOFTWARE FOR (A) C-SCAN IMAGES AND (B) B-SCAN PLOTS (ADAPTED FROM [189]).....	108
FIGURE 2.17: C-SCAN IMAGE FROM SET 5 OF THE R88 SAMPLE AT THE SLOWER ENCODER VELOCITY RATE. THE EDGE EFFECTS HAVE BEEN CORRECTED FOR THE CENTER ROW OF HOLES BUT REMAIN IN THE TOP AND BOTTOM ROWS	109
FIGURE 2.18: LIFT-OFF SCANS FOR R88 SAMPLE (A) SET 5 AND (B) SET 6 WITH 5MIL (0.13MM) SHIM ADDED	110
FIGURE 2.19: SIGNAL RESPONSE LOCATION ON THE PRE-COMPUTED MEASUREMENT GRID FOR SCAN SET 5 AND SET 6.....	110
FIGURE 2.20: (A)C-SCAN AND (B) B-SCAN RESULTS OF THE CONDUCTIVITY SCAN FOR SET 6 AT THE 15.84MHZ TEST FREQUENCY AFTER ADDITION OF SHIM AND USE OF AUTOMATIC THRESHOLD CORRECTION	112
FIGURE 2.21: THE EFFECT ON SIGNAL RESPONSE FOR THE CENTER ROW OF HOLES IN FIGURE 2.20(A) WHEN TWO ADJACENT CHANNELS DETECT THE SAME FLAT BOTTOM HOLES.....	113
FIGURE 2.22: C-SCAN IMAGE FOR SAMPLE H [190]	113
FIGURE 2.23: C-SCAN IMAGE FOR SAMPLE L	114
FIGURE 2.24: C-SCAN IMAGE FOR SAMPLE U	114
FIGURE 2.25: B-SCAN CONDUCTIVITY VERSUS POSITION PLOT FOR SET 8. THE SIGNAL RESPONSE FROM CHANNELS 18 AND 19 ARE NEARLY IDENTICAL.	115
FIGURE 2.26: (A) C-SCAN IMAGE OF SAMPLE L AFTER A 0.5MM (20 MIL) DIAGONAL ADJUSTMENT. (B) COMPARISON OF SIGNAL RESPONSE FROM CHANNELS 17-21 WITH FIGURE 2.25	116

FIGURE 2.27: (A) B-SCAN SIGNAL RESPONSE FROM CHANNELS 1-25 FOR SET 9. (B) LOCATION ON MEASUREMENT GRID FOR SELECTED CHANNELS OF SCAN SET 9	117
FIGURE 2.28: B-SCAN DATA FOR THE THREE CHANNELS IN SET 10 THAT SCANNED OVER THE INDIVIDUAL FBH ROWS. THE SIGNAL RESPONSE AMONG THE THREE CHANNELS IS NEARLY IDENTICAL RESULTING IN IMPROVED SENSITIVITY [190].	118
FIGURE 2.29: (A-C) B-SCANS MAGNIFIED AT THE X-AXIS LOCATIONS OF THE FBH ROWS	118
FIGURE 2.30: (A) C-SCAN IMAGE FOR SET 11 (B) B-SCAN PLOT OF THE THREE CHANNELS THAT SCANNED OVER THE INDIVIDUAL FBH ROWS FOR SET 11 (C) COMPARISON BETWEEN THE MEASUREMENT GRID LOCATION OF TWO CHANNELS IN SET 10 AND SET 11	120
FIGURE 2.31: (A) DUCT SEGMENT ORIENTED 45° RELATIVE TO SENSOR, WITH BUSINESS CARDS USED AS SHIMS TO ACCOUNT FOR LIFT-OFF (B) COMPONENT PLACED ON TOP OF REAM OF PAPER TO PROVIDE SOME COMPLIANCE DURING TESTING (C) IMAGE OF THE DUCT SEGMENT SCAN IN PROGRESS	121
FIGURE 2.32: (A) C-SCAN CONDUCTIVITY AND (B) LIFT-OFF SCANS FOR THE DUCT SEGMENT	122
FIGURE 2.33: (A) B-SCAN PLOT OF MULTIPLE CRACKS' SIGNAL RESPONSE AND (B) MEASUREMENT GRID FOR DUCT SEGMENT.....	122
FIGURE 2.34: (A) PROCESS OF CALIBRATING THE EDDY CURRENT ARRAY PROBE TO A REFERENCE STANDARD. (B) C-SCAN OUTPUT FOR THE INSPECTION OF SAMPLE H.	123
FIGURE 2.35: (A) CALIBRATION TO STANDARD DUCT SEGMENT OF KNOWN CRACKS (B) FLAW INDICATION APPEARS ON TRADITIONAL ECI EQUIPMENT DURING INSPECTION OF DUCT SEGMENT SPECIMEN (C) LISSAJOUS SIGNAL AT 45° ANGLE DURING INSPECTION A SIGN OF LIFT-OFF ISSUES (D) SCAN OF ANALOG DATA PRINT-OUT WITH A STRIP CHART REPRESENTATION TO THE RIGHT OF THE SINGLE FREQUENCY CHANNEL IMPEDANCE PLANE.....	125
FIGURE 3.1: ORIENTATION OF SAMPLES FOR THE MANUAL PHASED-ARRAY UT SCANS.....	129
FIGURE 3.2: (A) "BOTTOM-UP" SAMPLE ORIENTATION FOR TESI PA-UT INSPECTIONS (B) CENTERING TOOL USED FOR POSITIONAL REPEATABILITY AND ACCURACY BETWEEN SAMPLES	132
FIGURE 3.3: (A) STEEL WEDDING CAKE SAMPLE CENTERED (B) SAMPLE DURING SHEAR INSPECTION.....	132
FIGURE 3.4: (A-C) THREE PERSPECTIVES OF THE STEEL WEDDING CAKE AFTER INSPECTION DETAILING THE SEVERITY OF RUST CAUSED BY COMPLETE WATER IMMERSION.	132
FIGURE 3.5: (A) SCHEMATIC OF THE FOUR PROBE POSITIONS SELECTED ALONG THE PART FOR THE 10MHZ LONGITUDINAL INSPECTIONS (B) PROBE POSITION DURING INSPECTION AS SEEN THROUGH GRAPHICAL USER INTERFACE OF TESI SOFTWARE	133
FIGURE 3.6: SCHEMATIC REPRESENTATION OF THE TWO PROBE POSITIONS SELECTED FOR THE 10MHZ 45° SHEAR INSPECTIONS.....	134
FIGURE 3.7: (A) SCHEMATIC REPRESENTATION OF THE 5MHZ PROBE POSITION FOR BOTH THE LONGITUDINAL AND SHEAR INSPECTIONS (B) 5MHZ PROBE POSITION VISUALIZED WITH TESI GRAPHICAL USER INTERFACE	134
FIGURE 3.8: "BOTTOM-UP" SPECIMEN INSPECTION ORIENTATION	135
FIGURE 3.9: (A) APPLICATION OF GEL COUPLANT TO SAMPLE SURFACE (B) CALIBRATION OF FOCAL LAWS FOR EXPERIMENT	135
FIGURE 3.10: (A) OUTPUT FROM 5MHZ S-SCAN OF SAMPLE H DETAILING ONE ROW OF FBH (B) MARKERS PLACED ON IMAGE TO ESTIMATE HOLE DEPTH. FAINT INDICATIONS TO THE LEFT OF THREE HOLES REPRESENT THE BOTTOM DEPTH OF THE HOLES.	136
FIGURE 3.11: (A) RESULTS FROM 5MHZ LONGITUDINAL SCAN OF SAMPLE H. LONGITUDINAL SCAN AT 0° SHOWING 3X3 ARRAY OF FBH. (B) MARKERS PLACED ON IMAGE TO ESTIMATE DISTANCE BETWEEN HOLES IN BOTH X AND Y DIRECTIONS. (C) MAGNIFICATION AND DYNAMIC DEPTH FOCUSING OF TOP ROW OF FBH IN 3.11(B) <i>NOTE THIS WAS AN E-SCAN. THE S-SCAN HEADINGS WERE NOT UPDATED FROM FIGURE 3.10 DURING INSPECTION [190].</i>	137
FIGURE 3.12: (A) 17MHZ LONGITUDINAL E-SCAN OF SAMPLE R88. NOTE DIFFERENCE IN IMAGE RESOLUTION BETWEEN 5MHZ AND 17MHZ SCAN. (B) DISTANCE BETWEEN TWO HOLES ESTIMATED AT A PARTICULAR DEPTH. (C) IMAGE MAGNIFICATION OF TOP LEFT HOLE IN 3.12(A-B) <i>NOTE THIS WAS AN E-SCAN. THE S-SCAN HEADINGS WERE NOT UPDATED FROM FIGURE 3.10 DURING INSPECTION.</i>	138
FIGURE 3.13: (A) 17MHZ S-SCAN OF SAMPLE R88 (B) DEPTH AND DISTANCE MARKERS PLACED ON IMAGE	138
FIGURE 3.14: (A) TOMOVIEW™ SCREEN SHOT OF THE INITIAL LINEAR PASS ALONG THE SURFACE OF THE AL-WEDDING CAKE SAMPLE. A-SCAN SIGNAL SHOWN IN TOP LEFT, B-SCAN IN TOP RIGHT, AND C-SCAN IN BOTTOM HALF OF DISPLAY. MARKERS HAVE BEEN SLID OVER ONE OF THE LEVEL 1 HOLES. THREE	

LEVELS OF THE WEDDING CAKE SAMPLE ARE DISCERNABLE IN C-SCAN IMAGE. (B) MAGNIFIED VIEW OF LIFT-OFF VARIATION LIKELY CAUSED BY “STICKING” OF THE PROBE TO THE SAMPLE SURFACE NEAR THE EDGES OF THE CENTER HOLE REGION (C) IMAGE QUALITY IMPROVEMENT IN SUBSEQUENT MANUAL SCAN.....	140
FIGURE 3.15: (A-D) ITERATIVE PASSES REQUIRED TO IMAGE THE ENTIRE 6061 AL-WEDDING CAKE SAMPLE. FBH ON LEVEL 1 AND LEVEL 2 ARE OBSERVED IN (A-C); HOWEVER AS THE A-SCANS SHOW, THE VARIATION IN SIGNAL RESPONSE IS LARGE. THIS VARIABILITY COMPLICATES THE QUANTIFICATION OF SYSTEM CAPABILITY IN THE SENSITIVITY ANALYSIS.	141
FIGURE 3.16: (A) SAME SCAN AS IN FIGURE 3.14(A) BUT WITH THE RANGE TURNED DOWN IN ORDER TO BETTER EXAMINE LEVEL 1. (B) MAGNIFICATION OF B-SCAN REVEALS GHOST ECHOES (C) SUBSTANTIAL PIXILATION IN C-SCAN IMAGE.(D) IMPROVED RESOLUTION IN LARGER FBH LOCATED AT DIFFERENT LEVEL 3 POSITION.....	143
FIGURE 3.17: (A) LINEAR ARRAY PROBE PLACEMENT ON RUSTED STEEL SAMPLE (B) SAMPLE ORIENTATION WITH PROBE REMOVED (C) THRESHOLD NOT TRIPPED, GATED ALARM REMAINS WHITE AND NO FBH INDICATION OBSERVED (D) GATED THRESHOLD TRIPPED, ALARM GOES OFF AND GATE TURNS RED. THE RED ARROW IN (D) POINTS TO THE FBH INDICATION ON THE OMNISCAN® MONITOR.	144
FIGURE 3.18: (A) THE PROBE PLACEMENT ON THE EMBEDDED DEFECT WEDDING CAKE SAMPLE SURFACE (B) REFERENCE MEASUREMENT ON DIAMETER OF EMBEDDED DEFECT (C) S-SCAN IMAGE OF SAMPLE SHOWING DETECTION AND SIZING CAPABILITY OF MANUAL PA-UT.	145
FIGURE 3.19: ESTIMATION OF LEVEL 1 AND LEVEL 2 DEPTHS FROM A BOTTOM-UP ORIENTATION. THE ESTIMATED VALUES ARE VERY CLOSE TO THE ACTUAL VALUES SHOWN IN FIGURE 2.5.....	146
FIGURE 3.20: SELECTED A-SCAN, B-SCAN, AND C-SCAN DATA FOR THE 6061 ALUMINUM ALLOY WEDDING CAKE SAMPLE (A) CHANNEL 1 FROM 5MHZ LONGITUDINAL SCAN (B) CHANNEL 1 FROM 5MHZ 45° SHEAR SCAN (C) CHANNEL 2 FROM 5MHZ LONGITUDINAL SCAN (D) SAME C-SCAN IMAGE AS IN 3.20(C) BUT ZOOMED IN ON FBH TARGETS AND WITH GAIN ADDED TO IMAGE.....	149
FIGURE 3.21: SELECTED A-SCAN, B-SCAN, AND C-SCAN DATA FOR THE 8620 STEEL ALLOY WEDDING CAKE SAMPLE (A) CHANNEL 2 FROM 5MHZ LONGITUDINAL SCAN (B) CHANNEL 1 OF ZONE 3 FROM 10MHZ LONGITUDINAL SCAN (C) CHANNEL 2 OF ZONE 3 FROM 10MHZ LONGITUDINAL SCAN (D) CHANNEL 3 OF ZONE 3 FROM 10MHZ LONGITUDINAL SCAN.	150
FIGURE 3.22: SCHEMATIC OF LASER DRILLING PROCESS (A) LASER INITIALLY PULSES AND ABLATES COMPONENT SURFACE, BUT THE ABLATION PROCESS IS VERY VARIABLE AND BLOWBACK CAN OCCUR (B) LASER DRILLING BECOMES MORE UNIFORM ONCE STARTER HOLE IS FORMED (C) LASER PULSES ON AND OFF UNTIL DESIRED HOLE SIZE AND DEPTH IS OBTAINED.	151
FIGURE 3.23: TESI AUTOMATED CAD OUTPUT SHOWING ALL INDICATIONS FOR (A) STEEL AND (B) ALUMINUM SAMPLES. A LOT OF FALSE POSITIVE INDICATIONS WERE OBSERVED.	151
FIGURE 3.24: SCHEMATIC OF THE SYSTEM PROCESSING STEPS INVOLVED IN THE GENERATION OF A PULSE-ECHO SYSTEM RESPONSE FOR (A) FULLY IMMERSSED SAMPLE AND (B) ULTRASONIC SYSTEM IN CONTACT MODE (ADAPTED FROM [194]).....	153
FIGURE 3.25: (A-C) VARIOUS ADJUSTMENTS MADE TO GAIN AND MAGNIFICATION LEVELS OF THE EMBEDDED DEFECT ROI C-SCAN IMAGES WITH TOMOVIEWER®	154
FIGURE 3.26: (A) 10MHZ, 45° SHEAR INSPECTION OF EMBEDDED STEEL SAMPLE. FBH TARGETS IN LEVEL 1 DETECTED WHEN C-SCAN IMAGE FOCUSED AT A DEPTH OF 0.081IN. (0.21CM). RANGE SET FROM 3.2-9.1MM FOR C-SCAN IMAGE. (B) MAGNIFICATION OF FBH TARGET ALIGNED WITH MARKERS IN 3.26(A)	156
FIGURE 3.27: 10MHZ ACOUSTIC MICROSCOPY INSPECTION IMAGE OF (A) Ti-17 BILLET MATERIAL OF SAMPLE P AND (B) Ti-6-4 BILLET MATERIAL OF SAMPLE Q.....	157
FIGURE 3.28: (A-B) GRAPHICAL REPRESENTATION OF ALLOY BLOCK SPECIMEN SECTIONING AND NOMENCLATURE USED TO DISTINGUISH BLOCK ORIENTATION (REPRINTED FROM [184]).....	157
FIGURE 3.29: C-SAM IMAGE RESULTS FOR SIDES 1, 2, AND 3 OF (A) SAMPLE B AND (B) SAMPLE C	158
FIGURE 3.30: (A) SAMPLE R88 BLOCK UNDER INSPECTION WITH C-SAM SYSTEM (B) SAMPLE PROTRUDING ABOVE WATER LEVEL, RESULTING IN AN EXCESSIVE AMOUNT OF NOISE AND THE INABILITY TO OBTAIN DATA. THIS RESULT WAS OBSERVED FOR THE ENTIRE SET OF ALLOY BLOCK SPECIMENS INSPECTED WITH THE ADVANCED NDT TECHNIQUES.....	158
FIGURE 3.31: (A) TRADITIONAL C-SCAN UTI TEST SETUP LOCATED AT ATMC, UMASS DARTMOUTH (B-C) 2-D X-Y RASTERING OF SINGLE ELEMENT TRANSDUCER OVER SAMPLE R88.....	160

FIGURE 3.32: CONVERGENCE OF A FOCUSED SOUND BEAM ON A METAL SURFACE AND THE RESULTING ACOUSTIC EFFECT (ADAPTED FROM [194]).....	161
FIGURE 4.1: THE X-Tek® HMX-ST 225kV MICROCT IMAGING SYSTEM LOCATED AT THE CENTER FOR NANOSCALE SYSTEMS AT HARVARD UNIVERSITY	163
FIGURE 4.2: ELEMENTS OF THE MICROCT IMAGING SYSTEM. (A) THE TUNGSTEN X-RAY TRANSMISSION SOURCE. (B) USE OF A 1MM COPPER FILTER TO FILTER OUT SOFT X-RAYS AND REDUCE NOISE IN CT SCAN. (C) PICTURE OF THE INSIDE OF THE TARGET SHOWING THE FILAMENT (D) THE 2000x2000 ELEMENT DETECTOR AT THE BACK OF THE SYSTEM.	164
FIGURE 4.3: ASPECTS OF THE VG STUDIO MAX 2.0 TOMOGRAPHY VISUALIZATION SOFTWARE (A) SCREEN SHOT OF RECONSTRUCTED WEDDING CAKE SAMPLE WITH WINDOWS OF THE VARIOUS SAMPLE PERSPECTIVE VIEWS IN LEFT COLUMNS AND HISTOGRAM EDITING WINDOWS IN THE RIGHT COLUMNS (B) CLOSE UP OF HISTOGRAM EDITING WINDOWS.	164
FIGURE 4.4: (A) FRONT VIEW AND (B) ANGLED PERSPECTIVE VIEW OF THE SAMPLE L 3D VOLUME RENDERING [190].....	166
FIGURE 4.5: (A) 2D PROJECTION SLICE OF SAMPLE L SHOWING RING ARTIFACTS (B) ARROWS POINTING TO LOCATION OF A COLUMN OF #1FBH. [190].....	166
FIGURE 4.6: (A-D) DIFFERENT PERSPECTIVE VIEWS OF THE RENDERED 3D-CT 6061 AL-ALLOY WEDDING CAKE SAMPLE [190].	167
FIGURE 4.7: LACK OF X-RAY PENETRATION THROUGH LOWER LEVELS OF 8620 STEEL ALLOY WEDDING CAKE SAMPLE [190].	168
FIGURE 4.8: (A-B) PROCESS OF COLLECTING WHITE AND BLACK REFERENCE IMAGES FOR THE DUCT SEGMENT	169
FIGURE 4.9: (A) CENTER OF ROTATION SETTINGS TAB IN THE CT PRO™ MODULE (B) MAGNIFIED VIEW OF THE SETTINGS IN THE LEFT HAND PANEL OF THE MODULE THAT MUST BE SELECTED BEFORE VOLUME RECONSTRUCTION CAN PROCEED.	171
FIGURE 4.10: (A-B) REPRESENTATION OF HOW SELECTED VOLUME RENDERER INFLUENCES THE QUALITY OF A 3D RECONSTRUCTION. THE AMOUNT OF NOISE IS SIGNIFICANTLY GREATER IN (A) THAN IN (B).....	171
FIGURE 4.11: (A) NICK ON THE LEVEL 4 SURFACE OF THE ALUMINUM WEDDING CAKE (B) MAGNIFIED VIEW OF THE NICK TAKEN WITH A STEREO MICROSCOPE (C) NICK IS VISIBLE IN THE 3D-CT IMAGE AS A REGION OF SLIGHTLY LIGHTER GRAYSCALE.	172
FIGURE 4.12: SAMPLE SEGMENTATION VIA USE OF CUTAWAY PLANES AT (A) A PARTICULAR ANGLE (B-D) A PARTICULAR DEPTH. VISIBLE IN (B) AND (C) IS THE ABILITY TO TAKE MEASUREMENTS AT THE DESIRED ROI	175
FIGURE 4.13: (A-F) DIFFERENT 3D ORIENTATIONS FOR THE TURBINE BLADE WITH THE POST-WELD TIP CRACK	175
FIGURE 4.14: (A) TURBINE BLADE WITH LARGE DYNAMIC RANGE (B) TURBINE BLADE WITH LESS DYNAMIC RANGE RESULTING IN LESS IMAGE CONTRAST.....	176
FIGURE 4.15: (A) EQUIPMENT USED TO TAKE TRADITIONAL FILM X-RAYS (B) IDENTIFICATION MARKERS PLACED ON SAMPLE (C-D) FILM RADIOGRAPH IMAGES OF THE DUCT SEGMENT.....	177
FIGURE 4.16: (A-B) TRADITIONAL FILM RADIOGRAPHS OF TWO BLADES WITH WELD DROP THROUGH DEFECTS [190].....	178
FIGURE 4.17: INFLUENCE OF RADIOGRAPHIC VIEWER BRIGHTNESS ON IMAGE QUALITY	178
FIGURE 4.18: (A-B) TRADITIONAL RADIOGRAPHIC IMAGES OF TURBINE BLADE CONTAINING POST WELD TIP CRACK	178
FIGURE 4.19: (A) SELECTED 2D SLICE FROM THE 3D-CT SCAN OF THE POST WELD TIP CRACK BLADE SAMPLE AFTER ADJUSTMENT OF BRIGHTNESS, CONTRAST, EXPOSURE AND IMAGE INVERSION (B) INTERNAL CRACK ROI. NO INTERNAL CRACK IS DETECTABLE.....	179
FIGURE 4.20: (A-B) SAME IMAGE AS IN FIGURE 4.19 BUT ROTATED 3.2° DEGREES. COMPARE WITH FIG. 4.18.	179
FIGURE 4.21: BACK SIDE OF DUCT SEGMENT SHOWING (A) ORIGINAL 3D-CT INSPECTION SLICE (B) INVERTED IMAGE WITH NO BRIGHTNESS, CONTRAST, OR EXPOSURE LEVEL ADJUSTMENT (C) INVERTED IMAGE AFTER OPTIMIZATION.....	180
FIGURE 4.22: TOP SIDE OF DUCT SEGMENT SHOWING (A) ORIGINAL 3D-CT INSPECTION SLICE (B) INVERTED IMAGE WITH NO BRIGHTNESS, CONTRAST, OR EXPOSURE LEVEL ADJUSTMENT (C) INVERTED IMAGE AFTER OPTIMIZATION.....	180

FIGURE 4.23: (A-B) TRADITIONAL POINT PROBE EDDY CURRENT DETECTED THE POST WELD TIP CRACK WHEN THE MORE ADVANCED 3D-CT METHOD COULD NOT. THIS IS AN EXAMPLE OF WHEN A TRADITIONAL TECHNIQUE THAT IS BETTER SUITED TO THE PARTICULAR FLAW TYPE SHOULD BE USED INSTEAD OF AN ADVANCED TECHNIQUE.....	181
FIGURE 4.24: (A-E) RADIOGRAPHIC FILM IMAGES FOR LEVELS 1-5 OF STEEL WEDDING CAKE.....	182
FIGURE 4.25: (A-D) RADIOGRAPHIC FILM IMAGES FOR LEVELS 2-5 OF ALUMINUM WEDDING CAKE	183
FIGURE 4.26: EQUIPMENT SETUP FOR DR EXPERIMENTS	184
FIGURE 4.27: SELENIUM/PHOSPHOR MATERIAL USED IN THE IMAGING PLATE	185
FIGURE 4.28: (A) TURBINE BLADE WITH ROI CIRCLED WITH MARKER (B) DR IMAGE PRIOR TO ENHANCEMENT WITH IMAGE ANALYSIS SOFTWARE (C-E) IMAGE AFTER BRIGHTNESS AND CONTRAST LEVELS ALTERED TO ENHANCE GRAYSCALE CONTRAST IN ROI (F) IMAGE IN FIG. 4.28(E) MAGNIFIED FOR ADDITIONAL IMAGE ENHANCEMENT.....	189
FIGURE 4.29: EVOLUTION OF BLISTERS IN TURBINE BLADE FROM 2D SLICES TAKEN DURING CT INSPECTION	190
FIGURE 4.30: (A-F) ENLARGED 2D SLICES OF THE MOST RELEVANT IMAGES IN FIG. 4.29 CLEARLY SHOWING INTERNAL BLISTERS	191
FIGURE 5.1: CREATION OF PIPELINE IN CELLPROFILER.....	197
FIGURE 5.2: THRESHOLD CORRECTION FACTORS OF 0-8 APPLIED TO DR WEDDING CAKE IMAGES. ALUMINUM SAMPLE ON LEFT AND STEEL SAMPLE ON RIGHT.	203
FIGURE 5.3: CDR AND EDR PLOTTED AS A FUNCTION OF THRESHOLD CORRECTION FACTOR FOR (A) AL WEDDING CAKE AND (B) STEEL WEDDING CAKE	204
FIGURE 5.4: ORIGINAL 2D PROJECTION FROM LEVEL 5 FOR THE 3D-CT INSPECTION OF THE ALUMINUM WEDDING CAKE SAMPLE PROCESSED IN CELLPROFILER	205
FIGURE 5.5: IMAGES AFTER VARIOUS PIPELINE FILTERS WERE APPLIED.....	206
FIGURE 5.6: CLOSE-UP OF PROCESSED IMAGE	206
FIGURE 5.7: LEVEL 4 CELLPROFILER ANALYSIS OF 3D-CT SLICE.....	208
FIGURE 5.8: LEVEL 3 CELLPROFILER ANALYSIS CAN DISTINGUISH FBH IN 3D-CT SLICE.	208
FIGURE 5.9: THE SAME 2D PROJECTION IMAGE FROM THE 3D-CT INSPECTION AS IN FIG. 5.8. A THRESHOLD CORRECTION FACTOR OF 1.0 HAS BEEN APPLIED, BUT NO ADDITION PIPELINE OR FILTERS WERE SELECTED FOR THIS IMAGE. COMPARE THE RING ARTIFACTS AND GENERAL NOISE IN THIS SLICE WITH FIG 5.8.....	209
FIGURE 5.10: (A) POD CURVE FOR DATA AT SINGLE THRESHOLD CORRECTION FACTOR (B) POD CURVE FROM THREE COMBINED THRESHOLD FACTORS.....	210
FIGURE 5.11: REALISTIC VS. IDEALIZED POD CURVE.....	210
FIGURE 5.12: (A)TRADITIONAL FILM AND (B) DR IMAGES USED FOR POD ANALYSIS	213
FIGURE 5.13: 2D-DR IMAGE AFTER THE INVERSION AND FILTERING PIPELINE PROCESSES	214
FIGURE 5.14: FINAL (A) 2D-DR AND (B) TRADITIONAL IMAGES AFTER PIPELINE APPLICATION.....	215
FIGURE 5.15: USE OF COLOR SCHEME OPTION IN CELLPROFILER TO ASSIST IN HIT/MISS DETERMINATION... ..	216
FIGURE 5.16: POD CURVE FOR TRADITIONAL X-RAY FILM RADIOGRAPHY	216
FIGURE 5.17: POD CURVE GENERATED FOR DIGITAL RADIOGRAPHIC TECHNIQUE	217
FIGURE 5.18: EIGHT POSSIBLE POD VS. A MODELS OFFERED IN POD SOFTWARE.....	218
FIGURE 5.19: POD CURVE FROM FIG. 5.16 WITH CONFIDENCE BOUNDS AND STATISTICAL ANALYSIS INCLUDED	219
FIGURE 6.1: ELEMENTS OF RELIABILITY BLOCK DIAGRAMS (ADAPTED FROM [204])	224
FIGURE 6.2: BAYESIAN UPDATING OF THE RISK CALCULATION FOR A STRUCTURAL COMPONENT BASED ON INSPECTION POD AND SERVICE LIFE DATA (REPRINTED FROM [7])	232
FIGURE 6.3: (A-D) MANUAL PROCESSES INVOLVED IN AN ENGINE TEAR-DOWN INSPECTION AT AN OVERHAUL FACILITY	233
FIGURE 6.4: SPATIALLY FILTERED MWM-ARRAY SCAN IMAGES OF A CRACK PRODUCED INSIDE OF A HOLE IN A Ti-6-4 FATIGUE COUPON. THE FA43 SENSOR ARCHITECTURE WAS USED TO OBTAIN THESE IMAGES AT VARIOUS STAGES OF THE FATIGUE TEST. PHOTOMICROGRAPHS ON THE LEFT ARE FROM ACETATE REPLICAS TAKEN AFTER EACH MWM-ARRAY SCAN (REPRINTED FROM [112]).....	234
FIGURE 6.5: FRACTURE CONTROL PLAN FOR STRUCTURAL COMPONENTS IN SERVICE	237
FIGURE 6.6: RELIABILITY BLOCK DIAGRAM FOR THE CASE OF INITIAL DISK SURFACE INSPECTION.....	239
FIGURE 6.7: RELIABILITY BLOCK DIAGRAM FOR THE CASE OF INITIAL DISK NEAR SURFACE INSPECTION	239
FIGURE 6.8: RELIABILITY BLOCK DIAGRAM FOR THE CASE OF INITIAL DISK SUBSURFACE INSPECTION.....	239

FIGURE 6.9: RELIABILITY BLOCK DIAGRAM FOR 100% INITIAL COMPONENT INSPECTION OF DISK COMPONENTS.....	240
FIGURE 6.10: RELIABILITY BLOCK DIAGRAM FOR THE CASE OF CONTINUED DISK SURFACE INSPECTION	241
FIGURE 6.11: RELIABILITY BLOCK DIAGRAM FOR THE CASE OF CONTINUED DISK NEAR SURFACE INSPECTION	241
FIGURE 6.12: RELIABILITY BLOCK DIAGRAM FOR THE CASE OF CONTINUED DISK SUBSURFACE INSPECTION.....	242
FIGURE 6.13: RELIABILITY BLOCK DIAGRAM FOR THE CASE OF CONTINUED 100% DISK INSPECTION AFTER INITIAL GENERATION OF INSPECTION DATABASE.....	242
FIGURE 6.14: RELIABILITY BLOCK DIAGRAM FOR THE CASE OF INITIAL BLADE SURFACE INSPECTION.....	243
FIGURE 6.15: RELIABILITY BLOCK DIAGRAM FOR THE CASE OF INITIAL BLADE NEAR-SURFACE INSPECTION.....	243
FIGURE 6.16: RELIABILITY BLOCK DIAGRAM FOR THE CASE OF INITIAL BLADE SUB-SURFACE INSPECTION	244
FIGURE 6.17: RELIABILITY BLOCK DIAGRAM FOR THE INITIAL CASE OF 100% ZONE INSPECTION FOR BLADE COMPONENTS.....	245
FIGURE 6.18: RELIABILITY BLOCK DIAGRAM FOR THE CASE OF CONTINUED BLADE SURFACE INSPECTION AFTER SUFFICIENT INSPECTION HISTORY RESULTS ARE INCORPORATED INTO THE DIGITAL DATABASE	245
FIGURE 6.19: RELIABILITY BLOCK DIAGRAM FOR THE CASE OF CONTINUED BLADE NEAR-SURFACE INSPECTION AFTER SUFFICIENT INSPECTION HISTORY RESULTS ARE INCORPORATED INTO THE DIGITAL DATABASE	246
FIGURE 6.20: RELIABILITY BLOCK DIAGRAM FOR THE CASE OF CONTINUED BLADE SURFACE INSPECTION AFTER SUFFICIENT INSPECTION HISTORY RESULTS ARE INCORPORATED INTO THE DIGITAL DATABASE	246
FIGURE 6.21: RELIABILITY BLOCK DIAGRAM FOR THE CASE OF CONTINUED 100% BLADE COMPONENT INSPECTION AFTER SUFFICIENT INSPECTION DATA HAS BEEN INCORPORATED INTO THE DIGITAL DATABASE	247
FIGURE B.1: CROSS SECTION VIEW OF TYPICAL GAS TURBINE ENGINE (REPRINTED FROM [230])	280
FIGURE B.2: TEMPERATURE AND PRESSURE DEMANDS IN DIFFERENT ENGINE SECTIONS (REPRINTED FROM [231])	281
FIGURE B.3: TYPICAL GAS TURBINE COMPONENT MATERIALS (REPRINTED FROM [106])	282
FIGURE B.4: EXAMPLE OF THE DETERIORATION OF MECHANICAL PROPERTIES OF AN IN-SERVICE ENGINE COMPONENT DUE TO ENVIRONMENTAL ATTACK [190].....	284
FIGURE B.5: MICROSTRUCTURAL AGING OF γ' IN ALLOY IN738 AFTER 24,000 HOURS OF SERVICE (REPRINTED FROM [106]).....	285
FIGURE B.6: (A) TYPICAL TURBINE DISK DESIGN (B) DOVETAIL ATTACHMENT AT DISK RIM	286
FIGURE B.7: EVOLUTION OF TURBINE BLADE DESIGN AND GRAIN STRUCTURE (ADAPTED FROM [228])	289
FIGURE B.8: LOCATIONS OF SERVICE DAMAGE ON TURBINE BLADES (REPRINTED FROM [106])	290
FIGURE B.9: (A-B) TURBINE BLADE REMOVED FROM SERVICE EXHIBITING SERVICE DAMAGE INCLUDING FOD, TIP WEAR, OXIDATION, AND LEADING EDGE EROSION.	291
FIGURE B.10:(A)CROSS-SECTION VIEW OF THE INTERNAL MULTI-PASS COOLING CHANNELS AND (B) FILM COOLING SLOTS AND HOLES USED EXTENSIVELY IN THE DESIGN OF TURBINE BLADES (REPRINTED FROM [228])	291
FIGURE B.11: CUTAWAY SCHEMATIC OF A THERMAL BARRIER COATING (REPRINTED FROM [228])	292
FIGURE C.1: PROCESSING ROUTES FOR Ni-BASE SUPERALLOY BLADES AND DISKS (REPRINTED FROM [106])	298
FIGURE C.2:(A) FRECKLE AND WHITE SPOT DEFECTS IN IN718 (B) CHANGE IN MICROSTRUCTURE OF A POWDER-PROCESSED Ni-BASE SUPERALLOY DUE TO ELEVATED LEVELS OF REFRACTORY ALLOYING ELEMENTS (REPRINTED FROM [234]).....	300
FIGURE C.3: SURFACE CRACKING OBSERVED IN RUN-OUT SPECIMEN AFTER 1.63×10^7 CYCLES (REPRINTED FROM [292]).....	302
FIGURE C.4: (A) ALPHA CASE LAYER ON SURFACE OF Ti-6-4 AFTER HEAT TREATING (B) REMOVAL OF A SECTION OF ALPHA CASE LAYER VIA MACHINING.....	306
FIGURE C.5: (A-B) MICROGRAPHS FROM TWO DIFFERENT LOCATIONS WITHIN THE SAME Ti-6Al-4V TENSILE SPECIMEN. MICROGRAPHS IN (C-D) FROM TWO LOCATIONS IN A Ti-6Al-4V TENSILE SPECIMEN DIFFERENT FROM (A-B) SHOWING MICROSTRUCTURAL VARIATION DESPITE IDENTICAL HEAT TREATMENT. ALL MICROGRAPHS TAKEN ON OLYMPUS VANOX-T OPTICAL MICROSCOPE AT 50X	

MAGNIFICATION. SCALE BAR IN (A) APPLICABLE TO (A-D). KELLER'S REAGENT USED AS ETCHANT IN (A-D).....	308
FIGURE C.6: DEPENDENCE OF ΔK_{th} ON CRACK SIZE FOR VARIOUS STEEL ALLOYS (REPRINTED FROM [318])	313
FIGURE D.1: CALIBRATION TEST #1 FOR TRADITIONAL ULTRASONIC C-SCAN SYSTEM. (A) GATED AMPLITUDE (B) LIFT-OFF (C) GRAYSCALE PIXEL RESOLUTION FOR #1FBH.....	315
FIGURE D.2: CALIBRATION TEST #2 FOR TRADITIONAL ULTRASONIC C-SCAN SYSTEM. (A) GATED AMPLITUDE (B) FOCUSED GATED AMPLITUDE (C) GRAYSCALE PIXEL RESOLUTION FOR #1FBH.....	315
FIGURE D.3: TOP SURFACE INSPECTION OF SAMPLE R88. COLOR AMPLITUDE TEST DATA. (A) FULL RANGE (B) MANUALLY OPTIMIZED LIMITED RANGE (C) FBH-ARRAY ROI AT MANUALLY OPTIMIZED LIMITED RANGE	316
FIGURE D.4: TOP SURFACE INSPECTION OF SAMPLE R88. GRAYSCALE AMPLITUDE TEST DATA. (A) FULL RANGE (B) MANUALLY OPTIMIZED LIMITED RANGE (C) FBH-ARRAY ROI AT MANUALLY OPTIMIZED LIMITED RANGE.....	317
FIGURE D.5: TOP SURFACE INSPECTION OF SAMPLE R88. COLOR TIME OF FLIGHT TEST DATA. (A) FULL RANGE (B) MANUALLY OPTIMIZED LIMITED RANGE (C) FBH-ARRAY ROI AT MANUALLY OPTIMIZED LIMITED RANGE.....	318
FIGURE D.6: TOP SURFACE INSPECTION OF SAMPLE R88. GRAYSCALE TOF TEST DATA. (A) FULL RANGE (B) MANUALLY OPTIMIZED LIMITED RANGE (C) FBH-ARRAY ROI AT MANUALLY OPTIMIZED LIMITED RANGE	319
FIGURE D.7: BACK SURFACE INSPECTION OF SAMPLE R88. COLOR AMPLITUDE TEST DATA. (A) FULL RANGE (B) MANUALLY OPTIMIZED LIMITED RANGE	320
FIGURE D.8: BACK SURFACE INSPECTION OF SAMPLE R88. GRAYSCALE AMPLITUDE TEST DATA. (A) FULL RANGE (B) MANUALLY OPTIMIZED LIMITED RANGE.....	321
FIGURE D.9: BACK SURFACE INSPECTION OF SAMPLE R88. TOF TEST DATA. (A) MANUALLY OPTIMIZED LIMITED RANGE IN COLOR (B) MANUALLY OPTIMIZED LIMITED RANGE IN GRAYSCALE	322
FIGURE D.10: TOP SURFACE INSPECTION OF SAMPLE H. COLOR AMPLITUDE TEST DATA. (A) FULL RANGE (B) MANUALLY OPTIMIZED LIMITED RANGE (C) FBH-ARRAY ROI AT MANUALLY OPTIMIZED LIMITED RANGE	323
FIGURE D.11: TOP SURFACE INSPECTION OF SAMPLE H. GRAYSCALE AMPLITUDE TEST DATA. (A) FULL RANGE (B) MANUALLY OPTIMIZED LIMITED RANGE (C) FBH-ARRAY ROI AT MANUALLY OPTIMIZED LIMITED RANGE.....	324
FIGURE D.12: TOP SURFACE INSPECTION OF SAMPLE H. COLOR TOF TEST DATA. (A) FULL RANGE (B) MANUALLY OPTIMIZED LIMITED RANGE (C) FBH-ARRAY ROI AT MANUALLY OPTIMIZED LIMITED RANGE	325
FIGURE D.13: TOP SURFACE INSPECTION OF SAMPLE H. GRAYSCALE TOF TEST DATA. (A) FULL RANGE (B) MANUALLY OPTIMIZED LIMITED RANGE (C) FBH-ARRAY ROI AT MANUALLY OPTIMIZED LIMITED RANGE	326
FIGURE D.14: TOP SURFACE INSPECTION OF SAMPLE U. COLOR AMPLITUDE TEST DATA. (A) FULL RANGE (B) MANUALLY OPTIMIZED LIMITED RANGE (C) FBH-ARRAY ROI AT MANUALLY OPTIMIZED LIMITED RANGE	327
FIGURE D.15: TOP SURFACE INSPECTION OF SAMPLE U. GRAYSCALE AMPLITUDE TEST DATA. (A) FULL RANGE (B) MANUALLY OPTIMIZED LIMITED RANGE (C) FBH-ARRAY ROI AT MANUALLY OPTIMIZED LIMITED RANGE.....	328
FIGURE D.16: TOP SURFACE INSPECTION OF SAMPLE U. COLOR TOF TEST DATA. (A) FULL RANGE (B) MANUALLY OPTIMIZED LIMITED RANGE (C) FBH-ARRAY ROI AT MANUALLY OPTIMIZED LIMITED RANGE	329
FIGURE D.17: TOP SURFACE INSPECTION OF SAMPLE U. GRAYSCALE TOF TEST DATA. (A) FULL RANGE (B) MANUALLY OPTIMIZED LIMITED RANGE (C) FBH-ARRAY ROI AT MANUALLY OPTIMIZED LIMITED RANGE	330
FIGURE D.18: TOP SURFACE INSPECTION OF SAMPLE M. AMPLITUDE TEST DATA. (A) COLOR FULL RANGE (B) COLOR MANUALLY OPTIMIZED LIMITED RANGE (C) GRAYSCALE FULL RANGE (D) GRAYSCALE MANUALLY OPTIMIZED LIMITED RANGE.....	331
FIGURE D.19: TOP SURFACE INSPECTION OF SAMPLE M. TIME OF FLIGHT TEST DATA. (A) COLOR FULL RANGE (B) COLOR MANUALLY OPTIMIZED LIMITED RANGE (C) GRAYSCALE FULL RANGE (D) GRAYSCALE MANUALLY OPTIMIZED LIMITED RANGE.....	332
FIGURE E.1: IMAGE #1 FROM TABLE 4.2	333

FIGURE E.2: IMAGE #2 FROM TABLE 4.2	333
FIGURE E.3: IMAGE #3 FROM TABLE 4.2	333
FIGURE E.4: IMAGE #4 FROM TABLE 4.2	334
FIGURE E.5: IMAGE #5 FROM TABLE 4.2	334
FIGURE E.6: IMAGE #6 FROM TABLE 4.2	334
FIGURE E.7: IMAGE #7 FROM TABLE 4.2	335
FIGURE E.8: IMAGE #8 FROM TABLE 4.2	335
FIGURE E.9: IMAGE #9 FROM TABLE 4.2	335
FIGURE E.10: IMAGE #10 FROM TABLE 4.2	336
FIGURE E.11: IMAGE #11 FROM TABLE 4.2	336

List of Tables

TABLE 1.1: SIGNIFICANT VARIABLES THAT NDT RELIABILITY AND POD ARE DEPENDANT ON	22
TABLE 1.2: NDT METHODS APPLICABLE FOR FLAW DETECTION ON AEROSPACE COMPONENTS	25
TABLE 1.3: FACTORS THAT AFFECT THE SENSITIVITY LEVEL OF A FLUORESCENT PENETRANT INSPECTION ...	28
TABLE 1.4: THE PRINCIPAL OPERATING VARIABLES ENCOUNTERED IN ECI.....	33
TABLE 1.5: ELECTRICAL RESISTIVITY AND CONDUCTIVITY OF COMMON METALS AND ALLOYS	36
TABLE 1.6: THE ACOUSTIC PROPERTIES OF SELECTED MATERIALS	42
TABLE 1.7: EMBEDDED DEFECT TARGET DEPTHS AND SIZES EXAMINED UNDER THE TESI PROGRAM (REPRINTED FROM [97] COURTESY OF V. KRAMB, UNIV. OF DAYTON RESEARCH INSTITUTE).....	57
TABLE 1.8: OPTIONS ALLOWED BY THE FAA TO SATISFY DTR VALUES IN THE EVENT OF AN OFF-DESIGN CONDITION.....	88
TABLE 2.1: SELECTED PHYSICAL PROPERTY DATA FOR THE 6061-T6 ALUMINUM AND 8620 STEEL ALLOYS .	95
TABLE 2.2: HOLE MEASUREMENTS IN SI UNITS FOR THE ALUMINUM ALLOY WEDDING CAKE SAMPLE	99
TABLE 2.3: HOLE MEASUREMENTS IN US CUSTOMARY UNITS FOR THE AL-ALLOY WEDDING CAKE SAMPLE	100
TABLE 3.1: TESI INSPECTION RESULTS ON STEEL WEDDING CAKE SAMPLE	147
TABLE 3.2: TESI INSPECTION RESULTS ON 6061 AL-ALLOY WEDDING CAKE SAMPLE.....	148
TABLE 4.1: PARAMETERS FOR THE X-RAY FILM IMAGES TAKEN OF ALUMINUM WEDDING CAKE	182
TABLE 4.2: PARAMETERS AND A DESCRIPTION OF THE DR IMAGES TAKEN AT BAKER TESTING.....	184
TABLE 4.3: COMPARISON OF THE SUITABILITY OF TRADITIONAL X-RAY FILM RADIOGRAPHY AND DIGITAL RADIOGRAPHY FOR NUMEROUS LIGHT METAL AND HEAVY METAL STRUCTURAL COMPONENT INSPECTION APPLICATIONS DURING THE COMPONENT’S LIFE-CYCLE (ADAPTED FROM [27]).....	186
TABLE 4.4: COMPARISON OF ULTRASONIC, RADIOGRAPHIC, AND X-RAY CT TECHNIQUES (ADAPTED FROM [199])	188
TABLE 4.5: COMPARISON OF PERFORMANCE CHARACTERISTICS FOR TRADITIONAL FILM RADIOGRAPHY, REAL-TIME RADIOGRAPHY, AND 3D-COMPUTED TOMOGRAPHY (ADAPTED FROM [199])	193
TABLE 5.1: PIPELINE SELECTED FOR THE WEDDING CAKE SAMPLES	198
TABLE 6.1: RELEVANT PROBABILITIES TO STATISTICAL ANALYSIS	221
TABLE 6.2: NOMENCLATURE USED IN STATISTICAL ANALYSIS (ADAPTED FROM [203]).....	223
TABLE 6.3: AVERAGE COSTS ASSOCIATED WITH IN-SERVICE MAINTENANCE OR AIRCRAFT	248
TABLE 6.4: COSTS ASSOCIATED WITH CATASTROPHIC AIRCRAFT FAILURE OF THE RELEVANT DATA SET FOR TIME PERIOD 1989-2009	251
TABLE 6.5: RELEVANT STANDARDS RECENTLY ISSUED FOR THE ADVANCED NDT TECHNIQUES OF THE PROPOSED METHODOLOGY.....	262
TABLE B.1: COMPARISON OF COMMERCIAL GAS TURBINE ENGINE EFFICIENCIES AT TAKEOFF AND CRUISE FLIGHT CONDITIONS (ADAPTED FROM [179])	283
TABLE C.1: CHEMICAL COMPOSITION (IN WT. %) OF SOME COMMERCIALY AVAILABLE DISK COMPONENT ALLOYS.....	299
TABLE C.2: CHEMICAL COMPOSITION (IN WT. %) OF SOME COMMERCIALY AVAILABLE BLADE COMPONENT ALLOYS.....	299
TABLE C.3: RECOMMENDED HEAT TREATMENTS FOR Ti-6-4 AND Ti-17	305
TABLE C.4: DETERMINISTIC MATERIAL VALUES USED AS INPUTS IN MICROSTRUCTURAL BASED FCI AND FCG MODELS (ADAPTED FROM [178])	310

Chapter 1: Introduction

Aircraft gas turbine engines are complex structural systems that demand high performance and high reliability. The life-limited, fracture-critical components in turbine engines utilize a range of the most advanced structural materials. In particular, disks and blades are two such components that are required to operate at elevated temperatures in aggressive environments, and over extended periods of time. The manufacture of these complex components necessitates knowledge of the inter-relationship between the various processes required to achieve a finished component. These processes have a considerable impact on component failure modes, structural capability, strength, and component life. Undetected flaws due to manufacturing anomalies have been found to deteriorate mechanical properties, reduce service life, and in some instances result in catastrophic failure. In addition, degradation of a component's mechanical properties naturally occurs during operational life as a result of thermo-mechanical fatigue and the cyclic stresses that can be withstood. The dynamic mixed-mode interaction of the many structural, processing, environmental and operational variables makes remnant life prediction of critical aerospace components a challenging task.

In the aviation industry manufacturing and operational risks, from a local component perspective up to a global systems view of the aircraft, are controlled by specifying the minimum acceptable standards required for flight through both national and international regulations. The Federal Aviation Administration (FAA) is the agency responsible for setting these airworthiness standards in the US. A complete list of the acronyms and nomenclature referenced in this thesis can be found in Appendix A. The current methodology specified by the FAA for engine life-limited parts (LLPs) is based on a probabilistic “safe-life” [1-14] approach, where components are retired from service when they reach an established life limit. This life is generally defined as the point in time when the probability of developing a fatigue crack or another flaw typically of 0.030”x0.015” (0.8mm x 0.4mm) in size reaches 0.001 [2, 6, 7, 9, 10, 14, 15]. This low cycle fatigue (LCF) based approach necessitates discarding 1000 components to ensure the removal of the single part that is theoretically predicted to have developed a crack of specified size. The “safe-life” methodology mandates retirement at a specified lifetime

regardless of the potential life that may still remain for a majority of components. For high value LLPs such as disks there are serious deficiencies with the safe-life methodology from a cost-benefit perspective.

Recently, the “damage-tolerance” [3, 7, 8, 16-19] element of life management for aircraft engines has been incorporated into the safe-life methodology. Damage tolerance addresses the potential existence of component imperfections resulting from inherent material structure, material processing, design, manufacturing, or usage via the implementation of fracture mechanics analyses and nondestructive inspection. While the inclusion of damage tolerance to the safe-life methodology has resulted in an enhanced life management process, shortcomings remain and the current methodology is particularly lacking with respect to the treatment of aging aircraft. Credit is not given for surface treatments, such as shot peening, that impart compressive residual stresses, and a distinction is not addressed between fatigue crack growth rates (FCGR) and creep crack growth rates (CCGR) in the short crack and long crack regimes. In addition, the conventional life management methodology relies on the use of empirical constants based on deterministic assumptions in the fracture mechanics analyses. Lastly, the use of antiquated nondestructive testing (NDT) techniques is currently the industrial standard. Each of these factors adds a level of uncertainty to remnant life prediction on a part-specific basis.

Prior to service, critical engine components are inspected during manufacture for voids and inclusions in the billet or forging state. However, when the FAA decides to extend the life of engine components that have already been in service for an extended period of time, a need to find smaller defects than were originally screened for in the manufacturing process exists [20]. This has created a need for in-service inspection protocols. Two major challenges associated with operating aging aircraft are maintaining structural reliability standards throughout the extended operational life, while minimizing maintenance costs [21]. The fracture critical locations of an assembled engine are often the most difficult to nondestructively inspect [21-23], however it is specifically these highly loaded and difficult to access components that may benefit from an improved inspection and monitoring approach relying on advanced NDT technologies. A significant source of scatter with current life methodologies lies in the uncertainty

associated with the equivalent initial flaw size distribution that is used as an input for FCGR and CCGR models [23]. Uncertainty from three primary sources seriously hinders effective life management of aerospace engine parts. These sources of uncertainty are the variability and unknowns in the engine history (i.e. deviations from the specified mission profile), inaccuracy in the models that predict material damage and lifetime, and variability in material behavior from feature to feature and component to component [15]. The influence of these sources of uncertainty can result in a 6X variability in fatigue life and 10X-100X variability in probability of failure (POF) at a given life [22] for critical engine components. The ability to reliably detect smaller flaws than are currently capable with mature NDT technologies can potentially mitigate these sources of uncertainty if accumulated damage and flaw growth can be sensitively tracked throughout component life.

The objective of this thesis is to provide a rigorous methodology based on the redundant application of progressive NDT techniques to extend remnant life of structural components. Inspection of critical engine components in aging aircraft is the primary application analyzed; however this study applies to other structural components as well. Appendix B and Appendix C provide an analysis into design, processing, and mechanical property aspects of the Nickel-base superalloys and Titanium alloys that comprise the blades and disks of critical engine components. For the reader who is not familiar with the aerodynamic and material constraints involved in turbine engine design, these appendices should be read. The remainder of this chapter contains a discussion of the scientific theories behind NDT techniques that are currently the standard for the aerospace industry. The flaw detection limitations of these mature techniques are reviewed and compared to the advanced NDT processes of the proposed life methodology. An analysis into the history of airplane engine inspection methodology concludes the first chapter. Chapters 2 through 4 detail the results of sensitivity analyses of the Meandering Winding Magnetometer array (MWM-array ®) eddy current, phased array ultrasonic (PA-UT), and 3D X-ray computed tomography (3D CT) techniques that are the basis of the proposed methodology. A comparison of these three processes with their traditional counterparts is included in each chapter. Chapter 5 delves into the use of image analysis and probability of detection (POD) software to improve repeatability,

increase confidence, and quantify the benefit of redundancy. Chapter 6 provides an in-depth analysis of the recommended NDT methodology, details the statistical approach for monitoring aging aircraft, and comments on obstacles to implementing the methodology. Chapter 6 also contains a cost-benefit analysis that is inclusive of both direct equipment cost comparisons as well as peripheral benefits of the advanced NDT processes that are difficult to quantify with a monetary value.

The scope of this thesis is limited to critical engine components in domestic civilian commercial aircraft. While much of the advanced NDT technology is transferable to military aircraft, the differences in mission profile and quantification of cost to benefit ratio between military and commercial aircraft is significant. Regulatory discrepancies between the FAA and international agencies such as the EASA preclude an extension of the proposed lifing methodology to foreign aircraft. Manufacturing processes that occur prior to finished component certification, such as forging, billet conversion, and heat treatment will not be individually accounted for within the proposed methodology. These operations do indeed have a significant effect on a part's structural capability and are discussed in Appendix B and Appendix C. However, the lifing analysis in Chapter 6 uses the generic 0.030"x0.015" (0.8mm x 0.4mm) flaw size specified by the FAA as the basis for comparison with the progressive NDT approach to life management, rather than comparing particular anomalies that result during component fabrication or repair. It will be assumed that the baseline NDT scan, performed with the aforementioned cutting-edge techniques prior to the structural components' service life introduction, will detect any anomalies larger than the threshold flaw size. It is hypothesized that implementation of a systems approach to nondestructive inspection that incorporates redundancy and state-of-the-art techniques can significantly enhance the life management methodology currently endorsed by the FAA, and provide considerable cost savings for aging aircraft engine components despite the increased capital equipment costs.

1.1 NDT/NDE Processes

Nondestructive testing (NDT) is also often referred to as nondestructive evaluation (NDE) or nondestructive inspection (NDI). Regardless of the nomenclature used, NDT is a vital element of risk analysis and life prediction for critical airplane

engine components. Nondestructive inspection is used as a primary foundation for assuring structural integrity and fitness for service during maintenance and overhaul operations [24-26]. The metric used to quantify the capability of a particular nondestructive technique to detect flaws is known as the probability of detection (POD) [26-31]. The concept of POD was introduced in the 1970's as a necessary input for fracture mechanics models [32-35], and statistical methods were incorporated into the POD methodology to provide confidence bounds on the POD quantification [25-27]. It should be mentioned that in ensuring structural integrity, knowledge of the smallest flaw ever detected is of little use. Rather, it is the largest flaw that might be missed by the NDT procedure that is of primary interest [24, 25, 27, 29, 36], because that flaw size then becomes the starting point for fracture mechanics analyses and for crack growth models in remnant fatigue life predictions. As Rummel [25] indicated, it is clearly desirable to start with a very small flaw size.

The reliability of an NDT/NDE procedure is defined as a quantitative measure of the efficiency of that procedure in finding flaws of specific type and size. In the initial stages of using the damage tolerance approach in the 1970's, a one-number characterization of NDE capability was in use. The number is referred to as the 90/95 (POD/CL) crack length, and signifies the minimum crack length at the 95% confidence level (CL) from which at least 90% of all cracks greater than this length will be detected [2, 14, 27, 29, 31]. Inspection reliability is based on not only the capability to detect a given flaw size, but also the reproducibility and repeatability of the NDT process. Another way of saying this is inspection reliability is based not solely on POD, but also on the calibration and process control of the NDT system [25, 26]. The CL quantifies only statistical uncertainty due to limited data, and does not quantify model uncertainty nor process variability [31, 37]. Table 1.1 lists some of the variables that NDT reliability and POD are dependent on.

The variables in Table 1.1 all yield an inherent level of uncertainty to the inspection process, meaning that repeat inspections on the same flaw will not necessarily produce consistent hit or miss indications, and different flaws of the same size may have different detection capabilities. As a result of this uncertainty, efficacy of an NDT

Table 1.1: Significant variables that NDT reliability and POD are dependant on

• Flaw (Artifact) Variables
• Test Object Variables
• NDT Method Variables
• NDT Materials Variables
• NDT Equipment Variables
• NDT Procedure Variables
• NDT Process Variables
• Calibration Variables
• Acceptance Criteria / Decision Variables
• Human Factors

process is characterized by the POD as a function of a , the flaw size [27]. The $POD(a)$ function can be determined statistically through hit/miss data, or from signal response data in the form of an “ a vs. \hat{a} ” indication, where \hat{a} (pronounced a-hat) is a parameter of the inspection equipment or system that can be correlated with flaw size. The $POD(a)$ function is defined slightly differently for the two types of data, and Equations (1.1) and (1.2) highlight the subtleties between them.

$$POD(a) = \int_0^1 pf_a(p) dp \quad \text{[from hit/miss data]} \quad (1.1)$$

$$POD(a) = \int_{\hat{a}_{dec}}^{\infty} g_a(\hat{a}) d\hat{a} \quad \text{[from signal response data]} \quad (1.2)$$

where in (1.1) p is the distinct crack detection probability for each crack of size a , $f_a(p)$ is the probability density function of the detection probabilities, $pf_a(p) dp$ is the conditional probability of a randomly selected crack from the population that has a detection probability of p being detected at inspection, and the summation of the conditional probabilities from 0 to 1 represents the unconditional probability. In (1.2) $g_a(\hat{a})$ represents the probability density of the \hat{a} values for a fixed crack size a , \hat{a} is a parameter that is correlated with flaw size, and the integral is summed over all signal responses from some pre-defined decision threshold \hat{a}_{dec} to infinity.

Equation (1.1) implies that the $POD(a)$ function is the curve through the averages of the individual density functions of the detection probabilities. This curve is the regression equation and forms the basis for testing assumptions about the applicability of various POD models [27]. The log odds model is commonly used in the analysis of the

binary hit/miss data. Equation (1.2) is often modeled as a cumulative log normal distribution function, and methods for estimating maximum likelihood parameters from a vs. \hat{a} data typically involve assumptions about the flaw size distribution [23, 27, 38, 39]. As the above equations show, the $POD(a)$ function is akin to a cumulative distribution function (CDF) of a_{th} , where a_{th} is the recording signal threshold flaw size below which the signal and noise from the NDT system are indistinguishable [29, 40]. The assumptions made about the distribution of the $POD(a)$ function can have a significant influence on minimum detectable flaw size. The POD model discussed in Chapter 5 will highlight factors that affect model robustness.

The 90/95 POD/CL value is normally only used with NDT techniques to qualify surface flaw detection capability, but surface flaws are not the only relevant category of flaws for critical aerospace parts. The three specimen location categories of nondestructive inspection include surface, near surface, and subsurface (or embedded) [41]. An NDE reliability experiment consists of a test matrix of inspections on a set of specimens with known flaw locations and sizes. In an industrial setting, the specimens should be inspected under conditions meant to simulate actual service conditions as close as possible [27, 29, 40]. This typically involves experiments in a test cell, similar to Figure 1.1, where a number of strain gages and sensors are mounted onto an engine that gets revved up to operating speed during testing. The experimental design determines the test matrix, and the following four analysis concerns must be addressed: 1) the method of controlling the factors to be evaluated in the experiment, 2) the method of accounting for the uncontrolled factors in the experiment, 3) the sizes of the specimen flaws, and 4) the number of flawed and unflawed inspection sites [27]. Governmental guidelines for performing a statistically significant POD analysis are contained in Appendices F and G of MIL-HDBK-1823 [29]. The cost to perform a single test cell run is typically in the range of \$500,000 [42, 43], which was not feasible for the laboratory scale experiments performed on this project. Collaboration with the FAA and industry would be required to defray the substantial costs of testing specimens in a simulated service environment.



Figure 1.1: Industrial test cell used to simulate actual turbine engine service operating conditions

The remainder of this section will discuss the NDT processes that are currently the industrial standard for the aerospace industry. The terminology “traditional” will be used to describe these techniques, which include visual inspection (VI), fluorescent penetrant inspection (FPI), magnetic particle inspection (MPI), eddy current inspection (ECI), radiographic (X-ray) inspection, and finally ultrasonic inspection (UTI). The limitations of these traditional NDT processes will be explored in terms of the sensitivity and sources of variability inherent to each technique. The detection problems posed by embedded defects, the subjectivity and variance associated with human interpretation of NDT output, and finally prior catastrophic failures resulting from these limitations are also reviewed in this chapter. The review of these topics will serve as a comparative foundation to the three NDT processes of the proposed methodology. These three processes are dubbed “advanced” and include MWM-array® eddy current inspection, phased array ultrasonic inspection (PA-UT), and three dimensional computed tomography (3D-CT), which is a technique that incorporates digital radiography (DR). An additional section is included that focuses on imaging analysis and process automation techniques that have the potential to vastly improve repeatability and eliminate sources of process uncertainty.

1.2 A Discussion of “Traditional” NDT Processes Applicable to Aerospace Applications

The selection of a useful NDE method or combination of methods first requires a clear understanding of the problem to be solved. Appendix B and Appendix C provide an in depth summary of the complicated situation. Airplane engines are complex systems requiring the interaction of numerous moving parts in a precise yet constrained manner. Disks and blades comprise two of the more demanding components in this system, and numerous processing and manufacturing steps are required in the fabrication of these high-value parts. The complexities of the manufacturing process as well as the dynamic deformation mechanisms experienced during service expose the potential introduction of flaws. Extension of service life and prevention of catastrophic failure for these structural members is the problem to be solved. The unique characteristics of these components, including, but not limited to shape, size, and failure critical location preclude the use of a sole NDT technique to provide 100% inspection. Flaw detection is usually considered the most important aspect of NDE [27]. Flaws may be classified as volumetric or planar, and the location of these flaws is further classified as surface, near-surface, or interior. Volumetric flaws are three dimensional in nature, and can be of varied size as well as randomly oriented. Examples of volumetric flaws include porosity, voids, and inclusions. Planar flaws are thin in one dimension but larger in the other two dimensions, and examples include cracks and lack of penetration (LOP) defects. Table 1.2 lists the flaw types detectable by the six traditional NDT techniques mentioned in the previous paragraph. These six techniques, VI, FPI, MPI, ECI, X-ray, and UTI make up the most relevant nondestructive processes applicable to inspection of aerospace engine components. The science behind each technique as well as generic benefits and limitations are discussed next.

Table 1.2: NDT methods applicable for flaw detection on aerospace components

NDT Method	Flaw Classification			
	<u>Volumetric</u>	<u>Planar</u>	<u>Surface</u>	<u>Interior</u>
VI	X(surface only)	X	X	
FPI/LPI	X(surface only)		X	
MPI	X	X	X	X (near surface only)
ECI	X	X	X	X (near surface only)
X-ray	X			X
UTI	X	X	X	X

1.2.1 Visual Inspection

Visual inspection is typically a first line of defense in the inspection process for aerospace components. As shown in Table 1.2, visual inspection is only capable of detecting surface flaws. A variety of potential surface imperfections including corrosion, contamination, improper surface finish, and improper or incomplete welds/joints can be detected with VI from a trained and accredited inspector [27, 44, 45]. Direct visual inspection is by far the most common NDT technique, because it is the cheapest and quickest method for assessing the general condition of a specimen [44-46]. Size of a system or component under inspection is not an issue with VI, and almost any specimen regardless of geometrical complexity can be visually examined to determine the accuracy of its fabrication [45, 47, 48]. Visual inspection by the unassisted eye can determine little detail about the damage mechanism or severity [21]. Additionally, the sensitivity of flaw detection is limited to flaws around 6mm (0.25 inch) [44, 45]. Inspector variability and subjectivity in flaw detection is also a source of problems and a limitation to this technique. In one study, results showed the “human error” associated with individual inspector variability to be significant, with the 90% POD crack length ranging from 4.1-9.1mm (0.16-0.36 in.) [45]. Inspector level of training, as well as fatigue can affect both correct detection capability as well as the level of false positive indications. Visual inspection is ranked very low in terms of operator independence, capability for automation, data capture capability, and ease of quantification for NDE of cracks, geometric anomalies, and holes of varying length to diameter (L/D) aspect ratio [36]. Typically, VI is used in conjunction with a more sensitive technique such as ECI when critical components are inspected.

In addition to direct visual inspection with the unaided eye, aided visual inspection also falls under the category of VI. The use of equipment, ranging from a simple magnifying glass to a borescope, is often specified in the inspection of airplane components. A borescope is a long, tubular optical device that can be rigid or flexible, and allows the inspection of hard to reach areas, such as disks and blades in an assembled engine, to be performed [27]. Figure 1.2 is an image from a borescope inspection that revealed damage to HPT section blades. Aided visual inspection is also heavily



Figure 1.2: Image from a borescope inspection revealing blade damage

dependent on inspector capability. The cost of equipment used in aided VI can range from very low to modest, but both direct and aided visual inspection can be labor intensive. Labor costs associated with inspections that take a long time are an important factor in selecting an NDT method, and one reason automated NDT processes may be worthwhile despite increased capital equipment cost.

1.2.2 FPI/LPI

Fluorescent penetrant inspection (FPI) is also commonly referred to as liquid penetrant inspection; however the two techniques slightly differ. FPI utilizes penetrants that are usually green in color that fluoresce distinctly under UV light, while LPI employs penetrants that are usually red in color and produce vivid red indications under visible light [27]. For the purpose of this paper the terms FPI and LPI will be used interchangeably to describe an inspection process that involves the application of a penetrant that renders indications from cracks and other surface imperfections under a specified light source. The major limitation of FPI is that it is only applicable to surface cracks and is not appropriate for the detection of internal flaws. Penetrants are classified in terms of sensitivity levels ranging from *ultralow* (Level ½) to *ultrahigh* (Level 4) [27, 44]. The required degree of inspection sensitivity is a key element of the FPI inspection process, because many factors affect the sensitivity of the technique. Table 1.3 lists some factors that affect the sensitivity of FPI. The finest cracks capable of being detected by FPI have been estimated to be about $5\mu\text{m}$ ($0.2 \times 10^{-3}\text{in.}$) wide by $10\mu\text{m}$ ($0.4 \times 10^{-3}\text{in.}$) deep, however these numbers were based on inspections of cracks in flat samples and the

Table 1.3: Factors that affect the sensitivity level of a fluorescent penetrant inspection

• Wetting of the sample surface by the penetrant
• Crack geometry; including width, depth, aspect ratio, and length
• Cleanliness of crack and specimen surface preparation
• Time available for inspection
• Skill level of inspector
• Method of observation, visibility and contrast of indication
• Quality and condition of penetrant materials in industrial setting
• Effects of UV light, heat, water, and particulate contamination

overall POD for this crack size is much less than 90% [44]. As previously stated, it is the largest flaw that can be missed by a technique and not the smallest ever detected that is of greatest significance to POD measurements.

The scientific principle that forms the basis of FPI is surface wetting via capillary action. Young's equation, described by Equation (1.3), can be used to relate the contact

$$\gamma_{SG} = \gamma_{SL} + \gamma_{LG} \cos \theta \quad (1.3)$$

angle θ to the surface energies of the solid (S), liquid (L), and gas (G) phases. Figure 1.3 schematically shows the penetration of a liquid into a surface crack. The depth, d , that a liquid penetrates into a crack depends on the balance between the capillary forces and the weight of the liquid [27, 44] such that:

$$d = \frac{2\gamma_{LV} \cos \theta}{rg \rho} \quad (1.4)$$

where r is the crack radius, g is the acceleration due to gravity and ρ is the density of the liquid. The depth the liquid penetrates into a crack requires a contact angle of less than 90° , increases as the crack width increases, and does not depend on the viscosity of the liquid [44]. The viscosity does however affect the time it takes for the liquid to penetrate the crack, therefore adequate dwell time is required for the detection of very fine cracks.

There are both advantages and disadvantages to fluorescent penetrant inspection. Advantages of LPI include its applicability to virtually any sized part as well as complexly shaped parts. FPI is relatively inexpensive and can be applied to a wide range of materials including metals, plastics, and ceramics. Porous materials and some thermally sprayed coatings are notable exceptions [36]. Limitations of the technique include the high dependence on inspector quality. As Table 1.3 shows, human error in

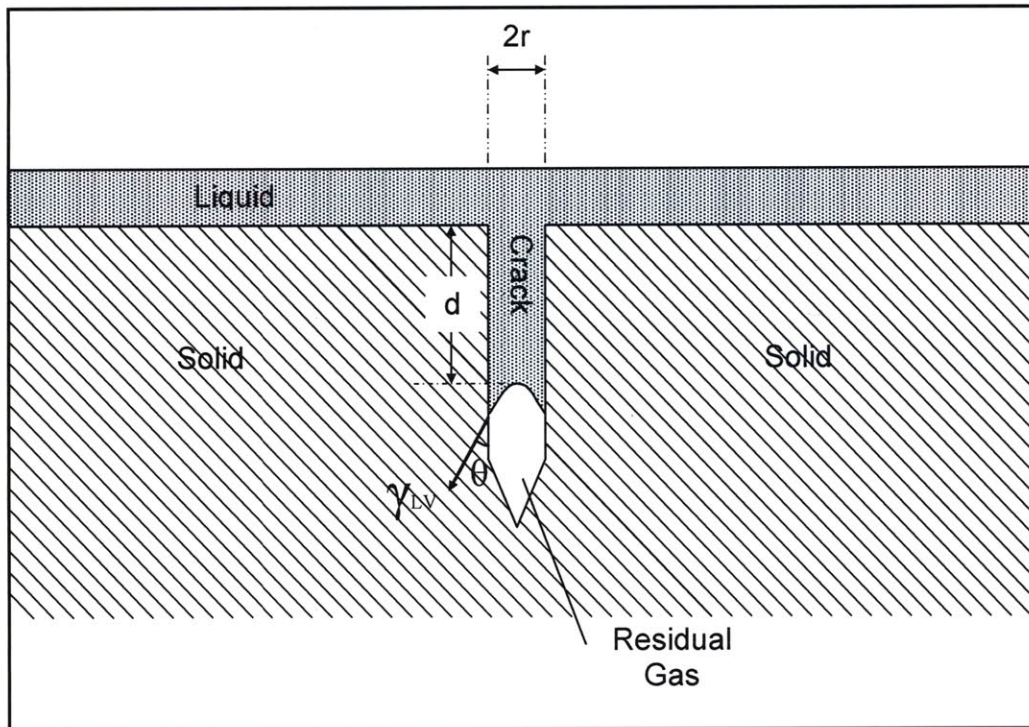


Figure 1.3: Schematic showing liquid penetrant into a surface crack via capillary action (adapted from [44])

the sample preparation or method of observation are the major factors that cause inspection variability. These human factors can lead to false positive indications or missed detections, both of which reduce POD, especially if process parameters like surface condition and cleanliness are not closely controlled [29, 36, 44]. The equipment requirements for FPI are significant in terms of space, and Figure 1.4(a-b) represents this extensive equipment arrangement in an aerospace facility. The equipment consists of multiple stations (or sub-units) including cleaning, pre- and post-wash, dwell, drying, developer, and inspection stations. These stations are shown in Figure 1.4(a), while Figure 1.4(b) shows a close-up of a dry-developer station. FPI is not a very fast process, and about 20 minutes is needed at the dwell station alone for the liquid penetrant to adsorb into the surface before the test can be run [27, 44]. FPI can be automated but for most applications is still performed manually. Finally, data generated from a fluorescent penetrant inspection generally consists of only qualitative observations by the inspector. This data is not necessarily retained after the inspection, and if observations are retained they are usually on paper with a limited shelf life [29, 36]. This poor record retention policy and lack of data preservation in a digital format limits the effectiveness

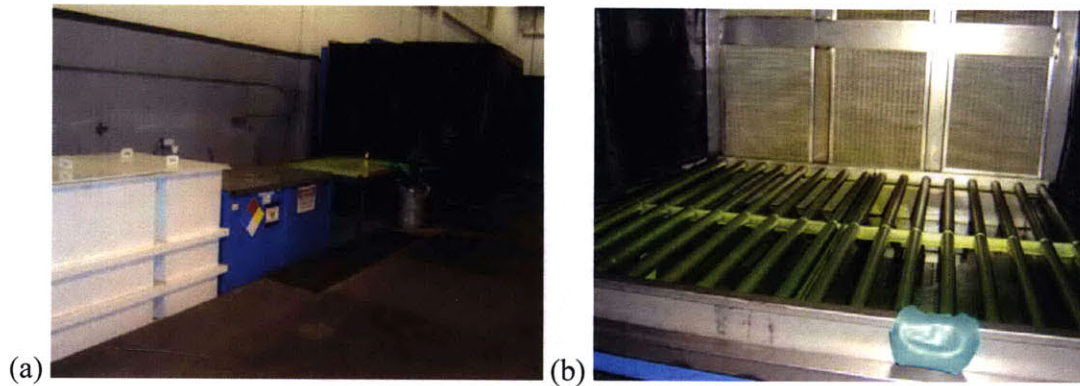


Figure 1.4: (a) Various stations required for FPI (b) Dry-developer bin with dust control and liquid reclamation system

of FPI inspection results via subsequent comparison to prior service inspections over a component's service life.

1.2.3 Magnetic Particle Inspection

Magnetic particle inspection (MPI) is a very mature NDT technique. As early as 1868, Saxby used a magnetic compass to locate inhomogeneities in iron gun barrels [44]. The basis of MPI is that when a component under test is magnetized, magnetic discontinuities that lie in a direction generally transverse to the direction of the magnetic field will cause a leakage field to form at and above the surface of the part [27]. When fine ferromagnetic particles are applied to the surface of the part, they will align over the source of the leakage field where the flaw exists. The use of iron particles to locate defects in magnetized components was originally observed in 1917 by Hoke in the US and others in the UK, who noticed that the iron grindings from machined steel parts formed patterns around surface cracks while being held in a magnetic chuck [44]. Advantages of the MPI technique include the ability to detect both surface and near-surface anomalies. Sensitivity to defect detection varies from 6.3-0.25 mm (0.25-0.01 in.) below the sample surface based on the choice of magnetic powder and type of magnetization (ac or dc current) [44]. Techniques can be developed for nearly all part geometries and sizes, and MPI is relatively inexpensive when compared to alternatives [27, 36]. As with VI and FPI, MPI is highly inspector dependent and line of sight limited. Surface preparation is very critical to inspection reliability, as the component surface must be free of grease and dust to permit free movement of the magnetic particles [27, 44]. Part geometry can severely negate the effectiveness of the inspection by making

certain areas difficult to view. The orientation of the flaw with respect to the magnetic field has a significant effect on MPI sensitivity, and a further inconvenience is that demagnetization of the component may be needed after testing [27, 36, 44]. As it pertains to this research the most significant limitation of magnetic particle inspection is that parts inspected must be ferromagnetic, making MPI not applicable to nickel- and titanium-alloy based parts [27, 36]. MPI works well on disk shaped components, and could be used for inspection of land based turbine engines whose disks are manufactured from steel alloys.

1.2.4 Eddy Current Inspection

Eddy current inspection is based on the scientific principles of electromagnetic induction. Electromagnetic induction was discovered by Michael Faraday in 1831 [27]. Faraday found that when the current in a loop of wire was caused to vary an electric current was induced in a second loop. In an eddy current probe, an alternating current flows through a wire coil and generates an oscillating magnetic field [49, 50]. When the probe is brought close to a conductive material, a circular flow of electrons known as an eddy current will flow and generate its own magnetic field, which results in mutual inductance with the probe coil [50]. This effect is used in ECI to both cause the eddy currents to flow as well as to monitor them in the material under inspection. Figure 1.5 represents this schematically. If a crack or other type of surface imperfection exists in the sample, the eddy current circulation in the material will be disturbed and the resulting coil impedance variation can be measured to indicate the presence of a defect.

Since electricity and magnetism form the foundation from which ECI is based on, a discussion of Maxwell's equations is necessary. In 1864, James Clerk Maxwell presented his dissertation on a dynamic theory of the electromagnetic (EM) field, which included a set of equations that described all large scale EM phenomena [27, 51]. The four partial differential equations, which bear Maxwell's name, relate the electric and magnetic fields to the charge density and current density that are the sources for the fields [51]. Maxwell's equations in their differential form are expressed in Equations (1.5-1.9).

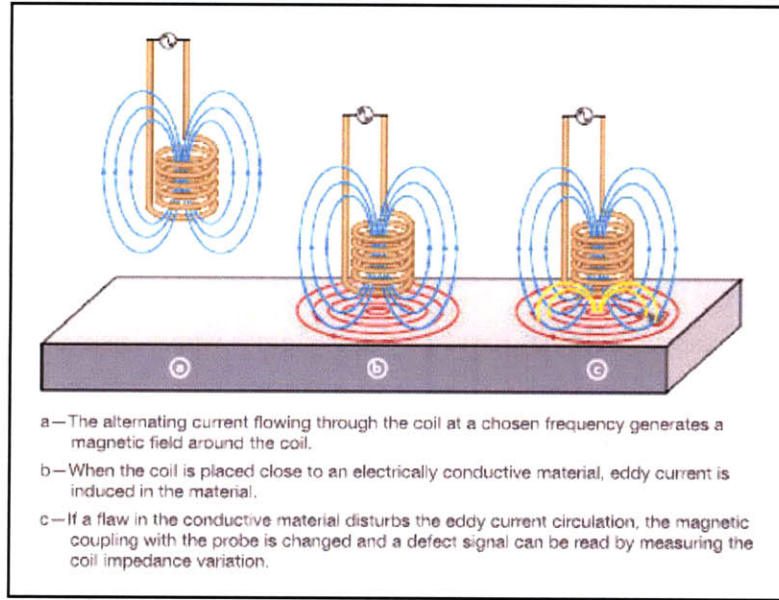


Figure 1.5: The underlying principle behind eddy current inspection (reprinted from [50])

$$\nabla \cdot \epsilon \mathbf{E} = \rho \quad (\text{Gauss' Law}) \quad (1.5)$$

$$\nabla \cdot \mu \mathbf{H} = 0 \quad (\text{Gauss' Law for Magnetism}) \quad (1.6)$$

$$\nabla \times \mathbf{E} = -\frac{\partial \mu \mathbf{H}}{\partial t} \quad (\text{Faraday's Law}) \quad (1.7)$$

$$\nabla \times \mathbf{H} = \mathbf{J} + \frac{\partial \epsilon \mathbf{E}}{\partial t} \quad (\text{Ampere's Law}) \quad (1.8)$$

$$\nabla \cdot \mathbf{J} + \frac{\partial \rho}{\partial t} = 0 \quad (\text{Charge Conservation}) \quad (1.9)$$

where \mathbf{H} is the magnetizing field, \mathbf{E} is the electric field, \mathbf{J} is the electric current density, ϵ is the electric permittivity and ρ is the electric charge density. Equation (1.9) is not one of Maxwell's Laws but rather a boundary condition requiring charge conservation.

Additionally, the following two relationships can be made:

$$\mathbf{B} = \mu \mathbf{H} \quad (1.10)$$

$$\mathbf{J} = \rho \mathbf{v} = \sigma \mathbf{E} \quad (\text{Ohm's Law}) \quad (1.11)$$

where μ is the magnetic permeability, \mathbf{v} is velocity, and σ is the electrical conductivity.

In non-ferromagnetic materials, the induced EM field is derived exclusively from eddy currents. Conversely, with ferromagnetic materials, additional magnetic effects occur that are of sufficient magnitude to overshadow the field effects caused by the eddy currents [27]. These additional magnetic effects result from the magnetic permeability of

the inspected part and are undesirable. This permeability effect is normally eliminated by magnetizing the component to saturation in a direct current magnetic field [27]. This is a distinction between ECI and MPI. When the permeability effect is not eliminated, the inspection method is categorized as electromagnetic or magneto-inductive inspection [27, 52]. The signal to noise ratio is lowered when the added background noise from the permeability effect is not eliminated.

Eddy current inspection is extremely versatile; however this versatility can be both an advantage and a liability. A wide variety of physical, structural, and metallurgical conditions can be differentiated with ECI for both ferromagnetic and non-ferromagnetic metal parts. Properties such as electrical conductivity and magnetic permeability, and conditions including grain size, hardness, heat treatment temper can be identified and measured with ECI [27, 44, 46]. Besides crack detection, eddy current testing can also be used for certain metal thickness measurements, such as identifying corrosion underneath aircraft skin, or to determine the thickness of nonconductive coatings over conductive substrates [50]. Eddy current inspection is limited to materials that conduct electricity and is not applicable to plastics. In many applications, the sensitivity of ECI to the many properties and characteristics within a material can be a disadvantage. Processing variables related to component fabrication, such as surface treatment, may mask relevant signals or cause instrument signals to be incorrectly interpreted [27]. Important operating variables that can affect the sensitivity of a traditional eddy current inspection are listed in Table 1.4. Traditional ECI also requires

Table 1.4: The principal operating variables encountered in ECI

• Coil impedance
• Electrical conductivity of sample
• Magnetic permeability of sample
• Lift-off distance between coil and sample
• Edge effects
• Skin effects
• Inspection frequency or frequencies
• Design of inspection coils: size, shape, and number of windings

extensive calibration prior to flaw characterization [21]. A reference standard, similar to the one shown in Figure 1.6, is typically made from electrical discharge machining

Figure 1 shows a metal plate with various markings and labels. The plate is divided into sections by vertical lines. Labels include "Bottom layer cracks at fasteners", "Sound", "0.200\" (Alodyne)", "0.200\" Tape", "Corrosion spots", "15%", "10%", "5%", "Bottom of top layer", "Top of bottom layer", and "5%". There are also some handwritten notes and a small diagram of a fastener.

newer techniques (i.e. the publication of codes and standards with regulating societies such as ASTM, AWS, ANSI, NIST, ASNT, etc.), is one potential barrier to implementation for an advanced NDT-based life methodology. This topic will be revisited in Chapter 6.

$$\delta = \frac{1}{\sqrt{\pi \nu \mu_o \mu_r \sigma}} \quad (1.12)$$

34

alloys is provided in Table 1.5. Edge effects occur when an inspection coil approaches the end or edge of a material under inspection, causing distortion of the eddy current because they are unable to flow beyond the edge of the part [27, 50]. Unlike life-off, little can be done to eliminate edge effects. Also, eddy current inspection near edges is limited because the magnitude of the effect is very large [27]. When multi-frequency techniques are used, the coil arrangement influences the response signal. With a differential coil arrangement, flaw depth can be related to the change in the angle of what's known as the *Lissajous signal* [27]. One disadvantage of ECI is the difficulty in interpreting data such as Lissajous signals, resulting in the need for specialized operator training and certification. Despite this hindrance, eddy current inspection is the 3rd most common NDT technique used on aerospace components, behind VI and ultrasonic inspection.

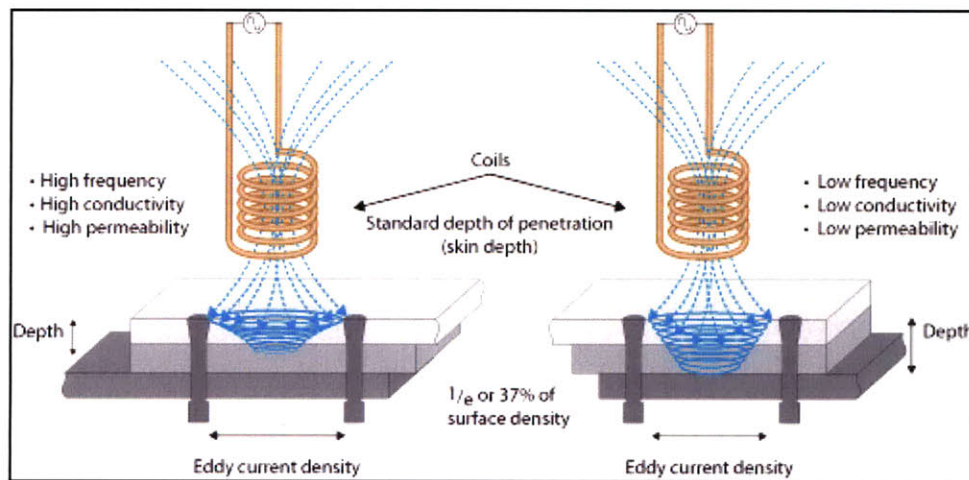


Figure 1.7: Schematic representation of the trade-off between inspection frequency and sensitivity and the affect on ECI depth of penetration (reprinted from [50])

Table 1.5: Electrical resistivity and conductivity of common metals and alloys

Metal or Alloy	Resistivity, $\mu\Omega \cdot \text{mm}$	Conductivity, % IACS
Silver	16.3	105
Copper, annealed	17.2	100
Gold	24.4	70
Aluminum	28.2	61
Aluminum alloys		
6061-T6	41	42
7075-T6	53	32
2024-T4	52	30
Magnesium	46	37
70-30 brass	62	28
Monel	482	3.6
Zirconium	500	3.4
Titanium	548	3.1
Ti-6Al-4V alloy	1720	1.0
Type 304 stainless steel	700	2.5
Inconel 600	980	1.7
Hastelloy X	1150	1.5
Waspaloy.	1230	1.4

1.2.5 X-ray Inspection

X-ray inspection is a very mature NDT technique. W.C. Roentgen discovered x-rays in 1895 when he observed a fluorescent glow of crystals on a table near his cathode ray tube [44]. In the years since this discovery, radiography has been incorporated into many industries including the medical, semiconductor, nuclear, automotive, and aerospace sectors. Radiography is the technique of obtaining a shadow image of a solid using penetrating radiation such as x-rays or gamma-rays [21, 27, 44, 56]. Gamma rays will not be considered in this document, therefore the term radiography will infer the use of x-rays from this point on. As depicted in Figure 1.8, x-rays are electromagnetic radiation just like visible light, infra-red light, and UV light. X-rays have a much shorter wavelength, and thus more energy than any of these methods, enabling the penetration of x-rays into dense materials including metals [44, 56-58]. This is the reason x-ray inspection is applicable for the detection of internal and volumetric flaws.

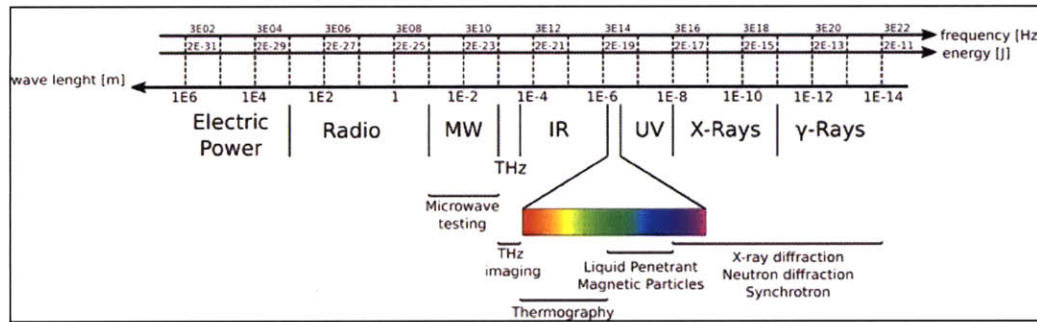


Figure 1.8: NDT techniques based on the EM spectrum. X-rays have a much shorter wavelength, and thus more energy than other techniques including VI, LPI, and MPI. [59]

X-rays are generated when an electron beam impinges on a solid metal target. Electrons are produced from a hot filament, and are accelerated using a high voltage toward the anode target [27, 44, 57, 58]. The electrons travel at velocities up to 80% the speed of light, resulting in electron energies in the 30-450 keV range [57]. A vacuum of about 10^{-2} Pa (10^{-7} atm) is required to achieve the desired acceleration [27, 44]. When the accelerated electrons interact with the electrons surrounding the target's atoms, they are suddenly decelerated. Sudden deceleration of an electrical charge in an electric field produces electromagnetic radiation [57, 58]. If the produced EM radiation has enough energy then it is classified as x-rays. Over 99% of the EM radiation produced upon impact of the electrons onto the target is converted to heat, meaning less than 1% of the radiation has enough energy to be called x-rays [57]. This explains why the target must be cooled very carefully and the anode is a high melting point metal such as tungsten [44]. Maxwell's equations can be used to describe the scientific theory behind the generation of x-rays. Figure 1.9 is a schematic of one potential cathode x-ray tube assembly.

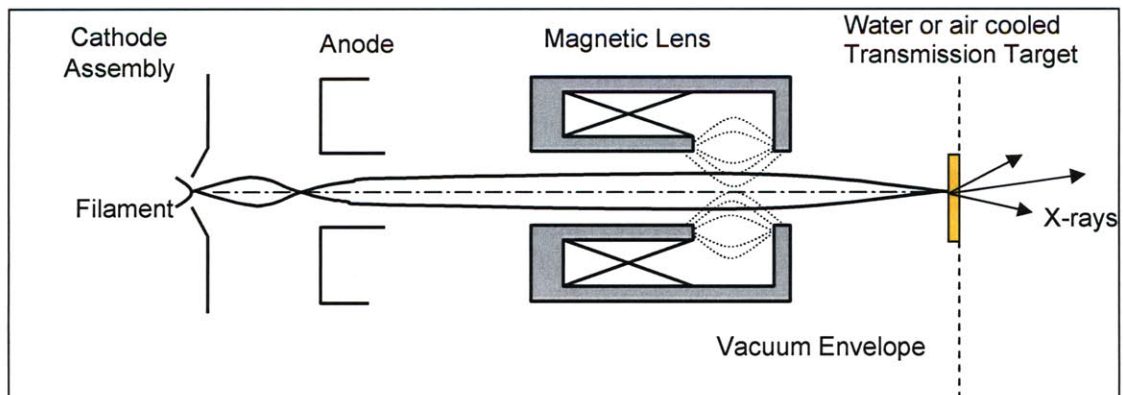


Figure 1.9: Schematic of x-ray tube (adapted from [57])

The three basic elements of x-ray inspection include the radiation (x-ray) source, the specimen under inspection, and a sensing material. The sensing material can be x-ray film as it is in traditional radiography, an amorphous silicon or amorphous selenium imaging plate as in digital radiography, or a linear array x-ray detector as in computed tomography [27, 60]. The x-rays travel in straight lines and pass through the sample, however some of the x-rays are absorbed by the sample. This causes the x-rays to lose energy, and the reduction in x-ray intensity results in the formation of a shadow image [27, 44, 57]. Since x-rays cannot be focused under normal conditions, the focal spot size becomes an important parameter in defining the image. Focal spot sizes range from 1.5-5.0mm (0.06-0.2 in.) in conventional x-ray tubes, 0.2-0.5mm (0.008-0.02 in.) in some focused x-ray tubes, and 5-50 μm (2×10^{-4} -0.002 in.) in special microfocused x-ray tubes [44]. The newest microfocal CT systems now have spot sizes as small as 1 μm (4×10^{-5} in.) [61]. The use of a microfocal x-ray source permits the magnification of the x-ray image onto the detector, thus allowing more detail and a sharper image to be obtained. In contrast with a microfocal source, the typical medical x-ray source is on the order of 1mm (0.04in.) [57]. Another critical parameter is the selection of the x-ray energy. Attenuation of the x-ray beam occurs due to absorption and scattering, therefore x-rays of the appropriate energy are required to obtain optimal image contrast [27, 44]. ASTM E1742-06 [62] is a specification issued on the standard practice for radiographic examination, and provides a thorough detail of test requirements and recommended methods for dealing with the many variables involved with traditional film radiography. A more extensive technical discussion on the principles of radiography can be found in [27, 44].

Unsharpness, contrast, and resolution are all factors in overall x-ray image quality. Unsharpness is commonly referred to as penumbra in industry. The penumbra, denoted by p , of a radiographic image is defined as the inability to faithfully reproduce the boundary of a given object [44]. The total unsharpness, U_T , is composed of several terms and takes the form:

$$U_T = U_g + U_m + U_s + U_f \quad (1.13)$$

where U_g is the geometric unsharpness, U_m is the motion unsharpness caused if the object moves during inspection, U_s is the unsharpness due to use of an intensifying screen, and

U_f is the inherent film unsharpness associated with traditional radiography. An intensifying screen is a sheet of crystals of inorganic salts called phosphors that emits fluorescent light when excited by x-ray radiation. The sheets are used to intensify the effect of the x-rays during exposure of x-ray film [63]. Screen unsharpness is related to the phosphor particle size and the diffusion of light from the phosphor screen. Imaging plates used in digital radiography, which is also known as computed radiography, also utilize phosphors. When x-rays are absorbed by the AgBr grains in traditional film photographic emulsion, secondary electrons are emitted from the AgBr that can affect adjacent grains [44]. Film unsharpness is due to these secondary electrons and is dependent on the x-ray photon energy level.

Geometric unsharpness is a result of the x-ray focal spot source in an x-ray tube being of finite size [27, 44], and is determined by geometry to be:

$$U_g = p = F \times \frac{l}{L_o} \quad (1.14)$$

where F is the effective width of the source, l is the distance from object to screen, and L_o is the distance from the x-ray source to the object. Projection radiography is the term used when l is large enough to produce a magnified image. The image magnification, M , for an object of size S_o and image of size S_i , is equal to Equation (1.15). Equation (1.16)

$$M = \frac{S_i}{S_o} = \frac{L_i}{L_o} \quad (1.15)$$

$$L_i = L_o + l \quad (1.16)$$

shows the source-to-film distance, also known as the source-to-detector distance, is labeled L_i . Knowledge of these values enables calculation of the minimum detectable flaw size, $S_{min,flaw}$, as follows:

$$S_{min,flaw} = \frac{F \times l}{L_o + l} = \frac{F \times l}{L_i} \quad (1.17)$$

Radiography, like all NDT methods, has advantages and limitations associated with it that factor into where and when x-ray inspection is applied. The three main advantages of radiography are: the ability to detect internal flaws, the ability to detect significant compositional variations, and the ability to establish a permanent record of raw inspection data [56]. Radiography inspection results are pictorial in nature and thus

more readily interpreted than numerical data. A main disadvantage of traditional film radiography is that only a two-dimensional image projection is obtained and no information pertaining to the flaw depth is ascertainable. Film radiography is extremely sensitive to the orientation of the inspection sample [27, 44, 56]. Radiography is not as effective in flaw detection when flaws are oriented in a planar direction with respect to the radiation source. Additionally, shielding requirements are necessary to limit operator exposure to harmful radiation. This results in higher equipment costs than other NDT methods and places an effective limit on the sample size that can be inspected. The portability of film radiography is seriously impaired by this requirement. The quality of the resulting film image is dependent on a number of factors including film speed, gradient, and graininess [27]. These factors, as well as film exposure, are functions of the selected film type and the development procedure. The control of these factors and the interpretation of the radiograph are highly reliant on inspector subjectivity. Finally, inspection of thick samples can be difficult because image quality and radiographic contrast decrease as thickness increases [27, 44]. An image quality indicator (IQI) is typically placed on top of the thickest part of the inspection sample to verify that the x-rays penetrated through the sample thickness [44, 62]. Use of the IQI is the most common way to evaluate the sensitivity and quality of the radiographic technique.

1.2.6 Ultrasonic Inspection

Unlike the previous five NDT methods that were based off the electromagnetic spectrum, the principles of ultrasonic inspection are grounded in the acoustic spectrum. Ultrasonic inspection is a nondestructive method in which beams of high frequency sound waves are introduced into materials for the detection of surface and subsurface flaws. Imperfections and inclusions in solids cause the sound waves to be scattered, resulting in echoes, reverberations, and general damping of the sound wave [27, 44]. The relationship between frequency, wavelength, and the velocity of ultrasound is given by Equations (1.18-1.19), where λ = *wavelength*, c = *material sound velocity*, f = *frequency*,

$$\lambda = \frac{c}{f} \quad (1.18)$$

$$\lambda = c \cdot T \quad (1.19)$$

and T = *the period of time required for a complete cycle*. In ultrasonic flaw detection, the generally accepted lower limit of detection for a small flaw is one half of the wavelength, and anything smaller than that will be below the threshold detection limit [64]. The most common methods of ultrasonic inspection utilize either longitudinal or shear waves, but other forms of sound propagation exist, including Rayleigh (surface) waves and Lamb waves [65]. The three frequency ranges of the acoustic spectrum are shown in Figure 1.10(a), while Fig. 1.10(b) provides an illustration of the particle motion direction versus the direction of wave propagation for longitudinal and transverse (shear) waves. A longitudinal wave, sometimes called a compression wave, is the type of UT wave most often used in ultrasonic inspection. The particle motion is in the same direction as the wave propagation for longitudinal waves, while in shear waves the direction of particle motion is perpendicular to the direction of the propagation [27, 44, 64-67]. Table 1.6 lists the longitudinal and shear wave velocities of materials that are commonly tested with ultrasonics. Rayleigh waves have an elliptical particle motion and travel across the surface of a material. Their velocity is about 90% that of a shear wave and the depth of penetration of Rayleigh waves is about equal to one wavelength [65]. Lamb waves, also known as plate waves, consist of complex vibrations that occur in materials whose thickness is less than the wavelength of ultrasound introduced into them [27, 44, 65]. Ultrasonic waves are mechanical rather than electromagnetic waves, such as light or x-rays, and UT waves involve the oscillation and vibration of particles under inspection.

The history of ultrasonic testing dates back to 1912. After the sinking of the *Titanic*, Richardson patented a proposed idea on the echo ranging detection of objects at sea [44]. World War II saw extensive use of ultrasonic wave technology for SONAR applications. In 1945, Simmons developed the pulse-echo method in which the same transducer transmits and receives the UT pulse [44]. The pulse-echo method is the most widely used ultrasonic method, and is used to measure both transit time and signal attenuation. This method is used in flaw detection and thickness measurements, and allows for the determination of both flaw depth and size [66]. Pulse-echo inspection information can be displayed as A-scans, B-scans, or C-scans corresponding to one dimensional, 2D, and 3D manifestations of the output data [27, 66]. The pitch-catch (pulse-transmission) and pulse-resonance techniques are two additional UT methods [68].

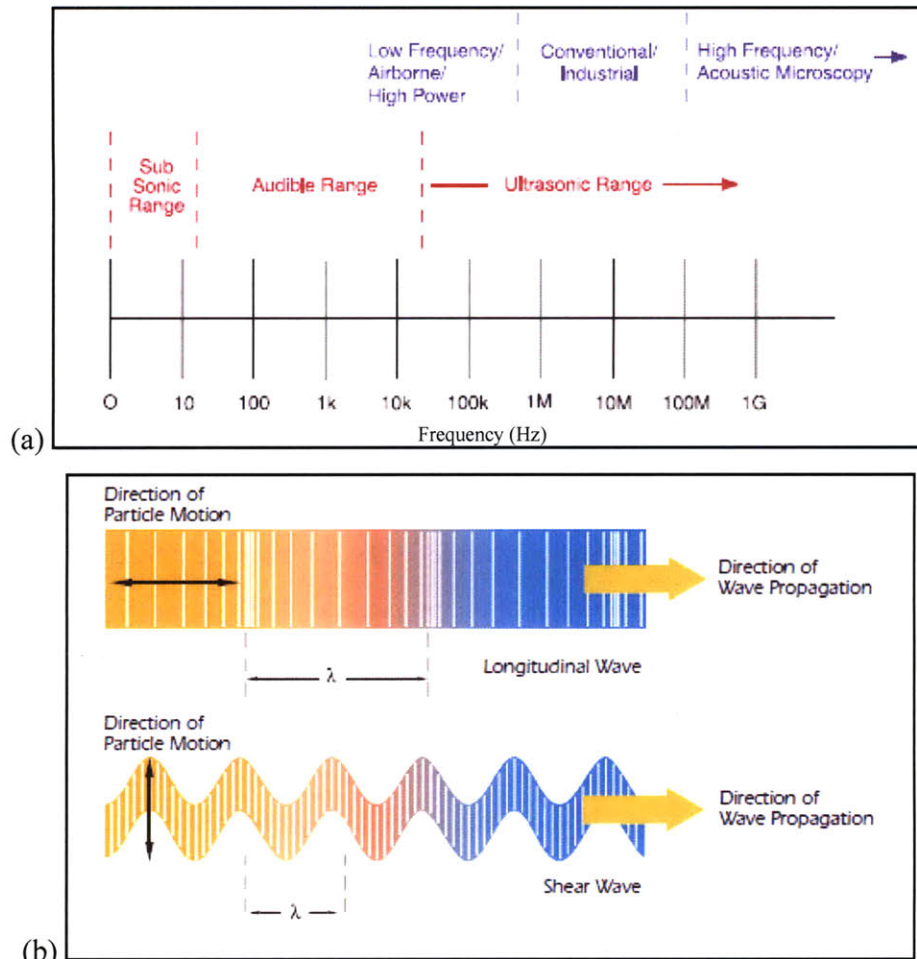


Figure 1.10: (a) The acoustic spectrum showing the three sub-sections of the ultrasonic frequency range. (b) Illustration of the direction of particle motion versus the direction of wave propagation for longitudinal and shear waves. (reprinted from [65])

Table 1.6: The acoustic properties of selected materials

Material	Longitudinal Velocity		Shear Velocity		Acoustic Impedance $M\Omega$ $(\frac{MPa \cdot s}{m^3})$
	(in/ μs)*	(m/s)	(in/ μs)*	(m/s)	
Aluminum	0.249	6,320	0.123	3,130	17.06
Copper	0.183	4,660	0.089	2,260	41.61
Gold	0.128	3,240	0.047	1,200	62.60
Inconel	0.29	5,820	0.119	3,020	49.47
Iron	0.232	5,900	0.127	3,230	45.43
Lead	0.085	2,160	0.028	700	24.49
Nickel, pure	0.222	5,630	0.117	2,960	49.99
Steel, 4340	0.230	5,850	0.128	3,240	45.63
Austenitic stainless Steel, 347	0.226	5,740	0.122	3,090	45.40
Titanium, Ti 150A	0.240	6,100	0.123	3,120	27.69
Water (20°)	0.058	1,480	-	-	1.48

The rapid development of instrumentation such as transducers for ultrasonics was spurred by the technological advances of the 1950's [66]. A transducer is any device that converts one form of energy into another. An ultrasonic transducer converts electrical energy to mechanical energy in the form of sound, and the main components of an ultrasonic transducer include the active element, backing, and wear plate [27, 65]. The active element is typically a piezoelectric or ferroelectric material that converts electrical energy, like an excitation pulse from a flaw detector, into ultrasonic energy. The backing is a high attenuation, high density material that is used to control the transducer's vibration by absorbing the radiating energy from the back face of the active element [65]. The purpose of the wear plate is to protect the transducer element from the testing environment. A thorough analysis of the advanced UT methods and transducer design currently being developed for NDT and material characterization is provided by C.H. Chen in [69].

As shown in Figure 1.10(a), most ultrasonic inspections are performed at frequencies between 0.1-25.0 MHz. This frequency range is well above the 20Hz - 20kHz range of human hearing [27, 66]. A sound wave is launched by transducer excitation in the form of either a voltage spike or a continuous wave impulse. The sound wave then travels through the material under inspection and either reflects off the back side returning to its point of origin, as in pulse-echo, or is received by a second transducer at the back face as in pulse-transmission [44, 67]. Traditional UTI approaches require either the use of gel as a couplant between the probe and the material under inspection, or complete immersion of the sample in water which acts as the couplant [21, 27, 44]. The changes in relative signal amplitude measurements can be used for sizing flaws or for measuring the material attenuation. This value is commonly measured in decibels [65, 70, 71]. Equation 1.20 equates decibel level with signal amplitude ratio such that:

$$dB = 20 \log_{10} \left(\frac{A_1}{A_2} \right) \quad (1.20)$$

where dB is the decibel value, A_1 is the amplitude of signal 1, and A_2 is the amplitude of signal 2. Major variables that affect the sensitivity of UTI and must be considered are the frequency of the ultrasonic waves, acoustic impedance, angle of incidence, beam attenuation, and beam scattering [27, 64, 65]. Shorter wavelengths are more responsive

to changes in the medium through which they pass, so many inspections benefit from using the highest possible frequency allowable in the material under test [67]. The acoustic impedance of a material is the opposition to displacement of its particles by sound and is calculated as:

$$Z = \rho \cdot c \quad (1.21)$$

where Z is the acoustic impedance, c is the sound velocity of the inspected sample, and ρ is the density of the sample. The decibel loss of energy associated with transmission of a signal from an interface boundary in medium 1 into medium 2 is given by:

$$\text{dB loss} = 10\text{Log}_{10} \left[4Z_1Z_2 / (Z_1 + Z_2)^2 \right] \quad (1.22)$$

where Z_1 is the acoustic impedance of the first material and Z_2 the acoustic impedance of the second material. The energy decibel loss of the echo signal in medium 1 reflected from an interface boundary with medium 2 is:

$$\text{dB loss} = 10\text{Log}_{10} \left[(Z_2 - Z_1)^2 / (Z_1 + Z_2)^2 \right] \quad (1.23)$$

At any other angle of incidence besides 0° , the phenomena of wave mode conversion and refraction must be considered. The general law that describes wave behavior at an interface is Snell's Law:

$$\text{Sin}\theta_i / c_i = \text{Sin}\theta_{rl} / c_{rl} = \text{Sin}\theta_{rs} / c_{rs} \quad (1.24)$$

The variables in Snell's law are as follows: θ_i = Incidence angle of the wedge; θ_{rl} = Angle of the refracted longitudinal wave; θ_{rs} = Angle of the refracted shear wave; c_i = Velocity of the incidence material (longitudinal); c_{rl} = Material sound velocity (longitudinal) and c_{rs} = Velocity of the test material (shear). Snell's law does not hold valid at low frequency and small active element size due to the effects of beam spread [65, 67]. The factors primarily responsible for beam attenuation are classified as transmission losses, interference effects, and beam spreading [27]. Scattering of a UT wave occurs due to inhomogeneities in material microstructure. Scattering is highly dependent on grain size, and for highly alloyed components such as turbine and compressor disks scattering effects cannot be overlooked.

Ultrasonic inspection is capable of detecting a wide array of anomalies including cracks, shrinkage cavities, pores, de-bonding, and other discontinuities. The main

advantages of UT over other NDT methods include the superior penetrating power that enables detection of deep internal flaws, the high sensitivity of the process that permits detection of small flaws, and the ability to create a permanent electronic record of inspection results for future reference [27]. Disadvantages of UT are that extensive technical knowledge is required for the development of inspection procedures and scan plans, parts that have either complex shapes or are not homogenous are difficult to inspect, and discontinuities that are present in the shallow near-surface layer may not be detectable [27, 44]. There are additional issues of concern with traditional ultrasonic inspection systems that rely on the rastering of a single transducer to perform an inspection, as depicted in Figure 1.11. Cracks or other discontinuities oriented perpendicular to the surface of the test sample are usually undetectable with conventional transducers because of their orientation with respect to the sound beam [64, 67]. Ultrasonic inspection equipment is available in both automated and manual operation type systems, with manual operation requiring careful attention by experienced technicians to avoid test variability [66]. Finally, the need for physical reference standards both for calibrating equipment and characterizing flaws is a disadvantage of UT inspection.

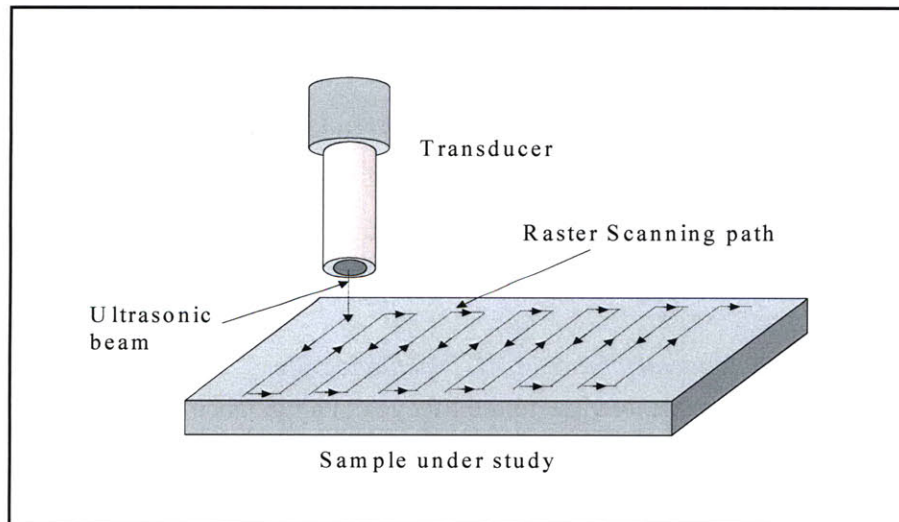


Figure 1.11: X-Y raster scanning used to obtain C-scan with traditional ultrasonic system (figure provided by Prof C.H. Chen, UMass Dartmouth)

1.3 The Limitations of the Traditional NDT Processes

The preceding subsections have provided a theoretical background on the scientific principles that form the basis for a number of NDT techniques. Each of the “traditional” techniques described does have utility in aerospace component inspection, but these same techniques also have drawbacks and limitations. If the purpose of inspection is solely qualitative, as in batch inspections during manufacture [72], then traditional techniques may suffice and be the most cost-effective inspection processes. On the other hand, if a quantitative measure of a particular inspection technique’s capability is required, as it is for in-service inspection of turbine engine components, then POD becomes an important metric for comparison. NDE methods are influenced by a number of factors, ranging from test variables such as the size and location of the defect to be inspected, to equipment and human factors such as technician skill and data analysis capability [24, 73, 74]. The sources of variability (i.e. “noise”) in remnant life prediction methodologies that rely on traditional NDT processes, as well as the sources of error associated with human inspection factors are two topics that will be highlighted. In turbine disks and blades the fracture-critical inspection locations, such as the disk bore region or the base of the dovetail blade slot [75, 76], are often difficult to access for inspection. In these instances NDT techniques that require line-of-sight for detection, such as visual, FPI, and MPI, have been determined in government reports [28, 36] to be inadequate. Detection of embedded defects is a particular limitation for many of the traditional NDT techniques, and a limitation that has resulted in catastrophic engine failure in the past. These are two additional points that will be broached in the following subsections.

1.3.1 Sources of noise and variability in NDT methodologies

In taking a systems level view to the lifecycle maintenance and reliability of a turbine engine structure, it is clear there are many potential sources of “noise”. Table 1.1 listed ten significant variables on which NDT reliability and POD are dependent. Each of these variables contributes a distribution of noise levels to the inspection process. Numerous examples from literature on component life variability are examined in Appendix B and Appendix C. Some of these included flaw variables due to processing [77-79], or variability caused by the manufacturing process or operating environment.

Additionally, details on inherent microstructural (grain) noise from the raw material or alloy being tested have been published [80-83]. This section focuses on the acceptance criteria, NDT method, and NDT equipment variables. Nondestructive testing is only one element of the life management system, with the end goal being structural reliability. It is posited that individual component variability, stemming from the numerous processing and fabrication steps, is unavoidable. To this end, reliable in-service nondestructive testing is deemed the only option capable of accurately quantifying remnant life of aging aircraft on a discrete part basis.

For most nondestructive testing techniques, the ability to successfully detect a flaw or anomaly in an interrogated material depends on a metric such as the signal to noise (S/N) ratio. The criticality of the component being tested and the required threshold discrimination level of the testing technique are the determinants in which NDT processes are applicable and ultimately chosen [27]. Figure 1.12 shows how the S/N density distribution varies with flaw size. As flaw size decreases it becomes harder to distinguish the response signal/noise density distribution from the flaw with the inherent noise of the system.

Magnitude of flaw size is only one of the relevant parameters that influence acceptance criterion. Other variables include flaw type, flaw location, flaw orientation, and flaw nearest neighbor [24, 25]. For critical aerospace components that involve complex machining procedures in their fabrication, these variables can be inherently random or highly dependent on processing. If they are the former they can have a significant impact on signal to noise ratio. The inability to distinguish the response signal from the inherent grain noise increases the probability for false negative (type I error) and false positive (type II error) indications. Figure 1.13 shows the 2x2 outcome matrix for an NDT flaw detection procedure. The correct placement of the discrimination threshold level is a critical parameter in the acceptance criteria, especially in the attempt to detect extremely small flaws. Proper placement of the discrimination (detection) threshold will ensure the minimization of type I and type II errors, resulting in a smaller flaw size, a , attainable for the 90/95 POD/CL value. Figure 1.14(a-c) and Figure 1.15 depict the effect of discrimination threshold level on POD.

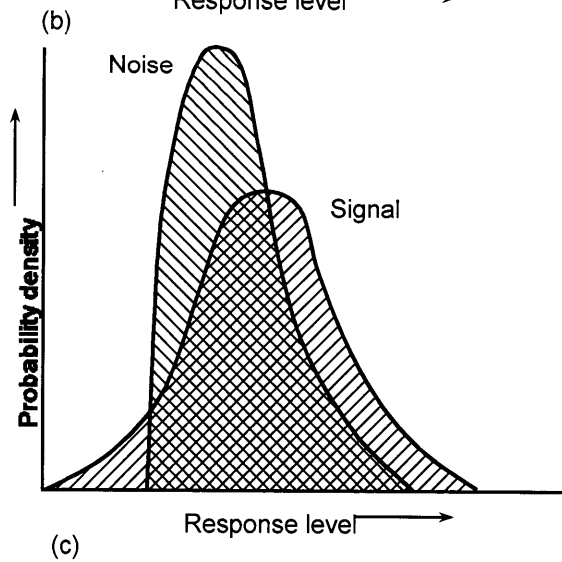
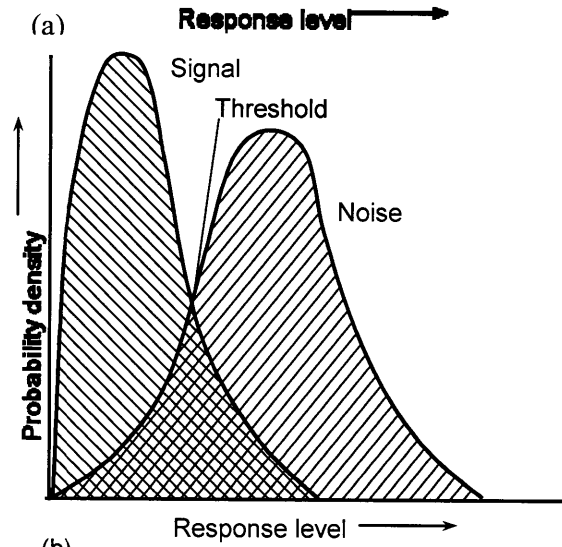
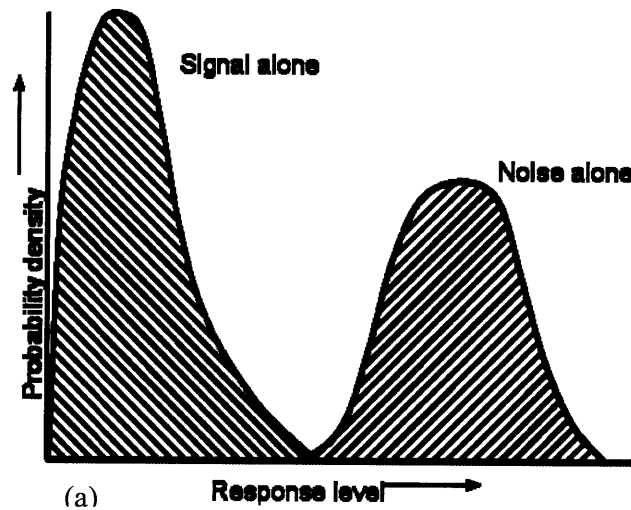


Figure 1.12: S/N density distribution for (a) a large flaw (b) a small flaw and (c) an extremely small flaw whose signal response is below the inherent microstructural (grain) noise of the material under test. (adapted from [84])

		Inspection stimuli	
		Positive, a	Negative, n
Inspection response	Positive, A	True positive (flaws detected) $M(A,a)$ $P(A,a)$ (no error)	False positive (false alarm) $M(A,n)$ $P(A,n)$ (type II error)
	Negative, N	False negative (undetected flaw) $M(N,a)$ $P(N,a)$ (type I error)	True negative (no flaw) $M(N,n)$ $P(N,n)$ (no error)

Figure 1.13: The four potential outcomes for an NDT flaw detection procedure shown in a 2x2 matrix (adapted from [84])

Makeev [85] and Cross [86] have recently proposed the use of a Bayesian inference technique for the simultaneous estimation of the equivalent initial flaw size (EIFS) and crack growth rate (CGR) variability distributions in fracture mechanics (FM) based life prediction models from inspection data. Uncertainty in the EIFS and CGR accounts for a significant amount of scatter, and thus noise, in fatigue life predictions [85, 86]. Data sets for these two parameters are usually obtained through component inspections, however data is scarce because current NDT techniques are neither sensitive nor reliable enough to provide an accurate measure [86]. Gandossi [87] applied this Bayesian inference approach to data obtained from traditional and advanced ultrasonic techniques on defect-containing dissimilar metal welds for nuclear pressure vessels. Bayesian analysis is an appropriate technique for generating posterior probability density distributions for sparse data sets [86, 87]. These posterior distributions provide not only a rigorous means to calculate confidence intervals on important quantities such as EIFS and damage accumulation, but also a systematic way to update prior knowledge as more inspection data is obtained [85-87]. The methodology proposed in Chapter 6 will rely

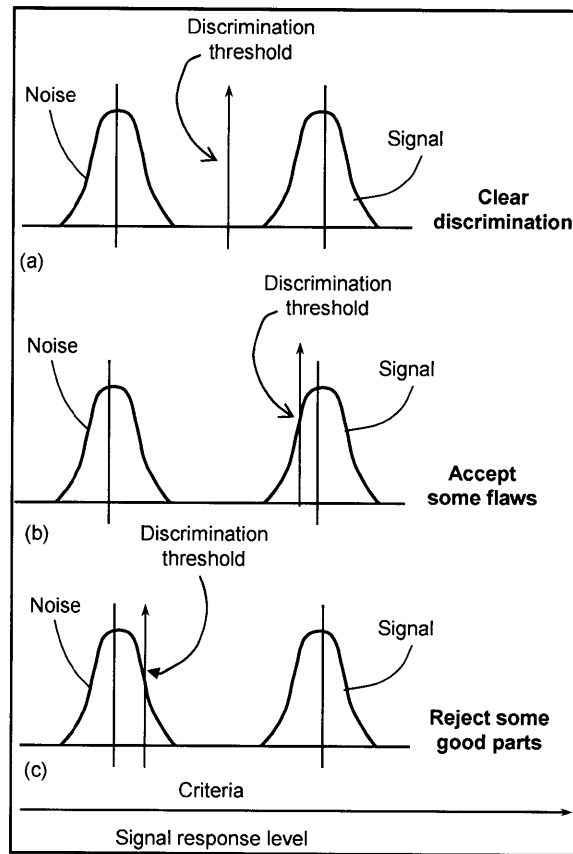


Figure 1.14: The effect of discrimination threshold level on POD (a) Clear discrimination (b) Accept some flaws (c) Reject some good parts

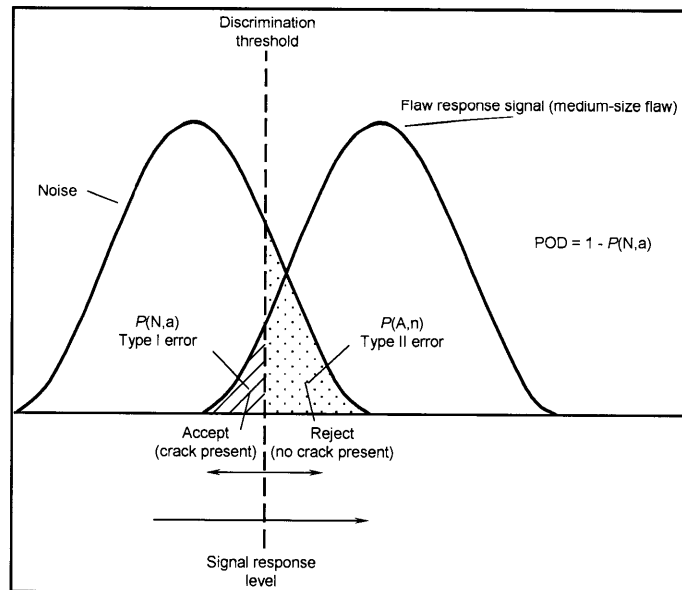
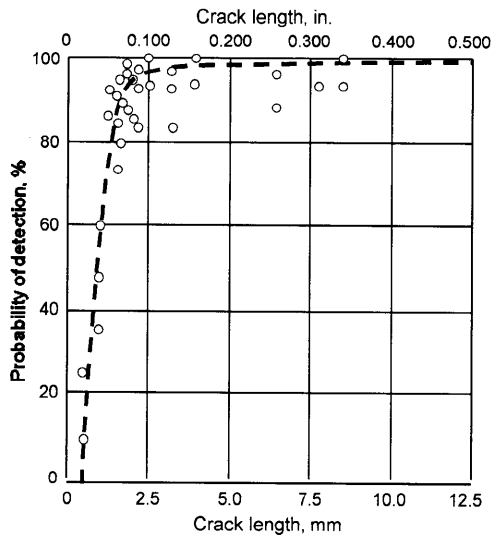


Figure 1.15: False positive (type II) and false negative (type I) inspection responses based on placement of discrimination threshold (adapted from [84])

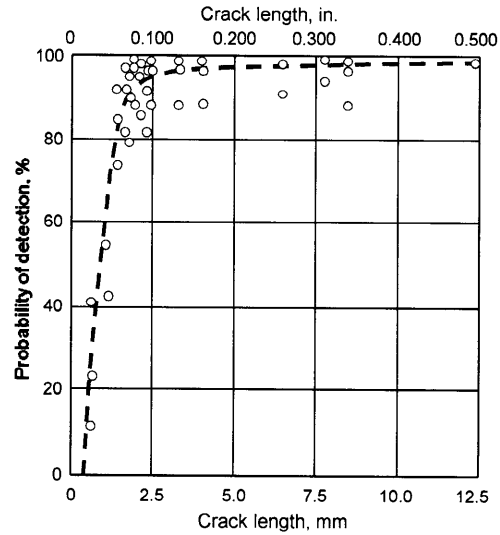
heavily on the incorporation of Bayesian inference to quantify the sources of uncertainty associated with each of the advanced NDT processes. An understanding of the variability associated with the EIFS distribution with respect to time is desired. An inspection methodology integrating multiple advanced nondestructive testing techniques at specified tear-down inspections can accomplish this goal. The use of multiple techniques adds a level of redundancy to the inspection reliability while simultaneously enabling the detection of smaller flaw sizes than traditional NDT methods currently allow. After an exhaustive search of the literature, it is the author's belief this is the first time such a methodology has ever been suggested.

Figure 1.16(a-d) shows POD plots for four different NDT methods used on the same set of specimens. The flaw lengths, which were only surface in nature, ranged from 0.3 – 18mm (0.012 -0.700 in.) and the POD curves generated were only valid for samples in the machined and etched surface condition [27]. The variability in POD from the choice of NDT method is evident. Conclusions drawn from this research included that FPI detection of small flaws was adversely affected by many variables including surface condition, orientation of flaw, and inspector skill. Due to these factors the FPI method did not have the necessary reliability to detect very small flaws in critical locations [27]. Another conclusion was that eddy current methods appeared to have the best potential for detecting small flaws at the required confidence level. Hasanzadeh [88] very recently studied the optimization of maximum likelihood filters for enhancement of defects in C-scan eddy current images. Simulated and experimental results demonstrated the successful performance of these filters in the enhancement of defect details and removal of noise associated with the eddy current method [88].

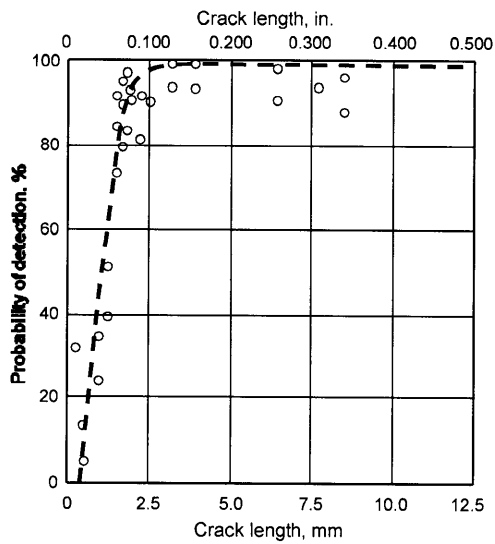
The equipment used to perform a nondestructive inspection is itself a potential source of variability. Even the most advanced NDT techniques are susceptible to equipment variables. Figure 1.17(a) shows the effect of random noise on the image quality of a CT projection, while Figure 1.17(b) depicts the deleterious effects of ring artifacts on CT image quality. Often a compromise must be made between the speed of inspection (i.e. time) and the quality of the data (i.e. noise) [57]. Additionally, the maintenance of the NDE equipment should be considered a source of variability.



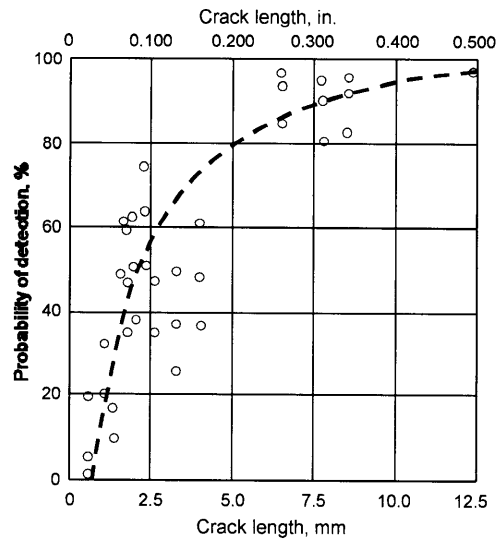
(a)



(b)



(c)



(d)

Figure 1.16: POD plots for four NDT methods on the same set of specimens. The POD curves are only applicable to surface flaws of specified surface condition a) Penetrant inspection b) Ultrasonic inspection c) Eddy current inspection d) X-ray inspection (adapted from [84])

An example would be the need to replace transducers on traditional ultrasonic test systems over the course of the equipment's lifespan. Equipment calibration must be performed when maintenance or repair operations alter any aspect of the NDT equipment system. The ability to automate the inspection process can significantly abate variability stemming from the NDT equipment.

1.3.2 Embedded defects

Embedded defects are a particularly challenging problem for engine designers and NDT technicians. The POD plots in Figure 1.16(a-d) were only valid for surface flaws. Traditional x-ray inspection and FPI performed poorest in terms of detection capability and reliability. For surface defects, traditional UTI is not as good as ECI in small flaw detection capability. Eddy current methods are potentially applicable for near surface defect detection depending on frequency [89], but are not applicable to internal defect detection because of their exponential decay in sensitivity with depth [20, 90, 91]. For eddy current inspections, the probe scans over a crack that is typically perpendicular to the surface and has a known aspect ratio. Surface cracks can be characterized by one number, the 90/95 (POD/CL) value, with good results which simplifies the POD test and analysis significantly [20]. Ultrasonic inspection methods are most apt for internal defect detection due to their excellent depth of penetration capabilities, but the complex nature of naturally occurring embedded defects makes it very difficult for the POD of UTI systems to be established with the same confidence that is achieved when using fatigue crack specimens for eddy current POD analyses [20, 92]. Traditional ultrasonic inspections attempt to detect three dimensional objects, such as voids or inclusions, which may have complex shapes, random orientations, and unknown depths [20, 28]. Each of these factors adds a level of unpredictability to ultrasonic reflection amplitudes.

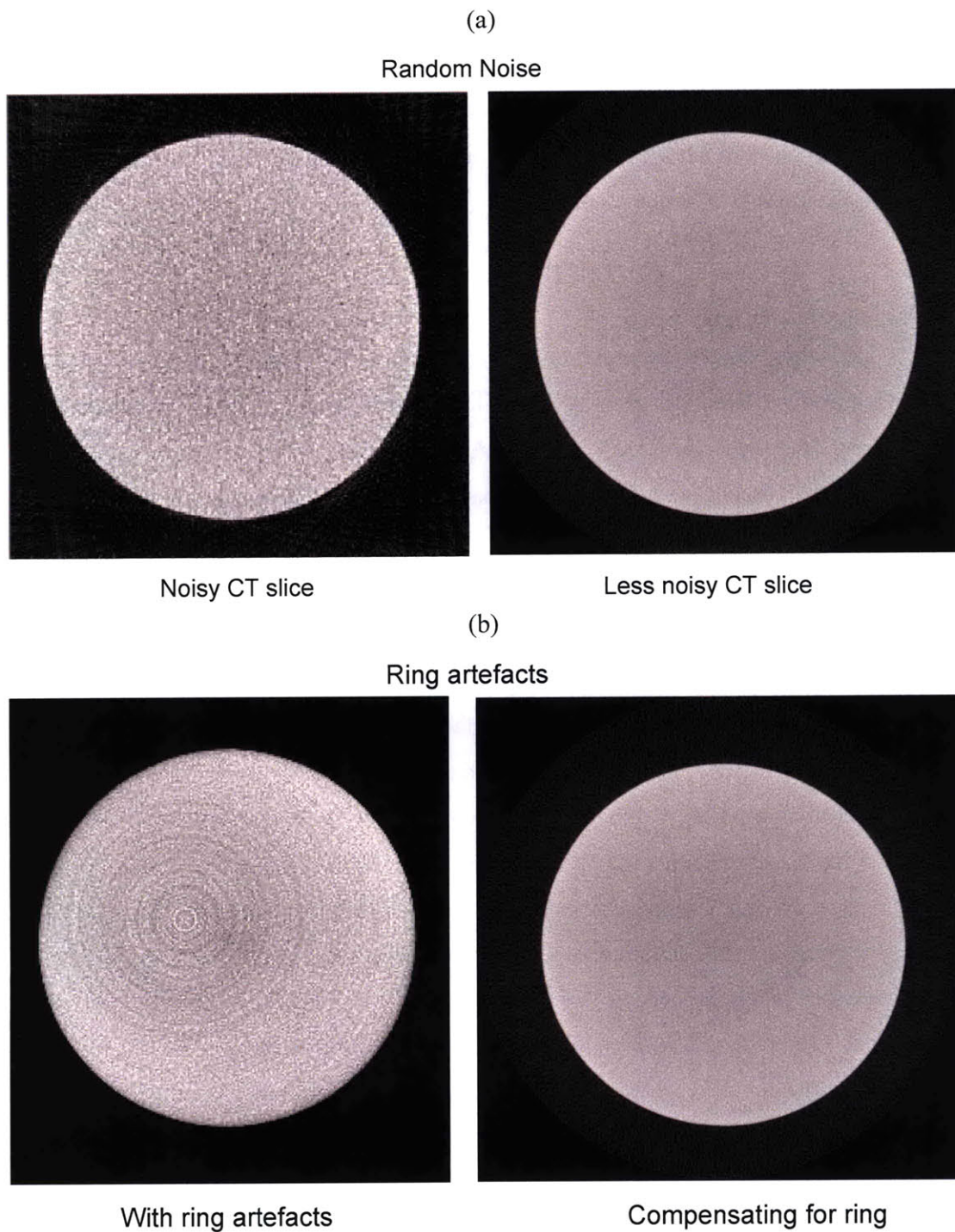


Figure 1.17: (a) Effect of random noise on CT image (b) CT image quality deterioration due to ring artifacts (reprinted from [57])

A particular example highlighting the aforementioned challenges is the detection of embedded hard alpha anomalies in titanium alloys. The presence of interstitial impurities due to the HA region result in density and elastic constant variations on the order of 10% from the nominal $\alpha+\beta$ microstructure [28]. HA defects are often caused by the presence of excess nitrogen, and the inherent gradient in nitrogen content leads to very weak ultrasonic reflections that are difficult to distinguish from the microstructural grain noise [20, 28, 92]. The background noise from the microstructure can result in missed detections and a high false indication rate, both of which can be costly. According to a 2002 FAA report [28], the distribution of grain noise in the detection process has been a known parameter for many years but has by and large been ignored in NDE applications for conventional life prediction methodologies. Under the direction of the Engine Titanium Consortium (ETC), synthetic hard alpha (SHA) specimens were produced with varying percent Nitrogen content [78, 93]. The cylindrically shaped inclusions were embedded in a Ti-6-4 ring forging via hot isostatic pressing (HIP) bonding procedures [28, 78, 93]. Full details on the SHA sample production and initial experimental results can be found in Appendix A of [28]. A similar HA embedded defect seeding procedure is described by Srivatsa [94]. In this case, the embedded defect samples were tested to determine the effect of forging on defect morphology, and to validate a FEM based deformation microcode developed to predict the change in shape and orientation of HA anomalies during the metal forming process.

An additional challenge posed by embedded defects is the difficulty in creating specimens with internal defects of known size and location, which are required to test the inspection capability of a particular NDT method. Multiple attempts have been made by industry and academia at simulating embedded defects. Generally, flat bottom holes (FBH) have been used by the aerospace industry to simulate defects [20, 28, 93, 95, 96]. There is disagreement over the validity of these types of simulated defects, because it has been argued a flat bottom hole signal is not representative of the signal from an in-service flaw [20, 28]. Despite this disagreement, the FBH is of considerable interest because of its current role as an industrial reference standard. Side drilled holes (SDH) and notches are used in the same manner as the FBH. Under the Turbine Engine Sustainment Initiative (TESI), specimens containing spherical targets were produced that mimicked

the range of reflectivities expected for embedded defects in turbine engine components [29, 92, 95-100]. The spherical defect targets ranged from 0.5-6.0mm (0.020-0.24 in.). The targets included alumina, tungsten, carbon, silicon carbide and silica balls that were embedded in a matrix of clean titanium or nickel base alloys via diffusion bonding to provide the range of reflectivities [92, 93, 95, 97, 101, 102]. Figure 1.18(a) provides a layout of the targets in the “spherical defect ring specimen”, and a schematic of the diffusion bonding process is shown in Figure 1.18(b). A total of 80 targets were contained at various depths within the ring specimen. Details on the depth and size of embedded defect targets examined under the TESI program as of 2004 are provided in Table 1.7. Two criticisms regarding these samples include their substantial cost to manufacture, and in that actual defects rarely have a perfectly spherical shape. Due to their complexity, industrial engineering assistance was required in the manufacture of the ETC specimens.

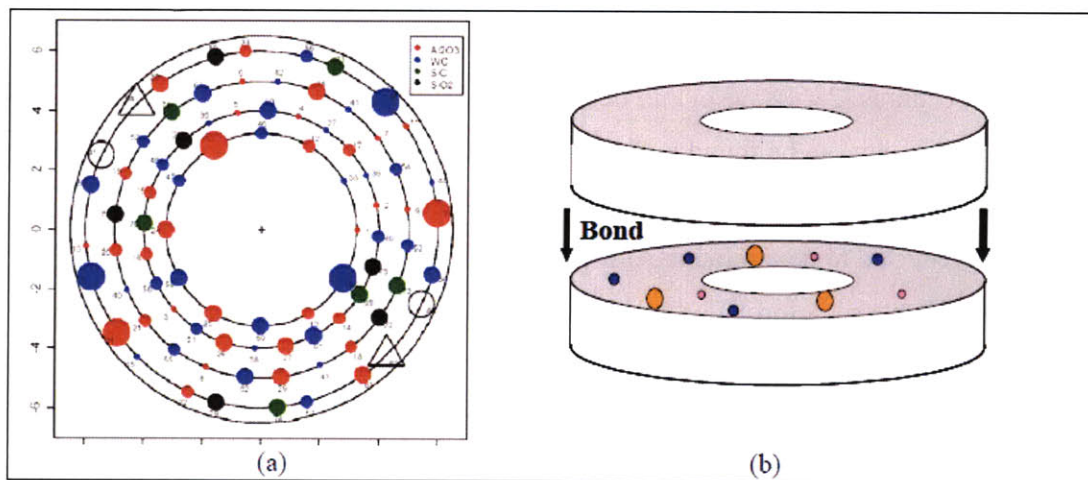


Figure 1.18: (a) Target layout in defect ring specimen (b) Schematic of the diffusion bonding process. (reprinted from [101] courtesy of V. Kramb, Univ. of Dayton Research Institute)

In addition to hard alpha anomalies in forged titanium alloys, embedded defects are also a significant concern for P/M Ni-base superalloys. The presence of non-metallic inclusions introduced into the alloy during powder metallurgy processing have been shown to seriously degrade LCF mechanical properties [103-105]. Typical inclusions are Al₂O₃ and SiO₂. Numerous experimental results have shown that the LCF life of a P/M superalloy is closely related to the size, location, and number of these inclusions [103, 105]. Xie and coworkers [105] performed in-situ SEM tensile tests on Al₂O₃ seeded P/M

Table 1.7: Embedded defect target depths and sizes examined under the TESI program (reprinted from [97] courtesy of V. Kramb, Univ. of Dayton Research Institute)

Specimen number	Matrix material	Target	Target Depth (mm)	Size (diameter)
1.	Titanium	W	12.7	3mm
		C	12.7	3mm
		Al ₂ O ₃	12.7	3mm
		void	12.7	irregular
2.	Titanium	SHA* (1.6, 2.7, 5.9%aN)	25.4	#2-5 FBH
3.	Titanium	FBH	3.175-76.4	#1-5
4.	Rene95	W	12.7	3mm
		C	12.7	3mm
		Al ₂ O ₃	12.7	3mm
		void	12.7	irregular
5.	Rene95	SDH	3.175-76.4	0.020 in.
6.	IN100	FBH	1.5-76.4	#1/2-3FBH
7.	PM IN100	SiO ₂	10.0	0.177-0.250mm
8.	PM IN100	Al ₂ O ₃	12.0	0.149-0.297mm
9.	IN100	mal-oriented, penny shaped defects	3.8-42.5	#1-5FBH
10.	Aluminum	SDH	1.5-70.2	0.4-1.6mm
11.	Aluminum	FBH	12.7	0.4-1.6mm

Rene' 95 superalloy samples, and determined that a critical inclusion size does exist based on experimental results. They found that for small sized inclusions, cracks did not initiate at the inclusion, but rather at the interface of the primary γ' /matrix from where propagation along the primary γ' then occurred. This result demonstrates that small sized inclusions below a critical value may not be harmful to LCF mechanical properties [105]. The significance for in-service disk components is that if small sized inclusions go undetected in initial inspections there may still be an opportunity to detect them during engine tear-down inspections if they are below a critical size.

It was previously discussed that surface crack initiation generally leads to the shortest lifetimes; however the detection of surface cracks is much less arduous than embedded defect detection. The risk of catastrophic failure is greater for embedded defects because of the required intricacy in the NDT process. Also, the lifetimes for specimens failing from subsurface cracks with isolated facets and macroscopically planar subsurface sites do not differ significantly from surface crack lifetimes for $\alpha+\beta$ titanium alloys [104]. Deyber [103] studied the competition between surface and subsurface crack initiation in DA718 (direct-aged Inconel 718), and found at both 450 °C (842 °F) and

600 °C (1112 °F) the applied load was the predominant determinant of crack initiation location. At high loads surface crack initiation was predominant; at low loads sub-surface or internal initiation prevailed; and at intermediate loads a transition zone where both initiation sites coexisted, leading to significant scatter in the results [103]. FEA simulation results at intermediate loads and 600 °C (1112 °F) calculated this transition from surface to subsurface dominance occurred at approximately 1×10^5 cycles [103]. An integrated inspection process that accounts for both surface and embedded defects is the only way to assure dynamic mixed-mode failure mechanisms are assessed.

The removal of internal voids in disks and blades via component rejuvenation processes can significantly extend the service lives of critical life-limited parts. Hot isostatic pressing is used in both new manufacture and repair processes to eliminate internal defects [106]. Parts are exposed to high pressures in excess of 100MPa (15ksi) at temperatures exceeding 1100 °C (2000 °F). Under these conditions the internal voids collapse and are “healed” by a creep mechanism [106]. This is shown schematically for a blade in Figure 1.19. Successful component rejuvenation can allow a 2nd or 3rd service life to be achieved [106, 107], resulting in substantial cost savings. NDT becomes increasingly critical for life-extended parts because of the higher probability of failure with aged components.

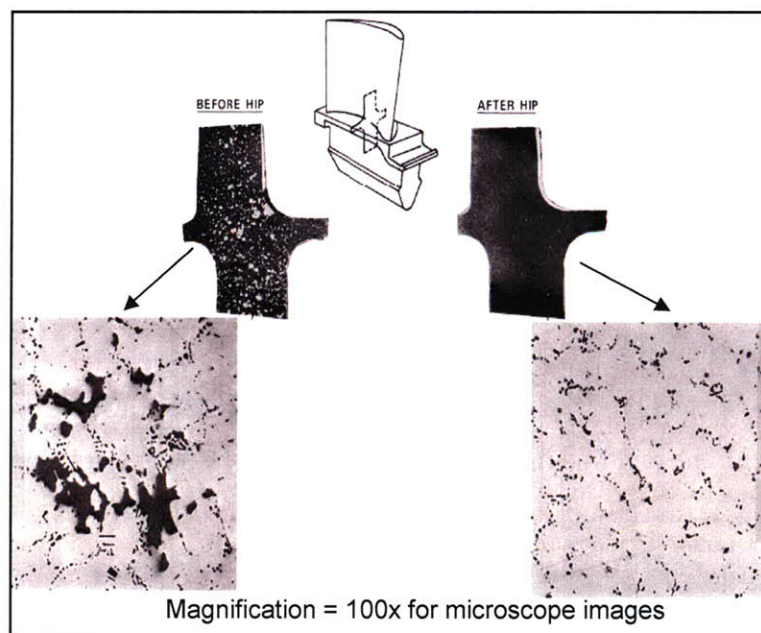


Figure 1.19: Rejuvenation HIP process for a blade showing internal void collapse (adapted from [106])

The extensive alloying in aerospace titanium and nickel-base superalloy components results in ultrasonically noisy materials. This makes billet and forging inspection with traditional UTI particularly challenging at detecting embedded defects because of the high sensitivity and substantial penetration depth required [92, 97]. Voids and inclusions which were below the detection threshold for the inspection of virgin components may develop new features during service that pushes them above the detection threshold. The operating environment may induce microstructural changes in the defect morphology, leading to void growth or crack initiation [92, 97]. No P/M raw material is completely inclusion free so the risk of an embedded defect is intrinsic. Currently ultrasonic inspection is the only inspection technique capable of subsurface defect detection. Incorporation of computed tomography (CT) with advanced phased array ultrasonic techniques will add redundancy and permit the detection of smaller flaws to an in-service inspection procedure. This may also prevent uncontained burst-type failure events.

1.3.3 Error Associated with Human Factors

The traditional NDT processes utilized in aircraft inspections are generally performed manually. A major limitation of current life management methodologies that incorporate traditional NDT is the influence the operator or inspector performing the nondestructive test has on the inspection outcome [21, 92, 97, 100, 108]. Rather than simply failing in the manner physical components often do, humans tend to more often degrade in their performance [109]. Operator skill, attention span, stress and fatigue are all human factors of degradation, and each can have a significant influence on the calculated POD [92, 108-110]. Functions performed by an operator, such as transducer selection, alignment, calibration, positioning, and decision making into pass/fail criteria are highly variable making a precise description of the inspection condition difficult to define [92, 97, 108]. Additionally, the development of a truly reliable inspection is extremely difficult in the absence of specimens that contain actual known defects to be detected [97]. Inspection requirements are often developed based on empirical inspector experience in this case, which is highly subjective and not easily quantifiable in a POD analysis [92, 97, 100]. Various research programs into the development of semi- and

fully-automated inspection systems for aerospace components are ongoing [95, 96, 100, 111-113]. The major idea is to use robots for NDT scanning in the fully automated systems [21]. Automation of the inspection process would reduce the number of human factors related to operator judgment that must be defined for the POD test [92]. The TESI phased array ultrasonic inspection system, located at the University of Dayton Research Institute (UDRI), is one example of a research program into a fully automated system where no human interaction with the inspection process occurs [92, 93, 95, 96, 98, 99, 102, 108]. The six-axis robot used in the TESI system is shown in Figure 1.20. Error associated with human factors in the inspection set-up, calibration, and decision making can be mitigated by inspection automation.

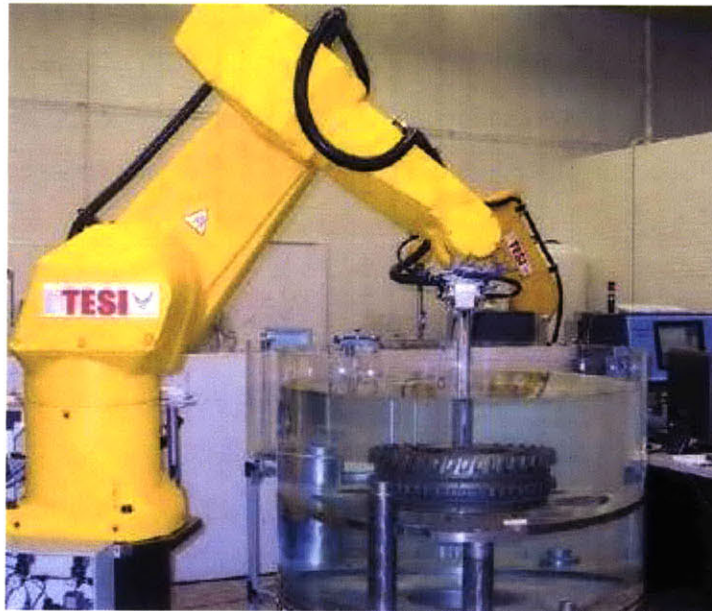


Figure 1.20: The fully automated TESI inspection system at UDRI showing the robot manipulator and inspection tank (reprinted from[100])

In aviation, there are three categories of safety. These categories include personal safety, aircraft safety, and flight safety [109]. Personal safety refers to injuries suffered by individuals while at work, for instance in a maintenance, repair, and overhaul (MRO) facility. Aircraft safety refers to incidents such as incorrect repairs, incorrect documentation, or ground damage to aircraft while not in flight [109]. Flight safety includes events that happen during flight, so both the aircraft as well as individuals are affected by these events. Human reliability is a key factor in each of these safety categories. According to the 1998 report *Uncontained Turbine Engine Rotor Events*

[110], data from 1984-1989 showed deterioration in human factors as the second most significant cause for uncontained rotor events for all classes of aircraft behind mechanical causes. Human factors were the cause for nearly 30% of all the more serious Category 3 and 4 events, where loss of aircraft or loss of life resulted [110]. A further manifestation of the worsening in maintenance, repair, assembly, and inspection reliability was an increase in the percentage of the “Unknown causes” category of uncontained turbine engine events, especially in Category 3 and 4 events [110]. An example on the effect from this deterioration in inspection reliability is given by A.K. Koul in [18], in which the lack of knowledge into the root cause of a missed flaw during inspection affected the determination of the most sensitive and reliable NDT technique. If it was assumed that operator error caused the missed detection, an eddy current method came out as most reliable. If no assumption was made an ultrasonic leaky wave technique appeared superior to the eddy current technique on the basis of combined reliability and sensitivity [18]. It is unacceptable to make such assumptions when inspecting critical components, therefore minimizing the effect of human errors is paramount.

There are two schools of thought in the theory of human reliability. High-reliability theorists believe that all accidents are avoidable. According to high-reliability theorists, if appropriate processes and redundancies are implemented such that systemic weaknesses are remedied and local level failures are contained, global level accidents can be avoided [109]. Normal-accident theorists counter this with a belief that accidents are unavoidable in complex, highly coupled systems. The normal-accident theorists believe that systemic redundancies and safety nets are not always effective, and especially not over a long period of time [109]. High-reliability theorists contend that even though individual humans are not very reliable, the system can be made reliable by incorporating these redundancies. This divergence in human reliability theory will be revisited in Chapter 6.

Regardless of the school of thought believed to be correct, it is obvious that human reliability influences risk assessments in aerospace design, inspection, and regulation. In order to minimize risk, aircraft designers envision the life and expected mission profile of an aircraft and design an engine so it will have a very low probability of failure (POF) with those predictions in mind. When either the life expectancy or the

operating environment is altered from these predictions the risk is increased [109]. This can be in the form of a life extension for the aircraft engine or a deterioration of its environment. Risk is introduced into the system from human errors committed in all aspects connected to the aircraft operation. There is a compounding essence to risks associated with aircraft maintenance. Maintenance related flaws are more likely to remain dormant for a longer time than flaws caused by other factors. This period of dormancy can serve as an opportunity to solve the problem via detection during in-service inspection, or inadvertently as a means to mask the problem thus increasing the probability of catastrophic failure [109]. An example of the latter is the August 1995 crash of an Southeast Airlines Embraer EMB-120RT near Carrollton, GA [109, 114]. The NTSB determined the probable cause was the in-flight fatigue fracture and separation of a propeller blade caused from multiple corrosion pits. Hamilton Standard (HS), the company responsible for the in-service maintenance and inspection, did not discover these corrosion pits due to, “...*inadequate and ineffective corporate inspection and repair techniques, training, documentation, and communications [114].*” Hamilton Standard previously discovered two similar composite propeller blades had failed in March 1994 and initiated an ultrasonic inspection program in which blades found to be defective were to be removed and sent to HS [109]. The blade from the 1995 accident had previously been removed from service on May 19, 1994. The subsequent HS shop UTI confirmed the flaw indication, but a technician concluded “*No visible faults found, blend rejected area*” upon inspection of the taper bore [109, 114]. The blade was blended and reinstalled on the left propeller assembly of the accident airplane on Sept. 30, 1994. The blade had accumulated nearly 2,400 hours and 2,425 cycles in the 11 months since the blend repair by the time the accident occurred [109, 114]. While this was not a failure involving critical turbomachinery in the HPT or HPC engine sections, the accident resulted in eight fatalities and loss of aircraft [114]. This accident illustrates the devastating effect human error can have on inspection reliability and POF calculations.

1.3.4 Prior Catastrophic Failures

The most frequently used NDT methods for turbine engine inspection, discussed in Sections 1.2.1-1.2.6, are for the most part effective and reliable. Be that as it may, there have still been numerous instances in the aviation industry over the years where the

designated methods have not been able to identify flaws of detectable size, and as a result catastrophic failures occurred. The FAA and NTSB have been publishing accident records for uncontained engine failures and damage for over 50 years [110, 115-117]. SAE Report AIR1537 [117] documented aircraft engine containment failures for the data period 1962-1975. SAE Report AIR4003 [116] covered the time period 1975-1983, and SAE Report SP-1270 [110] spanned the time period 1984-1989. Accident statistics and data from the past 20 years are now maintained online at FAA [118] and NTSB [115] websites. The report for the 1976-1983 time period indicated there were 203 non-containment events involving turboprop, turbojet, low-, and high-bypass ratio turbofan engine types [116, 119]. There were 52 disk failures out of the 203 total events, of which 15, or 29%, resulted in significant or severe aircraft damage. Of all the uncontained turbine engine rotor events during this period, 12.3% resulted in Category 3 or 4 events [116, 119]. There are considerable ramifications from a cost perspective associated with catastrophic disk or blade failure due to human errors or unreliability in the nondestructive inspection process. An analysis is presented in Section 6.4 on the monetary repercussions of component failure.

When a catastrophic failure occurs, especially if passenger fatality is involved, there are usually diverging views as to root cause on the part of the airline carrier and OEM due to the litigious nature of the industry. The report for the data period 1984-1989 took 9 years to complete and is considered a special publication (SP) and not an aerospace information report (AIR) because consensus on some of the report's findings could not be obtained by all committee members [110]. The committee was comprised of representatives from engine manufacturers, fixed-wing and rotorcraft aircraft manufacturers, air carriers, and the FAA [110]. This document is referenced in current FAA advisory circulars (AC) [2-11], and conclusions drawn in SP-1270 are used as justification for recent policies on engine LLP airworthiness assessment methodologies [1, 12-14] despite the lack of consensus by the parties involved in the committee. In SP-1270, aircraft engines were classified as either commercial transport (CT) if they powered fixed-wing aircraft with passenger capacity in excess of 19 or cargo capacity above 6000 pounds, general aviation (GA) if they powered fixed-wing aircraft with passenger capacity of 19 or fewer or cargo capacity below 6000 pounds, or rotorcraft

(RC) for rotary wing aircraft such as helicopters [110]. Conclusions of the report that apply broadly across all engine types are classified as civil aviation overall (CAO) fleet data. The CAO data showed 49 disk, 13 blade, and 4 spacer Category 3 and 4 events occurred during the 6 year data period [110]. This data can be misleading because RC events accounted for 35 of the 49 uncontained disk failures, while CT numbered 10 and GA accounted for the other 4 disk events in the same time period [110]. The 10 Category 3 and 4 uncontained disk events for CT engines are noteworthy because they represented a 17.2% increase in the event rate per million flight cycles. This is equivalent to a 5.6% increase in average event rate per million hours over the previous 1976-1983 data period [110]. In the development of a cost-benefit analysis, it is critical that only the appropriate data be considered so as to not skew the results. Only Category 3 and 4 CT events involving disk and blade components, in which a deficiency in the traditional nondestructive inspection process contributed to the failure, will be considered in the POF and cost calculations in Chapter 6.

One of the most influential catastrophic failures in the history of the aviation industry would fall under the situation described above. On July 19, 1989 a United Airlines McDonnell Douglas DC-10-10 crashed at the Sioux Gateway Airport in Sioux City, Iowa following the uncontained failure of the No. 2 rear engine during flight [119-121]. Failure analysis revealed the accident was the result of a fatigue crack that initiated from a small 1.4mm long by 1.4mm wide by 0.4mm deep (0.055 x 0.055 x 0.016 inch) cavity in the bore of the 1st stage rotor disk assembly [119, 121]. The 1st stage Ti-6Al-4V fan disk weighed about 168 kilograms (370 lbs), and was machined from a forging approximately 81 cm. (32 in.) and subsequently a billet nearly 41 cm. (16 in.) in diameter [119]. A nitrogen stabilized HA anomaly surrounded the cavity, and the NTSB concluded that it was formed during the final bore-machining operation prior to the component being introduced into service. The total time on the failed engine was 42,436 hours and 16,899 cycles [119, 120]. Analysis of the major fatigue striations indicated the fatigue crack had begun to propagate very early in the life of the disk, nearly 18 years before the fatal accident [119, 121]. During the manufacturing process the disk underwent four nondestructive inspections to detect internal and surface defects. These included contact-ultrasonic, immersion-ultrasonic, macroetch, and FPI. After the disk

entered service, six FPI inspections were performed during the life of the accident fan disk, including one 760 cycles before the accident [119, 121]. None of these inspections detected any material anomaly, even though the fatigue crack had grown to a detectable size of 13mm (0.51 in.) before the final penetrant inspection. The final FPI performed should have detected the crack because a discolored area from the FPI was found on the fracture surface [121]. Pieces of shrapnel from the burst disk severed all three of the hydraulic system's lines on the plane. Failure of all three hydraulic systems had been considered impossible by aircraft engineers and designers, so there was no backup means of controlling the aircraft once this occurred [120]. Even though 185 people survived as a result of the skilled maneuvering on the part of the flight crew, there were 111 fatalities [119, 120]. Also, the aircraft was destroyed upon ground impact.

In response to the Sioux City accident, the FAA formed numerous committees to examine the circumstances surrounding this incident and to recommend enhanced procedures. Metallurgical examination found that the microstructure of the HA anomaly had been altered at various stages of manufacturing, making detection of the inclusion more difficult [119]. The contact-ultrasonic inspection that was first performed on the 41 cm. (16 in.) diameter billet in 1970 had since been replaced by a more sensitive immersion-UT, with a greater sensitivity to subsurface flaw detection, as of 1990 [119]. General Electric Aircraft Engines (GEAE) performed the first immersion ultrasonic inspection on the accident disk material in its rectilinear machine-forged shape in 1971. The testing equipment for this inspection was calibrated to a standard maximized at 80% of the full scale height (FSH), with an additional 12 dB of gain added to the output signal to further increase sensitivity by a factor of 4 above the standard calibration [119]. The immersion-UT equipment specified for disks produced as of the NTSB report in 1990 required a 6dB gain rather than 12dB, added automatic depth compensating features, and allowed more scan modes. These were added to assist the operator in making a judgment on borderline flaw indications less subjectively [119]. The NTSB concluded that the probable cause of the accident was the, “ *inadequate consideration given to human factors limitations in the inspection and quality control procedures used by United Airlines' engine overhaul facility, which resulted in the failure to detect a fatigue crack emanating from a previously undetected metallurgical defect located in a critical*

area...[121].” The FAA Titanium Rotating Components Review Team recommended an enhanced damage tolerance design strategy employing a probabilistic relative risk assessment methodology intended to reduce the rate of uncontained rotor events [72]. The DTR values and POD curves based off the review team’s recommended risk assessment methodology have had to be updated more than once [36, 122] due to incorrect assumptions in the model, or when service data deviations required revision. Despite industrial improvements in engine safety that resulted from the recommendations of the various committees formed in the wake of the Sioux City accident, additional catastrophic failures have since occurred. These accidents also could have been prevented by use of improved inspection systems.

Two recent disastrous uncontained engine failures were the 1995 ValuJet Airlines Flight 597 crash and the 1996 engine failure accident during takeoff in Pensacola, Florida. Details on the events surrounding the accidents can be found in [109, 121, 123] for the ValuJet crash and [121, 124, 125] for the Pensacola accident. The NTSB determined the probable cause of the June 8, 1995 ValuJet accident was the failure by the Turk Hava Yollari maintenance and inspection personnel to perform a proper inspection of a 7th stage HPC disk [109]. The disk ruptured because poor inspection processes and ambiguous procedures, at the Turkish repair station where the engine had been overhauled 4 years prior to failure, allowed a detectable crack to grow to a critical length [109]. The HPC disk had a life limit of 30,000 hours or 18,932 cycles, and was made from AISI 9310, a low alloy steel [121]. Maintenance records indicated the failed disk had accumulated 24,101 hours and 16,340 cycles [121]. Fluorescent MPI missed a detectable 13mm (0.51 in.) crack in 1991, 4433 cycles before the accident [121]. The uncontained engine failure of Delta Airlines Flight 1288 on July 6, 1996 was caused by the failure of Delta’s FPI process to expose a detectable fatigue crack initiating from an area of altered microstructure in the left engine’s front compressor fan hub [121, 125]. The fatigue crack initiated from a near-surface HA anomaly, formed during the tiered hole drilling process, that went undetected at the time of manufacture [125]. The fan hub was designated as a safe life part and would have been retired after a total of 20,000 cycles. Also, according to the safe-life methodology, if the fan hub was not removed from the engine it did not have to be inspected [121]. The left engine’s fan hub had

acquired a total of 16,542 hours and 13,835 cycles at the time of the accident [121]. Maintenance work requiring a teardown of the hub assembly took place only 1142 cycles before failure. During the teardown, FPI and visual inspection were both performed [121, 125]. The NTSB determined a lack of sufficient redundancy in the in-service inspection program contributed to this accident [125]. These two accidents illustrate how flaws that remain dormant for an extended amount of time can result in catastrophic failure when the effects of inspection variability, stemming from the use of insensitive and unreliable NDT techniques, and human error are compounded.

1.4 Advanced NDT Processes of Proposed Methodology

All of the traditional NDT techniques are well established, and procedures for their use in airplane engine inspection have changed little in the past 40-50 years. Many of these procedures were developed with electronic devices that are now considered obsolete; however the electronics used with traditional NDT have generally not been updated to incorporate advancements in technology [46, 102]. In his review of in-service NDE of aerospace structures [46], Yoseph Bar-Cohen, of the jet propulsion lab at Caltech, pointed out that a series of advancements related to computers, electronics, material science and other interdisciplinary fields has made a major impact on all or many of the NDE methods. Implementation of newer technologies for the in-service inspection of critical aerospace components has the potential to overcome many of the current limitations traditional techniques face. Advanced techniques that incorporate newer technology provide increased detection capability as well as data storage and processing opportunities [98, 99, 102]. The understanding that no single method can provide all the necessary NDE information makes it apparent that integration of several methods is the only way to provide total inspection coverage for life-limited parts. The integration of complimenting NDT techniques yields improved flaw detection capability, while the level of redundancy provided by the overlapping techniques enhances reliability.

1.4.1 MWM®-Array Eddy Current Inspection

The Meandering Winding Magnetometer Array (MWM®-Array), is a conformable eddy current sensor array that produces high resolution two-dimensional C-scan images for crack and flaw detection. The MWM was originally conceptualized at

MIT's Laboratory for Electromagnetic and Electronic Systems by the late Prof. James Melcher [126] in the mid 1980's. The technology was further developed by Melcher and Neil Goldfine [127, 128] in the early 1990's. Over the past 20 years the MWM-array sensor technology has evolved at JENTEK Sensors, Inc. [Waltham, MA] [91, 128-131]. The MWM-array sensor has been successfully applied to a number of aerospace applications, including material damage accumulation and health monitoring [53, 91, 111, 112, 132], hidden corrosion imaging [54, 133], TBC characterization [134], and detection of cracks in critical regions with fretting fatigue damage [52, 53, 112, 135]. The MWM may be thought of as an eddy current sensor with periodic geometry, and many of the technical terms discussed for the traditional eddy current inspection technique are also relevant to the analysis of MWM-arrays.

Figure 1.21 depicts the typical layout of the early MWM sensors. This is an

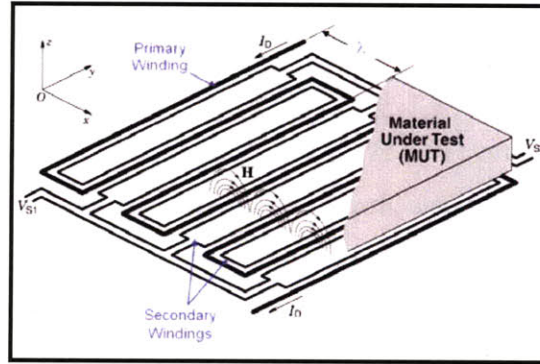


Figure 1.21: Schematic of the basic structure of the MWM Sensor as originally conceived (reprinted from [52])

example of a periodic field magnetic sensor with a spatial wavelength of λ that does not use a shaped-field current drive. It consists of a primary winding driven with a current I_D , and one or more secondary windings laid out in a periodic fashion on an insulating flexible substrate [131]. The imposed spatial periodicity of the current excitation results in a magnetic field H , shown for three meanders in Figure 1.21. The time varying magnetic field induces eddy currents in the material under test. The secondary windings couple some of the magnetic flux, and the voltages induced at their terminals are V_{S1} and V_{S2} [127, 128, 131]. The summation of the voltages, V_S , is given by the equation in (1.25), where V_{Sf} is the final winding if the secondary windings are connected in series. If they are connected in parallel then (1.26) is used. The sensors' complex transimpedance, Z , for the original MWM shown in Figure 1.21, is defined by the

$$V_S = V_{S1} + V_{S2} + \dots V_{Sf} \quad (1.25)$$

$$V_S = V_{S1} = V_{S2} = \dots V_{Sf} \quad (1.26)$$

$$Z_{21} = V_S / I_D = V_2 / I_1 \quad (1.27)$$

equation in (1.27). The transimpedance is the voltage measured at the two terminals of the sensing elements V_S , divided by the applied current I_D [52, 128, 131, 136]. The transinductance is equal to the transimpedance divided by the angular frequency, $\omega = 2\pi f$, where f is the excitation frequency of the applied drive winding current [135]. The sensor's complex transimpedance is directly linked to the properties of the material under test.

In most cases for aerospace materials, the material under test is metal. The governing equation for metallic samples is the magnetic diffusion equation, where the characteristic decay rate, also known as the depth of penetration, is a function of both the imposed spatial wavelength and the skin depth of the material, with the smaller of these two lengths dominating [131]. MWM-arrays operate in the magnetoquasistatic (MQS) regime, where changing magnetic fields are ignored. Starting with the four Maxwell's equations previously described and ignoring magnetic fields results in:

$$\nabla \cdot \mu \mathbf{H} = 0 \quad (1.28)$$

$$\nabla \times \mathbf{H} = \mathbf{J} \quad (1.29)$$

$$\nabla \times \mathbf{E} = -\frac{\partial \mu \mathbf{H}}{\partial t} \quad (1.30)$$

Introduction of the magnetic vector potential, \mathbf{A} , via (1.31) and Ohm's law by the second relationship in (1.11) gives the solution to the magnetic diffusion equation in (1.32).

$$\mu \mathbf{H} = \nabla \times \mathbf{A} \quad (1.31)$$

$$\nabla^2 \mathbf{A} = \mu \sigma \frac{\partial \mathbf{A}}{\partial t} \quad (\text{Magnetic Diffusion Equation}) \quad (1.32)$$

Rewriting the diffusion equation in (1.32) in complex number notation with $j = \sqrt{-1}$ gives:

$$\nabla^2 \mathbf{A} = j 2\pi f \mu \sigma \mathbf{A} \quad (1.33)$$

In the MQS regime, if it is assumed that the sensor is periodic in the x -direction with period (wavelength) λ , nothing changes in the y -direction, currents flow in the y -direction, and the material under test is uniform, then the depth of penetration γ and skin depth δ can be calculated by the equations in (1.34)-(1.35) to be:

$$\gamma = \sqrt{(2\pi/\lambda)^2 - j2\pi f \mu \sigma} = \sqrt{(2\pi/\lambda)^2 - 2j/\delta^2} \quad (1.34)$$

$$\delta = \sqrt{1/\pi f \mu \sigma} \quad (1.35)$$

The material properties affect the sensor response at the step where the magnetic field is derived from the magnetic vector potential [52, 131]. Electrically non-conducting materials satisfy Laplace's equation, given in (1.36). These materials operate in

$$\nabla^2 \Phi = 0 \quad (\text{Laplace's equation, no free charge, } \rho = 0) \quad (1.36)$$

the electroquasistatic (EQS) regime and can be tested with an Interdigitated Electrode Dielectrometer (IDED®) sensor [52, 53, 126, 131]. Only the MWM-array sensors, which are used to inspect metallic samples, will be discussed henceforth.

The previous paragraph has described what is known as the *Forward Problem*. The *Forward Problem* computes the sensor transimpedance given all relevant model inputs, including material properties such electric conductivity and magnetic permeability, material geometry, and sensor geometry [52, 128, 135, 136]. To solve for multiple material property and geometric unknowns, a patented multivariate inverse method using precomputed databases [126-128] is implemented into the Gridstation® software that is used in concert with the MWM-array sensor. First, the *Forward Model* is used to precompute all the potential sensor responses for all combinations of relevant unknowns over their dynamic range. The results from the precomputed databases are plotted, as depicted in Figure 1.22, as a grid for two unknowns. Other potential databases take the form of a lattice for three unknowns, or a hyperlattice for more than three unknowns [91, 126-129]. Complex nonlinear problems involving multiple unknowns are typically estimated using iterative root searching methods. These methods attempt to minimize the error between the measured sensor response and the model predicted response [52]. This is a time consuming process that is unacceptable in a production environment or inspection depot facility, where thousands or possibly even millions of unknowns must

be solved for each minute. One advantage of the precomputed databases is that as long as the data points from the inspection lie within the grid space, the measurements are valid if calibration was correctly performed. This approach is advantageous in situations where processing power and time is limited at the instant an inspection decision must be made, but massive data storage is readily available at low cost so that the inspection output can be analyzed at a later time [52-54]. These situations are common in NDT applications.

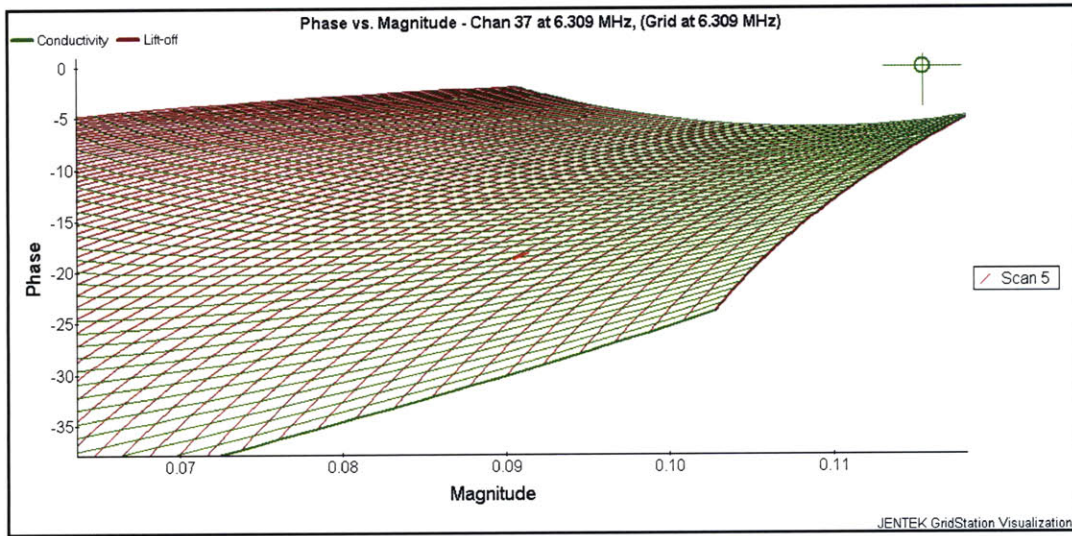


Figure 1.22: Precomputed grid containing all potential sensor responses for the case where the two unknowns are conductivity and lift-off. The grid is for a particular channel of the MWM-array sensor at a particular frequency.

To solve the *Inverse Problem* the Jacobian matrix that relates the measurement vector must be inverted. This involves inversion of the real and imaginary parts of the transimpedance for each measurement condition, such as at each frequency in multiple frequency measurements or for all sensor proximities for multiple lift-off procedures [52, 127, 136]. The number of measurements that can be taken simultaneously by the sensor has a direct effect on the number of unknown material properties that can be solved. Therefore information about sensitivity, and also the system capability to independently measure multiple unknowns, is provided by the rank of the Jacobian matrix [52, 130, 136]. Improvements in MWM-array sensor design, since the original MWM depicted in Figure 1.21, are described in [53, 135]. Figure 1.23 depicts the architecture for one of these improved sensors: the multi-channel FA28 MWM-array sensor.

The multiple channel MWM-array sensors are capable of taking data at *each* sensing element as it traverses a component to produce simultaneous images of multiple unknown properties [52, 127, 128, 130, 136]. The multivariate inverse method permits thousands of independent eddy current measurements to be viewed in real time as high resolution images of electrical conductivity, magnetic permeability, layer thickness and lift-off [53, 54, 112, 135]. These measured properties can be related to dependent

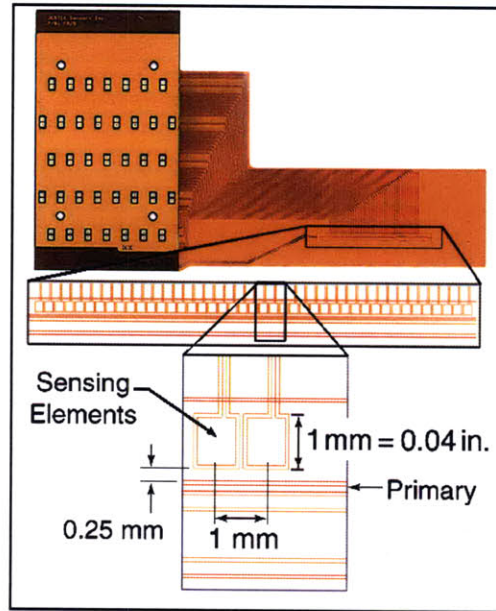


Figure 1.23: Multiple channel FA28 MWM-array sensor (reprinted from [52])

properties of interest such as crack depth, surface roughness, paint thickness, stress, or material loss from corrosion. The use of relatively small sensing elements, on the order of 1 mm x 1 mm (0.04 in. x 0.04 in.), enables high resolution images of absolute properties to be generated. High resolution imaging is critical for detection of very small cracks, while imaging of absolute properties is necessary to correct for lift-off variations or to provide reliable crack responses for cracks that form in clusters [135]. Cracks in the fretting regions of engine disk slots are one example of such a crack group that form in clusters.

1.4.2 Phased Array Ultrasonic Inspection

Conventional ultrasonic inspection for NDT commonly consists of either a single active element that both generates and receives high frequency sound waves, or two paired elements, with one for transmitting and one for receiving [137]. An ultrasonic

array is a single transducer that contains a number of individually connected elements. Phased array probes consist of a transducer assembly with from 16 to as many as 256 small individual elements that can each be pulsed separately [137-139]. The wave physics principle of “phasing” is utilized in a phased array system, such that the time between a series of outgoing ultrasonic pulses is varied and the individual wave fronts generated by each element in the array combine with each other to add or cancel in predictable ways that effectively steer and shape the sound beam [137-139]. The operator can sweep the beam through a selected volume of the test piece by varying the sequence in which the elements are pulsed [138]. Frequently, the elements are pulsed in groups of 4 to 32 in order to improve the effective sensitivity by increasing aperture, thereby reducing unwanted beam spreading and enabling sharper focusing [99, 137, 140]. Additionally, phased array systems are capable of multizone inspections, where *dynamic depth focusing* of maximum sound energy at selected depths that correspond to potential flaw locations is simultaneously performed [70, 71, 113, 122, 138, 141]. A 2008 FAA report [122] determined the POD curves generated by use of the multizone technique were clearly superior to those of the conventional UTI technique for the ultrasonic detection of hard alpha inclusions in Ti-alloy billets. Sonograms used for medical imaging were one of the first applications to incorporate phased arrays [137, 142]. In recent years the use of PA-UT inspection for NDE has gained more attention.

Sophisticated technology is incorporated into the design of a phased array ultrasonic system. Computer-based instrumentation is required that is capable of driving the multi-element probe, both receiving and digitizing the returning echoes, and plotting the echo information in various standard formats [137]. Software known as a focal law calculator is used to establish specific delay times for the firing of each group of elements, and takes into account probe and wedge characteristics as well as the acoustical properties of the test material to generate the desired beam shape [137, 143]. The programmed pulsing sequence selected by the software launches a number of wave fronts that constructively or destructively combine to form a single wave front beam that can be dynamically steered through various angles, focal distances, and focal spot sizes [137, 142]. PA-UT systems can operate in manual direct contact use, semi-automated as part of an angle beam assembly with a wedge, or fully automated modes. As in conventional

UTI, phased arrays can operate in immersion with sound coupling obtained through a water path. The arrays can perform beam sweeping through an angular range (known as sectorial S-scans), beam scanning at a fixed angle (known as longitudinal E-scans), beam focusing, lateral scanning, and a variety of other scans depending on the array and software programming [138, 142]. Figure 1.24(a-b) is an example of beam scanning at a fixed angle and beam steering through an angular range. A phased array transducer can spatially sort the returning wavelength according to the arrival time and amplitude at each element, unlike a conventional single element UT transducer where the influences of all the beam components that strike its area are effectively merged [137]. A review of ultrasonic array design, modeling, and signal processing for NDE applications is provided in [142] by B.W. Drinkwater and P.D. Wilcox. Phased array technology has great potential to increase inspection quality and reduce inspection time.

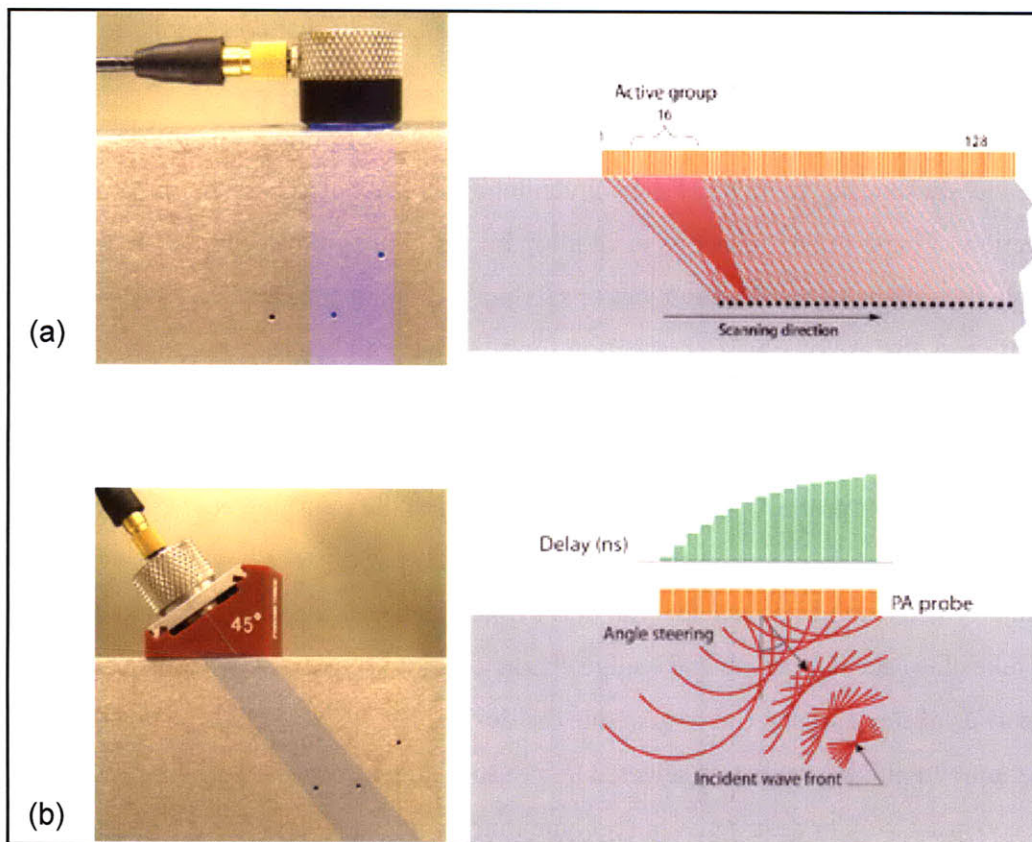


Figure 1.24: (a) Schematic of beam scanning in longitudinal E-scan (b) Schematic of beam sweeping in sectorial S-scan (adapted from [137])

1.4.3 Computed Tomography

Tomography originates from the Greek words *tomos* meaning “slice” or “section” and *graphia* meaning describing. Three dimensional x-ray computed tomography (3D-CT) is the reconstruction of a large number of two-dimensional digital radiographic (DR) projections, or slices, taken at different viewing angles around an object’s periphery with the aid of a computer [27, 144-146]. The first commercial X-ray CT system was invented in 1972 by British engineer G. Hounsfield of EMI Laboratories for medical applications [27, 145]. In the medical industry CT systems are also referred to as computerized assisted tomography (CAT) scanners [27, 147]. The medical industry continues to be the primary application for CT and over the past two decades there has been a dramatic increase in the usage of CT, with an estimated 72 million scans performed in the US in 2007 alone [144, 145, 147]. Since the early 1990’s the use of industrial computed tomography for NDT applications has seen a growing potential.

The general principles of a modern 3D-CT scanning system are shown in Figure 1.25. The three main components of the system are the x-ray source tube, the x-ray

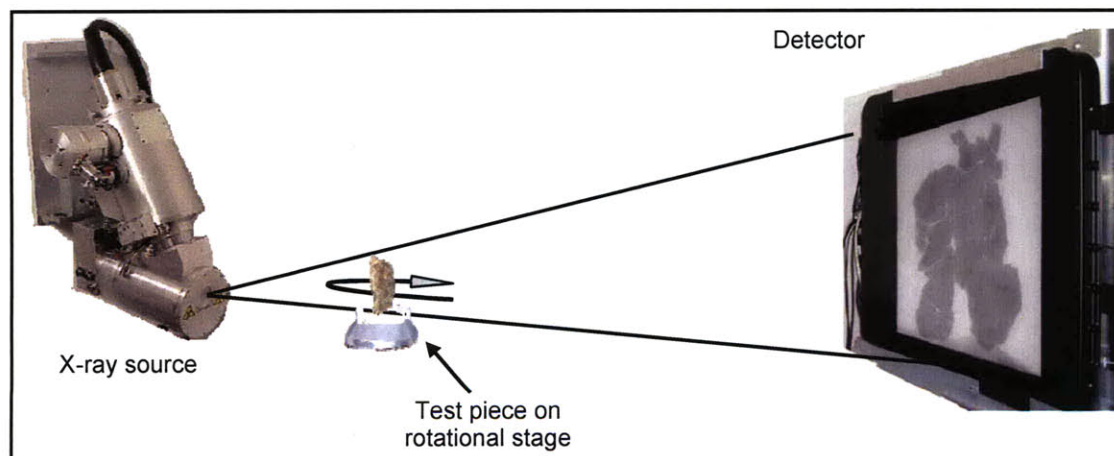


Figure 1.25: Schematic of the general components in a modern industrial 3D-CT scan (adapted from [57]).

detector, and the rotational stage. As in traditional film radiography, the x-ray source and detector lie in the same plane as the test piece. X-rays travel in straight lines and pass through the sample. Some of the x-rays are absorbed by the sample, and the fraction of the x-ray beam that is attenuated is directly related to the density and thickness of material through which the beam has traveled as well as the composition of the sample and the energy of the x-ray beam [27, 57, 58, 148, 149]. The test piece rotates 360°

during the scan with 2D projection images acquired at a rate of one image every 0.1° to 1.0° , depending on the desired resolution [149, 150]. Each projection image is between 3-10 megapixels, and is both averaged and filtered to reduce noise [149]. The 2D-DR images are used in the reconstruction and visualization of the 3D-CT volume.

Once the acquisition process of the CT scan is completed, the 3D-CT volume is rendered using computer reconstruction algorithms. The first step in the reconstruction of a CT image is the calculation of projection data. The measured transmitted intensity projection data are normalized by the expected unattenuated intensity. The values used for image normalization are represented by I_{white} and I_{black} , the intensity of the black and white reference images taken prior to CT reconstruction [27, 57]. The projection data values correspond to the integral or sum of the linear attenuation coefficient values along the line of the transmitted radiation [27, 148]. For a narrow mono-energetic beam of x-ray radiation this data can be theoretically modeled by Lambert's law of absorption:

$$I = I_0 \exp(-\mu t) \quad (1.37)$$

where I is the intensity of the beam transmitted through the sample, I_0 is the initial intensity of the beam, t is the thickness of the sample, and μ is the linear attenuation coefficient of the absorber material [27, 57, 148]. When a sample of complex geometry is considered, the intensity of radiation transmitted along a particular path is given by line integrals, also called ray sums, of the following form:

$$I = I_0 \exp \left[- \int_{\text{source}}^{\text{detector}} \mu(x, y) dt \right] \quad (1.38)$$

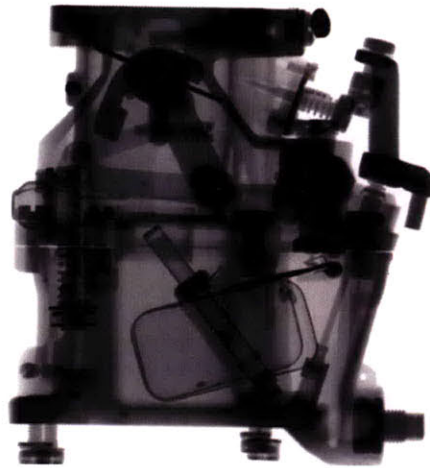
where dt is the differential of the path length along the ray. The objective of a CT reconstruction is to determine the distribution of $\mu(x, y)$ from a series of intensity measurements through the sample [27, 57]. For a particular CT scan where reference images have been taken this can be written as follows:

$$\mu = \frac{\ln \left[\frac{(I_{white} - I_{black})}{(I_{measured} - I_{black})} \right]}{t} \quad (1.39)$$

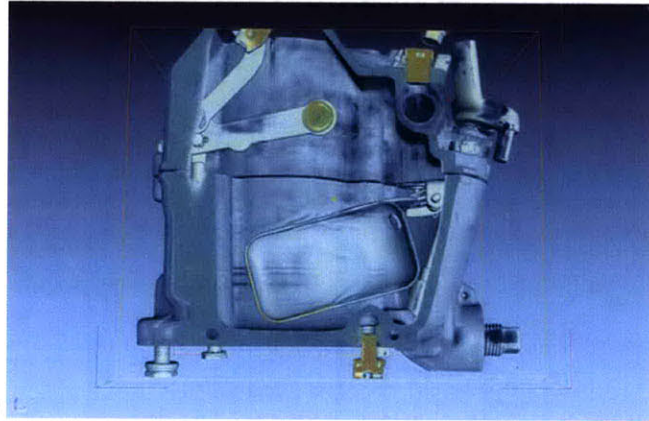
In (1.39), $I_{measured}$ is the measured intensity of the sample at a particular projection. The linear attenuation coefficients can be thought of as x-ray densities in a sample.

After the values of the linear attenuation coefficients have been determined from the reconstruction algorithms, the use of 3D visualization software can transform the pixels in each slice into voxels. A voxel, short for volume pixel, is a three dimensional pixel that contains volumetric data [145]. Years ago the generation of a few CT slices would have taken hours to complete. Technology and visualization software have progressed to the point where complete 3D models containing billions of voxels can be reconstructed in just seconds [149]. It is now possible to view slices through any internal plane of a sample and inspect for internal defects and discontinuities, as Figure 1.26 represents. This technological capability has allowed real time manipulation of 3D-CT volumes of complex samples. Also, 3D reconstructions can be directly compared to CAD model databases or other CT models in order to discern component verification via relative differences in measurements, densities, or the presence of internal defects [27, 146, 149]. This is a benefit that CT has over other NDT techniques, and which has been exploited in the reverse engineering of aerospace components [147, 148, 151]. Wall thickness measurements for turbine blades are an industrial application that has especially made use of this capability.

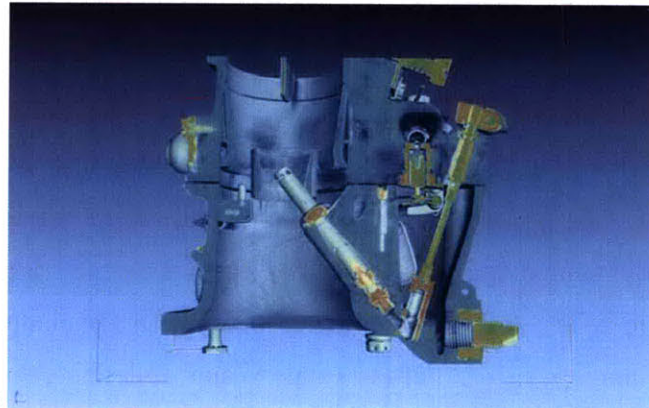
Computed tomography has detection capabilities that are dependant on the specific system and operating parameters. Many of these are the same as in traditional radiography, such as x-ray voltage and focal spot size. Some of the newer CT systems incorporate micro-focus tube instead of a traditional tube. The x-ray source in a micro-CT scan is only a few microns in length, allowing better scan resolution [57, 149]. For comparison, micro-CT resolution is 100X better than the best CAT scan in the medical field [149]. The dynamic range of the detector system is characterized by the ratio of the maximum signal to noise. An important factor affecting image quality is the amount of contrast on a CT image [27, 74]. For the image to appear defined, the black object details need to be seen as black, the white object details as white, and all the gray scale values in between need to be accurately imaged. The relative contrast between a feature and the surrounding background material is the normalized difference between the two linear attenuation coefficients [27]. In addition to image contrast, spatial resolution and image artifacts are the other primary factors that affect image quality.



(a)



(b)



(c)

Figure 1.26: (a) 2D slice of a complex component acquired during CT scan (b-c) 3D CT reconstruction of the sample with various cutaway planes for inspection of internal defects

Three dimensional CT has many benefits over traditional radiographic and other NDT techniques. The principal benefit of using 3D CT is that a complete model with both external and internal surfaces of an object is obtained nondestructively [149]. Voids, inclusions, and porosity are readily detectable high-contrast targets [27]. Separated or displaced cracks, delaminations, and machining defects are all seen when using CT. Additionally, in the reconstructed 3D model a threshold value for radiodensity can be chosen which allows different colors to represent each component of an assembly [149]. This is visible in Figure 1.26(b-c). Adding color to the reconstructed CT volume can make interpretation of flaws easier for an operator.

CT is limited by many of the same aspects of traditional radiography. Penetration of the x-rays through the sample is required. If x-ray penetration doesn't occur, the full dynamic range is not utilized resulting in poor image contrast and noisy 2D image projections. One problem with CT is that many aircraft structures have a shape with a high aspect ratio, causing difficulty with x-ray penetration in the long direction [148]. Artifacts and noise in the 2D slices can also have important effect on 3D-CT volume quality. To produce sharp detail in the CT volume an inverse filter is applied to suppress low frequency information and enhance high frequency information in the projection images [57]. Noise is usually high frequency meaning it gets enhanced, and this amplification of noise is further exaggerated when converting from a set of 2D projection images to a 3D reconstructed volume. The stability of the x-ray source is especially important in CT. Disruptive voltage variations can change the effective energy of the beam and cause image artifacts, such as the beam hardening shown in Figure 1.27. The CT system must have shielding for the safe use of the radiation. For industrial systems with x-ray sources operating below 500kV, self-contained shielding cabinet systems are often used [27, 147]. The steel/lead/steel cabinet usually ranges between 0.1-0.3 m³ (4-10 ft³), and this places a practical size limit on the potential sample that may be scanned [149]. Although not common, portable CT systems have been used to rapidly inspect trees and telephone poles *in situ* [148]. CT is a powerful technique that when used in conjunction with other NDE processes results in better flaw detection capability.

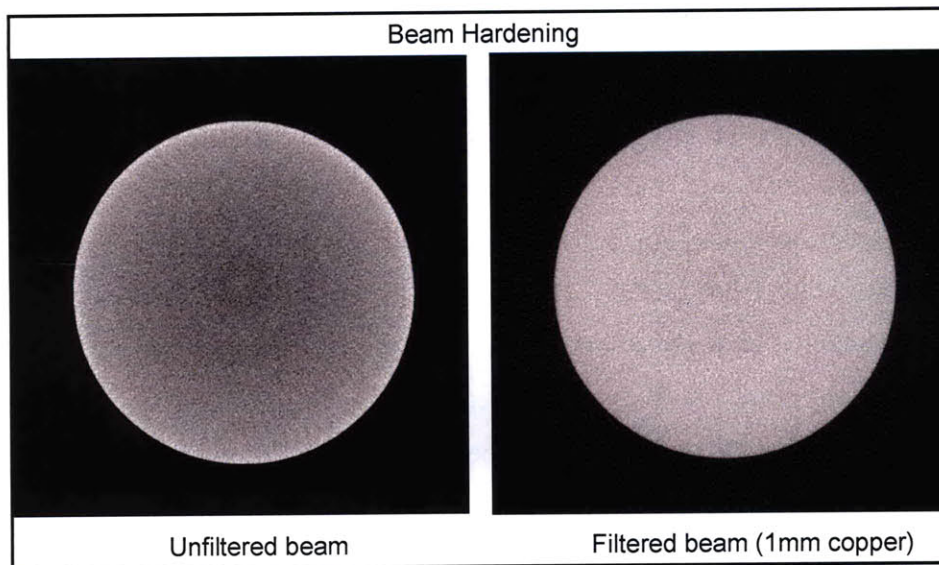


Figure 1.27: Effect of beam hardening on image quality (reprinted from [57])

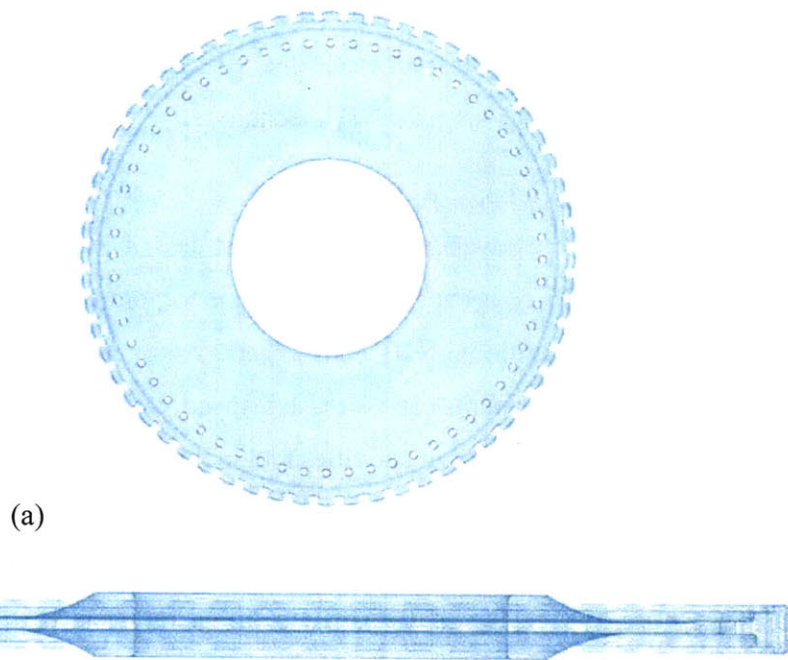
Digital radiography is used as an acquisition mode in computed tomography to obtain the 2D slices, but it is also an NDT technique in its own right. The method of data acquisition is different for DR in CT systems than when used as an individual NDT technique. In CT the high resolution detector of the rotate-only system normally requires a z-axis translation to produce a high quality DR image [27]. The principles of digital radiography when exclusively used are essentially the same as traditional film radiography; however DR has many advantages over film radiography. For over a decade the NDT community has been discussing effective x-ray film replacement methods, and in 2005 several standards were published in ASTM and ASME to support the application of DR phosphor imaging plates in lieu of x-ray film [60, 152, 153]. Besides the obvious advantage of obtaining data in a digital format without the need to develop x-ray film, amorphous silicon flat panels have been developed that are capable of being up to 100X more sensitive than film [152]. The imaging plates can be reused between 200 and 5,000 times, unlike traditional x-ray film that can only be used once [60]. The improved sensitivity enables high signal to noise ratios leading to improved POD. Digital radiography also can be set up on site, overcoming one of the shortfalls of CT in portability and sample size capability [152, 153]. Image processing times are reduced from a minimum of 12 minutes for film to about 1 minute for DR, and operators are exposed to significantly less radiation with DR [60]. Compensation principles for

enhancing digital image quality in industrial DR are described by Ewert in [153]. Digital radiography offers many benefits over traditional film radiography when used as an imaging mode in CT and as a singular NDT technique.

1.4.4 Imaging Analysis and Process Automation

In each of the three advanced techniques just described, a level of process automation and image analysis capability has been incorporated to improve reliability and sensitivity over its traditional NDT counterpart. Automation of key inspection processes for aircraft components can increase inspection repeatability, throughput, and thoroughness both in field overhaul activities and in manufacturing [102, 146]. Often, the programmable industrial robots utilized reduce overall manufacturing and inspection costs by eliminating process variability caused by human factors [95, 154]. A technique known as *error budgeting* [155] has been used with automated technology to compare the actual tolerances to the design tolerances of a manufactured product as it is being assembled. In addition to industrial robots, equipment used to increase process automation include coordinate measurement machines (CMM [27]), 3D laser scanners [156], and advanced topometric sensors (ATOS) [157]. Figure 1.28(a-b) shows two views from an ATOS scan of the disk component in Figure B.6(a). Up to 1.3 million data points can be generated from a single part measurement in a matter of minutes [157], and these points can be exported as point cloud data to compare with CAD models for component tolerance verification.

In addition to automated equipment, the use of image analysis software in conjunction with advanced NDT techniques can significantly, if not completely, remove human subjectivity from the process of flaw detection and classification. Computer technology has advanced to the point where new image recognition software systems [158-160] can automatically detect a range of flaws, surprisingly needing only a small amount of pixels. This technology can be applied to a wide range of industrial applications from microprocessors [161], photocopiers [162], and even biological cell analyses [163-165]. One of the image analysis software systems originally designed for biological cell analysis is Cellprofiler [166]. The Cellprofiler image recognition software system has previously demonstrated the capability of “scoring” diverse cellular morphologies in image-based screens with *iterative feedback* and *machine*



(b)
Figure 1.28: (a-b) Two views from an ATOS scan of the disk component in Figure B.6(a)

learning [164, 167]. Application of the *machine learning* concept to industrial NDT could significantly improve POD. If the data output from the inspection could be integrated into the image analysis software, the potential to automatically ‘learn’ where critical regions that may contain defects are located could be exploited. This option could be applied to component inspection in a production, or industrial maintenance/service environment, if a sole component was the object of the repetitive inspections and identical test parameters were selected during setup [163-165]. Medical research recently published has concluded that use of advanced imaging algorithms makes for clearer ultrasound images [168], and advances in imaging software now allow computers to be as good as a second pair of eyes at reading mammograms [169]. However, a report from the American Gastroenterological Association on a specific esophageal condition cautioned that new image analysis techniques have improved image quality but *not* diagnosis [170]. This shows human error factors involved in the interpretation of an inspection image is not a challenge unique to the industrial NDE of structural components. Many of the advanced NDT techniques proposed were originally developed for the medical industry, so a lot can be gained by adapting procedures used in

medical inspections to industrial NDE. An example of this idea put into practice was the adaptation of the Cellprofiler imaging software for use in the POD analysis of the aluminum alloy wedding cake, which is discussed in Chapter 5.

Results from inspections that utilize image analysis software could serve as baseline references for flaw detection in future inspections. Another potential outcome from the integration of digital NDT techniques and image analysis software could be the ability to “map and track” accumulated damage in a structural component after an indication has been observed [112]. Methods to secure these images from tampering or alteration, such as generating a date-stamped image quality database [162], are beyond the scope of this discussion. However, including those types of controls on digital data generated by NDT systems is a necessity to the concept’s feasibility in an industrial environment. Since the mid-1980’s, the DICOM (Digital Imaging and Communication in Medicine) standard has been applied to the generation and distribution of medical images [171]. More recently, the DICOM standard has been adapted by the NDT industry as digital inspection techniques have demonstrated reliability and become more accepted in industry [171-173]. DICONDE is the term used when the DICOM standard is applied to the nondestructive evaluation of structural components. In 2006, ASTM Standard E2339 [172], *Standard Practice for Digital Imaging and Communication in Nondestructive Evaluation (DICONDE)*, was introduced. The standardization of industrial best practices, in this case for nondestructive testing techniques that incorporate progressive digital technologies, is an important step toward gaining regulatory approval to allow a new methodology on structural component life prediction to be implemented.

1.5 Background on Airplane Engine Inspection Methodology

Inspection methodologies for airplane engine components have evolved over the years. Often catastrophic failures resulting in the loss of life, such as the 1989 accident in Sioux City, have precipitated regulatory changes made by the FAA. The number one mandate of the FAA is to ensure the safety of the general flying public [6, 13, 14], and life prediction models are used to make judgments on the level of aircraft safety. Life prediction models generally fall under two broad categories: a parametric approach or a physics-based approach [174, 175]. Parametric approaches are based on empirical observations, and do not attempt to separate processes such as creep and fatigue in

accumulated damage calculations. Fatigue life prediction has historically been based on safe-life or crack-growth approaches, both of which are empirically based [38, 39]. On the other hand, physics-based approaches do attempt to distinguish the various damage mechanisms by taking component microstructure into account [174, 175]. Damage tolerant (DT) design is a type of physics based model. Despite this enhancement, a level of empiricism cannot be avoided even in physics-based models, due to the difficulty in uniquely identifying and accurately modeling the complex linkage between damage indicators at the microstructural level [38, 39, 174, 176]. Consequently, neither safe-life nor damage tolerant approaches adequately represent the long-term operating conditions in aging aircraft. Neither attempts to identify the sources of variability nor the extent to which these sources contribute to variability in component life.

1.5.1 Safe Life/Damage Tolerant Approach

The incorporation of damage tolerance assessments to the safe life approach has resulted in the “enhanced” life management process currently accepted in the design and operation of aircraft engine. The aspects of this enhanced life management process are portrayed in Figure 1.29. The safe-life approach is a low cycle fatigue-based process in which components are designed and substantiated to have a specified service life, which is stated in operating cycles, operating hours, or both. This approach requires that parts be removed from service prior to the development of an unsafe condition, and when a component reaches its published life limit, it is retired from service regardless of its condition [2-9].

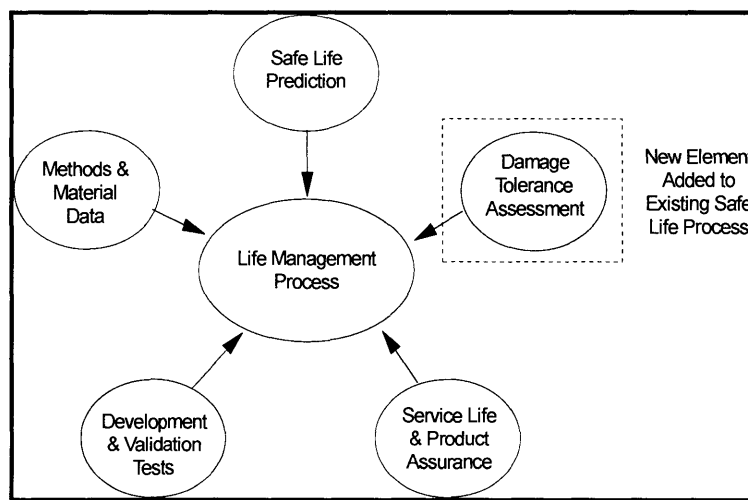


Figure 1.29: Aspects of the enhanced life management process (reprinted from [8])

The United States Air force (USAF) initiated the Aircraft Structural Integrity Program (ASIP) in 1958 and this is where the “safe-life” process originated [17]. Aircraft failures in service arising from the safe-life process demanded a fundamental change be made in the approach to design, qualification, and inspection of aircraft. The DT approach emerged as the candidate chosen for this change and was formally integrated into ASIP in 1975 [17]. Damage tolerance is an element of the life management process that recognizes the potential existence of component imperfections that are the result of inherent material structure, material processing, component design, manufacturing, or usage [2-9]. Damage tolerance addresses this situation through the incorporation of fracture resistant design, fracture-mechanics, process control, or nondestructive inspection. When the safe-life/damage tolerant approach is used, a probabilistic risk assessment is obtained that is compared to a DTR value to satisfy FAA requirements. A probabilistic risk assessment is defined by the FAA as:

“A fracture-mechanics based simulation procedure that uses statistical techniques to mathematically model and combine the influence of two or more variables to estimate the likelihood of various outcomes for a product. Since not all variables may be considered or may not be capable of being accurately quantified, the numerical predictions are used on a comparative basis to evaluate various options. Results from these analyses are typically used for design optimization to meet a predefined target or to conduct parametric studies [6-9].”

This type of procedure differs from an absolute risk analysis, which attempts to consider all significant variables, and is used to quantify, on an absolute basis, the predicted number of future events with safety and reliability ramifications [6-9]. Incorporation of an absolute risk assessment would allow component retirement for cause rather than retirement at a specified service life.

The safe-life/damage tolerant approach currently used for critical aerospace engine components is part of the Engine Structural Integrity Program (ENSIP) and was developed primarily from experimental data. There is a risk associated with the use of

empirical models that do not effectively reflect the influence of internal variables such as microstructure and operating environment. As many researchers [23, 38, 39, 176-178] have pointed out, empirical models that are based on statistical fleet wide data are only appropriate for interpolations over the available data. In addition, most of the data used to construct these empirical models is generated through accelerated testing, and as such may not adequately reflect long term operating characteristics. Rummel [24-26] made the point that anomaly-containing structural components whose degradation or failure results in a catastrophic event are typically statistical outliers, and therefore are not captured by statistical distributions of empirical fleet wide data. For instance, previous investigations have shown empirical approaches to creep life prediction, such as the Larson-Miller parameter, can be off by as much as a factor of 20 relative to observed field experience [106, 175]. Identification and quantification of these internal variables is critical to the prediction of damage evolution and accumulation [38, 39]. The methodology of Chapter 6 is fundamentally distinct from the safe-life methodology in its approach to structural health monitoring.

1.5.2 Structural Health Monitoring

Structural health monitoring (SHM) is the process of implementing a damage detection and characterization strategy for engineering structures. Real structures in service are not inherently defect free, as assumed in the safe-life methodology [179], and therefore contain flaws. These flaws may be pre-existing from the manufacturing process or may be formed during service with the application of stress [32-34, 180]. *Fitness-for-service* is the quantitative engineering evaluation of the suitability for continued service of equipment that is known to contain flaws [32, 33, 35, 181, 182]. For the current life methodology depicted by the flowchart in Figure 1.30, NDT is but one aspect of SHM among many required to obtain life certification approval [6, 7]. Other empirically observed variables weigh heavily upon the life limit that is ultimately approved. The design target risk, DTR, is the design metric used in probabilistic risk assessments based on the conventional life management approach. The DTR metric defines the risk of a component failure at the end of design life [23], however failure often occurs before the end of design life has been reached. Component degradation during service is inevitable,

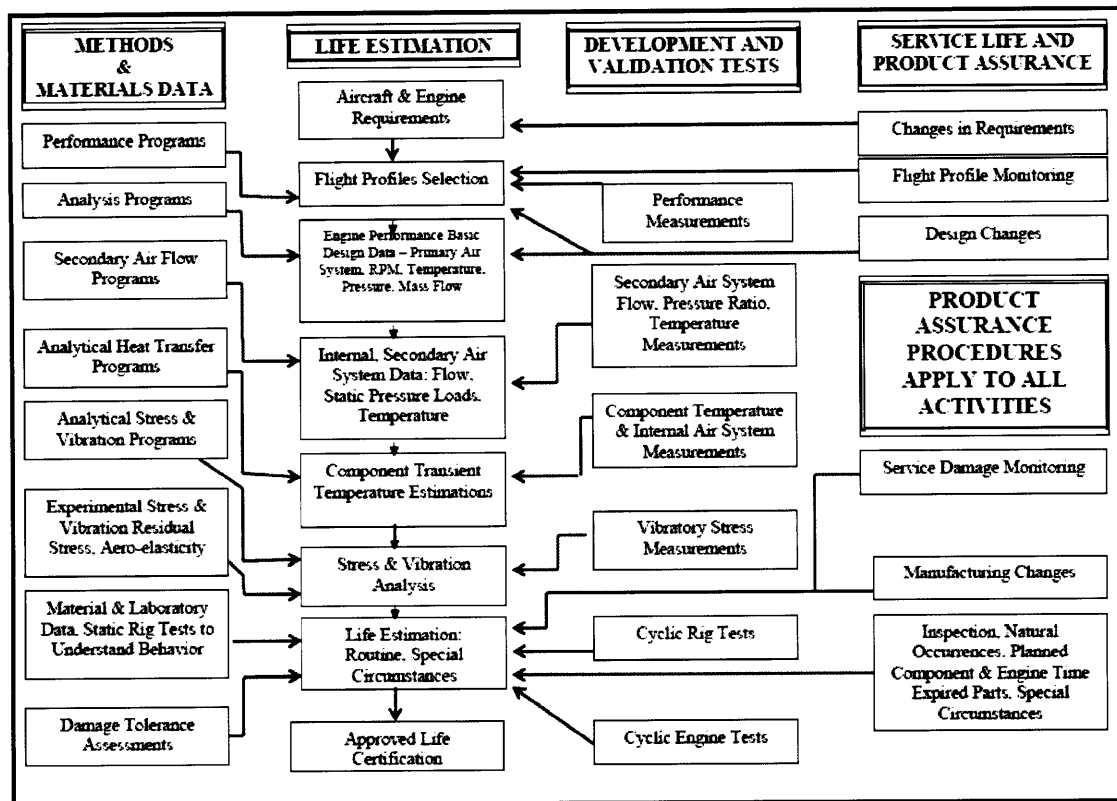


Figure 1.30: SHM aspects of the conventional life management process (reprinted from [6])

and this degradation is the driving factor in component failure. An in-service metric that provides the instantaneous risk of failure for a component during service is more useful to remnant life prediction than the DTR metric. One such metric is the single flight probability of failure, which is calculated from all available service data to calculate the risk of failure in the next operating cycle [23]. The use of advanced NDT techniques implies that more reliable data would be available to make a better informed judgment as to the single flight POF.

The current life management methodology uses a very reactive approach to structural health monitoring. This approach calls for “hard”, mandatory inspection intervals based on DTR values, with “soft”, non-mandatory inspections to be performed when the opportunity presents itself [2, 9, 11]. If no detections are found during these soft inspections, the number of cycles allowed until the next hard inspection is essentially the full DTR value starting from zero cycles if disassembly of the module is not required. Visual inspection, FPI, and ECI are the methods most often used with these hard and soft inspections. Typically, hot gas path components are inspected by FPI or ECI during full

tear-down (i.e. hard) inspections once every 2-3 years [106]. Additionally, design credits may be given for fracture resistant features, such as shot peening, that demonstrate a reduction in the potential for failure [2-4, 6, 7]. These design credits may significantly affect the FAA certified DTR value, but variability in quality control of the surface treatment process is not considered. In the 1989 Sioux City crash, statistical data indicated the fan module was disassembled for maintenance once every 2,500 cycles [119]. Fracture mechanics analyses performed after the accident indicated the threshold detectable defect size in the most critical area of the fan disk, based on the immersion-UTI process, was a 2.5mm (0.1 inch) radius crack, resulting in a predicted residual life of 1,500 cycles [119]. However, that methodology did not account for the missed FPI of a detectable crack 760 cycles before catastrophic failure.

If an off-design condition occurs during service, the FAA allows many options to achieve the certified DTR value. Some of these options are included in Table 1.8. As recently as January 2009 [1], the FAA issued a memorandum on a shortfall in the current

Table 1.8: Options allowed by the FAA to satisfy DTR values in the event of an off-design condition

• Component redesign
• Material changes
• Material process improvements
• Manufacturing process improvements
• Manufacturing inspection improvements
• Enhanced in-service inspections
• Life limit reductions

LLP assessment methodology. In previous instances when a known unsafe condition existed, the FAA worked on a case-by-case basis with the engine part OEM/MRO and airline owner to remedy the situation [11]. The actions taken in these cases typically included inspection, repair, or replacement of specific primary structural parts. However, the FAA has acknowledged that in-service experience has shown actions taken to address one unsafe condition have allowed subsequent unsafe conditions to develop [11, 13, 14]. The enhanced life methodology proposed in Chapter 6 is proactive rather than reactive in its approach to structural health monitoring. The proactive approach calls for enhanced

in-service inspections combined with inspection redundancy. State-of-the-art NDT techniques that utilize advanced technologies are a fundamental component of the approach presented. The digital capabilities of these advanced techniques enable damage accumulation to be uniquely tracked throughout the life of individual components, as opposed to assuming a level of damage based on average fleet wide data. This methodology allows a retirement for cause (RFC) approach to be implemented for critical aerospace components.

1.5.3 Retirement for Cause Approach

Aspects of the life management process currently regulated by the FAA, and detailed by the flowchart in Figure 1.30, incorporate the safe-life/damage-tolerant methodology. The guidelines and public policy formed by the methodology stem from data and conclusions drawn in previous reports, such as SP-1270 [110, 116, 117]. Conflicting opinions on the part of industry members who comprised the SP-1270 committee resulted in the document taking nine years to complete without consensus being reached [110]. Consensus was not obtained on specific conclusions made about engine component safety, drawn from selective analysis of the uncontained event data. One particular point of contention among the committee members involved discussion of the safety results for the CT subclass called “Second-Generation” high bypass turbofans. This subclass of engines was introduced into service during the 1980’s, and incorporated new technology, design improvements, and improved manufacturing processes [110]. In particular, the committee could not agree on a statement attributing no Category 3 or 4 events to this engine subclass, with the resulting safety improvement due in large part to advances in design technology used with these engines. Since the publication date of SP-1270 in 1990, uncontained engine events and catastrophic failures have occurred in these engines in spite of those design improvements. An additional example that would have been included in the AIR4003 report was the 1983 rupture of a GE CFM-56 stage 1 HPC rotor disk having only 256 cycles [121]. This particular disk incorporated advanced triple-melt VIM+ESR+VAR technology, yet a hard alpha anomaly still went undetected during inspection and resulted in failure [121]. While technological advances in processing and design have improved the quality of critical rotating components, only a

robust in-service NDT/NDE methodology can ensure the detection of these rare anomalies in specific components prior to catastrophic failure.

The retirement-for-cause (RFC) lifing concept involves the periodic nondestructive evaluation of components to assess their current damage state. This approach allows parts with low remnant life to be detected and discarded before they can cause an incident, and parts with high remnant life to be used to their full potential [183]. Damage tolerance is used to its fullest extent when the RFC concept is employed. Contrary to the safe-life process, where components are retired at a specified time when 0.1% of them may theoretically have an initiated fatigue crack 0.8mm (0.030 in.) in length, the RFC approach allows the continual return to service for components as long as irreversible damage has not been detected during inspection. This is shown schematically in Figure 1.31. Intrinsic to this approach is knowledge of the threshold flaw size that is just below the detection limit of the NDT technique employed. This threshold flaw size becomes the starting crack size for the fracture mechanics analysis. The RFC approach permits continued inspection and service of a component, primarily a disk, until the point in time where accumulated damage reaches a condition where the component must be retired for cause.

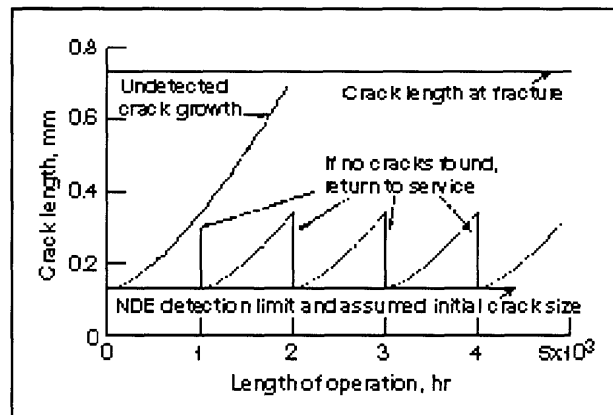


Figure 1.31: Fatigue crack growth under a RFC inspection approach. Parts are inspected every 1000 hrs. (reprinted from [183])

Chapter 2: MWM-array® Eddy Current Inspection

Chapter 1 has provided a background on the science and theory of the three advanced NDT techniques proposed for the improved critical component remnant life methodology. A discussion on inadequacies associated with certain elements of the safe life/damage tolerant methodology has also been included in this introductory chapter to show there are opportunities for improvement that can potentially extend the operating lives of critical life-limited parts. Chapters 2, 3, and 4 provide results from experiments performed on each of the advanced NDT technologies. The experiments were meant to quantify the sensitivity of each technique while collecting data in the form of C-scan digital images and A-scan signal to noise ratio plots. The C-scan image data is presented to allow a visual comparison of the “advanced” techniques to be made with their “traditional” counterparts. Chapter 2 examines the MWM-array® eddy current inspection technique. The first section of this chapter details the sample design and preparation for the different test specimens utilized in the experimentation. Three different sample types of varying size and increasing geometrical complexity were analyzed. Samples are classified as alloy blocks, “wedding cake” samples, or actual engine components. Sample preparation is only described in Chapter 2 to avoid repetition in subsequent chapters. The experimental procedures are described independently for each technique in the next three chapters.

2.1 Sample Preparation

It has previously been explained in Chapter 1 that certain NDT processes are not always applicable to the detection of particular flaw types in a component. For instance, eddy current inspection is most sensitive to surface cracks and is not really appropriate for detection of deep embedded flaws, while the acoustic transmission of sound waves in UTI allows for deep penetration through thick samples. In the attempt to design a robust NDT reliability test matrix multiple sample categories were needed. The range of samples span Ni-base superalloy and Ti-alloy test blocks containing arrays of identically sized holes drilled into a flat surface, layered wedding cake samples containing a bevy of varying sized flat bottom and side drilled holes at different locations and depths, an engine duct segment component with surface cracks, and finally turbine blades of

complex geometry that contain flaws generated during service repair welding operations. These specimen classes encompass flaws in the surface, near-surface, and subsurface regimes. Because of specimen geometry or size constraints not every sample was inspected with every proposed technique. In the following chapters, experiments that have been performed are discussed. If particular samples have not been tested by a certain method an explanation for the exclusion is provided.

2.1.1 Alloy blocks

A set of alloy test blocks were loaned to the author from the Center for NDE (CNDE) at Iowa State University. These test blocks were fabricated as part of the Engine Titanium Consortium (ETC) phase I program, under the auspice of the FAA. The objective of the ETC was to promote collaboration among industry, academia, and the FAA in the search for reliable, cost-effective new methods and improvements in mature technologies for detecting cracks, inclusions, and imperfections in premium rotor-grade Ti-alloys [184]. In Chapter 1 it was stated that titanium is an ultrasonically noisy material, and this can result in false positive indications or missed detections upon inspection. These alloy block specimens were originally manufactured as part of a fundamental study to quantify the inspection properties of Ti-alloys used in jet engines. The full details and results from that study can be found in a 2002 FAA document titled *Report No. DOT/FAA/AR-02/114* [184]. The block samples were designated by the letters A through N in the 2002 report. This designation will also be used in the present work to differentiate between samples.

The experiments performed for this research project fundamentally differ from those of *Report No. DOT/FAA/AR-02/114*. In the 2002 FAA report, velocity, attenuation, and noise figure of merit (FOM) measurements were made on the alloy blocks using a common set of ultrasonic transducers. The objective of the tests described in Chapters 2-4 was to examine the detection capability of progressive NDT techniques based on threshold flaw size and flaw depth measurements. For this reason, not all of the 14 alloy block samples (A through N) were applicable. The relevant samples were H, L, U, and an undesignated sample that will be referred to as the R88 block, because these were the only samples that contained a 3x3 array of flat bottom holes (FBH). These alloy block samples are shown in Figure 2.1(a-d). In all four samples, every hole in the 3x3 array

had a diameter of approximately 0.4 mm (0.016 in.). This hole diameter is known in the industry as a #1 FBH, because it is equivalent to 1/64th of an inch. A close-up view of the 3x3 FBH array for Sample R88 is pictured in Figure 2.2. The FBH array was drilled to a depth of 6.3 mm (0.25 in.) into one flat face on the R88 and H samples. Sample U had arrays drilled into two faces and Sample L had arrays drilled into three orthogonal faces, but testing of one array-containing surface was deemed sufficient to demonstrate flaw detection capability.

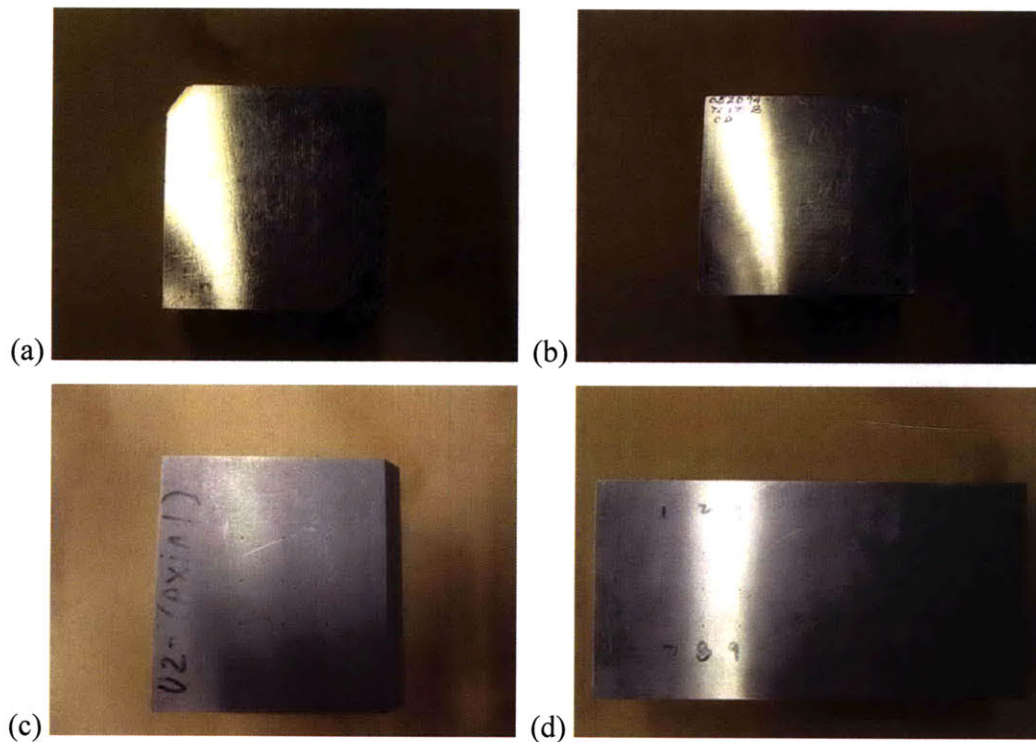


Figure 2.1: (a) Sample H (b) Sample L (c) Sample U (d) Sample R88



Figure 2.2: Close up view of 3x3 array of #1FBH on Sample R88

The four alloy block samples were fabricated from different raw materials. Sample H was cut from the outer diameter (OD) region of a 23.5 cm (9.25 in.) diameter billet manufactured from Ti-6Al-4V raw material. Sample L was cut from the near OD region of a 17.8 cm (7.0 in.) diameter billet manufactured from Ti-17 stock. Sample U was cut from the aft rim region of a large Ti-6-4 forged disk. The R88 sample was manufactured from Rene' 88, a Ni-base superalloy processed via the powder metallurgy technique. The dimensions for all the blocks tested were approximately 7.6 x 7.6 x 7.6 centimeters (3x3x3 in.), except for the R88 reference block sample which was 15.2cm x 7.6cm x 7.6cm (6x3x3 in.). As Figure 2.1(a) shows, on some of the alloy block samples one edge was beveled. This was done as part of the original attenuation measurements and did not impact the data collected or results drawn from this project.

2.1.2 Wedding Cake Samples

The second class of test specimens are referred to as a “wedding cake” samples because of their multi-layer design. The wedding cake design was selected due to the abundance of data related to the NDT system coverage and sensitivity that can be obtained from a single sample. An additional reason for selection of a wedding cake design was the geometrical similarities with more complex engine disk components, thus enabling reasonable conclusions on the POD capability of actual disk-shaped LLPs to be drawn from wedding cake inspection data. Figure 2.3 depicts a CAD model of the original wedding cake design. Two alloys were chosen from to machine the wedding

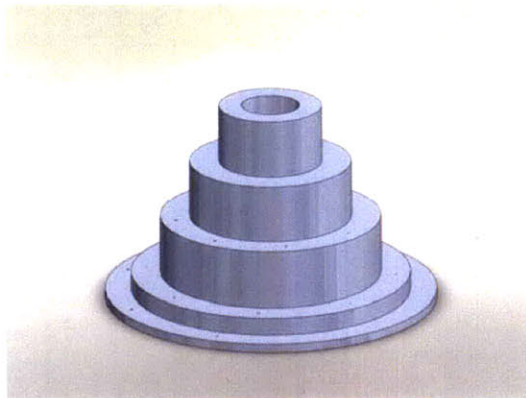


Figure 2.3: CAD model of the original wedding cake sample design
cake samples: a 6061-T6 aluminum alloy and an 8620 steel alloy. These alloys were selected in lieu of traditional aerospace engine alloys due to their machinability,

availability, and also to enable a comparison to be made of the various NDT system responses between alloys of relatively high and low value with respect to modulus and density. Values of selected physical properties for the 6061-T6 aluminum and 8620 (chrome-nickel-molybdenum) steel alloys are provided in Table 2.1.

Table 2.1: Selected physical property data for the 6061-T6 aluminum and 8620 steel alloys

Material	Tensile Strength		Yield Stress		Brinell Hardness	Density	
	(MPa)	(psi)	(MPa)	(psi)		(kg/m ³)	(lb/ft ³)
Al 6061-T6	310	45000	276	40000	95	2700	169
Steel alloy 8620	669	97000	393	57000	201	7872	491

The samples were machined in the Welding and Joining Laboratory at MIT on a Southwestern Industries Proto Trak SLX ® CNC lathe [Model:TRAK 1630 SX]. To obtain the sample profile shown in Figure 2.3, the wedding cake samples were turned down from cylindrical rod stock of 61 cm (2 ft.) length and 15.2 cm (6 in.) diameter. Figure 2.4 contains images of various machining processes performed during the wedding cake sample preparation. As shown in Figure 2.4(b-d), a 30.5 cm (1 ft.) length piece of cylindrical stock was clamped in the chuck region, stabilized with a centering tailstock quill, and the layers of the wedding cake were turned down from the tailstock end and cut off with a flat end mill attachment. The CNC lathe was programmed to add a small fillet between the base and surface of adjoining layers to provide a smooth transition rather than a hard edge between layers of the sample.

All of the machined wedding cake samples consisted of five layers, also referred to as levels, of varying height and outer diameter. A total sample height of 8.9 cm (3.5 in.) was specified. Heights for the individual levels are shown in Figure 2.5. The outer diameter of Level 1 was 13.2 cm (5.2 in.) in diameter, and when the sample is oriented as in Figure 2.5 this is the base level. The OD was 10.8 cm (4.3 in.) for Level 2, 8.3 cm (3.3 in.) for Level 3, 6.4 cm (2.5 in.) for Level 4, and 4.4 cm (1.75 in.) for Level 5. A 2.54 cm (1.0 in.) inner diameter (ID) center hole was bore out of the aluminum and steel alloy wedding cake samples tested. A drill bit broke and fused within the center hole region while machining a second steel alloy sample. The broken drill bit was machined flush with the base of the sample and plugged. The appearance of this sample is

illustrated in Figure 2.6. This sample was tested to determine the capability of detecting the embedded drill bit defect. Additionally, this steel sample had a total of 18 FBH of varying diameter located on Levels 1-3.

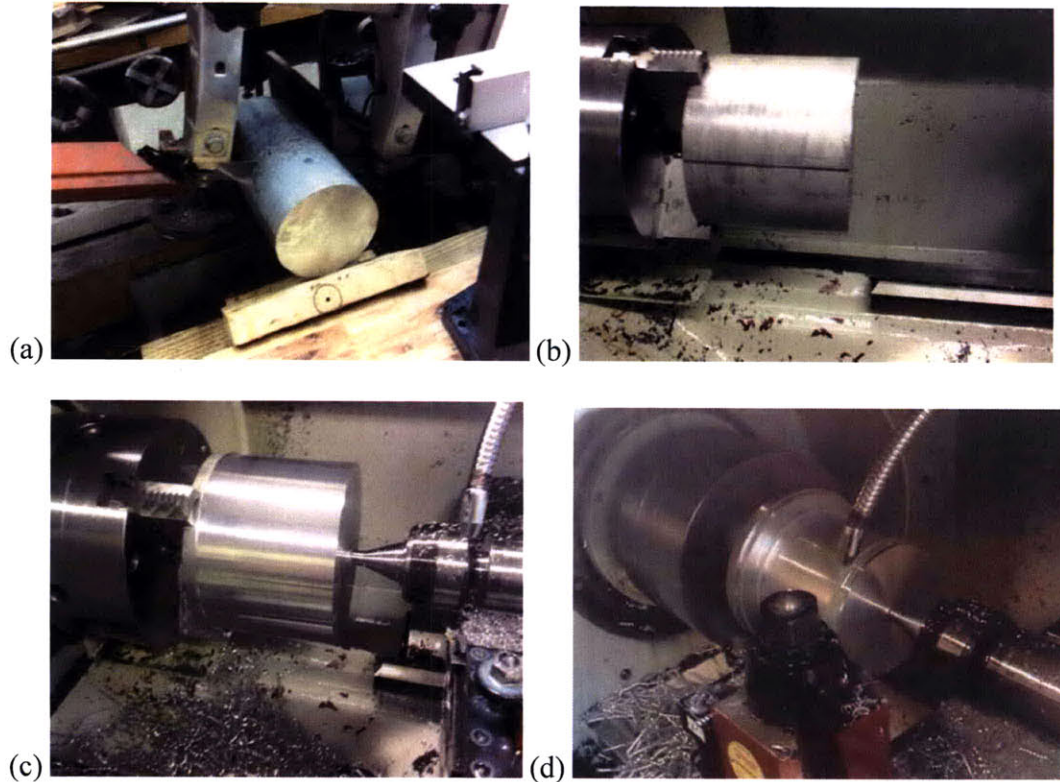


Figure 2.4: Machining processes performed in the wedding cake sample preparation (a) Cutting cylindrical rod stock in half on band saw (b) clamping cut stock in chuck of CNC lathe (c) stabilizing stock with centering tailstock quill (d) turning down the layers of the wedding cake sample

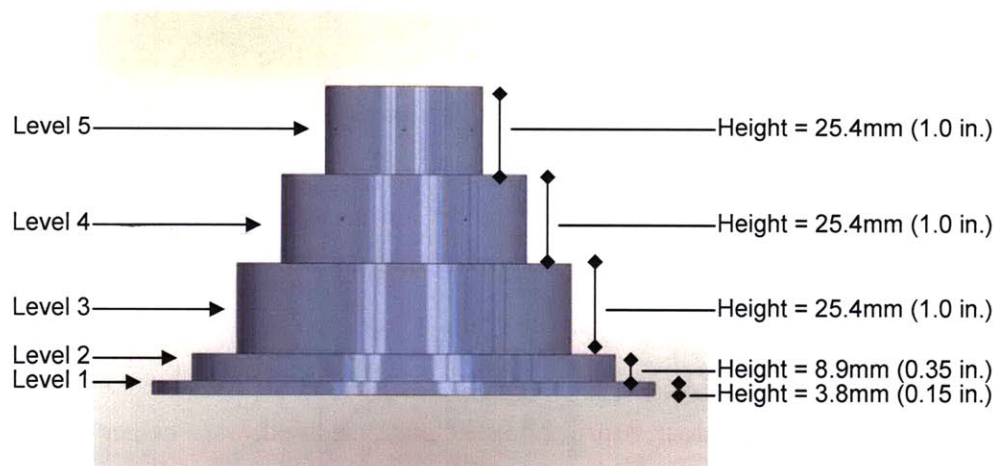


Figure 2.5: The specified heights for the five levels in the wedding cake specimens

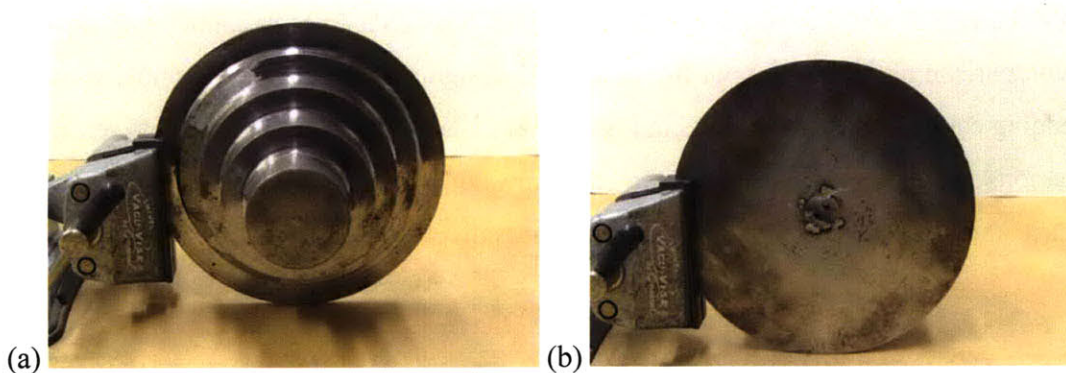


Figure 2.6: (a) Front-side top down view of embedded defect sample (b) Back-side view of the embedded drill bit defect from the rear base of Level 1

For the two wedding cake samples containing the ID center hole, simulated defects of varying sizes and orientations were incorporated during sample fabrication. On these samples eight FBH per level, ranging in diameter from 0.254 mm (0.010 in.) to 1.27 mm (0.050 in.), were placed on Levels 1-3 via a laser drilling process. The laser drilling procedure was performed at an aerospace MRO facility in Orangeburg, NY. The eight holes drilled for each of the lower three layers were placed at 45° intervals along the sample circumference and were centered approximately halfway between the difference in radial length of adjacent levels. Since the total difference in OD length ranged from 1.9-2.54 cm (0.75-1.0 in.) for the various adjoining levels, the holes were drilled at a horizontal distance of approximately 4.8-6.3 mm (0.19-0.25 in.) into the sample from the outer edge of each level. The 0° reference starting position for the initial flat bottom hole was offset by 15° between Level 1 and Level 2, and an additional 15° between Level 2 and Level 3. Figure 2.7(a-b) shows a transparent view of the FBH layout from a top-down and bottom-up perspective. Variability and inconsistency in laser intensity during the hole drilling process required the use of a pin gage set to verify all specified FBH diameters. A pin gage set [Fowler Co. Inc., Boston MA] with gage members that ranged from 0.152-1.52 mm (0.006-0.060 in.) in diameter was used to verify FBH diameter sizes. The gage set had a 25.4 μm (1×10^{-3} in.) size interval between nearest members and a tolerance of $\pm 5.1 \mu\text{m}$ (2×10^{-4} in.). The hole diameters were found to be within $\pm 25.4 - 76.2 \mu\text{m}$ (0.001-0.003 in.) of the specified hole layout. On both Level 4 and Level 5, six side drilled features were machined into the surface edge at a perpendicular angle using a wire EDM. These features will be referred to as SDH even though they are technically

not circular holes. Like the flat bottom holes they too varied in both diameter and length. A comparison of the hole layout from the CAD design with the fabricated 6061 Al-alloy wedding cake sample is presented in Figure 2.8(a-b). Pin gage dimensions and reference locations for each hole feature in the aluminum wedding cake sample are provided in metric units in Table 2.2 and US customary units in Table 2.3.

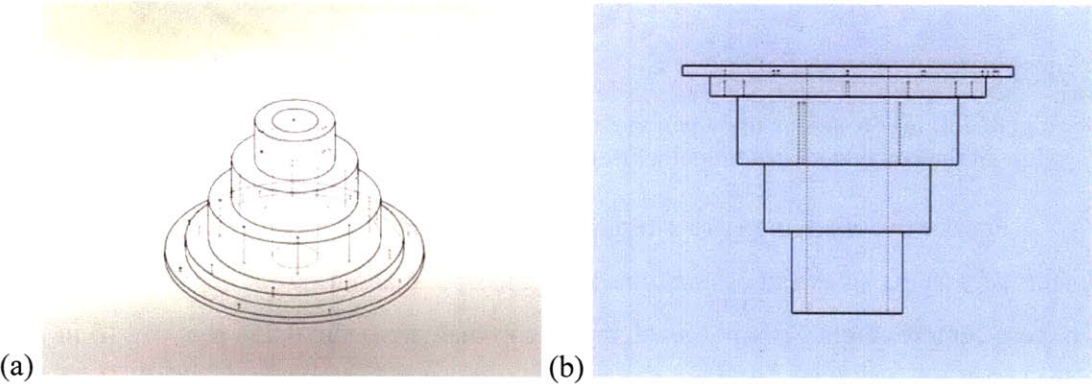


Figure 2.7: (a) Top-down and (b) Bottom-up perspective of the specified hole layout

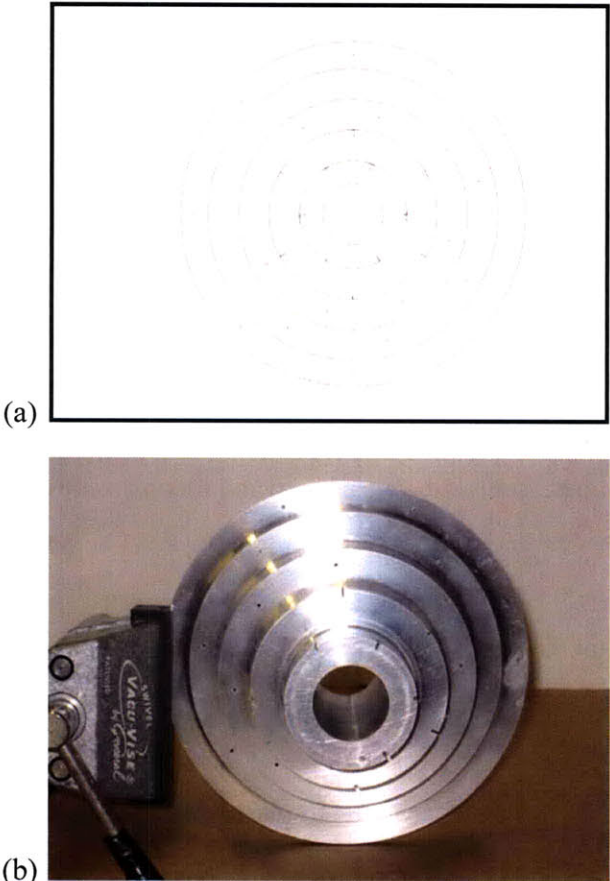


Figure 2.8: Comparison of the hole layout from (a) sample CAD design and (b) fabricated sample

Table 2.2: Hole measurements in SI units for the aluminum alloy wedding cake sample

Level	Level Thickness (mm)	Hole	Hole Drill Depth (mm)	FBH Diameter (mm)	Radius (mm)	θ	X	Y
1	3.8	1	2.032	0.3048	66.04	0	66.0400	0.0000
		2		0.4064		45	46.6973	46.6973
		3		0.8128		90	0.0000	66.0400
		4		0.5334		135	-46.6973	1.8385
		5		1.1684		180	-66.0400	0.0000
		6		1.3208		225	-46.6973	-46.6973
		7		0.9906		270	0.0000	-66.0400
		8		0.3048		315	46.6973	-46.6973
2	8.9	9	5.588	0.5080	54.17	15	52.3199	14.0191
		10		0.3810		60	27.0828	46.9087
		11		0.7620		105	-14.0191	52.3199
		12		0.3556		150	-46.9087	27.0828
		13		0.3810		195	-52.3199	-14.0191
		14		0.7620		240	-27.0828	-46.9087
		15		1.1684		285	14.0191	-52.3199
		16		1.1684		330	46.9087	-27.0828
3	25.4	17	23.114	0.4826	41.47	30	35.9102	20.7328
		18		0.4826		75	10.7321	40.0526
		19		0.8890		120	-20.7328	35.9102
		20		0.4572		165	-40.0526	10.7321
		21		1.3462		210	-35.9102	-20.7328
		22		1.0922		255	-10.7321	-40.0526
		23		1.0922		300	20.7328	-35.9102
		24		1.0160		345	40.0526	-10.7321
Level	Level Thickness (mm)	Hole	SDH Diameter (mm)	SDH Length (mm)	SDH Depth (mm)			
4	25.40	1	0.203	1.270	12.700			
		2	0.254	2.032	12.700			
		3	0.559	1.651	12.700			
		4	0.787	2.413	12.700			
		5	1.321	1.397	12.700			
		6	1.270	2.540	12.700			
5	25.40	7	0.279	2.286	12.700			
		8	0.254	1.270	12.700			
		9	0.584	2.540	12.700			
		10	0.737	1.397	12.700			
		11	0.965	2.540	12.700			
		12	1.219	1.270	12.700			

Table 2.3: Hole measurements in US customary units for the Al-alloy wedding cake sample

Level	Level Thickness (in)	Hole	Hole Drill Depth (in)	FBH Diameter (in)	Radius (in)	θ	X	Y
1	0.15	1	0.08	0.0120	2.6	0	2.6000	0.0000
		2		0.0160		45	1.8385	1.8385
		3		0.0320		90	0.0000	2.6000
		4		0.0210		135	-1.8385	1.8385
		5		0.0460		180	-2.6000	0.0000
		6		0.0520		225	-1.8385	-1.8385
		7		0.0390		270	0.0000	-2.6000
		8		0.0120		315	1.8385	-1.8385
2	0.35	9	0.22	0.0200	2.133	15	2.0598	0.5519
		10		0.0150		60	1.0663	1.8468
		11		0.0300		105	-0.5519	2.0598
		12		0.0140		150	-1.8468	1.0663
		13		0.0150		195	-2.0598	-0.5519
		14		0.0300		240	-1.0663	-1.8468
		15		0.0460		285	0.5519	-2.0598
		16		0.0460		330	1.8468	-1.0663
3	1.00	17	0.91	0.0190	1.633	30	1.4138	0.8163
		18		0.0190		75	0.4225	1.5769
		19		0.0350		120	-0.8163	1.4138
		20		0.0180		165	-1.5769	0.4225
		21		0.0530		210	-1.4138	-0.8163
		22		0.0430		255	-0.4225	-1.5769
		23		0.0430		300	0.8163	-1.4138
		24		0.0400		345	1.5769	-0.4225
Level	Level Thickness (in)	Hole	SDH Diameter (in)	SDH Length (in)	SDH Depth (in)			
4	1.00	1	0.008	0.050	0.500			
		2	0.010	0.080	0.500			
		3	0.022	0.065	0.500			
		4	0.031	0.095	0.500			
		5	0.052	0.055	0.500			
		6	0.050	0.100	0.500			
5	1.00	7	0.011	0.090	0.500			
		8	0.010	0.050	0.500			
		9	0.023	0.100	0.500			
		10	0.029	0.055	0.500			
		11	0.038	0.100	0.500			
		12	0.048	0.050	0.500			

2.1.3 Actual Engine Components

The third class of specimen was actual airplane engine components. This included three 1st stage HPT blades that were removed from service due to defects introduced during weld repair operations. Front, back, and top views from one of these blades are showcased in Figure 2.9(a-c). Defects included post-weld tip crack and weld drop through anomalies. These blades were manufactured from PW1484, a Ni-base superalloy used in the manufacture of turbine blades.

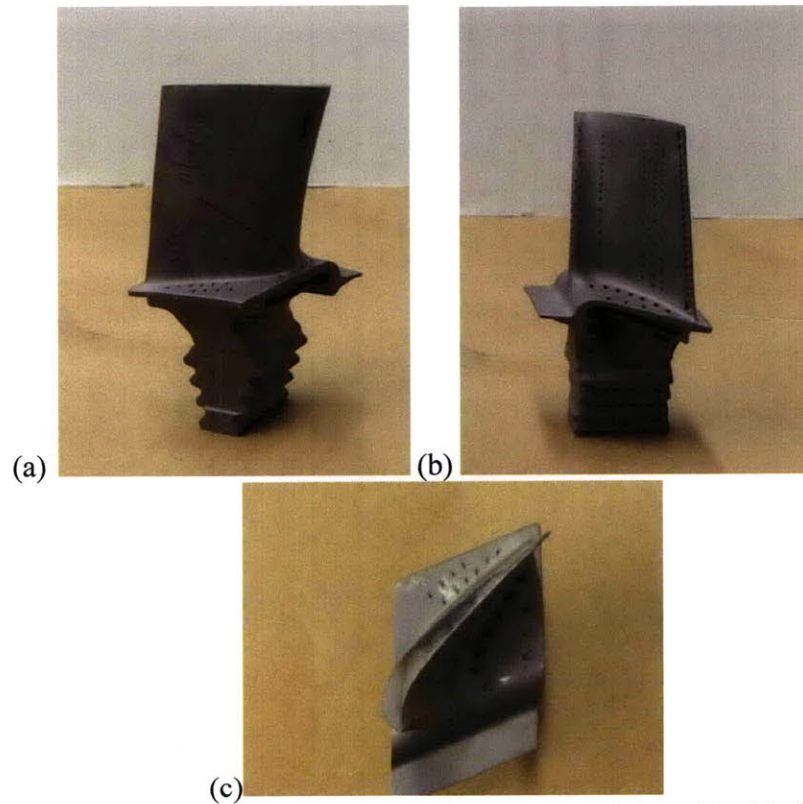


Figure 2.9: (a-c) Front, back, and top view from one of the turbine blade samples

In addition to the HPT blades, a 1st stage HPT duct segment was also inspected. Figure 2.10(a-b) illustrates the front and back geometry of this component. This sample contained a number of surface cracks. As illustrated in the stereomicroscope image in Figure 2.11, the cracks were oriented in the same direction but their lengths varied. The duct segment was also manufactured from PW1484. Surface cracks in duct segments are typically inspected with an eddy current technique.

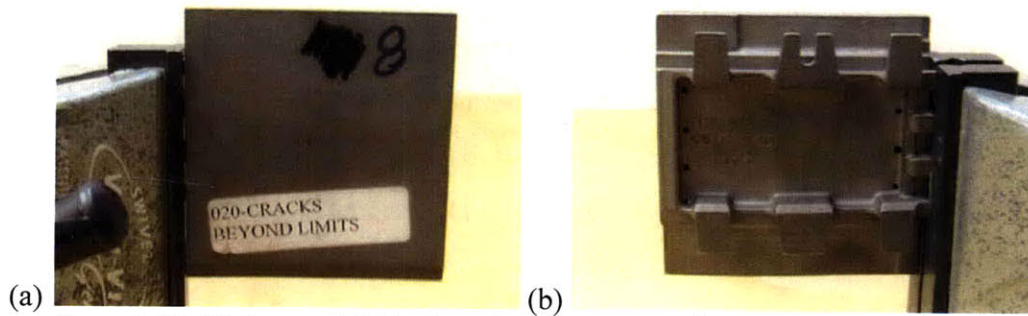


Figure 2.10: (a) Front and (b) back surface view of the 1st stage duct segment

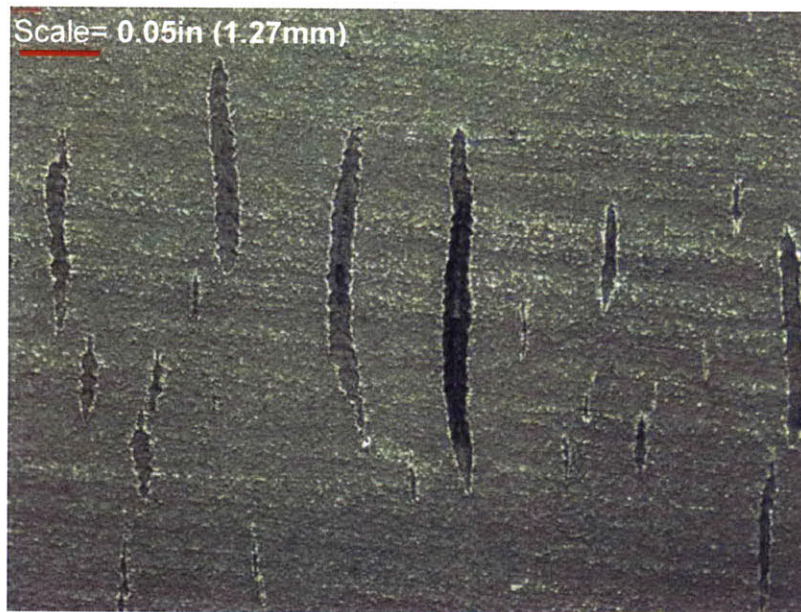


Figure 2.11: Stereomicroscope image of the duct segment surface cracks. Image size is 0.5 x 0.375 in. (12.7x9.5mm)

2.2 Experimental Procedure

The four alloy block specimens and the duct segment HPT component were tested with the MWM-array® eddy current technique. The wedding cake specimens and the turbine blades were not tested because their complex curvature required specialized attachment fixtures for the MWM-array sensors to compensate for the varying sensor lift-off distance. The equipment required to utilize such fixtures was not readily available. Also, capability of the MWM-array sensor had already been demonstrated in the automated inspection of critical disk slot and blade dovetail connections [52, 112, 135, 185], so it was determined that inspection of the turbine blades was unessential. Figure 2.12(a-b) depict the concept design for the automated inspection system and a fabricated

system already in use for the detection of fretting damage in critical turbine blade dovetail regions. Additionally, the footprint of the multi-channel MWM-array sensor, although flexible, could not be easily adapted to inspect within the small clearances on the wedding cake samples where the FBH were located. For these reasons the MWM-array technique was only used to inspect samples with relatively flat surfaces.

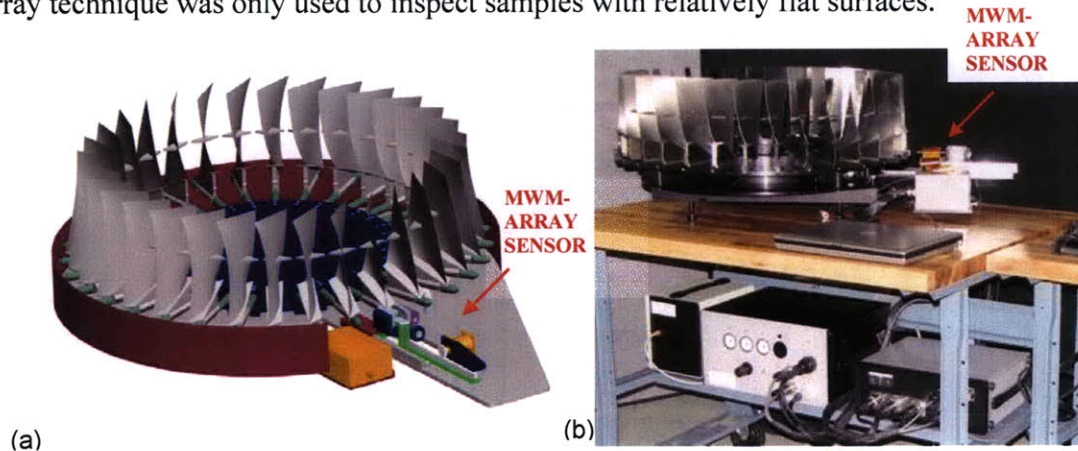


Figure 2.12: (a) Early CAD concept design for the automated blade dovetail inspection system (b) photograph of a fabricated system currently in use (adapted from [112])

The MWM-array inspections were performed at JENTEK Sensors Inc., in Waltham, Massachusetts. The patented MWM® sensor technology and Gridstation® visualization software were used to obtain digital C-scan images and B-scan conductivity versus location plots from which S/N measurements and flaw size data were obtained. The inspections of the alloy block and duct segment samples were set up using an X-Y encoder gantry system so that flaws could be more accurately sized and their location more reliably calculated. Information on the X-Y sensor position was automatically encoded into the Gridstation software using a software package called Quick Controls. A macro program called Scan Table was used to run the encoder system off a PC. The use of the gantry system, shown in Figure 2.13(a), added a level of automation to the inspections and eliminated any potential lift-off and scan velocity variability stemming from manual sensor operation. Figure 2.13(b) shows a 2kg (4.4lb) weight placed on top of the sensor to minimize lift-off variation and ensure intimate contact between the sensor and the test sample. For all the inspections, a second alloy block was positioned next to the test sample, as in Figure 2.13(b). This was done to allow the MWM-array sensor to

traverse over the entire region of interest without edge effects from the corners of the test samples deteriorating image quality.

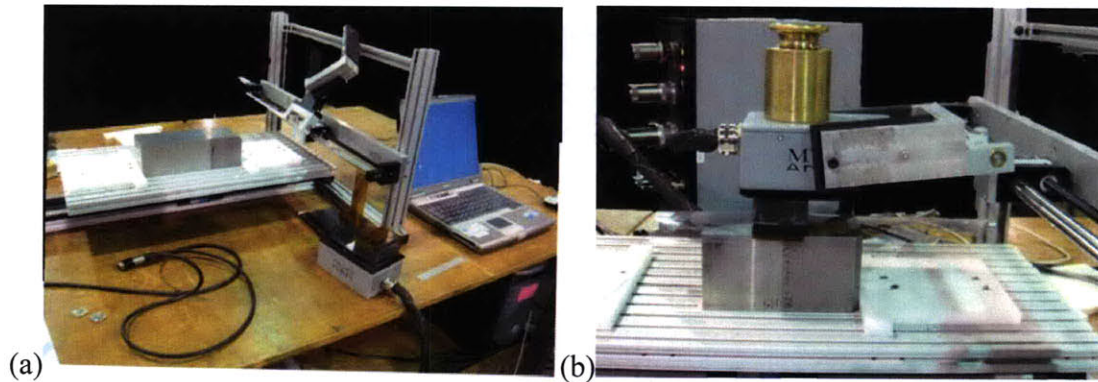


Figure 2.13: (a) X-Y encoder gantry system test setup prior to inspection (b) Encoder setup during inspection. A 2kg (4.4lb) weight was placed on top of the sensor to minimize lift-off variation and ensure intimate contact between the sensor and the test sample.

Before testing could commence, a number of test parameters were required to be specified in the Gridstation software. A new inspection session was opened in the software, the appropriate sensor was selected, and the correct data response grid or grids were loaded based on the material/s under test and the desired minimum detectable flaw size. Over the past 20 years, JENTEK has developed various sensors with individual channel architectures and arrangements for a variety of applications [52-54, 91, 112, 133, 135, 186], so selection of the appropriate sensor was not trivial. A 35 channel array probe [Model No. FA35] was selected as the sensor for all inspections. General information required for the alloy block and duct segment inspections were chosen in the *Session Settings* window. For these inspections the following were selected:

Conductivity/Lift-off Measurement Module, Set Data Acquisition Mode, 200 for the *Number of Sets*, and **3000 Meas./Set**. Recall from Section 1.2.4 that depth of penetration is relatively high at lower frequencies, but the flaw detection sensitivity is relatively low. At higher frequencies the reverse is true. Since high flaw detection sensitivity was desired, the test frequencies for all the samples were chosen to be 6.309MHz and 15.84 MHz. The specific values of these test frequencies stems from the particular grid set selected.

A unique aspect of MWM sensors is the ease with which calibration is performed and the many different types of calibration from which the operator is permitted to select.

The two most common types of calibration are the *Air and Shunt Calibration* and the *Reference Part Calibration*. The reference part calibration requires a sensor tip and specimen of known properties (i.e. conductivity), and the calibration anchors the two points specified by the user to the actual points measured [187]. Typically these two points refer to the same location on the reference part with and without the use of a shim of specified thickness. In this manner this lift-off distance can be calibrated against the known shim thickness. Air and shunt calibration requires no reference parts, but does require a shunt tip. The shunt tip provides a measure of all the system variables not explicitly accounted for by the software, such as the cable capacitance, and then subtracts the signal response from these parasitic variables so that only the measured signal response from the test-piece is obtained. The first step performed in the air and shunt calibration of the sensor probe is called *Ranging*, where generally a minimum of 25 measurements are taken in air and on the part. These measurements provide the range of values from which the measurement grids, which are pre-computed databases used for rapid conversion from raw sensor impedance data to absolute material property values, are generated [52, 54, 187, 188]. The advantages of these calibration methods over traditional eddy current techniques that rely on the use of calibration blocks will be discussed in Section 2.4. For the experiments on the alloy blocks and duct segment component the air and shunt calibration method was selected, and a follow up scan using the reference part calibration method on one of the alloy blocks was performed to validate the results.

2.3 Results of Sensitivity Analysis

The first sample scanned with the JENTEK equipment was the P/M Rene' 88 block. Figure 2.14 shows the initial C-scan image taken of the sample at 6.309MHz. There are many subtleties of the Gridstation® visualization software in Figure 2.14 that will appear in subsequent images, therefore pertinent features have been pointed out and described. The values along the lower horizontal and left-hand vertical axes are measurements of length in inches. Occasionally a vertical axis on the right-hand side will appear in the C-scan; this axis denotes the particular channel of the array sensor located at that Y distance. Since Figure 2.14 is a conductivity scan the rainbow colored scale below the X-axis is the range of electrical conductivities, in units of %IACS. The lower

and upper bounds of the %IACS scale are the determined discrimination thresholds. Correct selection of the upper and lower bound discrimination thresholds is critical to

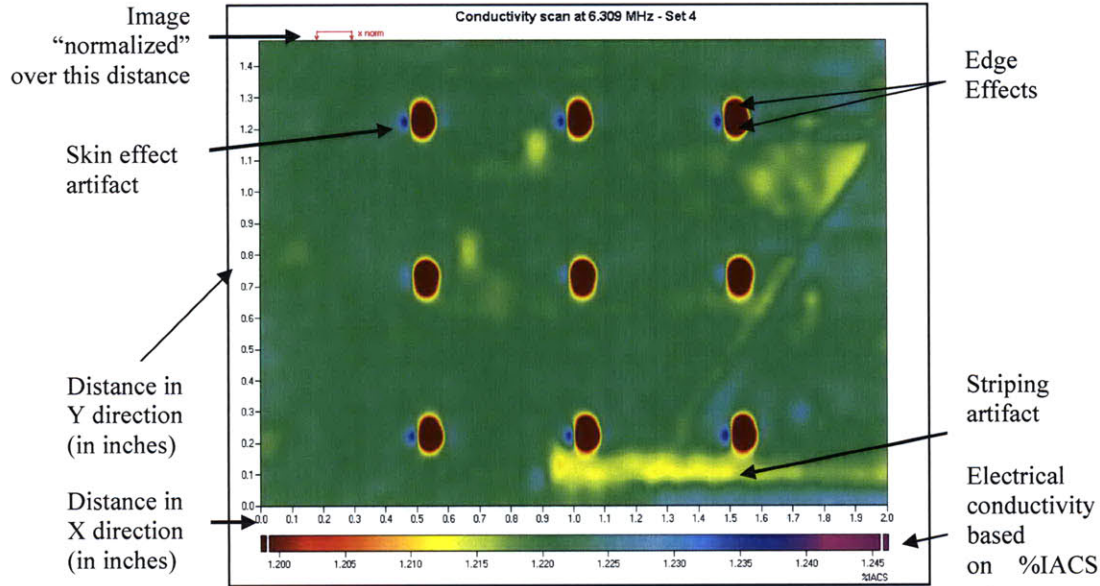


Figure 2.14: C-scan image of R88 sample with a description of image features

maximizing S/N ratio and minimizing false positives and missed detections. For lift-off scans the multi-colored scale would represent the lift-off distance in mils (where 1mil=0.001in.=0.0254mm). Along the top horizontal axis there is an “x-norm” scale bar. Normalization collects data between two measurement points and divides all the values of the selected region within those two points by that region’s average. Then all of the other measurements in the C-scan image are divided by their respective average (normalized) channel value. In the case of Figure 2.14, channel values were normalized over a prescribed distance in the x-direction, but normalization can also be performed over other absolute material property values such as lift-off.

Normalization is used to get rid of striping artifacts, which are caused by slight variations in complex transimpedance between channels of the same probe. The striping artifact seen in Figure 2.14 most likely resulted because normalization was not performed over a sufficiently large area. The small blue features that appear to the left of the larger, red circular features are indicative of skin effects. The red circular features are the nine flat bottom holes of the 3x3 array for the R88 sample. Edge effects are observed in all of these holes. As the MWM-array probe approached the edges of the holes, distortion of

the eddy currents resulted because they were unable to flow beyond the edge of the part. The severity of the skin effect artifacts in Figure 2.14 was attributed to the 6.309MHz inspection frequency. Interestingly, the excessively slow velocity of the probe caused too many data points to be collected while spanning the flat bottom holes, thus skewing the material property average of the surrounding material. Fine-tuning of the many inspection variables was required before quality C-scan images were obtained. The conductivity scan in Figure 2.14 states “Set 4” because the first three data sets were needed to resolve bugs in the encoder programming. Subsequent inspections yielded improved results as well as interesting observations about the NDT system.

A clear improvement in C-scan image quality was observed at the higher 15.84MHz test frequency than in the 6.309MHz scan in Figure 2.14. In Figure 2.15(a-b), the C-scan and B-scan results from the same inspection as in Figure 2.14 are shown, but at the higher 15.84MHz test frequency. Skin effects are seen more distinctly in Figure 2.14 than in Figure 2.15(a) because the 6.309MHz frequency had a greater depth of penetration than the 15.84MHz test frequency. Since the FBH array for Sample R88 was drilled to a depth of 6.3mm (0.25 in.), it is likely the 6.309MHz scan penetrated into the near-surface regime of the sample. This conclusion is supported by the difference in

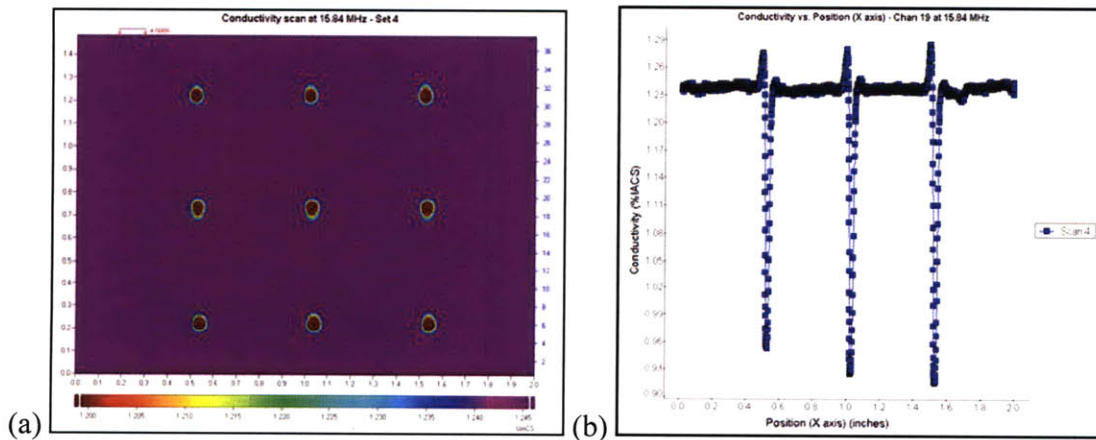


Figure 2.15: (a) C-scan and (b) B-scan data at 15.84MHz for inspection Set 4 of Sample R88

background color for the two C-scan images. While Figure 2.15(a) has a purple image background near the 1.245% IACS upper bound threshold level, the image background of Figure 2.14 is around 1.220% IACS. The 3x3 FBH array exhibits a lower conductivity of 1.200% IACS because of their 6.3mm (0.25 in.) hole depth. The skin effects visible in

Figure 2.14 have a blue shade signifying an approximate conductivity of 1.235% IACS. An advantage of the MWM-array system is that comparisons between NDT system response and *absolute* material property values can be made because of the patented multivariate inverse method. Since %IACS can be correlated with penetration depth, this shows that the sample surface is located at the 1.245%IACS value, and 1.200%IACS is 6.3mm (0.25 in.) below this surface. The approximate depth, δ , of the skin effect is calculated by equation (2.1).

$$\delta = \frac{\%IACS_{Surf} - \%IACS_{EdgeEffect}}{\%IACS_{Surf} - \%IACS_{FBH}} = \frac{0.01}{0.045} \times 6.3mm = 1.4mm(.055in.) \quad (2.1)$$

Simple crack (or in this case FBH diameter), sizing methods can be used with the MWM data generated in both the B-scan and C-scan images. These two sizing methods are depicted in Figure 2.16(a-b). Application of these methods to the images in Figure 2.15 revealed that although all nine of the flat bottom holes were easily detected, there was an error in the manually selected values for the upper and lower %IACS discrimination threshold bounds. This error is significant, with the FBH diameter estimated at 2mm (0.080 in.) from the C-scan image in Figure 2.15(a). The excessively slow scan velocity is a secondary source of error in the flaw size measurements. The

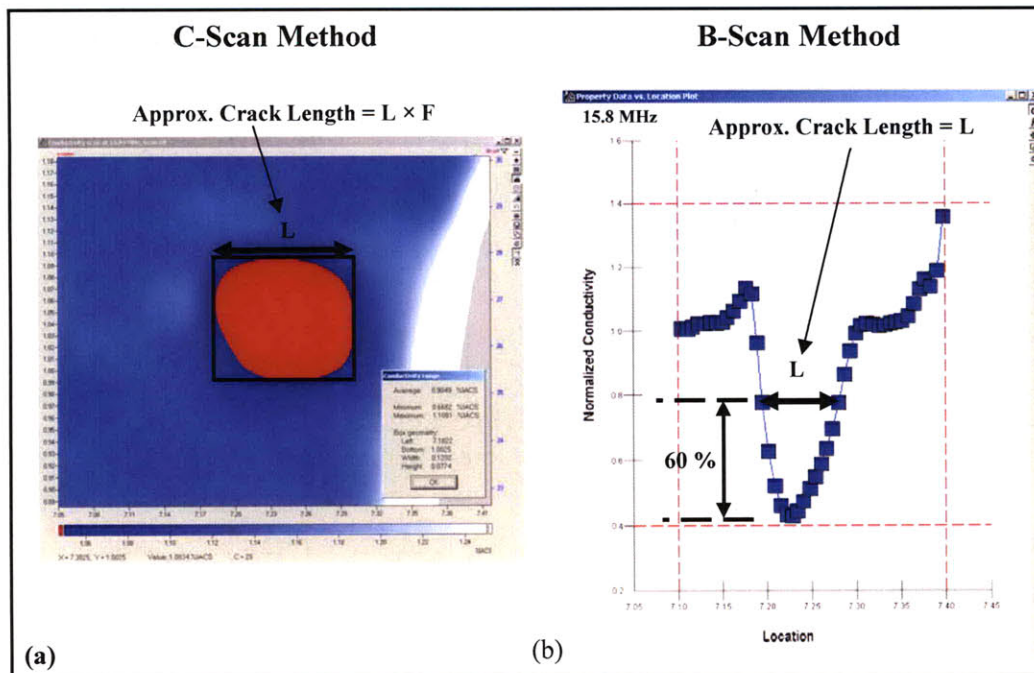


Figure 2.16: Simple crack sizing methods with the Gridstation® software for (a) C-scan images and (b) B-scan plots (adapted from [189])

initially selected encoder velocity resulted in a rate of approximately 1000 data points/inch to be taken. This caused the average conductivity calculations near the holes to be skewed to the lower threshold discrimination bound upon normalization, resulting in a larger apparent flaw size. This same effect can be visualized from the B-scan plot in Figure 2.15(b). The data points at the hole locations on the conductivity versus position plot are very jagged, making an estimate of the hole diameter based on the flaw sizing method in Figure 2.16(b) extremely difficult. Additionally, errors in the shape of the hole features due to edge effects are evident in Figure 2.15(a). The snail-like scan velocity enhanced the edge effects around these holes.

The edge effects seen in Figure 2.15(a) were improved by slowing the encoder velocity by approximately 2.5 times below the initial value chosen in Set 4. Figure 2.17 is the C-scan image for the R88 sample at this slower Set 5 data rate. The edge effects have been corrected for the center row of holes but remain in the top and bottom rows. In the top and bottom rows the edge effects were caused by two channels rather than one channel of the FA35 sensor detecting the hole during inspection. At these small flaw

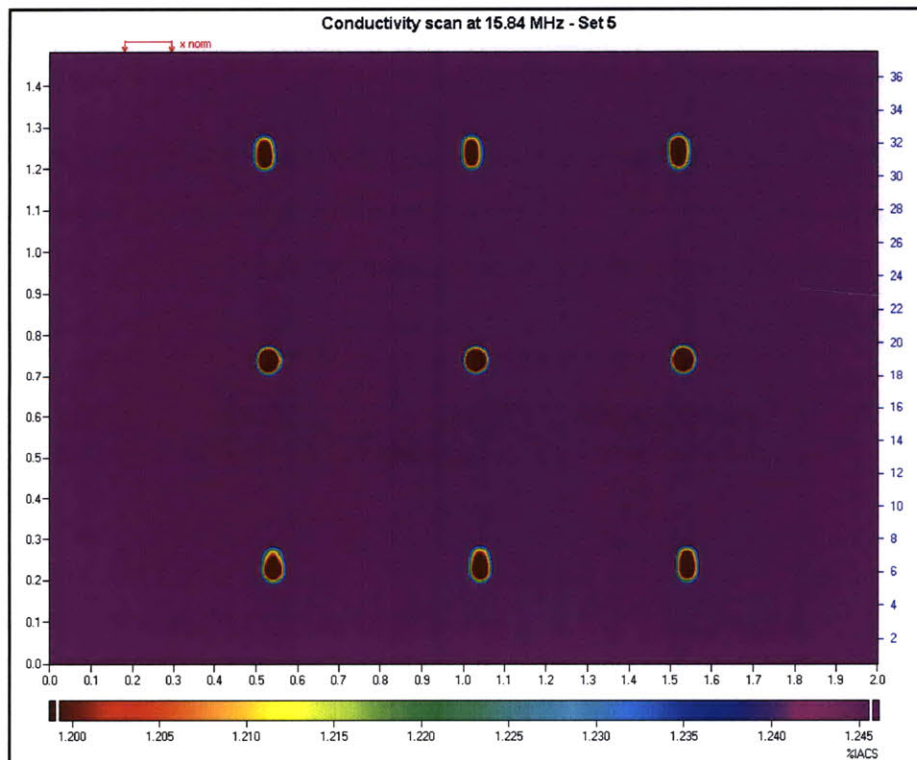


Figure 2.17: C-scan image from Set 5 of the R88 sample at the slower encoder velocity rate. The edge effects have been corrected for the center row of holes but remain in the top and bottom rows

sizes that are on the order of the individual sense element length, little can be done to eliminate the edge effects. For this reason, the footprint of the sensor architecture is an important factor in image quality. The upper and lower threshold bounds were again manually determined for data set 5 in Figure 2.17, therefore error in the C-scan crack sizing method remained.

In Set 6, two procedural changes were made to the inspection of the R88 sample. The first was the addition of a 5 mil (0.13mm) shim to minimize the lift-off effect, as evidenced in Figure 2.18(a-b) by the lift-off comparison between Set 5 and Set 6. The

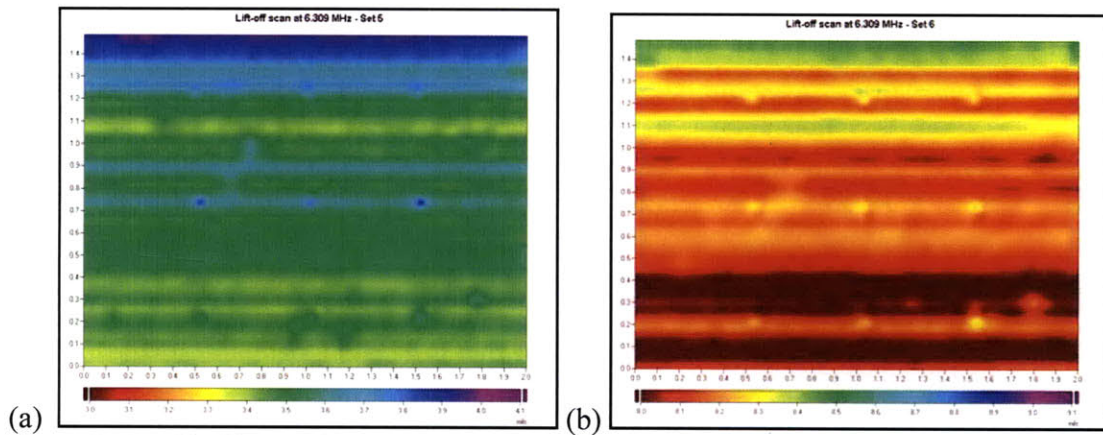


Figure 2.18: Lift-off scans for R88 sample (a) Set 5 and (b) Set 6 with 5mil (0.13mm) shim added

addition of the shim changed the location on the measurement grid where the precomputed sensor responses were determined by the multivariate inverse method. As long as the sensor responses remained on the measurement grid, as in Figure 2.19, the measured material property values should be considered within range and acceptable.

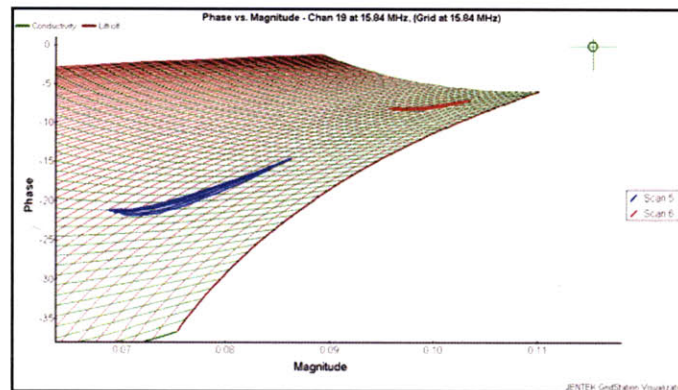


Figure 2.19: Signal response location on the pre-computed measurement grid for scan Set 5 and Set 6

The second procedural change was use of the automatic threshold option in the Gridstation ® software in lieu of manual threshold discrimination. The C-scan and B-scan results of the conductivity scan for Set 6 at the 15.84MHz test frequency are shown in Figure 2.20(a-b). Use of the automatic threshold option resulted in much better flaw size estimation, with the FBH diameter now represented by the smaller red circular features in Figure 2.20(a). Also, the B-scan data was much improved in Figure 2.20(b) over Figure 2.15(b) after automatic selection of the upper and lower bounds. One disadvantage of using the automatic bound selection was that the edge effects became more pronounced, as observed in Figure 2.20(a). Figure 2.21 shows the effect on signal response for the center row of holes in Figure 2.20(a) when two adjacent channels detect the same flat bottom holes.

Results similar to the R88 sample were obtained for the other alloy block specimens. The C-scan images for Samples H, L, and U are presented in Figures 2.22-2.24. Normalization over a larger area in Figure 2.22 resulted in improved sensitivity and accuracy in C-scan flaw size results when compared to the C-scan images of the other alloy block samples. A difference between Figures 2.22-2.24 was the upper and lower conductivity threshold bounds, which varied slightly due to compositional deviations in the three Ti-alloy blocks. A peculiar characteristic observed in Figure 2.23 for the Set 8 C-scan image of Sample L was that the center row of FBH was not detected by any of the sensor channels. Only the edge effects are visible in the center row of this image, while the top and bottom rows have the most accurate and uniform signal response of all the images. This is attributed to the rows and columns of the flat bottom holes being separated by a distance of 12.7mm (0.5 in.), while the individual sense elements of the MWM-array probe were separated by approximately 1mm (0.04 in.). When the FA35 sensor and the alloy block test sample were oriented in parallel one on top of the other, these particular lengths can never perfectly align for all three rows of holes. This observation is represented graphically in Figure 2.25, which is the B-scan conductivity versus position plot for Set 8. The signal response from Channels 18 and 19, the two sensor channels that scanned over the center row of FBH, are nearly identical and

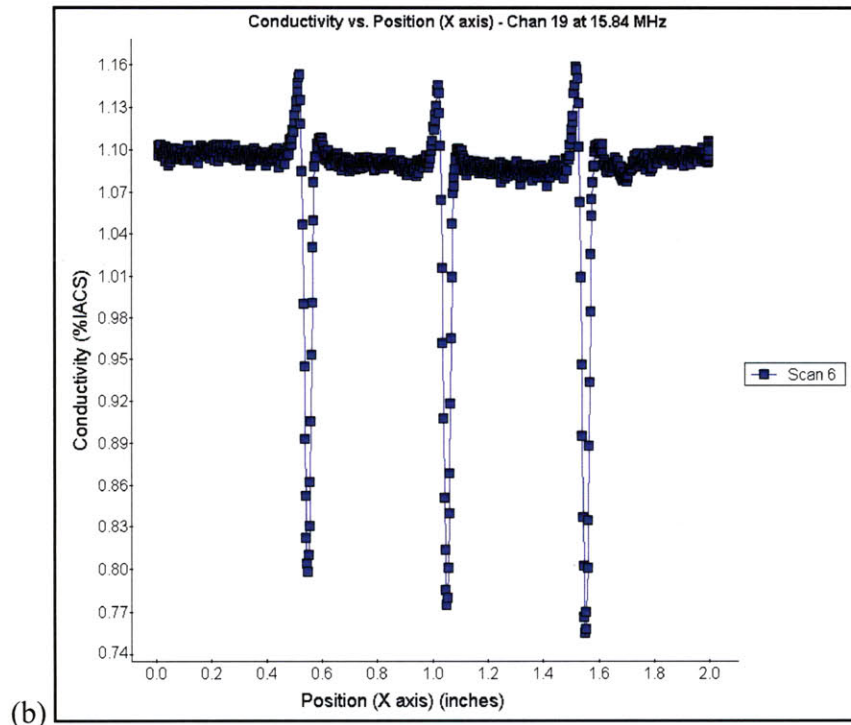
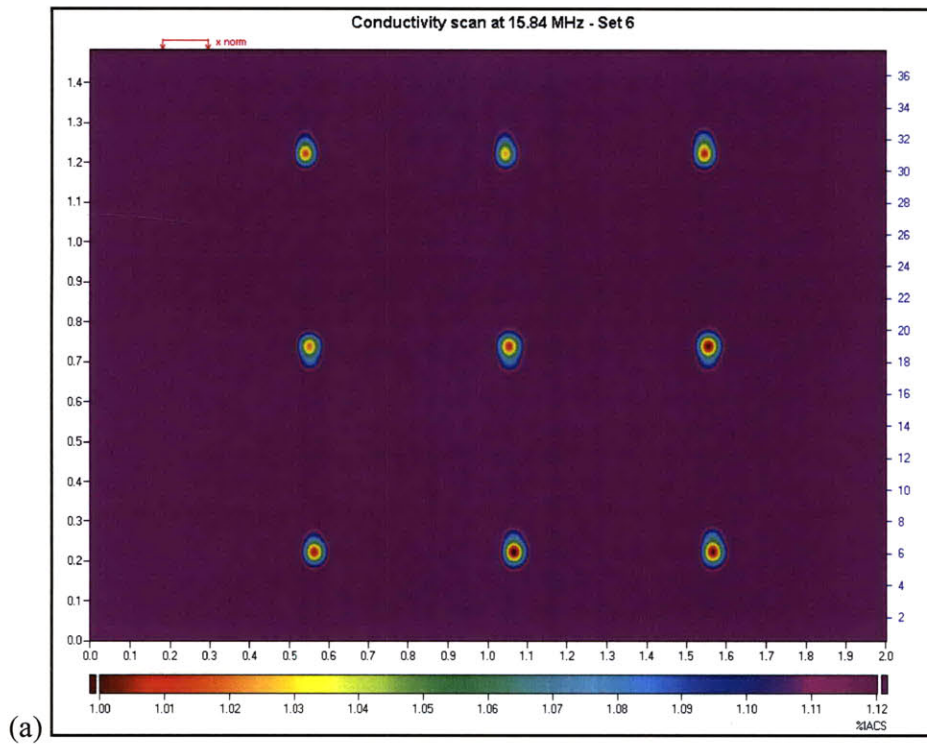


Figure 2.20: (a) C-scan and (b) B-scan results of the conductivity scan for Set 6 at the 15.84 MHz test frequency after addition of shim and use of automatic threshold correction

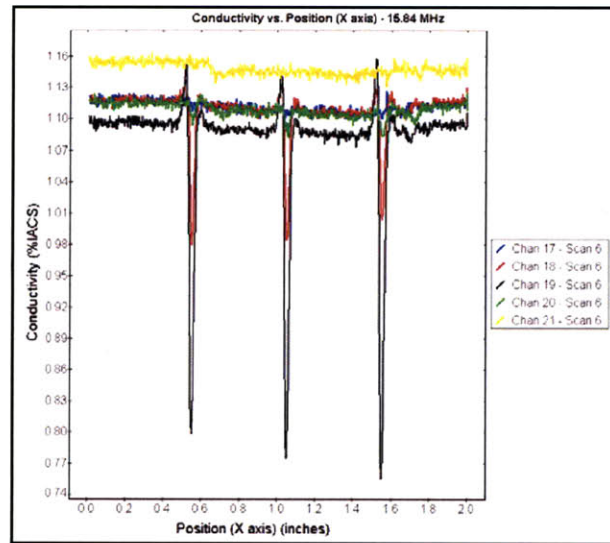


Figure 2.21: The effect on signal response for the center row of holes in Figure 2.20(a) when two adjacent channels detect the same flat bottom holes.

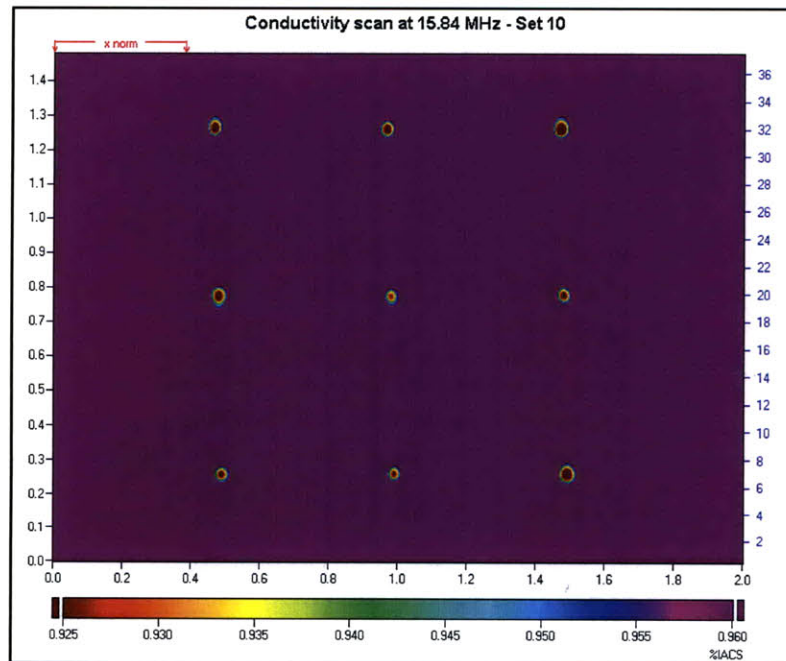


Figure 2.22: C-scan image for Sample H [190]

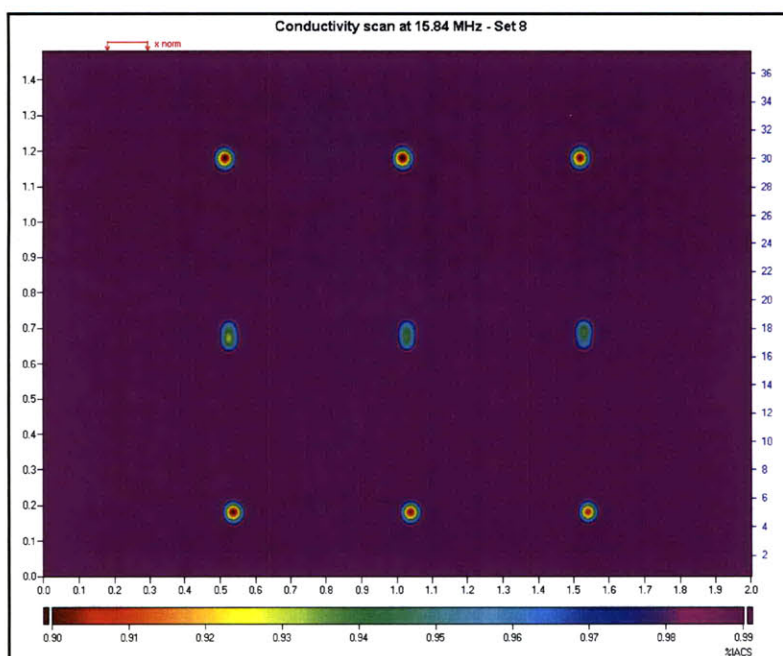


Figure 2.23: C-scan image for Sample L

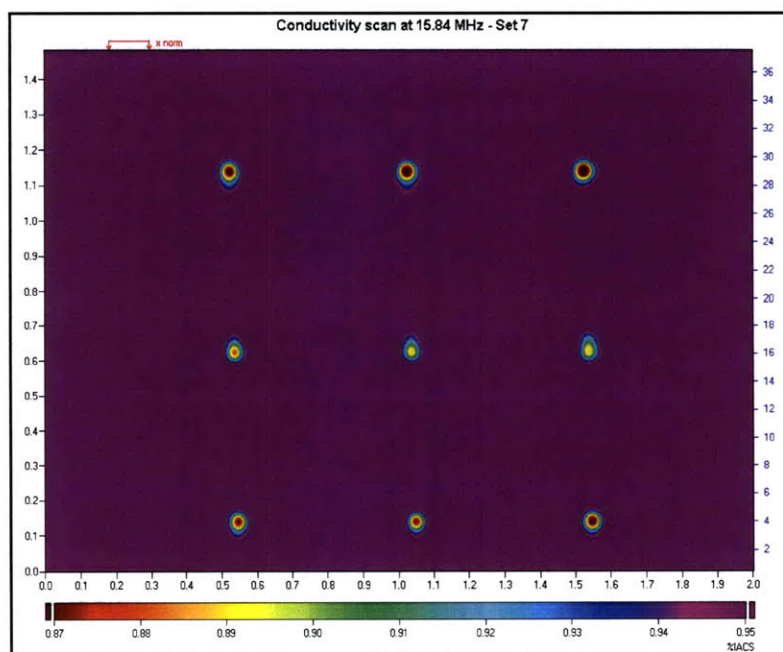


Figure 2.24: C-scan image for Sample U

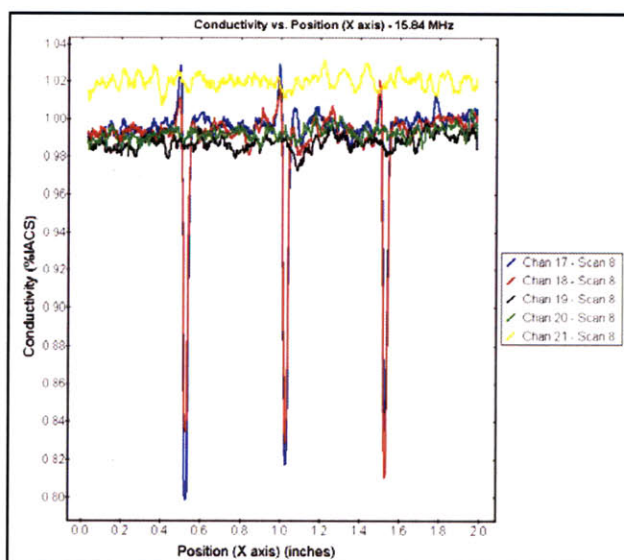


Figure 2.25: B-scan conductivity versus position plot for Set 8. The signal response from Channels 18 and 19 are nearly identical.

essentially cancel each other out. The signal response from channels adjacent to Channels 18 and 19 have a distinctly different profile. Sample L was moved 0.5mm (20 mils) diagonally and re-scanned in Set 9. Figure 2.26(a-b) shows the significant difference in image quality and signal response obtained in Set 9 from this slight adjustment of sample orientation, while the signal response from a number of channels in a B-scan plot and the location of the channels on the measurement grid are provided in Figure 2.27(a-b) .

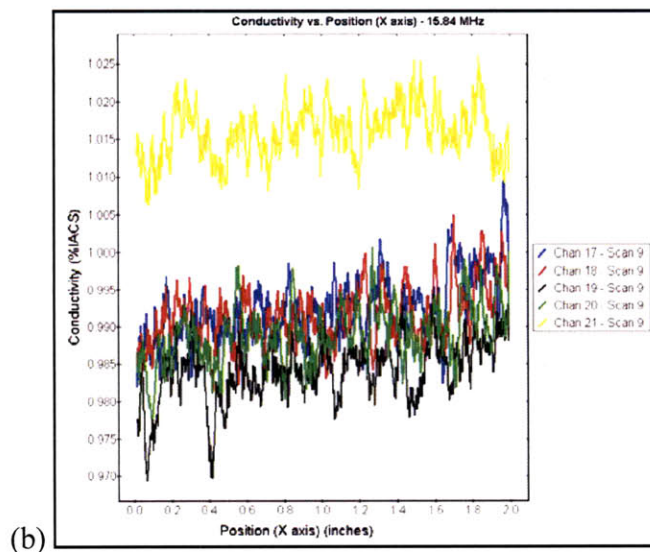
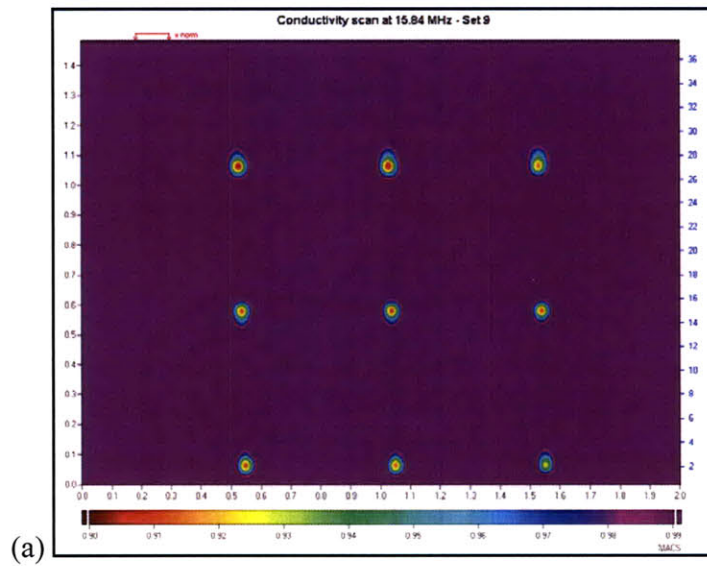


Figure 2.26: (a) C-scan image of Sample L after a 0.5mm (20 mil) diagonal adjustment. (b) Comparison of signal response from Channels 17-21 with Figure 2.25

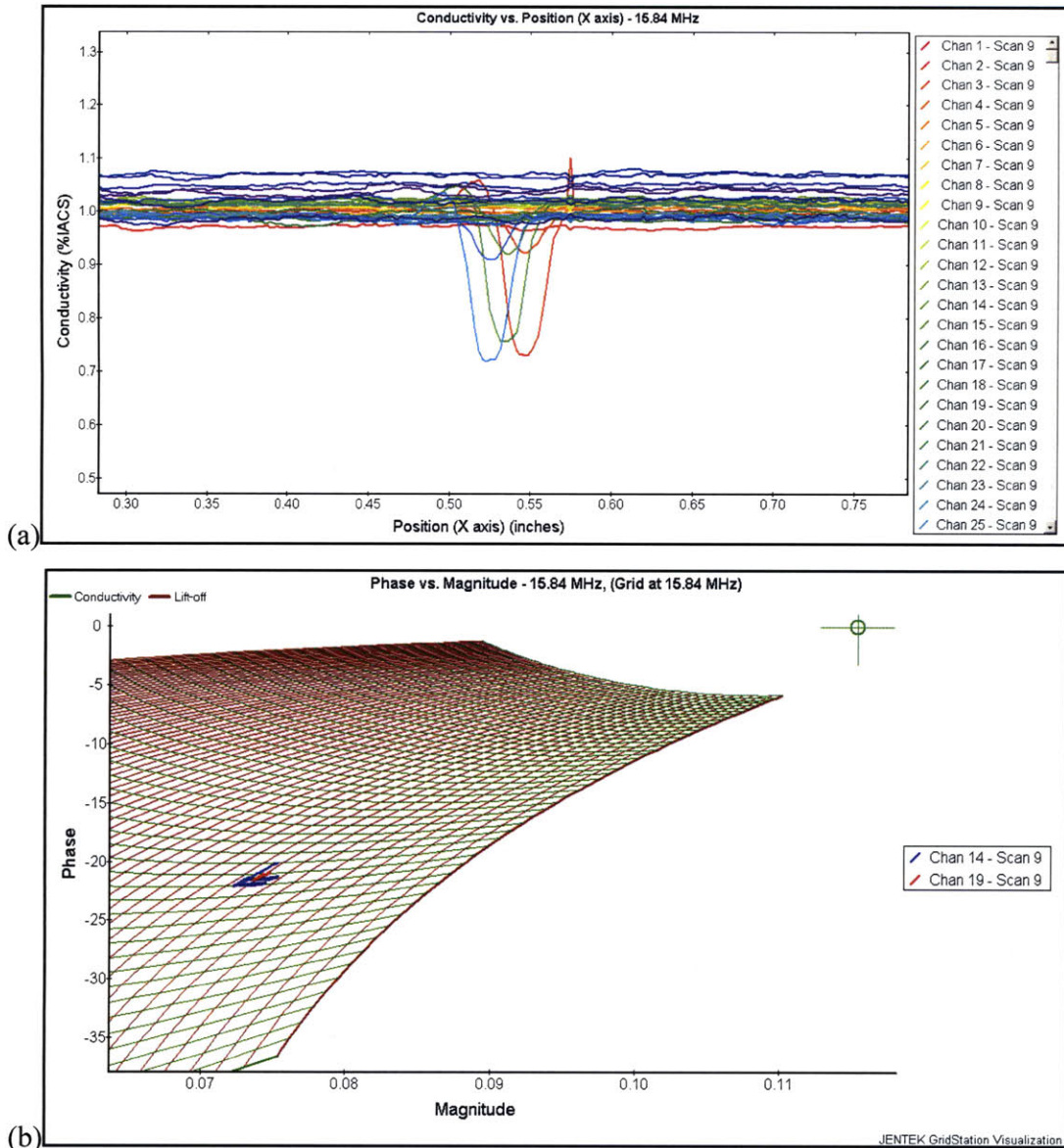


Figure 2.27: (a) B-scan signal response from Channels 1-25 for Set 9. (b) Location on measurement grid for selected channels of scan Set 9

The C-scan image of Sample H in Figure 2.22 revealed that normalization over a larger area can improve flaw detection sensitivity. Additionally, repeatability in individual channel signal response was improved by increasing the “ x_{norm} ” distance. Figure 2.28 contains the B-scan data for the three channels in Set 10 that scanned over the individual FBH rows. The uniformity in the signal responses from the three sense elements in Figure 2.28 is much better than any of the previous B-scan figures, resulting in improved flaw detection capability and sensitivity. B-scans magnified at the x-axis

locations of the FBH rows are pictured in Figure 2.29(a-c). Using the B-scan crack sizing method illustrated in Figure 2.16(b), the FBH diameter, ΔL , was calculated as follows:

$$\sigma_L = 0.65\%IACS + 0.65\%IACS[(0.6(1.0\%IACS - 0.65\%IACS))] = 0.787\%IACS \quad (2.2)$$

$$\Delta L_{0.787} \approx 1.505in. - 1.49in. \approx 0.015in. \quad (2.3)$$

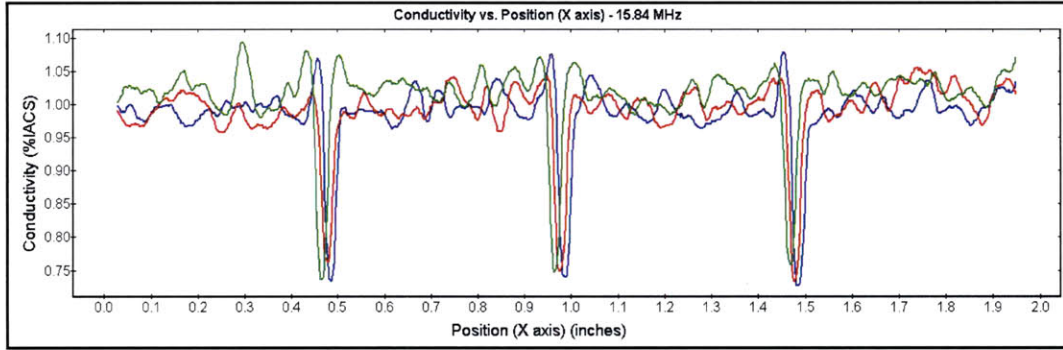


Figure 2.28: B-scan data for the three channels in Set 10 that scanned over the individual FBH rows. The signal response among the three channels is nearly identical resulting in improved sensitivity [190].

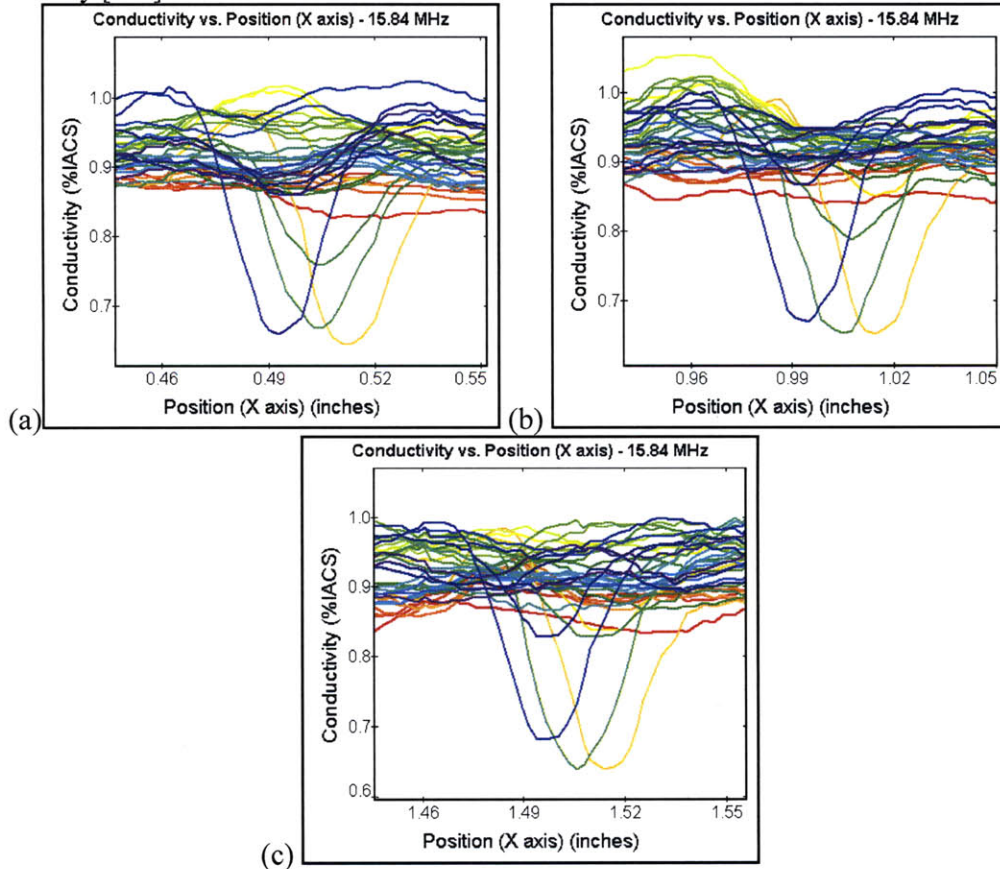


Figure 2.29: (a-c) B-scans magnified at the x-axis locations of the FBH rows

Equation (2.2) is the calculation for the electrical conductivity value that is 60% of the full scale signal response height. From Figure 2.29(a-c), the base of the signal is approximately at a conductivity of 0.65%IACS. Ti-6Al-4V has a conductivity of 1.0%IACS, obtained from Table 1.5 and shown in Figure 2.29(a-c). Since the conductivity of the alloy is 1.0%IACS, the conductivity values used in Equation (2.2) do not need to be normalized. The calculated FBH diameter of 0.015 in. (0.38mm) in equation (2.3) is almost identical to the standard #1FBH size of 0.0156 in. (0.397mm).

The results from scan Set 10 were obtained using the *Air and Shunt Calibration* method. To validate these results an additional scan was performed on Sample H using the *Reference Part Calibration*. A 5 mil (0.127 mm) mylar shim was placed on the surface of Sample H and scan Set 11 was taken at the same 15.84MHz inspection frequency as Set 10. The C-scan image for Set 11, B-scan plot of the three channels that scanned over the individual FBH rows for Set 11, and comparison between the measurement grid location of two channels in Set 10 and Set 11 are presented in Figure 2.30(a-c). Validation of the measurement results for Set 10 as well as demonstration of the repeatability, reliability, and sensitivity of the MWM-array® system were concluded from the results of Figure 2.30(a-c).

The duct segment was also scanned using the X-Y encoder gantry. As shown in Figure 2.31(a-c), the duct segment was oriented at a 45° angle relative to the probe to obtain the greatest sensor sensitivity to crack detection. Because the component's shape was not perfectly horizontal, business cards were used as shims to level the lift-off and the part was set atop a ream of paper to provide some compliance and enable intimate contact at the sensor/component interface during inspection. Figure 2.32(a-b) are the C-scan conductivity and lift-off scans of the duct segment. Note that the region in the lower right hand corner of both scans is the label on the duct segment surface that reads, "020-CRACKS BEYOND LIMITS". Multiple cracks were detected in the conductivity image, ranging from 0.5-1.1%IACS. The threshold detectable crack size appears to be 0.005in. x 0.05in (0.127x1.27mm) in size based on Fig. 2.32(a). A slight variation in lift-off is discernable in Figure 2.32(b) for the largest crack, possibly due to its increased crack depth versus the more shallow cracks. Figure 2.33(a) shows results from the B-scan plot, and sizes for the multiple cracks can be estimated as in Figure 2.16(b). The measurement

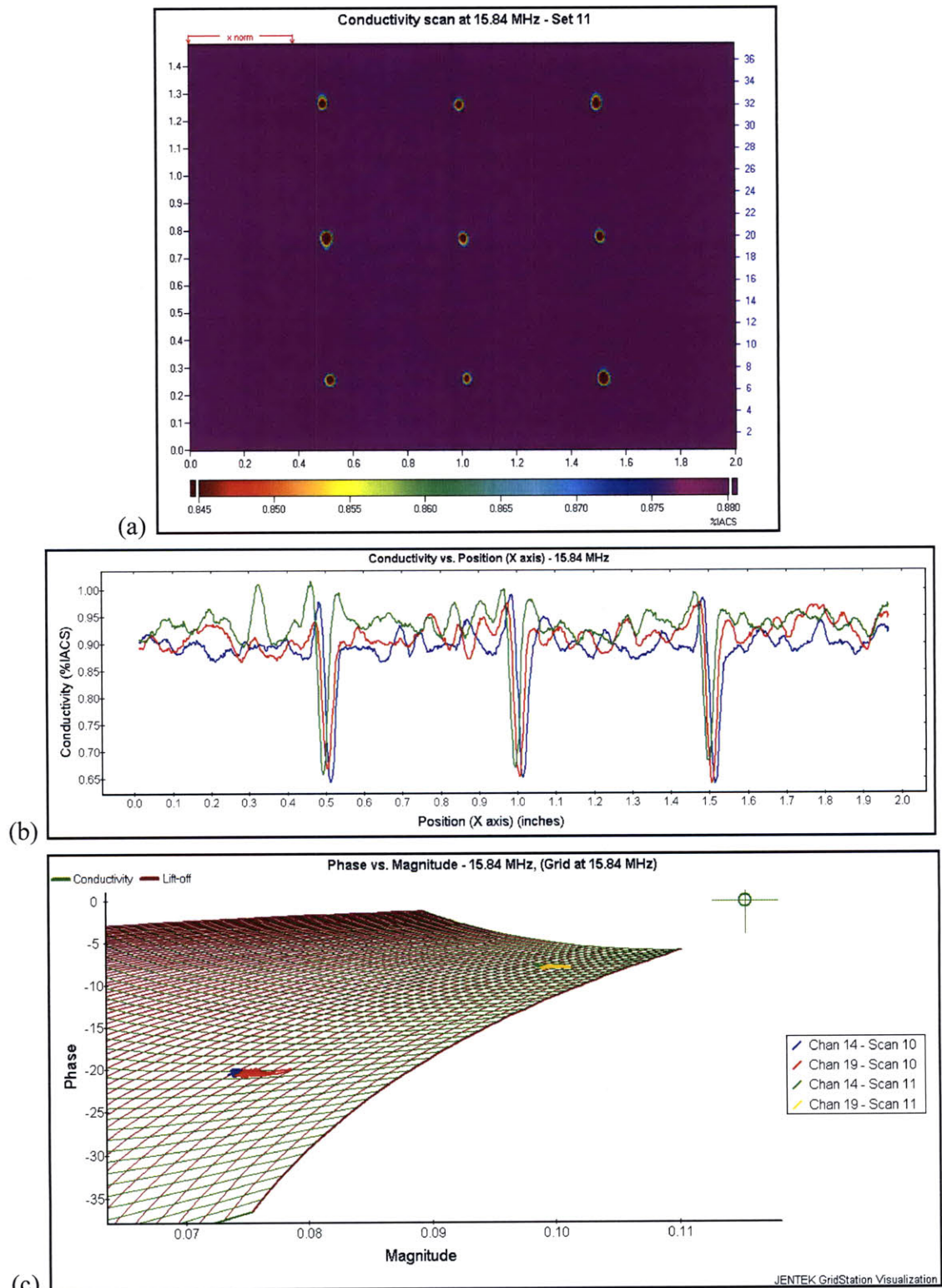


Figure 2.30: (a) C-scan image for Set 11 (b) B-scan plot of the three channels that scanned over the individual FBH rows for Set 11 (c) Comparison between the measurement grid location of two channels in Set 10 and Set 11

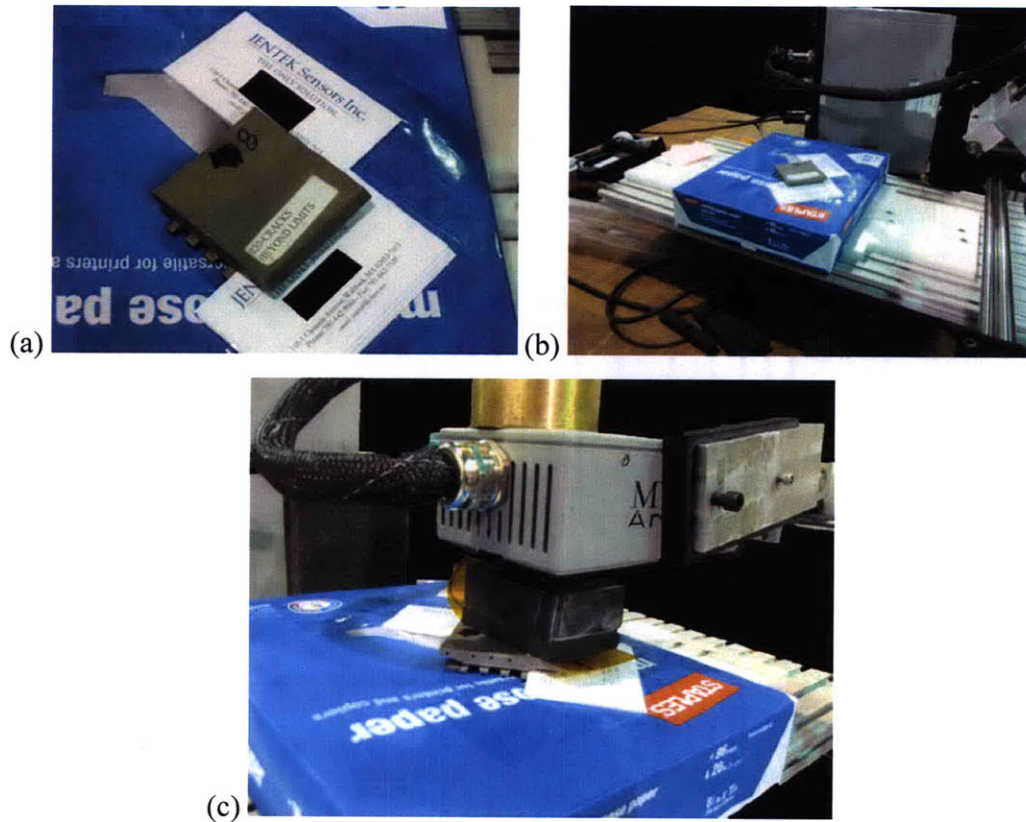
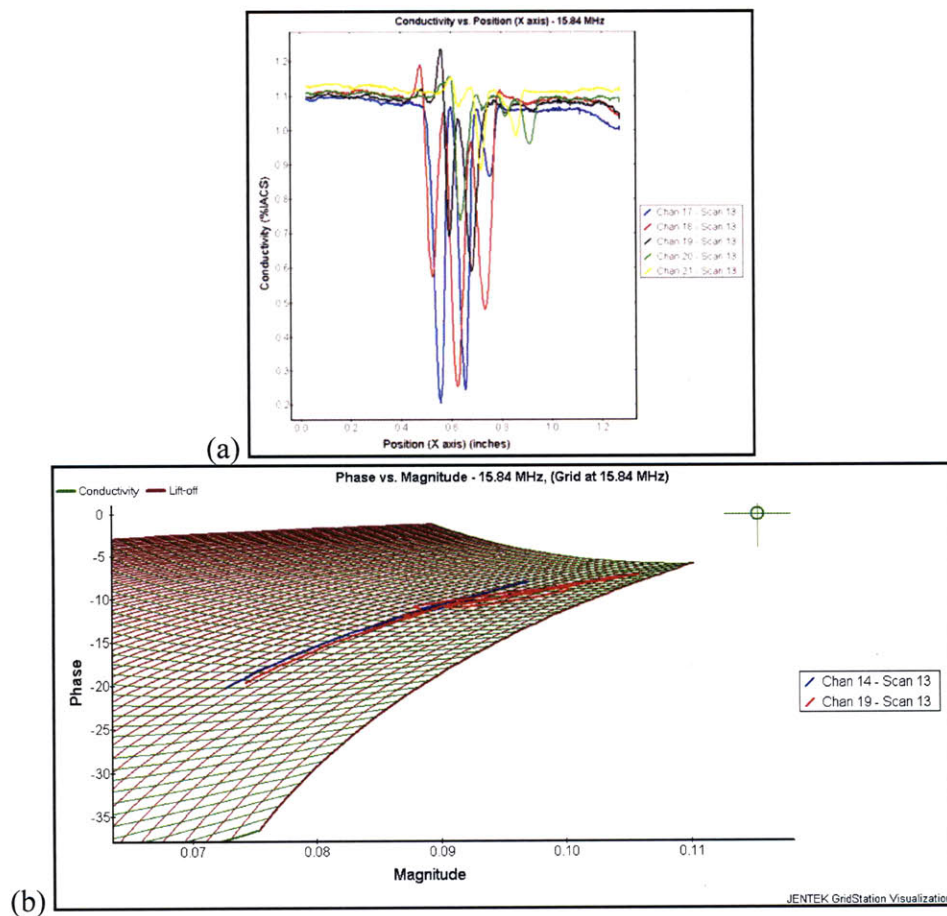
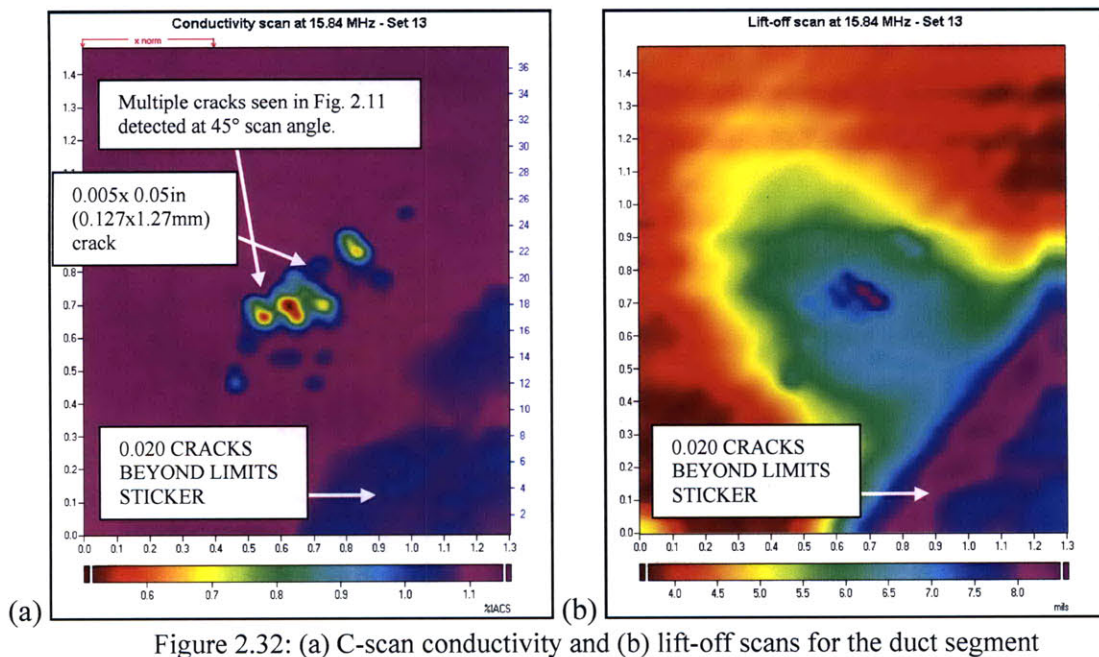


Figure 2.31: (a) Duct segment oriented 45° relative to sensor, with business cards used as shims to account for lift-off (b) Component placed on top of ream of paper to provide some compliance during testing (c) Image of the duct segment scan in progress

grid for the duct segment scan is provided in Figure 2.33(b), and shows that real cracks have more variability than the flat bottom holes. The applicability of FBH to represent real service cracks will be one topic discussed in Section 2.4.

2.4 Comparison with Traditional EC Technique

There are many types of eddy current probes and arrays commercially available to the NDT community. Important variables that affect the output of an inspection include the amount of channels (coils) in a selected sensor, as well as the test frequencies chosen for the available ECI equipment. A single frequency, single channel eddy current point probe and a 32-channel eddy current array probe with an internal multiplexer were the traditional eddy current inspection systems selected. The Sample H alloy block was tested on an Omniscan™ MX system capable of performing both eddy current array and UT phased array inspections. The Omniscan™ MX system is portable and its instrumentation is in a modular platform that allows for easy switching between PA-UT



and ECA inspection configurations [70]. Physical detection and recognition of the probe connected to the mainframe is automatically programmed in the Omniscan™ MX system to determine what type of inspection is being performed. The eddy current array probe used to inspect Sample H was the R/D Tech® Crack EC Array [Model #SAB-067-005-032]. This probe required calibration to a reference standard like the one shown in Figure 1.6, before an inspection could be made. Figure 2.34(a) shows the calibration standard used to test Sample H. A Ti-6Al-4V standard was not available at the time of testing, so a standard used for aluminum alloys had to be used instead. The conductivity difference between Al-alloys and Ti-6-4 is about a factor of 30, as reference values in Table 1.5 indicate. Figure 2.34(b) shows the output from the eddy current array inspection. This test was performed at a 6MHz frequency, which was the maximum frequency possible with the system. The lack of a calibration standard for the material being inspected had a significant impact on the quality of the C-scan image obtained. Regardless, it is doubtful that this system would have been capable of detecting the #1FBH array even with the proper calibration standard due to the electronic noise from the coil design.

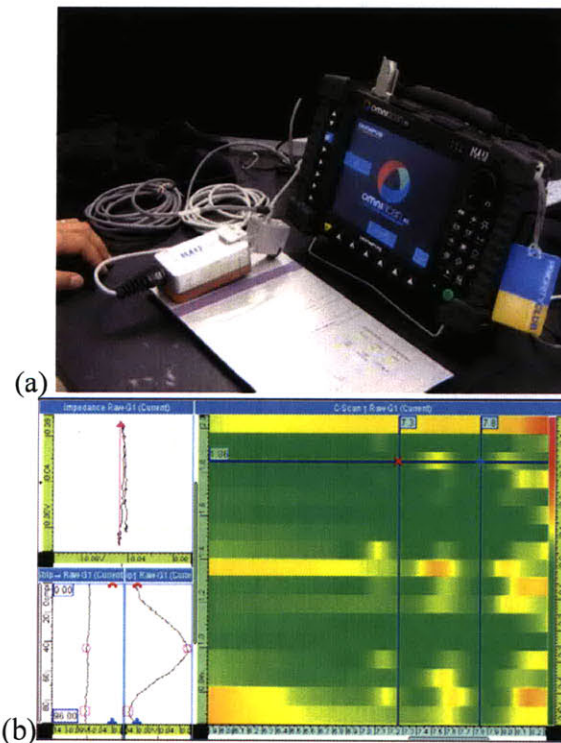


Figure 2.34: (a) Process of calibrating the eddy current array probe to a reference standard. (b) C-scan output for the inspection of Sample H.

A major difference between the MWM-array® system and other eddy current systems is the calibration aspect of the equipment. The MWM system allows the operator to choose between multiple calibration options that include the air, air and shunt, or reference part calibration methods. In 2004, ASTM Standard E2338-04 was issued under the title, *Standard Practice for Characterization of Coatings Using Conformable Eddy-Current Sensors without Coating Reference Standards* [52, 112, 185, 186]. Having a standard in place to qualify an operational aspect of a particular NDT technique, such as calibration, is critical to overcome the barrier of implementation into an industry. Companies can now specify this ASTM code and use the MWM®-array sensors in their facility in lieu of traditional eddy current systems. It is apparent from Figure 2.34 the calibration procedure for traditional eddy current array systems is inferior to the method used with MWM®-arrays. An easier and more robust calibration process has a direct impact on image quality and minimum flaw size for POD capability.

In the aerospace industry, flat bottom holes are used for two primary purposes. The first is to simulate real surface cracks, which are difficult to incorporate into fabricated test samples. The second is to calibrate an NDT system's response to the particular size and depth of the simulated FBH defect. The latter is traditionally performed for in-service inspections on components of a specific size. FBH with a larger diameter than the inspected alloy block samples are common. Simulated FBH defects in the #2-#8FBH range may be used, with #2FBH referring to a hole diameter 2/64th inch (approximately 0.8mm or 0.03 in.) and so on. Once the human factor sources of error, such as the manual selection of the upper and lower threshold bounds, were minimized in the MWM® system the C-scan and B-scan images were very accurate in sizing the #1FBH. Certain traditional ECI systems are only capable of detecting #2-#3FBH under optimal inspection conditions.

There is disagreement over the validity of using flat bottom holes and EDM notches to simulate defects within the NDT community. It has been argued that FBH and EDM notches are not representative of real service cracks, especially in regions with shot peening or fretting damage [189]. Additionally, it has been noted the use of starter notches to generate fatigue cracks results in open cracks. These open cracks produce a greater signal response and are thus more easily detected [112, 185, 189]. The MWM-

array® system has demonstrated the ability to detect and successfully track accumulated damage from fatigue cracks formed without the use of starter notches for Al-alloy, Ti-alloy, and high-strength steel specimens [132]. Crack detection and characterization for samples after the application of various surface enhancement processes, such as shot peening, is ongoing. These topics will be revisited in Chapter 6 with the discussion of the proposed life methodology.

The duct segment was inspected with a UniWest® US-454 EddyView™ traditional ECI point probe. This probe operates at a single frequency channel. One frequency that is sent to the EC probe is generated by the single frequency channel, and the signal that comes back is detected by two phase sensitive detectors. This results in two analog signals which are displayed as horizontal and vertical axes in the impedance plane. These analog signals are shown in the equipment monitor in Figure 2.35(a-c).

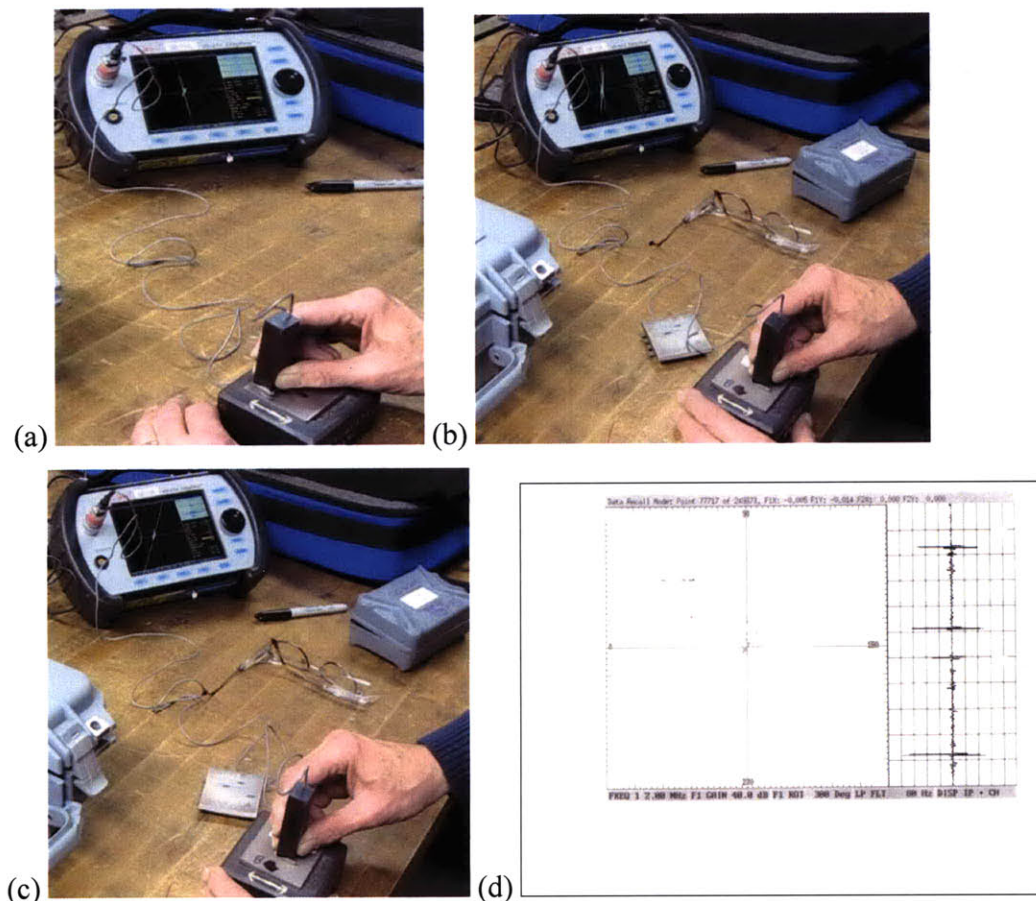


Figure 2.35: (a) Calibration to standard duct segment of known cracks (b) Flaw indication appears on traditional ECI equipment during inspection of duct segment specimen (c) Lissajous signal at 45° angle during inspection a sign of lift-off issues (d) Scan of analog data print-out with a strip chart representation to the right of the single frequency channel impedance plane

Similar to the Omniscan™ EC array probe, this system must also be calibrated to a standard. In this case, the standard is a duct segment component of known crack depth. The calibration duct segment contains notches of known depth, and the probe is traversed perpendicularly over the notches to produce vertical peaks such as the one shown in Figure 2.35(a). The probe is manually operated and the scan velocity should be around 2.5cm/sec (1in/sec). A test frequency of 2MHz with a gain of 40 ± 1 dB was selected for those test parameters. The inspection output is not in units of length, but rather in number of grid boxes. Each grid box represents 10% of the monitor screen therefore the screen height is a total of 10 grid boxes. Inspection acceptance and rejection criteria must be empirically determined using a statistical regression of results obtained during maintenance inspections.

Compared to the sensitivity of the MWM®-array inspection of the duct segment in Figures 2.32-2.33, this type of EC point probe provides a very crude form of analysis. Figure 2.35(b) shows the indication for the duct segment, however Figure 2.35(c) shows the inherent variability in lift-off for this probe design. The 45° angle for the Lissajous signal is indicative of lift-off variation during inspection. Additionally, the output for this inspection is not in a digital form. The UniWest® equipment must be manually connected to a printing device in order to obtain an analog print out of the data; otherwise the inspection data is lost and the operator's notes are all that remains from the inspection. Figure 2.35(d) is a scan of the duct segment print-out, with a strip chart on the right hand side that shows the signal response of the frequency channel. This system is currently the standard used for NDT eddy current inspection of aerospace duct segments at a particular MRO facility visited during the course of research. The transition from this technologically mature system to a more advanced system, such as the MWM®-array with Gridstation® software platform, would result in a significant improvement in inspection sensitivity, reliability, minimum flaw detection capability, and records (data) retention capacity. Each of these factors is significant in the feasibility of an RFC approach to life prediction of structural components.

Chapter 3: Phased Array Ultrasonic Inspection

This chapter discusses the phased array ultrasonic inspection experiments that were performed. Two PA-UT systems were analyzed: a manual phased array system utilizing gel as the coupling medium through which the sound waves were passed, and a fully-automated, water immersion PA-UT system. The first section of this chapter reviews the experimental procedure performed for these two phased array NDT systems. The test setup for the relevant samples is described, and an explanation is given for samples not examined. Results from these experiments are included in the sensitivity analysis section of this chapter. Finally, Section 3.3 contains a comparative analysis for the phased array techniques with their traditional UT counterpart. Pertinent factors not previously mentioned that affected the PA-UT experimental results are also considered.

3.1 Experimental Procedure

As the previous chapter detailing the experimental results of the MWM-array® eddy current inspection technique demonstrated, the NDT system response between the Ti-alloy block samples did not significantly vary. Even though the three samples were fabricated from varying alloys and processing routes, including a Ti-6-4 forging, Ti-6-4 billet, and Ti-17 billet, they essentially responded identically to the stated experimental objectives of first detecting the #1FBH array and second accurately sizing the array holes. A similar response from the three Ti-alloy block samples was also expected for the manual phased array inspections. This assumption was confirmed by the results of the traditional UT experiments discussed in Section 3.3, which were performed prior to any of the phased array UT testing. For this reason, only one of these samples was selected along with the P/M R88 sample for testing with the manual PA-UT system.

The TESI phased array system, located at the University of Dayton Research Institute (UDRI), was chosen for the fully automated PA-UT experiments. This selection was based on two main considerations: 1) prior research performed at the site relevant to airplane disk components, and 2) technical proficiency of the UDRI staff in the field of phased array ultrasonic inspection. This system was designed for fully automated inspection of turbine engine disk components, and as a result was only programmed to accommodate samples with circular symmetry. This factor excluded all samples other

than the wedding cake specimens from analysis. In spite of this, the wedding cake samples provided the most utility in the PA-UT flaw threshold sensitivity analysis performed due to the wide range of flaw sizes and varied flaw depths of the three specimens. The multitude of flaw sizes and depths at specified circumferential locations, described in Tables 2.2-2.3 specifically for the Al-6061 wedding cake but generally indicative of all the samples, provided many opportunities for inspection on a single sample. The number of opportunities for inspection is statistically significant in the determination of POD. Appendices F and G of [29] include a thorough discussion on this topic.

The three wedding cake samples were also analyzed with the manual PA-UT system so a comparison between the manual and automated PA-UT systems could be made. In addition to this, Section 3.3 contains a comparison between the manual PA-UT system and a traditional immersion-UT system. The wedding cake specimens were not tested with this traditional immersion-UT system, and the reasoning for that decision will be discussed in Section 3.3. The complex geometry of the turbine blades prevented their inspection by either of the PA-UT systems or the traditional UT system. Also, the duct segment component was not tested as part of the phased array experiments. The surface cracks of the duct segment would typically be inspected with an eddy current or FPI technique rather than an ultrasonic one. However, as the traditional UT results on the alloy block specimens in Section 3.3 will show, UTI is capable of detecting surface cracks. It was decided to not inspect the duct segment by PA-UT based on these results combined with the successful flaw detection of the duct segment's surface cracks previously demonstrated by the MWM-array® technique. Because they were not inspected, neither the sensitivity analysis nor the discussion on PA-UT system capability mentions the actual engine component samples. Determination of detection capability with respect to sub-surface flaws was the main objective of the PA-UT experiments.

3.1.1 Alloy Blocks

Sample H and Sample R88 were the respective Ti-alloy and Ni-base superalloy block specimens examined with the manual PA-UT system. The experiments were performed at the Olympus® NDT Inc. facility in Waltham, MA. An Omniscan® MX phased array system built with the Tomoview™ software package was used to inspect the

parts. A 64 element PA-UT probe [Model #5L64-A2] of 9.6mm (0.378 in.) aperture, with a refracted L-wedge [Model #SA2-0L] was selected to inspect Sample H. The wedge angle was 0° . Of the 64 elements, the 16 elements numbered 40-55 were used to generate the phased arrays. A 5MHz probe frequency at a system voltage of 80V and gain of 34dB was used in pulse-echo mode to inspect the sample. The samples were oriented as shown in Figure 3.1. A $17.239\mu\text{s}$ beam delay was used to phase the sound waves through the 5.45cm (2.147 in.) wave distance range through the samples to the 3x3

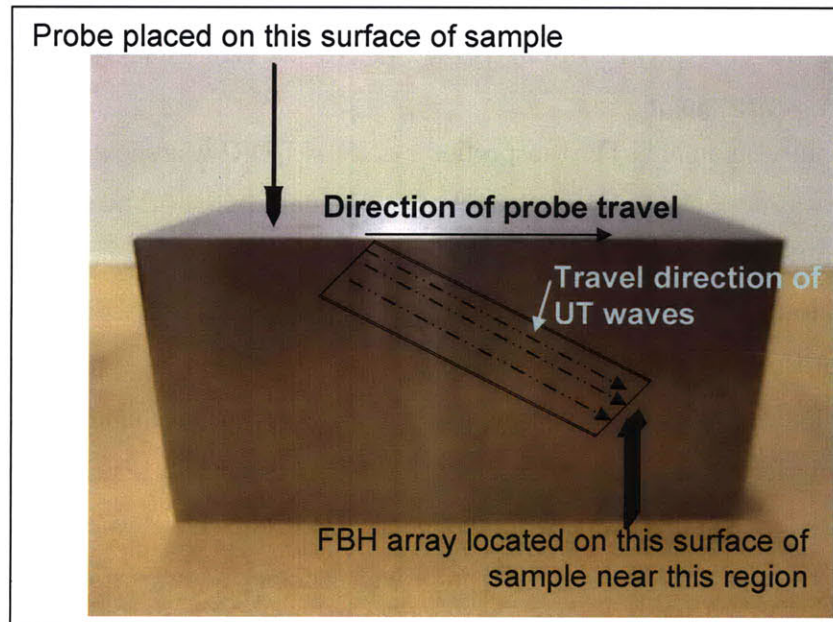


Figure 3.1: Orientation of samples for the manual phased-array UT scans

FBH array. The wave type was longitudinal with a sound velocity of $6.1 \text{ mm}/\mu\text{s}$ ($0.24 \text{ in.}/\mu\text{s}$) and 100ns pulse width specified. The Tomoview™ advanced calculator automatically programmed the angle beams and focal point laws for the inspections. A focal depth of 3.8cm (1.5in.) was calculated. A scan speed of 21mm/s ($0.827 \text{ in.}/\text{s}$) and scan resolution of 0.99mm (0.039in.) were calculated for the 7.6cm (3in.) thick samples. Sample H was inspected with both *Sectorial* (S-scan) and *Longitudinal at 0°* (E-scan) focal law configurations. The S-scan was performed through a $0\text{-}30^\circ$ range of angles at a 0.5° angle resolution.

The P/M Rene88 sample was inspected at a higher probe frequency of 17MHz. A 100 element probe [Model #17L100E35-4] of aperture 4.6mm (0.18 in.) was used with the refracted L-wedge for this S-scan inspection. The 16 elements numbered 80-95 of the

100 element array were selected. A system voltage of 80V and higher 59dB gain were used in pulse-echo mode to inspect the sample. A 17.18 μ s beam delay was used to phase the sound waves through a half path range of 5.38cm (2.118 in.). The wave type and material sound velocity values were the same as for Sample H, but the pulse width was lowered to 30ns. The S-scan was performed through a 0-30° range of angles at a 1.0° angle resolution and 5.1cm (2.0 in.) focal depth. The scan speed and resolution values were not changed from Sample H. After each inspection, the Omniscan® system software automatically generated a report containing all these test setup parameters.

3.1.2 *Wedding cake samples*

The fully automated TESI inspection system at UDRI was shown in Figure 1.20. The system was designed to be fully automatic. The definition of fully automatic can have many different meanings depending on context and the individual using the term. With regard to the TESI inspection system, it means no human interaction with the inspection process [100, 191]. Some of the components of the system that enable the removal of human interaction are: a six-axis robot used as the mechanical manipulator; a water control system that fills and empties the 600 liter capacity cylindrical water tank automatically for each inspection; a turntable that rotates the entire water tank rather than the individual component in the tank for improved accuracy and repeatability during inspection; a 128-channel PA-UT instrument designed to allow automatic changing between the various PA-UT transducers; and finally a graphical user interface for designing inspections and scan plans [100]. The R/D Tech® Tomoscan III phased array ultrasonic instrument was the one selected, because it supported the simultaneous use of up to 32 of the total 128 channels attached to the multi-element probe [108]. These multiple-transducer elements can be individually pulsed with one of the 32 pulsers (channels). The pulsers can then be multiplexed to obtain the total 128-channel capability.

The term *multiplexing* refers to the ability of the different active channels to simultaneously acquire data at different test parameters specified for the same ultrasonic inspection. The conditions that change between channels are the focusing depth, number of elements used to create the focused beam, and electronic scanning along the probe [191]. Additionally, gain settings, gate position, or data acquired may be changed

between channels. Multiplexing significantly improves the detection sensitivity and scan coverage during an ultrasonic inspection [92, 101]. This is a particularly important aspect to the POD for sub-surface defects. A design requirement for the TESI PA-UT system was to use state-of-the-art technology while incorporating off the shelf components as much as possible. To this end, it was found that a majority of inspections could be performed using a 10MHz, 64 element linear array probe [108]. This particular array probe has 0.45mm x 5.0mm (0.018x0.197 in.) sized elements with an element spacing of 0.5mm (0.02in.) from center to center [108]. This commercially available linear array transducer has been used in industrial applications, and was one of the transducers selected to inspect the wedding cake samples. A 5MHz linear array probe containing 128 elements with an element spacing of 1.0mm (0.04in.) was also available and used in the fully automated PA-UT inspections.

The wedding cake samples were inspected with the two linear array probes described above in both longitudinal and shear modes. The 6061 Al-alloy wedding cake was inspected in the “bottom-up” orientation shown in Figure 3.2(a). The centering tool used in Figure 3.2(b) enabled positional repeatability within 0.05mm (0.002in.) and a positional accuracy of 0.05mm per 300mm (0.002 inches per foot) [96, 100]. Similarly, the test setup for the steel wedding cake sample is illustrated in Figure 3.3(a-b). One unintended consequence of using the 8620 alloy mild steel instead of a stainless steel alloy was the severity of environmental attack on the steel wedding cake. A significant amount of rust on the sample is evident in Figure 3.4(a-c), caused by the specimen’s complete submersion for an extended period of time during inspection. Since the fully-automated inspection was performed before the manual PA-UT inspection, it is unknown what affect this corrosive oxide scale had on the signal response of the latter inspection. Fortunately, the inspection of the steel wedding cake containing the embedded defect was performed on the manual PA-UT system first. Therefore an unbiased signal response was obtained for a single wedding cake sample by both the manual and fully automated phased array setups.

The 10 MHz, 64 element linear array probe was focused at depths of 3.8, 8.9, 19.1, or 38.1mm (0.15, 0.35, 0.75, or 1.5 inches). Electronic scanning along the

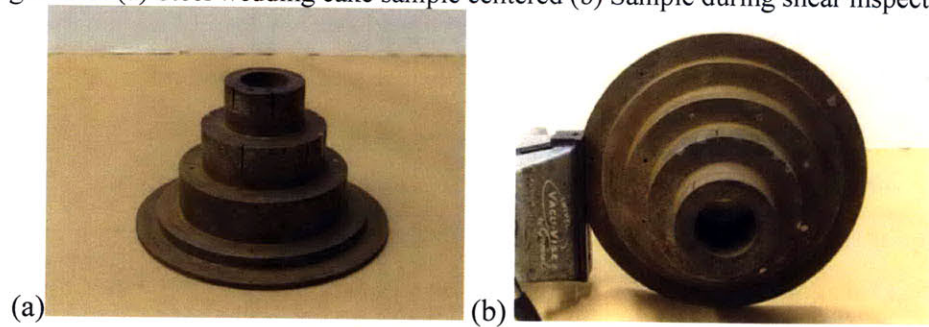
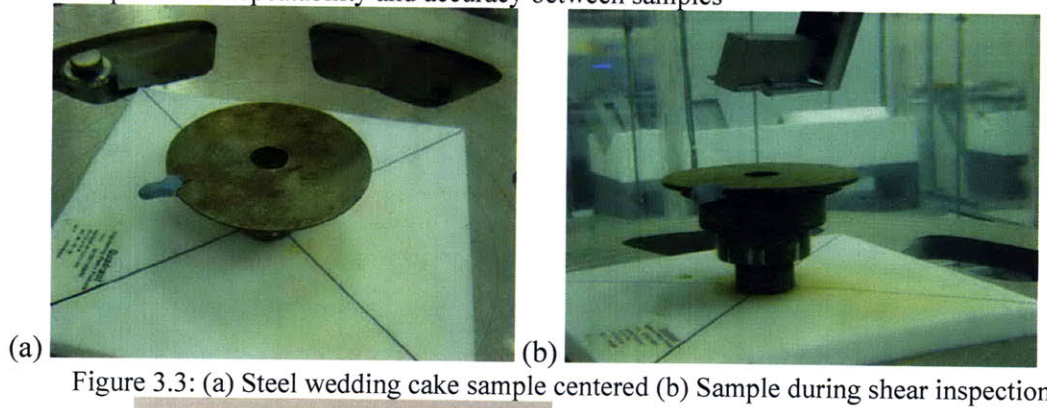
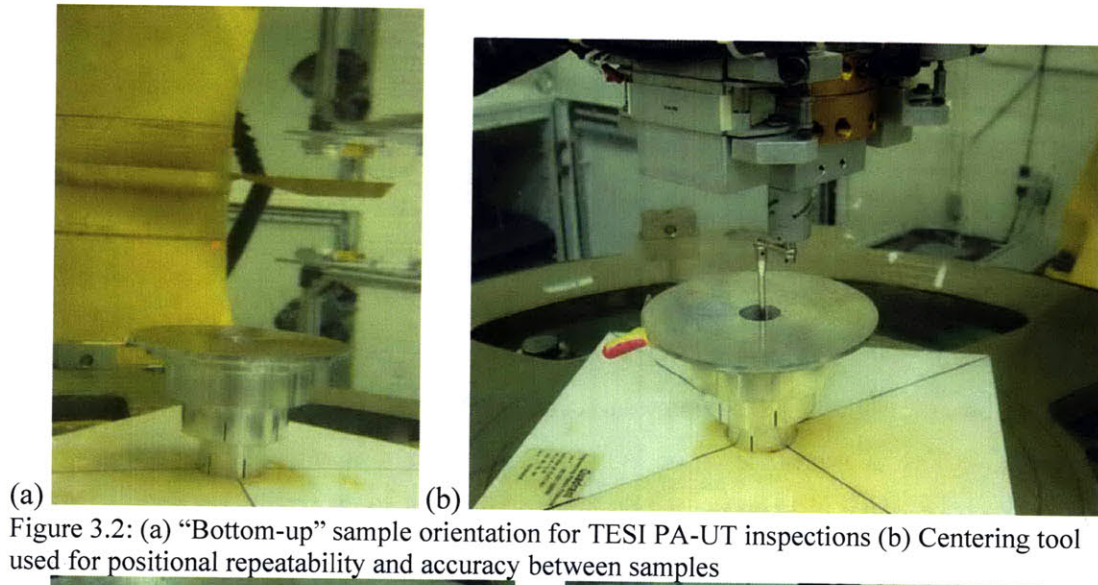


Figure 3.4: (a-c) Three perspectives of the steel wedding cake after inspection detailing the severity of rust caused by complete water immersion.

probe was used to acquire data from approximately 12.7mm (0.5in.) sections of the part simultaneously. The electronic scan index spacing was one element width, or 0.5mm (0.02in.). The longitudinal (at 0°) inspections for the 10MHz probe were broken up into 4 separate data files with 4 different physical probe positions along the part. This is pictured schematically in Figure 3.5(a) and through the graphical user interface of the TESI software in Figure 3.5(b). Hardware setup and control of the Tomoscan III instrument is accomplished with the Quickview™ PC based software application [108].

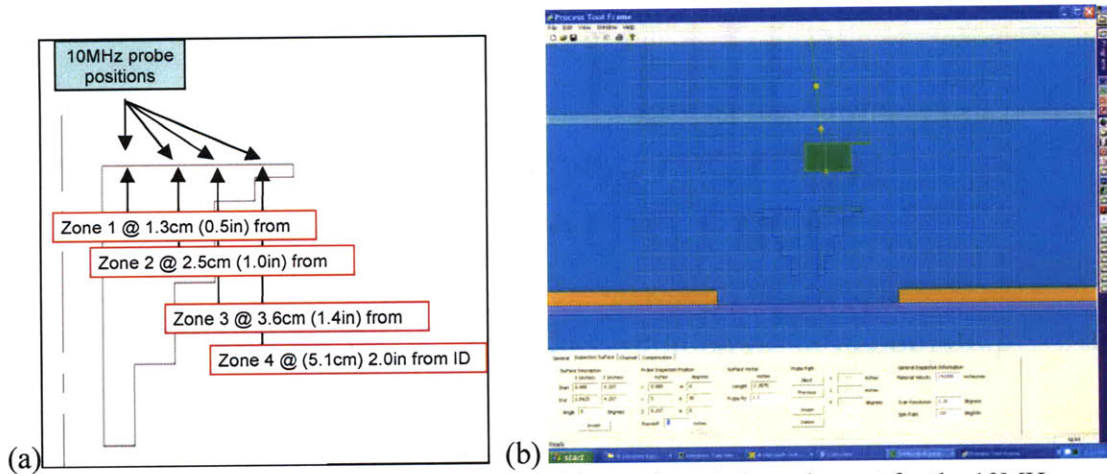


Figure 3.5: (a) Schematic of the four probe positions selected along the part for the 10MHz longitudinal inspections (b) Probe position during inspection as seen through graphical user interface of TESI software

The 45 degree shear inspections were only performed near the outside edge of the part, since the targets could not be inspected below about a 2.5cm (1 in.) depth. Focal depths in shear were located at 0.21, 0.83, and 2.47cm (0.081, 0.325 and 0.974 in.). These focal depths were based on earlier work [93, 97, 102, 191] performed on aerospace materials. Figure 3.6 provides a similar representation for the shear scans that Figure 3.5(a) provided for the longitudinal scans. For the 5MHz linear array, the electronic scan index spacing was one element width, which for the 5MHz probe was 1.0mm (0.04in.). This larger scan index size and longer electronic scan range allowed data acquisition over the entire width of the specimen in a single data file for this frequency. Focusing depths used with the 5MHz linear array probe were 0.25, 1.9, and 4.3cm (0.1, 0.75 and 1.7in.) for the longitudinal inspections. The 45° shear data utilized 1.0, 2.5, and 4.3cm (0.375, 1.0 and 1.7 in.) focal depths. Figure 3.7(a-b) presents the probe position both figuratively and via the TESI Quickview™ software interface.

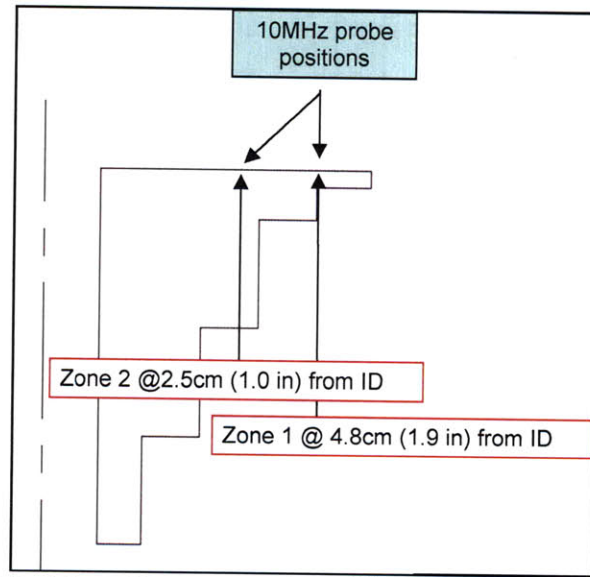


Figure 3.6: Schematic representation of the two probe positions selected for the 10MHz 45° shear inspections

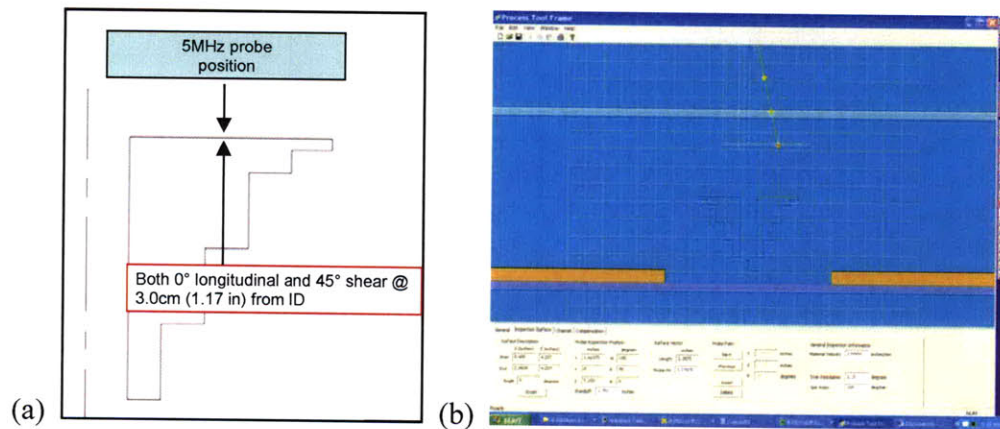


Figure 3.7: (a) Schematic representation of the 5MHz probe position for both the longitudinal and shear inspections (b) 5MHz probe position visualized with TESI graphical user interface

The same Olympus Omniscan® MX phased array system used to inspect the alloy block samples was also operated for the wedding cake specimen inspections. As was the case for the inspections at UDRI, the specimens were oriented in the “bottom-up” position shown in Figure 3.8. Unlike the experiments at UDRI, a water soluble gel was applied to the Level 1 sample base only. This is shown in Figure 3.9(a), while Figure 3.9(b) shows the calibration of the Omniscan® system, including the automatic software calculation of every element’s focal law. The aluminum wedding cake was initially examined with a 10MHz probe, however it was determined that a higher frequency was

needed to detect the smallest 0.28mm (0.011 in.) laser drilled hole diameter. For this reason the 17MHz, 100-element probe [Model #17L100E35-4] used to inspect the P/M R88 specimen was also used for all three of the wedding cake samples inspected.



Figure 3.8: "Bottom-up" specimen inspection orientation

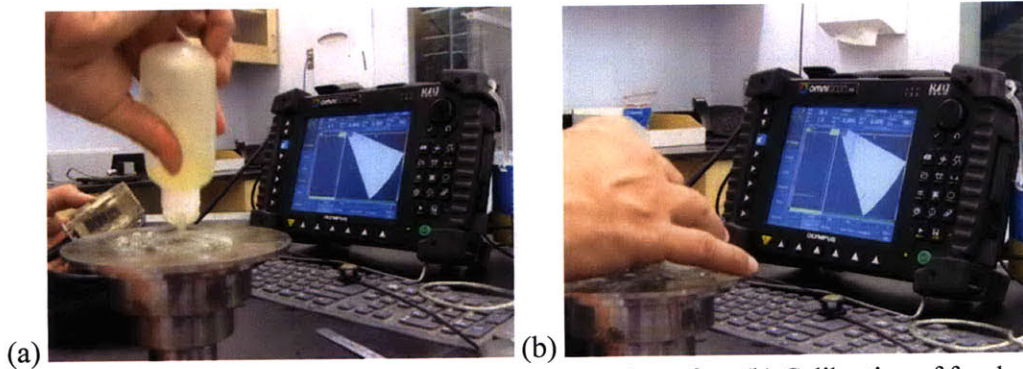


Figure 3.9: (a) Application of gel couplant to sample surface (b) Calibration of focal laws for experiment

3.2 Results of Sensitivity Analysis

The results for the manual phased array ultrasonic inspections on the alloy block samples are shown in Figures 3.10-3.13. The inspection data was viewed with Tomoview™ Version 2.8R7. The axes of the figures are in units of inches. Figure 3.10(a) contains the output from the 5MHz S-scan of Sample H detailing one row of FBH. In Figure 3.10(b) markers were placed on the image to estimate hole depth. The vertical marker placed over the faint indications at the 3.500 in. (8.9cm) index length represented the bottom depth of the holes. The 0.226 inch (0.57cm) estimation of hole depth has an

error of approximately 10% from the true value of 0.25 in. (0.64cm). Human factors contributed to this error. The marker placement was performed manually and was subject to the personal discretion of the operator.

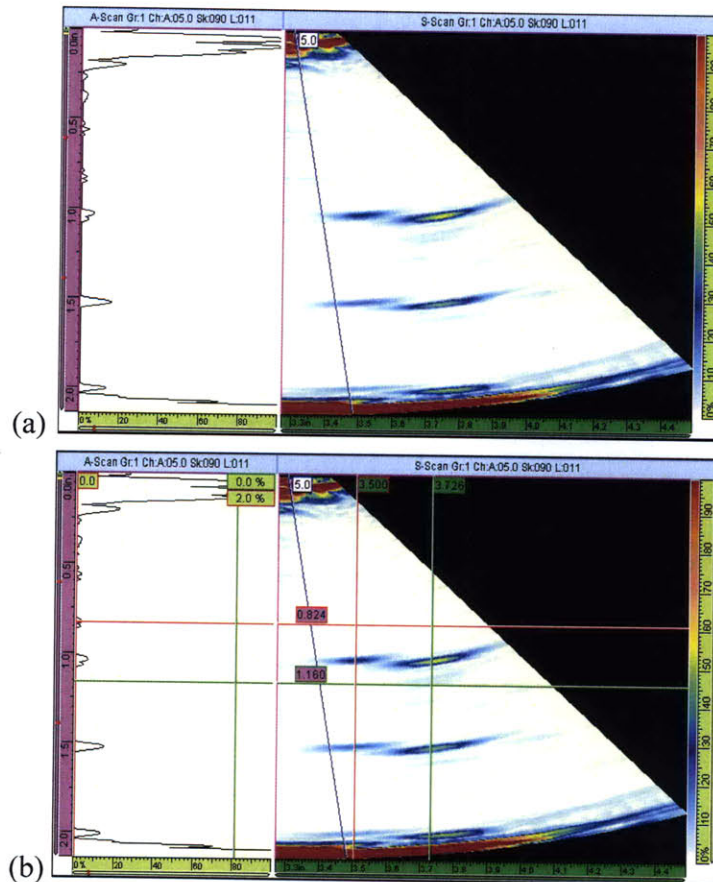


Figure 3.10: (a) Output from 5MHz S-scan of Sample H detailing one row of FBH (b) Markers placed on image to estimate hole depth. Faint indications to the left of three holes represent the bottom depth of the holes.

The 5MHz longitudinal E-scan results for Sample H are presented in Figure 3.11(a-c). All nine flat bottom holes were visible in a single longitudinal scan, however the image resolution decreased with increasing wavelength. The distance between holes in the X and Y directions were estimated at 0.501 in.(1.27cm) and 0.515 inches (1.31cm) respectively. These values show very good agreement with the actual length of 0.5in. (1.27cm). In Figure 3.11(c), magnification and dynamic depth focusing were used to obtain a C-scan image with a more accurate hole aspect ratio. Figure 3.12(a-c) contains similar images for the R88 sample at 17MHz. It can be seen that the 3x3 FBH array

image resolution is worse at the higher frequency. The C-scan image degradation is attributable to material property differences between the Ti-6-4 and P/M Rene' 88 Ni-

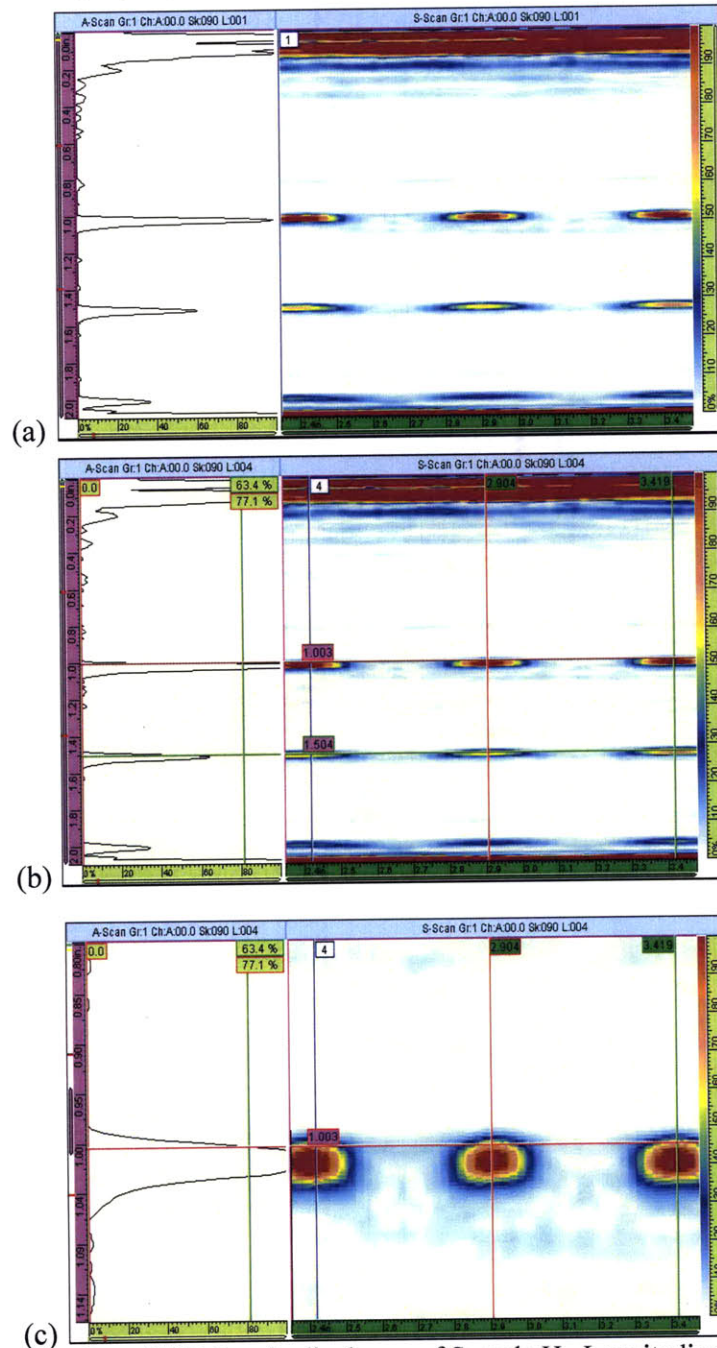


Figure 3.11: (a) Results from 5MHz longitudinal scan of Sample H. Longitudinal scan at 0° showing 3x3 array of FBH. (b) Markers placed on image to estimate distance between holes in both X and Y directions. (c) Magnification and dynamic depth focusing of top row of FBH in 3.11(b) Note this was an E-scan. The S-scan headings were not updated from Figure 3.10 during inspection [190].

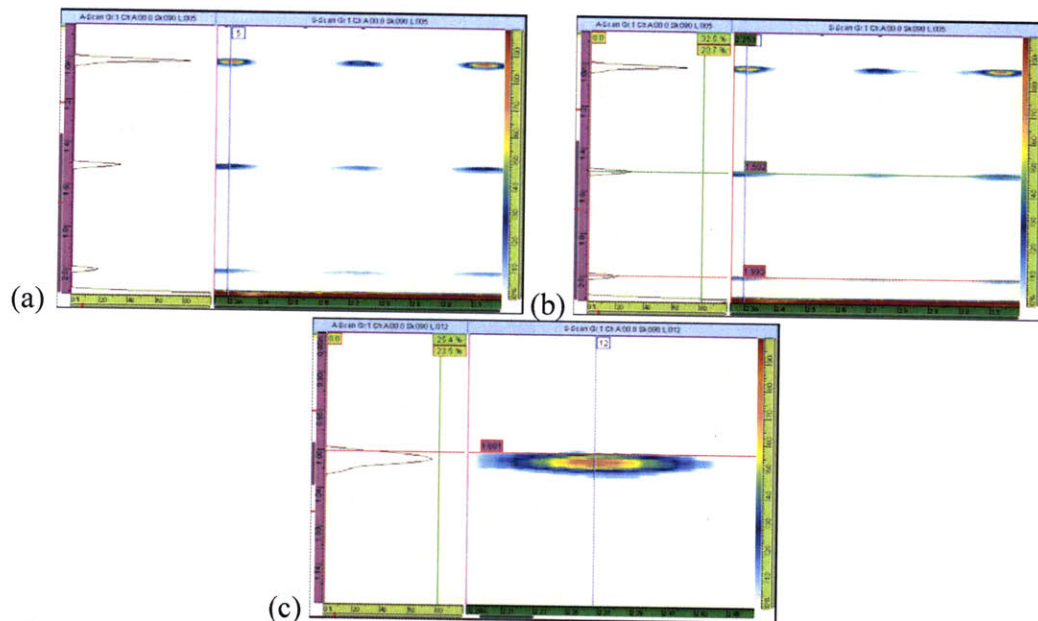


Figure 3.12: (a) 17MHz longitudinal E-scan of Sample R88. Note difference in image resolution between 5MHz and 17MHz scan. (b) Distance between two holes estimated at a particular depth. (c) Image magnification of top left hole in 3.12(a-b) *Note this was an E-scan. The S-scan headings were not updated from Figure 3.10 during inspection.*

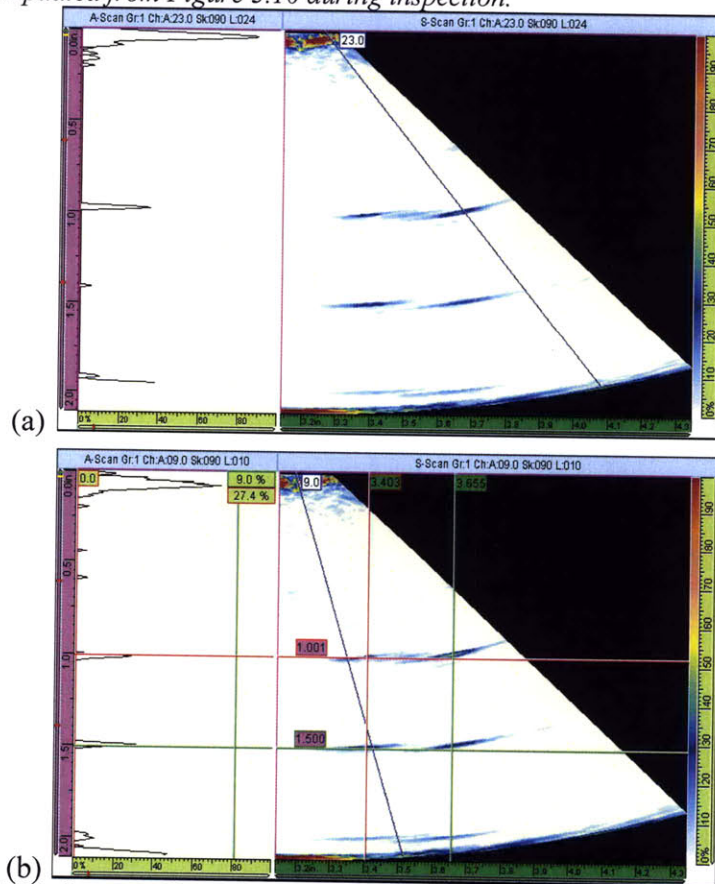


Figure 3.13: (a) 17MHz S-scan of Sample R88 (b) Depth and distance markers placed on image

base superalloy specimens. While it is well known that Ti-alloys are ultrasonically “noisy” materials, the high alloying content of the nickel-base superalloys imparted a comparable level of inherent microstructural grain noise. This grain noise combined with the high material density for the R88 sample required a higher test frequency to penetrate through the specified sample depth. Sound wave attenuation due to both absorption and scattering appeared to result in significant dB loss of energy in the pulse-echo signal for holes that were the greatest distance from the probe, as evidenced by the 2nd and 3rd rows in Figure 3.12(a).

The 17MHz sectorial scan for Sample R88 is shown in Figure 3.13(a-b). Again, the C-scan sectorial image for the R88 sample is not as well characterized as the image for the Ti-6-4 Sample H. Attenuation has already been mentioned as a factor, but acoustic impedance is an equally important factor in the image quality difference between Figures 3.10-3.11 and Figures 3.12-3.13. Acoustic impedance values for these two particular alloys was not found in the literature, but the acoustic impedance for Inconel® was about twice that of Titanium [65, 70]. As shown in Figure 3.13(b), despite the materials-science related challenges with ultrasonic characterization of a highly-alloyed specimen, very accurate measurements on flaw depth and distance were made. A hole depth of 0.252 inches (0.64cm) and a distance of 0.499 inches (1.27cm) between adjacent holes was calculated. The error between these measurements and their true values were 0.8% and 0.2% respectively. More attention to the accurate placement of the image markers resulted in the improved accuracy for the manual PA-UT alloy block results.

The sensitivity analysis results for the wedding cake samples with the manual Olympus® phased array system are next to be discussed. Particular emphasis will be placed on the inspection results for the embedded defect steel wedding cake sample, but the other two samples will be briefly discussed first. The bottom surface of the aluminum wedding cake sample was scanned with the 17MHz, 100-element probe. Figure 3.14(a) contains a screen shot from the Tomoview™ software with A-scan, B-scan, and C-scan plots from the first linear probe pass over the edge of the sample. In the B-scan, the multi-colored horizontal lines are indicative of a sound wave multiple. These artifacts are caused because the sound waves have nothing to reflect off of back to the probe once they exit the bottom of the flat holes. Instead they strike air, so they are visible at every

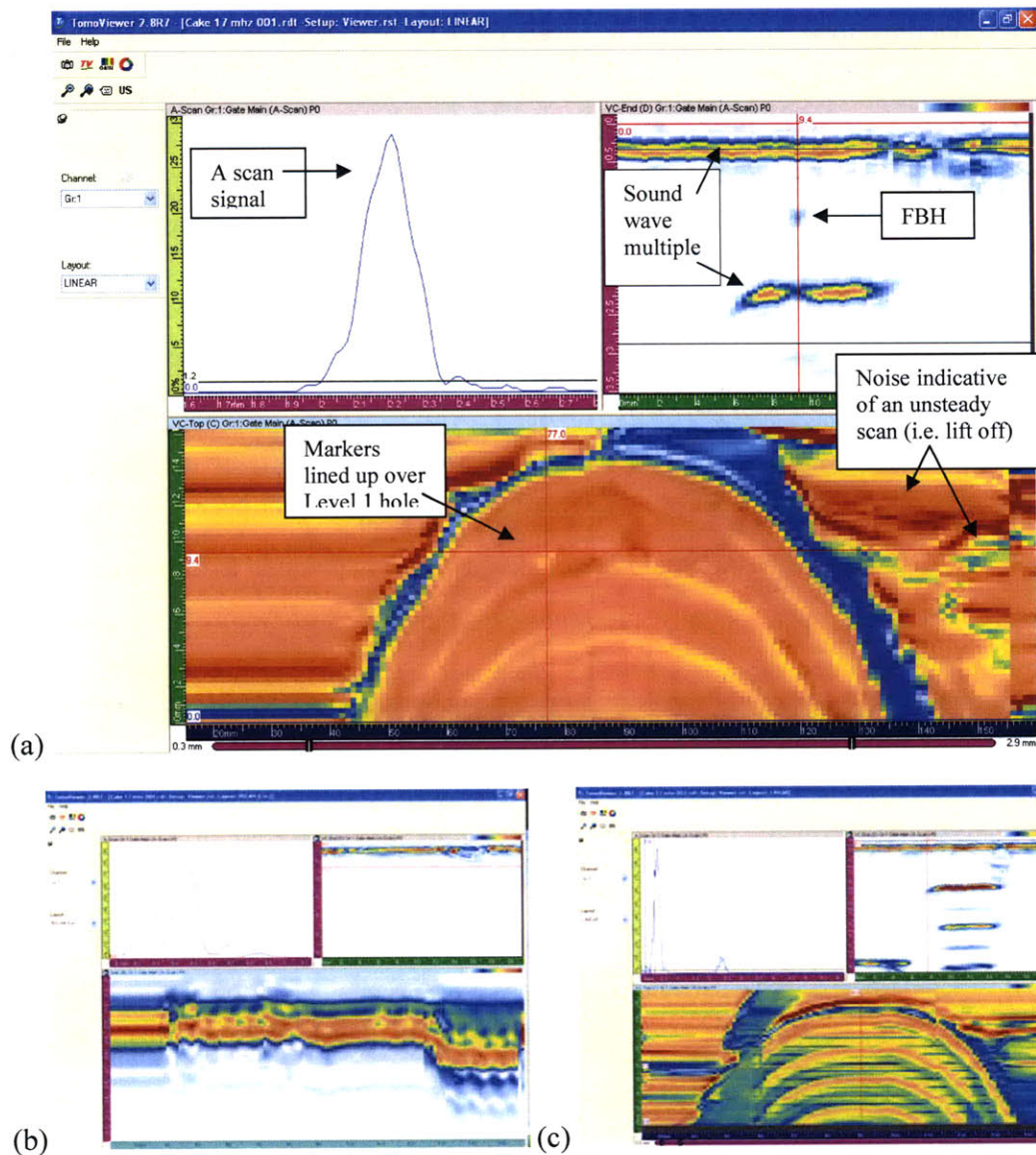


Figure 3.14: (a) Tomoview™ screen shot of the initial linear pass along the surface of the Al-wedding cake sample. A-scan signal shown in top left, B-scan in top right, and C-scan in bottom half of display. Markers have been slid over one of the Level 1 holes. Three levels of the wedding cake sample are discernable in C-scan image. (b) Magnified view of lift-off variation likely caused by “sticking” of the probe to the sample surface near the edges of the center hole (c) Image quality improvement in subsequent manual scan.

wavelength multiple of their echo. The 0.28mm (0.011in.) diameter FBH is the indication seen about halfway between the sound wave multiples. Since the FBH depth was drilled about halfway in the outermost Level 1, the FBH indication at that position in the B-scan was expected. The *time corrected gain* (TCG) option in the Omniscan® software was turned on to minimize noise due to scattering and thus maximize signal

response. The C-scan image in Figure 3.14(a) also contains a lot of noise from probe lift-off. Figure 3.14(b) is a magnified view depicting the severity in lift-off variation across the sample surface. This was attributed to operator error, and resulted from hand unsteadiness while holding the probe during the longitudinal scan. The design of the wedding cake, with its bored-out center hole region, caused the probe to “stick” and made maintaining a uniform lift-off more difficult. Figure 3.14(c) was a subsequent manual scan. The image quality improvement resulting from the more uniform probe lift-off is evident, but the presence of noise is still obvious. In a manner similar to the X-Y encoder gantry used in the MWM® scans, incorporating a level of automation into the manual phased array inspection could significantly reduce these sources of variability and noise. Additionally, the use of an encoder gantry system would precisely calculate the correct locations for multi-pass scans so that images from the individual scan passes could be integrated into one homogenous figure. As seen in Figure 3.15(a-d), flat bottom

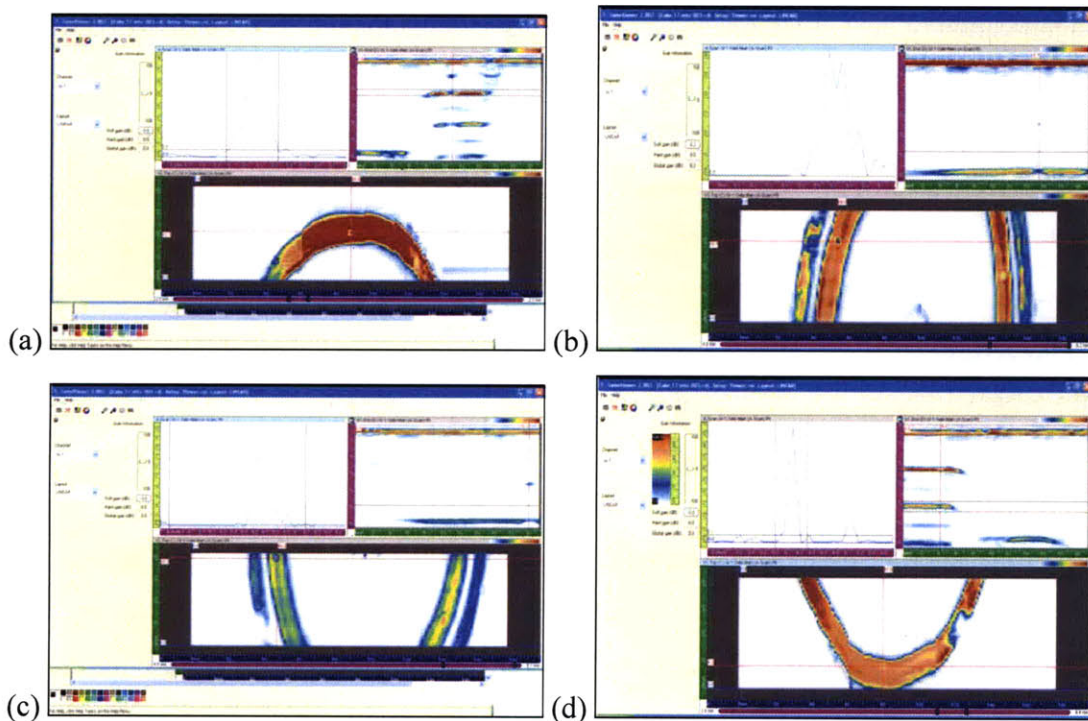


Figure 3.15: (a-d) Iterative passes required to image the entire 6061 Al-wedding cake sample. FBH on Level 1 and Level 2 are observed in (a-c); however as the A-scans show, the variation in signal response is large. This variability complicates the quantification of system capability in the sensitivity analysis.

holes were detected on multiple levels, but the variability between iterative surface scans of the same inspection sample complicates the sensitivity analysis. In general, none of the side drilled holes (SDH) on Level 4 or 5 were able to be distinguished due to a combination of noise from inspection variables and attenuation masking the SDH signal. A level of scattering and transmission losses were expected since the sound waves had to penetrate through Levels 1-3 before reaching the SDH. The use of an X-Y encoder would have changed the inspection classification from manual to semi-automated and most likely improved flaw detection of both SDH and FBH.

Figure 3.16(a) is the same image from Figure 3.14(a), only with the range turned down in order to examine the thinnest layer, i.e. Level 1. Magnification of the B-scan reveals the presence of *ghost echoes* in Figure 3.16(b), which are artifacts especially relevant when small flaws are the object of detection. Ghost echoes are due to high pulse repetition frequency (PRF), and can be mitigated by editing the element firing sequence in the Omniscan® advanced focal law calculator [65, 70, 71, 113, 192]. In Figure 3.16(c), magnification of the C-scan image reveals a substantial amount of pixilation. A flaw of this size is pushing the capability limits of the manual PA-UT system. Based on the contiguous dark blue portion of the C-scan, the FBH diameter was estimated to be 1mm (0.039 in.) in size. The error in the flaw size estimate for this particular FBH was around 250% for the image in Figure 3.16(c). Figure 3.16(d) shows a much better image resolution for a larger FBH located on Level 3 at a different position. An error as large as in Fig. 3.16(c) could result in the forced use of hit vs. miss data in lieu of a vs. \hat{a} data. This topic will be broached in Chapter 5.

The variation in surface condition between the two steel wedding cake samples had a significant impact on inspection sensitivity. Both samples were inspected with the same 17MHz probe used on the aluminum wedding cake sample. The steel wedding cake sample without the embedded defect had previously been tested at UDRI on the TESI system. As detailed in Figure 3.4, the complete immersion of the sample for the fully automated inspection resulted in extensive rusting on the sample surface. Nevertheless, Figure 3.17(a-d) portrays the detection of a 0.5mm (0.020 in.) FBH in the oxidized steel sample. The utilization of a gated signal threshold technique was helpful in the analysis. The placement of the probe is shown in Figure 3.17(a-b), while Figure

3.17(c) shows no defect below the response threshold and Fig. 3.17(d) shows the flaw after the gated threshold level has been tripped by its signal. As exhibited in Figure 3.17(b-c), the background noise is much higher in the steel sample because of the surface rust. The increased background noise necessitated the use of the gated threshold to observe the FBH indication more reliably. At the time the manual PA-UT inspection

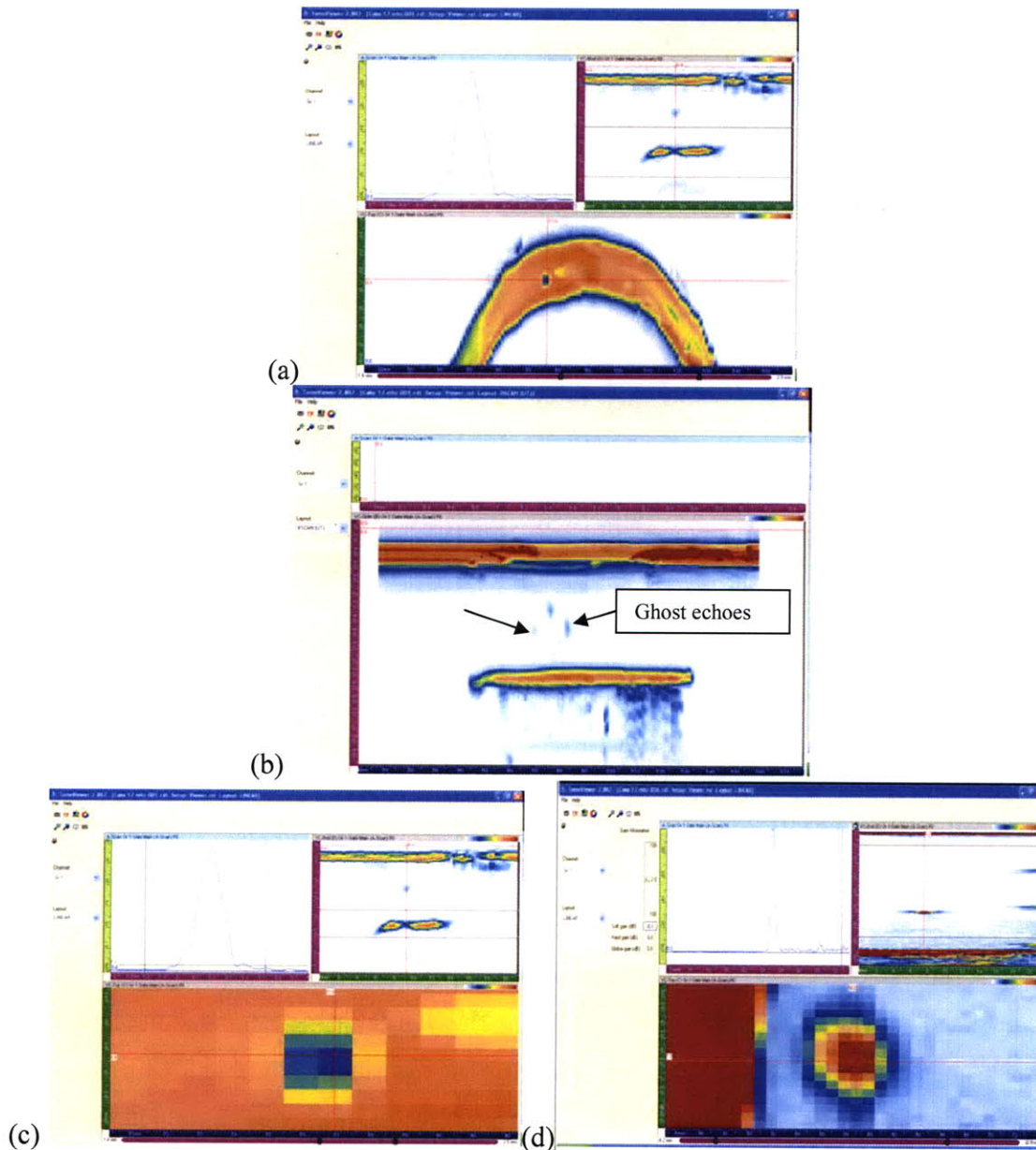


Figure 3.16: (a) Same scan as in Figure 3.14(a) but with the range turned down in order to better examine Level 1. (b) Magnification of B-scan reveals ghost echoes (c) Substantial pixilation in C-scan image.(d) Improved resolution in larger FBH located at different Level 3 position.

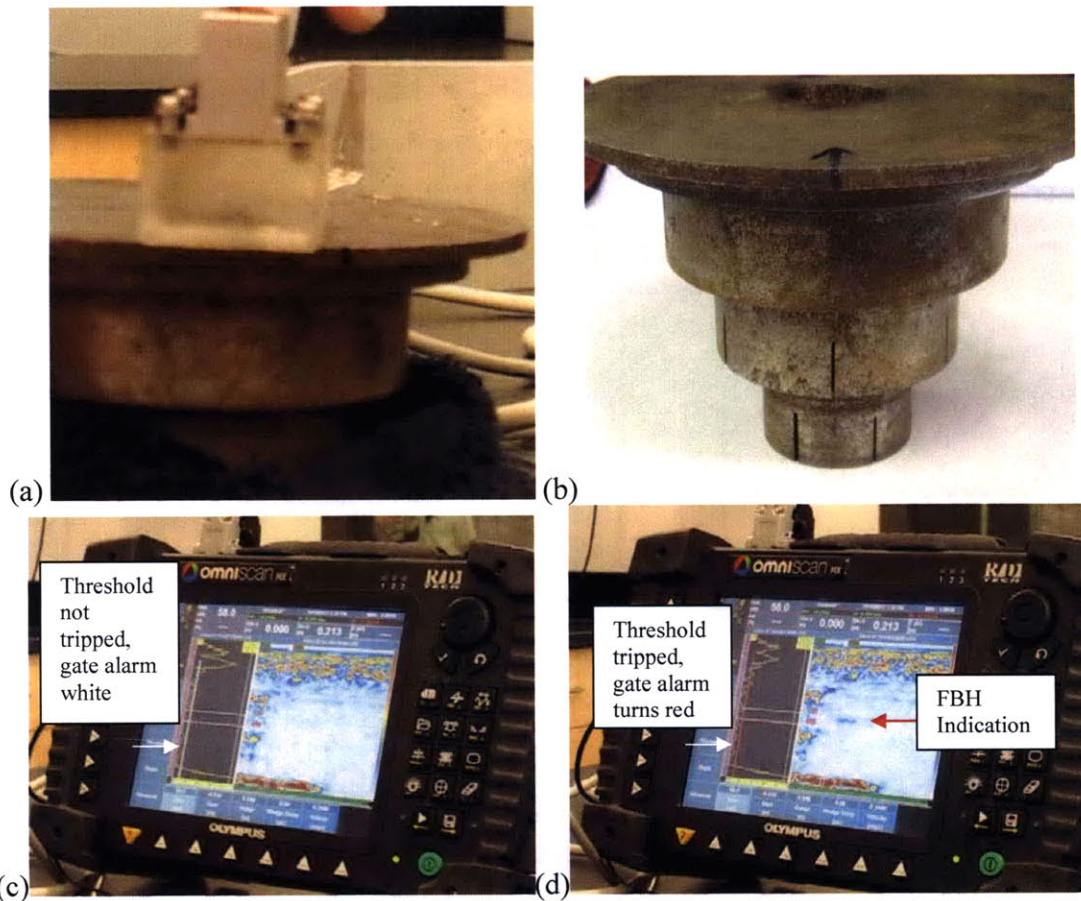


Figure 3.17: (a) Linear array probe placement on rusted steel sample (b) Sample orientation with probe removed (c) Threshold not tripped, gated alarm remains white and no FBH indication observed (d) Gated threshold tripped, alarm goes off and gate turns red. The red arrow in (d) points to the FBH indication on the Omniscan® monitor.

with the gel couplant was completed, the embedded defect steel sample had not yet been tested at UDRI. Therefore its surface condition had not been adversely affected by the water immersion inspection. Figure 3.18(a) shows the probe placement on the sample surface. A ruler placed between the array probe and the embedded defect is provided in Fig. 3.18(b) to serve as a reference length to compare with the S-scan result and calculated embedded flaw size in Fig. 3.18(c). The S-scan image estimated the length of the broken drill bit defect to be 0.35 in. (9mm). The measurement in Fig 3.18(b) shows the drill bit diameter was actually 0.375in. (9.5mm). Also, the actual drill bit depth was not known a priori. Unlike the simulated defects that had known sizes and depths, this embedded defect was an actual defect of an unknown size, morphology, and depth. The Omniscan® system estimated the base of the drill bit at a depth of 0.975 in. (2.48cm).

This was believed to be a reasonable estimate because the drill bit broke approximately a third of the way through the sample. The last observation on the Olympus® phased array system is included in Figure 3.19. A number of sound wave multiples from Level 1 and Level 2 are seen. The NDT system estimated the depths of these two levels to be 0.16in.(4mm) and 0.47in.(12mm) from the bottom-up orientation. The top-down schematic of the wedding cake in Figure 2.5 indicated the true heights (depths in bottom-up orientation) to be 0.15in.(3.8mm) for Level 1 and 0.5in.(1.27cm) for Level 2. Accuracy in size estimation was demonstrated for both flaws and surface features.

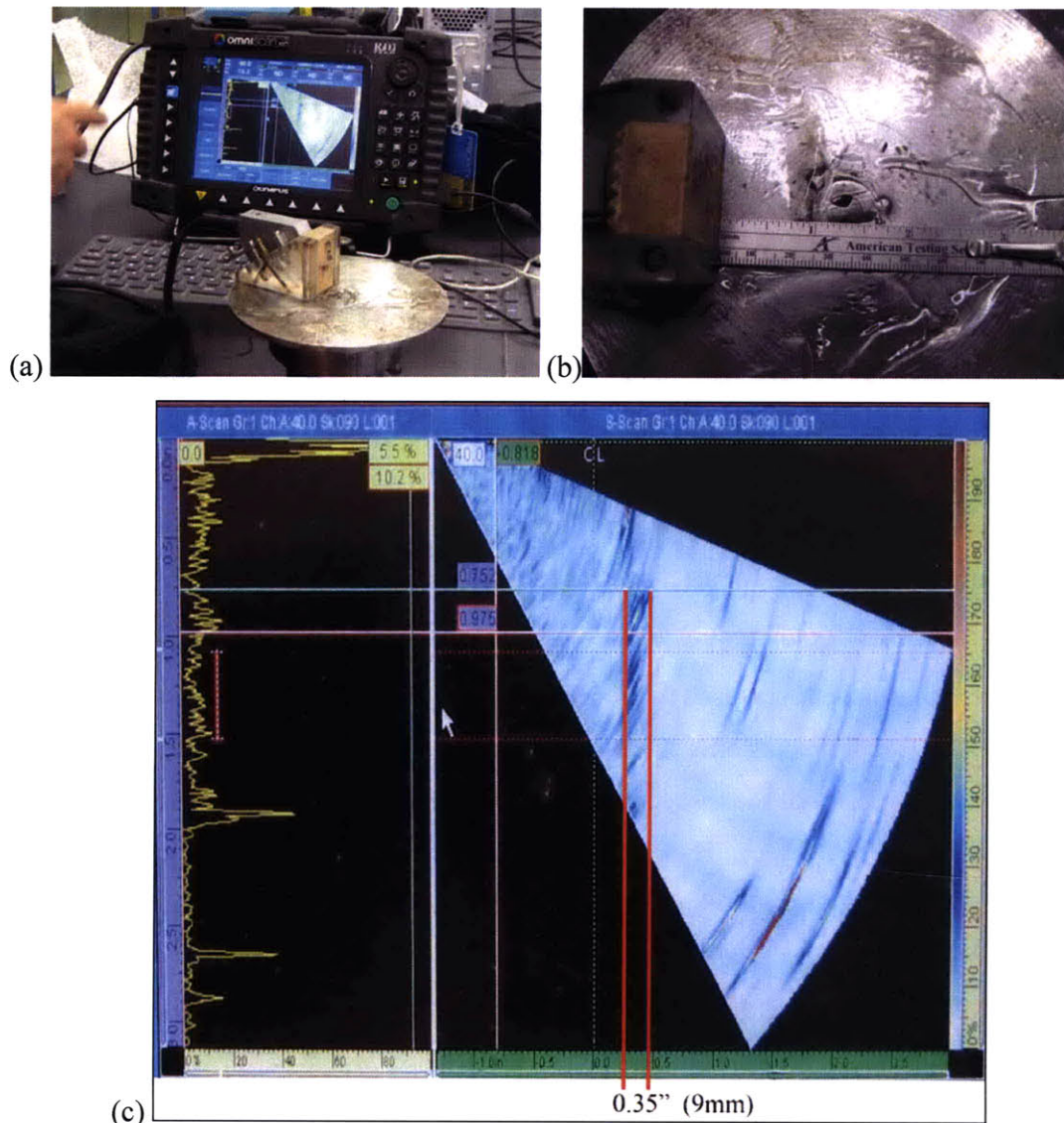


Figure 3.18: (a) The probe placement on the embedded defect wedding cake sample surface (b) Reference measurement on diameter of embedded defect (c) S-scan image of sample showing detection and sizing capability of manual PA-UT.

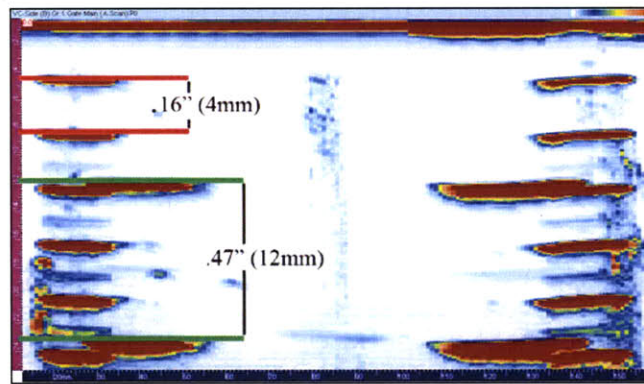


Figure 3.19: Estimation of Level 1 and Level 2 depths from a bottom-up orientation. The estimated values are very close to the actual values shown in Figure 2.5

The fully automated experiments at UDRI were based off scan plans previously used on actual Ni-base superalloy and Ti-alloy engine disk components. The scan plan used with the 10MHz inspections was originally developed for inspections up to a 2.5cm (1in.) depth on an IN100 alloy component. The 5MHz inspection scan plans were developed for titanium forgings that had a maximum depth of 7.6-10.2 centimeters (3-4 in.). The creation of a unique scan plan is a time consuming process. It was determined the use of these prior scan plans was acceptable since the wedding cake samples were meant to be a simplified representation of a disk-like component. Also, the steel attenuation and impedance values were comparable to the IN100. Table 1.6 shows the acoustic impedance values for steel and Inconel® differ by only about 8%, while the acoustic impedance for aluminum was about $\frac{1}{3}$ that of IN100 and $\frac{2}{3}$ that of titanium. The TESI system has never been used to precisely “size” defects [193], therefore unlike the manual PA-UT experiments only “hit vs. miss” data could be obtained. Tables 3.1 and 3.2 provide a summary of the inspection results for the wedding cake samples that did not contain the embedded defect. The results are broken down not only by sample, but also by zone and channel as pictured in Figures 3.5-3.7. Since the scan plans used in these inspections were not specifically designed for steel and aluminum wedding cake samples, a definitive analysis on the detection sensitivity of the TESI system to FBH and SDH cannot be made. This is because some level of *inspection process* error was introduced into the analysis which cannot be distinguished and filtered from the inspection data. Nevertheless, observations based on data from the different wedding cake samples are relevant. These results are presented only to highlight pertinent factors related to adding

Table 3.1: TESI inspection results on Steel wedding cake sample

Specimen and Test Setup Description	Zone	Channel	Description of Inspection Results
Steel wedding cake w/out embedded defect 10MHz frequency Longitudinal Inspection	1	1	No useful data
		2	Nothing detected in C-scan
		3	C-scan shows attenuation of back wall signal in the presence of slotted SDH targets. Targets not directly detected when A-scan channel data focused to 1.5 in. (3.8cm), using 32 elements of array and 30dB channel gain.
	2	1	No useful data
		2	FBH detected at low amplitude C-scan focused to 1.0 in. (2.5cm) channel depth
		3	C-scan shows FBH targets at approx. 40% FSH amplitude when A-scan settings set to 1.5 in. (3.8cm) channel focus depth, 32 elements, 35dB channel gain, 40dB DAC gain
	3	1	FBH targets detected in Level 2 at 0.25 in. (0.63cm) depth when channel focused to 0.15in. (0.38cm)
		2	FBH Targets detected in Level 2 at 0.25 in. (0.63cm) depth when channel focused to 0.35in. (0.89cm)
		3	FBH detected in Level 3 at 1.0 in. (2.5cm) depth when channel focused to 0.75 in. (1.9cm)
	4	1	FBH targets detected in Level 1 along very top row of scan at approx. 0.1 in. (0.25cm) depth when channel focused to 0.15in. (0.38cm)
		2	FBH targets detected in Level 2 at 0.25 in (0.63cm) depth when channel focused to 0.35in. (0.89cm)
		3	No useful data
Steel wedding cake w/out embedded defect 10MHz frequency ±45° Shear Inspection	1	1	FBH targets detected in Level 1 at approx. 0.1 in. (0.25cm) depth when channel focused to 0.081 in. (0.2cm)
		2	FBH targets detected in Level 2 at 0.5 in (1.27cm) depth when channel focused to 0.325in. (0.83cm)
		3	No useful data
	2	1	No useful data
		2	FBH targets detected in Level 2 at 0.5 in (1.27cm) depth when channel focused to 0.325in. (0.83cm)
		3	No targets detected in Level 3 when channel focused to 0.975in. (2.48cm) depth
Steel wedding cake w/out embedded defect 5MHz frequency Longitudinal Inspection	1	1	One possible indication at 131°. No other targets detected
		2	FBH targets detected in Level 2 at 0.5in. (1.27cm) depth when channel focused to 0.75in. (1.9cm)
		3	No FBH targets in Level 3 or SDH slots in Level 4 located when channel focused at 1.7in. (4.3cm) depth
Steel wedding cake w/out embedded defect 5MHz frequency ±45° Shear Inspection	1	1	FBH targets detected in Level 2 with max. amplitude when channel focused to 0.375 in. (0.95cm)
		2	FBH targets detected in Level 2 at 0.5in. (1.27cm) depth, FBH targets detected in Level 3 at 0.8in. (2cm) depth, and SDH slots detected in Level 4 at approx. 1.5in.(3.8cm) depth all when channel focused to 0.75in. (1.9cm)
		3	SDH slots in Level 4 detected at approx. 1.5in. (3.8cm)depth and SDH slots in Level 5 detected at approx. 2in. (5.1cm) depth when channel focused at 1.7in. (4.3cm) depth

Table 3.2: TESI inspection results on 6061 Al-alloy wedding cake sample

Specimen and Test Setup Description	Zone	Channel	Description of Inspection Results
6061 Aluminum Alloy Wedding Cake 10MHz frequency Longitudinal Inspection	1	1	No useful data
		2	Nothing detected in C-scan
		3	C-scan shows SDH slotted targets detected in Level 4 at 1.6in. (4.1cm) depth. SDH targets in Level 5 produced only slight attenuation of signal at 3in (7.6cm) depth. Targets detected for A-scan channel data focused to 1.5 in. (3.8cm), using 32 elements of array and 30dB channel gain.
	2	1	No useful data
		2	Level 3 FBH detected with max. amplitude C-scan focused to 1.0 in. (2.5cm) channel depth
		3	Level 3 FBH detected with max. amplitude C-scan focused to 1.5 in. (3.8cm) channel depth
	3	1	FBH targets detected with max. amplitude in Level 2 at 0.25 in. (0.63cm) depth when channel focused to 0.15in. (0.38cm)
		2	FBH Targets detected with max. amplitude in Level 2 at 0.25 in. (0.63cm) depth when channel focused to 0.35in. (0.89cm)
		3	FBH detected with max. amplitude in Level 3 at 1.0 in. (2.5cm) depth when channel focused to 0.75 in. (1.9cm)
	4	1	FBH targets detected with max. amplitude in Level 1 along very top row of scan at approx. 0.1 in. (0.25cm) depth when channel focused to 0.15in. (0.38cm)
		2	FBH targets detected with max. amplitude in Level 2 at 0.25 in (0.63cm) depth when channel focused to 0.35in. (0.89cm)
		3	No useful data
6061 Aluminum Alloy Wedding Cake 10MHz frequency ±45° Shear Inspection	1	1	FBH targets detected in Level 1 at approx. 0.1 in. (0.25cm) depth when channel focused to 0.081in. (0.2cm)
		2	FBH targets detected in Level 2 at 0.5 in (1.27cm) depth when channel focused to 0.325in. (0.83cm)
		3	No useful data
	2	1	No useful data
		2	FBH targets detected in Level 2 at 0.5 in (1.27cm) depth when channel focused to 0.325in. (0.83cm)
		3	FBH targets detected in Level 3 at 1in. (2.5cm) depth when channel focused to 0.975in. (2.48cm) depth
6061 Aluminum Alloy Wedding Cake 5MHz frequency Longitudinal Inspection	1	1	FBH targets detected in Level 2 at 0.25in. (0.63cm) depth
		2	FBH targets detected in Level 3 at 0.8in. (2cm) depth when channel focused to 0.75in. (1.9cm)
		3	SDH slots in Level 4 detected when channel focused at 1.7in. (4.3cm) depth
6061 Aluminum Alloy Wedding Cake 5MHz frequency ±45° Shear Inspection	1	1	FBH targets detected in Level 2 with max. amplitude when channel focused to 0.375 in. (0.95cm)
		2	FBH targets detected in Level 2 at 0.5in. (1.27cm) depth, FBH targets detected in Level 3 at 0.8in. (2cm) depth, and SDH slots detected in Level 4 at approx. 1.5in.(3.8cm) depth all when channel focused to 0.75in. (1.9cm)
		3	SDH slots in Level 4 detected at approx. 1.5in. (3.8cm)depth and SDH slots in Level 5 detected at approx. 2in. (5.1cm) depth when channel focused at 1.7in. (4.3cm) depth

a fully automated PA-UT inspection system as an element of a multi-technique, redundant in-service NDT inspection program.

Based on the inspection results in Table 3.1 and Table 3.2, a general conclusion on the TESI system is that a high level of repeatability between the 6061 Al-alloy and 8620 steel alloy wedding cake was obtained despite the material property differences. Figure 3.20(a-d) contains A-scan, B-scan, and C-scan images from selected 6061 Al-alloy sample data, while Figure 3.21(a-d) contains A-scan, B-scan, and C-scan images from selected 8620 steel alloy sample data. It can be seen from these images that there exists a variable background noise between Zone, Channel, and inspected material. Some of this background noise can be attributed to inconsistencies in the laser drilling process. The hole bottoms were not perfectly flat due to the difficulty in maintaining laser stability and uniform intensity while drilling such small holes, as depicted in Figure 3.22(a-c). The ability to drill the smallest 0.011 in (0.28mm) FBH without plugging the hole verged on the capability limit of the aerospace production facility. Since the

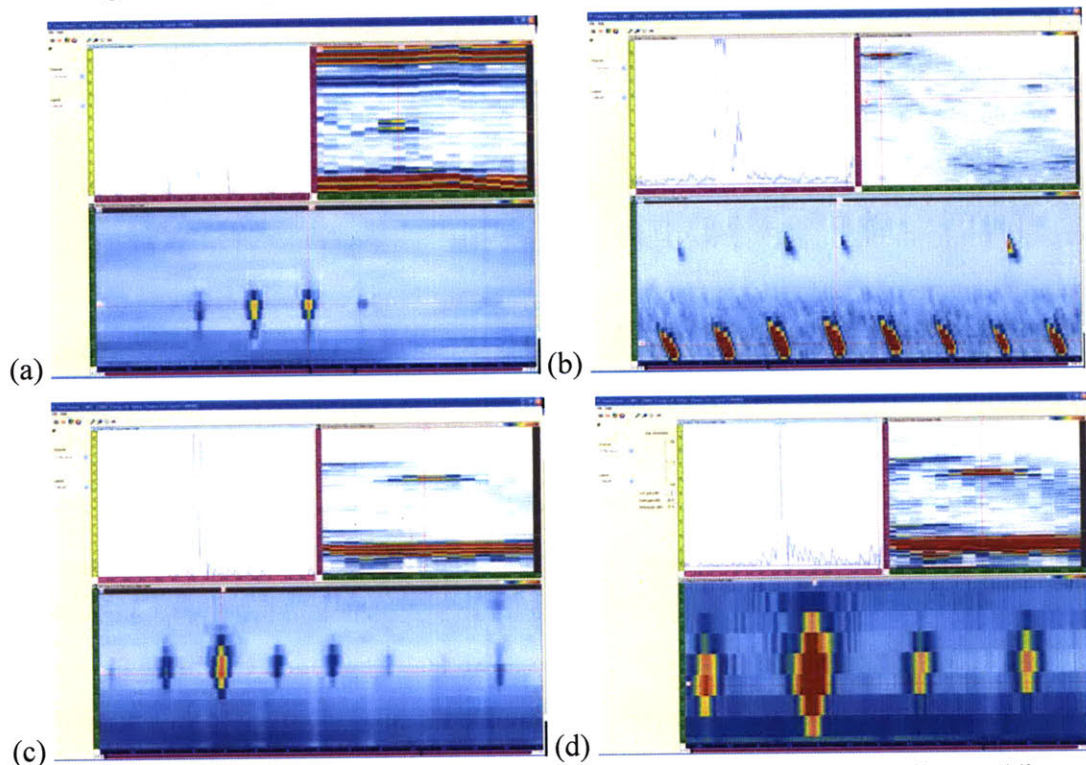


Figure 3.20: Selected A-scan, B-scan, and C-scan data for the 6061 aluminum alloy wedding cake sample (a) Channel 1 from 5MHz Longitudinal scan (b) Channel 1 from 5MHz 45° shear scan (c) Channel 2 from 5MHz Longitudinal scan (d) Same C-scan image as in 3.20(c) but zoomed in on FBH targets and with gain added to image.

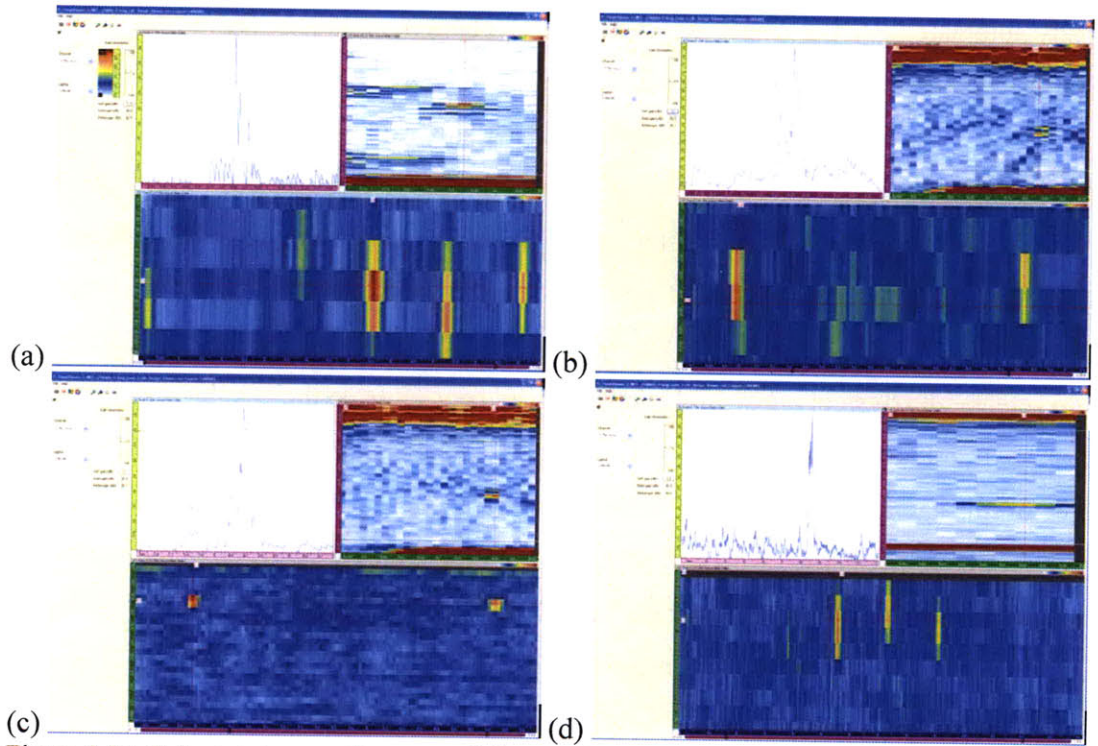


Figure 3.21: Selected A-scan, B-scan, and C-scan data for the 8620 steel alloy wedding cake sample (a) Channel 2 from 5MHz Longitudinal scan (b) Channel 1 of Zone 3 from 10MHz Longitudinal scan (c) Channel 2 of Zone 3 from 10MHz Longitudinal scan (d) Channel 3 of Zone 3 from 10MHz Longitudinal scan.

morphologies at the hole bottoms were not characterized, the acoustic reflectances there were not uniform because they were not perfectly flat. This resulted in some of the holes exhibiting more of a scattering effect from the back wall than a unique reflectance. The affect of this non-uniform FBH morphology was most pronounced in Level 3, because the hole depth was greatest for this level. Accordingly, the variability in the laser drilling process increased with increasing hole depth.

The terms *FBH target detected* or *SDH slot detected* used in Tables 3.1-3.2 do not specify the resolution of the detection, nor the quantity of targets detected. As shown in the selected C-scan images of Figure 3.20 and Figure 3.21, some indications are much easier to interpret than others. The background noise, gain level, and C-scan region of interest are all parameters that affect the resulting image quality. Since the purpose of the TESI experiments was to generate a limited amount of raw data for three wedding cake samples and not to generate a robust scan plan for the reliable inspection of actual disk components, a lot of false detections in the data are observed. Figure 3.23 shows a CAD

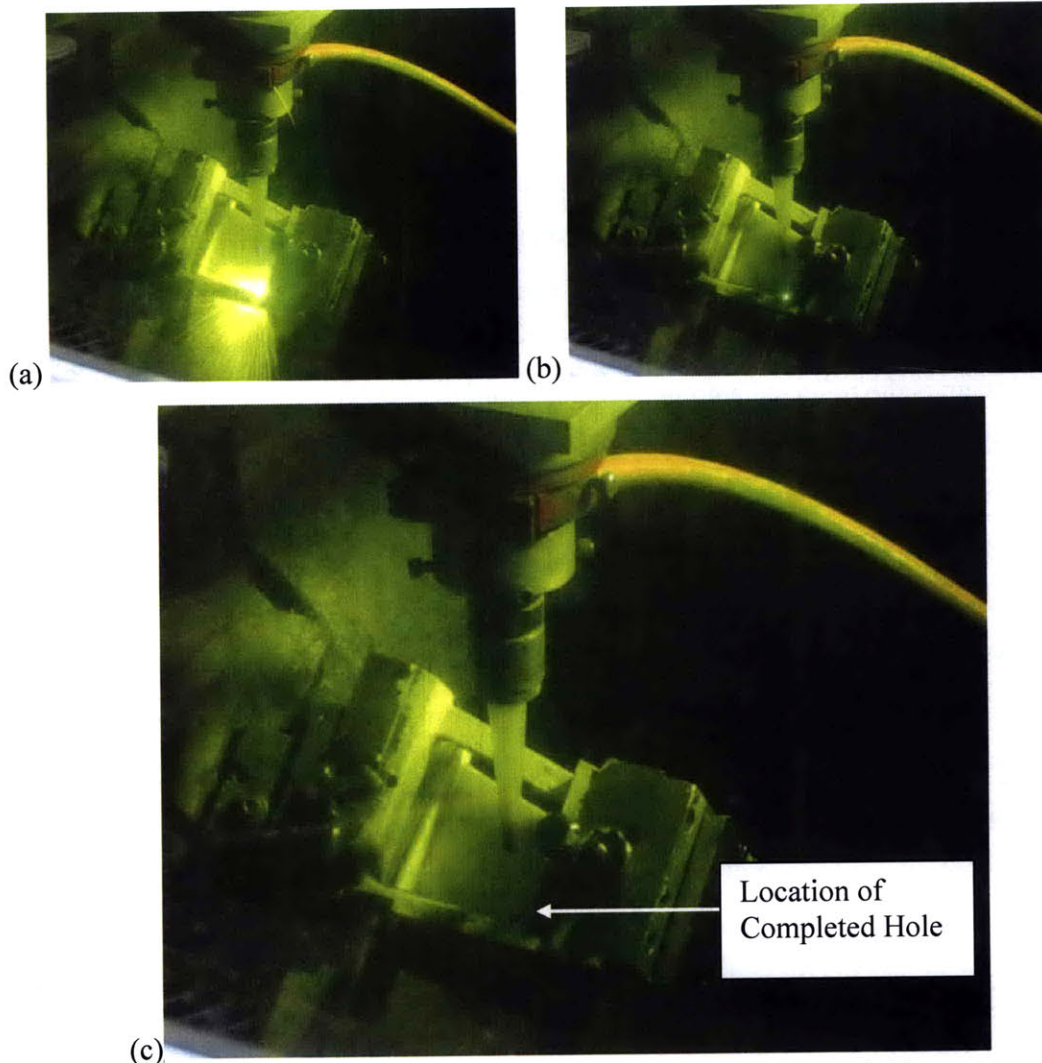


Figure 3.22: Schematic of laser drilling process (a) Laser initially pulses and ablates component surface, but the ablation process is very variable and blowback can occur (b) Laser drilling becomes more uniform once starter hole is formed (c) Laser pulses on and off until desired hole size and depth is obtained.

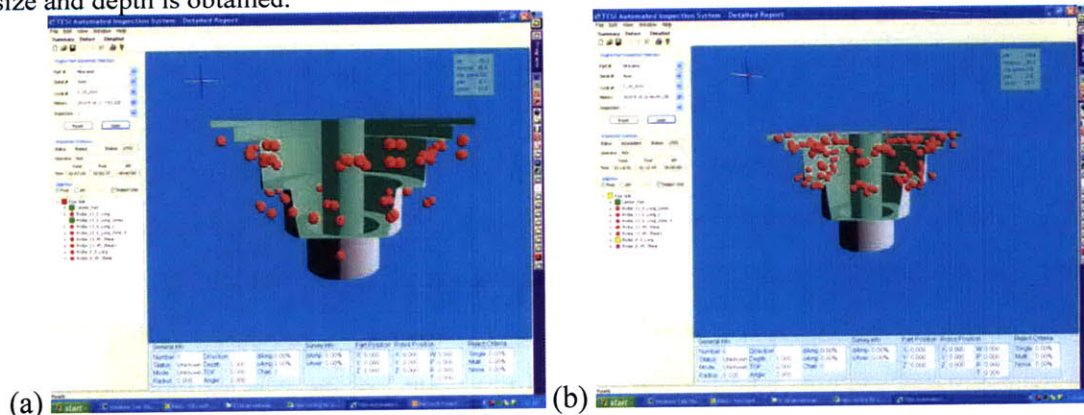
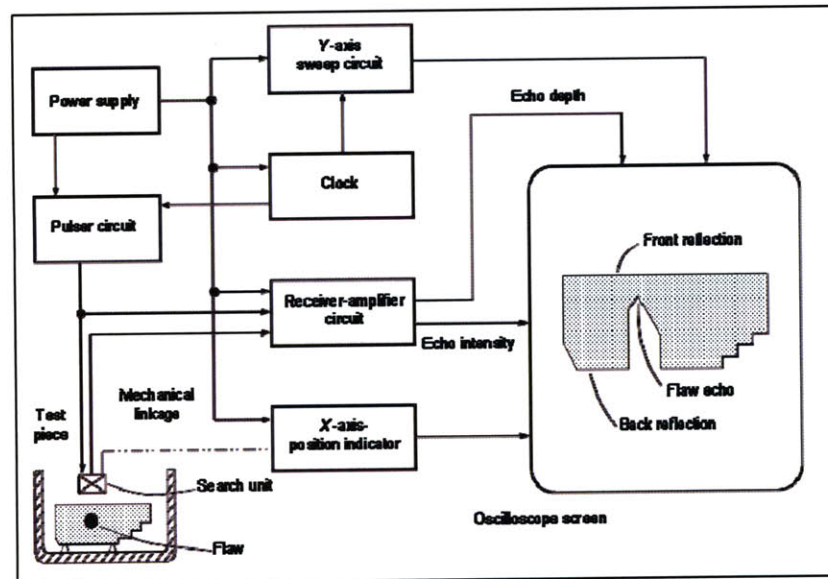


Figure 3.23: TESI automated CAD output showing all indications for (a) steel and (b) aluminum samples. A lot of false positive indications were observed.

image automatically generated by the TESI system upon completion of the fully-automated PA-UT inspection. In addition to the correctly detected FBH, a substantial amount of false positive indications are seen. This is because a threshold of 40% FSH (full scale height) was specified for these PA-UT inspections, which was not the optimal threshold discrimination value. In production facilities that perform UTI, threshold discrimination values of 60%FSH, or more commonly 80%FSH, are typically selected [95, 101, 142, 191]. The performance metric by which defects should be judged with the TESI system is the reflected amplitude signal. In these experiments, every UT signal that exceeded the 40% threshold value appears in Figure 3.23(a-b) as an indication. This means any extraneous signals from the back wall or front surface of the sample could have been misinterpreted as a flaw by the automated system if the signal response exceeded 40%. The inherent differences between the signal generation method from an immersion ultrasonic system and a contact mode system are shown schematically in Figure 3.24(a-b) for an A-scan and B-scan setup. From this figure, it is observed that extraneous signals generated from the back wall or front surface can negatively impact both techniques. However, the adverse impact is more severe in the fully immersed specimen because of the use of water as the transmission medium. An additional difference observed between the TESI immersion system and the Omniscan® manual contact system was the inspection time. In Figure 3.23(a-b) the total inspection times for the aluminum and steel wedding cakes are included. The aluminum sample took about 1.25 hours to complete, while the steel sample required nearly 3 hours for inspection. Comparatively, the contact PA-UT system inspections averaged about 20-30 minutes per sample, including time associated with programming the focal law and group wizards. The total inspection time required is a factor in the overall cost-benefit of any NDT system.

The results from the fully automated PA-UT of the steel wedding cake containing the embedded defect correlated well with the manual phased array results obtained on the Omniscan® system. Figure 3.25(a) shows a C-scan image of the overall region of interest (ROI), and Fig. 3.25(b) has a focused and magnified C-scan view of the embedded defect region. These images were from Zone 1 of the 10MHz longitudinal inspection. In the C-scan image of Fig. 3.25(b), instead of seeing a horizontal line,

(a)



(b)

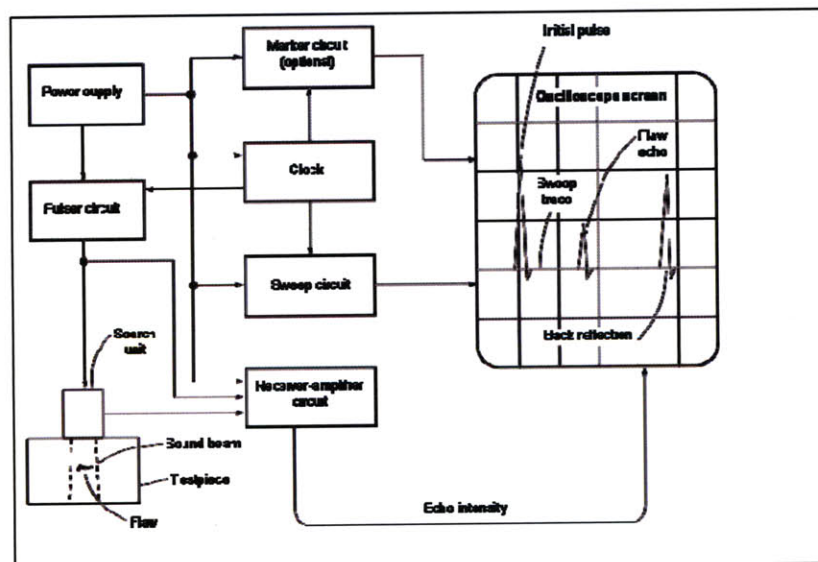


Figure 3.24: Schematic of the system processing steps involved in the generation of a pulse-echo system response for (a) fully immersed sample and (b) ultrasonic system in contact mode (adapted from [194])

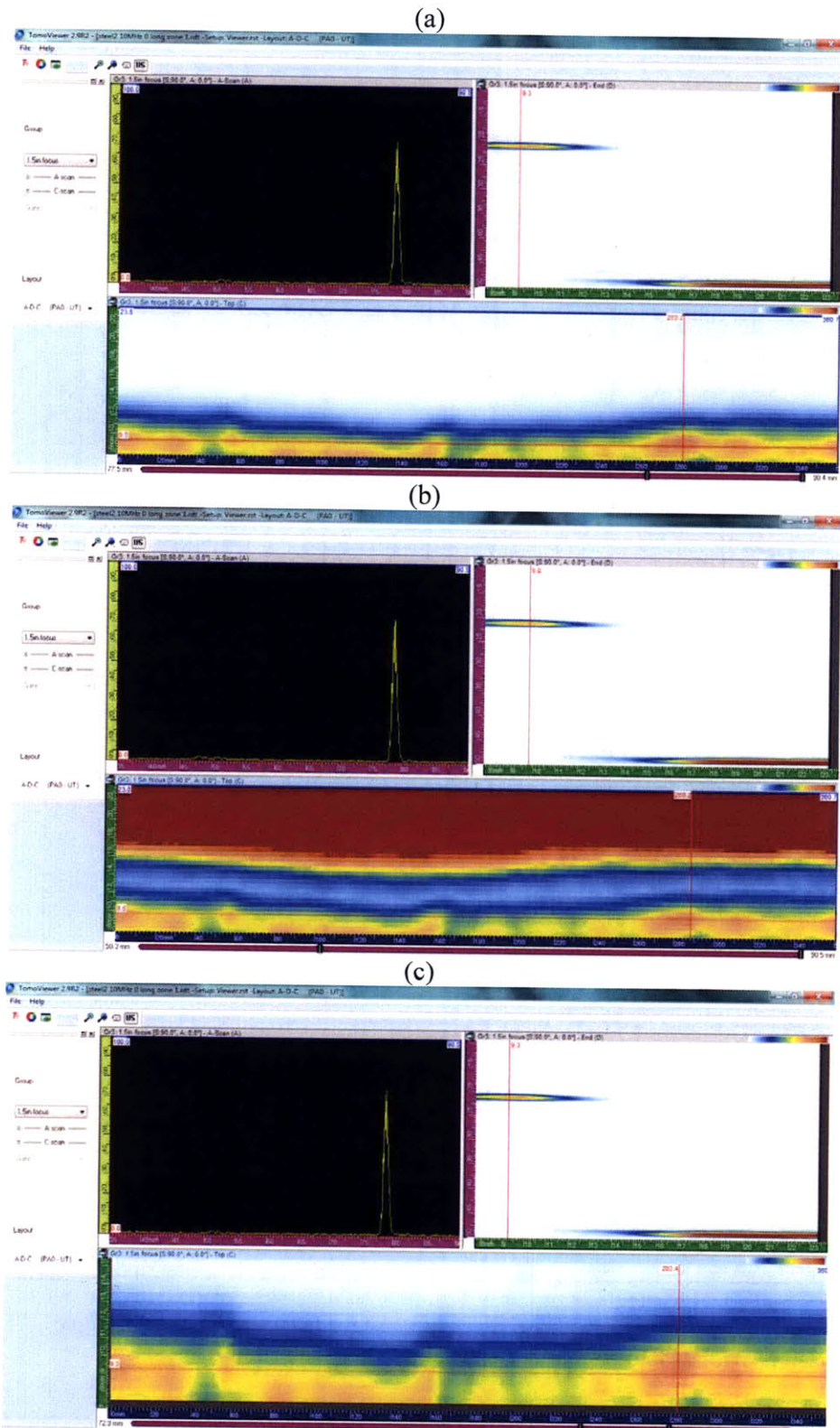


Figure 3.25: (a-c) Various adjustments made to gain and magnification levels of the embedded defect ROI C-scan images with Tomoviewer® .

curvature is apparent in the ROI with the bluish hue. This curvature appears to have been caused by the drill bit *walking* instead of *cutting* as it progressed through the steel sample. Walking is a machining term also known as “climb cutting,” and refers to the direction of feed in relation to cutter rotation that produces cutting forces perpendicular to the feed direction. The vibrations and shaking caused by the climb cutting are evident in Figure 3.25(c). From this image the radius of the embedded drill bit was estimated to be 4.5mm (0.18cm). This would indicate a tool diameter of about 9mm (0.36cm), which is extremely close to both the Omniscan® data and the actual drill bit diameter of 9.5mm (0.375in.). A newly released version of Tomoviewer® was used to image the embedded defect sample, and that was the cause of the slight display appearance differences between Figure 3.25 and previous figures.

The embedded steel sample was also inspected at 10MHz for the 45° shear inspection. Figure 3.26(a-b) shows the output from two channels for the Zone 1 inspection. The shear scans showed the best capability at detecting all of the FBH (or SDH) from multiple levels in a single inspection. This is a major advantage of phased array UTI over traditional ultrasonic inspection techniques. Traditional UTI is limited to the longitudinal mode because the single element transducer is only able to raster back and forth in the X-Y plane, as was previously shown in Figure 1.11. The use of focal law wizards enabled both the contact and immersion PA-UT systems to focus and steer the sound beam through the desired angles. This resulted in improved sample interrogation, and an ability to estimate flaw depth as well as flaw size. Section 3.3 provides additional comparative analysis for results obtained with the phased array and the traditional ultrasonic C-scan units.

3.3 Comparison with Traditional UT Technique

An acoustic microscopy imaging (AMI) inspection technique was initially considered for comparison with the phased array results. Acoustic microscopy is the general term applied to high-resolution, high-frequency UTI techniques that produce images of subsurface features in samples [27]. Alloy blocks were taken to the Sonoscan® Inc. field office [formerly in Burlington, MA] for inspection on a C-mode scanning acoustic microscope (C-SAM). Slight differences in alloy composition and microstructure between Ti-6-4 billet and Ti-17 billet block samples had a much more

profound affect with the AMI technique than with either the PA-UT or traditional-UT inspection methods. Two of the 14 ETC blocks loaned by Iowa State University,

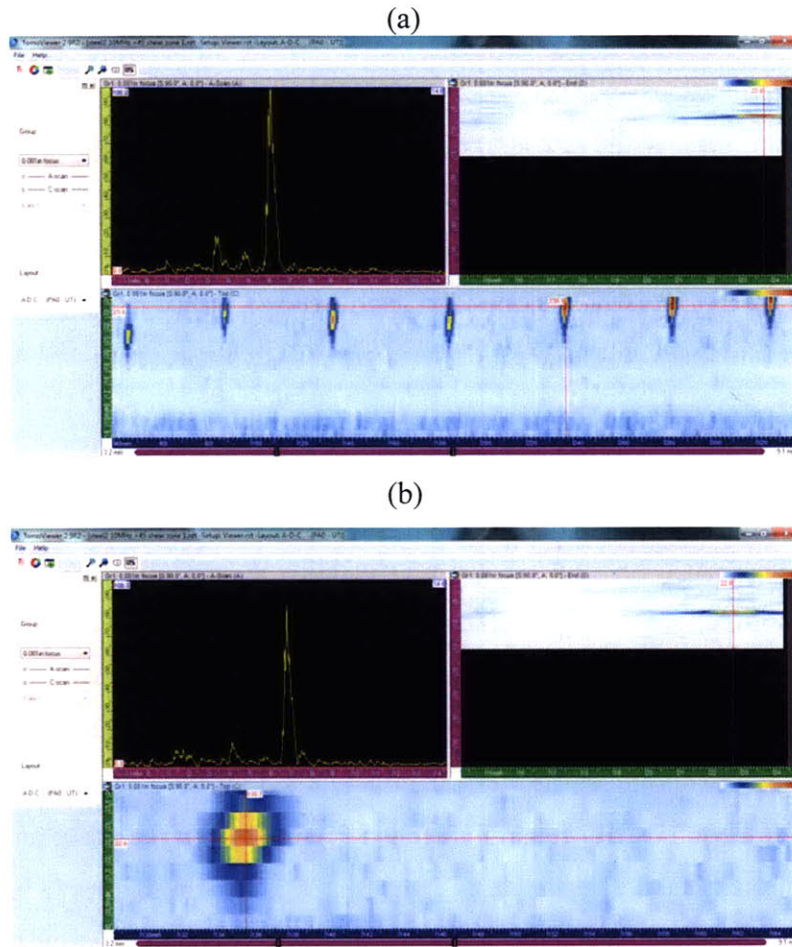


Figure 3.26: (a) 10MHz, 45° shear inspection of embedded steel sample. FBH targets in Level 1 detected when C-scan image focused at a depth of 0.081in. (0.21cm). Range set from 3.2-9.1mm for C-scan image. (b) Magnification of FBH target aligned with markers in 3.26(a)

designated as Sample P and Sample Q, were analyzed at a 5.1cm (2in.) focal length with a 10MHz transducer. These samples had been sliced from their original 7.6cm (3in.) length into 2.5cm (1in.) and 5.1cm (2in.) sections. The resulting AMI images from the 2.5cm (1in.) section of both samples are displayed in Figure 3.27(a-b), and show a stark contrast between the Ti-6-4 Sample Q block and the Ti-17 Sample P block. An additional inspection parameter deemed paramount to the image quality for the acoustic microscopy technique, but which was essentially ignored for the phased array and

traditional UT inspections, was the variation in acoustic impedance for the X-, Y-, and Z- directions. Figure 3.28(a-b) contains nomenclature from [184] used to describe the various block directions.

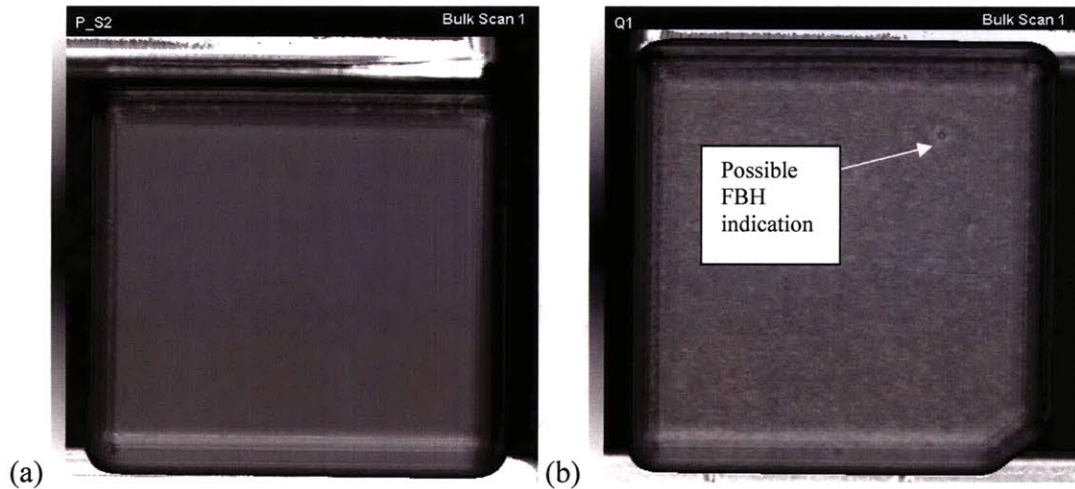


Figure 3.27: 10MHz acoustic microscopy inspection image of (a) Ti-17 billet material of Sample P and (b) Ti-6-4 billet material of Sample Q

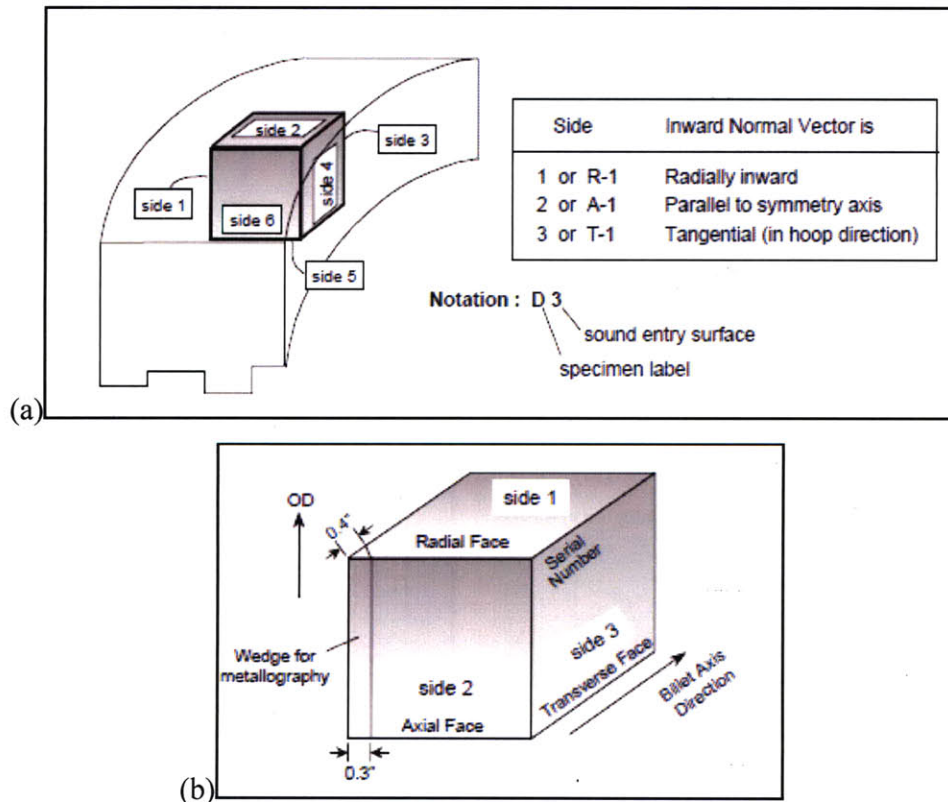


Figure 3.28: (a-b) Graphical representation of alloy block specimen sectioning and nomenclature used to distinguish block orientation (reprinted from [184])

Figure 3.29(a-b) shows the variation in C-SAM image results for 3 sides of both Samples B and C. These two samples were also included in the set of 14 ETC blocks. Samples B and C were smaller in size than the other blocks, having a length of only 3.3cm (1.3in.) on each side, whereas the other samples had a length of 7.6cm (3in.). Unfortunately, all of the alloy block samples used in the advanced NDT inspections were too thick for use with the C-SAM system at Sonoscan®. As Figure 3.30(a-b) shows, the samples protruded above the water surface, resulting in an excessive amount of noise and an inability to obtain C-SAM images.

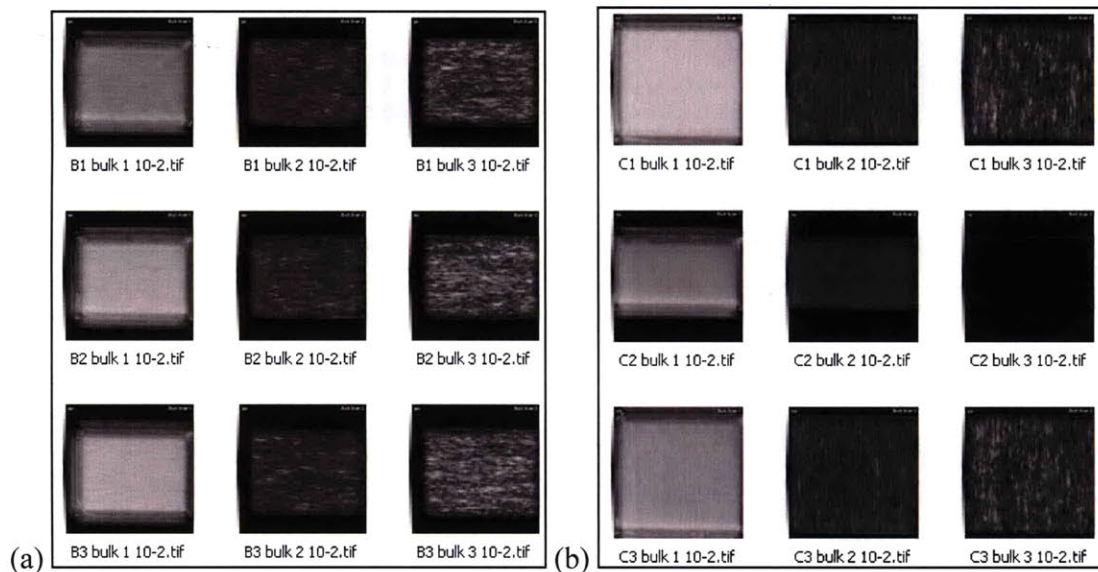


Figure 3.29: C-SAM image results for Sides 1, 2, and 3 of (a) Sample B and (b) Sample C

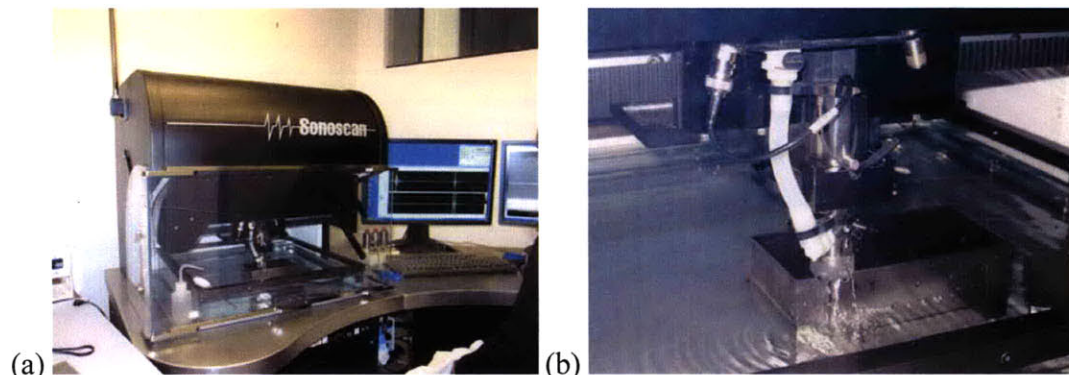


Figure 3.30: (a) Sample R88 block under inspection with C-SAM system (b) Sample protruding above water level, resulting in an excessive amount of noise and the inability to obtain data. This result was observed for the entire set of alloy block specimens inspected with the advanced NDT techniques.

The results from the fully automated and manual phased array inspections were able to be compared with inspection results from a traditional ultrasonic C-scan system. A Panametrics® LSC “Off-the-Shelf” Scanning System was used to perform the traditional UT experiments. This system was located at the Advanced Technology and Manufacturing Center (ATMC) of UMass Dartmouth in the Ultrasonic NDE Laboratory. The test setup for this system is shown in Figure 3.31(a-c). Sample R88, Sample H, Sample U, and Sample M were the only specimens inspected with this system. Sample M was one of the ETC specimens from the near outer diameter region of a Ti-17 billet. Sample M did not contain any flat bottom holes and was inspected so a comparison between samples with and without the 3x3 FBH array could be made from data taken on the traditional C-scan system. After analyzing the data from the alloy block specimens, it was determined the Panametrics® system did not have the capability required to inspect the non-planar wedding cake specimens. Dr. Chi Chen, a highly regarded expert in ultrasonic inspection methods and head of the Ultrasonic NDE lab, advised that a contact mode system would work much better than the traditional C-scan immersion system used to test the alloy blocks [195]. Therefore, only data on the alloy blocks is presented. Appendix D contains C-scan images for both amplitude and time of flight (TOF) data taken from these four samples.

The alloy blocks were each scanned in two orientations. In separate tests, samples were oriented with the FBH array located at both the sample surface facing up, and flipped 180° such that at the sample base they were facing down relative to the single element UT transducer. Since the transducer for this system scans over a 2-D surface by rastering back and forth in the X-Y plane, sectorial scans cannot be performed and samples can only be interrogated via longitudinal scans. A 10MHz focused transducer was used for the inspections with the FBH oriented at the sample surface. The transducer was focused to the known depth of 0.25 in. (0.64cm) for the flat bottom holes. Focused beams reduce background noise by reducing the volume of material inspected. This in turn reduced the probability that the sound beam would be attenuated by small reflectors such as grain boundaries or micro-porosity at that same focus depth [27]. A schematic representation of the convergence of a focused sound beam on a flat metal surface is shown in Figure 3.32. A scan increment of 0.004 in. (0.1mm), scan speed of 0.5

inch/second (1.27 cm/sec), and scan extent of 4 inches (10.2cm) was specified in the scan plan for the inspection with the holes orientated at the surface. The receiver attenuation was between 10-13dB. Also, each scan took approximately 1.5 hours to complete because of the minimal scan increment, but setting this parameter at a very small value

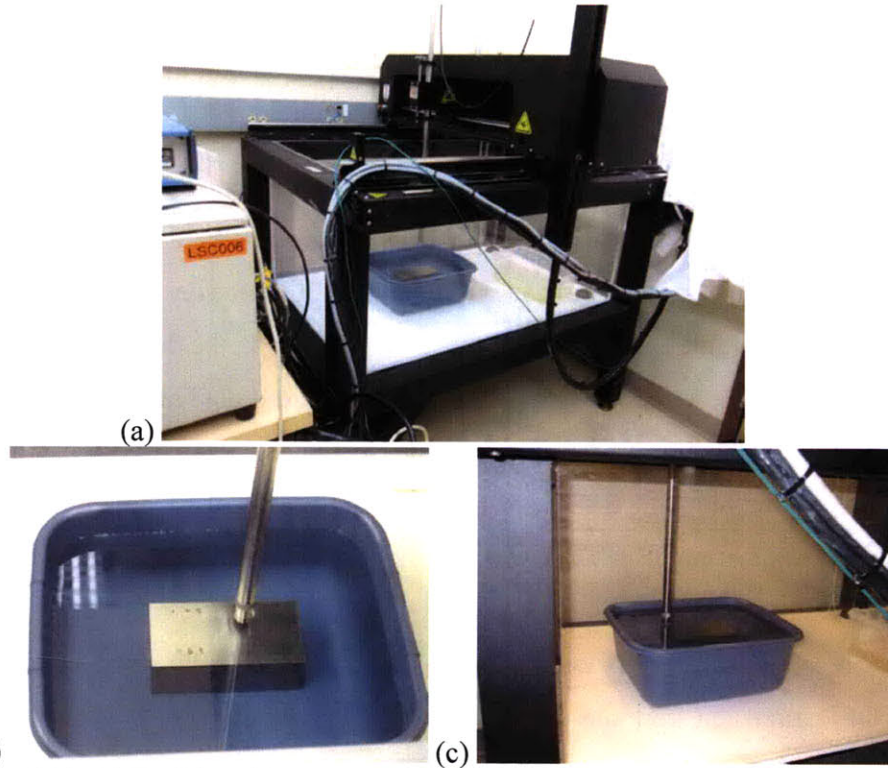


Figure 3.31: (a) Traditional C-scan UTI test setup located at ATMC, UMass Dartmouth (b-c) 2-D X-Y rastering of single element transducer over Sample R88

was required to obtain the highest sensitivity. The figures in Appendix D show C-scan image results from the full amplitude range (%FSH), as well as a limited amplitude range for both the complete sample surface and the 3x3 FBH-array ROI, obtained by manual optimization. In general, very good discrimination of the flat bottom holes at the surface orientation was obtained for the three samples which contained the FBH array, at these inspection parameters. Time of flight (TOF) images are also included in Appendix D. The TOF C-scans show slight variation in the sound wave pulse-echo time at different sample locations. These results demonstrate the capability for UTI to detect small surface flaws or cracks with good discrimination. However, ultrasonic inspection of surface cracks is generally performed only as a secondary technique to confirm or validate indications from primary surface techniques such as FPI and ECI.

The main advantage of ultrasonic inspections over other NDT processes which are rooted in the electromagnetic regime is the superior penetrating power of the acoustic waves. The primary objective of the PA-UT inspections on both the fully automatic and manual systems was to determine the sensitivity and coverage of the systems with respect to detection of subsurface defects. Since the wedding cake samples were not

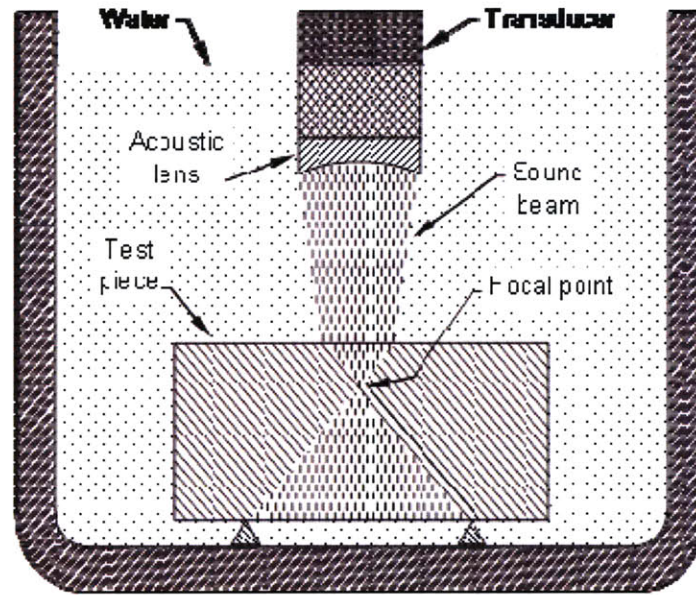


Figure 3.32: Convergence of a focused sound beam on a metal surface and the resulting acoustic effect (adapted from [194])

inspected with the traditional C-scan system, the only way to determine the traditional UTI system's sensitivity to subsurface flaws was to flip the alloy blocks 180° and inspect from the back surface reflection of the simulated flaws. When the FBH array was oriented with the FBH array in the bottom position a 2.25MHz unfocused transducer was used. In this case, the selection of an unfocused transducer was made to increase the penetration depth into the dense samples. The selection of a lower frequency transducer was made to decrease the receiver attenuation from the prior value of 10-13dB to nearly 0dB. Despite these modifications to the scan plan, which were meant to improve the system's sensitivity to subsurface flaw detection, there was still too much noise to enable detection of the hole features. This is presented in Figures D.7-D.8 for the reflected

amplitude signal of Sample R88. Air bubbles that formed along the edges of the back-surface holes contributed to this noise. These bubbles interfered with the reflected signal, but the traditional C-scan system was not sensitive enough to detect the holes regardless of the presence of air bubbles. The single element transducer encountered too much acoustic impedance in the dense, thick alloy blocks. This attenuation prevented detection of the #1FBH with optimal inspection settings and no air bubbles. The ability to focus and steer multiple element transducer arrays in both the longitudinal and sectorial inspection modes resulted in superior detection capability and sensitivity. This was the case for both the manual contact PA system and automated immersion TESI phased array system. Both of the phased array systems outperformed the traditional ultrasonic inspection system with respect to subsurface flaw detection as well as overall system sensitivity.

Chapter 4: Computed Tomography Inspection

This chapter focuses on advanced radiographic NDT techniques. Three dimensional computed tomography (3D-CT) inspections of the alloy block, wedding cake, and actual component samples were performed. A discussion of the experimental procedures for each class of samples is provided in Section 4.1. Results of the sensitivity analyses are detailed in Section 4.2. In addition, inspections were performed on selected samples using digital radiographic and traditional film radiographic techniques. The results of these inspections form the basis of the comparative analysis included in Section 4.3.

4.1 Experimental Procedure

An X-Tek® HMX-ST 225kV MicroCT Imaging System located at the Center for Nanoscale Systems at Harvard University was used for the CT scans. This system is pictured in Figure 4.1. This system has a microfocal source approximately $5\mu\text{m}$ ($2 \times 10^{-4}\text{in.}$) in size. The use of such a small x-ray source enabled magnification of the x-ray images onto the detector, so greater image detail was obtained. Elements of the CT system are pictured in Figure 4.2. Included in this figure are: the tungsten x-ray transmission source, filters placed on the target to minimize soft x-rays (which increase image noise during inspection), the filament inside the internal vacuum chamber of the target, and the 2000x2000 array element detector at the back of the system.

Once sample inspection was completed, the resulting 2D image projections (also known as slices) were reconstructed into the 3D-CT volume using VG Studio MAX 2.0®



Figure 4.1: The X-Tek® HMX-ST 225kV MicroCT Imaging System located at the Center for Nanoscale Systems at Harvard University

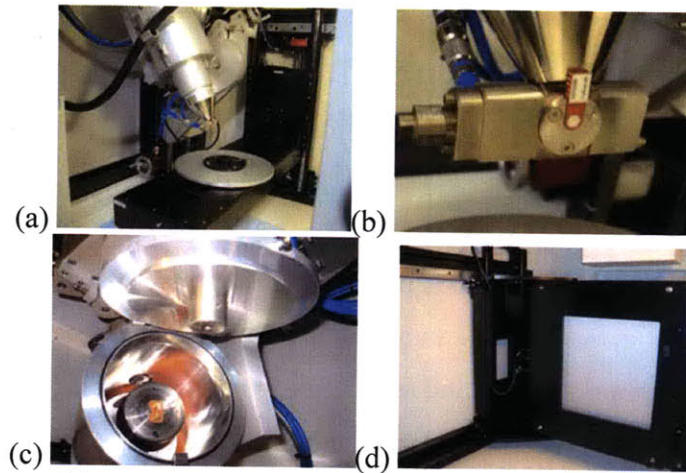


Figure 4.2: Elements of the MicroCT imaging system. (a) The tungsten x-ray transmission source. (b) Use of a 1mm copper filter to filter out soft x-rays and reduce noise in CT scan. (c) Picture of the inside of the target showing the filament (d) The 2000x2000 element detector at the back of the system.

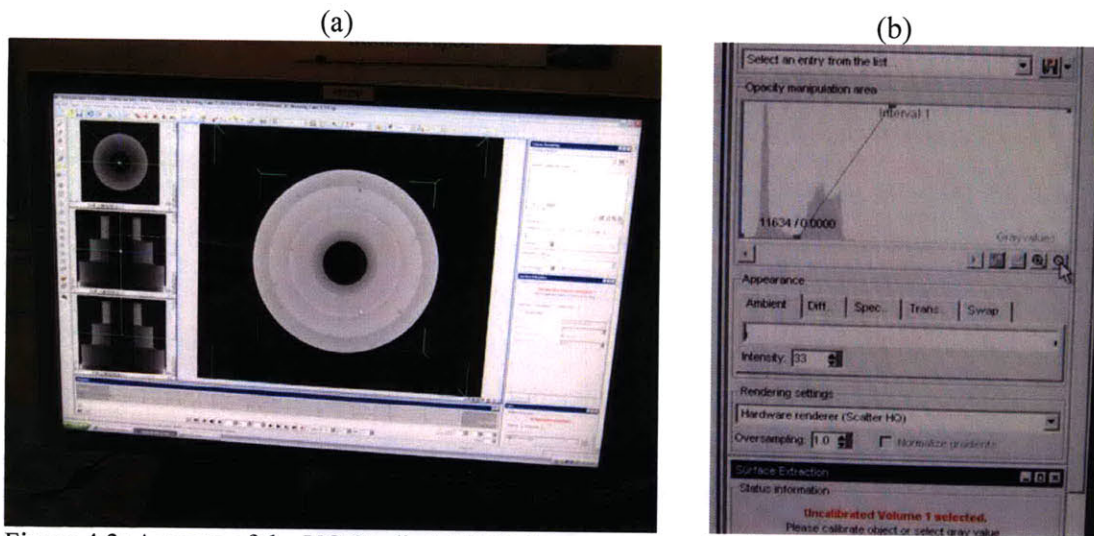


Figure 4.3: Aspects of the VG Studio MAX 2.0 tomography visualization software (a) Screen shot of reconstructed wedding cake sample with windows of the various sample perspective views in left columns and histogram editing windows in the right columns (b) Close up of histogram editing windows.

tomography visualization software [Volume Graphics GmbH]. Figure 4.3 pictures some aspects of the software, including windows containing various perspective views of the 2D projections and windows with options for manipulating the histogram. The dynamic range of image grayscale levels for each individual inspection is contained in the histogram. For the CT inspections performed, the histogram was manually adjusted to

optimize the contrast in the reconstructed volume. The MicroCT system discriminates slices over a 16bit grayscale range, and there are 65,535 unique grayscale values in this range. The histogram adjustments depended on a number of factors. Sample size, geometry, and material alloy all affected the resulting dynamic range for a particular inspection. Since the histogram adjustments were manually performed, the dynamic range was different for each of the inspected samples. The dynamic range was a primary determinant of the reconstructed 3D volume quality, and a source of variability between similar samples. This topic will be discussed in greater detail in Section 4.2.

4.1.1 Alloy Block Samples

It was unknown whether the 225kV x-ray voltage would be sufficient to fully penetrate the alloy block samples prior to the initial CT inspection. For this reason, a single alloy block was scanned before a decision on the entire set of samples was made. Sample L was inspected at the Harvard CNS facility with the assistance of technical experts in CT from Nikon® Metrology Ltd. The sample was oriented corner to corner to make sure x-ray penetration of the thickest sample region occurred. The scan of the Ti-6-4 alloy block was performed at a 220kV x-ray voltage and 95 μ A x-ray current. This was the capability limit of the system, and certain controls on the CT system had to be manually overridden to even permit such values to be obtained. At these high settings the power density had to be defocused to avoid melting the target and sputtering material onto the detector. A 2mm (0.079in) Cu filter was used to filter out the soft x-rays. The number of frames averaged at each scan position was increased from a recommended amount of 45 to 128 to improve CT quality by increasing the total x-ray detection. Figure 4.4(a-b) shows two perspective views of the CT reconstruction of Sample L. Figure 4.5(a) shows one of the approximately 1600 2D projections taken to create the 3D volume rendering, and Figure 4.5(b) is the same 2D projection as in Fig.4.5(a) but with arrows indicating the location of one column of the FBH array that was somewhat observable.

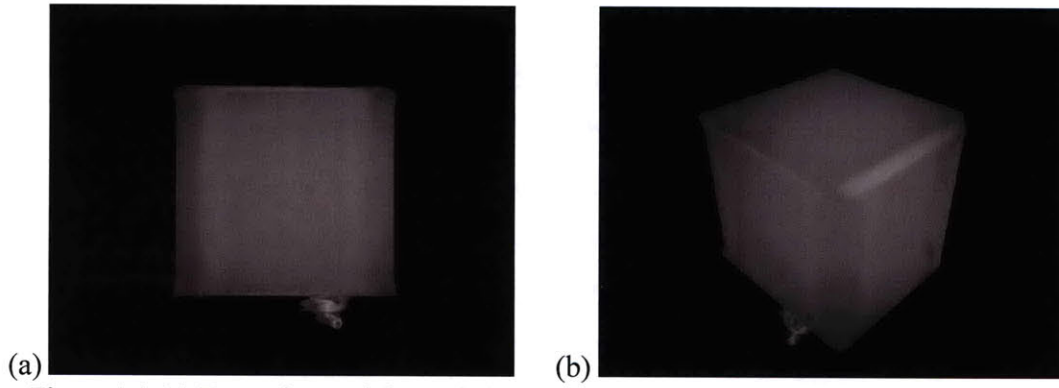


Figure 4.4: (a) Front view and (b) angled perspective view of the Sample L 3D volume rendering [190]

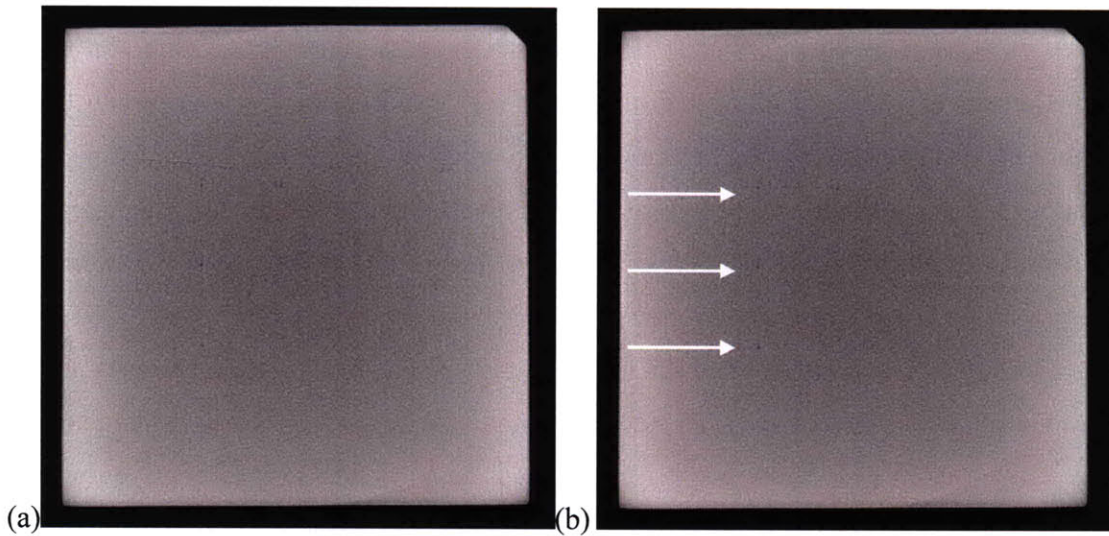


Figure 4.5: (a) 2D projection slice of Sample L showing ring artifacts (b) Arrows pointing to location of a column of #1FBH. [190]

Based on these settings, a 14.5GB volume size was obtained with a calculated resolution of 60 microns (2.4×10^{-3} in.). However, detection of the #1FBH array was generally unobtainable except for a few individual 2D slices, like the one shown in Figure 4.5, where some of the holes were barely observable. The presence of image artifacts added noise to the slices and caused the poor resolution. Artifacts in CT data degrade image quality and image resolution. In Figure 4.5, ring artifacts and streak artifacts were both observed in the CT slice. Ring artifacts are caused by non-linear detector noise in the projection images. Noise in the black reference image gives the worst ring artifacts because it is re-used to correct each projection, and is therefore amplified [57]. Most streak artifacts are caused by beam-hardening or lack of penetration

through the sample by the x-ray beam. For Sample L, a 2mm (0.079in) Cu filter was used to reduce beam hardening. Lack of penetration can typically be corrected by increasing x-ray voltage. Unfortunately, the system was operating at maximum voltage for the inspection of this sample. The only solution in this instance would be the use a higher x-ray energy system, such as a 450 kV system. Such a system was not locally available. As a result, no other alloy block samples were inspected with the 225kV system due to its limited voltage.

4.1.2 Wedding Cake Samples

The aluminum wedding cake sample was scanned with the following settings: an x-ray voltage of 216kV, current of 57 μ A, 1.0mm (0.04in) Cu filter, and 256 frames averaged per projection. The scan time took approximately one hour, not including time to render the image. Figure 4.6(a-d) shows the resulting output of the aluminum sample after reconstruction. Noticeable in Figure 4.6 is the fact that only Levels 3-5 of the

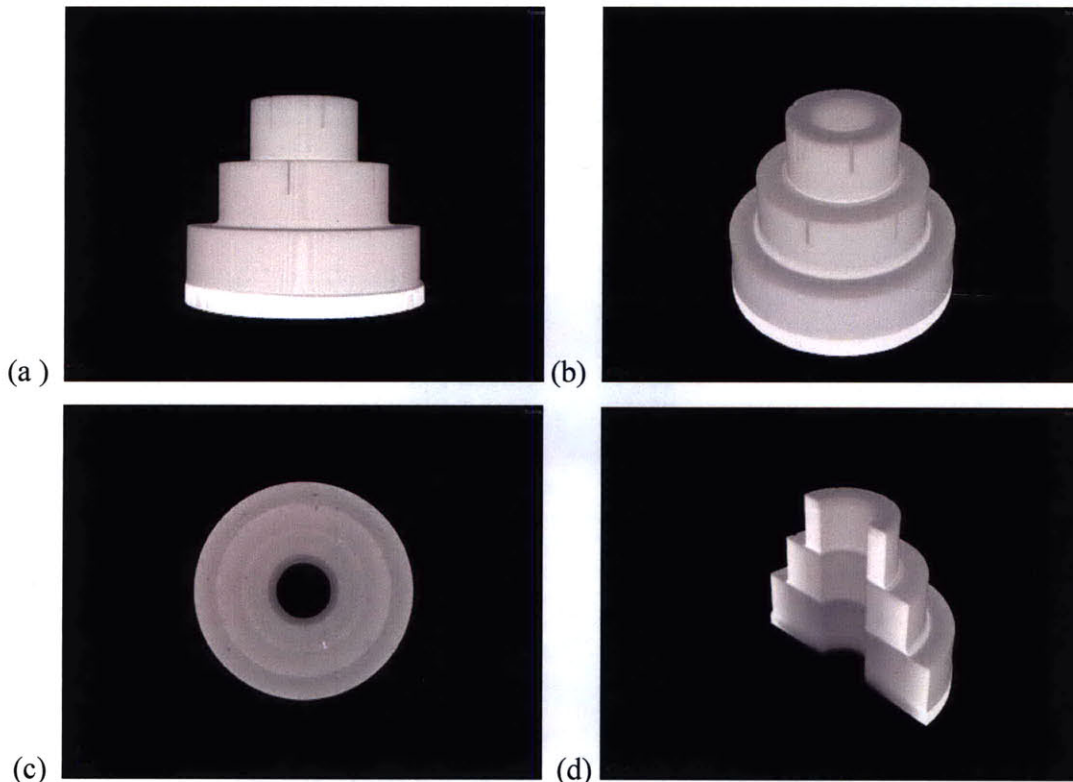


Figure 4.6: (a-d) Different perspective views of the rendered 3D-CT 6061 Al-alloy wedding cake sample [190].

wedding cake are shown. The MicroCT system was meant to be a research CT system and as such was not designed for industrial-type inspections of large components. Therefore, sample size was a limitation of the system and the entire aluminum wedding cake could not be adequately rendered. This will be discussed more in Section 4.2.

While x-ray penetration through the cross-section of the aluminum wedding cake sample was obtained, the same cannot be said for the 8620 steel alloy wedding cake. Because the source and detector remain stationary and the sample rotates in 3D-CT, x-ray penetration through the thickest section of any sample must be obtained for an acceptable volume reconstruction to be obtained. If penetration through the thickest sample section at all angles of rotation does not occur, there will be dropped images in the inspection. All 2D slices are required for the CT reconstruction, so dropped images are unacceptable. For the steel wedding cake this meant that the x-rays would have had to penetrate through approximately 15.2centimeters (6in.) of material at the base of Level 1. This was not possible with the 225kV system. Figure 4.7 shows the lack of penetration observed when taking the black and white reference images of the sample. Since x-ray penetration through the sample was not feasible with this CT system, neither of the steel wedding cake samples were scanned.



Figure 4.7: Lack of x-ray penetration through lower levels of 8620 steel alloy wedding cake sample [190].

4.1.3 Actual Components

The three turbine blades and the duct segment component were also inspected with the Micro CT system. The system settings for the three blades were nominally identical, with slight changes in current required due to filament usage. The blades were scanned at voltages between 210-220kV and currents between 60-70 μ A. A 1.0mm (0.04in) Cu filter was used for the blades. A secondary scan was done on one of the blades with a weld drop-through defect using a 1.6mm (0.06in) Cu filter. The settings selected for the duct segment component were similar to those chosen for the blades. Both components had similar cross-section thicknesses and were fabricated from the same PW1484 Ni-base superalloy. The duct segment was inspected at a voltage of 220kV and current of 60 μ A. Figure 4.8(a-b) shows the process of collecting the white and black reference images for the duct segment at 0° and 90° rotations of the part. This is a very important procedural step, because it sets the dynamic range of grayscale values for the inspection. Variations in the dynamic range will result in differences in image quality even if similar components are inspected with identical x-ray voltage and current parameters.

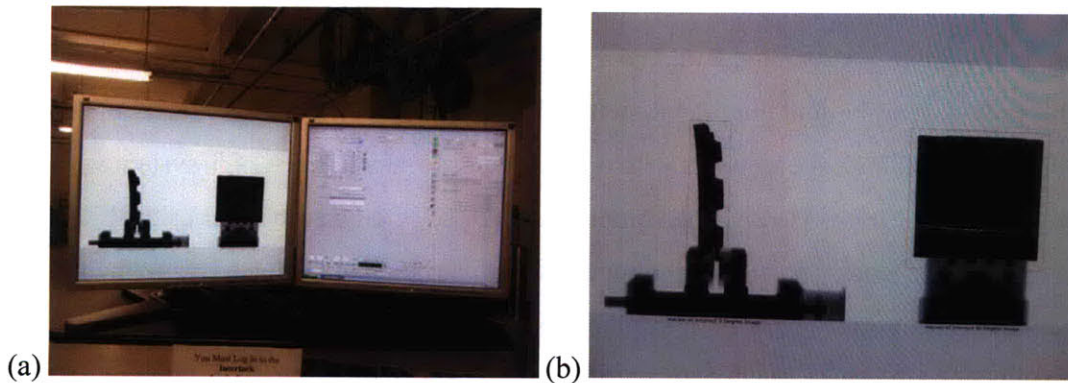


Figure 4.8: (a-b) Process of collecting white and black reference images for the duct segment

Once the scans of the blades and duct segment were completed, certain parameters had to be selected in CT Pro™, which was the software program used to reconstruct the volume. CT Pro™ and VG StudioMax™ are distinct software packages and serve separate functions. In CT Pro™, the user determines the center of rotation of the sample and selects a level that ranges from 1-6 for two parameters: *Noise Reduction* and *Beam Hardening*. Figure 4.9(a-b) displays one of the settings tabs of the CT Pro™ module that is required to be selected before the 3D volume can be reconstructed.

Selection of the correct value for each of these parameters is critical to minimizing noise in the volume reconstruction. The reconstruction process enhances noise when converting the 2D projection slices into a 3D volume rendering. To produce sharp detail in the CT volume an inverse filter is applied to suppress low frequency information and enhance high frequency information in the projection images [57]. Noise is usually in the high frequency regime, meaning it gets enhanced in the volume reconstruction. Therefore any noise from the sample set of 2D projection images is further exaggerated when converted to a 3D reconstructed volume. The settings selected in CT Pro™ have a direct impact on the quality of the images and visualization renderings produced with the VG Studio Max software.

4.2 Results of Sensitivity Analysis

The maximum voltage of the X-Tek® HMX-ST 225kV MicroCT Imaging System was a limiting factor in the inspections of both the alloy block specimens and the steel wedding cake samples. An industrial CT system on the order of 450kV would have been satisfactory for the Ti-alloy block samples, while an advanced CT system most likely in the 600-800kV range would have been required to penetrate through the steel wedding cake samples and the P/M Rene88 alloy block [196]. The estimated scan time for the steel wedding cake samples with a linear detector array (LDA) CT system was approximately 12 hours [197]. The *volume renderer* selected was another critical parameter that affected the resulting image and simulation quality. There were many volume renderer options to choose from in the VG StudioMax™ software. The renderer ultimately chosen generally depends on whether fast inspection time or high image quality is more critical. Figure 4.10 represents the change in appearance of the surface containing the 3x3 FBH array for Sample L caused by the selection of volume renderer.

For samples in which x-ray penetration was not a limiting factor, the resulting image quality of the 3D-CT reconstruction was impressive. In Figure 4.11(c), all eight of the flat bottom holes on Level 3 as well as the 12 SDH on Levels 4 and 5 are observed for the three levels of the aluminum wedding cake that were able to be inspected. Figure 4.11(a-b) shows a surface imperfection on Level 4 of the aluminum

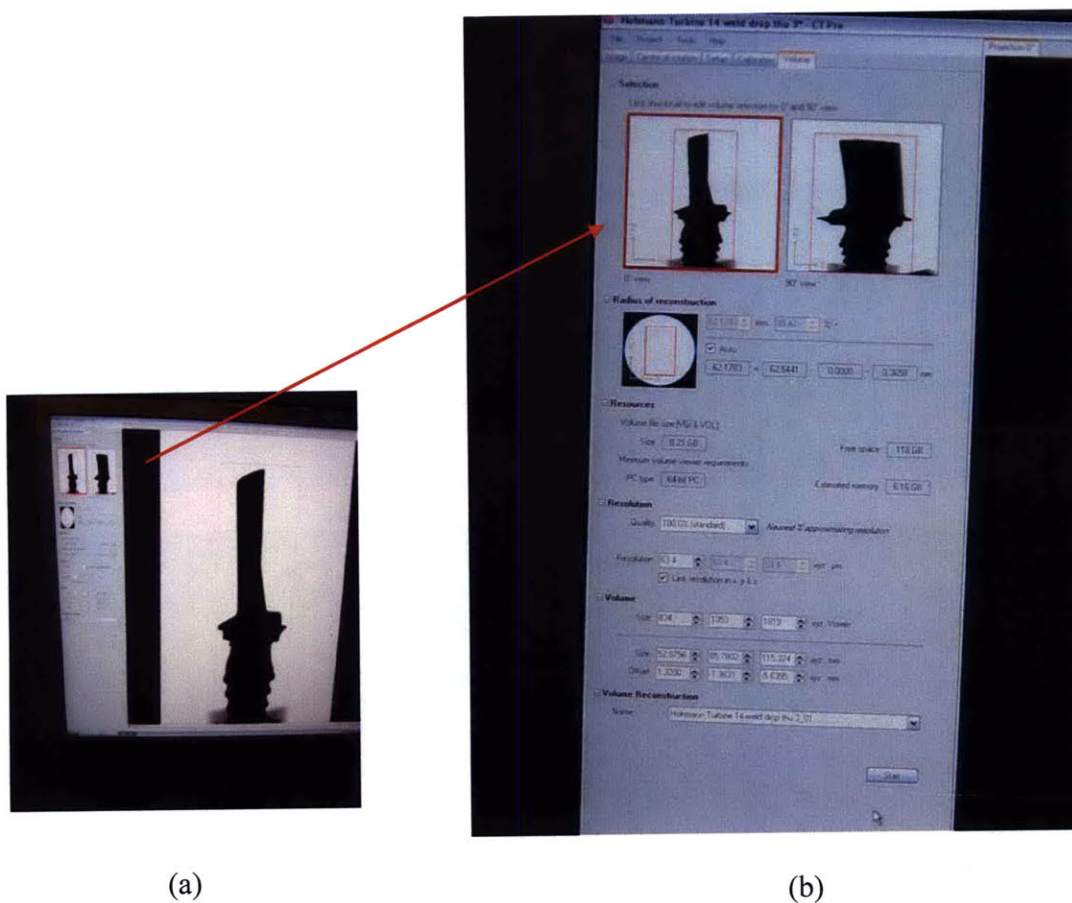


Figure 4.9: (a) Center of rotation settings tab in the CT Pro™ module (b) Magnified view of the settings in the left hand panel of the module that must be selected before volume reconstruction can proceed.

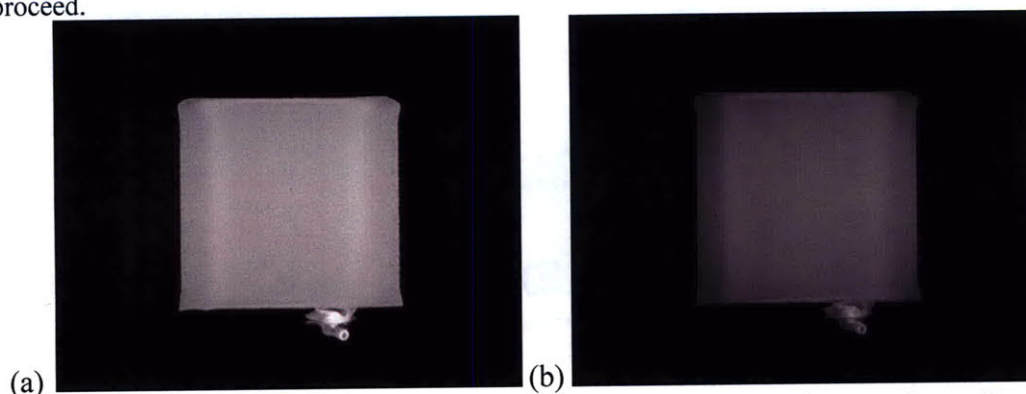


Figure 4.10: (a-b) Representation of how selected volume renderer influences the quality of a 3D reconstruction. The amount of noise is significantly greater in (a) than in (b)

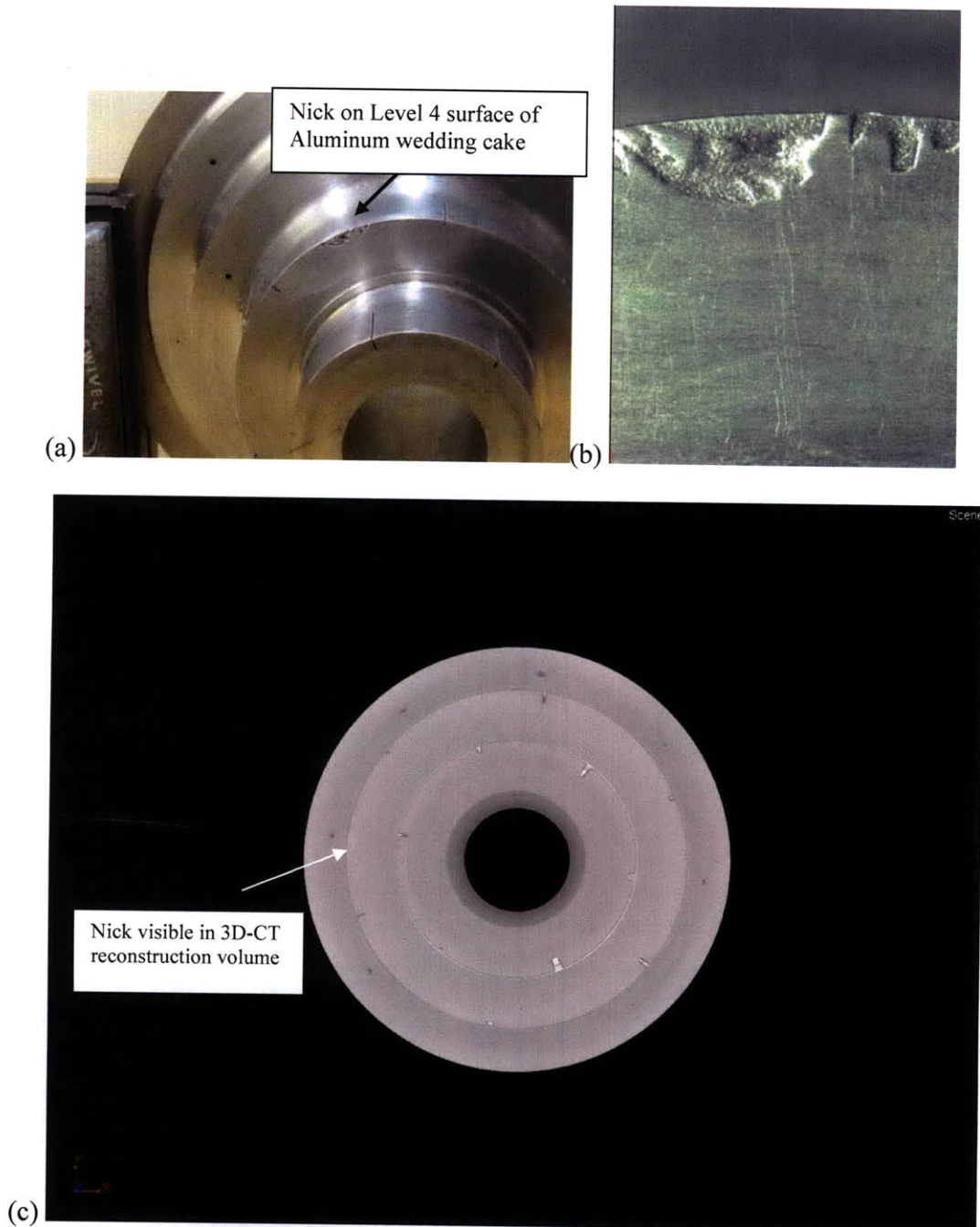


Figure 4.11: (a) Nick on the Level 4 surface of the aluminum wedding cake (b) Magnified view of the nick taken with a stereo microscope (c) Nick is visible in the 3D-CT image as a region of slightly lighter grayscale.

wedding cake that is also visible in Figure 4.11(c) as a region of slightly lighter than nominal grayscale. This is one of the benefits of 3D-CT inspection over ultrasonic techniques. Whereas UTI techniques provide unsurpassed depth of penetration for thick samples, they are not adept at characterizing the material properties of the sample under inspection. On the other hand, 3D-CT is very well suited for material characterization but x-ray attenuation through thick components and the upper limit on x-ray penetration depth are drawbacks. An additional advantage of CT over acoustic techniques is the ability to inspect very complexly shaped parts with ease. The images from the turbine blade and duct segment inspections are evidence of this. Newer features available in 3D-CT reconstruction software allow thresholds to be set for radiodensity values. In this manner subsurface defects that have a different density than the bulk material, such as hard alpha anomalies, can be more easily detected. Additionally, the ability to apply an image threshold based on a material property value enables the simultaneous inspection of multi-component assemblies, as was previously shown in Figure 1.26. With regard to penetration depth and material characterization capabilities, 3D-CT and PA-UT are complementary techniques when simultaneously incorporated into an inspection program.

For the detection of subsurface defects, three dimensional computed tomography reconstructions provide a number of benefits other radiographic techniques cannot. Segmentation techniques, such as the use of cutaway planes, can be applied to the reconstructed volume. As shown for the aluminum wedding cake in Figure 4.12(a-d), samples may be segmented at a particular angle or at a unique depth. Neither traditional film radiography nor digital radiography can provide this type of information on feature depth. As shown in Figure 4.12(b), once a particular depth has been selected measurements can then be made in the ROI. For situations where the indication of a defect requires subsequent removal of that section from a large structural component, there may be significant cost savings gained from knowledge of the defect's depth if that results in the removal of substantially less material. Also, as Figure 4.13(a-f) shows for one of the turbine blades, the sample orientation can be easily manipulated by the visualization software. This capability overcomes line of sight limitations inherent to film radiography and two dimensional digital radiography (2D-DR). Section 4.3

provides a more in-depth analysis on the differences between these three radiographic techniques.

The results of these inspections also show that computed tomography is not without its limitations. The limitation of sample size has already been mentioned, however this is a significant obstacle to implementation of 3D-CT for large parts or parts with a particularly large aspect ratio in one direction. Scattering of the x-rays can give rise to noise. In the aluminum wedding cake sample, the bored out center hole region caused a lot of x-ray scattering. This is visible in Figure 4.6(d) by the coarseness of the image quality around the center hole region. Variability in the dynamic range for CT scans of two separate turbine blades significantly affected the resulting image quality and thus sensitivity to flaw detection. Figure 4.14(a-b) shows the contrast difference for the two blades as a result of the different dynamic ranges. At least for the 225kV MicroCT system used, inspection parameters that were subjectively selected by the operator had a major influence on scan quality and inspection outcome. While the weld drop-through defects can still be observed in Figure 4.14(b), the loss of image contrast would seriously limit the sensitivity of a CT system to detect internal defects for thicker components. The ability to automate these decisions in a production environment would be a critical factor to implementing a RFC approach to predicting remnant life in structural components. The inspection results corroborated the general principle that 3D-CT is not adept at detecting surface flaws. The surface cracks in the duct segment could not be identified after inspection. Also, the post weld tip crack was not identified by 3D-CT. Section 4.3 goes into greater detail on the results for this particular turbine blade.

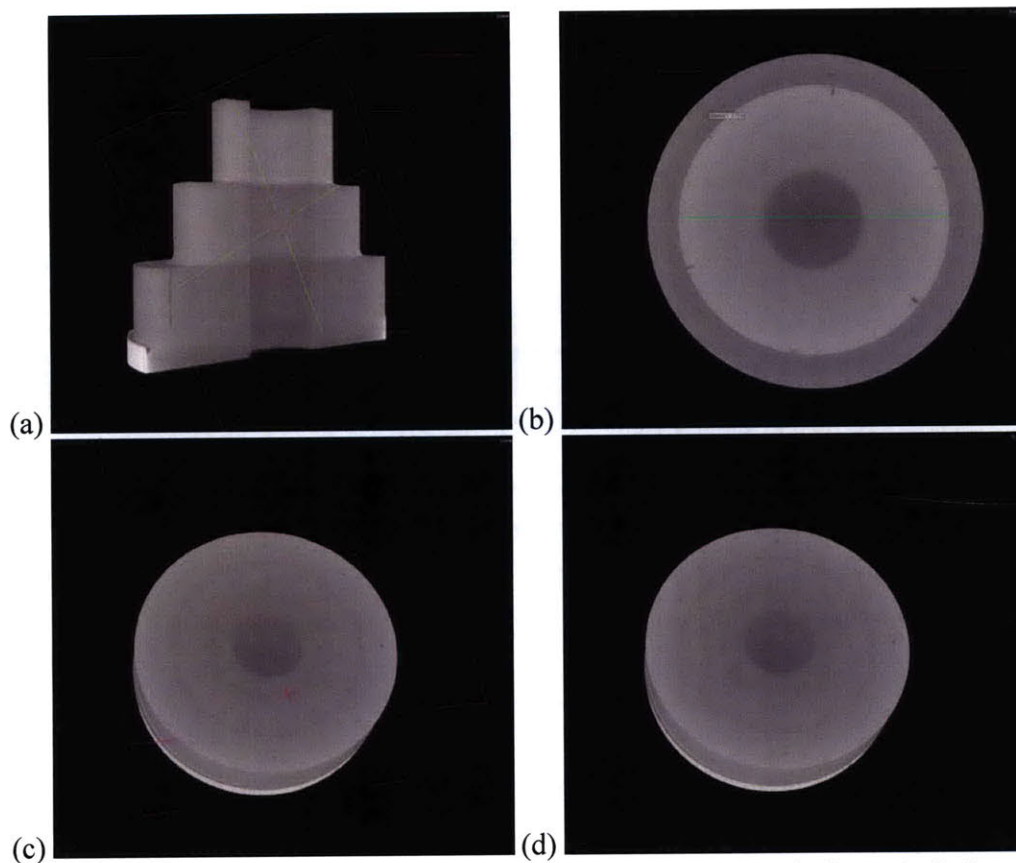


Figure 4.12: Sample segmentation via use of cutaway planes at (a) a particular angle (b-d) a particular depth. Visible in (b) and (c) is the ability to take measurements at the desired ROI

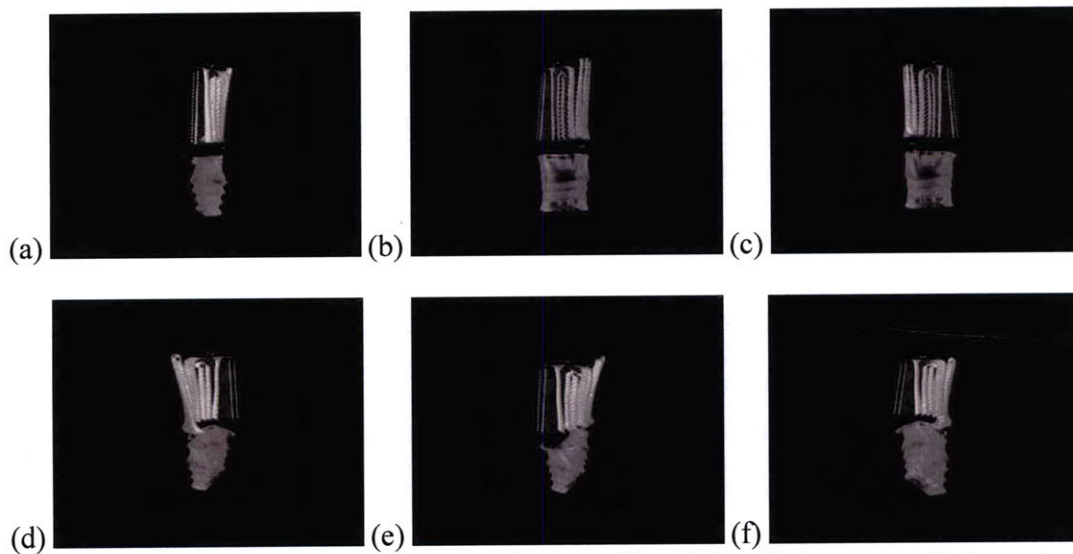


Figure 4.13: (a-f) Different 3D orientations for the turbine blade with the post-weld tip crack

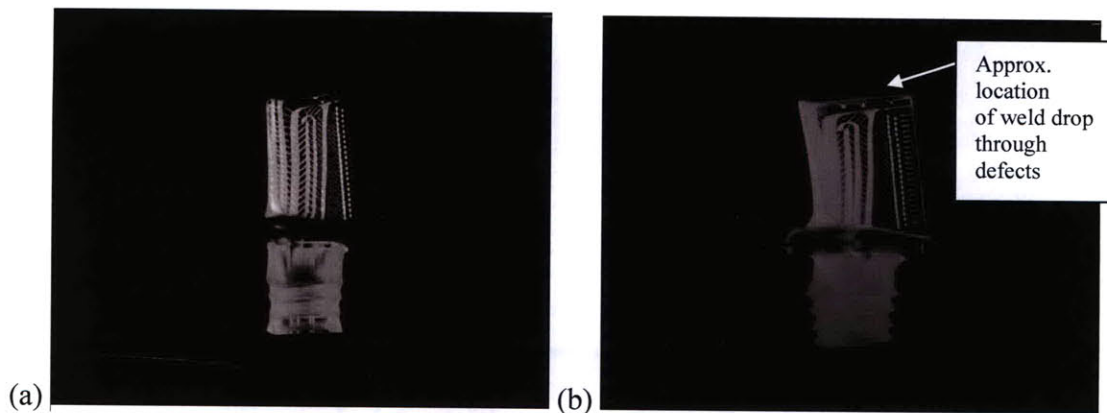


Figure 4.14: (a) Turbine blade with large dynamic range (b) Turbine blade with less dynamic range resulting in less image contrast

4.3 Comparison with Traditional X-ray Technique

Traditional film radiography was performed on the wedding cake specimens and actual engine component samples at the aerospace MRO facility in New York. Settings for the duct segment and two of the blade inspections included a 175kV x-ray voltage, 10.0mA current, and 2 minute exposure time. Figure 4.15(a-d) shows the equipment used to take the radiographic images, sample setup, and resulting images for the duct segment. Since film is not a digital form of media, a digital camera was used to photograph the x-ray film while it was exposed under a radiographic viewer. Traditional film radiographic images for the two turbine blades with weld drop-through defects are shown in Figure 4.16(a-b). Figure 4.17 shows the influence of the selected brightness level from the radiographic viewer on ultimate film image quality. It was attempted to maintain brightness levels as equal as possible between samples, however variability between image brightness was unavoidable. The images for the post weld tip crack are observed in Figure 4.18(a-b) for the traditional radiographic technique. A crack at the tip of the trailing edge as well as a crack in the internal cooling channel region can be observed. For the post weld tip crack film exposure, a ^{60}Co -gamma radiation source was used rather than an x-ray source.

The use of the gamma radiation source was a contributing factor to the ability of the traditional technique to detect this internal crack, while both CT and DR digital techniques were not able. Also, the specific orientation of the blade with respect to the direction of incoming x-rays significantly affects detection sensitivity. Based off the

images in Figure 4.18(a-b), a 2D slice from the 3D-CT scan of the post weld tip cracked blade was selected for comparison. Projection slice 2080 out of 2682 total 2D slices was used for the analysis because its orientation most closely matched that of Figure 4.18. Since the 3D-CT sample rotates 360° during inspection, the 2D slice seen in Fig 4.19 was taken at a rotational angle of approximately 280° from the nominal starting position. The original CT slice had to be inverted because 3D-CT takes 2D images with respect to a black reference image while traditional film radiographs are exposed with respect to a white reference image. Adobe® Photoshop CS4 edition was used to alter the brightness, contrast and exposure of the CT slice to mimic the levels of Figure 4.18. Figure 4.19(a-b) show the resulting digital slice after doubling the brightness level, reducing the contrast by 50%, and increasing the exposure by a factor of 2.4. The features of the cooling channels are almost identical for the two figures, however no cracks are observed in the digital image. The reason for this is because there is approximately a 3° difference

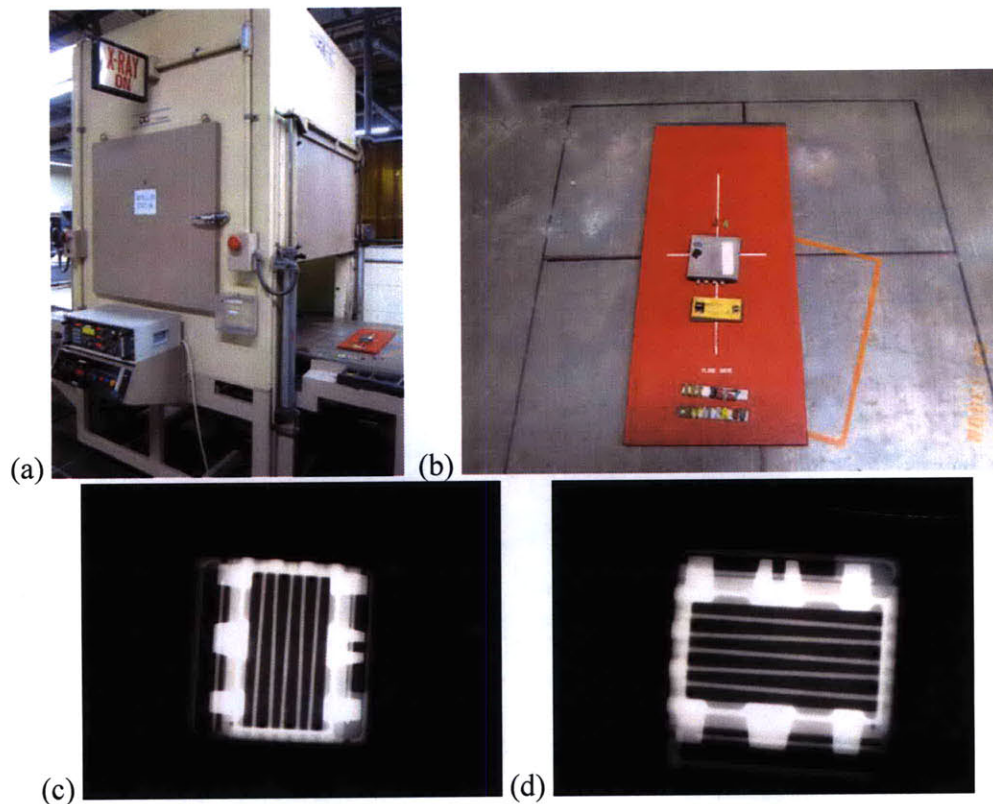


Figure 4.15: (a) Equipment used to take traditional film x-rays (b) identification markers placed on sample (c-d) Film radiograph images of the duct segment.

in the sample orientation between Figure 4.18 and Figure 4.19. Figure 4.20(a-b) shows the image in Figure 4.19 after rotating by 3.2° with the Photoshop™ software. Unfortunately, the use of image analysis software cannot correct for sample misalignment after the inspection has already occurred, and the internal crack was not detectable by either of the digital techniques.

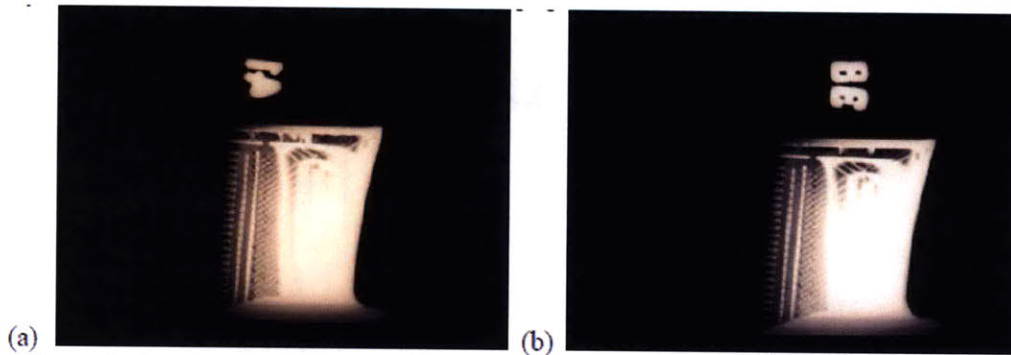


Figure 4.16: (a-b) Traditional film radiographs of two blades with weld drop through defects [190].

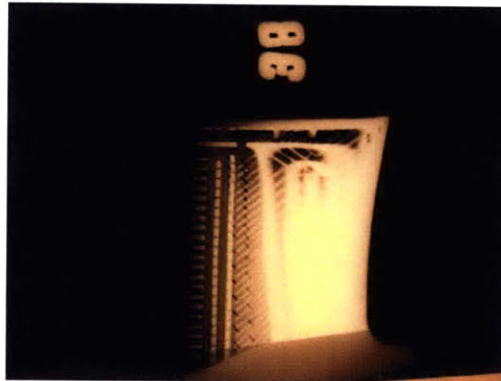


Figure 4.17: Influence of radiographic viewer brightness on image quality

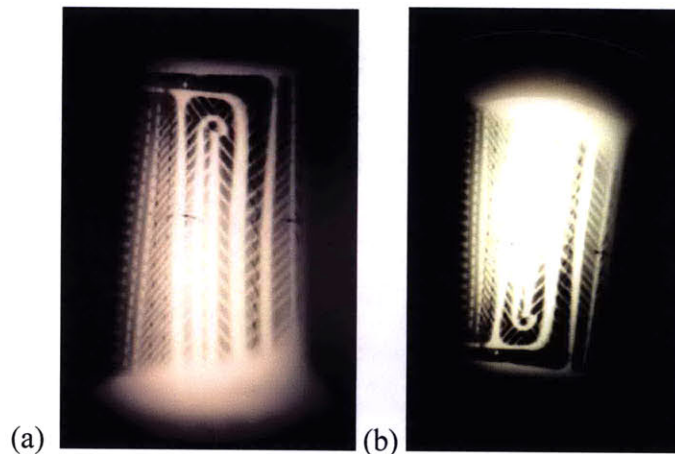


Figure 4.18: (a-b) Traditional radiographic images of turbine blade containing post weld tip crack

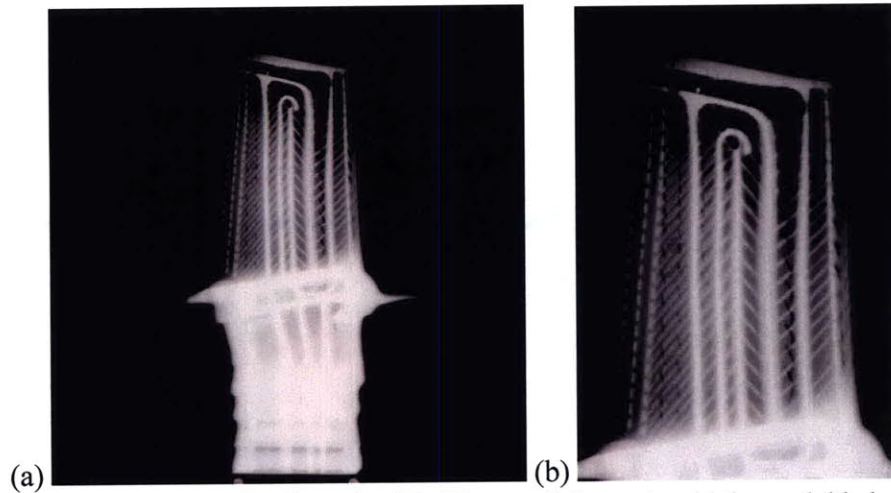


Figure 4.19: (a) Selected 2D slice from the 3D-CT scan of the post weld tip crack blade sample after adjustment of brightness, contrast, exposure and image inversion (b) Internal crack ROI. No internal crack is detectable.

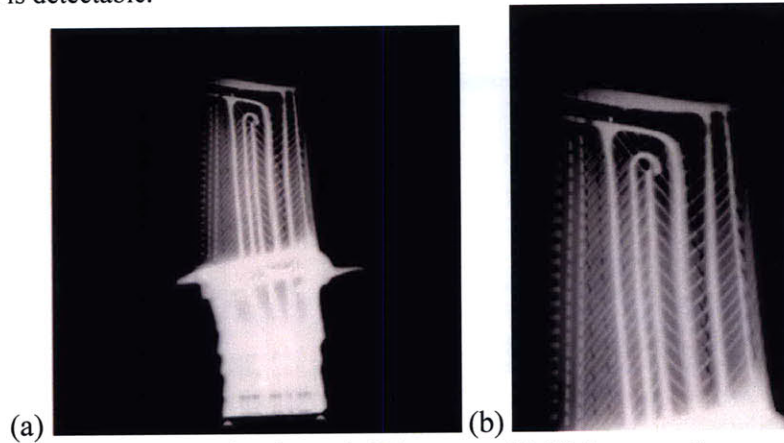


Figure 4.20: (a-b) Same image as in Figure 4.19 but rotated 3.2° degrees. Compare with Fig. 4.18.

A similar image inversion and grayscale optimization procedure using the Adobe® CS4 Photoshop software was performed on a slice from the 3D-CT inspection of the duct segment. Figure 4.21(a-c) shows the original slice, the inverted slice without adjustment, and the inverted slice after exposure optimization for the back side of the sample. Similarly, Figure 4.22(a-c) shows the same perspectives for the front side of the duct segment. The surface cracks of the duct segment are not detectable in any of the images, further supporting the conclusion that 3D-CT inspection is not applicable for detection of surface cracks. On the other hand, the level of image detail and resolution for the software-optimized images in Fig. 4.21(c) and Fig. 4.22(c) are superior to those of the traditional film radiographs. Chapter 5 will further explore the inspection benefits

gained via usage of image analysis software, however in Chapter 5 the Cellprofiler software rather than Photoshop™ was used. The main reason for the change in image analysis programs was the high image throughput and batch analysis capabilities of Cellprofiler.

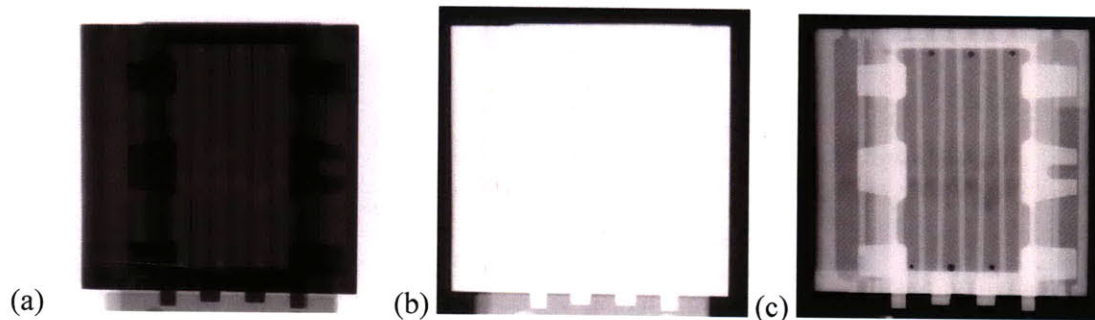


Figure 4.21: Back side of duct segment showing (a) Original 3D-CT inspection slice (b) Inverted image with no brightness, contrast, or exposure level adjustment (c) Inverted image after optimization

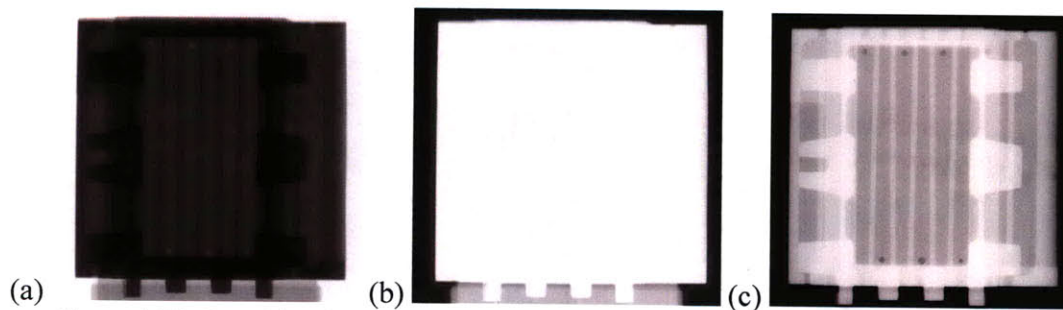


Figure 4.22: Top side of duct segment showing (a) Original 3D-CT inspection slice (b) Inverted image with no brightness, contrast, or exposure level adjustment (c) Inverted image after optimization

An important point observed by the inability of the 3D-CT or DR techniques to detect the surface cracks on the duct segment and near surface crack on the post-weld tip cracked turbine blade is that regardless of how advanced the NDT system being used is, it must be applicable to detection of the particular defect present. Neither the 3D-CT nor DR technique is very good at detecting surface or near-surface cracks. The cracks seen in Figure 4.18 are near-surface cracks. However, the traditional eddy current technique detected the post-weld crack tip. Figure 4.23(a-b) shows the crack indication with traditional EDI. The need to use image analysis software to invert the grayscale levels of the image also contributed to the lack of sensitivity for the 3D-CT technique. During the CT inspection, the crack was indistinguishable from the black background level while for the traditional film radiograph the crack was enhanced.

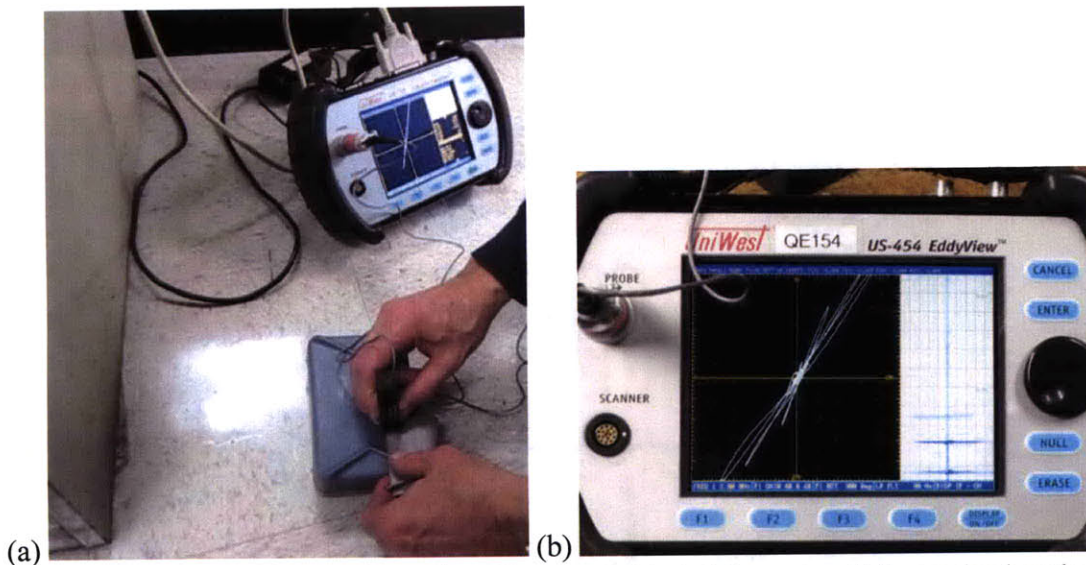


Figure 4.23: (a-b) Traditional point probe eddy current detected the post weld tip crack when the more advanced 3D-CT method could not. This is an example of when a traditional technique that is better suited to the particular flaw type should be used instead of an advanced technique.

A limitation of traditional film radiography is that film can only inspect one region of a sample at a time. Therefore, a single film exposure was needed at each of the five surface levels. A masking technique was used to shield the x-rays so that only one level per film exposure was obtained. Figure 4.24(a-e) contains the images for the five steel layers for the sample without the embedded defect. For all of the steel sample levels, neither the FBH nor the SDH were well resolved. The steel wedding cake without the embedded defect was shot at a voltage of approximately 300kV, while the parameters for the aluminum x-ray films varied by level. Table 4.1 includes these settings and also the H/D values for the film images. These H/D values are used in conjunction with what is known as the film characteristic curve. The purpose of this curve is to characterize x-ray film based on the applied exposure and the resulting film density. The film characteristic curve enables a comparison between different sets of x-ray film to be made based on those two values. Figure 4.25(a-d) contains the aluminum wedding cake film images. A film exposure that was in focus could not be obtained for Level 1 of the aluminum cake due to distortion from penumbra. This penumbra is unavoidable unless higher energy x-rays can be used at a longer distance from the wedding cake and film [198]. These

images were incorporated into the POD analysis by the use of the Cellprofiler image analysis software. The results of this analysis are discussed in Chapter 5.

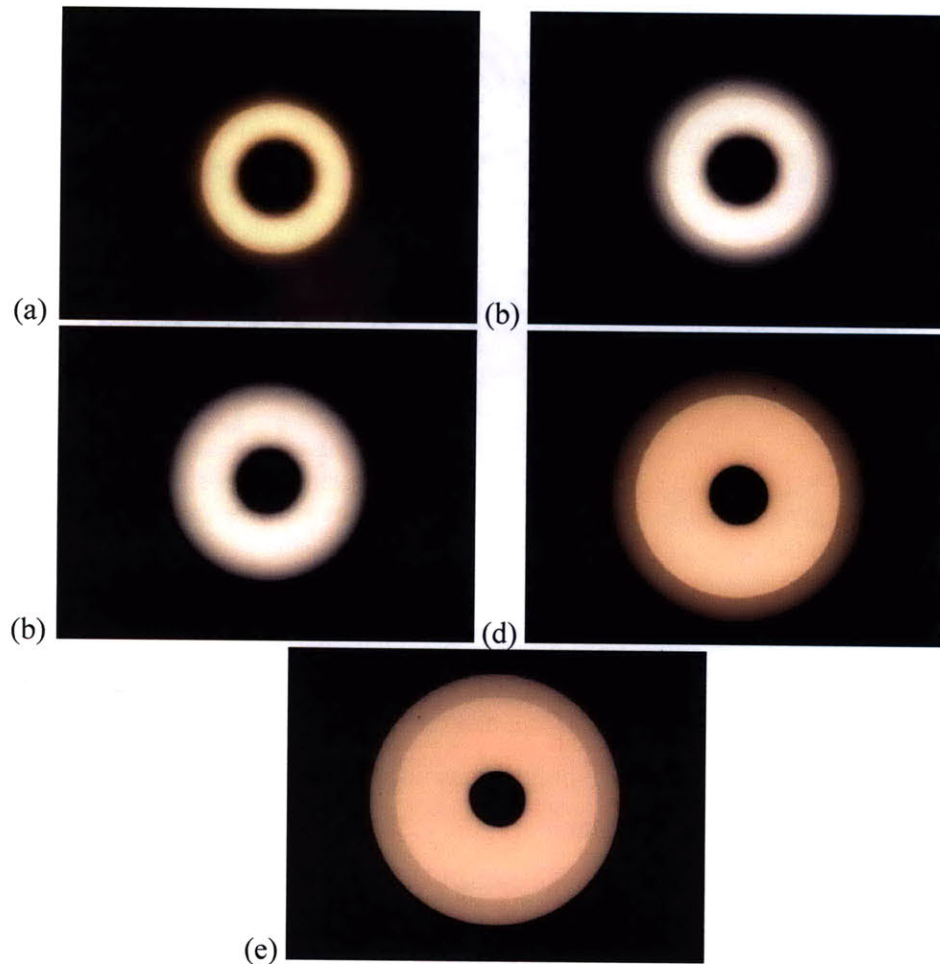


Figure 4.24: (a-e) Radiographic film images for Levels 1-5 of steel wedding cake

Table 4.1: Parameters for the x-ray film images taken of aluminum wedding cake

Level	Voltage (kV)	Current (mA)	Exposure (min)	H/D value
1	95	10	1	3.06
2	110	10	1	3.09
3	140	10	1	2.08
4	165	15	1	2.19
5	185	15	1	2.15

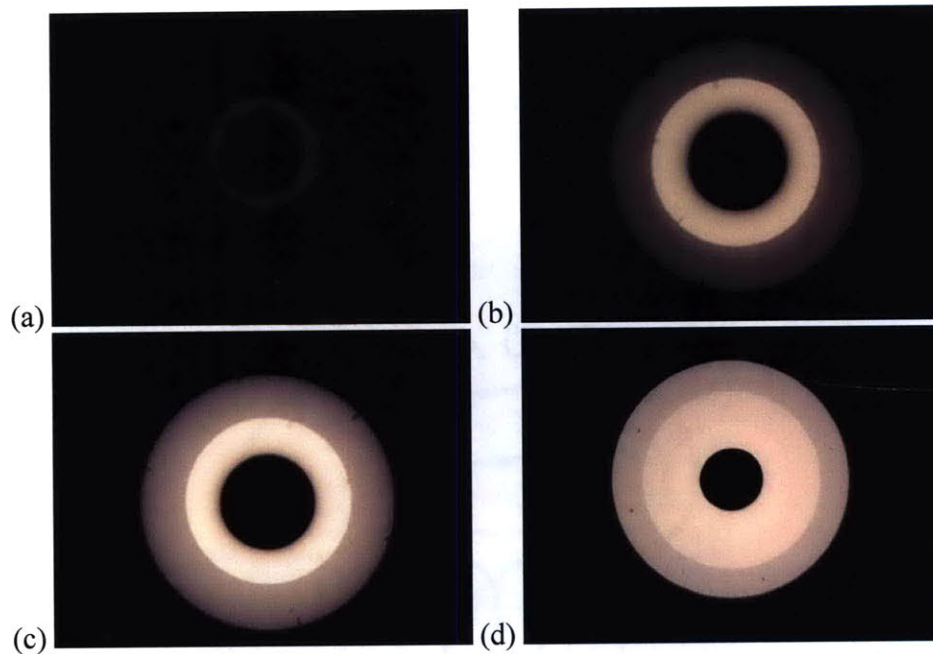


Figure 4.25: (a-d) Radiographic film images for Levels 2-5 of aluminum wedding cake

Digital radiographic (also known as Computed Radiography) images were taken at Baker Testing Services, Inc. [Rockland, MA]. The equipment used and test setup for the DR inspections are shown in Figure 4.26. Figure 4.27 shows the selenium/phosphor material used in the image plate. All four of the alloy block specimens, all three of the wedding cake specimens, the three turbine blades, and the duct segment were imaged with the DR. The DR technique was able to inspect multiple samples in a single exposure in some instances, which is a capability not afforded to film radiography. Table 4.2 includes an image description, as well as voltage, current, and exposure values. Appendix E contains the images acquired during the DR inspections for the images listed in Table 4.2. The focal spot size of the x-ray source was 1.8mm (0.07in.) and the source to object distance was approximately 203cm (80in.). The large distance between the source and object allowed good image resolution from all sample layers with minimal penumbra. As shown in Figure E.3 and Figure E.7, FBH indications from multiple levels were obtained from a single exposure with the DR technique. For the aluminum wedding cake sample, the side drilled holes could also be observed from a single digital radiographic exposure. Because of the high energy radiation generated, shielding in the form of a 30cm (1 ft) thick wall of concrete reinforcement was required.



Figure 4.26: Equipment setup for DR experiments

Table 4.2: Parameters and a description of the DR images taken at Baker Testing

Image #	Voltage (kV)	Current (mA)	Exposure (min)	Description
1	180	3	0.5	Three turbine blades
2	230	3	0.5	Steel wedding cake with embedded defect-Top down
3	230	3	0.5	Steel wedding cake w/out embedded defect-Top down
4	320	5	2	Steel wedding cake with embedded defect cross section exposure
5	320	5	3	Steel wedding cake with embedded defect -Top down/Higer kV
6	220	3	0.5	Duct segment
7	100	3	0.5	Aluminum wedding cake Top down
8	320	5	3	Sample H
9	225	5	6	Sample H
10	320	5	5	Sample R88
11	320	5	3	Sample L and sample U Side by side

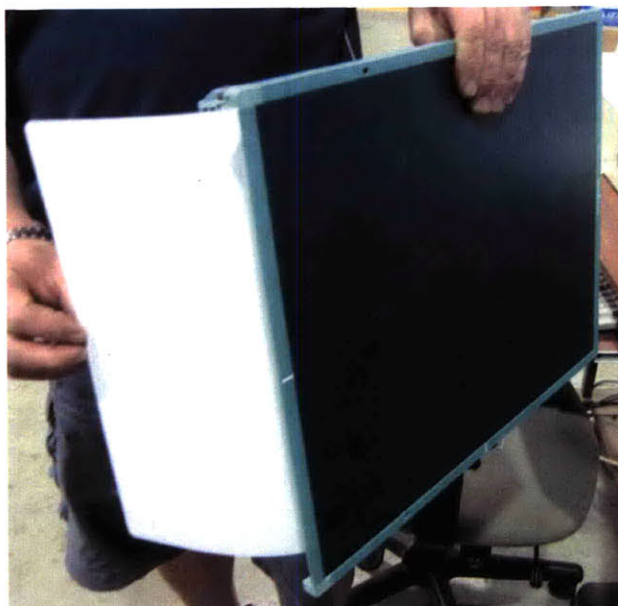


Figure 4.27: Selenium/phosphor material used in the imaging plate

The digital radiographic images for the wedding cake samples were taken with both top down and cross section orientations. As was the case for the CT images of the steel wedding cake samples, the DR technique was not able to penetrate through the cross section of the sample at the 320kV voltage capacity of the system at Baker Testing. It was estimated a higher voltage CT system in the range of 600-800kV would be needed in order to penetrate through all of the five levels of the steel sample with the embedded drill bit defect [196]. Commercially available systems with this voltage capability will be available in the next 1-2 years, and higher CT systems in the 6MV range are currently available for DR although they use linear accelerators and have additional radiation and shielding issues. Table 4.3 provides a comparison between the suitability of traditional x-ray film radiography and digital radiography NDT techniques for the inspection of both light and heavy metal structural components. The inspection sensitivity of both radiographic processes for a number of potential applications is provided, including the inspection of sheet, plate, bar and tube structural component geometries. Table 4.3 also classifies the flaw detection sensitivity for potential defects in castings, forgings, welds, processing, and service environments as good, fair, poor, or unsatisfactory.

The inspection results for the alloy block, wedding cake, and actual component sample classes corroborate with the various flaw detection sensitivity “grades” provided in Table 4.3. In terms of general thickness, DR is graded as “good” while x-ray film only

Table 4.3: Comparison of the suitability of traditional x-ray film radiography and digital radiography for numerous light metal and heavy metal structural component inspection applications during the component's life-cycle (adapted from [27])

<u>Inspection application</u>	<u>Suitability for light metals(a)</u>		<u>Suitability for heavy metals(a)</u>	
	<u>Traditional x-ray radiography with film</u>	<u>Digital radiography</u>	<u>Traditional x-ray radiography with film</u>	<u>Digital radiography</u>
General				
Surface cracks (b)	F(c)	F	F(c)	F
Internal cracks	F(c)	F	F(c)	F
Voids	G	G	G	G
Thickness	F	G	F	G
Metallurgical variations	F	F	F	F
Sheet and plate				
Thickness	G(d)	G	G(d)	G
Laminations	U	U	U	U
Voids	G	G	G	G
Bar and tubes				
Seams	P	P	P	P
Pipe	G	G	G	G
Cupping	G	G	G	G
Inclusions	F	F	F	F
Castings				
Cold shuts	G	G	G	G
Surface cracks	F(c)	F	F(c)	F
Internal shrinkage	G	G	G	G
Voids, pores	G	G	G	G
Core shift	G	G	G	G
Forgings				
Laps	P(c)	P(c)	P	P
Inclusions	F	F	F	F
Internal bursts	G	G	F	F
Internal flakes	P(c)	P	P(c)	P
Cracks and tears	F(c)	F	F(c)	F
Welds				
Shrinkage cracks	G(c)	G	G(c)	G
Slag inclusions	G	G	G	G
Incomplete fusion	G	G	G	G
Pores	G	G	G	G
Incomplete penetration.	G	G	G	G
Processing				
Heat-treat cracks	U	U	P	U
Grinding cracks	U	U	U	U
Service				
Fatigue and heat cracks	F(c)	F	P	P
Stress corrosion	F	F	F	F
Blistering	P	P	P	P
Thinning	F	F	F	F
Corrosion pits	F	F	G	G
(a) G, good; F, fair; P, poor; U, unsatisfactory. (b) Includes only visible cracks. Minute surface cracks are undetectable by radiographic inspection methods. (c) Radiation beam must be parallel to the cracks, laps, or flakes. In real-time radiography, the sample can be manipulated for proper orientation. (d) When calibrated using special thickness gages				

does a “fair” job for both light and heavy metals. This was observed for the top-down radiographic analyses of the aluminum and steel wedding cake samples, and the POD analysis in Chapter 5 will go into greater detail on this subject. Both techniques only do a fair job for surface crack and internal crack inspections, as was witnessed by the duct segment and post-weld tip crack turbine blade inspections. The importance of the sample orientation with respect to the x-ray beam is noted in the footnotes at the bottom of Table 4.3. As the results for the inspections of the turbine blades with the weld drop-through defects showed, both radiographic techniques generally do a “good” job with respect to the detection of weld defects. The traditional film and DR techniques are both poor at the detection of “blister” service defects, and both are classified as “unsatisfactory” for cracks formed during component processing steps. An example of the improved detection capability and sensitivity of 3D-CT over both of these radiographic techniques for a particular case of internal blisters caused by sulfidation on in-service LPT blades will be reviewed at the end of this section.

An additional factor that must be considered is the scan time required. For a dense component such as the steel wedding cake with the embedded defect, the inspection time was estimated at 12 hours [197]. In an aerospace maintenance, repair, and overhaul facility, a critical parameter in the economic feasibility of a *retirement-for-cause* type approach is the total required inspection time per component. When the inspection time for a large structural component is deemed prohibitively long, the best alternative is to inspect the part via an ultrasonic technique. Table 4.4 contains a comparison of ultrasonic, radiographic (generic to both traditional and digital processes), and 3D-CT NDT techniques. The comparison is based on various NDT system performance characteristics as well as detection capabilities for particular flaw-types. From Table 4.4 it can be concluded that 3D-CT has many of the same benefits or limitations as DR or traditional x-ray film radiography, as a consequence of being a radiographic technique subject to the laws of the electromagnetic spectrum. The primary difference between 3D-CT and both DR and traditional radiography is the fundamental nature of the radiographic inspection image. In both digital and film radiography, the structural information from a three dimensional sample is compressed onto a two dimensional image [199]. A positive consequence of this is that a relatively large volume

Table 4.4: Comparison of ultrasonic, radiographic, and x-ray CT techniques (adapted from [199])

Performance characteristic	Ultrasound	Radiography (Traditional or Digital)	Computed tomography
Parameter imaged	Acoustic impedance differences, attenuation, velocity	Attenuation	Attenuation
Handling of Sample	Immersion, contact system With gel couplant	Flexible but portability limited by shielding requirements	Scanner size limitation
Surface roughness imaging	Poor	Fair	Good
Complexity of sample	Poor	Fair	Good
General Limitations	Needs acoustic coupling; sensitivity lowered for acoustically noisy materials	Penetration through one side only. No knowledge of flaw depth gained.	Penetration over a 360° scan; limited volume imaged per scan
General NDT System Costs	Medium	Medium	High
Specific Flaw-type Detection Capability	Ultrasound	Radiography (Traditional or Digital)	Computed tomography
Voids	Good	Good	Good
Inclusions	Good	Fair	Good
Porosity, hot tears, etc.	Good	Fair	Good
Density variations	Fair	Fair	Good
Cracks	Good (not aligned)	Fair (separated and aligned)	Fair (separated)
Debonding	Good	Fair (separated and aligned)	Fair (separated)

can be interrogated and resolved in a single exposure, but the trade-off is a loss of depth resolution. The main advantage of 3D-CT over DR and film radiography is the ability to quantify the depth of embedded voids and cracks. This is a very important aspect of subsurface defect sensitivity.

An example of this advantage is shown by the difference in image quality and image resolution in Figure 4.28 and Figure 4.29. Figure 4.28(a-f) displays DR images for a turbine blade. Image software was used to adjust the brightness and contrast levels for the DR exposure, as seen in Fig. 4.28(c-e). What appeared to be two flaw indications are circled in Fig. 4.28(e-f), however the indications could not be conclusively identified as defects based on the DR image. Computed tomography was subsequently performed on the blade. Individual 2D projection slices from the 3D-CT scan that show the damage progression of the internal sulfidation blisters are included in Figure 4.29. The 2D slices were taken subject to two conditions: a 2D slice was taken at either a specified depth

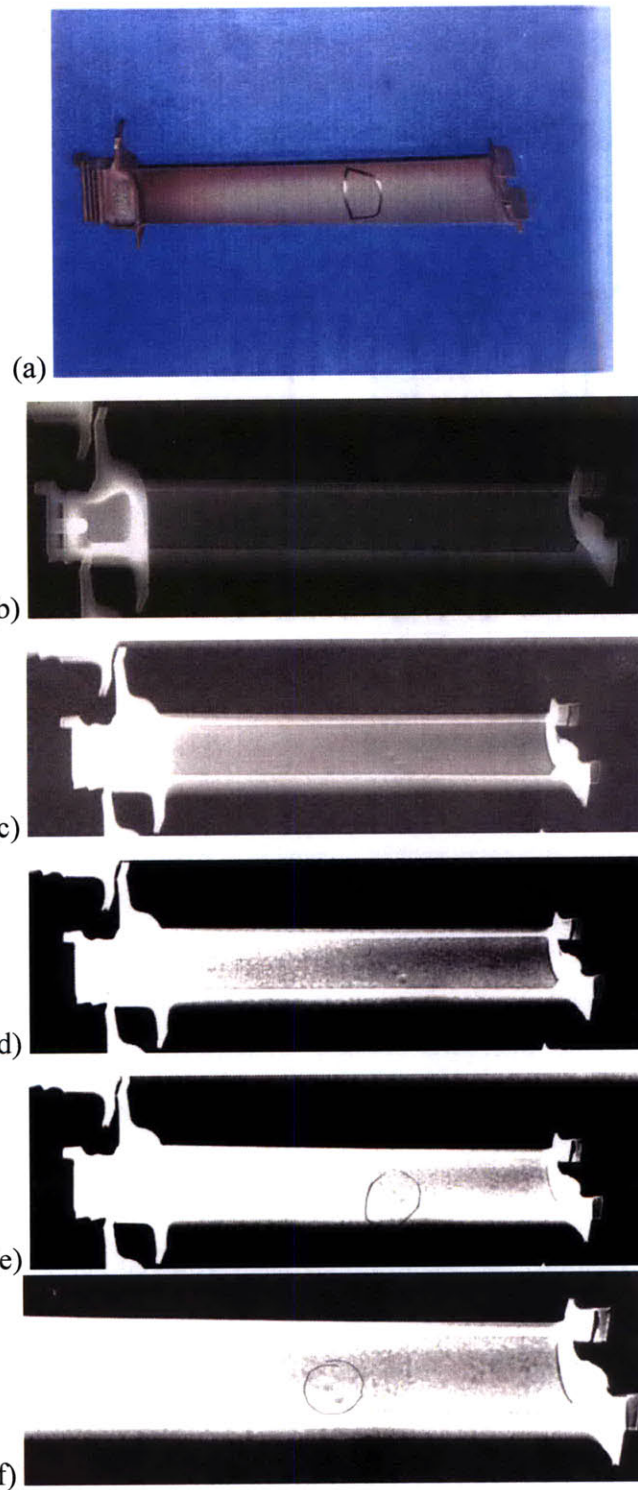


Figure 4.28: (a) Turbine blade with ROI circled with marker (b) DR image prior to enhancement with image analysis software (c-e) Image after brightness and contrast levels altered to enhance grayscale contrast in ROI (f) Image in Fig. 4.28(e) magnified for additional image enhancement

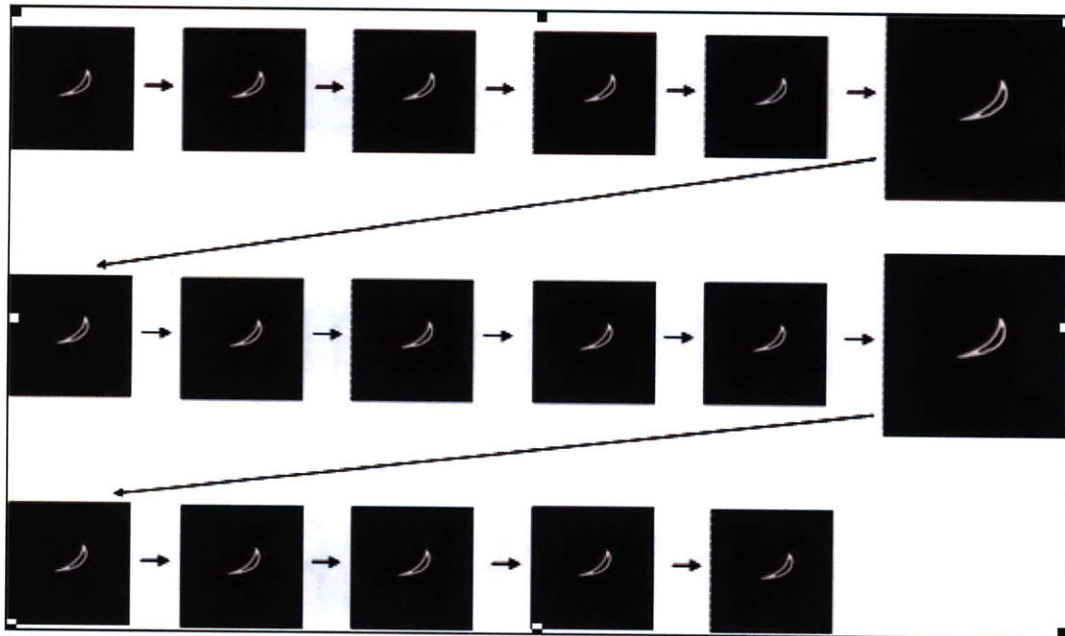


Figure 4.29: Evolution of blisters in turbine blade from 2D slices taken during CT inspection

interval of 0.5mm (0.020in.) or when a gated threshold was crossed. The threshold was applied based on a chosen relative percentage difference in grayscale level (i.e. dynamic range) between adjacent 2D scan slices. In Figure 4.29, the smaller 2D images represent the specified 0.5mm (0.020in.) slice intervals, while the two larger images to the right represent where the grayscale threshold was tripped. Figure 4.30(a-f) contains enlarged 2D images of the most relevant projection slices from Figure 4.29.

The CT inspection images in Figure 4.30 conclusively show the detected near-surface regime blister defects. They also allow a quantitative estimate of the percent total wall thickness to be calculated for each of the blisters, because blister depth, length, and width can be calculated from information contained in the individual projection slices. The 3D-CT scan slices were then reconstructed and rendered into a 3D volume where the evolution of the two sulfidation blisters was even more apparent. In cases like this where service defects result in indications that are inconclusive and subject to operator discretion, the ability to observe and segment a reconstructed CT volume is a significant benefit for the NDT technician who must make the ultimate decision on the inspection data. Whereas the images from the 2D digital radiographic NDT technique in Figure 4.28 were difficult to interpret because of shadows superimposed from overlying and

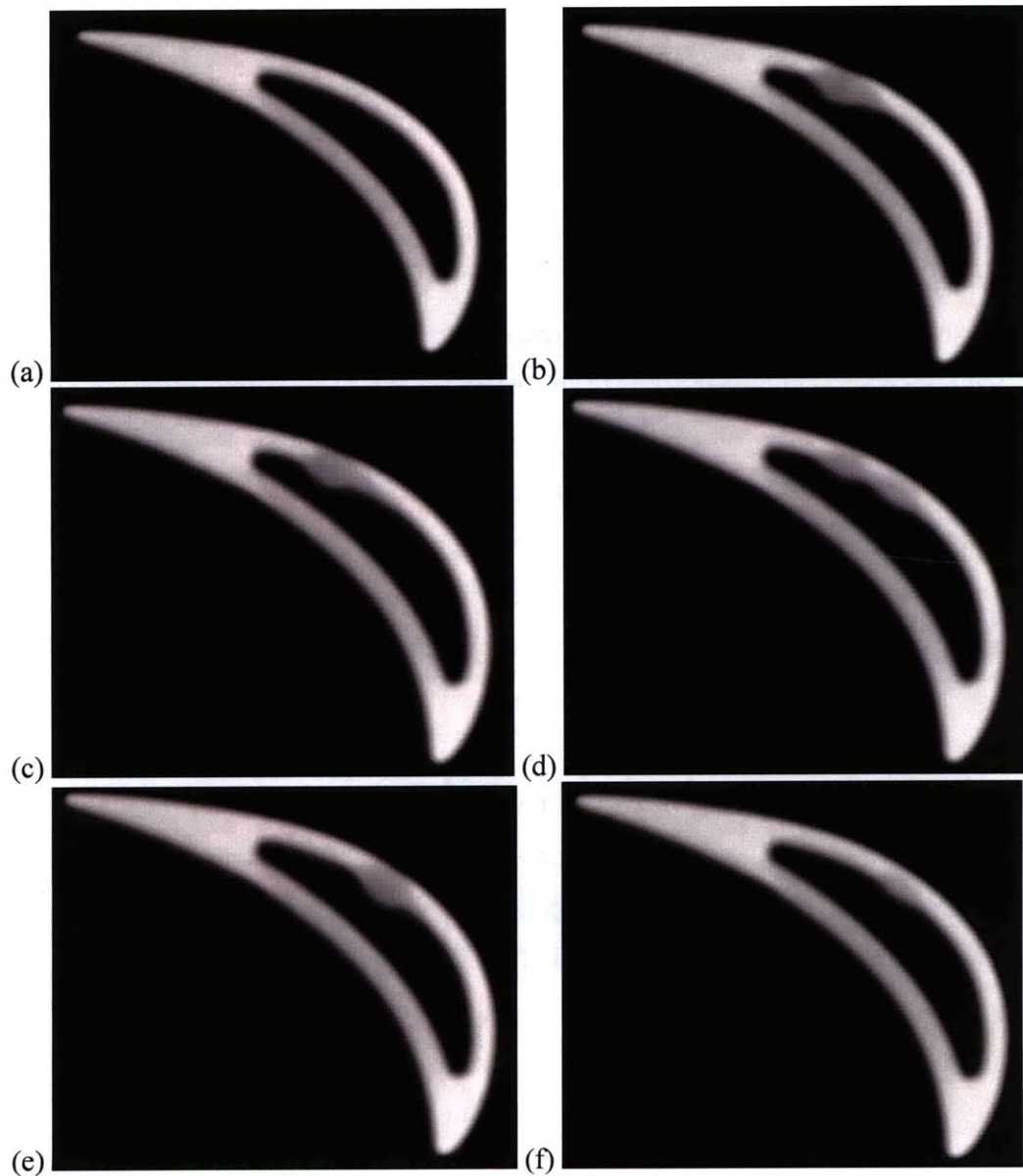


Figure 4.30: (a-f) Enlarged 2D slices of the most relevant images in Fig. 4.29 clearly showing internal blisters

underlying features, the 3D-CT scan was not subject to that same limitation (caused by compression of a 3D object onto a 2D image plane). Furthermore, neither 2D-DR nor traditional film NDT are able to sufficiently characterize three dimensional flaws such as internal voids or porosity. These two techniques can only provide POD information on surface flaws. The 90/95 POD/CL value that is used as a metric to judge the POD of various NDT techniques is not sufficient for quantifying the sensitivity, component coverage, or capability of an NDT system with respect to subsurface defect detection. In

order to implement the proposed methodology a new three parameter metric for characterizing embedded defects is required. Specific details regarding this newly proposed three parameter quality metric and the implications of its incorporation into remnant life prediction models for structural components are discussed in Chapter 6.

Table 4.5 contains a comparison of performance characteristics for traditional x-ray film radiography, real-time radiography and 3D-CT. A fluorescent screen TV camera system or an image intensifier is utilized in real-time radiography. As seen in Table 4.5 the spatial resolution is quoted in terms of line pairs/mm, and 3D-CT generally has lower spatial resolution than x-ray film or real-time radiographic. The reason for the lower spatial resolution stems from the decreased source to detector distance in a compact 3D-CT system versus a traditional x-ray film system. However, newer CT systems with microfocus x-ray tubes now result in increased spatial resolution and enhanced flaw detection sensitivity versus other radiographic techniques. The improvement in 3D-CT technology is noteworthy. Until a few years ago x-ray sources with focal spot sizes less than $50\mu\text{m}$ (0.002 in.) were not commercially available; approximately a decade later CT systems with $1\mu\text{m}$ ($4\times 10^{-5}\text{ in.}$) and higher voltage capability are possible for the most advanced models. The technological advances gained in CT have outpaced other techniques in the past 25 years. Additional benefits of CT include significant advantages in absorption efficiency, dynamic range, digital image processing, and dimensioning capability over traditional x-ray techniques. A global conclusion determined from the 3D-CT experiments performed is that advancements in NDT technology have resulted in nearly a 10X improvement in POD for advanced 3D-CT systems versus the data in Figure 1.16 for radiographic techniques in the mid-1980's. Conversely, NDT processes that are currently used in the aerospace industry have not shown the significant improvement in POD that 3D-CT has. Fluorescent penetrant inspection has only seen approximately a 1-1.5X improvement over the same time span.

Results from the experimental inspections performed on the three sample classes also confirmed what is described in Table 4.4. The C-scan inspection data verified the complementary inspection capabilities of the PA-UT and 3D-CT methods. When penetration of thick structural steel wedding cake samples was required, the phased array ultrasonic techniques were shown to be superior to the radiographic techniques.

Table 4.5: Comparison of performance characteristics for traditional film radiography, real-time radiography, and 3D-computed tomography (adapted from [199])

Performance characteristic	Film radiography	Real-time radiography (a)	3D-Computed Tomography
Spatial resolution (b)	7-8 line pairs/mm	2.5-5 line pairs/mm	0.2-4.5 line pairs/mm
Absorption efficiencies, %			
Absorption efficiency (80 keV)	5	20	99
Absorption efficiency (420 keV)	2	8	95
Absorption efficiency (2 MeV)	0.5	2	80
Sources of noise	Scatter, poor photon statistics	Scatter, poor photon statistics	Minimal scatter
Dynamic range	200-1000	500-2000	Up to 1×10^6
Digital image processing	Poor; requires film scanner	Moderate to good; typically 8-bit data	Excellent; typically 16-bit data
Dimensioning capability	Moderate; affected by structural visibility and variable radiographic magnification	Moderate to poor; affected by structure visibility, resolution, variable radiographic magnification, and optical distortions	Excellent; affected by resolution, enhanced by low contrast detectability
(a) General characteristics of real-time radiography with fluorescent screen-TV camera system or an image intensifier. (b) Can be improved with microfocus x-ray source and geometric magnification.			

However, for components such as turbine blades, computed tomography was the best available technique. Compared to 3D-CT, there was a higher probability of false detections stemming from the poor detection sensitivity associated with ultrasonic inspection of complexly shaped parts. In addition to sample complexity, Table 4.4 also shows that UTI and 3D-CT techniques also complement each other in the detection of surface roughness, density variations, cracks, and debonding. Both ultrasonic and CT techniques are known to be good at the detection of voids, inclusion, and porosity. The performance characteristic comparisons included in Table 4.4 are for traditional ultrasonic techniques. It was shown in Chapter 3 that use of both the manual contact PA-UT and fully automated TESI phased array NDT systems in lieu of traditional UT techniques resulted in an improvement to inspection sensitivity, inspection coverage, and minimum detectable flaw size. The use of the more advanced phased array ultrasonic inspection systems in conjunction with microfocal 3D-CT systems can drastically improve inspection reliability and defect detection sensitivity in structural components for each of the three depth regimes. In particular, an ability to characterize the

contribution from shot peening or laser shock processing treatments in the near-surface regime could potentially be calculated based on the redundancy of the processes.

There are instances where 3D-CT or DR can be used interchangeably without a significant loss in image quality. The performance characteristics contained in Table 4.5 are comparable for 2D-DR systems with discrete element detector arrays and 3D-CT systems. Codes such as ASTM E1647-09, *Standard Practice for Determining Contrast Sensitivity in Radioscopy*, can be used to provide guidance on particular situations where the divergence in image quality between 3D-CT and DR is unacceptable. A new industrial standard for quantifying the inspection uncertainty in 3D-CT systems is soon to be released in Germany [200]. This German standard is part of the VDI 2630 guideline and is the first of its kind in the NDT industry. Additional efforts are underway in the US to expand the DICONDE standard for ultrasonic, eddy current, 2D-DR, and 3D-CT techniques that utilize advanced technology and rely on digital data output. This work on the “codification” of NDT standards for advanced digital imaging techniques will be discussed further in Chapter 5. In an integrated life-cycle inspection plan for structural components, there are costs associated with both increasing the total number of required in-service inspections and using advanced techniques that have increased equipment costs. However, over the lifetime of a structural component situations will arise where a choice between NDT methods of comparable sensitivity can result in significant cost savings without sacrificing flaw detection capability or increasing the risk of catastrophic failure. The methodology proposed in Chapter 6 describes a way to use Bayesian updating techniques to enable the substitution of advanced NDT techniques to optimize the life cycle cost-benefit ratio for the redundant system level inspection process.

Chapter 5: Image Analysis and POD Modeling

The previous three chapters have shown that the advanced techniques which are proposed for use in the improved NDT methodology enable the detection of smaller flaws with improved component reliability, coverage and sensitivity as compared to the mature traditional NDT technique. One of the main reasons the FAA has not adopted a RFC lifing approach is because the NDT techniques currently used lack the sensitivity required. The purpose of this chapter is to attempt to quantify the contribution of image analysis software in further reducing the minimum threshold flaw size that can be reliably detected. In the remnant life prediction of structural components, the minimum threshold flaw size is a significant parameter because it is a primary input variable incorporated into fracture mechanics analyses.

5.1 Experimental Procedure for Cellprofiler

There are many commercially available image analysis programs on the market, however Cellprofiler was selected over these commercial options for a number of reasons. A main reason for the selection of Cellprofiler was that the code was originally written for inspection of biological cells at the Broad Institute at MIT, therefore the technical knowledge of the individuals who wrote the code was in close proximity and readily available. Second, Cellprofiler is free and the code is available open source, so an individual user can modify Cellprofiler for a particular application other than biological image cytometry (automated cell image analysis) by writing custom macro programs to the open source code. This flexibility to the software code is a critical benefit of Cellprofiler over commercial image analysis tools. The algorithms used in commercial software packages are generally proprietary, and as such cannot be directly compared between various software programs because image analysis is heavily skewed by how the software is “tuned” [163]. Prior to Cellprofiler, the only other flexible, open-source biological image analysis package was ImageJ/NIH Image; however its design was geared more towards the analysis of individual images whereas Cellprofiler is designed to handle thousands of images in a high-throughput mode [163].

By properly “tuning” the inspection output between different NDT equipment, Cellprofiler can remove the variability associated with the *NDT inspection system*. This

variability between the inspection signal responses of different NDT systems is inherent to different inspection equipment based on the same general technique. In this manner, Cellprofiler was used to analyze the results from the traditional x-ray, digital radiographic, and CT aluminum wedding cake inspection data. The individual inspection data from the three techniques was optimized via pipeline development, application of image filters, and use of thresholding for individual image pixels. Intensity values for all of the relevant image filters and modules are included in a spreadsheet that is generated upon completion of the Cellprofiler image analysis. These values were normalized on a 0-1 scale for all three radiographic techniques to enable a direct comparison between the signal/noise response ratio of the different NDT techniques. The absolute intensity values were not significantly different for each technique; however normalization enabled a further reduction in the overall noise level between systems. With this experimental approach, an “apples-to-apples” comparison between the minimum detectable flaw size and POD for each radiographic NDT technique was made. The quality metric selected for the POD analysis was defined as the normalized signal response in a hit/miss type form after Cellprofiler was used to minimize the noise and artifacts from the 2D inspection data.

For the POD analysis described in Section 5.3, a range of detectable and non-detectable flaw sizes was required to generate the POD curve. For this reason, only the aluminum wedding cake sample was analyzed, since the steel wedding cake inspection results suffered from lack of penetration issues and the alloy block samples were all of identical flaw size. Each of the FBH and SDH flaws were of known size, location, and depth for the aluminum wedding cake sample. A pin gage had been used to verify the actual flaw sizes, calipers were used to quantify the thickness of the various SDH, and the NDT inspection output could be oriented so that the FBH were identically aligned when inputted into Cellprofiler. In this manner additional comparisons beyond just a hit/miss analysis were made, and a direct comparison quantifying the difference between the POD and flaw detection sensitivity from the traditional film and advanced DR techniques was obtained. A similar approach is described in [163], where Cellprofiler output was compared to images scored via visual inspection by expert biologists in order to quantify and validate the benefit gained from image cytometry. A slight difference in the

approach described in Section 5.3 was that since the aluminum wedding cake had been machined to known FBH and SDH values and oriented in such a distinct manner, visual inspection by experts was unnecessary since all the data needed to quantify the benefit of Cellprofiler was already known.

CellProfiler enables automated image processing through the application of “pipelines” with customizable modules and parameters. Specifically, a pipeline is composed of many individual modules and a progression of image analyses is run through these modules in order to yield the desired results. For most applications, pipelines will be composed of similar modules to handle the initial image uploading process. Image analysis results, however, are optimized by the addition of specific module filters and the manipulation of threshold correction factors as well as other parameters. Figure 5.1 shows the window in Cellprofiler where the user builds a personalized pipeline. The pipeline includes the various filters applied to the image to optimize its sensitivity and resolution. Table 5.1 contains the pipeline chosen for the optimized threshold analysis of the DR wedding cake sample images. Once the filters are applied various image threshold values can then be selected.

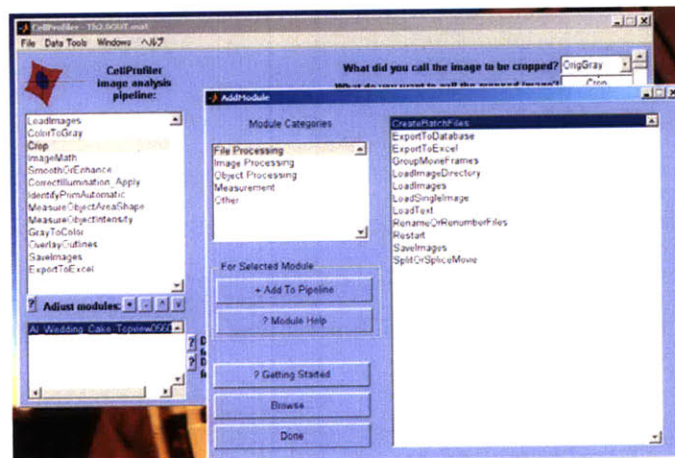


Figure 5.1: Creation of pipeline in Cellprofiler

The purpose of the Cellprofiler analysis was to determine the threshold ratio that optimized the correct detection ratio (CDR), while keeping the excess detection ratio (EDR) as low as possible. Another term for EDR is the level of false positive indications. After this was known, the optimized threshold values could then be selected for the POD analysis. An additional reason Cellprofiler was only used on the images from the

Table 5.1: Pipeline selected for the wedding cake samples

LoadImages
ColorToGray
Crop
ImageMath
SmoothOrEnhance
CorrectIllumination_Apply
IdentifyPrimAutomatic
MeasureObjectAreaShape
MeasureObjectIntensity
GrayToColor
OverlayOutlines
SaveImages
ExportToExcel

traditional x-ray film, DR, and 3D-CT radiographic techniques was because the radiographic inspection data was the most applicable for analysis with the existing Cellprofiler code. The top down radiographic data required little modification to the existing software because the FBH indications were cell-shaped and could be defined based on the difference in relative grayscale value from the nominal surface levels. On the contrary, the phased array results (especially for the 45° shear inspections) had FBH indications with skewed aspect ratios which complicated the ability to reliably size the detected flaws. Additionally, the data output from the TESI system was generated in such a manner that the information pertaining to the known FBH and SDH orientations was lost. As seen in the images in Chapter 3, the FBH appear linearly rather than circumferentially for the TESI inspection output. Since the system was programmed in such a way that the sample remained stationary and the probe and tank rotated during the inspection, it was impossible to know which FBH was nominally at the 0° position at the start of the inspections.

One limitation of the Cellprofiler software was the need for fairly circular hole features to be used in the image analysis. Also, only 2D slices from the various radiographic techniques could be inputted into Cellprofiler, since it was originally designed and optimized for the most common high-content screening image format (which is 2D). Cellprofiler has very limited support for time-lapse and 3D image stack analysis [163], which would be very beneficial for subsurface defect depth quantification via 3D-CT techniques. It should be noted that modules compatible for that type of inspection could be built due to the flexibility to personalize the Cellprofiler software;

however such an effort would require a lot of work and a lot of time programming macros. For CellProfiler to be feasible in a real inspection environment, the ability to detect service cracks with varying aspect ratios and orientations is required. The software currently does not have that capability, although the ability to detect non-circular morphologies is in progress. Continued work on this topic could lead to the expansion of image analysis software capabilities in the future.

For the detection of FBH and SDH flaws in the individual levels of the aluminum wedding cake sample, CellProfiler was very effective in filtering the image and contrasting the defects from the nominal material surface. With an idealized material geometry and optimized image quality, the software could be used to automatically identify defects during inspection. Automating the defect detection process would greatly reduce the necessary inspection time. Once the pipeline had been adjusted for the given application, CellProfiler is designed to quickly analyze large batches of images. For instance, the approximately 2500 two dimensional image slices taken during the 3D-CT scan of the aluminum wedding cake sample could be analyzed with CellProfiler in a few minutes to a few hours, depending on computer processing speed. Comparatively, this would take a technician anywhere from a couple days to a week to look at. However, for the image analyses performed, selections were manually made through the pipeline module progression and threshold correction processes. The sequence of modules in the wedding cake pipeline is shown in Table 5.1. The first two modules introduce images to CellProfiler in the appropriate format, enabling further analysis. The *ColorToGray* module was used because the image analysis was being performed on radiographic images with features based on grayscale contrast differences. The *ImageMath* module consisted of a variety of image process operations, such as addition, subtraction, and averaging. For the chosen pipeline, the *ImageMath* module was utilized to invert the grayscale levels of the DR image, making the voids stand out as white spots on a black background. One of the most critical steps in image analysis is illumination correction. Illumination can vary by more than 150% across the field of view, which adds an unacceptable level of noise to the image that obscures real quantitative differences [163]. Next, the *Morph* module performed a series of low level alterations to the images based on selected operations. The voids were further accentuated by using the

Dilate operation. This operation scans the image and replaces pixel color with the maximum pixel level of the adjacent pixels, making the outlines of the voids more defined. Conversely, the *Erode* operation, which replaces pixel color with the minimum level of the adjacent pixels, would effectively shrink the voids and make them harder to detect.


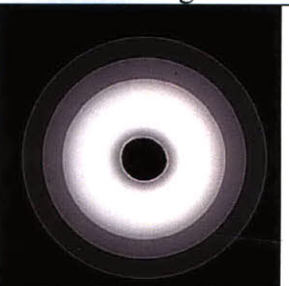


The *Smooth* module (also known as *SmoothOrEnhance* in Version 1 of CellProfiler), “smooths out” the image by reducing noise and artifacts. In order for CellProfiler to distinguish between actual defects and noise, the filter type and parameters must be adjusted accordingly. For the radiographic wedding cake images a median filter was applied, which removed features that were smaller than a specified pixel diameter. The void pixel diameter was determined by the void geometry and picture resolution, and was measured in CellProfiler in the previous step. If the filter size was too small the smooth filter could not “clean up” the image, but if the filter size was too high CellProfiler blurred out the voids. In the next step, *ImageMath* was used again, but this time for an absolute difference measurement between the images from the *Morph* and *Smooth* steps. The order of operations in the pipeline can be performed in a number of permutations, either individually or in succession, resulting in slightly different output. This is because the pipeline builds off the filters used in previous modules. For this pipeline, the *Morph* and *Smooth* steps were applied to the same original image, yielding one with accentuated voids (from *Morph*) and another with minimal noise (from *Smooth*). Taking the difference of these two pictures resulted in an image with accentuated voids and reduced artifacts. In this manner a pipeline was created that would enable optimized flaw detection.


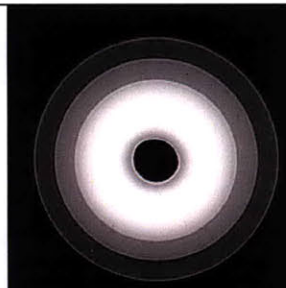

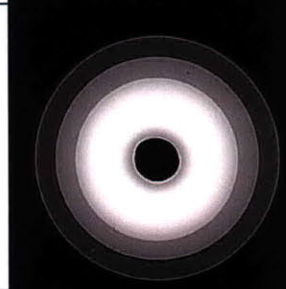
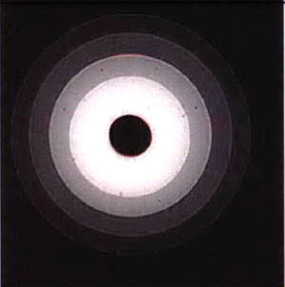
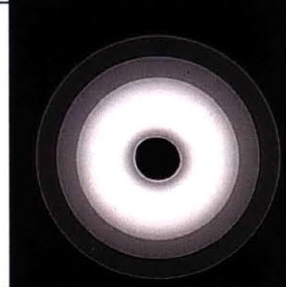


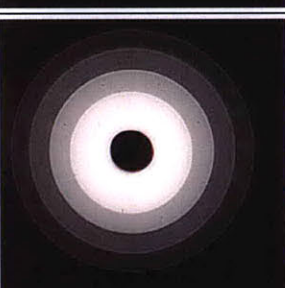
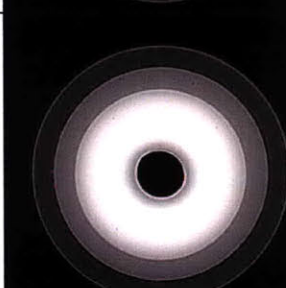
For the ideal situation where image quality is high, noise is minimal, and material geometry is simple, CellProfiler is a viable tool for automatically filtering images and detecting flaws on and within material surfaces. However, even when the images are not ideal, as was the case with the varying noise from the different wedding cake levels and center hole region of the sample, CellProfiler is still highly useful for preparing the images for human hit/miss inspection. The center hole of the wedding cake increased the contribution from x-ray scattering. This added a level of complexity to the selection of filters for the image analysis. The results from the Cellprofiler image analysis are

discussed in the following section. Prior to the analysis on the radiographic wedding cake images, the traditional C-scan ultrasonic data contained in Appendix D was imported into Cellprofiler to practice optimizing the threshold correction factor for both color and grayscale images. However, the results were not relevant to the POD analysis because only the single #1FBH defect size was contained on the Rene 88 and Ti-alloy blocks.

5.2 Image Analysis Results

The image analysis comparison shown in Figure 5.2 (which spans multiple pages) is for the aluminum and steel wedding cake sample exposures taken with the 2D digital radiographic technique at the Baker Testing Services Inc. facility. Threshold correction factors between 0.0 and 8.0 were applied to both images and the CDR and EDR were calculated. Flaw indications appear as red dots on the DR images. The optimized threshold correction factors were determined to be 5.0 for the aluminum sample and 2.0 for the steel wedding cake without the embedded defect. A number of false detections due to burrs at edges of the two wedding cake samples were observed. Figure 5.3(a-b) provides the statistics on the EDR and CDR for the specimens. The aluminum wedding cake is representative of a light metal, while steel was chosen to represent the heavy metal class.

		Aluminum Wedding Cake	Steel Wedding Cake
Threshold correction factor	0.0		
	1.0		

Threshold correction factor	2.0		
	3.0		
	4.0		
	5.0		
	6.0		

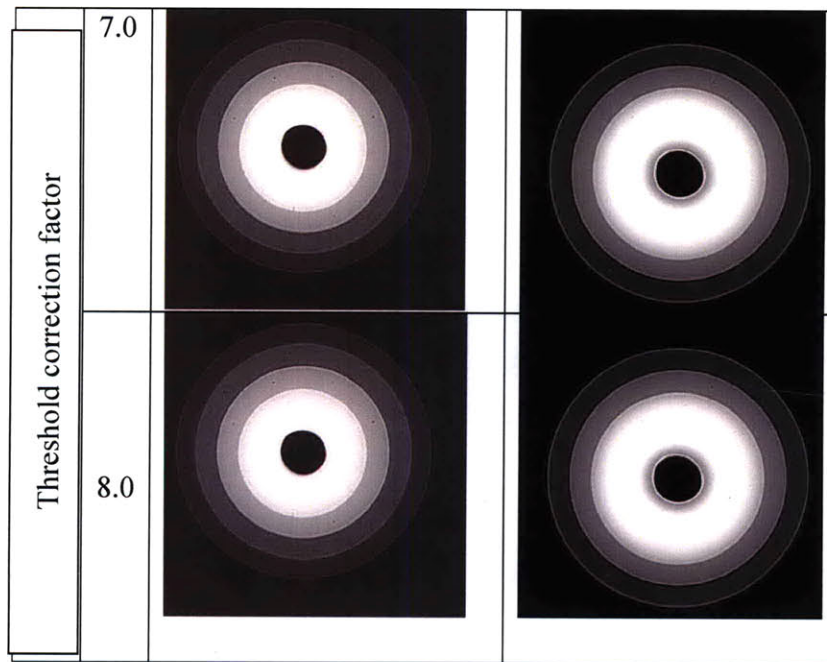


Figure 5.2: Threshold correction factors of 0-8 applied to DR wedding cake images. Aluminum sample on left and Steel sample on right.

It can be seen in Figure 5.2 that the aluminum DR wedding cake image had better depth resolution than the image for the steel sample. Some of the SDH in Levels 4 and 5 are observed in the aluminum sample but not in the steel sample. This is a direct result of the density difference between the two materials, which resulted in a greater depth of penetration and less scattering in the aluminum sample. Figure 5.3(a) shows that at a threshold level of 4.0, the CDR is greatest for the aluminum sample. However, the number of false positives is also the greatest at that same threshold correction value. The left vertical scale is for the CDR percentage, while the right vertical scale is for the EDR percentage. The relatively low number of potential FBH indications explains why the EDR scale is significantly greater than 100 percent. Penumbra from the DR images is a factor in the high EDR percentages that were observed. Since a single digital radiographic exposure was used to image all five levels of the samples, Level 3 was selected as the location to focus the image. Therefore the layers above and below Level 3 are slightly out of focus. The compression of the three dimensional sample onto a 2D image plate resulted in shadow images. The added noise from the shadow images, in addition to the observed penumbra (image “unsharpness”), resulted in numerous false

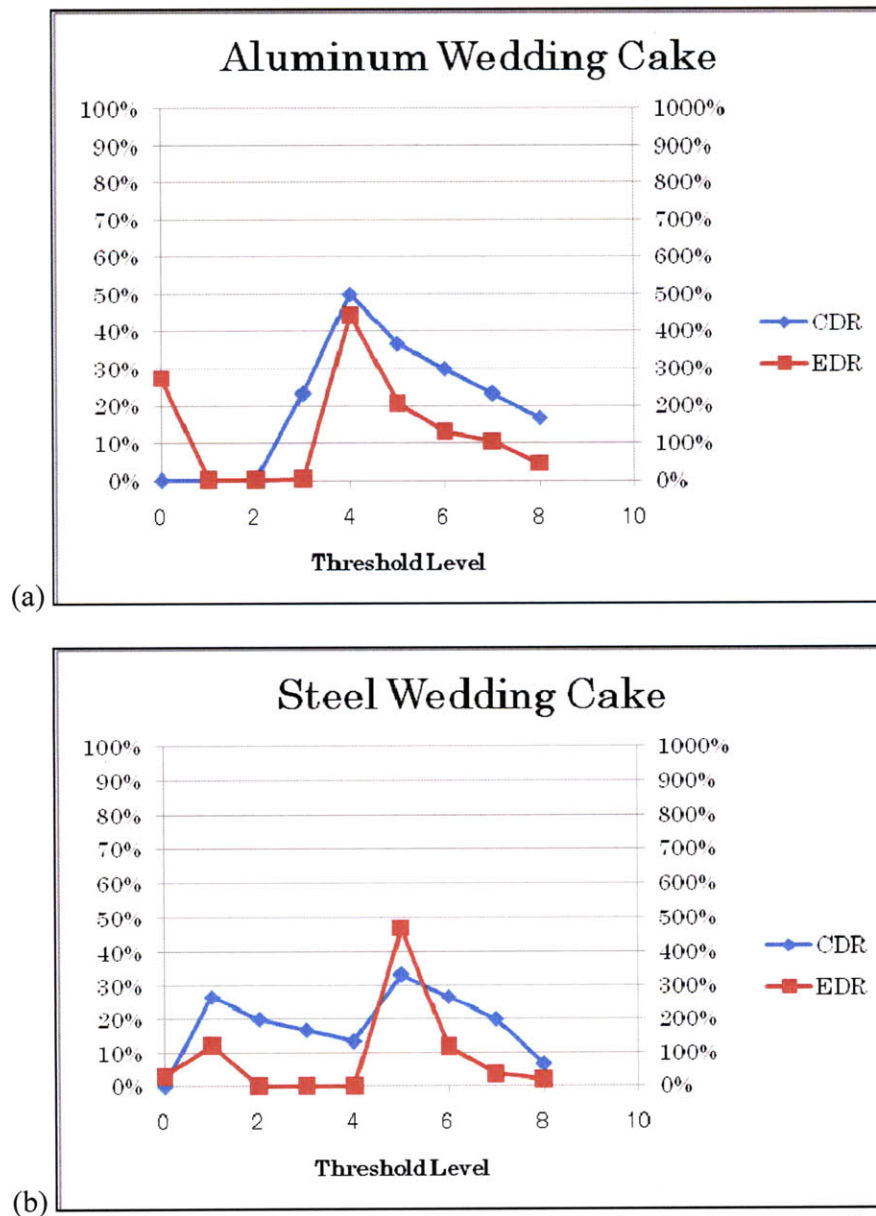


Figure 5.3: CDR and EDR plotted as a function of threshold correction factor for (a) Al wedding cake and (b) Steel wedding cake

positive indications. Most of the false positive indications were observed at the edges of the inexactly focused levels, especially at the higher threshold correction factors.

Figures 5.4-5.6 show the progression of steps in the Cellprofiler analysis for a 2D image slice from the 3D-CT inspection of the aluminum wedding cake sample at the

selected Level 5 height/depth. Figure 5.4 displays the original grayscale image before any modules or filters were applied. Figure 5.5 shows the effect of the *Morph* and *Smooth* filters, as well as the output after the *ImageMath* pipeline module is re-applied to accentuate the voids and reduce the artifacts for the six SDH at the Level 5 surface interface. Figure 5.6 shows the Cellprofiler output of the image after going through the selected pipeline. A considerable amount of image noise can still be seen in Figure 5.6 despite the efforts to minimize the noise and maximize the S/N response ratio.

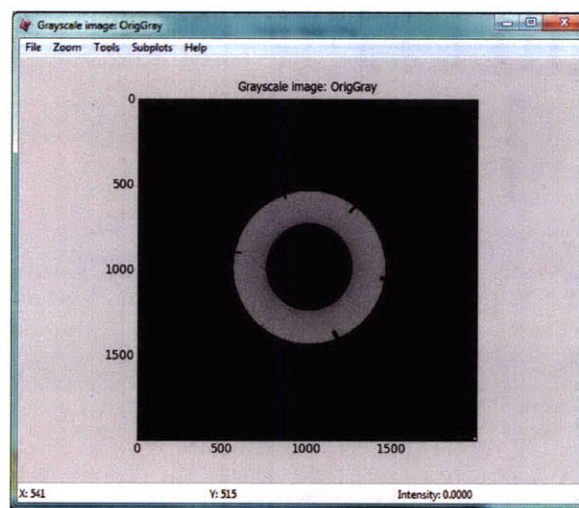


Figure 5.4: Original 2D projection from Level 5 for the 3D-CT inspection of the aluminum wedding cake sample processed in Cellprofiler

An attempt was made to program CellProfiler to automatically detect the SDH for this particular image. Based on the digital output of Figure 5.6, it was determined that automatic detection of the SDH defects failed in this case. There was an unacceptable level of noise in the solid center area where the wedding cake was bored out that resulted in decreased dynamic range (and thus discrimination) between the grayscale levels of the Level 5 surface. Unlike the flat bottom holes, the SDH geometry at this specified depth was not a void per se (as Cellprofiler determined it to be), but rather a geometrical feature particular to this individual 2D slice. As a result, CellProfiler identified the outline of the SDH, but did not identify it correctly because it was not an enclosed cellular shape. This

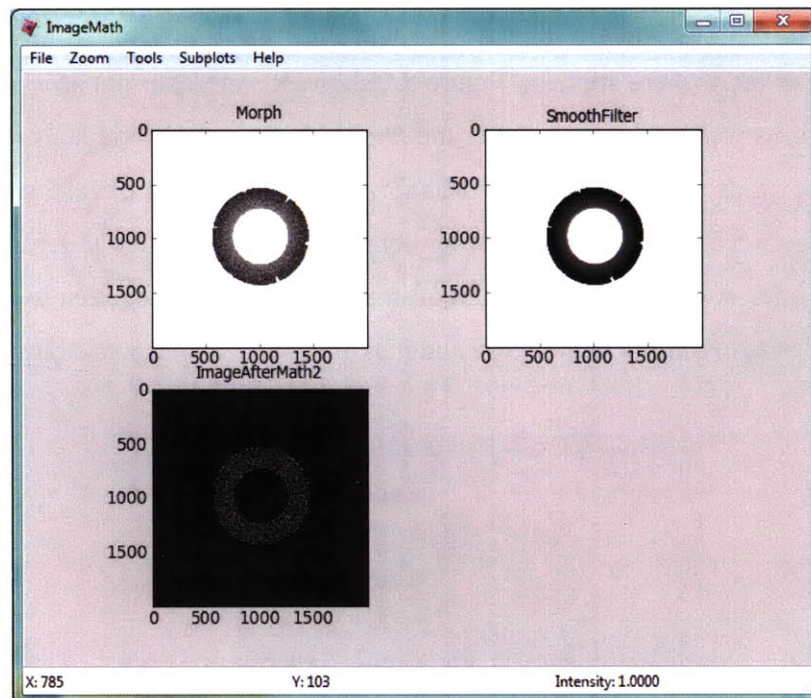


Figure 5.5: Images after various pipeline filters were applied

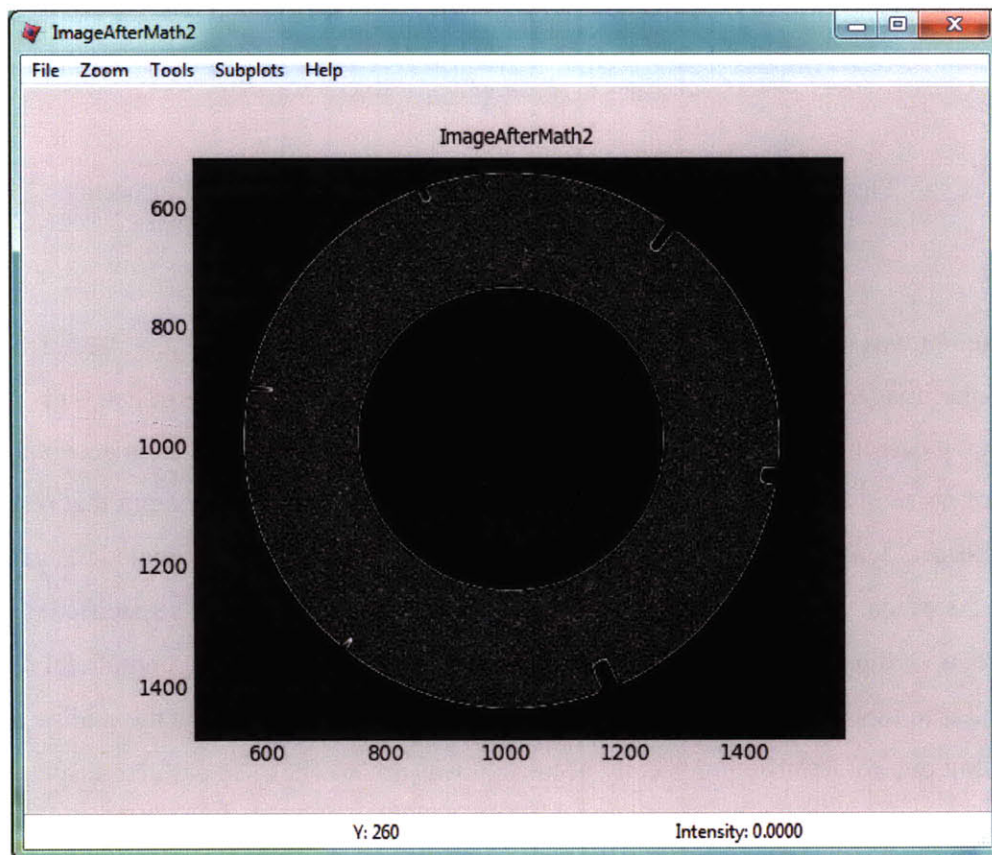


Figure 5.6: Close-up of processed image

resulted in an unacceptable level of missed flaw detections. Cellprofiler would need to be modified to better deal with the morphological aspects of complexly designed forgings if it were to be implemented in an industrial setting.

The same problems with noise also existed in the 2D slices of the 3D-CT aluminum wedding cake inspection images at the Level 4 and Level 3 sample depths. A positive result observed from the use of the Cellprofiler pipeline and filters was that the flat bottom holes at the Level 3 depth were much more detectable than they originally were. As shown in Figures 5.7 and 5.8 below, all of the 6 SDH from Level 4 and all eight of the FBH from Level 3 are distinguishable. The diameters of the detected FBH defects ranged from 0.28mm (0.011in.) to 1.27mm (0.050in.) for Level 3. This is significantly smaller than the 0.76mm (0.030in.) detectable flaw size specified in FAA documents as the starting flaw size for fracture mechanics calculations. Noise, in the form of ring artifacts from the inspection, unfortunately could not be removed completely from the image analysis. However, as Figure 5.9 shows, the deleterious effect from the ring artifacts on inspection sensitivity is much more pronounced in the original inspection data slice. The conclusion drawn from this observation was that an image analysis program is only as good as the resulting NDT inspection data uploaded into it. Therefore, it follows that the most significant improvement to both POD and minimum detectable flaw size from an image analysis requires the use of the correct NDT technique that initially will provide the highest quality inspection images with the least artifacts and noise. For this particular example, Cellprofiler was able to lower the overall image noise contribution to the subjective decision-making process by approximately a factor of two. In this regard, the general capability of image analysis programs to improve POD was demonstrated. Section 5.3 includes additional analysis into quantifying and incorporating the benefits from automated image analysis into an NDE/NDI program.

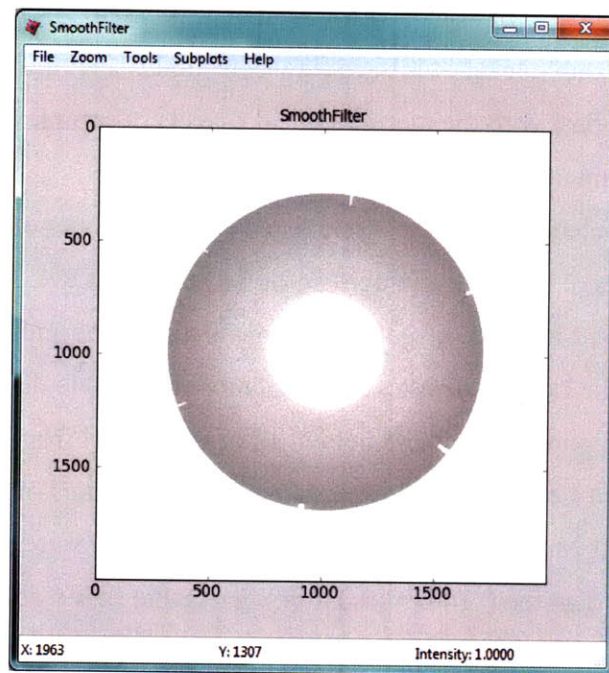


Figure 5.7: Level 4 Cellprofiler analysis of 3D-CT slice

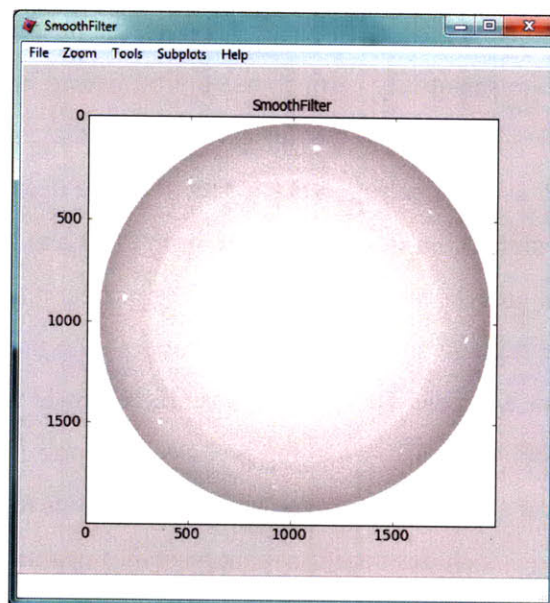


Figure 5.8: Level 3 Cellprofiler analysis can distinguish FBH in 3D-CT slice.

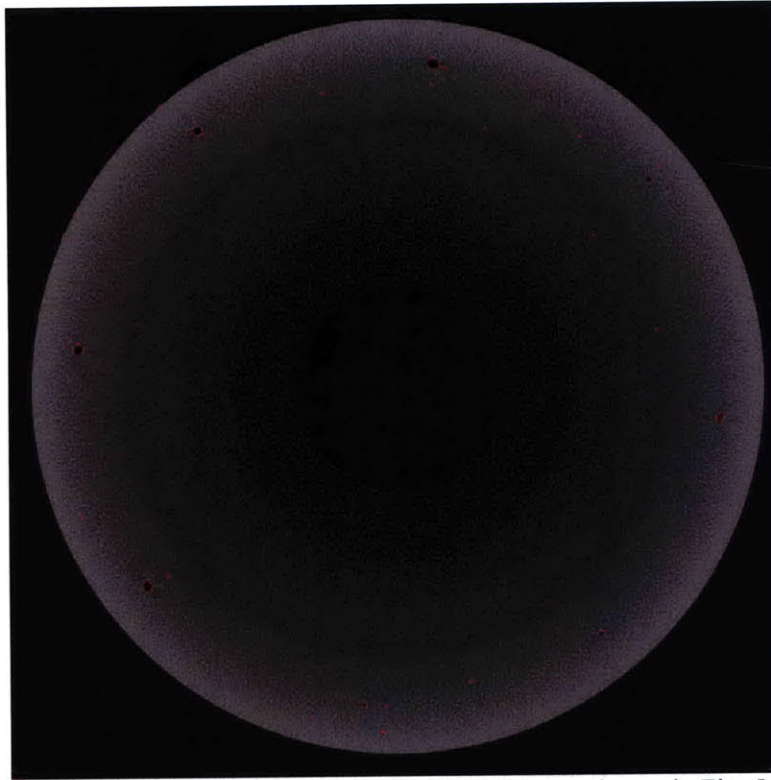


Figure 5.9: The same 2D projection image from the 3D-CT inspection as in Fig. 5.8. A threshold correction factor of 1.0 has been applied, but no additional pipeline or filters were selected for this image. Compare the ring artifacts and general noise in this slice with Fig 5.8

5.3 POD Model

Based on the Cellprofiler results from the aluminum wedding cake slices in Section 5.2, an analysis into the effect on POD from inspecting images at multiple threshold correction factors versus at a single threshold correction value was attempted. The Level 3 slice shown in Figure 5.8 and Figure 5.9 was used in the analysis. Threshold correction factors of 1.3, 2.0, 3.0, and 4.0 were applied to the image shown in Figure 5.9 in a manner similar to that described for the 2D-DR wedding cake images in Figure 5.2. The POD software used was freely available, and was the same software used to generate the POD curves in the MH-1823 [201] document. Figure 5.10(a) shows the POD curve at a single threshold value of 1.3, while Figure 5.10(b) shows a combined POD curve that incorporated the three threshold correction factors with the best ratio of CDR to EDR. It is seen that the POD curve is both steeper and slightly shifted to the left for the combined threshold curve. This is a better representation of the idealistic POD curve shown in Figure 5.11. In contrast, Figure 5.10(a) has a more realistic S-shape to its POD curve.

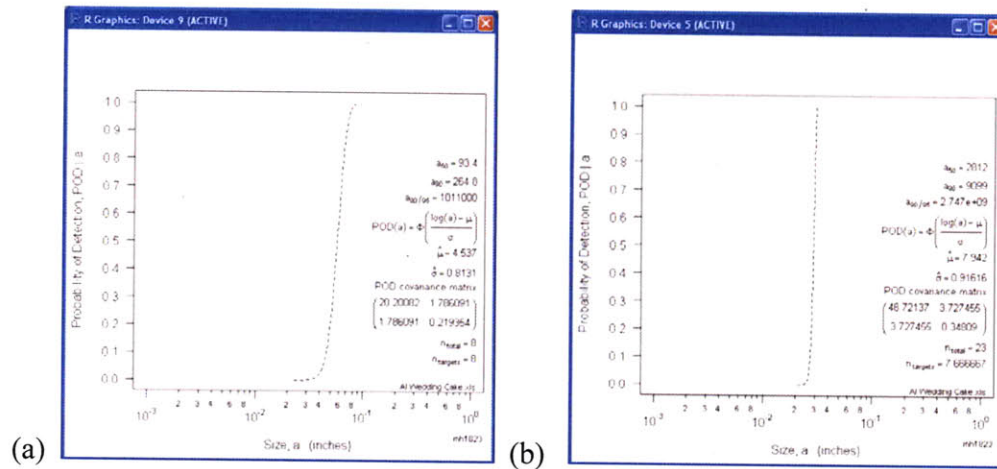


Figure 5.10: (a) POD curve for data at single threshold correction factor (b) POD curve from three combined threshold factors

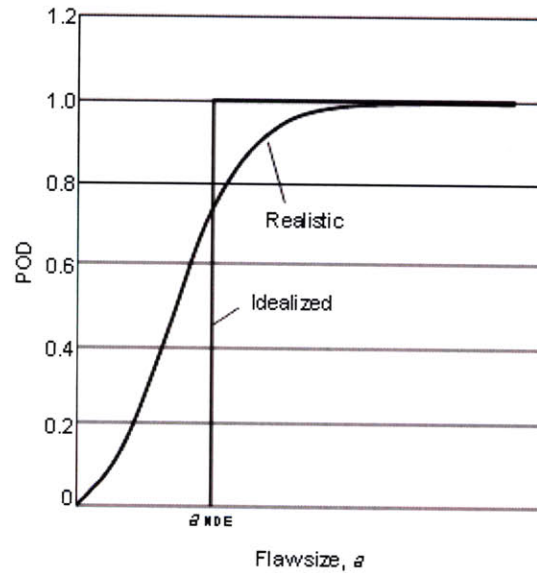


Figure 5.11: Realistic vs. Idealized POD curve.

In general, a POD curve is based on a regression equation, and provides the basis for testing assumptions about the applicability of various $POD(a)$ function models. Many different functional forms were available to calculate the POD curves described in this section from, but it has been determined that the log-logistics (also known as the log-odds) model best represents hit/miss data [202]. For the data used in the generated POD curves, hit/miss data was used. However, since information on location was known as well, a correlation to a vs. \hat{a} data was also made. Equations (5.1) and (5.2) are two

mathematically equivalent forms used to represent the log odds model. In (5.1) and (5.2), the variables α and β are known as the maximum likelihood parameters. The log odds

$$\text{POD}(a) = \frac{\exp(\alpha + \beta \ln a)}{1 + \exp(\alpha + \beta \ln a)} \quad (5.1)$$

$$\ln \left[\frac{\text{POD}(a)}{1 - \text{POD}(a)} \right] = \alpha + \beta \ln(a) \quad (5.2)$$

model is especially applicable to the analyses described in this section, because a regression analysis can be applied to the maximum likelihood parameters which results in equivalence for both large sample sizes and much smaller sample sizes. This is significant since only a limited number of data points were available in the generated POD curves because of both the sample design and size limitations of the CT equipment used. The log odds model got its name based on the left side of the equation in (5.2), and it is practically equivalent to a cumulative log normal distribution.

The parameters α and β in the above equations are not easily interpretable in physical terms. In order to gain a better physical representation, a mathematically equivalent form of the log odds models is given in Equation (5.3).

$$\text{POD}(a) = \left\{ 1 + \exp - \left[\frac{\pi}{\sqrt{3}} \left(\frac{\ln a - \mu}{\sigma} \right) \right] \right\}^{-1} \quad (5.3)$$

In the form of the POD model described by the above equation, the parameter μ is equal to $\ln a_{0.5}$ (where $a_{0.5}$ = the flaw size that is detected 50% of the time, aka the median detectable crack size) and σ is the standard deviation. The parameters in (5.1) and (5.3) are related by:

$$\mu = \frac{-\alpha}{\beta} \quad (5.4)$$

$$\sigma = \frac{\pi}{(\beta\sqrt{3})} \quad (5.5)$$

The parameters defined in (5.4) and (5.5) appear in the POD curves shown in Figure 5.10 and are significant. The steepness of the $\text{POD}(a)$ function is inversely proportional to the parameter σ defined in (5.5). Therefore, the smaller the value of σ , the steeper the curve. The goal of NDT inspection is to obtain the steepest POD curve at

the smallest possible flaw size. However, as the values included in Figure 5.10(a-b) show, there was an error made when calculating these POD curves. This initial analysis cannot be considered an “apples-to-apples” comparison, because the data for the combined threshold curve was not normalized on a 0-1 scale. The values generated for the 90/95 POD/CL and likelihood parameters shown in Figure 5.10 therefore have no significance. This error in the analysis also explains why the value for σ is larger instead of smaller for the steeper POD curve in Fig. 5.10(b). Despite this error, the benefit of increasing the number of data points in the POD analysis can be deduced from Figure 5.10(a-b). The greater the value of n_{total} , the tighter the curve fit. This allows both a more accurate and more reliable determination of POD, because there is inherent error in POD curves associated simply by the finite number of potential data points. Unfortunately the size limitation of the CT system only enabled one FBH-containing layer of the sample to be imaged. Because of the lack of statistically significant data points for the 3D-CT inspection slices, the DR aluminum wedding cake image was used in the POD comparison with the traditional film x-ray image.

Traditional x-ray film and digital radiographic images for the aluminum wedding cake sample were compared via integration of Cellprofiler analysis with POD software. The objective was to remove, as much as possible, the sources of variability inherent to each individual NDT technique and to develop a POD curve based on an “apples to apples” comparison from the signal response of the curves. Figure 5.12(a-b) shows the two images used in the comparison. Notice that the digital x-ray was able to pick up the FBH on Level 1, the thinnest layer of the sample. The traditional x-ray film technique was not able to distinguish Level 1. Most likely, the specimen was oriented in the “top-down” position for the inspection. In this orientation, Level 1 is the bottom layer at the base of the sample approximately 8.9 centimeters (3.5 inches) away from the Level 5 surface. The larger focal spot size of the traditional radiographic technique increased the overall image unsharpness, making it especially hard to distinguish the bottom layer with the traditional film exposure. This resulted in the availability of only two levels of the aluminum wedding cake for the traditional POD curve, while the POD curve generated with the DR image had three levels. The CellProfiler Pipeline applied to convert the

image was as follows: *LoadImages*; *ImageMath* – inverted the original image so the voids became white spots on white background; *Morph* – performed dilation on holes,

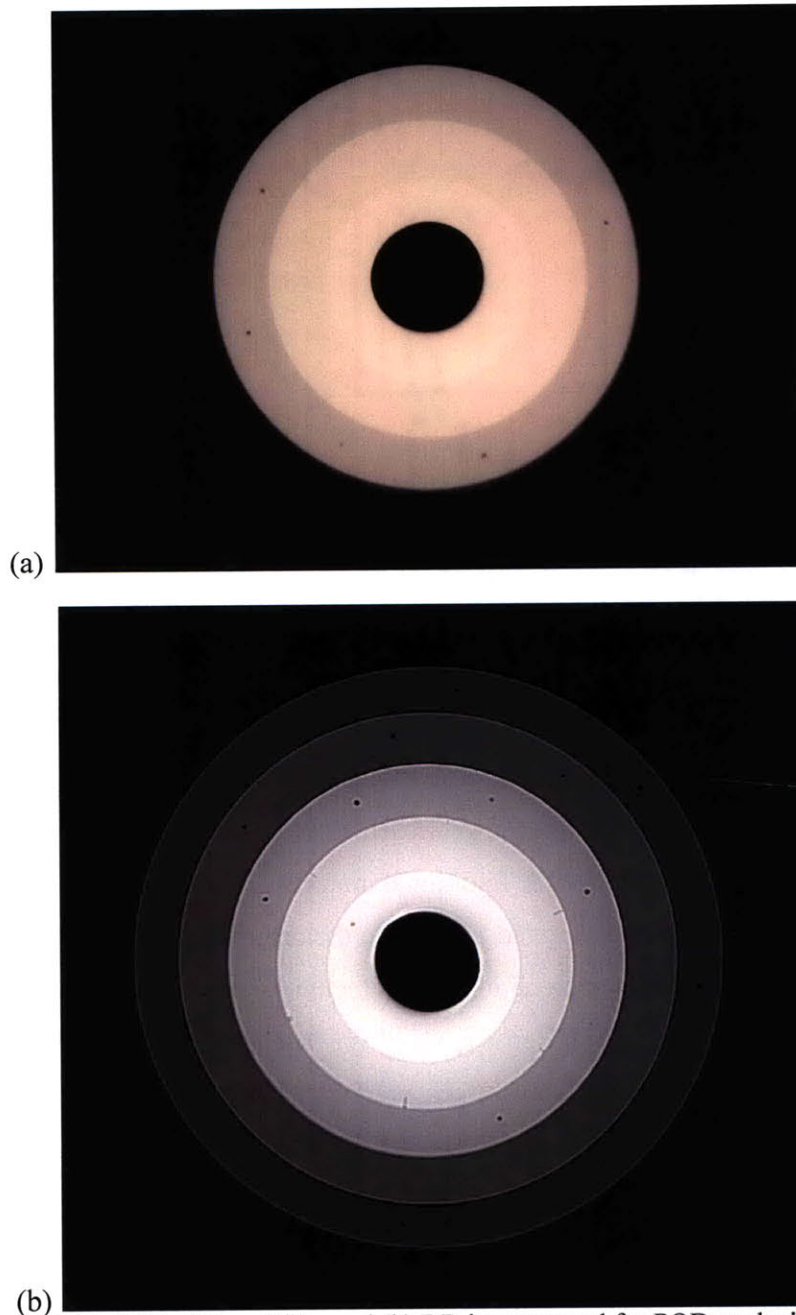


Figure 5.12: (a) Traditional film and (b) DR images used for POD analysis

replacing surrounding grey pixels with white, effectively making the holes more defined; *Smooth* – filters to remove noise; *CorrectIlluminationApply* – illuminated the morphed

image using a mask of the smooth filter. Figure 5.13 shows the DR image after the inversion and filter pipeline processes.

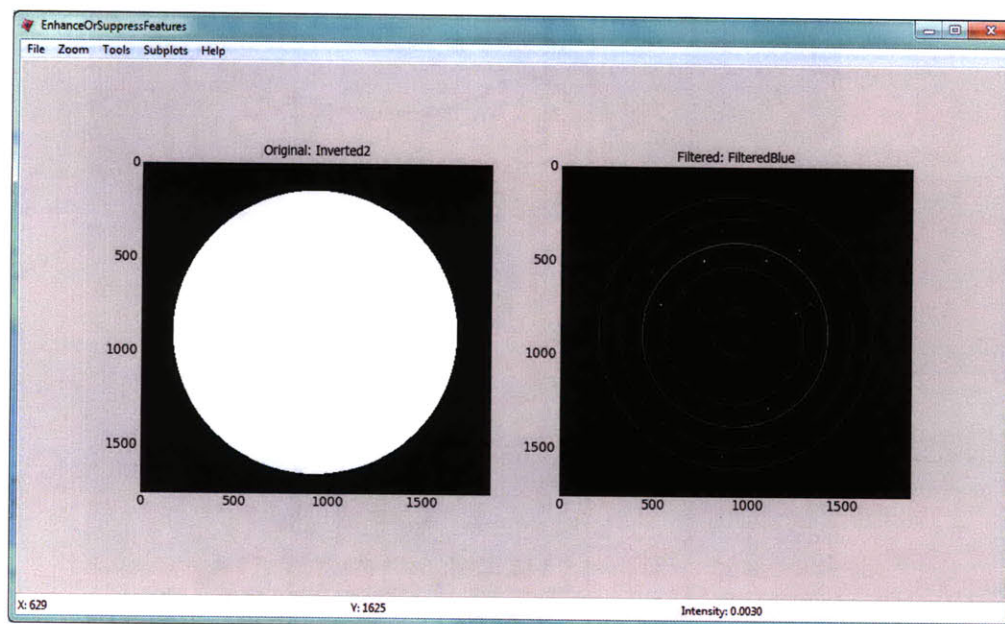


Figure 5.13: 2D-DR image after the inversion and filtering pipeline processes

The resulting images were all black with light colors for the well defined features, as shown in Figure 5.14(a-b) below. The filters purpose was to extract the defects into plain view (and resultantly make the geometric effects visible). Although the FBH indications appear brighter for the traditional image in Fig. 5.14(b), Cellprofiler enables various color schemes to be applied to assist in the determination of the hit/miss data. Figure 5.15 shows how such an option makes technician determination easier.

In order to perform a hit/miss analysis for POD software, the holes on the x-rays needed to be aligned with the known measured sizes of the holes. A spreadsheet was then compiled with two columns, the first being the known hole size, and the second the corresponding hit/miss data for that detection method. Figure 5.16 is the POD curve generated for the traditional film method and Figure 5.17 is the POD curve generated for the digital method. The analysis for both POD curves was performed at the same specified sample depth. It was concluded that the POD for the digital radiographic NDT technique has a significantly smaller detectable flaw size at the 90/95 POD/CL level than the traditional film method. An approximate factor of three reduction in threshold flaw sized was obtained by incorporating the image analysis software. The use of the

Cellprofiler automated image analysis software removed inspection process variability and enabled a comparison on the output signal response alone.

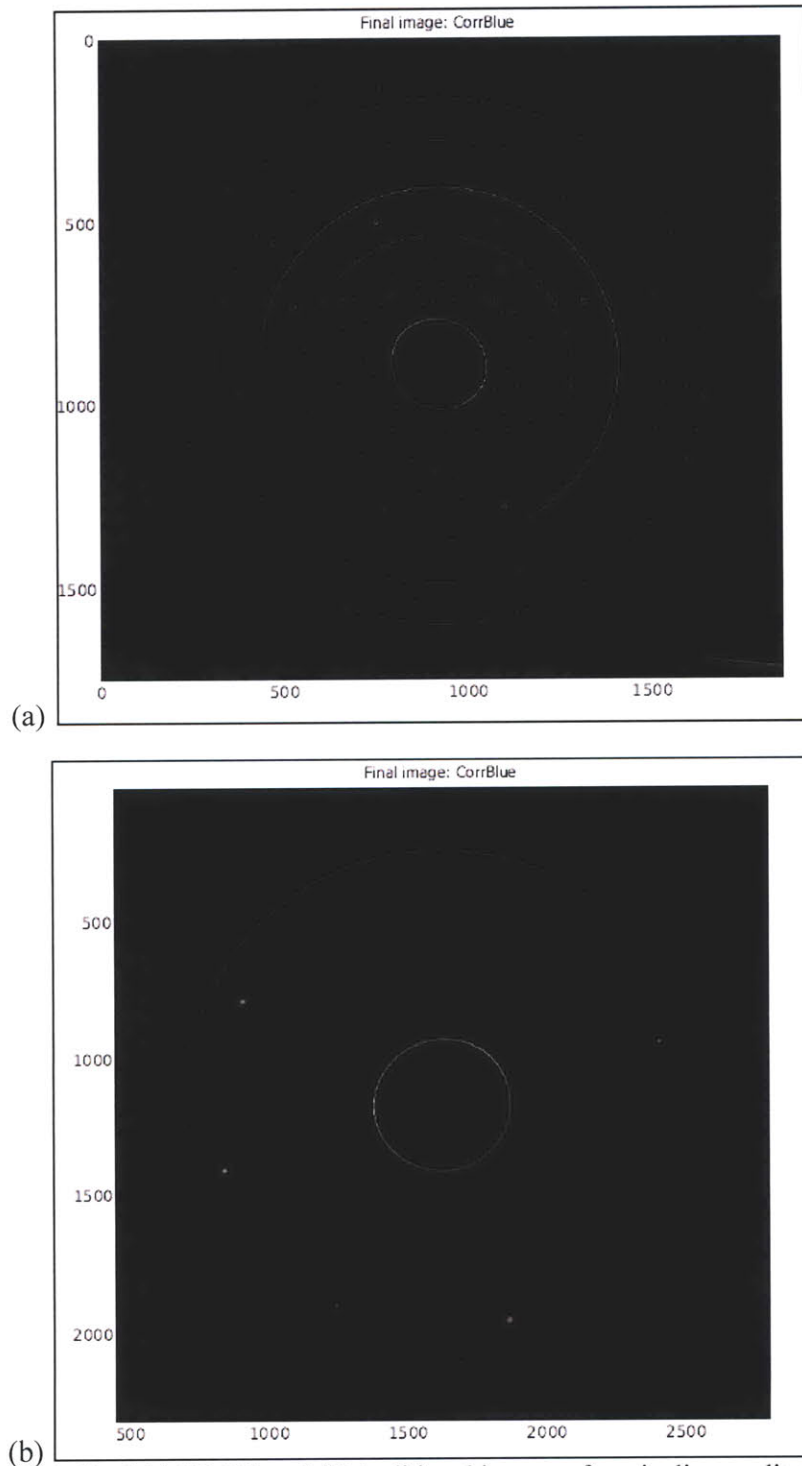


Figure 5.14: Final (a) 2D-DR and (b) traditional images after pipeline application

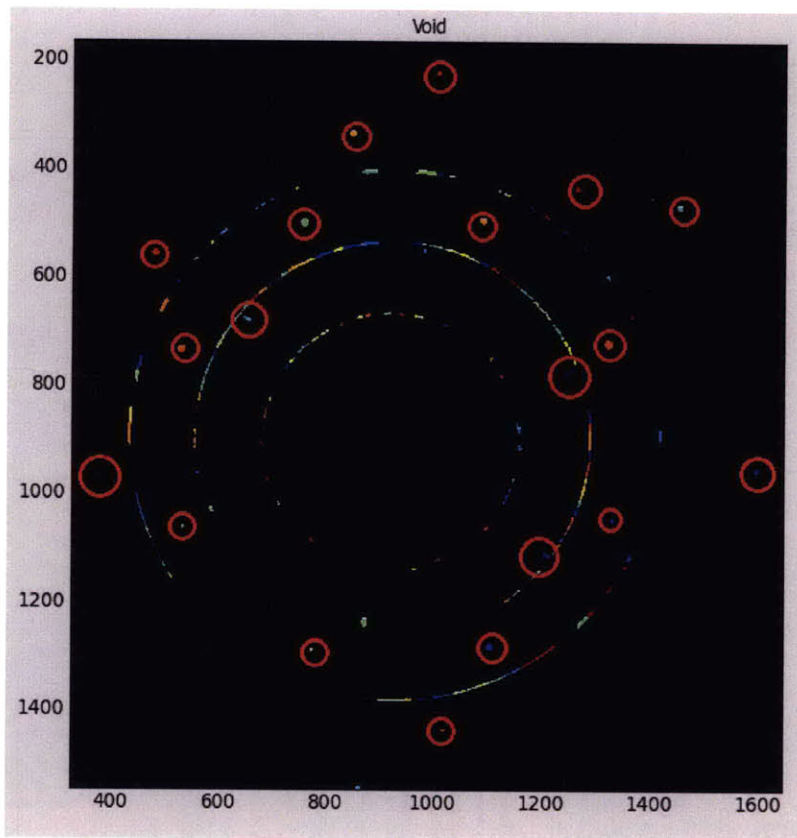


Figure 5.15: Use of color scheme option in Cellprofiler to assist in hit/miss determination

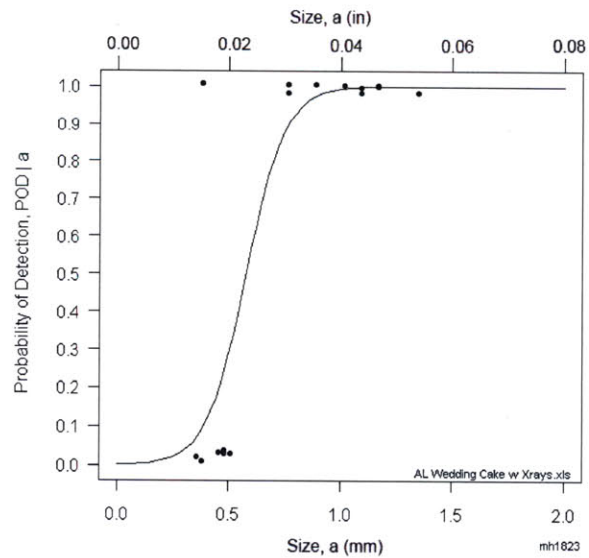


Figure 5.16: POD curve for traditional x-ray film radiography

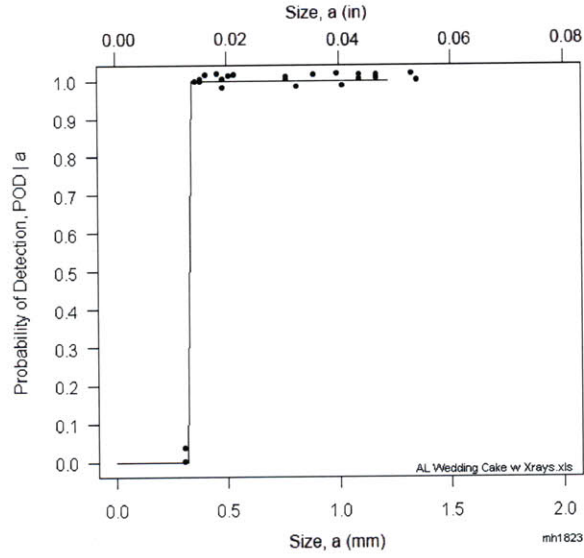


Figure 5.17: POD curve generated for Digital Radiographic technique

The parameters in (5.4) and (5.5) can be adapted for various POD curve distribution functions. The POD software allows eight potential POD vs. a models to be generated, as shown in Figure 5.18. For a vs. a -hat analyses, the following equations are utilized:

$$\hat{a} = \mu(a) + \delta \quad (5.6)$$

$$\ln(\hat{a}) = \beta_0 + \beta_1 \ln(a) + \delta \quad (5.7)$$

where $\mu(a)$ is the mean of the $g_a(\hat{a})$ function and δ is a random error term accounting for the differences between \hat{a} and $\mu(a)$. The use of normally distributed deviations for the $\ln(\hat{a})$ and δ terms in (5.6) and (5.7) has proved to be an acceptable assumption for these types of analyses [202], although this assumption would need to be verified for application of integrated Cellprofiler/POD analyses in industrial OEM or MRO environments. If the assumption proves valid, the POD function is calculated from (5.8)-(5.10):

$$\text{POD}(a) = \text{Probability} [\hat{a} > \hat{a}_{dec}] \quad (5.8)$$

$$\text{POD}(a) = \text{Probability} [\ln(\hat{a}) > \ln(\hat{a}_{dec})] \quad (5.9)$$

$$\text{POD}(a) = 1 - \Phi \left[\frac{\ln(\hat{a}_{dec}) - \beta_0 + \beta_1 \ln(a)}{\sigma_\delta} \right] \quad (5.10)$$

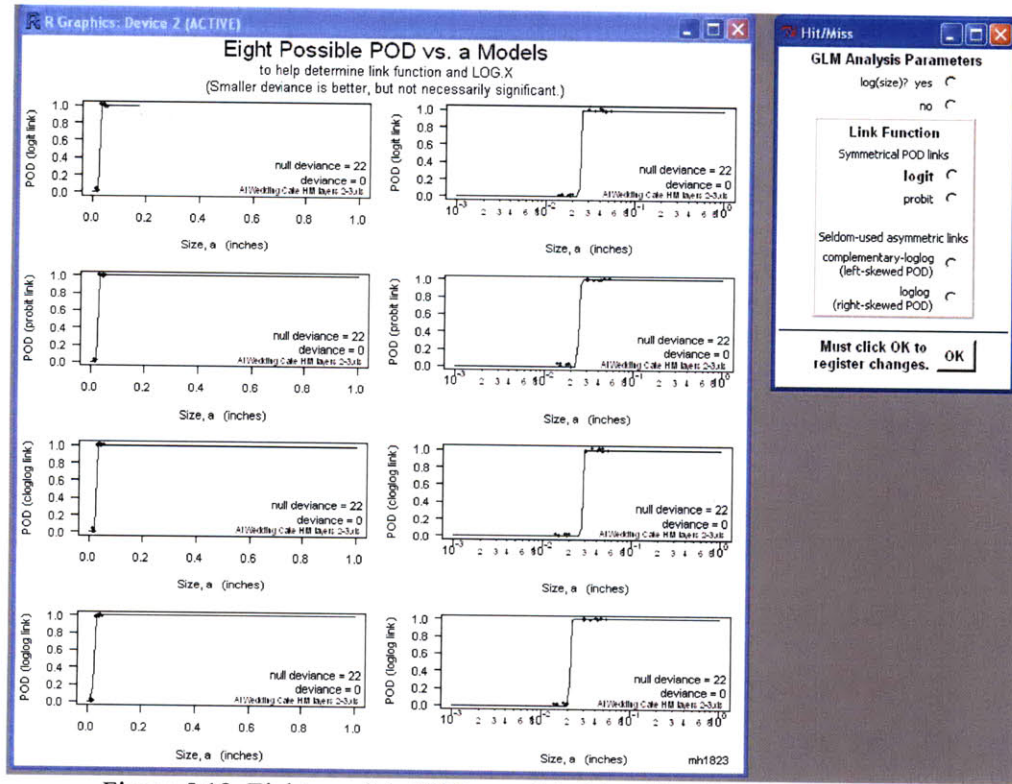


Figure 5.18: Eight possible POD vs. a Models offered in POD software

In (5.10), Φ represents the standard normal deviation function. Equation (5.10) can be reduced to a cumulative log normal distribution function that takes the following form:

$$\text{POD}(a) = \Phi \left\{ \frac{\ln(a) - [\ln(\hat{a}_{dec}) - \beta_0] / \beta_1}{\sigma_\delta / \beta_1} \right\} \quad (5.11)$$

The mean and standard deviation values of log flaw length for (5.11) are calculated by:

$$\mu = \frac{\ln(\hat{a}_{dec}) - \beta_0}{\beta_1} \quad (5.12)$$

$$\sigma = \frac{\sigma_\delta}{\beta_1} \quad (5.13)$$

The equations discussed above can be used to generate confidence bounds on the calculated POD curves. Figure 5.19 is the POD curve for the traditional x-ray technique shown in Fig. 5.16, but with confidence bounds and statistical data included. For the traditional radiographic NDT technique, the $a_{90/95}$ value was determined to be 1.246mm (0.050in.). This value was affected by the sample design and number of inspection opportunities, and future work into developing new wedding cake samples with wider

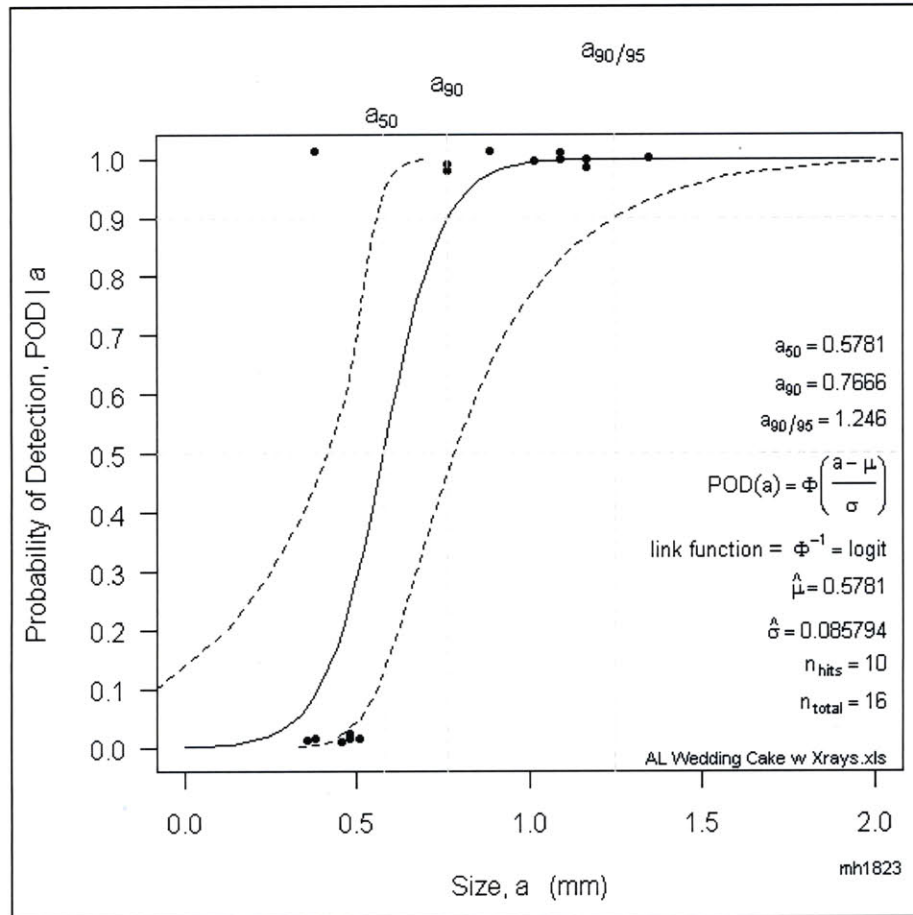


Figure 5.19: POD curve from Fig. 5.16 with confidence bounds and statistical analysis included

flaw ranges could significantly alter this value. However, for the samples used in this analysis, the use of digital NDT technology enabled a factor of two improvement in the minimal threshold $a_{90/95}$ value. This is based on the data in Figure 5.17. To validate this conclusion, future tests need to be performed to significantly increase the data sets of the inspection results for the various NDT techniques that were used to generate the curves.

Chapter 6: Advanced NDT Methodology

The advanced NDT methodology that is proposed in this chapter enables a retirement-for-cause remnant life management approach to be used to extend the useful service lives for structural components. The main aspects of the proposed methodology include the application of a Bayesian updating technique to POD inspection data, and redundancy in the selection of NDT methods with overlapping flaw detection capabilities. As Chapter 5 described, the ability to integrate an automated image analysis process as an additional aspect of the methodology can further improve sensitivity as well as reduce inspection variability. In this way a robust inspection plan for in-service inspection of structural components is described. Sections 6.2 and 6.3 provide an analysis of the methodology applied to disk and blade turbine engine components. A cost-benefit analysis of the approach is included in Section 6.4, and obstacles to implementation of the proposed approach are outlined in Section 6.5.

6.1 Statistical Approach to Quantifying Variables

Bayes' theorem is a formula used to calculate posterior probabilities based on prior probabilities and the likelihood ratios that a given event will occur. Bayes' theorem is given by the following formula:

$$P\left(\frac{E}{O}\right) = \frac{P(E) \cdot P\left(\frac{O}{E}\right)}{P(O)} \quad (6.1)$$

In Equation (6.1), $P(E)$ is the prior probability of Event E , $P(E/O)$ is the posterior probability of $P(E)$ after observation O is made, $P(O/E)$ is the conditional probability that O is associated with E , and $P(O)$ is the probability of observation O . The conditional probability term can also be thought of as the likelihood of the evidence from an inspection. Additionally, the term $P(\bar{E})$ is read as $P(E \text{ does not occur})$. From the requirement that the total probability of the sample space, which is the set of all possible outcomes of an experiment, total 1.0 the relation in (6.2) is obtained. An equivalent form of Bayes' theorem is given by Equation (6.3).

$$P(E) + P(\bar{E}) = 1.0 \quad (6.2)$$

$$P(E) = \left[P\left(\frac{E}{O}\right) \cdot P(O) + P\left(\frac{E}{\bar{O}}\right) \cdot P(\bar{O}) \right] \quad (6.3)$$

Likelihood ratios, denoted by LR, are continually updated as more evidence is obtained. Equation (6.4) contains the formula used to calculate the likelihood ratio, and (6.5) gives the probability of an event in terms of these likelihood ratios.

$$LR = \frac{P(E)}{P(\bar{E})} \quad (6.4)$$

$$P(E) = \frac{LR}{1 + LR} \quad (6.5)$$

The use of Bayesian updating is a fundamental aspect of the proposed methodology, because Bayes' theorem allows for continuous updating of a structural component's remnant life based on posterior probabilities generated from the information gained in successive inspections. Equations (6.6) and (6.7) provide the form of Bayes' used for continually updating posterior probabilities for in-service inspection.

$$LR_k = LR \quad (\text{after } k \text{ inspections [i.e. observations]}) \quad (6.6)$$

$$P\left(\frac{E_k}{O}\right) = \frac{P(E_k) \cdot P\left(\frac{O}{E_k}\right)}{\sum_1^N P(E_k) \cdot P\left(\frac{O}{E_k}\right)} \quad (6.7)$$

In (6.7), N is the total number of inspections and k is the number of inspections for which event E has been observed. It is precisely in this Bayesian form given by (6.7) that the integration of multiple NDT techniques in a redundant manner has the greatest impact. Table 6.1 includes the relevant probabilities to the statistical analysis that will be discussed in the proposed methodology.

Table 6.1: Relevant probabilities to statistical analysis

p_a	=	probability of detecting a flaw of size a
$p_{(\text{surf})}$	=	probability of surface flaw
$p_{(\text{near-surf})}$	=	probability of near surface flaw
$p_{(\text{sub-surf})}$	=	probability of subsurface flaw
p_{MWM}	=	probability of detection with MWM test method
$p_{\text{PA-UT}}$	=	probability of detection with phased array UT test method
$p_{\text{3D-CT}}$	=	probability of detection with 3D CT test method
$p_{\text{2D-DR}}$	=	probability of detection with digital x-ray test method

From Table 6.1, it can be seen that flaw detection probabilities for the MWM-array ®, PA-UT (both automated and semi-automated/manual), 3D-CT, and 2D-DR nondestructive evaluation techniques analyzed in Chapters 2-4 are required for the statistical analysis. Additionally, the probabilities of the three location depths, also referred to as *zones*, for which a potential anomaly could be present in the structural component under inspection are required for the analysis. The entire structural component volume, V , is defined by the summation of the volumes of the surface, near-surface, and subsurface zones. In order for an RFC-type approach to be implemented, a comprehensive inspection over 100% of the component's volume must be performed. Because there is an increased risk of catastrophic failure inherently associated with keeping structural components in service past their initial service life, the most sensitive and reliable NDT techniques available must be incorporated into the methodology to offset this increased risk. However, the experimental results provided in Chapters 2-4 have shown that no single NDT technique is applicable for detection of all potential flaws. Generally, the sensitivity of an NDT technique is coupled to the volumetric region of interest under inspection. The POD of an NDT technique is heavily influenced by factors such as component geometry, surface conditions, and the location of critical life-limiting regions in the component volume. Therefore it is critical that the selected NDT inspection techniques be capable of reliably detecting all the potential types of service flaws in all of the relevant zones for the part-specific inspection methodology.

Table 6.2 contains nomenclature for the additional variables incorporated into the statistical analysis. In the table, the variable i is used to define the inspection zone. For the methodology proposed for disks and blades the three relevant inspection zones are classified as *surf*, *near-surf*, or *sub-surf*. There exists the potential for more than a single anomaly to be present in a structural component, so the variable j is used to define the number of anomalies present in a particular zone. Variables associated with fracture mechanics calculations, such as crack growth rate, crack growth life, and fracture toughness are additional values needed to accurately predict the remnant life of an in-service structural component. The methodology attempts to provide enhanced in-service inspection reliability by incorporating digital techniques whose detection capabilities overlap in terms of their applicable zone classes. The reasoning behind this is that the

simultaneous application of inspection techniques means that the probability of a missed detection for any flaw-type in any of the structural component's volumetric zones is reduced by the series operator. The methodology proposed is unique in both the specific

Table 6.2: Nomenclature used in statistical analysis (adapted from [203])

A	=	occurrence of anomaly in zone i
A_j	=	occurrence of j anomalies in zone
da/dN	=	crack growth rate
$F_{i A}$	=	fracture failure event in zone i given anomaly in zone i
$F_{i A_j}$	=	fracture failure event associated with zone i given that j anomalies are present
$F_{i A,L}$	=	fracture event of component given that anomaly is placed at life limiting location
K_C	=	fracture toughness
$K_{i A,L}$	=	stress intensity factor associated with anomaly at life limiting location in zone i
N	=	crack growth life
p_A	=	probability associated with event A
p_i	=	probability of fracture of zone i
$p_{i A}$	=	probability associated with event $F_{i A}$
$p_{i A,L}$	=	probability associated with event $F_{i A,L}$
V	=	component, volume
V_i	=	volume of zone i
λ_i	=	mean anomaly occurrence rate associated with zone i
λ_V	=	mean anomaly occurrence rate associated component volume

NDE techniques selected and the sequencing of the redundant NDE inspections for the particular component being evaluated. When multiple NDT inspection techniques are required the total inspection time becomes a more significant parameter in a cost benefit analysis. Section 6.4 delves into cost aspects associated with increasing the amount of inspections and the costs incurred from catastrophic structural failure.

Figure 6.1 shows elements of reliability block diagrams that will be developed in the fault tree analyses of Sections 6.2 and 6.3 via examples of the proposed methodology applied to aerospace disk and blade components at various times in the components' service lives. In Figure 6.1 it is shown that the union of two events is described by the "OR" operator and the intersection of two events is described by the "AND" operator.

These operators are mathematically described by the \cup and \cap symbols shown in Figure 6.1. The overall inspection coverage for a component for which the NDT techniques were specified in a redundant manner to all three potential zones would imply use of the “AND” operator such that:

$$X_{i/a,NDT} = X_{surf} \cdot X_{near-surf} \cdot X_{sub-surf} \quad (6.8)$$

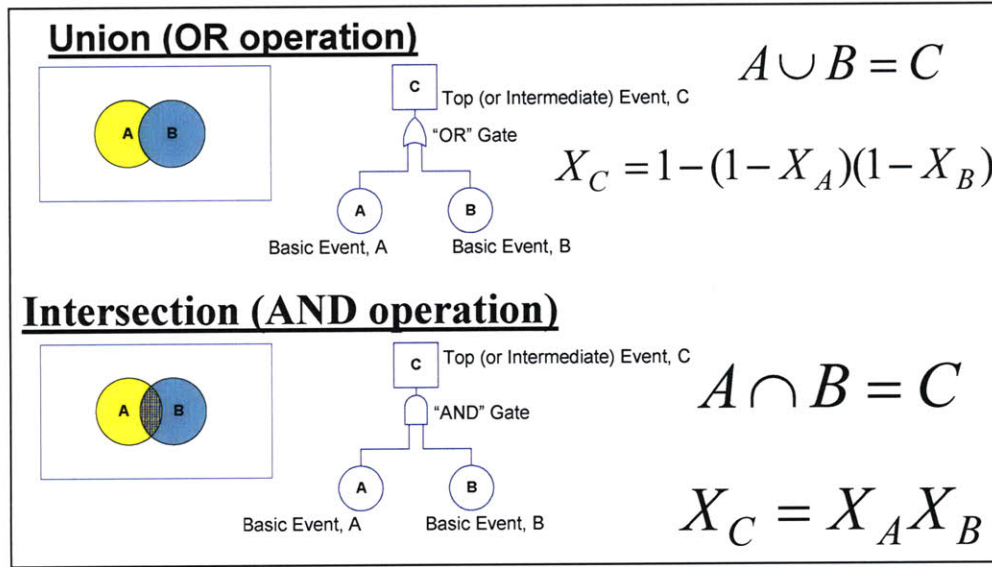


Figure 6.1: Elements of reliability block diagrams (adapted from [204])

In (6.8), the variable $X_{i/a,NDT}$ represents the overall ability of the redundant NDT inspection system to detect a flaw of size a in a particular zone i . It can be seen that this overall ability is represented by the multiplicative series of inspection zones. The improved reliability and sensitivity of the advanced NDT techniques which are proposed has already been shown to be superior to their traditional counterparts. The application of a redundant design further decreases the overall probability of fracture, because in order for a flaw to be missed at least two advanced techniques must fail for every inspection opportunity.

In instances when the proposed methodology allows a choice of NDT technique to be made, the “OR” operator should be used. An example of when the “OR” operator could be used is when either the manual contact Olympus® PA-UT or the fully automated TESI PA-UT technique could be used for subsurface flaw detection

interchangeably without a loss in overall inspection sensitivity. This example is mathematically represented by (6.9) and (6.10):

$$X_{\text{sub-surf}} = 1 - [(1 - X_{\text{manual PA-UT}})(1 - X_{\text{fully auto PA-UT}})] \quad (6.9)$$

$$PA-UT_{\text{manual}} \cup PA-UT_{\text{fully-auto}} = X_{\text{sub-surf}} \quad (6.10)$$

In the statistical analysis that follows, the variable X that appears in the above equations can represent any of the variables in Table 6.1 and 6.2. Generally, the flaw detection probability of a particular NDT technique or the probability associated with an anomaly in a particular volumetric inspection zone will take the place of X in the analysis.

Catastrophic airplane accidents that occur as a direct result of an NDT technique missing a flaw of detectable size during an in-service inspection are extremely rare events. As such, the Poisson distribution in (6.11) is used to model their occurrence.

$$p_A = \left[e^{-\lambda t} \cdot \left(\frac{(\lambda t)^A}{A!} \right) \right] \quad (6.11)$$

In the above equation, the probability of having exactly A number of events associated with anomalies in a particular zone i is given for the time period $(0, t)$. With the Poisson distribution, the anomaly occurrence rate, λ , is constant for the case of catastrophic aerospace accident events. Additionally, with the Poisson distribution the mean anomaly occurrence rate is proportional to the volume of material in each zone and is given by:

$$\lambda_i = (V_i / V) \lambda_v \quad (6.12)$$

The failure events which do occur in time period t are independent of one another. This means that the average number of events, μ , and the variance of the events, σ^2 , are both equal to λt [204]. These are the same likelihood parameters included on the POD curves generated in Chapter 5, only the POD curves are based on a log-normal distribution. Formulas for converting the values of these likelihood parameters between different statistical distributions are readily available.

For a structural aerospace component, the probability of fracture within a zone, p_i , is given by:

$$p_i = P(F_{i|A} \cap A) \quad (6.13)$$

The events $F_{i|A}$ and A are statistically independent, therefore (6.12) can be expressed as:

$$p_i = p_{i|A} \cdot p_A \quad (6.14)$$

The conditional probability of fracture within each of the three zones selected in this analysis is greatest at the critical life-limiting locations. Appendix B and Appendix C provide a thorough analysis of the critical locations for disk and blade aerospace components. For any structural component under inspection, the specific critical failure locations for that particular component are influenced by design assumptions and become the upper bounds for estimates of the probability of fracture within the relevant zone. This is expressed mathematically by the equivalent forms given in (6.15) and (6.16).

$$P(F_{i|A}) \leq P(F_{i|A,L}) \quad (6.15)$$

$$p_{i|A} \leq p_{i|A,L} \quad (6.16)$$

The surface, near-surface, and subsurface zones were chosen in this analysis due to the relatively straightforward method in which applicability of the advanced NDT techniques could be classified into one of those three location regimes. However, as the number of zones included in the inspection analysis increases, the value of $p_{i|A}$ approaches $p_{i|A,L}$. The probability of fracture of any structural component can generically be modeled by a system of m total zones as seen in (6.17).

$$p_F = P[F_1 \cup F_2 \cup \dots \cup F_m] = 1 - P\left[\bigcap_{i=1}^m \bar{F}_i\right] \quad (6.17)$$

The probability of fracture equals the union of probabilities for the m total zones, or one minus the probability intersection for those m zones for the case where fracture does not occur. This can be stated in the following ways: (1) the total probability of failure is equal to the zone failure probability if either zone 1 **OR** zone 2 **OR**...zone m fails (2) the total probability of failure is equal to 1 minus the multiplicative series of the m zones when failure does not occur in zone 1 **AND** zone 2 **AND**...zone m . Therefore, for the transfer of this methodology to structural applications other than aerospace engine components, it may be beneficial to use another zone classification system with an increased number of zones. The NDT techniques selected must be capable of distinguishing between zones, but optimization of the total number of component zones could improve the conditional probabilities and thus the posterior probabilities of the analysis. Future work into correlating the total number of volumetric inspection zones for a component with monte carlo simulations and finite element (FE) mesh size could

improve the predictive ability of analytical software to minimize the equivalent initial flaw size (EIFS) distribution. The variability and lack of accuracy in EIFS calculations are significant limitations to current software programs that perform fracture mechanics analyses. However, for the disk and blade reliability block diagrams in Section 6.2 and Section 6.3, only flaws at surface, near-surface, and subsurface zones were considered.

The anomaly occurrence rate is highly dependent on the condition of the raw material and the manufacturing processing steps used to fabricate the component into its final shape. The materials considered in this analysis are detailed in Appendix B and Appendix C for rotating airplane engine turbomachinery applications. These structural components are typically manufactured from premium grade Ni-alloy and Ti-alloy materials as mandated by FAA regulations [4, 5]. As such, these components have an extremely low anomaly occurrence rate. If the mean anomaly occurrence rate is very small, the probability of more than one significant flaw in the component is negligible and the probability of multiple anomalies in a particular zone is even more unlikely [203]. This allows Equation (6.17) to be reduced to:

$$p_F \cong \sum_{i=1}^m p_i \quad (6.18)$$

For the analysis considered in Section 6.2 and Section 6.3, it was assumed that (6.18) was valid, because the premium raw materials would limit the number of potentially catastrophic anomalies that could potentially be present in the aerospace components. Application of this methodology to other structural components that exhibit significantly higher anomaly rates because of the use of lower quality raw materials would preclude the use of Equation (6.18) in the analysis. In that case, the conditional probability of fracture would need to be modeled to account for the potential possibility of j anomalies in each zone. Enright and Huyse [203] provide an analysis for these cases.

Since the presence of anomalies such as hard alpha anomalies in Ti-6-4 compressor disks occur so infrequently, they cannot be accurately modeled by fleet-wide statistics. The use of fleet-wide statistics is currently the accepted practice for calculating risks associated with component failure of aging aircraft. The anomalies that result in catastrophic failure are typically unaccounted for in current life prediction methodologies, because they reside at the extreme tail ends of the statistical distributions used. A branch

of statistics dealing with the extreme deviations from the median of probability distributions is known as the Extreme Value Theory (EVT) [205-207]. The use of EVT has been successfully applied to the assessment of risk in rare events, such as 100 year floods. Also, EVT theory has been used to calculate risk in other industries; such as equity risks with day to day fluctuations in the stock market, pipeline failures due to pitting corrosion, and extreme weather. The prediction of future catastrophic aerospace events resulting from traditional NDT techniques missing flaws of a detectable size during inspection could be made using EVT theory. However, such an analysis would require a significant amount of work and could be a separate thesis in its own right. Instead, for predicting the amount of future catastrophic events, statistical data from past events were extrapolated in this analysis. Data from NTSB reports [119, 125, 208-212], FAA databases [115, 118], and other sources [120, 124, 213-218] for the time period 1989-2009 were used in the analysis. The relevant data set for that 20 year period consisted of the four Category 3 and 4 events described in Section 1.3.2.4. This data was used to approximate the costs associated with catastrophic failure in the cost-benefit analysis of Section 6.4.

6.1.1 In-service Inspection

The POD analysis performed in Chapter 5 was based on wedding cake samples where the flaw size, depth, and location were all known prior to inspection. Comparison between the proposed advanced techniques and their traditional counterparts showed the sensitivity and minimum detectable flaw size were superior for the advanced techniques. Based on the experiments performed in Chapter 2, it is concluded the use of the MWM-array® eddy current technique would result in approximately a 2-3X improvement over traditional eddy current array systems. The benefit of MWM technology over single channel point probes currently used at MRO facilities to inspect blade components is even greater, because the MWM-array® technique allows data to be simultaneously collected from multiple channels at multiple frequencies. A traditional eddy current point probe only provides information from one channel at one frequency. Approximately 75X more data was obtained at *every* inspection point with the MWM sensor used in the Chapter 2 analysis than a point probe is capable of collecting. The C-scans in Chapter 2 are comprised of many thousands of inspection points. Additionally, traditional eddy

current point probe inspection systems are analog and the printed hardcopy output from that inspection equipment is typically not retained for more than a couple years.

Based on the experiments performed in Chapter 3, it is concluded the flaw detection coverage of the contact Olympus® PA-UT system and the fully automated TESI PA-UT system were comparable. Both PA-UT systems provide greater penetration depth capabilities for subsurface flaw detection than any of the other NDT techniques considered. Additionally, the detection of both surface and near-surface flaws was more reliable with phased array systems than traditional UT systems. The flaw detection *sensitivities* of the two systems would be comparable if component inspection using the Olympus® system was semi-automated with a controllable X-Y gantry encoder system. Compared to traditional ultrasonic C-scan equipment, use of these phased array systems can result in approximately a factor of three improvement to $a_{min-Threshold}$, the threshold minimum flaw size at a specified POD level and depth. This significant reduction in $a_{min-Threshold}$ in the PA-UT equipment versus traditional UTI C-scan systems was observed due in part to the added sectorial shear inspection capability. Traditional UT inspection systems can only do single element longitudinal scans. Also, the zone multiplexing capability of the TESI PA-UT system and dynamic depth focusing (DDF) capability of the Omniscan™ PA-UT system allow the simultaneous analysis at varying component depths for a single inspection. This zone based approach drastically improves the overall in-service inspection coverage and sensitivity for flaw detection at non-surface zones.

The benefits of the digital radiographic techniques over traditional x-ray film radiography were quantified in Chapter 4. As the analysis in Chapter 5 showed, the integration of these advanced digital NDT techniques with image analysis software further improves POD and NDE inspection reliability. In the experiments performed, all of the advanced techniques were able to consistently locate flaws smaller than the 0.030in. x 0.015in. (0.8mm x 0.4mm) surface fatigue crack flaw size specified by the FAA for fracture mechanics analyses. Additionally, the 3D-CT and both the PA-UT systems offer the capability to reliably detect subsurface flaws. The 3D-CT and PA-UT inspection systems are complementary with regard to the applicable flaw types that can be detected, the NDT system depth of penetration capability, and the NDT system component characterization capability. Incorporation of these advanced techniques in a redundant

systems methodology to in-service NDT of structural components enables a retirement for cause life prediction approach to be feasible.

The statistical approach described in Section 6.1 utilized a component zone-based approach to flaw detection at various component depths. The in-service inspection analysis proposed in this section expands upon that zone-based approach. For structural components where multiple anomalies may be present within any single zone, the probability of fracture occurring in one of those zones is:

$$p_i = P \left[1 - \bigcap_{j=1}^n (\bar{F}_{i|A_j} \cap A_j) \right] \quad (6.19)$$

If (6.19) quantifies the probability of fracture in a zone, it follows from (6.2) that the probability of catastrophic component failure not occurring in a zone is given by:

$$\bar{p}_i = P(\bar{F}_i) = P \left[\bigcap_{j=1}^n (\bar{F}_{i|A_j} \cap A_j) \right] \quad (6.20)$$

From (6.20) it can be seen that the probability of fracture not occurring in zone i is conditional upon preventing a fracture failure event associated with zone i from happening, given that j anomalies are present in that zone. The overall probability of fracture for a structural component is then equal to the probability union for all m zones that the component is divided into. Substituting (6.19) into (6.17) gives:

$$p_F = 1 - P \left[\bigcap_{i=1}^m \left(\bigcap_{j=1}^n \bar{F}_{i|A_j} \cap A_j \right) \right] \quad (6.21)$$

For the analysis of disks and blades described by the reliability block diagrams in Section 6.2 and Section 6.3, m is equal to three for the specified surface, near-surface, and subsurface zones. The selection of these three zones was arbitrarily made, and was based on the convenience with which the advanced NDT techniques could be classified. Future research could be performed to optimize the number of zones used in the methodology for structural components of various volumes and aspect ratios. Since the zone failures can be treated as independent events, Equation (6.21) can be written as:

$$p_F = 1 - \prod_{i=1}^m (1 - p_i) \quad (6.22)$$

If the proposed methodology is to be implemented for in-service inspection of structural components in an industrial environment, the advanced NDT techniques must

be capable of reliably detecting service flaws on real components of complex geometry. For the wedding cake samples, flat bottom holes and side drilled holes were used to simulate possible flaws. The FBH and SDH were an idealistic representation, and there are diverging opinions in the NDT community on the validity of these simulated flaws. Real service cracks are much tighter than FBH, and do not have a uniform aspect ratio. For these reasons, the S/N ratio between real flaws and FBH could substantially differ. For aging structural aerospace components that are still in service, the potential for flaws to exist is high because of the aggressive environment these components operate in. Unlike the POD curve generated for the 2D-DR technique in Chapter 5, the location, size, AR, and depth will not be known a priori. A quality metric that takes into account the sensitivity of a particular NDT technique to these parameters is therefore needed, because the 90/95 POD/CL single value metric currently used cannot adequately describe service flaws in three dimensions. As part of the improved methodology, the development of a new 3-parameter POD metric for characterization of non-surface flaw features is proposed. The three parameters suggested for inclusion in the proposed POD metric are:

- (1) 90/95 POD/CL @ a particular component depth, D
 - (2) An AR parameter that describes flaw feature orientation @ D
 - (3) Correlation parameter between positive sub-surface NDT indications
- This would be known as the 3D-CT/PA-UT indicator

The selection of the 90/95 level as the single value quality metric for an NDT inspection technique in the 1970's was arbitrary. The selection was based on the capability of the technology at the time. However, advanced technology has been integrated into NDT inspection systems to such an extent that a single 90/95 level is no longer sufficient to describe the POD capability. The time has come for the NDT industry to embrace the advanced capabilities afforded by digital technology. Future research to further characterize the three parameters suggested in the new quality metric for all applicable techniques would require industry-wide collaboration and would take years to complete. Nonetheless, if the advanced techniques are shown to be reliable and sensitive in their flaw detection capabilities, a paradigm shift to a 95/95 or even 99/95 POD/CL curve for surface and/or non-surface zone-depths could be established in lieu of the current 90/95 level. The improved sensitivity and reliability of the advanced

techniques would more than cancel out the increased risk of failure associated with keeping critical components in service longer.

The elegance of the proposed methodology is that the added value of information gained by the use of redundant NDT methods and Bayesian analysis continually refines and improves the predictive power of the remnant life model as the structural component progresses through its life-cycle. This is shown schematically in Figure 6.2. Since the methodology calls for increased inspections at smaller cyclic intervals between in-service tear-downs, there will be less variability associated with the calculated conditional and posterior probabilities. The results from every in-service inspection that incorporates the redundant NDT methodology can have a Bayesian updating treatment applied. A key element of implementing an RFC approach is accurately determining the $a_{min-Threshold}$ and quantifying the variability in the EIFS distribution. Use of Bayesian analysis with respect to these two inspection parameters could significantly reduce the overall variability and scatter in fracture mechanics models used in the remnant life prediction of structural components.

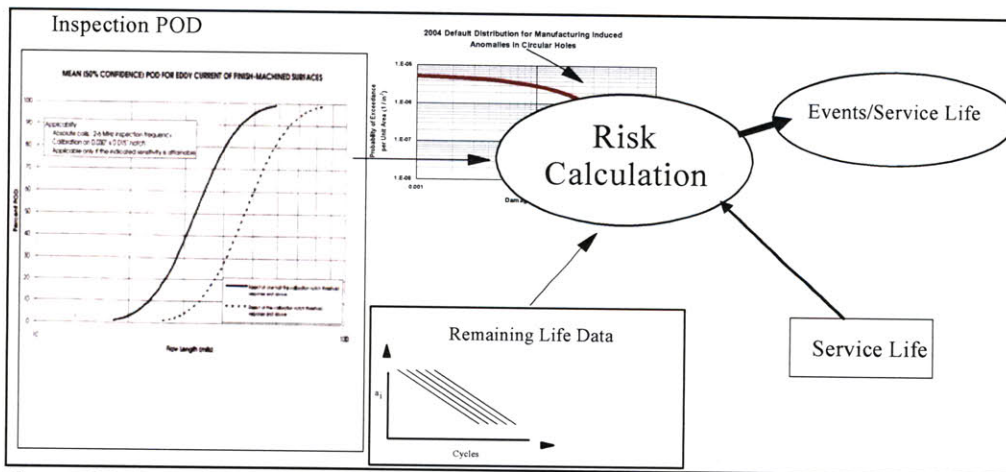


Figure 6.2: Bayesian updating of the risk calculation for a structural component based on inspection POD and service life data (reprinted from [7])

Safety factors will have to be applied to the calculated additional component service life, due to the potential damage to the components during tear-down and reassembly processes. Figure 6.3(a-d) shows some of the many manual operations performed during engine tear-down inspections. There is a risk associated with initiating a defect at the MRO facility during a teardown inspection. An additional knockdown

factor would be required for when refurbishment and rejuvenation processes were performed. While these processes can indeed extend a component's usable service life by a factor of one to three times, the knowledge gained from the accumulation of in-service inspection data is no longer valid once the component has undergone a process meant to erase its "microstructural memory". The baseline in-service NDT inspection data generated prior to refurbishment is no longer valid after component rejuvenation. Similarly, a knockdown factor must be incorporated when new blades or other components are swapped into or out of an older legacy engine. From a global perspective, this changes the dynamic contribution associated with the unique mission profile of an engine to the single flight probability of engine failure. However, since the proposed methodology calls for inspection on a part-specific basis, the digital inspection history database can be transferred for individual components. The analysis in Section 6.4 estimates the additional service life that can be gained from the proposed NDT methodology despite these safety and knockdown factors.

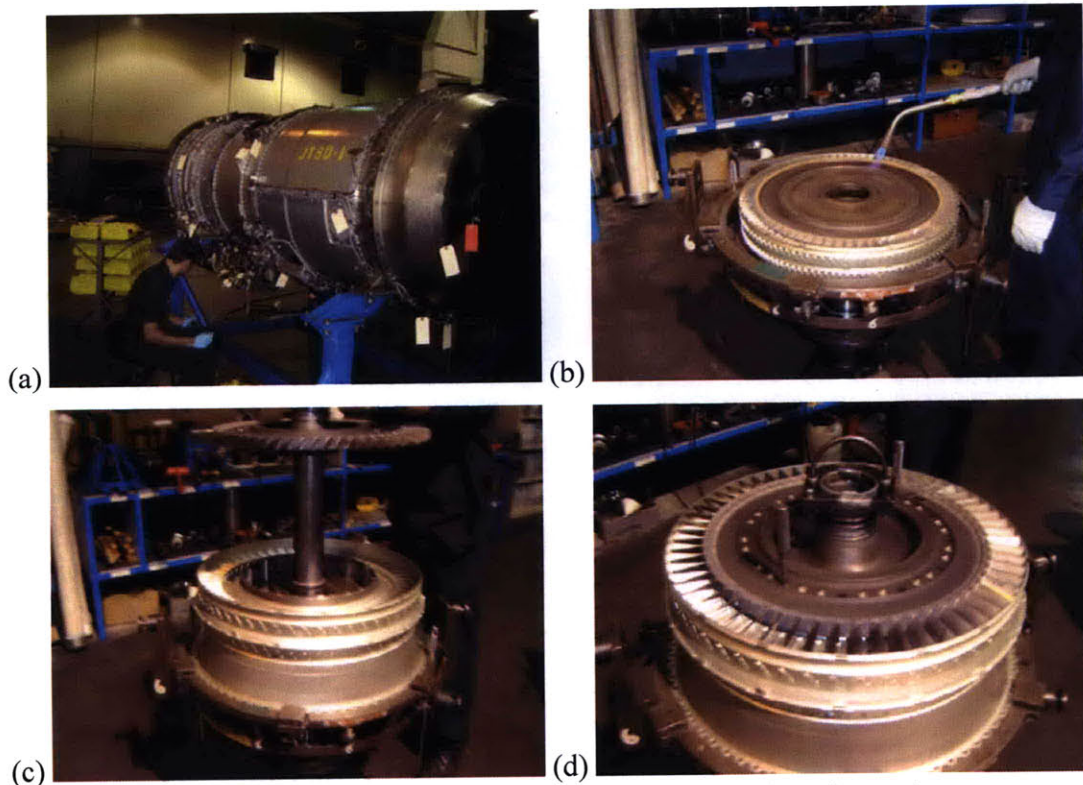


Figure 6.3: (a-d) Manual processes involved in an engine tear-down inspection at an overhaul facility

As Equation (6.21) shows, the union of all the volumetric zones that a structural component is divided into can be used to determine the overall probability of fracture. In the proposed methodology, there are at least two advanced NDT techniques not only applicable to every zone, but actually integrated into the in-service inspection program. The data obtained from these advanced techniques are digital in nature, whereas most of traditional NDT techniques can only provide data in analog format. Digital inspection data can be used with image analysis software as Chapter 5 showed. Additionally, digital data can be easily stored so that every inspection for every structural turbine engine component can be added to a digital inspection outcome database. This database would allow an NDT technician to reference previous inspection results so that remnant life predictions could be based on *differential* analyses of accumulated damage in structural components. This would allow cracks which have been detected in an inspection, but are not yet of a critical size to warrant removal from service, to be “mapped and tracked” in subsequent inspections. Figure 6.4 is an example of this mapping and tracking capability provided by the MWM-array® technique on a Ti-6-4 alloy part.

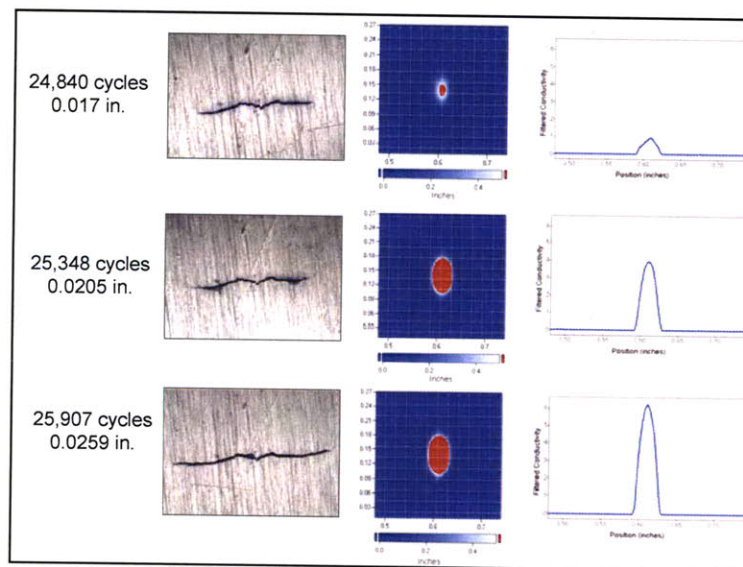


Figure 6.4: Spatially filtered MWM-Array scan images of a crack produced inside of a hole in a Ti-6-4 fatigue coupon. The FA43 sensor architecture was used to obtain these images at various stages of the fatigue test. Photomicrographs on the left are from acetate replicas taken after each MWM-Array scan (reprinted from [112])

Given a flaw is present, the conditional probability that one of the applicable techniques of the redundant NDT methodology will detect a flaw of size a in zone i is given by:

$$p(NDT/a_i) = 1 - P\left[\bigcup_{\text{applicable_NDT}=1}^n X_{\text{applicable_NDT}}\right] = 1 - \prod_{\text{applicable_NDT}=1}^n (1 - X_{\text{applicable_NDT}}) \quad (6.23)$$

where $X_{\text{applicable_NDT}}$ are the probabilities for the advanced NDT techniques listed at the bottom of Table 6.1 which are relevant to the particular component under inspection. Equation (6.23) can be re-written in the disjunctive normal form as shown in (6.24).

$$P(X_{NDT}) = \prod_{i=1}^m M_i = 1 - (1 - M_1)(1 - M_2) \cdot \dots \cdot (1 - M_m) \quad (6.24)$$

In (6.24), X_{NDT} is the total probability for the redundant system and $[M_i, M_{i+1}, \dots, M_m]$ are the relevant minimal cut sets for all of the m zone-depths that make up the fault tree in the reliability block analysis. A cut set is defined as any set of events that causes system failure and a minimal cut set is a cut set that does not contain another cut set as a subset [204]. One example of a potential minimal cut set associated with subsurface component failure would be:

$$M_{\text{sub-surf}} = X_{PA-UT} X_{3D-CT} \quad (6.25)$$

From this it follows that the failure of the applicable advanced NDT techniques to detect a flaw of size a , which is within the POD capability of the NDT system, can be generalized by the minimal cut set relevant to a particular zone i and modeled as:

$$\bar{p}_i = (1 - M_i) \quad (6.26)$$

For the particular example of both 3D-CT and PA-UT failing to detect a subsurface flaw of size a , the probability of failure for this zone would be calculated as:

$$\bar{p}_{\text{sub-surf}} = 1 - [(1 - \bar{p}_{3D-CT}) \cdot (1 - \bar{p}_{PA-UT})] \quad (6.27)$$

From (6.27) the benefit of a redundant NDT approach can be quantified. If the POD of detecting a flaw of given size with an advanced technique is very high for a particular zone, then that means that the chances of an inspection missing that flaw are very low. If two advanced techniques are used simultaneously, the probability of missed

detection exponentially drops off. In order for catastrophic failure to occur, the probability intersection from use of multiple NDT techniques for the probability union of the zones would be required. Additionally, the maximum likelihood parameters obtained from a POD analysis similar to the one performed in Section 5.3 could be used in conjunction with (6.4) and (6.6) to further reduce uncertainty in the inspection data. The likelihood function in (6.28) is used to estimate the likelihood, L , of a specific inspection result.

$$L(\theta) = \prod_{i=1}^{i=n} f(X_i; \theta) \quad (6.28)$$

In (6.28), X_i represents the outcome of the i th inspection, and $f(X_i; \theta)$ represents the probability of obtaining X_i for an inspection involving the set of θ parameters. The maximum likelihood analysis of hit/miss data involves the estimation of the parameters of the log odds model based directly on either a 0 or 1 value for the probability of each inspection result. If n represents the number of flaws and k represents the number of inspection opportunities resulting from an NDE reliability experiment, then the likelihood function in (6.28) can be written as:

$$L(\mu, \sigma) = \prod_{i=1}^n \prod_{j=1}^k p_i^{z_{ij}} (1 - p_i)^{1-z_{ij}} \quad (6.29)$$

where μ and σ were previously defined in Section 5.3 and z_{ij} equals 0 or 1 for the j th inspection of the i th flaw producing either a hit or miss response. The probability, p_i , of detecting a flaw of size a_i is then calculated as shown in (6.30)-(6.31).

$$p_i = \frac{h(a)}{1 + h(a)} \quad (6.30)$$

$$h(a) = \exp \left[\frac{\pi}{\sqrt{3}} \left(\frac{\ln(a_i) - \mu}{\sigma} \right) \right] \quad (6.31)$$

If the Cellprofiler image analysis software was able to be modified so that POD curves with these likelihood parameter values could be generated for not only the 3D-CT and 2D-DR radiographic but also the MWM-array® and both PA-UT techniques, the $a_{min-Threshold}$ value for the redundant NDT system methodology could be calculated. If

this value was known, it could be incorporated into remnant life fracture mechanics models to determine the instantaneous risk associated with the single flight probability of failure. The enhanced NDT methodology is only a part of the fracture control plan. Other components of the fracture control plan are shown in Figure 6.5. While the potential for catastrophic failure would be decreased for critical turbine engine components, other structural component sub-assemblies in the engine or at the entire airframe structure level could still potentially fail.

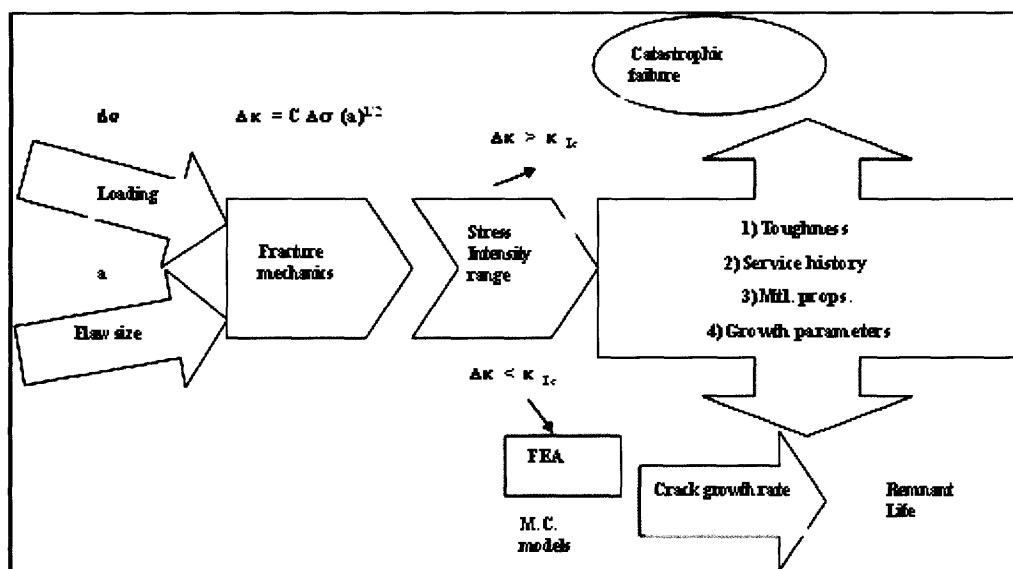


Figure 6.5: Fracture control plan for structural components in service

The advanced NDT methodology described above is adaptable to many industries in which structural components are critical. The digital NDT techniques should be specified based on their flaw detection sensitivity and capability with respect to the relevant structural component undergoing inspection. The methodology is distinct for the examples detailed in Section 6.2 and Section 6.3 for disk and blade components. The risk of uncontained catastrophic failure is much greater for disks than for blades. For disks, if subsurface defects are not detected during manufacturing processes, they are extremely difficult to detect once the disk is in-service with the traditional NDT techniques currently used in the aerospace industry. For this reason the detection of subsurface defects is the most critical zone depth for disk components, and the NDT inspection techniques associated with this zone are specified to occur first in the overall sequence of

inspections associated with the redundant systemic approach. Blades, on the other hand, suffer primarily from surface cracks and fretting fatigue cracks. For this reason, detection of surface defects with the MWM-array® eddy current technique is the initial zone-based inspection specified for blades. In this regard, the proposed methodology is more efficient than the traditional component life management inspection approach. Because the sequence of inspections under the proposed methodology allows disks and blades to be simultaneously inspected, the overall time required for a complete engine tear-down inspection is minimized.

A high-reliability theorist view of component inspection is intrinsic to the proposed methodology. While defects can never be completely eliminated from every critical turbine engine component, the use of technologically advanced NDT techniques and an integrated life-cycle inspection program can provide sufficient redundancy to detect flaws prior to catastrophic failure. The ability to “map and track” accumulated structural damage facilitates divergence from the current life management methodology to a new approach for on condition retirement of structural components for cause rather than on time.

6.2 Methodology Applied to Disks

Figure 6.1 provided an explanation for the meanings of the elements contained in the fault tree reliability block diagrams described in the next two sections. It is through these fault tree diagrams that the proposed methodology is uniquely detailed. The advanced NDT methodology will be applied to the in-service inspection of disks for two cases: when the component initially enters service and after the inspection database has generated enough data to reliably determine that uncontained LCF events have a sufficiently low probability of failure. After this determination is made, the second inspection case calls for comparable digital techniques to be substituted for the initial NDT techniques. These comparable techniques provide either a lower operating cost or less time required to perform the inspection. In this way, the methodology attempts to optimize the inspection sensitivity subject to cost and time constraints.

Figures 6.6-6.8 detail the suggested NDT techniques to be used for the initial component inspection. Included are the fully automated PA-UT system, a 3D-CT system

**Sequence of Inspections Performed
Ordered Left to Right**

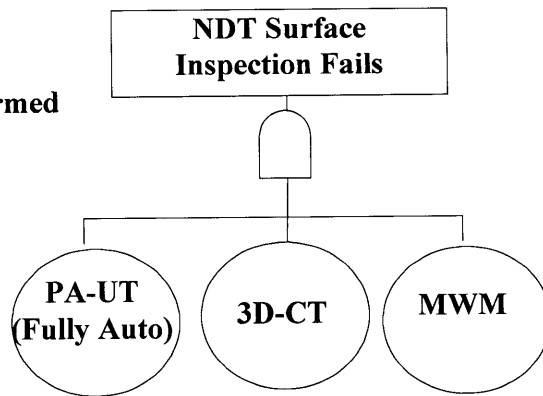


Figure 6.6: Reliability block diagram for the case of initial disk surface inspection

**Sequence of Inspections Performed
Ordered Left to Right**

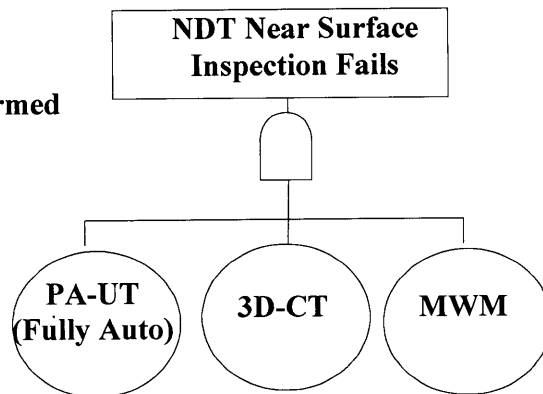


Figure 6.7: Reliability block diagram for the case of initial disk near surface inspection

**Sequence of Inspections Performed
Ordered Left to Right**

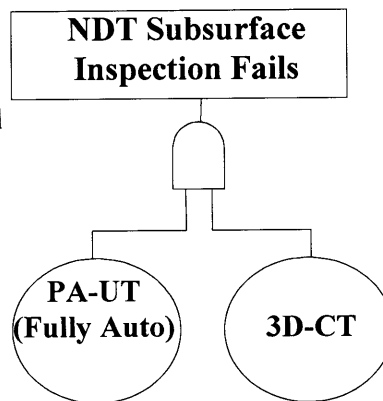


Figure 6.8: Reliability block diagram for the case of initial disk subsurface inspection

of sufficient voltage and size capacity to inspect the disk components, and the MWM-array® eddy current technique. The cut sets for catastrophic system failure are represented by the individual elements for each of the three inspection zones. In certain

instances, if an NDT technique was not sensitive enough to flaw detection in a certain zone it was removed from the fault tree for the combined 100% inspection. As the figures state, the sequence of inspections is ordered from left to right. The multiplexing capability of the fully-automated PA-UT system, and the volume reconstruction capability of the 3D-CT system allow all three inspection zones to be analyzed in a single inspection. The last inspection to be performed is the MWM-array® eddy current. The reasoning is that since that technique will be the first one performed on blades, it is most time efficient with respect to total combined NDT system inspection time to scan the disks with the MWM system last. Therefore, for 100% component inspection, the reliability block diagram shown in Figure 6.9 is proposed for the initial case where a newer disk component has just begun in-service inspections. In Figure 6.9, it can be seen that the minimal cut set for the surface zone does not include 3D-CT. As the results in Chapter 4 detailed, surface cracks are very sensitive to orientation with respect to radiographic techniques. Since 3D-CT does not easily allow adjusting of the component orientation to detection of surface flaws, it was not included in the minimal cut set for that zone.

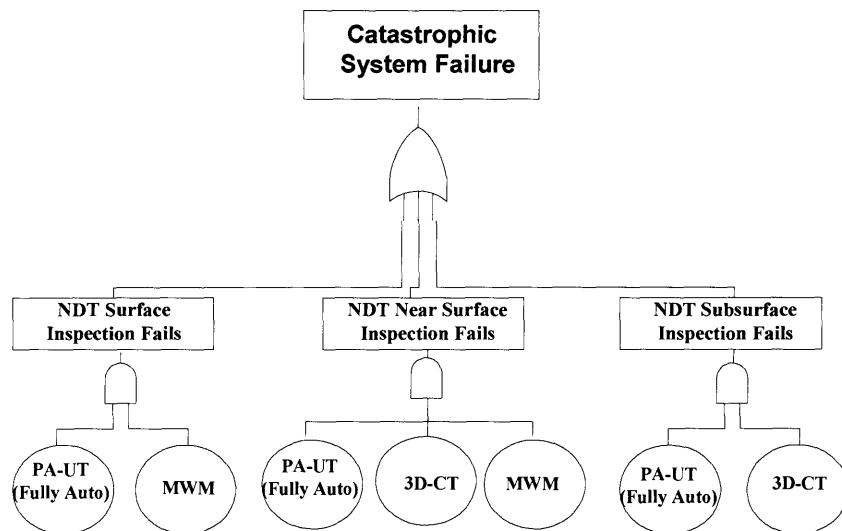


Figure 6.9: Reliability block diagram for 100% initial component inspection of disk components

Now, after the disk has been in service a while, a database of historic inspection results has been acquired. After the determination that the risk of catastrophic failure from sub-surface or near-surface anomalies is sufficiently minimal, the use of other digital NDT

techniques can be applied. It generally follows that substitution from one advanced NDT technique to another provides some cost savings without sacrificing inspection sensitivity. The fault trees of the three disk inspection zones for this second inspection case are provided in Figures 6.10-6.12.

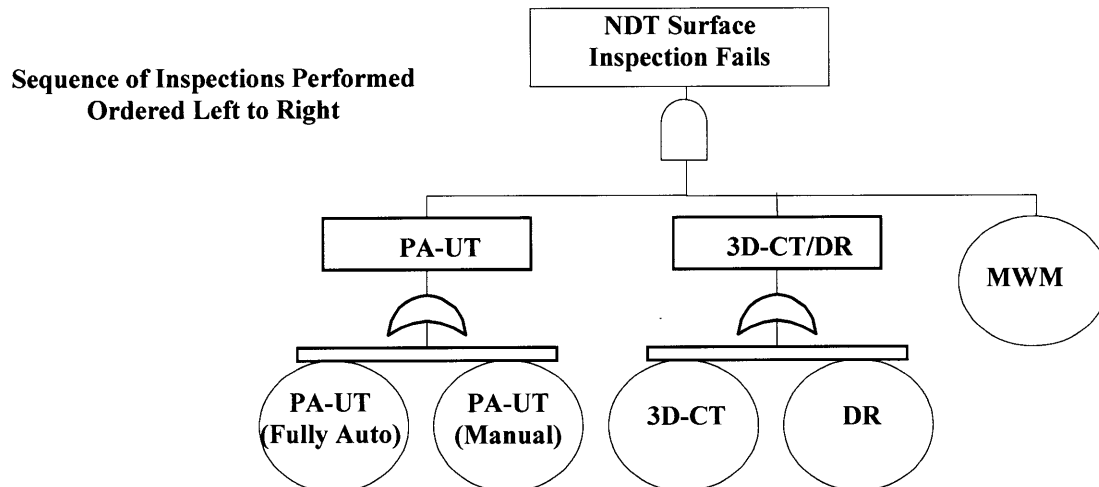


Figure 6.10: Reliability block diagram for the case of continued disk surface inspection

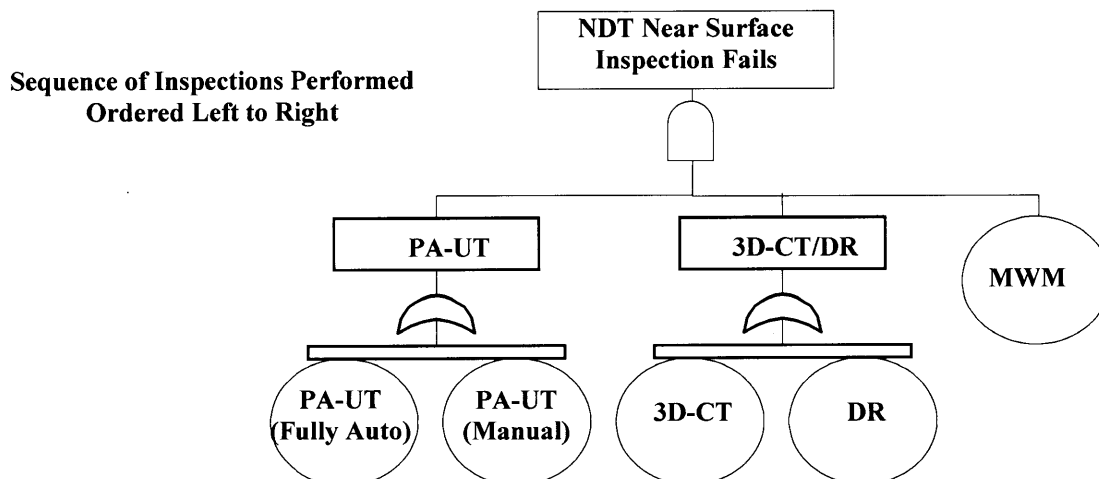


Figure 6.11: Reliability block diagram for the case of continued disk near surface inspection

From Figures 6.10-6.12 it can be seen that the 2D-DR and manual contact Omniscan™ PA-UT systems can now be substituted for the 3D-CT and fully automated PA-UT inspection techniques. Although the fault tree states that the “manual” contact PA-UT system can be used, it is highly recommended that the system be set up with an X-Y encoder gantry. The resulting semi-automated PA-UT inspection would

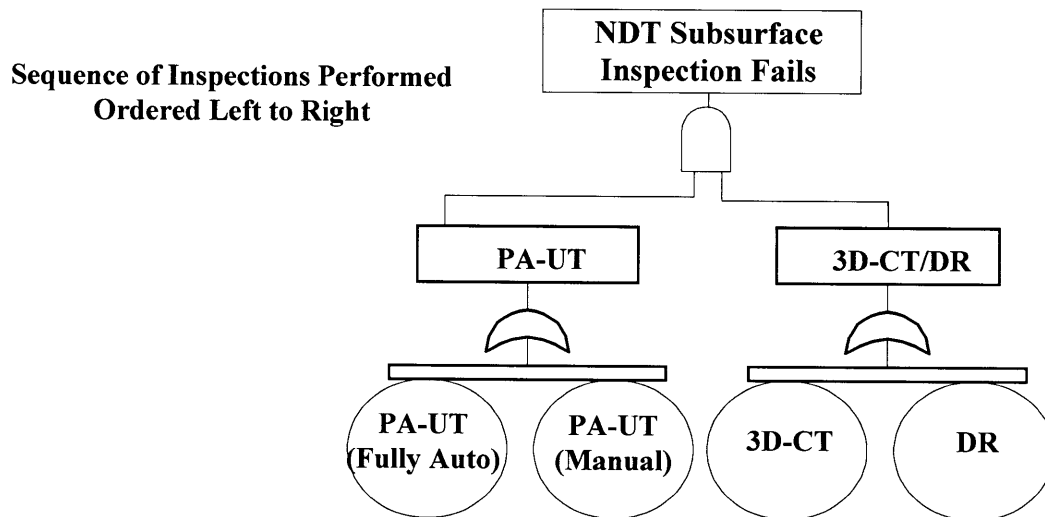


Figure 6.12: Reliability block diagram for the case of continued disk subsurface inspection

provide a much improved C-scan image. Also, the noise associated with operator hand unsteadiness would essentially be eliminated. For this inspection case the resulting overall system reliability block diagram is shown in Figure 6.13. The 2D-DR technique can be oriented for improved sensitivity to cracks in the surface zone, therefore if 2D-DR is substituted for 3D-CT it would be included in the surface zone minimal cut set.

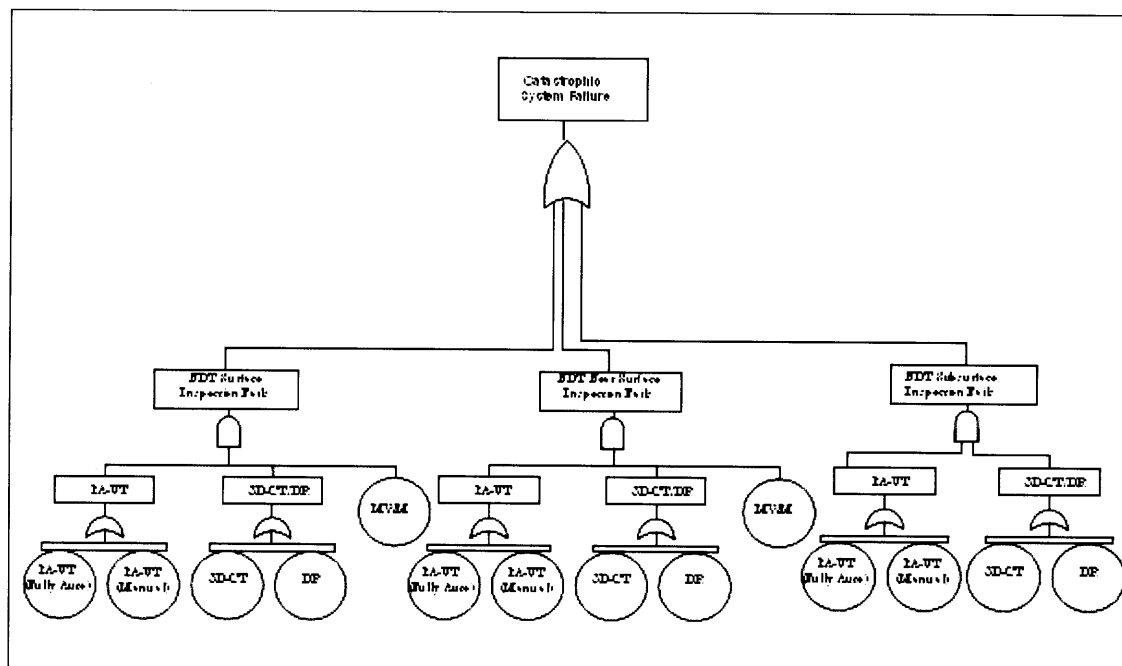


Figure 6.13: Reliability block diagram for the case of continued 100% disk inspection after initial generation of inspection database

6.3 Methodology Applied to Blades

The inspection of turbine engine blade components is presented similarly to the analysis in Section 6.2. The reliability block diagrams of the initial inspection case for turbine engine blade components are shown in Figure 6.14, Figure 6.15, and Figure 6.16 for the surface, near-surface, and subsurface inspection zones. Since surface damage is the life-limiting zone for these components, the MWM-array® technique is suggested as the initial inspection technique to be used. The experimental results on the duct segment component showed that the MWM-array® technique is capable of detecting real service flaws on the order of 0.005 in. (0.127mm) in size. Also observed in Figures 6.14-6.16 is the use of the manual PA-UT Omniscan™ contact system. The fully automated TESI

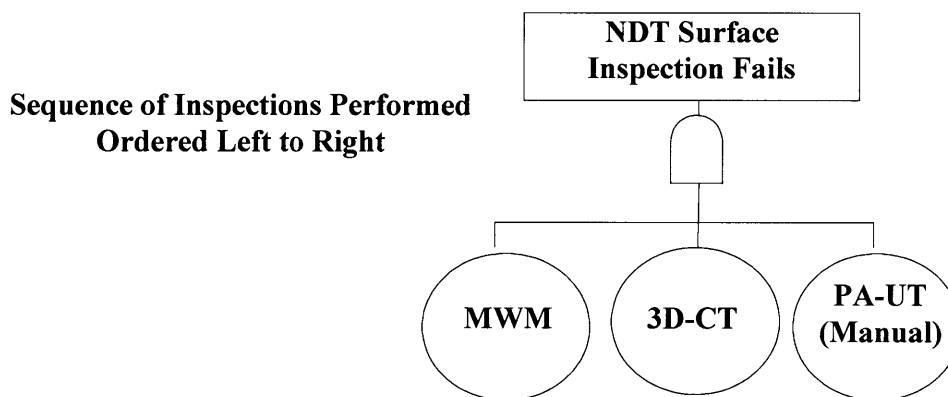


Figure 6.14: Reliability block diagram for the case of initial blade surface inspection

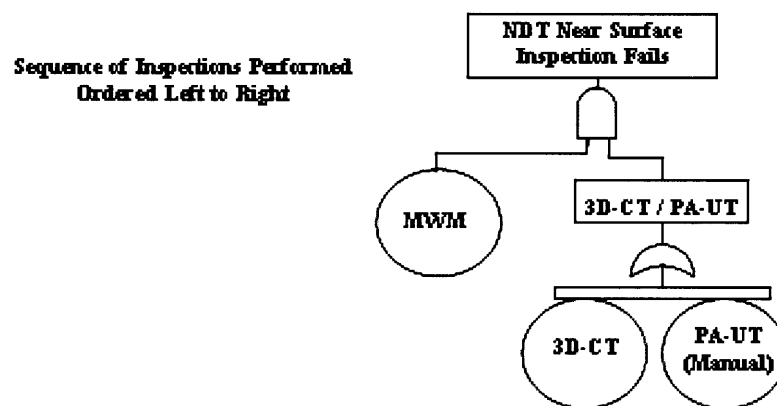


Figure 6.15: Reliability block diagram for the case of initial blade near-surface inspection

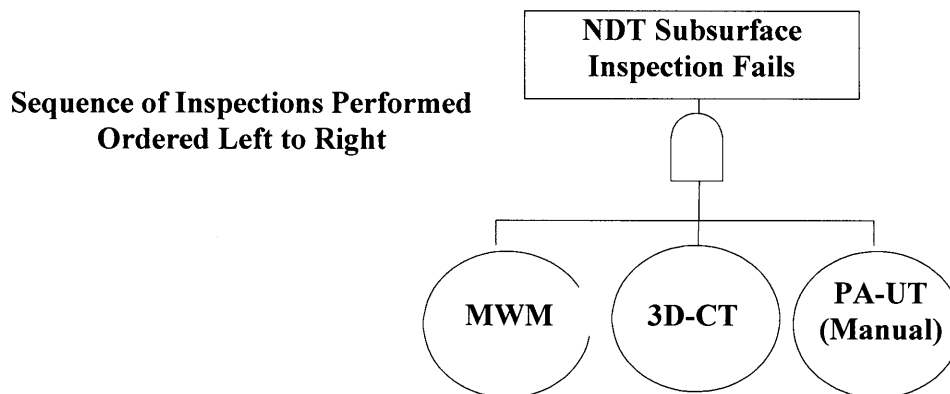


Figure 6.16: Reliability block diagram for the case of initial blade sub-surface inspection

phased array system is currently programmed and designed only for circular disk-like components. For this reason, the TESI fully-automated system is not applicable to blade components with their complex geometrical design. Additionally, while the 3D-CT system was shown in Chapter 4 to be unreliable at detecting surface cracks, for the case of initial blade inspections the benefit gained from the 3D volume rendering capability of the 3D-CT system resulted in the inclusion of that technique in the minimal cut set. Since blades are not large structural components, penetration depth of the selected NDT techniques is much less critical for blades than for disks. The complementary inspection capability in the near-surface regime for 3D-CT and manual PA-UT enable a choice of one or the other to be incorporated into the analysis of near-surface anomalies. However, this choice essentially becomes a moot point for the initial base because as Figure 6.16 shows both the 3D-CT and manual PA-UT are included in the minimal cut set. Also included in the minimal cut set is the MWM-array® eddy current technique, at a sufficiently low inspection frequency to improve its depth of penetration. Figure 6.17 contains the overall reliability block diagram for the initial case of 100% zone-based inspection for blade components.

Once the relevant blade parts have been in service and a sufficient digital inspection history database has been generated, Figures 6.18-6.21 can then be used to represent the proposed NDT methodology for the individual zones and the combination

of all the zones. Through these reliability block diagrams the NDT methodology for continued blade inspection throughout component service life is detailed.

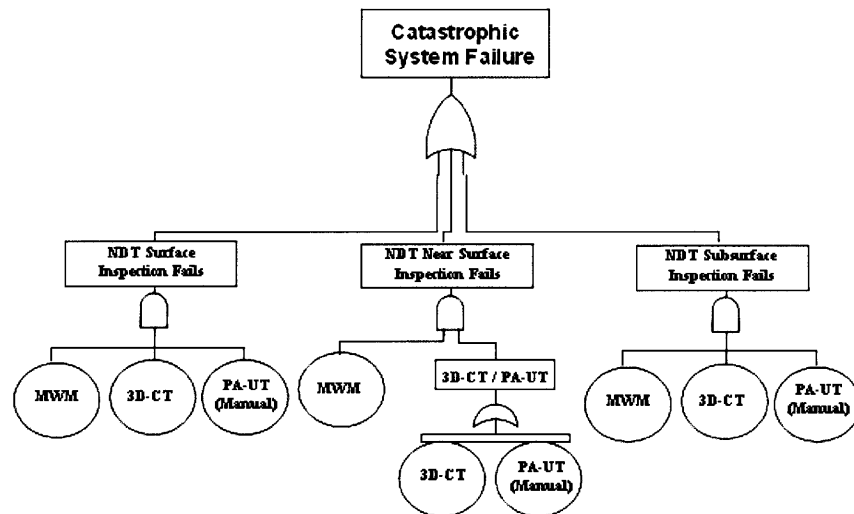


Figure 6.17: Reliability block diagram for the initial case of 100% zone inspection for blade components

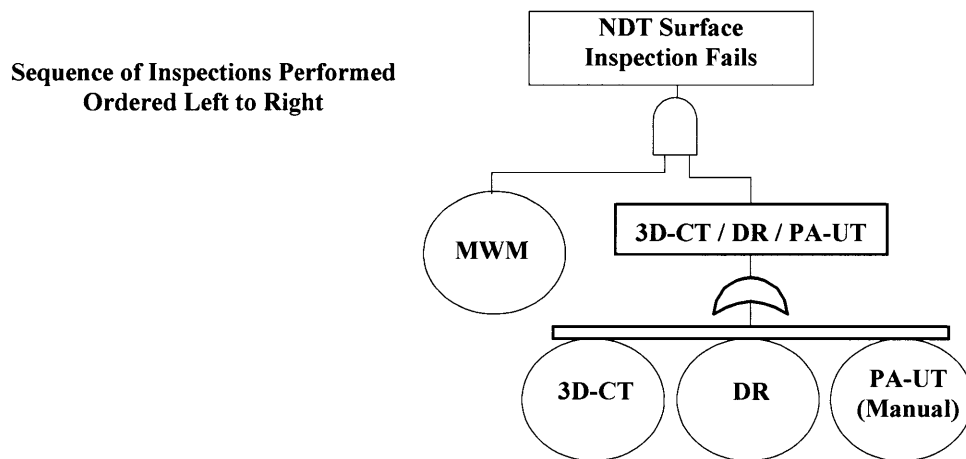


Figure 6.18: Reliability block diagram for the case of continued blade surface inspection after sufficient inspection history results are incorporated into the digital database

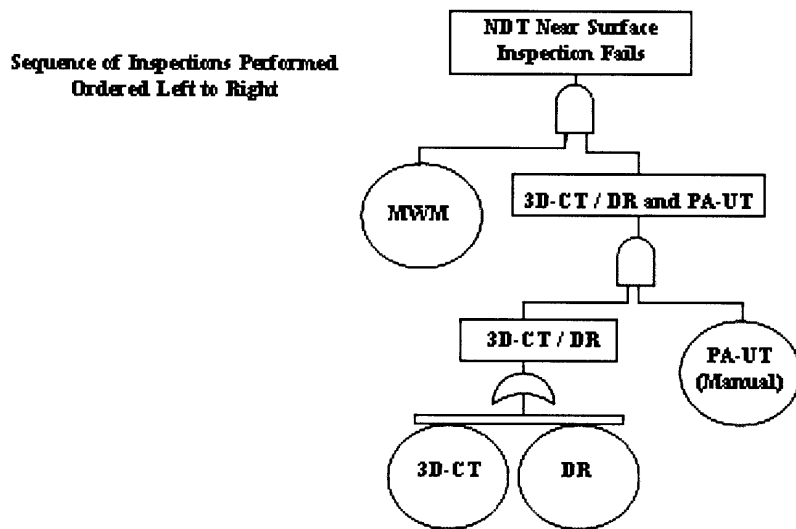


Figure 6.19: Reliability block diagram for the case of continued blade near-surface inspection after sufficient inspection history results are incorporated into the digital database

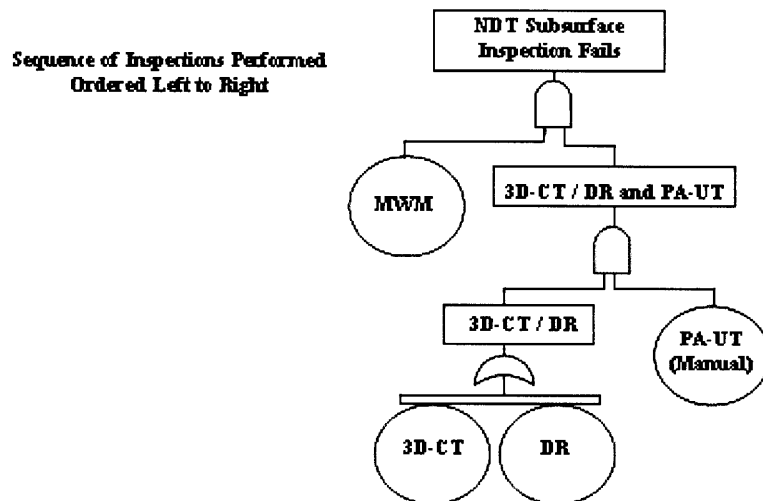


Figure 6.20: Reliability block diagram for the case of continued blade surface inspection after sufficient inspection history results are incorporated into the digital database

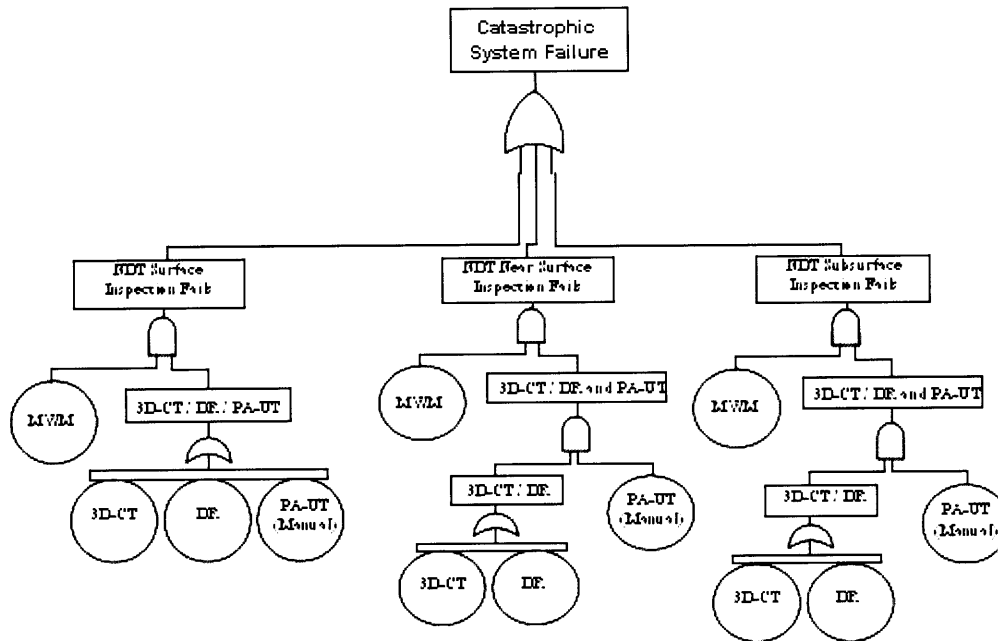


Figure 6.21: Reliability block diagram for the case of continued 100% blade component inspection after sufficient inspection data has been incorporated into the digital database

6.4 Discussion of Cost-Benefit Analysis

The cost of maintenance for aging aircraft is becoming a significant issue for the aerospace industry as the expected service lives of these aircraft are reached and surpassed. It has been mentioned that the risk of catastrophic failure increases with prolonged service life. Previous incidents such as the United Airlines Flight 232 crash in Sioux City, Iowa in 1989 [119], and more recently an uncontained engine failure in Pensacola, FL in 1996 [125], illustrate the importance of a robust NDT program to detect service flaws. Even if catastrophic failure does not occur the harsh operating environment of critical engine components, and in particular those in the HPT, LPT and HPC sections of the engine, can force an airplane to be grounded due to required (and unplanned for) maintenance and repair procedures. Table 6.3 provides some average costs associated with in-service maintenance costs. The average costs included in Table 6.3 were obtained from [216].

In 1978, the Airline Deregulation Act was passed which removed government control over fares, routes, and the creation of new commercial airlines. These changes

Table 6.3: Average costs associated with in-service maintenance or aircraft

<u>Cause of Maintenance</u>	<u>Associated Average Cost</u> (in 2009 dollars \$)
In-flight engine shutdown	\$500,000
Flight cancellation	\$50,000
Return to gate	\$15,000
Ground damage costs	\$850 million/year (Estimated by Airline Transport Association for entire aviation industry)
Each ground damage incident	\$70,000
Error (predominantly caused by human factors but all types of error in general)	\$75-\$100 million/year (Estimate for entire aviation industry)

brought about a surge in competition for commercial airline carriers, which in turn brought passenger ticket prices lower [214]. Passengers are currently paying on average half as much as in 1978 for airfare, when prices are compared on the basis of net present dollars. The cost of catastrophic failure was quantified for the four relevant Category 3 and 4 airplane accidents that occurred during the 1989-2009 timeframe, and which resulted from traditional NDT techniques missing detectable flaw sizes during in-service inspections that should have been observed. The dollar amounts calculated for the analysis of the costs associated with catastrophic failure were all normalized in terms of 2009 dollars. The equivalent past and present dollar amounts associated with the costs were calculated from (6.32) and (6.33).

$$(P/F, i, n) = \frac{1}{(1+i)^n} \quad (6.32)$$

$$(F/P, i, n) = (1+i)^n \quad (6.33)$$

In the above equations, a single payment present-worth factor or single payment compound amount factor was used with P equal to the present dollar amount, F equal to the future dollar amount, i equal to the interest rate, and n equal to the number of years between present and future times. The annual inflation rate can be determined from (6.34) and (6.35).

$$f_{t+1} = \frac{CPI_{t+1} - CPI_t}{CPI_t} \quad (6.34)$$

$$CPI_t(1+f)^n = CPI_{t+n} \quad (6.35)$$

In (6.34) and (6.35), f_{t+1} is the annual inflation rate for year $t+1$, and CPI is the consumer price index which is related to inflation and measures the changes in retail prices to maintain a fixed standard of living for the “average” consumer. The average annual inflation rate was calculated from data obtained at [219] for the time period of 1989-2009 relevant to this analysis. It was determined the average annual rate of inflation was just about 3.0%. Since 1980, the airlines have struggled, losing a cumulative \$20 billion since airline deregulation [214]. Therefore, the benefit gained from keeping components in-service past their certified design life via implementation of the advanced NDT inspection methodology must be significantly greater than the costs associated with the purchase of advanced NDT equipment and increased overall inspection time required.

From 1984-1989 industry data showed about 40% of turbine engine rotor cracking and failure events were caused by manufacturing induced anomalies [14]. During that same time period, uncontained engine failures due to raw material, manufacturing, and maintenance induced anomalies occurred at a rate of 1.2 per 10 million flights or approximately 3 events per year [2, 4, 9, 14]. In response to the Sioux City crash the FAA, engine manufacturers, raw material suppliers, and others in industry reevaluated many of the quality control practices in place, and documented guidelines to prevent future uncontained engine failures caused by metallurgical anomalies [28, 36, 220]. The efforts of these agencies has resulted in a sharp drop in air fatalities from all causes in the last two decades, from a rate one fatal accident in nearly 2 million departures in 1997 to one fatal accident in about 4.5 million departures in 2007 [123].

Despite this improvement in passenger safety, the risk of catastrophic in-service failure from aging aircraft is currently increasing due to the sheer magnitude of aircraft being operated near or past their intended design life. As of 1999, the number of US and European built civil aircraft over 15 years old was about 4,750, and the number greater than 25 years old was approximately 2,150 [21, 109]. From 1982-2006, airline activity has risen by more than 35% [118], and the number of U.S. domestic commercial flights is conservatively estimated at 20,000 daily [214]. The FAA has regulatory authority under Title 14, Part 121 of the Code of Federal Regulation (CFR). FAA Advisory Circular documents [1-4, 6, 7, 13, 14] have stated that if a RFC-type life approach were to be adopted by an airline, its use should not attempt to extend the approved safe-life of a

component. The position currently taken by the FAA is that the increased risk of catastrophic failure associated with operation of critical LLP's beyond FAA certified life limits would result in an unacceptable risk to the flying public. However, the methodology proposed earlier in this chapter is unlike any prior enhanced life management methodologies. The redundancy built into the model provides a robust framework geared specifically toward prevention of catastrophic failure never seen before. With the continued operation of an ever-aging fleet of commercial aircraft, the need for a paradigm shift toward implementation of technologically advanced NDT processes is more tangible now than ever for the aerospace industry. The use of state-of-the-art NDT processes in lieu of traditional techniques has been shown to reliably detect smaller flaws with greater sensitivity. The POD analysis and theory contained in Chapters 5 and 6 show the feasibility of an RFC approach with minimum detectable flaw size as the quality metric. Feasibility of the methodology must now also be demonstrated with the performance metric being lifecycle maintenance cost.

The costs associated with catastrophic airplane accidents resulting from failures in the traditional NDT inspection system approach are given in Table 6.4. From the table, a select set of cost parameters can be observed for the four relevant Category 3 and 4 events during the 20 year analysis period. The value of life used by the Department of Transportation (DOT) in estimating the cost of fatality was quoted as \$1.5 million (in 1996 dollars) from [209]. Placing a monetary value on human life is extremely difficult but essential to a cost-benefit analysis quantifying catastrophic failure. The future earning potential of the deceased individual can drastically alter the value of life from the quoted amount. In the literature, a \$15 million dollar settlement for an individual fatality in the Sioux City, IA crash was found. In addition to the cost associated with fatality, the cost associated per serious injury was estimated at \$350,000 (in 1996 dollars). The costs associated with damage to the aircraft for the four accidents were obtained from NTSB reports [119, 125, 208-212], and are also included in Table 6.4. The sum of the total primary costs associated with catastrophe were calculated for the year each specific accident occurred, and then that value was adjusted for inflation into 2009 dollars. The summation of net present costs for the four events totals approximately \$350 million (in 2009 dollars). The Sioux City accident in 1989 accounts for more than 80% of this total,

Table 6.4: Costs associated with catastrophic aircraft failure of the relevant data set for time period 1989-2009

	<u>Incident</u>			
	<u>Sioux City (United Airlines Flight 232)</u>	<u>Carrollton, GA (Atlantic Southeast Airlines Flight 529)</u>	<u>Valujet Flight 592</u>	<u>Pensacola (Delta Airlines Flight 1288)</u>
Parameter				
Year	1989	1995	1995	1996
# Fatalities	111	8	0	2
# Serious Injuries	47	12	1	2
Cost per Fatality	\$1,184,927	\$1,457,301	\$1,457,301	\$1,500,000
Cost per serious injury	\$276,483	\$340,037	\$340,037	\$350,000
Cost associated with fatalities	\$131,526,885	\$11,658,409	\$0	\$3,000,000
Cost associated with serious injuries	\$12,994,698	\$4,080,443	\$340,037	\$700,000
Cost associated with damage to aircraft	\$21,000,000	\$5,000,000	\$4,000,000	\$15,000,000
Total primary costs	\$165,521,583	\$20,738,852	\$4,340,037	\$18,700,000
Net present costs adjusted for inflation to (2009)	\$286,993,429	\$29,232,063	\$6,117,419	\$25,607,663

largely due to the enormous number of casualties. Failures resulting from human errors not related to in-service tear-down inspections, such as pilot error, were not deemed relevant to this analysis. Additionally, other forms of maintenance error, such as improper de-icing of wings, were not included.

There are additional “peripheral” costs not listed in Table 6.4 that are incurred when a significant accident occurs. In particular, no monetary values for costs associated with litigation were calculated, although it is assumed that value would be near 10-20% of the total adjusted value. Damage to an airline’s reputation after involvement in a catastrophic failure is a difficult cost to quantify, but a significant cost nevertheless. It was found in the literature that Valujet lost an estimated \$55 million in sales revenue in the 7 months following the 1996 Flight 592 crash in the Florida Everglades [210, 211]. Damage to corporate reputation often lingers for some time, because the consumer public is generally hesitant to fly a particular airline if they have recently been involved in a serious accident. Costs associated with environmental damage caused by crash impact were not considered, but could add an additional few million dollars to the total value

calculated for the cost of catastrophic failure. The “safe-life” and enhanced “safe-life/damage tolerant” life management methodologies were specified in all four cases, yet those approaches still failed to prevent the very thing they were supposed to (and which dictates their overly-conservative and uneconomical model of component life management). For each of these events, the failure was a latent event rather than an active event. In more than one instance, the flaw that initiated and propagated to failure remained undetected for an extended dormancy period. The length of dormancy ranged from about a year to almost 18 years. During this time, the aircraft remained in-service and the traditional NDT techniques did not exhibit the sensitivity or zone coverage to reveal the anomaly’s presence. The proposed methodology calls for both increased service inspection and the use of state-of-the-art techniques. This dormancy period could be viewed as an additional opportunity timeframe to detect a given anomaly with the advanced NDT approach.

Typically, the engines on a commercial aircraft represent about 20-25% of the total acquisition cost. Metal alloys account for 80% of jet engine components due to the severe operating environment and need for to compensate for component complexity during machining [221]. Ni-base superalloys and Ti-alloys comprise the bulk percentage of the metal alloy components. Appendix B goes into greater depth on the topic of material selection constraints associated with critical turbine engine components. Despite efficiency improvements in engineering and manufacturing operations, the escalation in engine system costs can be attributed primarily to the increased use of more expensive structural components and assemblies [221]. The extensive alloying in Ti- and Ni-alloys makes them ultrasonically noisy materials. This leads to greater risk for missed detections with traditional UTI techniques than with the redundant advanced NDT methodology proposed, which allows use of fully automated PA-UT, semi-automated PA-UT, and 3D-CT techniques. The inability of traditional inspection techniques to characterize the noise distribution and quantify the contribution from the microstructural noise to the inspection S/N ratio limits their POD capability for critical aerospace components. Because of this, an overly conservative “safe-life” methodology is required. However, studies indicate that nearly 80% of parts replaced at safe-life limits have at least a full order of magnitude of their fatigue life remaining [217]. Based on this statistic, the potential for substantial

cost savings to airlines that can keep high-value critical rotating components *safely* in-service for even a fraction of their remaining fatigue life is evident.

Turbine engine disks run anywhere between \$30,000 and \$300,000 per disk with approximately 20 disks per engine. For simplicity, it will be assumed that there are 5 total turbine section (HPT+LPT) and 15 total compressor section (HPC+LPC) per engine on average. Additionally, it will be estimated that the turbine section disks average \$200,000/disk and the compressor section disks average \$100,000/disk. This results in a total disk cost of \$2,500,000 per engine. If there are 1000 total engines in the entire commercial airline fleet, the monetary implication skyrockets to \$25,000,000,000 for a single airline fleet. This number does not take into account depreciation of the disks as they age, which could end up reducing this overall cost by a factor of 2. However, the replacement costs for disks are high because of the significant manufacturing precision required and need to use premium Ni-base superalloy raw material stock. This has created a fast-growing segment of the aircraft industry that specializes in service repair and rejuvenation. Billions of dollars can potentially be saved by aircraft carriers if FAA regulation allowing companies to abandon the “safe-life/damage tolerant” inspection methodology for the redundant advanced-NDT RFC approach is approved. Until then, application of the proposed methodology to military aerospace components will serve as the proving ground for the reliability and predictive capability gained by the methodology. The Air Force approximates that from 2004-2013, \$750 million can be saved by use of the TESI fully automated PA-UT system on military disk components [140]. If the methodology is successful for military components, the commercial side of the industry will most likely follow suit and transition to the new RFC approach.

The service of airplane components is becoming a larger source of revenue, because it's much cheaper to inspect and put engine components back into service rather than replace them. This has led to intensified competition between original equipment manufacturers (OEMs) and maintenance, repair, and overhaul facilities (MROs). MROs create more service options around the world, while OEMs are more aggressively seeking to increase aftermarket revenue due to slumping new part sales [222]. An interesting example is Pratt & Whitney (P&W), who are an OEM that decided to enter the MRO business. P&W doubled their service revenue from 2003-2008, in part by offering parts

and maintenance for a competitor's engine, CFM International's CFM56 engine [222]. There is international debate over the validity of the process, referred to as PMA (Parts Manufacturer Approval) [218]. For 2007, P&W's revenue was on the order of \$12.1 billion; 45% of this was from sales of new parts on the OEM side of the company, but 55% was from MRO [223]. Additionally, MRO sales for Pratt increased 30% from 2006 to 2007. The North American MRO market was valued at \$16.1 billion in 2009, and is expected to grow to \$18.9 billion by 2019 [222]. With increased uncertainty of the quality and mechanical properties of critical life-limited aerospace parts manufactured under PMA regulations, the benefit gained from a robust, redundant in-service NDE inspection methodology is substantial. OEMs and MROs use failure modes effects criticality analysis (FMECA) to assess the engine fleet reliability. However, both OEMs and MROs continually end up having to revise reliability predictions based on actual operating experience as it is accumulated [175]. This is because a statistically significant amount of service experience is required to make reliability predictions, and such experience is obviously missing when new engine designs are introduced into the market. Often OEMs use past experience with similar engine designs to make reliability predictions and users must wait a few years before enough data is accumulated to make reliable predictions [175]. Implementation of the advanced NDT methodology suggested in this chapter has been shown to generate more accurate structural component reliability predictions, predominantly from the Bayesian approach to updating posterior and conditional probabilities, as well as from the increased value of information gained via redundant techniques with overlapping detection capabilities. Successful application of the proposed NDT systems approach to remnant life methodology could result in greater MRO market share to be captured by the company that can correctly transfer the approach to specific high-value components. Additionally, the opportunity to reverse engineer a competitor's parts is gained by including 3D-CT in the redundant NDT systems approach. The proposed methodology adds further value at no additional cost when this factor is considered.

In addition to acquisition related costs, MRO costs for aircraft in service typically represent nearly 50% of the overall life-cycle cost of military aircraft. This percentage is not quite as high for commercial aircraft, due to the more aggressive mission profile

required of military aircraft resulting in greater damage accumulation rates. The elimination of premature failures in the field, efficient inspection techniques, reduced maintenance actions, and rapid tool-less production of spare parts are areas identified as having significant cost impact [140]. Although no specific jet-engine subsystem stands alone in relative cost inefficiency, a review determined that the nozzles, HPC, and HPT sections represent the best opportunity to maximize cost benefits resulting from metals-development activities [221]. In the aerospace industry, there is a trend toward the increased use of MC simulations and FEA analysis instead of actual design-of-experiment (DOE) testing to validate new engine designs. While an increase in computational turbine engine validation in lieu of experimentation can save time, money, and decrease the time to market implementation for new engine designs [224-226], it also increases the potential for invalid design assumptions to go unnoticed and unchecked. In an effort to further increase turbine inlet temperatures that have basically reached their design limit, OEMs have begun to alter the microstructures of critical components by adding trace amounts of exotic materials such as Rhenium and Hafnium [227]. Also, OEMs are using increasingly more complex cooling schemes, especially on turbine blades. Undesired consequences resulting from these design changes are usually not recognized until after in-service component failures occur. The daily cost associated with grounding a fleet of aircraft while solving an unexpected engine design error is estimated at 10X more than the maintenance costs for a teardown inspection [15, 32, 109, 216]. Because of this, the criticality of a robust NDT methodology to identify design errors prior to structural failure is greater than ever before.

Approximate costs for disks were estimated at \$100,000-\$200,000. Blades are not individually as highly valued as disks, but there are many more blades than disks in an airplane engine. This results in a nearly equal total component cost per engine. It is assumed the cost of blades can vary from \$5,000-\$12,500. Blade repair and rejuvenation procedures can potentially allow not only an additional 2nd service life to be achieved, but in certain cases a 3rd service life. However, if the repair or rejuvenation process is performed incorrectly, the result is a blade worth only its scrap metal value that cannot be put back into service. Additional risks are assumed with turbine blade rejuvenation processes when human error factors are considered. One relevant example was the ASA

Flight 529 accident in Carrollton, GA, where engine failure occurred as a result of an MRO technician incorrectly labeling a damaged blade as acceptable for re-use. In instances such as this, the ability to automate the inspection process can mitigate the risks associated with human error. After the recent failure of a weld-repaired F402 engine compressor blade, a decision was made to use the MWM-array® technique to inspect all of the 10,000 blades potentially affected by the faulty weld-repair process [91]. An automated inspection setup, similar to the one shown in Figure 2.12, has inspected over 8,000 of these blades to date and has detected numerous blades with weld-repair defects. The positive indications from the MWM-array® system have been verified on a subset of the blades with radiography, and *no false indications have been reported* [91]. The estimated cost savings from implementation of the MWM procedure for this specific short-term titanium blade weld inspection was over \$200,000 [91], however from a cost perspective the benefit is even more substantial when a long-term view of maintenance for aging structural engine components is taken. This is because the cost burden associated with the initial capital investment required in purchasing the advanced NDT system decreases with time. This is true for all of the proposed advanced NDT techniques.

The two performance characteristics used in the cost-benefit comparison between the advanced and the traditional NDT processes were equipment cost and inspection time. A ballpark estimate for the cost of the MWM-array® equipment, including the Gridstation® software, is about \$75,000-\$100,000 per system. If a large OEM or MRO were to implement the proposed methodology, numerous systems would obviously be required to inspect the multitude of components constantly entering the inspection stream. On the other hand, a traditional eddy current system, such as the UniWest™ single channel point probe system, only costs around \$5,000-\$10,000. Traditional eddy current array systems can significantly vary in cost, but \$25,000 per system is a reasonable estimate. The inspection time per blade is around 1-2 minutes for the MWM-array® technique in a fully-automated mode. Traditional eddy current techniques are approximately 10X-100X slower than this. If 100 advanced MWM eddy current systems were needed to handle the inspection demand at a production facility, and were bought at a bulk discount rate of \$50,000/system, the “sunk” equipment cost would total \$5 million.

The equipment cost for the traditional eddy current systems would be \$1.5 million if 50 point probes were bought at \$5,000/system and 50 traditional array probes were bought at \$25,000/system. Therefore an additional \$3.5 million would be required up front to pay for the more advanced eddy current system.

The cost of an industrial computed tomography system varies, and depends on many parameters including the voltage capacity, focal spot size, and maximum sample size that can be inspected. A 600keV compact CT system, capable of industrially inspecting blades, costs in the neighborhood of \$300,000 [196]. As voltage increases so does cost, and an 800keV system of similar capabilities costs around \$400,000-\$500,000 [196, 197]. Not including the time for reconstruction, a blade could be scanned with one of these systems in about 5-10 minutes. The prices for such compact CT systems have significantly decreased over the past decade as the technology has improved and become more industrially accepted. Also, the added value gained from the reverse engineering of components via 3D-CT cannot be achieved with any other radiographic techniques. Computed tomography systems capable of inspecting larger and denser components such as disks would need to have a voltage capacity anywhere in the 1MeV to 6MeV range. This would require the use of a linear accelerator as the radiation source and additional radiation shielding protection, which would increase the system cost to somewhere on the order of \$1 million per system. This higher 3D-CT system equipment cost compared to other radiographic techniques is currently the main barrier to implementing computed tomography on a large scale in the aerospace industry.

The equipment costs for digital radiography, on the other hand, are not prohibitively high when compared to traditional x-ray film processing. Typical DR systems are about twice as expensive as film processing systems and cost around \$125,000, meaning a traditional film x-ray system costs approximately \$60,000 [60]. In addition, the systems costs for DR are dropping while the costs of the film based systems are staying the same or increasing. In an industrial production inspection environment, it has been estimated the DR system cost of inspection per blade is around \$25 [91]. Digital radiography requires an image plate, which can cost around \$550 to \$700 per system. This is about the cost of 100 sheets of x-ray film, but the image plate can be used up to 5,000 times, so in terms of this parameter there is a benefit to going digital [60]. A

secondary benefit to DR over film radiography is the elimination of expensive hazardous waste removal of the chemicals required to develop the film. For each x-ray film system transitioned to a DR system, an annual savings of \$200,000 has been estimated based on the elimination of this waste removal cost [60]. The time required for inspection depends on the component being evaluated and the desired exposure, but for DR systems this is generally under 5 minutes for most aerospace components. With film x-ray inspection systems however, the required exposure time can considerably vary. For instance, the exposure time for blades is on the order of 1-2 minutes, which is comparable to DR, while for components with a longer aspect ratio (AR) the required inspection time can be over 20 minutes per exposure [60]. Both digital radiography and x-ray film radiography permit adjustment of a sample to a particular orientation, while 3D-CT systems are less flexible in this regard. As was seen with the post-weld tip cracked turbine blade in Chapter 4, proper sample orientation can significantly influence POD. Finally, as was observed with the DR image of the turbine blades in Appendix D, multiple blades can be accurately inspected on a single image plate (i.e. a single exposure). Generally, only one blade per exposure is capable with film radiographic systems due to the decreased focal range.

For certain structural components, digital radiography is the optimal radiographic NDT technique to be used with the proposed methodology, when reliable inspection data in a digital format is needed at the lowest cost. However, because 3D-CT provides information on the location and depth of potential flaws, it must be the technique initially used with the proposed RFC approach. Once enough inspection data has been generated for the digital database to rule out the presence of a subsurface defect, a switch from 3D-CT to DR could be made. Also, because the phased array ultrasonic inspection technique would be performed concurrently with the 3D-CT inspection, fewer inspections would be needed before an informed decision to switch to DR could be made. It is at this moment in the lifecycle of a structural component where the benefit of converting to the new proposed three-parameter POD quality metric is particularly significant to the overall cost effectiveness of the methodology. The 3D-CT/PA-UT correlation parameter is very significant to minimizing risk when the decision to shift from 3D-CT to DR is made. If both techniques indicate an anomaly is present, the probability that a flaw is actually

present is significantly increased over the case where only one of the advanced techniques is used. Aristotle's quote, "*The whole is greater than the sum of its parts.*" describes the situation well. In instances where either the 3D-CT or PA-UT inspection technique results in a potential subsurface indication, the component should be removed from service for further evaluation until a conclusive determination can be made. It is recommended that after the switch to DR is made no more than three consecutive DR inspections should occur between sequential 3D-CT scans, so that if the subsurface microstructural condition of a component is altered during service it has a better chance of being detected prior to catastrophe. The purchase of a number of both 3D-CT and DR systems would be required if these recommendations were scaled up to the level of an industrial OEM or MRO facility. A substantial investment on the order of \$10-20 million would be required per facility to cover the capital equipment costs of these advanced systems. Additional funds would also be required to set up a computer network that would store the digital inspection database for every component inspection. This is considerable when compared only to the costs associated with traditional radiography.

The cost of phased array systems similar to the Omniscan® equipment used for the experiments in Chapter 3 have also dramatically decreased in the past decade. In the mid-1990's NDT equipment such as this sold for around \$200,000, but that has dropped to only \$60,000 in recent years [160]. The portability of the PA-UT equipment and gear is also much improved over past models. The simplest traditional UT equipment is also hand-held and portable, and is intended for discontinuity detection and thickness gauging. A reasonable estimate for that system's cost would be \$10,000, while more elaborate traditional systems cost around \$25,000-\$30,000 [66]. Industrial production traditional UTI systems are often modular and cost around \$50,000. Other hardware, such as immersion tanks, water squirting systems, laser sound generation, and automated scanning systems can add another \$50,000 to the total cost [66]. For instance, the six-axis industrial robot used with the fully automated TESI PA-UT system alone adds \$65,000-\$100,000 to that system's equipment cost [100]. Since the TESI system is not commercially available, it is difficult to provide an estimate on that system's overall cost. However, since the TESI system utilizes off-the-shelf components as much as possible, certain equipment costs can be calculated. One of these is the cost for the actual phased

array transducer in comparison to a conventional flaw transducer. The multi element PA transducer costs around \$6,000 while the traditional transducer only costs about \$350 [139]. Over the life span of the ultrasonic NDT equipment, replacement costs for transducers and similar peripherals can add up. The multi-element phased array has a longer lifespan than a traditional ultrasonic flaw transducer, and can still remain functional despite damage to a single element or channel (although a loss in overall sensitivity an POD will occur). The inspection time can be drastically reduced by using a contact PA-UT modular system instead of an ultrasonic system that relies on the rastering back and forth of a single element in the X and Y directions. Inspection times are similar between the fully automated water immersion PA-UT and conventional C-scan water immersion systems.

Based on the above analysis, the added equipment costs for the advanced NDT systems of the proposed methodology may seem prohibitively high when a short-term outlook to component maintenance is made. However, when the potential long-term benefits of applying such a redundant inspection philosophy to structural components are made, the possible return on investment is overwhelming. For aerospace in particular, it is estimated that the transition to the proposed NDT inspection methodology can allow an additional $\frac{1}{2}$ service lives for disk and blade components. This estimate takes into account all potential “knockdown” factors previously discussed, and also includes an additional safety factor comparable to FAA imposed values. Based on the cost savings in replacement parts alone, an estimated \$1 billion per engine can be saved over the life of an aircraft by the proposed RFC approach. Additionally, if use of the proposed methodology can prevent one significant aircraft accident from occurring (per 20 year time period), costs ranging anywhere from \$10 million to \$1 billion can be avoided, depending on the severity of the crash and number of fatalities avoided. As equipment costs continue to decrease for advanced inspection systems, the feasibility of the methodology becomes increasingly viable from a cost perspective. Finally, automation of the advanced techniques can result in only a marginally increased total inspection time. This is estimated at about 25% more then the current times associated with manual inspection with traditional techniques.

6.5 Obstacles to Implementing Methodology

Despite the abundant cost savings that could be generated, there are significant obstacles to implementing the proposed methodology. Market acceptance of the advanced technologies mentioned is a critical restraint. Aircraft carriers and MRO companies are very risk averse, and the millions of dollars required to purchase the advanced NDT systems is a risk because this approach has never been attempted before. Also, there is currently no industry-wide agreed upon validation process to determine the POD for a particular NDT technique at a location other than at the surface of a component. The transition to a new three-parameter POD metric could allow an improved judgment on the POD of the best NDT techniques at surface and subsurface levels to be made. Aerospace companies are much more willing to purchase a particular NDT system once it has gained market acceptance. For the advanced systems mentioned acceptance is slowly being gained in the aerospace and NDT markets. This is one of the reasons for the significant decrease in equipment costs over the past decade.

The lack of codes and standards is the second significant obstacle to implementation. Codes that reference recommended practices and procedural guidelines for use of the advanced NDT techniques are a requirement in most industries. Some relevant industries that involve the inspection of critical structural components include the nuclear, automotive, petrochemical, transportation, and aerospace industries. Associations and societies that publish industrially accepted standards include ASME, ASTM, API, AWS, and ASNT. As Table 6.5 shows, in recent years many important standards have been published related to the proposed advanced NDT techniques. This is a very critical development in overcoming the barriers to implementation.

In addition to codes, regulatory agencies such as the FAA need to adapt from their current stance that an RFC approach poses too great a risk for catastrophe. The enhanced safe-life/damage tolerant approach has shown in multiple cases to be lacking with respect to the life management of aging aircraft. The proposed methodology has a level of redundancy added to improve the reliability and robustness of the approach, however years of testing may be required by the FAA before the bureaucratic red tape is cut through. Part of this resistance is due to OEMs not wanting an RFC approach allowed, because it cuts into new part sales and results in decreased corporate revenue. Some

Table 6.5: Relevant standards recently issued for the advanced NDT techniques of the proposed methodology

Advanced NDT Technique	Standard/Code (US Only)	Code Description
MWM-Array	ASTM E2338-04	Characterization of Coatings Using Conformable Eddy-Current Sensors without Coating Reference Standards
PA-UT (Primarily Olympus® manual PA-UT but also related to TESI fully automated system)	ASTM E1454	Data fields for Computerized Transfer of Digital Ultrasonic Examination Data
	ASTM E2663-08	Standard practice for digital Imaging and Communication in Nondestructive Evaluation (DICONDE) for Ultrasonic Test Methods
	ASME Code Case 2235-9 (2005)	Use of Ultrasonic Examination in Lieu of Radiography
	ASME Code Cases -2541, -2557, -2588, -2599, -2600	Manual PA-UT using single fixed beam, sectorial scan, linear scan, encoded (automated PA-UT) with E-scans, encoded (automated PA-UT with S-scans)
3D-CT	ASTM E1570-05	Standard practice for Computed Tomographic Examination
2D-DR	ASTM E1475-02 (2008)	Data fields for Computerized Transfer of Digital Radiographic Examination data
	ASTM E1742-08a	Standard practice for Radiographic Examination
Digital Image Analysis	ASTM E2339-06 (revised in 2008)	Standard practice for digital Imaging and Communication in Nondestructive Evaluation (DICONDE)
Digital Image Analysis	Current ASTM E2339-10 (revised in June 2010)	Newest revision to DICONDE standard

MROs are even resistant to a retirement-for-cause life management approach, because of the costs required to train their NDT operators on the advanced techniques. End-user training is a big challenge to implementation. Finally, in order for the methodology to work it must be easily adaptable to new technology as the current “advanced” techniques become mature and ultimately obsolete. The digital database created for each component must be able to account for the addition of new advanced NDT techniques. In this regard the incorporation of the Cellprofiler image analysis program could be beneficial. The

open-end code of the Cellprofiler software allows the individual end-user to easily adapt the program.

Conclusions

Based on the analysis in Chapter 6, it has been determined that a substantial cost savings can be achieved by implementing the proposed redundant NDT methodology despite the increased capital equipment costs associated with the advanced NDT techniques. After considering all the knockdown factors, it is estimated an additional ½ service life factor can be further accumulated by disk and blade components by conversion to an RFC approach. Successful implementation of this methodology would result in approximately cost savings of \$1 billion per engine. Furthermore, the approach calls for an increased quantity of in-service inspections, which should result in a further decrease of air fatalities and Category 3 and 4 events.

The experimental study performed was able to show improved flaw detection sensitivity on the part of the advanced nondestructive testing (NDT) techniques with respect to structural applications. The techniques analyzed exemplify the incorporation of digital technology into NDT and included the meandering winding magnetometer array (MWM-array®) eddy current, phased-array ultrasonic (PA-UT), three dimensional computed tomography (3D-CT), and digital radiography (DR) techniques. Three classes of samples were inspected with these techniques. They consisted of alloy block specimens containing flat bottom hole (FBH) arrays, probability of detection (POD) wedding cake samples, and actual airplane engine components. Results from the sensitivity analyses were compared to current NDT techniques used industrially and it was shown the advanced techniques were superior in their capability for subsurface defect detection. It is subsurface defects that provide the greatest risk for in-service catastrophic failure of aircraft. In the 25 years (circa 1985) since original POD curves were developed approximately a 100-150% improvement in the POD capability of FPI has been achieved due to advancements in NDT technology. Comparatively, the following are approximations for improvements of other NDT approaches versus 25 years ago:

- A factor of 10 improvement (i.e. 10X) in radiography
- A 3X improvement in UTI
- A 2-3X improvement in ECI

The combined use of PA-UT and 3D-CT methods in an inspection program compliments each other and allows a new metric for subsurface flaw detection to be achieved. This metric is based on three parameters and deviates from the single 90/95 POD/CL value currently used. As part of the improved methodology, the development of a new 3-parameter POD metric for characterization of non-surface flaw features is proposed. The three parameters suggested for inclusion in the proposed POD metric are:

- (1) A 90/95 POD/CL parameter @ a particular component depth, D
 - (2) An AR parameter that describes flaw feature orientation @ D
 - (3) A Correlation parameter between positive sub-surface NDT indications
- This would be known as the 3D-CT/PA-UT indicator

Because subsurface defects are inherently three dimensional in nature, a single value parameter is not sufficient in its description of potential flaws. The incorporation of this new metric for subsurface flaws, when integrated with the redundant NDT approach and automated image analysis software enable a retirement-for-cause approach to be utilized for structural applications.

The Cellprofiler image analysis program was used to optimize the threshold correction factor for selected radiographic results. The output from this program was analyzed in conjunction with POD software. The integration of digitally advanced NDT techniques with image analysis software was found to improve the minimum detectable flaw size at the 90/95 POD/CL level by 200-300%. Future work aimed at optimizing parameters in the image analysis software, modifying the Cellprofiler software code to work for 3D-CT batch analysis, and developing new pipelines for PA-UT and MWM-array® C-scan data could further reduce the detectable threshold flaw size by a factor of two at the 90/95 level.

An improved inspection methodology was presented which incorporated redundancy in the in-service inspection plan with the use of Bayesian updating techniques to forecast remnant life. Reliability block diagrams for structural disk and blade aircraft engine components were presented as examples of the methodology. Finally, implementation of the proposed NDT methodology was analyzed from a cost perspective rather than a POD perspective. The feasibility of implementing the suggested

retirement-for-cause (RFC) approach is cost-effective for aging structural components when high value structural components are able to remain in service for significantly extended amount of time without catastrophic failure occurring. Recommendations on ways to implement more cost-effective digital techniques without sacrificing NDE reliability were made. Obstacles to implementing the proposed NDT methodology were discussed. Many of these obstacles are actively being addressed by the NDT industry.

This page intentionally left blank

Appendix A: Nomenclature

a : Size of discontinuity, flaw, or target. Physical dimension of a target – can be its depth, surface length, or diameter of a circular discontinuity, or radius of semi-circular or corner crack having the same cross-sectional area.

\hat{a} , a -hat: Measured response of the NDE system, to a target of size, a . Units depend on inspection apparatus, and can be scale divisions, counts, number of contiguous illuminated pixels, or millivolts.

a_{50} : Target size at 50% POD

\hat{a}_{dec} , decision threshold: Value of \hat{a} above which the signal is interpreted as a hit, and below which the signal is interpreted as a miss. It is the \hat{a} value associated with 50% POD. Decision threshold is always greater than or equal to inspection threshold.

\hat{a}_{sat} , saturation: Value of \hat{a} as large, or larger than, the maximum output of the system or the largest value of \hat{a} that the system can record.

\hat{a}_{th} , inspection threshold, signal response threshold: Smallest value of \hat{a} that the system records; the value of \hat{a} below which the signal is indistinguishable from noise. Inspection threshold is always less than or equal to decision threshold.

AC: Advisory Circular. Document published by FAA recommending best practices for aerospace industry

AIR: Aerospace Information Report

α : Constraint factor

AMI: Acoustic Microscopy Imaging

ANSI: American National Standards Institute

APB: anti-phase boundary

ASIP: Aircraft Structural Integrity Program

ASNT: American Society for Nondestructive Testing

ASTM: American society for Testing and Materials

ATMC: Advanced Technology and Manufacturing Center at UMass Dartmouth

ATOS: Advanced Topometric Sensor (or Scanner)

AWS: American Welding Society

BCT: Body Centered Tetragonal crystal structure

$\hat{\beta}_0 \hat{\beta}_1$: Maximum likelihood estimators of parameters β_0, β_1

C: Crack length in width direction, in.

C_{1i} : Crack-growth coefficient for segment i

C_{2i}
Crack-growth power for segment i

Calibration: Process of determining the performance parameters of a system by comparing them with measurement standards.

CAD: Computer Aided Drafting (or Drawing)

CAO: Civil Aviation Overall engine category, including CT, GA, and RC

categorical variable: Discrete variable having levels that are inappropriately described by simply assigning them a numerical code, and instead have a measurement scale based on categories.

CCGR: Creep crack growth rate

CDF: Cumulative Distribution Function

CDR: Correct Detection Ratio

censored data: Signal response either smaller than \hat{a}_{th} , and therefore indistinguishable from the noise (left censored), or greater than \hat{a}_{sat} (right censored), and therefore a saturated response. Censored data require specialized statistical techniques because their likelihood function differs from uncensored observations at the same value.

Central Limit Theorem: The distribution of an average tends to be normal, and regression model parameters tend to be asymptotically multivariate normal. Thus while the assumption of Gaussian behavior is not always appropriate for physical parameters, it is often justified for regression parameters.

CHM: Cold Hearth Melting

CMC: Ceramic Matrix (or Metal) Composite

CMM: Coordinate Measuring Machine

Coefficient: Engineers and mathematicians say coefficient; statisticians say parameter, but these are not synonymous terms. A coefficient is a multiplier in a mathematical formula. A parameter is a numerical characteristic of a population or statistical model. μ, σ are parameters of the normal density. Their coefficients here are understood to be 1. The confusion arises in situations like this: $y = \beta_0 + \beta_1 x$, where β_0 and β_1 are model parameters, but β_1 is also the coefficient of x . Engineers and mathematicians see β_0 and β_1 as known, and x as unknown to be solved for, while

statisticians view (x, y) pairs as observed data and therefore known, from which the unknown β_0 and β_1 must be inferred.

Component feature: A unique location, structural shape, or surface of a component or part. For a disk, a component feature would be blade slots, bore or web locations. Other examples are grooves, slots, or holes. Usually different machining processes and practices are required to produce each unique feature.

Component event rate: The number of events for a given rotor component stage for each engine cycle, averaged over the projected life of the component.

Components of variance: In a designed experiment the total observed variance can be apportioned to its components (e.g.: probe, operator, underlying variance) so that improvements in inspection performance are possible, or the causes of substandard performance can be identified.

Conditional probability: Probability of one variable, given the value of another, and given the model parameters: $f(x|y, \Theta)$ where f is the probability of x by itself, given specific value of variable y , and the distribution parameters, Θ correlation A measure of the linear relationship between two variables. For example, when $-z < x < z$, the correlation between x and x^2 is zero.

Confidence: The long run frequency of being right. The maximum likelihood value for a_{90} is a best estimate for the target size with 90% POD, and so about half the time it is smaller than the true, but unknown, value and otherwise it is larger. A 95% confidence value for a_{90} (called $a_{90/95}$) will be greater than the true a_{90} , in 95% of similar experiments.

C-SAM: C-scan Scanning Acoustic Microscopy

C(T) : Compact specimen

CT: 1) Commercial Transport Engine Category
2) Computed Tomography

da/dN: Fatigue Crack Growth Rate

Damage Tolerance, DT: An element of the life management process that recognizes the potential existence of component imperfections that are the result of inherent material structure, material processing, component design, manufacturing, or usage. Damage tolerance addresses this situation through the incorporation of fracture resistant design, fracture-mechanics, process control, or nondestructive inspection.

Default POD values: Values representing mean probabilities of detecting anomalies of various types and sizes, under specified inspection conditions, and consistent with good industry practice.

ΔK : Stress-intensity factor range, ksi $\sqrt{\text{in}}$.

ΔK_{eff} : Effective stress-intensity factor range, ksi $\sqrt{\text{in}}$.

$(\Delta K_{\text{eff}})_T$: Effective stress-intensity factor range at flat-to-slant crack growth, ksi $\sqrt{\text{in}}$.

DEN(T): Double-edge-notch tensile specimen

Detection: Affirmative NDE system response, not necessarily rejectable

Disparate data: “Apples and Oranges” data – inspection data from difference specimen sets (usually from different equipment with different operators, probes, procedures) dubiously grouped to form one dataset.

DOE: Design of Experiments – Statistical methods for assigning test conditions to produce the maximum information with minimal expense.

DR: Digital Radiography

DTR: Design Target Risk value, the standard against which probabilistic assessment results (stated in terms of feature, component, and engine level event rates) are compared.

EASA: European Aviation Safety Agency

ECI: Eddy Current Inspection

EDM: Electrical Discharge Machining

EDR: Excess Detection Ratio, also known as ratio of false positive indications

EIFS- Equivalent initial flaw size

EM- Electromagnetic

ENSIP: Engine Structural Integrity Program

Engine event rate: The cumulative number of events predicted for a given anomaly type for each engine cycle, for all rotor life-limited parts in a given engine, calculated over the projected life of those components.

EQS: Electroquasistatic. Regime in which IDEDs operate in

ϵ :Random error between assumed statistical model and measured system response

ETC : Engine titanium consortium

Event : A rotor structural part separation, failure, or burst, with no assessment of consequence.

FAA: Federal Aviation Administration

Factor: Variable whose effect on POD(a) is to be evaluated, especially a categorical variable, e.g. operator or probe

False positive; false call: NDE system response interpreted as having detected a target when none is present at the inspection location.

FBH : Flat Bottom Hole

FCC : Face Centered Cubic crystal structure

FCGR : Fatigue crack growth rate

FCP: Fatigue crack propagation

FE: Finite Element

FEA: Finite Element Analysis

Fitness for service: Capability of a component or system to perform its intended function under given circumstances for a specified period of time.

FM: Fracture Mechanics

Focused inspection: Inspections in which any necessary specialized processing instructions have been provided, and the inspector has been instructed to pay special attention to specific component features.

FOD: Foreign Object Damage

FPI: Fluorescent Penetrant Inspection, also LPI (liquid)

Full field inspection: General inspection of a component without special attention to any specific component features.

FSH: Full scale height

GA-General aviation category of aircraft

Gamma-prime γ' : Microstructural feature in Ni-base superalloys

GB: Grain Boundary

GEAE: General Electric Aircraft Engines

GLM: Generalized Linear Model, a regression having a binary (or otherwise non-continuous) response, such as hit/miss.

HA: Hard Alpha anomaly

HAD aka Type II: High Aluminum Defect, defined as an aluminum-rich alpha stabilized region which may extend across a large number of beta grains

Hard time inspection interval: The number of engine cycles since new or since the most recent inspection, after which a rotor part must be made available and must receive the inspection specified in the Airworthiness Limitations Section (ALS) of the Instructions for Continued Airworthiness (ICA).

HCF: High Cycle Fatigue

HDI: High Density Inclusion. This is a region with a high concentration of refractory elements having a higher density than the matrix

HEE: Hazardous Engine Effect, limited to the non-containment of high-energy debris. Disks, hubs, impellers, large rotating seals and other similar large rotating components represent potential sources of high-energy debris

HID (aka LDI or HA) aka Type I: An alpha phase region of substantially higher hardness than the surrounding material. The higher hardness often results in a brittle alpha phase, and is caused from very high localized nitrogen, oxygen, or carbon concentrations that increase the beta transus

HIP: Hot Isostatic Pressing

Hit: Affirmative NDE system response: detection

Hole feature: A set of one or more circular holes at the same axial and radial location where any given hole falls at least partially within the circumferential (diametral) shadow of the largest hole and its size is greater than 25% of the diameter of the largest hole.

HPC: High Pressure Compressor section of engine

HPT: High Pressure Turbine section of engine

HS- Hamilton standard

%IACS: International Annealed Copper Standard. Eddy Current Inspections are compared to %IACS values

ID: Inner diameter

IDED: Interdigitated Electrode Dielectrometer sensor

IN718: Inconel® 718: A Ni-base superalloy used heavily in aerospace engine components

Independent: Two variables, A and B, are independent if their conditional probability is equal to their unconditional probability – A and B are independent if, and only if, $P(A|B) = P(A)$, and $P(B|A) = P(B)$. In engineering terms, A and B are independent if knowing something about one tells nothing about the other.

Inference : Process of drawing conclusions about a population based on measurements of samples from that population.

Inspection opportunity: An occasion when an engine is disassembled to at least the modular level and the hardware in question is accessible for inspection, whether or not the hardware has been reduced to the piece part level.

Inspector: Person administering the NDE technique who interprets the results and determines the acceptance of the material per specifications.

IQI: Initial quality Indicator

Joint probability: The probability of two or more things happening together, $f(x, y | \Theta)$ where f is the probability of x and y together as a pair, given the distribution parameters, Θ . A joint probability density two or more variables is called a multivariate distribution.

K: Stress-intensity factor, ksi $\sqrt{\text{in}}$.

K_{Ic} : Elastic stress-intensity factor at failure, ksi $\sqrt{\text{in}}$.

LDA: Linear Detector Array

LCF: Low cycle fatigue

Likelihood: The “probability of the data,” given specific model parameters, i.e. the probability that the experiment turned out the way it did.

Likelihood ratio method: Method for constructing confidence bounds based on the asymptotic χ^2 (chi-square) distribution of the log-likelihood. The likelihood ratio method produces confidence bounds on hit/miss POD(a) curves that are closer to their nominal values than does the Wald method.

LLP: Life Limited Part. Critical rotor or major static structural component whose failure is likely to result in a hazardous engine event.

Low Cycle Fatigue (LCF) Initiation.: The process of progressive and permanent local structural deterioration occurring in a material subject to cyclic variations, in stress and strain, of sufficient magnitude and number of repetitions. The process will culminate in detectable crack initiation typically within 10^5 cycles. FAA AC's state the detectable crack initiation is 0.030 inches in length and this length defines when the useful life of the part is exhausted. The term “detectable crack” does not refer to nor define inspection requirements and does not apply to the service or the manufacturing environments. The term is used by engineering to set life limits.

LPC: Low Pressure Compressor engine section

LPT: Low Pressure Turbine engine section

LSP: Laser Shock Peening (or Processing)

Maintenance exposure interval: Distribution of shop visits (in flight cycles) since new or last overhaul that an engine, module, or component is exposed to as a function of normal maintenance activity.

Manufacturing anomaly: A surface-related imperfection introduced during the manufacturing process (subsequent to melting) that is considered potentially detrimental to the structural integrity of the critical rotating part during its service life.

MAPOD: Model-Assisted POD – Methods for improving the effectiveness of POD models that require little or no further specimen testing.

Marginal probability: Probability of one variable for all possible values of another: $f(x|\Theta)$ where f is the probability density of x , for all possible values of y , given the distribution parameters, θ . The marginal probability of x is determined from the joint distribution of x and y by integrating over all values of y .

Maximum likelihood: Standard statistical method used to estimate numerical values for model parameters such as β_0 and β_1 by choosing values that are most likely to have produced the observed outcome.

MC: Monte carlo simulation technique

Mean POD: The 50-percent confidence level POD versus anomaly size curve.

Miss : NDE system response interpreted as not having detected a target when one was present.

Mixed models: Statistical models for which the influence of a factor is described with a probability density rather than with individual parameter values.

MMC: Metal-Matrix Composites

Module: A combination of assemblies, subassemblies, and parts contained in one package, or arranged to be installed in one maintenance action.

MPI: Magnetic Particle Inspection

MQS: Magnetoquasistatic. Regime MWM-arrays operate in.

MRO: Maintenance, Repair, and Overhaul facility

MWM-array: Meandering winding magnetomer

N : Number of cycles

NDE/NDT: Nondestructive evaluation/testing, which encompasses both the inspection itself and the subsequent statistical and engineering analyses of the inspection data

NDE system: Ensemble that can include hardware, software, materials, and procedures intended for the application of a specific NDE method. Can range from fully manually operated to fully automated.

NDI : Nondestructive inspection. Often used interchangeably with NDE, however should apply only to the inspection itself and not the subsequent data analysis.

NIST: National Institute of Standards and Technology

Noise: Signal response containing no useful target characterization information

NPV: Negative predictive value, $P(\text{no defect} \mid -)$: probability that the part is defect-free, given a negative indication.

NTSB: National Transportation Safety Board. Organization that inspects accidents and determines probable causes of failure.

OD: Outer diameter

OEM: Original Equipment Manufacturer

Operational induced anomaly: A surface imperfection that is introduced during service operations (includes flight operations and maintenance) that is potentially detrimental to the structural integrity of the critical rotating part.

Ordinal variable: Categorical variable that also has a hierarchical order. For example, “good,” “better,” “best,” are ordinal variables, and are based on an ordinal scale, where the distances between the ordered categories is unknown.

Parameter: A numerical characteristic of a population or statistical model. μ, σ are parameters of the normal density.

Part available: A part that can be inspected, as required by the ALS of the ICA, without any further disassembly. Depending on the inspection requirements, some parts may require a fully disassembled “piece part” condition, while other parts may be available for inspection while still in the assembled module.

PA-UT: Phased array ultrasonic testing

PDF: Probability Density Function- A function of a continuous random variable that describes the relative likelihood for this variable to occur at a given point in the observation space. The probability of a random variable falling within a given set is given by the integral of its density over the set.

PFP: Probability of False Positive, or false call. $PFP = 1 - \text{specificity}$

P/M: Powder metallurgy processing technique

POD, $POD \mid a$: Probability of detection, given target a exists. $POD = \text{sensitivity}$

POD(a): The fraction of targets of nominal size, a , expected to be found, given their existence.

POF: Probability of Failure

PPB: Prior particle boundary defect

PPV: Positive predictive value, $P(\text{defect} \mid +)$: probability that the part has a defect, given a positive indication.

PRF: Pulse repetitive frequency

Probabilistic risk assessment: A fracture-mechanics based simulation procedure that uses statistical techniques to mathematically model and combine the influence of two or more variables to estimate the likelihood of various outcomes for a product. Since not all variables may be considered or may not be capable of being accurately quantified, the numerical predictions are used on a comparative basis to evaluate various options. Results from these analyses are typically used for design optimization to meet a predefined target or to conduct parametric studies. This type of procedure differs from an absolute risk analysis, which attempts to consider all significant variables, and is used to quantify, on an absolute basis, the predicted number of future events with safety and reliability ramifications.

probability : i) Frequentist definition – the long-run expected frequency of occurrence, $P(\text{event}) = n/N$, where n is the number of times event occurs in N opportunities. ii) Bayesian definition – a measure of the plausibility of an event given incomplete knowledge. Both definitions of probability follow the same mathematical rules.

R : Powerful open-source (free) software environment for statistical computing and graphics.
<http://www.r-project.org/>
 ISBN 3-900051-07-0. The mh1823 POD software uses as its computational and graphics engine.

R : Stress ratio (S_{\min}/S_{\max})

r : Hole radius, mm or in.

RC- Rotorcraft class of aircraft

Regression: Statistical model of the influence independent variables (e.g.: target size, probe type) on system output signal (\hat{a}). Also called a “linear model.”

Repeatability and reproducibility: Two potential components of variance. Repeatability often refers to equipment variation, with a single operator. Reproducibility often refers to the influence of different operators, using the same instrument to measure nominally identical characteristics. NOTE: these definitions are not universally agreed on and the usages of “reliability,” “repeatability,” “reproducibility,” “variability” and “capability” are often contradictory.

Residual : Difference between an observed signal response and the response predicted from the statistical model. Residuals are only defined for non-censored observations.

ROI: Region of Interest

ρ : Electric charge density

S : Applied stress, ksi

S_{\max} : Maximum applied stress, ksi

S_{\min} : Minimum applied stress, ksi

S_{peak}
 Highest applied gross stress in spectra, ksi

SAE: Society of Automotive Engineers

Safe-life: A low cycle fatigue-based process in which components are designed and substantiated to have a specified service life, which is stated in operating cycles, operating hours, or both. The “safe life approach” requires that parts be removed from service prior to the development of an unsafe condition (i.e. crack initiation). When a component reaches its published life limit, it is retired from service.

SDH: Side Drilled Hole

Sensitivity: Probability of a true positive: $P(\text{detection} \mid \text{target present})$

SEN(T): Single-edge-notch tension specimen

σ_u : Ultimate tensile strength, ksi

σ_{ys} : Yield stress (0.2 % offset), ksi

SHM: Structural Health Monitoring

SII: Safe Inspection Interval

S/N ratio: Signal to Noise Ratio

Soft time inspection interval: The number of engine cycles since new, or the most recent inspection, after which a rotor part in an available module must receive the inspection specified in the ALS of the ICA.

SP: Special Publication

Specificity: Probability of a true negative: $P(\text{no indication} \mid \text{no target present})$

Stage: The rotor structure that supports and is attached to a single aerodynamic blade row.

System operator: The person responsible for an automated or semi-automated system, including the assuring that the mechanical, electrical, computer, and other systems are in proper operating condition.

Target: Object of an inspection. It can be a crack, flaw, defect, physical or chemical discontinuity, anomaly, or other origin of a positive NDE response.

τ : Standard error of residuals of regression of \hat{a} against a .

TBC: Thermal barrier coating

TCG: Time-corrected gain

TCP: Topologically close packed phase. An undesirable phase due to its plate like morphology

TESI: Turbine Engine Sustainment Initiative

TIT, T_{it} : Turbine Inlet Temperature. A major determinant of an engine’s thrust to weight ratio

TMF: thermo-mechanical fatigue

TOF: Time of Flight

UDRI: University of Dayton Research Institute

USAF: United states Air Force

UT/UTI: Ultrasonic testing/inspection

VAR: Vacuum arc remelt process

VI: Visual Inspection

VIM: Vacuum induction melt process

YSZ: Ytria Stabilized Zirconia: Used in TBC coating

Wald method: Method for constructing confidence bounds on \hat{a} vs a curves, and POD(a) curves derived from them, based the asymptotic normal distribution of the model parameters. The Wald method is less often used in recent years for hit/miss POD in favor of the likelihood ratio method which produces confidence boundaries that are closer to their nominal values. For \hat{a} vs a data the difference between the Wald method and the likelihood ratio method are negligible.

X-ray: Radiographic X-ray Inspection

3D CT: Three dimensional computed tomography NDT technique

90/95 POD/CL: The minimum crack length at the 95% confidence level (CL) from which at least 90% of all cracks greater than this length will be detected. Value is used as a one-number metric for NDE system capability.

Appendix B: Critical Turbine Engine Components

A typical gas turbine engine for an airplane consists of an inlet, a low pressure compressor (LPC), high pressure compressor (HPC), combustor, high pressure turbine (HPT), low pressure turbine (LPT), and exhaust section. Various numbers of stages comprise the compressor and turbine sections. Figure B.1 is a schematic of one such engine type, a two-spool turbofan. Turbofans are used in high subsonic commercial transport aircraft where engine weight and fuel consumption are important design considerations [179, 228, 229]. The inlet delivers and diffuses the air flow demanded by the compressor, while the fan and compressor does work on the air to raise its stagnation pressure and temperature. The combustor is where heat is added to the air at approximately constant pressure. The turbine extracts work from the air to drive the

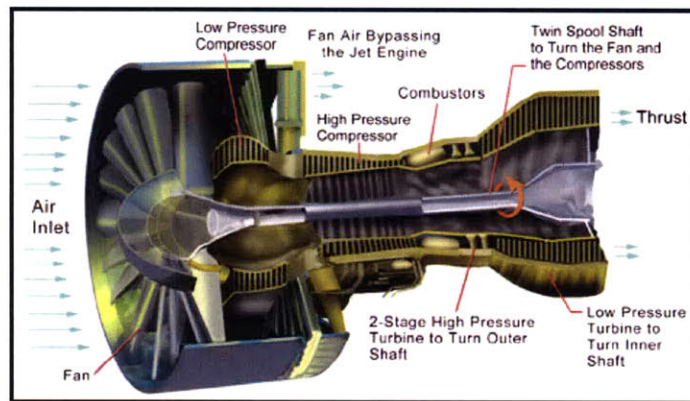


Figure B.1: Cross section view of typical gas turbine engine (reprinted from [230])

compressor and to power the aircraft via thrust. Lastly an exhaust nozzle raises the velocity of the exiting mass flow, and exhaust gases reject heat to the atmosphere at constant pressure [228]. The two-spool design imposes four constraints on the compressor-combustor-turbine subsystem. The first is that the LPC-LPT low speed spool and HPC-HPT high speed spool have independent rotor speeds. Flow compatibility between the spools requires aerodynamic coupling, which sets a ratio between the rotor speeds. The second constraint is mass flow conservation, and the turbine mass flow is required to equal the compressor mass flow. Third is a need for power balance across the compressor-turbine in both the low pressure and high pressure spools, since the turbine provides the power to drive the compressor. The last constraint is energy balance across

the combustor, since the stagnation enthalpy rise across the combustor is determined by the fuel/air ratio and the heat of combustion [179, 228, 229]. When these constraints are not met, off-design conditions such as engine surge and stall may occur that impose added stresses on engine components and increase the risks associated with engine failure.

The majority of the remaining discussion on critical engine components will be limited to disks and blades in the HPT, or “hot section” of the engine. As Figure B.2 shows, it is in the HPT section where the operating environment and temperature demands on these parts are greatest. However, as the previous paragraph explained, the HPT and HPC are intimately related due to aerodynamic constraints. For this reason, Section C.3 on non-HPT critical components in the HPC section has been included. Two main factors drive the design differences between turbine and compressor engine sections. The high turbine inlet temperature (TIT), T_{t4} , introduces material design problems such as the need for blade cooling schemes to prevent localized melting of components. Since the pressure falls through the turbine section, the tangential Mach number is lowered, which eases aerodynamic problems [228]. Conversely, since the pressure ratio rises

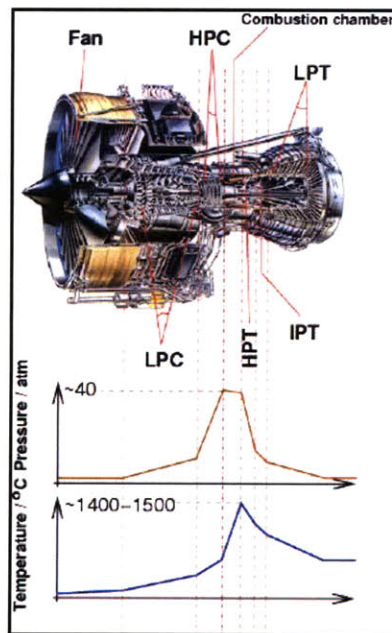


Figure B.2: Temperature and pressure demands in different engine sections (reprinted from [231])

through the compressor, the aerodynamic design is critical to ensuring the efficient rise in stagnation pressure ratio with minimal work and losses. These design differences give

rise to the different number of stages required and different alloy materials selected in each section. Typically there are 12-19 stages total for the LPC and HPC, 1-2 stages for the HPT, and 2-5 stages for the LPT in a twin-spool engine [106]. Figure B.3 lists some typical gas turbine component materials, including commercial trade names for many Nickel-base (Ni-base) superalloys.

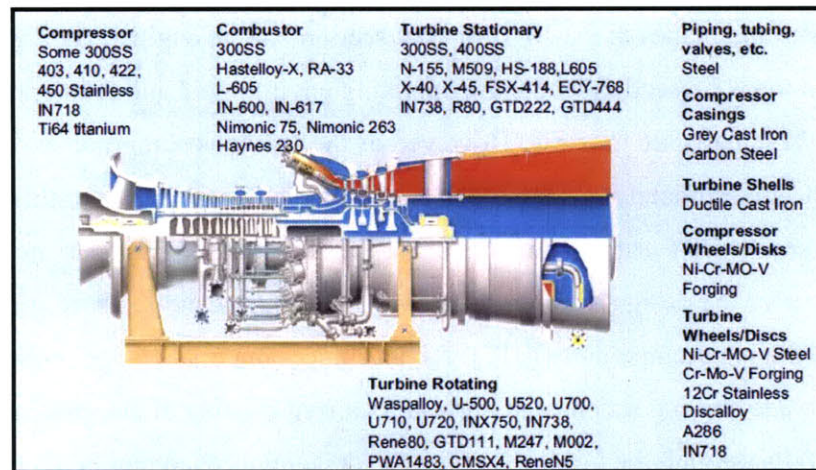


Figure B.3: Typical gas turbine component materials (reprinted from [106])

A performance metric used to judge the efficiency of an engine is the thrust to weight ratio, which is set according to the turbine inlet temperature, compressor pressure ratio, fan bypass ratio, axial Mach number, and engine length. Table B.1 includes data for some original equipment manufacturer (OEM) commercial gas turbine engines at takeoff and cruise flight conditions. Higher operating temperatures, and in particular a higher T_{t4} value, have historically been the primary means of improving aircraft engine thrust [232]. Additionally, a higher T_{t4} requires materials capable of withstanding those temperatures without compromising their mechanical properties. For every 10°C (50°F) increased in the turbine firing temperature, the combined cycle efficiency is improved by approximately 1% [232]. A 1% efficiency improvement results in millions of dollars in fuel savings on a fleet-wide basis.

The first propulsion jet engine was patented by Sir Frank Whittle in 1929. Named after its inventor, the first Whittle engine flew in 1941. The hot section components of these early engines utilized stainless steels. Whittle's original 840 pound engine generated a thrust/weight ratio of roughly 3:2 and could operate for a few hundred hours at most [41]. During the 1950's, materials available for gas turbine engines were

improved in temperature capability via alloy development and melt process improvements. The evolution of the vacuum induction melting (VIM) and vacuum arc remelting (VAR) processes permitted the elimination of detrimental trace elements, and the addition of the reactive elements titanium and aluminum to nickel based alloys

Table B.1: Comparison of commercial gas turbine engine efficiencies at takeoff and cruise flight conditions (adapted from [179])

Model No.	OEM	<u>Takeoff</u>				<u>Cruise</u>				
		Thrust, (lbf)	BR ^a	OPR ^b	Airflow, (lbm/s)	Alt, (kft)	Mach #	Thrust, (lbf)	TSFC ^c	Application
CF6-50-C2	GE	52,500	4.31	30.4	1,476	35	0.80	11,555	0.630	DC10-10, A300B, 747-200
CF6-80-C2	GE	52,500	5.31	27.4	1,650	35	0.80	12,000	0.576	767-200, -300, -200ER
GE90-B4	GE	87,400	8.40	39.3	3,037	35	0.80	17,500		777
JT8D-15A	P&W	15,500	1.04	16.6	327	30	0.80	4,920	0.779	727, 737, DC9
JT9D-59A	P&W	53,000	4.90	24.5	1,639	35	0.85	11,950	0.646	DC10-40, A300B, 747-200
PW2037	P&W	38,250	6.00	27.6	1,210	35	0.85	6,500	0.582	757-200
PW4052	P&W	52,000	5.00	27.5	1,700					767, A310-300
PW4084	P&W	87,900	6.41	34.4	2,550	35	0.83			777
CFM56-3	CFM Intl.	23,500	5.00	22.6	655	35	0.85	4,890	0.667	737-300, -400, -500
CFM56-5C	CFM Intl.	31,200	6.60	31.5	1,027	35	0.80	6,600	0.545	A340
^a BR = bypass ratio ^b OPR = overall pressure ratio ^c TSFC = thrust specific fuel consumption										

spawned the superalloy age [41, 233]. From 1950-1970 the TITs increased from 730 °C to 950 °C (1350-1750 °F). Design, alloy development, alloy processing and manufacturing improvements during the years 1970-1985 further increased T_{it} from 980-1120 °C (1800-2050 °F) [106]. In the past 25 years, the use of thermal barrier coatings (TBCs) and more efficient blade cooling schemes have enabled inlet temperatures in the 1260-1430 °C (2300-2600 °F) range to be realized [41, 106, 180, 234, 235]. Today, commercial jet engines have thrust/weight ratios of 6:1 and higher [41], largely due to increased thrust capability as a result of nickel-base superalloy development. There is a

cost associated with this increased thrust/weight ratio. Designing engines to prevent failure of their critical rotating turbomachinery becomes increasingly difficult due to the metallurgical effects of service on these components.

The operating conditions for hot section disks and blades are very severe and result in many potential modes of failure. Thermal gradients and stresses from load variations, especially during takeoff, result as a consequence of the cyclic start-up and shutdown nature of flight. Thermal stresses result from the tendency of materials to expand with increasing temperature [229], and lead to thermo-mechanical fatigue (TMF) and TBC spallation problems. For example, temperatures vary from about 150°C (300°F) at the hub up to 750°C (1382°F) at the rim of disks, and 550°C (1025°F) at the base to around 1100°C (2015°F) at the tips of turbine blades during operation [180, 228, 236]. During cruise, engines operate for considerable periods of time where conditions are constant, and the effects of these “hold times” gives rise to mixed-mode creep/fatigue interactions. High temperature creep and LCF are important failure modes to consider, as they frequently initiate at microstructural weak links in a component such as grain boundaries (GB). High cycle fatigue (HCF) is an important failure mode for aging aircraft. Overload and wear are damage mechanisms that can occur during rare off-design or service events and can be very difficult to account for in remnant life prediction analyses. Environmental attack in the form of oxidation, corrosion, and sulfidation are constant threats to hot gas path components. Figure B.4 is an example of the material degradation that can occur due to environmental attack.



Figure B.4: Example of the deterioration of mechanical properties of an in-service engine component due to environmental attack [190]

As Figure B.5 shows, the metal temperatures in the hot section are high enough that microstructural aging occurs [106]. Throughout service life in Ni-base parts, continued

growth of gamma-prime (γ') particles takes place by diffusion. This occurs as a way to minimize interfacial energy. In addition, the likelihood of foreign object damage (FOD) from ingested debris, undetected manufacturing flaws, handling damage during maintenance, or abnormal engine operating conditions may each add a level of unpredictable damage to parts [237]. A robust NDT methodology is required to account for these many sources of service accumulated damage.

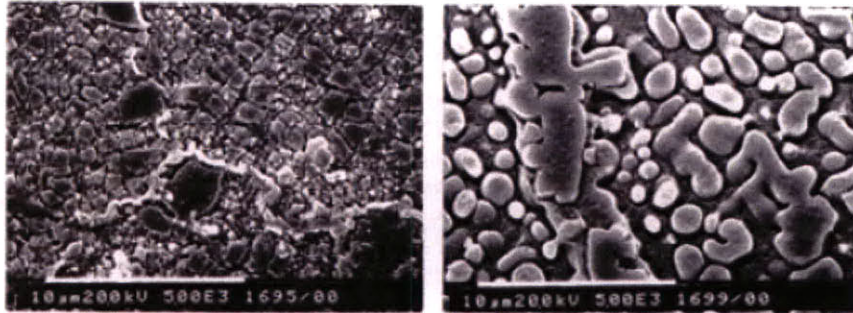


Figure B.5: Microstructural aging of γ' in Alloy IN738 after 24,000 hours of service (reprinted from [106])

As the previous paragraph has illustrated, the harsh conditions of critical HPT components can result in a myriad of failure mechanisms. Over 40% of engine failures are located in the turbine section [237]. The life cycle cost of turbine engines depends strongly on the durability of these hot section constituents. Refurbishment and repair processes are performed to return service exposed components to a usable condition, and restore metallurgical properties following extended use damage [106]. While these life extension processes can add value there are risks involved if parts are improperly treated. The extreme temperature and high gas flow velocity currently exclude the possibility of placing active sensors in the engine to monitor these parts [43]. The use of state-of-the-art NDT techniques during scheduled engine tear-down maintenance periods has the potential to detect and monitor these numerous forms of service damage prior to catastrophic failure. The failure mechanisms for disks and blades are distinct resulting from their geometrical design and service requirements. An individual assessment for both disks and blades will subsequently follow.

B.1 Disks

The need to manufacture disk components from Ni-base superalloys to withstand the harsh operating environment has previously been discussed. In addition to the

thermal stresses induced in disks, the rotational velocities required for operation cause centrifugal stresses to be a significant concern in turbine disk design. Nominal rotational speeds during operation in the range of 10,000-15,000 RPM have been reported [75, 236, 238]. In most high performance engines, certain locations on the disk are locally stressed above yield during high load conditions such as take-off [236]. Most engine parts are designed to be contained in the event of failure to allow for safe engine shutdown. Disks however cannot be contained. An important design criterion for disks is the “burst speed” at which the disks fails and separates in smaller pieces. The burst speed is typically 1.3-1.4 times the design speed [229]. Uncontained engine failures due to disk rupture have resulted in catastrophic failure and loss of life [2, 3, 5, 119, 125]. The potential for uncontained failure has resulted in the designation of disks as “critical” components, and causes NDT to be a vital factor in their life management.

Most turbine disks are cast and then forged into shape, and have a conventional dovetail design for blade attachment. Figure B.6(a-b) shows a typical disk and dovetail

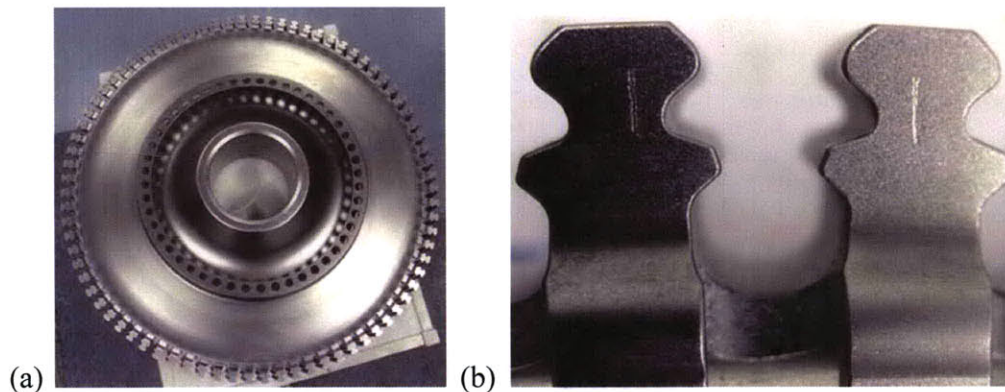


Figure B.6: (a) Typical turbine disk design (b) Dovetail attachment at disk rim

cross-section. The fir-tree slots and serration fitting of the dovetail attachment shown in Figure B.6(b) represent the most critical location in a disk from a LCF standpoint [238]. Fretting fatigue in this region of the disk is a cause for concern in both turbine and compressor disks [239]. The other critical regions in a disk are the assembly holes and the hub zone. Blisks, which are bladed disks cast as one piece, will not be considered although Bhaumik [240] provides a discussion on the topic. Geometric envelope requirements for disks include the maximum bore width (which is limited by adjacent parts), the minimum bore radius, and the required rim radius (which is set by the

flowpath and blade fastening) [228]. Operating data, materials data, and functional requirements must all be integrated.

As the operational demands on disks are pushed to new limits, new manufacturing techniques, processing techniques, and alloy development for disks have been evaluated as potential solutions to design dilemmas. The manufacture of bimetallic disks, via hot isostatic pressing augmented by isothermal forging, has been attempted to tailor the mechanical property requirements in the hub and rim section of a disk [241, 242]. Klotz and coworkers [241] found poor control of the deformation and shape of the bimetallic interface as well as internal cracking issues with the disks they manufactured. Articles by Fecht and Furrer [243, 244] provide a detailed analysis on the evolution in processing of turbine engine disk components. An integrated process model for tracking defects in aerospace disks throughout the entire manufacturing route was examined by Kermanpur [245]. The model was applied to a generic disk geometry and it was found that intrinsic defects such as freckles and white spots formed during VAR at mid-radius locations are undesirable because they have a high probability of remaining in the final disk [245]. The use of powder metallurgy (P/M) processing techniques for disk components has been introduced to extend the operating temperature and improve reliability [243, 246-248]. The effect of powder cleanliness on fatigue behavior of P/M disk alloys was shown by Kantzos [249] to be significant. Also, P/M superalloys are subject to their own drawbacks. P/M superalloys contain prior particle boundaries (PPB), which are MC carbides, oxides, and other phases that are harmful because they impede particle bonding and provide crack paths to precipitate $M_{23}C_6$ carbides on grain boundaries [243]. Porosity is also of particular concern because it is a major site for fatigue crack initiation. Silva [248] attempted to characterize the FCGR parameters for P/M disk alloys by analyzing da/dN vs. ΔK curves. Huron and coworkers [250] tried to optimize the major element chemistry of P/M alloys via a multi-iteration design of experiments (DOE) approach. Traditionally, disk alloys have been developed by empirical methods that have involved much iteration, significant cost, and relied on many years of experience. Thermodynamic modeling is seeing an increased presence in the development of new disk alloys [251]. While TD modeling can provide significant cost savings over full scale

component testing, it also underscores the need to have an advanced NDT methodology in place to determine if incorrect assumptions have been made in the model.

The effects of temperature on microstructure and fatigue life in turbine disks have been researched via experimental and computational approaches. Gabb and colleagues [252, 253] examined the relationship between heat treatment, microstructure, and mechanical properties experimentally. They concluded the effects of high temperature exposures, meant to simulate service conditions, reduced component life by up to 70% and increased the scatter in life as compared to unexposed levels [253]. The unexposed samples failed from cracks initiating internally at large grains or Al_2O_3 non-metallic inclusions, while the samples exposed to the 650-704°C (1202-1300°F) temperature in air more often failed from cracks initiating at an environmentally-affected surface layer than from internal sites [253]. Brockman and coworkers [75] estimated damage in turbine engine disks associated with flaws at unknown locations through the combined use of analytical finite element (FE) models and measured vibration signatures. Witek [238] presented a failure analysis model of a turbine disk incorporating extensive FEA of the dovetail-rim area where the disk and blade are joined together. Advanced health monitoring approaches that incorporate both experimental and analytical data are discussed in [254-256]. Abdul-Aziz incorporated image processing, filtering, and segmentation from data collected via an ultrasonic NDT imaging system to this approach in [254]. The combined use of experimental testing on disk samples and rotor finite element models can improve accuracy in damage prognosis and life prediction.

B.2 Blades

The design of turbine blades and vanes has also evolved over the years as inlet temperatures have increased. Polycrystalline conventionally cast and later directionally solidified blade designs have been superseded for a single crystal approach owing to the improved mechanical properties of single crystal turbine blades. Figure B.7 shows the grain structure for these various designs. In addition to the thermal and centrifugal stresses that have been discussed with disk components, blades must also endure bending stresses as the hot gas flows through the engine at high velocity. The axial and tangential gas-dynamic forces generate a bending moment about the root of a blade. The maximum stress due to these gas forces and the largest centrifugal forces are both at the blade root,

making it a critical location for failure [228, 229]. The non-uniformity of the hot gases creates a thermal environment susceptible to a number of failure modes. Oxidation, corrosion, and erosion of blade coatings and base material can be caused by chemical particulates in the hot gas [228, 229]. Creep and thermal fatigue in blades, resulting from prolonged exposure to high stresses at elevated temperatures, is a significant cause for concern. Dynamic mixed-mode creep/fatigue interaction makes remnant life prediction

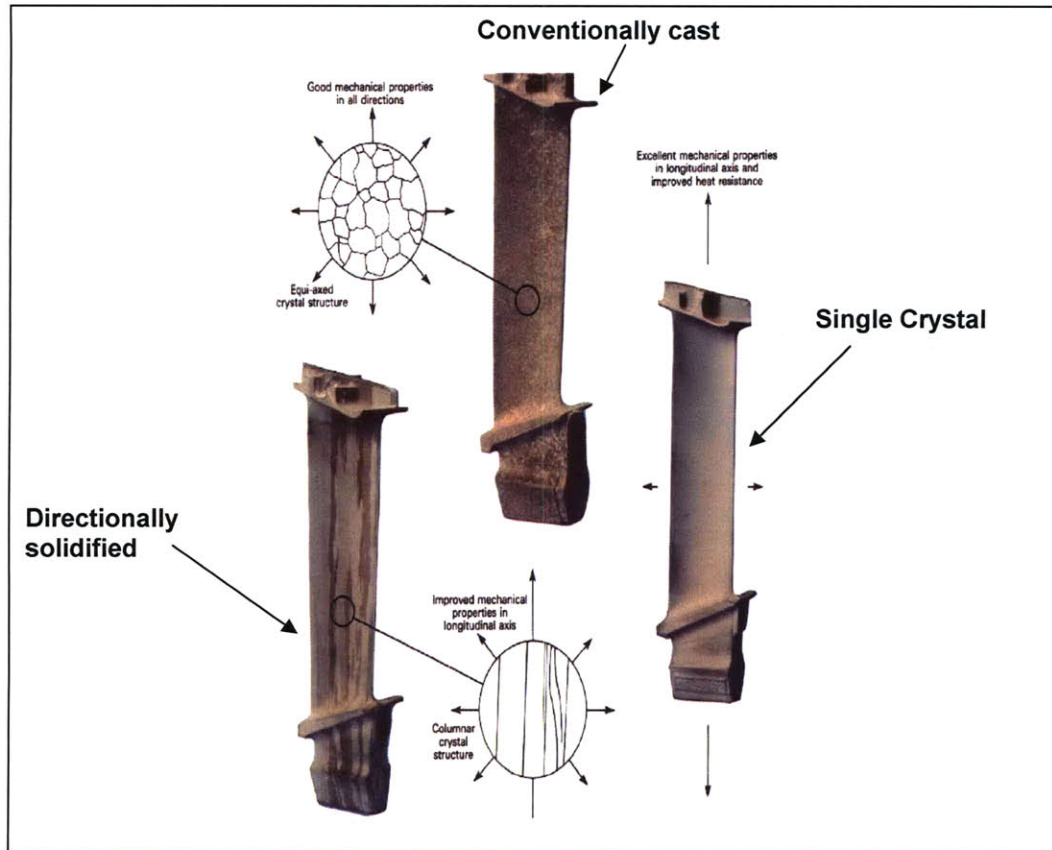


Figure B.7: Evolution of turbine blade design and grain structure (adapted from [228])

especially difficult for turbine blades. Figure B.8 depicts the prevalent blade locations for service induced damage. Figure B.9(a-b) shows an actual turbine blade removed from service that exhibits some of the failure modes described in Figure B.8. Early materials for turbine blade manufacture were based on high temperature steel forgings. Cast Ni-base superalloys are now used in blade manufacture due to their improved creep and fatigue properties over other materials.

To mitigate some of the deleterious thermal effects on blades, complex cooling schemes and thermal barrier coatings (TBC) have been integrated into the design and

manufacture of these critical rotating components. Direct air cooling occurs when air is bled from the compressor section and introduced to turbine blades through their blade roots. Direct air cooling results in the cooling of rotor blade, nozzle vane, casing, and the rim of disk components [228]. The addition of convective cooling from quintuple pass, multi-feed internal cooling channels and film cooling, introduced via 0.015-0.030 inch (0.4-0.8mm) holes and slots, has increased the geometrical complexity of blade designs [179, 229]. Figure B.10(a) shows a cross-section view of the complexity of multi-feed internal cooling channels, while Fig. B.10(b) provides a close up view of the film cooling slots in a turbine blade. While these complex cooling schemes have allowed an increase in turbine inlet temperature, there is an efficiency penalty associated with cooling schemes. Other design considerations with film cooling include hole plugging, hole to hole cracking, and hot zones between holes [228]. Additionally, cooling introduces thermal gradients that may lead to local deformation and cracking in blades.

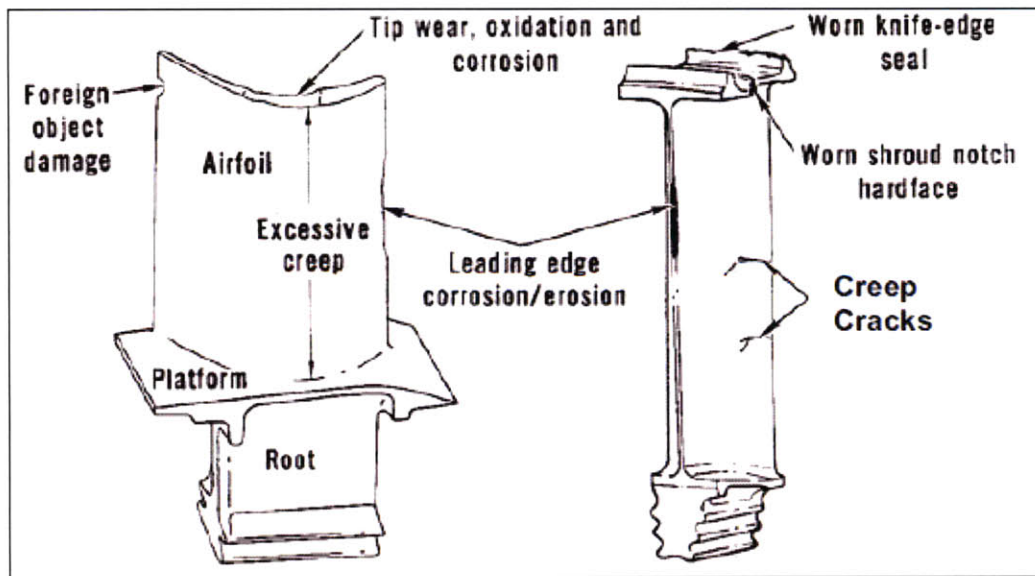
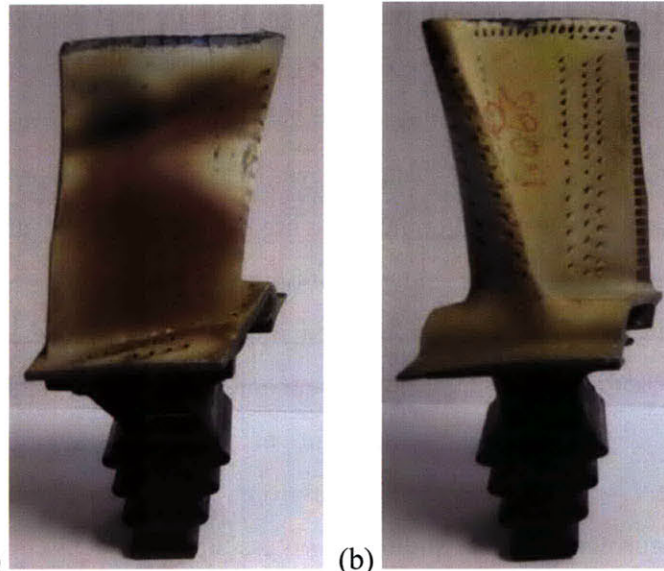
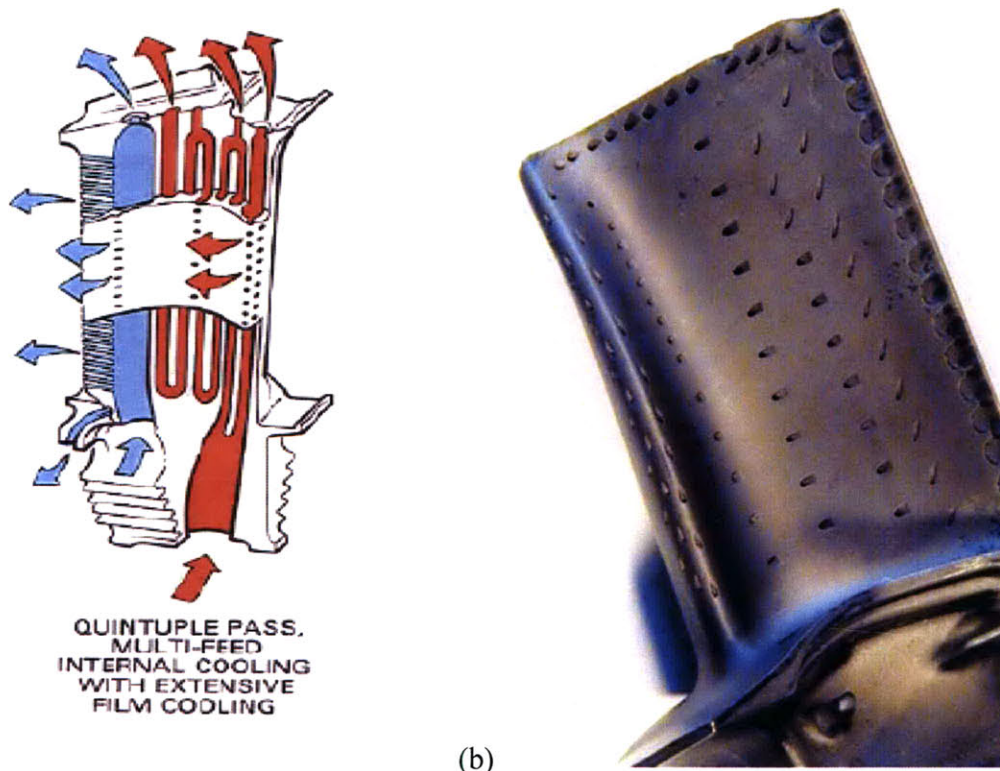


Figure B.8: Locations of service damage on turbine blades (reprinted from [106])



(a) (b)
Figure B.9: (a-b) Turbine blade removed from service exhibiting service damage including FOD, tip wear, oxidation, and leading edge erosion.



(a) (b)
Figure B.10: (a) Cross-section view of the internal multi-pass cooling channels and (b) film cooling slots and holes used extensively in the design of turbine blades (reprinted from [228])

The use of TBCs in conjunction with complex cooling schemes has further improved the effectiveness of cooling turbine blades. As shown schematically in Figure B.11, TBCs usually consist of an yttria-stabilized-zirconia (YSZ) insulating ceramic layer and a MCrAlY corrosion resistant metallic layer [228, 257]. Spallation of the TBC layer produces significant variability in component life expectancy, and Tamarin [257] provides a detailed review on the selection of optimum coatings for modern aircraft engine turbine blades. Critical to the life prediction of turbine blade components is maintaining uniformity in the superalloy base metal. Kerrebrock [229] noted that a difference of 15 °C (27 °F) in local temperature can result in a factor of two change in turbine life at the 975 °C (1787 °F) level. Environmental attack in the form of hot corrosion can occur when salts of sodium or potassium, present as contaminants in fuel, air, or water, deplete the TBC. Sulfur is usually present as a fuel contaminant [258], and it has been found that SO₂ infiltration significantly increases FCP rates [106, 180]. Oxides of vanadium are particularly detrimental to TBC coatings. Walston [259]

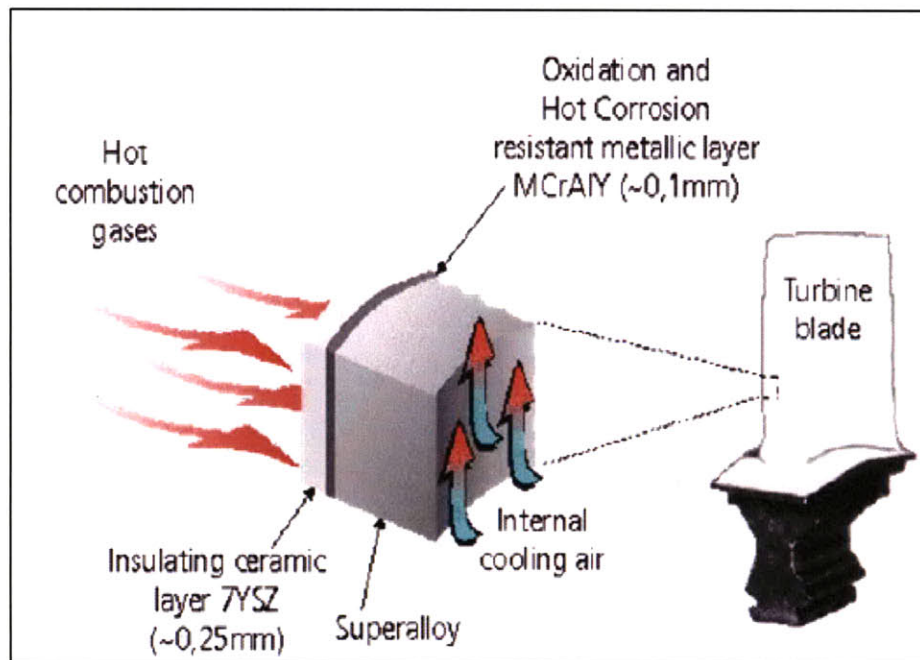


Figure B.11: Cutaway schematic of a thermal barrier coating (reprinted from [228])

discussed potential bond coat improvements for turbine airfoils, such as platinum-aluminide (Pt-Al) coatings or lowering the thermal conductivity of the 7% YSZ layer. Okazaki [260] researched the mechanisms of early crack growth in de-bonded TBCs

under cyclic load. Segregation in single crystal Ni-base superalloys due to carbide formation [261, 262], or ruthenium addition [263] have also been shown to alter microstructure and increase variability in life. Kunz and others [264] looked at the effects of vibration on the lifetime of single crystal alloys subjected to tensile stress, and observed a decreasing lifetime with increasing stress amplitude when fatigue damage due to crack initiation and propagation overrode the beneficial influence of high frequency cycling. A methodology for life extension of turbine blades must account for the potential variability due to these numerous service effects on a part basis rather than by statistical fleet-wide assumptions.

B.3 Non-HPT Critical Components

Thus far, only Ni-base superalloy components in the HPT section of the engine have been considered, however non-HPT components can also be critical to the function of an engine. For example, the premium-grade titanium materials used for fan and compressor rotors and disks may contain brittle “hard alpha” anomalies that form during the triple vacuum arc melting process [4, 203, 220]. Although rare, these hard alpha (HA) anomalies may occur anywhere within a billet if upsets during processing occur, and can change shape during the forging process. If undetected during manufacturing or subsequent field inspection, low cycle fatigue cracks initiated by HA defects can lead to uncontained engine failure [203, 220]. The accident at Sioux City, Iowa [119] is the most prominent catastrophic failure involving HA anomalies in titanium components.

The aerodynamic constraints on the design of HPC components are also a source of life-limiting behavior. High cycle fatigue and foreign object damage are particularly important failure modes considered in the design of fan and compressor airfoils. If blade tip speed is constant, the highest blade stress levels will occur in the first stage of a high pressure compressor [229]. Erosion in compressor blades due to particulates in the air flow stream can result in serious damage [265]. It has been noted in [265] that previous fault detection methods have been unable to suitably detect erosion in compressor blades with sufficient accuracy. Limited data available has added to the inadequacy for fault detection. Since it is aerodynamic and not temperature concerns that drive compressor design, titanium alloys, such as Ti-6Al-4V, or steel alloys are typically used for these components rather than Ni-base superalloys. As shown in Figure B.3, one notable

exception is the use of Inconel® 718 (IN718) in compressor disks due to its combined affordability, machineability, weldability, and good mechanical properties.

Titanium alloys, and in particular Ti-6Al-4V, are known to have microstructures and textures affected by processing that decidedly influence mechanical properties and crack initiation behavior. Whittaker and coworkers [266] examined six microstructural variations of Ti-6-4, and concluded the considerable fatigue life variability of the alloy variations could be attributed largely to grain size effects through the Hall-Petch relationship. Additionally, they determined crystallographic texture was of importance as a secondary effect when considering strain-life. Prismatic slip in the early part of testing accounted for varying degrees of stress relaxation, which in turn influenced fatigue performance [266]. Nalla [267] presented a thorough examination of the microstructural influence Ti-6Al-4V has on HCF for bimodal and lamellar structures. Although differences between the two structures are not large, the coarser lamellar structure has improved smooth bar stress-life (S/N) properties, an approximately 10% higher tensile strength in the HCF regime, and superior resistance to fatigue-crack propagation for pure mode I loading in the presence of cracks that are large compared to the size of the microstructure [267]. Under mixed-mode loading the lamellar structure is generally superior. However, in the presence of microstructurally small cracks, there is little difference in the HCF properties between the bimodal and lamellar structures [267]. The differences in mechanical properties and crack propagation rates between long and short cracks appear to be significant, and current safe-life/damage tolerant methodologies generally neglect these distinct crack regimes in their treatment.

Assumptions made in predictive models, such as in [72] where the impact of the forging process is assumed to have little impact on HA size and shape, can have serious consequences on residual life assessment. In separate case studies for residual life assessments of disks and blades in a land based industrial gas turbine fleet environment, Koul [175, 268-270] states that, “*Safe inspection interval limits based on traditional empirical methods are overly optimistic under creep crack propagation conditions and it is necessary to use physics based crack propagation models to make reliable life cycle management decisions* [269, 270]”. The case studies further acknowledge that use of sensitive inspection techniques at depot level is necessary to avoid catastrophic failures

during service. The materials selected for the disks in these studies included a stainless steel alloy and a Ni-base superalloy. In land-based turbines, the rim region of stainless steel turbine disks rarely exceed 500°C (932 °F) and superalloy disks are not exposed to temperatures greater than 600 °C (1112 °F) [268]. Despite the thermal discrepancies associated with airplane engine components at higher operating temperature, the use of sensitive NDT techniques at depot level inspections for both HPT and HPC components offers the possibility of detecting small regime cracks with greater reliability. The capability afforded by an approach based on advanced NDT is more accurate life prediction on a part-by-part basis. In order to be feasible the approach must take into account the distinct microstructural effects of the various alloys that comprise each component, as well as be cost effective and capable of an efficient total inspection time.

Appendix C: Material Selection for Critical Engine Components

As mentioned in the prior sections, most HPT life-critical components are manufactured from Ni-base superalloys. Disk and blade components in fan and critical HPC compressor sections experience lower operating temperatures. For this reason, Ti-alloys are often specified for these components. The safety of the general public is the guiding principle for the FAA's policy on mandatory inspection intervals and life-limiting of critical airplane engine components. A component is viewed as critical if its failure is likely to result in a catastrophic event (i.e. loss of life or loss of plane). Advisory circulars on best practices for the manufacture of premium nickel and titanium alloy components have been issued by the FAA [4, 5, 13, 14]. A review of the mechanical properties and processing effects of both nickel and titanium alloys is necessary in order to understand the ramifications of these factors on component failure modes.

C.1 Nickel-base Superalloys: Properties and Processing Effects

The compositions of Ni-base superalloys are extremely complex, and over a dozen elements may be present in certain alloys. Aluminum and Chromium are protective scale formers added for oxidation protection. Heavy "refractory" elements, such as molybdenum, niobium, rhenium, tantalum, and tungsten, are added for solution hardening [106, 233]. Precipitation forming elements added for strengthening include aluminum, titanium, and niobium. Carbon, hafnium, zirconium, and boron are added at trace levels to control and strengthen grain boundaries [106]. The primary phase present in such alloys is a FCC austenite matrix (γ) which contains solid solution strengtheners [233, 234]. The solid solution strengtheners are called gamma prime (γ') precipitates, and the γ' phase is based on an ordered $\text{Ni}_3(\text{Al}, \text{Ti})$ structure with Ni atoms at the face centers and Al or Ti atoms at the cube corners. Gamma prime precipitates introduce coherency strains in the matrix inhibiting dislocation penetration, as well as slow deformation via antiphase boundary (APB) formation [180, 233, 271]. Some Ni-base superalloys also contain a gamma double prime (γ'') phase that is an ordered BCT crystal

structure based on Ni_3Nb . These secondary phases are desired and result in excellent high temperature strength, creep resistance, and corrosion resistance properties.

Phases present in Ni-base superalloys that may be deleterious at high concentrations are carbides, borides, and topologically close packed (TCP) phases such as μ , σ , and Laves phases. These TCP phases generally have plate-like structures which promote crack formation [272-274]. Carbides precipitated on grain boundaries are known to be the initiation sites for high temperature creep cracking [275]. Conversely, carbide strengthening, also occurring on the grain boundaries, is desirable for certain superalloys. The control of carbide morphology in Ni-base superalloys is necessary to ensure beneficial and not deleterious properties, as this may be a source of fatigue life variability. The most common carbides found in Ni-base alloys are coarse cubic or script MC type carbides, which are hafnium, tantalum, niobium and titanium rich; fine M_6C type carbides, which are molybdenum and tungsten rich; and blocky M_{23}C_6 type carbides which are chromium rich [106, 233]. In the prior carbide types M is one of the locally abundant metals mentioned. Al-Jarba and Fuchs [261] studied the effect of carbon additions on as-cast microstructure and defect formation in the resulting grain size of single crystal Ni-base superalloys. In other studies on the effects of carbon additions, the choice of forming method as well as heat treatment influenced the microstructure and probability of defect inclusion in the alloy [276-279]. The mechanical properties of a superalloy are a function of the level of solid solution strengthening, the size, distribution, and volume fraction of γ' particles, the grain size, and the effect of carbide precipitation at grain boundaries [106, 233]. Controlling the microstructure and grain size in Ni-base superalloys is of utmost importance to limiting the fatigue variability and optimizing the mechanical properties of the manufactured part.

The processing routes for superalloy disks and blades are distinct, as represented by the process flowchart in Figure C.1. As previously stated, the choice of forming method in tandem with heat treatment selection influences the resulting alloy grain size, and the grain size drives optimal mechanical behavior. Cast, wrought, and powder forms of various alloys are commercially available. Slight modifications to alloy chemistry are often made to tailor an alloy against a particular failure mode, such as thermo-mechanical fatigue [280], creep resistance [251], or others. Many commercially available Ni-base

superalloys for disk and blade applications are based on similar constituent chemistries. Table C.1 lists some of these chemistries for disk components, while Table C.2 has compositions for blade components. The melting temperature for pure nickel is 1453 °C (2647 °F), and the addition of these alloying elements improves mechanical properties such as creep and oxidation resistance, but lowers the incipient melting point. Extensive processing and alloy development the past 30 years has resulted in Ni-base superalloys that can tolerate average temperatures of 1050 °C (1922 °F) and local hot spots near airfoil tips up to 1200 °C (2192 °F) [234].

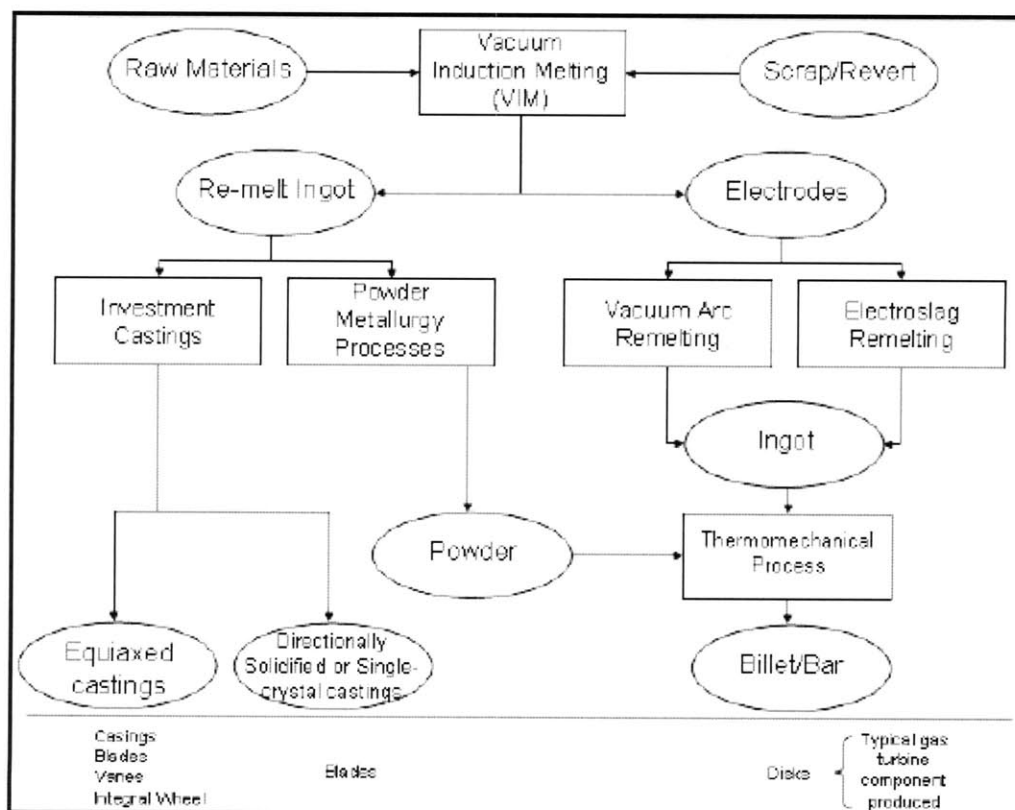


Figure C.1: Processing routes for Ni-base superalloy blades and disks (reprinted from [106])

These temperatures are 80-90% of the incipient melting temperature. As previously discussed, advanced cooling schemes and coating technologies have further extended the turbine inlet temperature.

The FAA has been at the forefront of issuing Advisory Circulars (AC) [5, 6] that recommend best practices for manufacturing premium quality nickel alloy for critical engine rotating parts. FAA data from 1984-1989 indicated that uncontained engine

Table C.1: Chemical composition (in wt. %) of some commercially available disk component alloys

Alloy	Ni	Cr	Co	Mo	W	Nb	Ti	Al	Fe	C	B	Other
Inconel 706	41.5	16	-	-	-	-	1.75	0.2	37.5	0.03	-	2.9(Nb+Ta), .15Cu
Inconel 718	52.5	19	-	3	-	5.1	0.9	0.5	18.5	0.08	-	0.15 Cu
Astroloy	56.5	15	15	5.25	-	-	3.5	4.4	<0.3	0.06	0.03	0.06 Zr
Discaloy	26	14	-	3	-	-	1.7	0.25	55	0.06	-	
IN100	60	10	15	3	-	-	4.7	5.5	<0.6	0.15	0.015	0.06Zr, 1.0V
Incoloy 901	42.5	12.5	-	6	-	-	2.7	-	36.2	0.10	-	
Incoloy 909	38	-	13	-	-	4.7	1.5	0.03	42	0.01	-	
Nimonic 95	52.4	19.5	18	-	-	-	2.9	2.0	5.0	0.15	-	
Nimonic 115	55	15	15	4	-	-	4	5	1.0	0.20	-	0.04 Zr
René 88	56.4	16	13.0	4	4	0.7	3.7	2.1	-	0.03	0.015	0.03 Zr
René 95	61	14	8	3.5	3.5	3.5	2.5	3.5	<0.3	0.16	0.01	0.05 Zr
Udimet 520	57	19	12	6	1	-	3	2	-	0.08	0.005	
Udimet 710	55	18	14.8	3	1.5	-	5	2.5	-	0.07	0.01	
Udimet 720	55	18	14.8	3	1.25	-	5	2.5	-	0.035	0.033	0.03 Zr
Udimet 720LI	57	16	15.0	3	1.25	-	5	2.5	-	0.025	0.018	0.03 Zr
Waspaloy	57	19.5	13.5	4.3	-	-	3	1.4	<2.0	0.07	0.006	0.09 Zr

Table C.2: Chemical composition (in wt. %) of some commercially available blade component alloys

Alloy	Ni	Cr	Co	Mo	W	Ta	Cb	Al	Ti	Hf	C	B	Zr	Other
B-1900	64	8.0	10.0	6.0	-	4.0	-	6.0	1.0	-	0.10	0.015	0.10	
CMSX-2	66	8.0	4.6	0.6	7.9	5.8	-	5.6	0.9	-	-	-	-	
GTD-222	51	22.5	19.0	-	2.0	1.0	0.8	1.2	2.3	-	0.10	0.010	0.01	
IN-738LC	61	16.0	8.5	1.7	2.6	1.7	0.9	3.4	3.4	-	0.11	0.010	0.05	
MarM-247	60	8.3	10.0	0.7	10	3.0	-	5.5	1.0	1.5	0.10	0.015	0.05	
PWA-1483	61	12.8	9.0	1.9	3.8	4.0	-	3.6	4.0	-	0.07	-	-	
Rene-N5	62	7.0	8.0	2.0	5.0	7.0	-	6.2	-	0.2	0.00	-	-	3.0Re
PWA 1480	62	10.0	5.0	0.0	4.0	12.0	-	5.0	1.5	-	0.04	-	-	
PWA 1484	59	5.0	10.0	2.0	6.0	9.0	-	5.6	-	0.1	0.02	-	-	3.0Re

failures occurred at a rate of 1.2 per 10 million flights, which translated into about 3 events per year [5, 13, 14]. Most critical rotating parts were manufactured from a “double-melt” process consisting of VIM+VAR during this timeframe. Improvements in all stages of melt, remelt, and conversion have resulted in a significant reduction in the occurrence of process-induced melt-related defects since the mid-1980’s [5, 281, 282]. In particular the transition to a “triple-melt” process consisting of VIM+ESR+VAR has decreased uncontained engine events.

Despite these processing improvements, defects still have multiple opportunities to work themselves into critical components. The main sources of anomalies are introduced via the raw materials used or due to upset conditions and human errors during the processing, manufacturing, and maintenance steps that encompass a product’s life

cycle. Billet macro-segregation is a result of increasing ingot size, and can be very deleterious to mechanical properties [243, 283]. Segregation causes variations in local transformation temperature, resulting in random grain size variations and grain size banding. Other defects possibly present in billet material include oxides, nitrides, carbo-nitrides (also known as slag stringers), and “white spots”. Carbo-nitrides degrade fatigue resistance capability and result in reduced component life [243]. A white spot is a region of negative alloy segregation generated during the remelt process as seen upon macroetching [5]. “Freckles” are solidification defects that can form in ingot metallurgy alloys from strong local convection currents due to local liquid density differences [243]. Figure C.2 exhibits freckle and white spot defects in IN718 in (a), while (b) illustrates the changes in grain size of a powder-processed Ni-base superalloy containing elevated refractory levels. Because of the limited ductility associated with the high levels of refractory alloying elements, isothermal forging of these alloys is generally required in lieu of conventional forging processes. Tin and Pollack [284] developed regression models capable of predicting the occurrence of freckle formation during solidification from detailed statistical analyses of the microstructures, segregation behavior, and phase

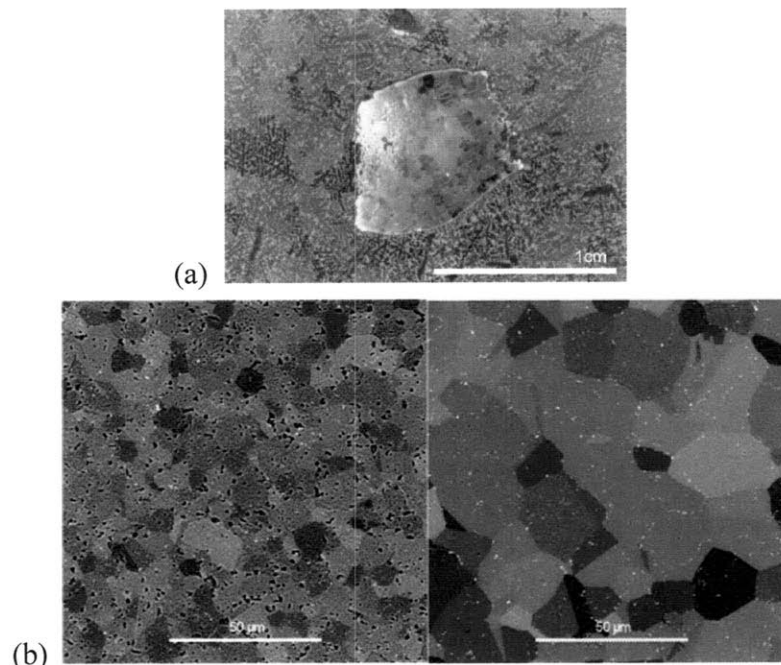


Figure C.2:(a) Freckle and white spot defects in IN718 (b) Change in microstructure of a powder-processed Ni-base superalloy due to elevated levels of refractory alloying elements (reprinted from [234])

transformation temperatures in single crystal Ni-base superalloys. They determined that although tungsten, rhenium, and tantalum are effective strengtheners the overall content of these additives must be carefully balanced to optimize physical and mechanical properties. It is proposed that the redundant NDT methodology will be capable of “mapping and tracking” damage accumulation. The “mapping and tracking” of damage accumulation in these parts during service is assisted by the use of digital image analysis. Since the NDT data is in a digital format that can be saved and stored for future reference, a more accurate quantification of damage incurred since the previous inspection is possible. This in turn improves the remaining life prediction capability and helps to ensure critical crack size is not reached. The mature NDT techniques currently used do not afford those benefits.

Service damage effects and improper maintenance of critical parts may significantly increase crack growth rates. The repair of turbine blades requires that the old, spent TBCs be removed via chemical stripping. Often, strong acid mixtures such as H_2SO_4 , $\text{H}_2\text{SO}_4\text{-HCl}$, and HNO_3 are used to dissolve the aluminide phases in the coating [106]. Excessive exposure to the stripping solutions can lead to intergranular attack of the base metal. Weld or braze repair of blades requires the appropriate pre-weld or pre-braze solution heat treatment followed by an aging heat treatment to restore the original properties to service-run parts [106]. Keeping this in mind, Mueller [285] published a failure analysis on B-1900 alloy weld-repaired turbine blade shrouds. His analysis of the broken blades found they had failed from fatigue resulting from cracks initiated in the heat affected weld repair zone. The cracks were nucleated from liquation at the grain boundaries and residual stresses that couldn't be relieved by way of the low-ductility weldments [285]. Kim and coworkers [286] researched the mechanical behavior of this same B-1900 alloy used in turbine blades, and found that γ' coarsening and coherency loss at the γ/γ' interface during thermal exposure were primarily responsible for the deterioration of mechanical properties. Both repair and rejuvenation processes for service-run critical components require extensive manual labor, and human error in any service repair process can result in fatigue variability or component failure during service.

Quantification of life-limiting fatigue behavior at elevated temperature has been the subject of numerous research studies. Morrissey [287] evaluated the fatigue

variability of single crystal superalloy PW1484 at a stress ratio, R , of 0.1, and a maximum stress of 860 MPa at a temperature of 593 °C (1100 °F). The results of these tests showed a large amount of variability in total life. Fatigue lives spanning over two orders of magnitude were seen, from 63,000 cycles to a run-out of over 16 million cycles [287]. Similar results have been published on other nickel superalloys and titanium alloys [287-292] where the large variability was attributed to different failure mechanisms. Wright [292] observed two major modes of failure in experiments on the HCF of PW1484 at high temperature. These failure modes were fatigue at low mean stress, and stress rupture at higher mean stress. In his analysis of endurance limit behavior, Wright states, “*Samples removed from test without failure after approximately 10^7 cycles often showed evidence of damage in the form of surface cracks.*” Figure C.3 is an example of this surface cracking accumulated service damage in a run-out specimen. Traditional approaches to life prediction treat fatigue life variability as a statistical

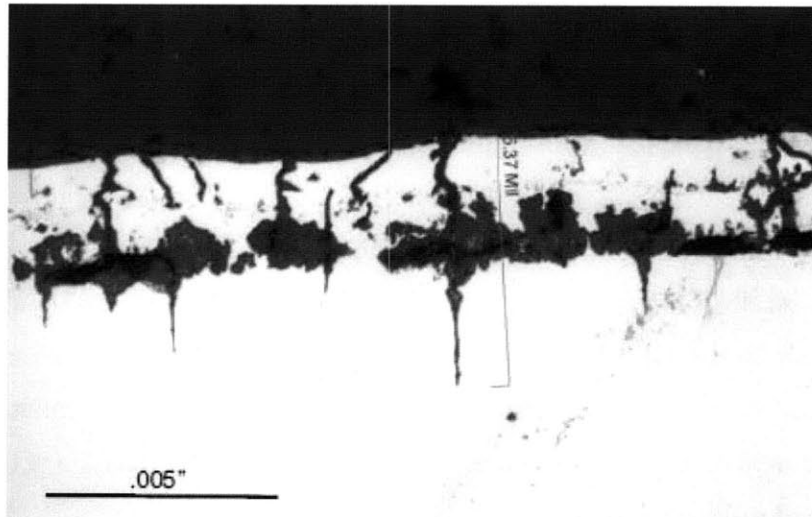


Figure C.3: Surface cracking observed in run-out specimen after 1.63×10^7 cycles (reprinted from [292])

problem where most of the fatigue life data is assumed to follow a standard statistical distribution. Shyam [293, 294] noted this approach is limited by the difficulty in coupling microstructural variability with fatigue life variability. Disk components manufactured via powder metallurgy (P/M) are touted for their FCG resistance due to a fine grain size and patents for the methods of making these components have been issued [246, 295]. However, as Caton [296] pointed out the character, size, shape and location of crack nucleation sites particularly influence the fatigue life in P/M processed

superalloys. Additionally, cracks growing from sub-surface initiation sites in P/M alloys are especially difficult to detect via NDT for in-service components and present a tangible risk for catastrophic failure.

Jha [289, 290], and others [293, 294, 297-300] have attributed this variation in FCG rates to a divergence in stress intensity thresholds, ΔK_{th} , for short and long cracks. In general, scatter in fatigue life increases at low stress amplitudes, where crack initiation and short crack propagation control lifetime and where long crack growth is less important [293]. In his study of fatigue variability behavior in P/M Rene' 88DT, Caton [296] concluded there existed a factor of 3 variability at a stress level of 1100MPa, while at 940MPa the variability factor increased to nearly 30. In this low stress/short crack regime, the sensitivity to microstructural variability complicates life prediction and poses a challenge for design of new alloys with optimum resistance to fatigue failure. Lu [291] investigated the effect of hold time on fatigue and creep crack growth rates. Ranjan [301] developed a method to calculate stress intensity factors as a function of crystallographic orientation, and found anisotropy at the crack tip plays an important role in life prediction calculations and the determination of a $K_{effective}$. Surface enhancement methods, such as shot peening, laser shock peening, and low plasticity burnishing significantly improve the fatigue resistance and FOD tolerance of critical components by introducing beneficial near-surface compressive residual stresses [90, 302, 303]. However, the fatigue life improvement gained via these methods is not explicitly accounted for in current engine component life methodologies because of a lack of accurate and reliable NDT methods that could verify the presence of these near-surface residual stresses. X-ray diffraction is an alternative nondestructive technique for the detection of near-surface residual stresses; however it is a relatively time consuming process and its use on larger aerospace components is limited due to x-ray shielding requirements. An improved lifing methodology should address FCGR divergence in short versus long cracks, account for component surface enhancement, and quantify the effect of service repair and rejuvenation.

C.2 Ti-alloys: Properties and Processing Effects

Titanium is an allotropic element, meaning it exists in more than one crystallographic form. At room temperature, Ti has a HCP crystal structure, which is

referred to as the α phase. This structure transforms to a BCC structure, the β phase, at 883 °C (1621 °F) [304]. Alloying elements are classified as α or β stabilizers. The α stabilizers, which include aluminum and oxygen, increase the temperature at which the α phase is stable, while β stabilizers, such as vanadium and molybdenum, result in stability of the β phase at lower temps [304]. The β transus temperature is defined as the lowest equilibrium temperature at which a material is 100% β [107, 304]. The β transus temperature is the temperature at which the following reactions occur.



Processing and heat treatment of Ti-alloys are often carried out with reference to some incremental temperature above or below the β transus, making it an important process parameter [107]. Titanium alloys are treated in a variety of ways to obtain the desired mechanical properties. Stress relieving and annealing may be employed to reduce residual stress and distortion developed during component fabrication, to prevent preferential chemical attack in some corrosive environments, or to condition the metal for future forming and fabrication operations [107, 305]. Solution treating and aging treatments are imposed to increase strength and achieve selected mechanical properties. Annealing treatments for Ti-alloys are various and examples include single, duplex, beta, and recrystallization annealing. Not all heat treating cycles are applicable to all titanium alloys, because various alloys are designed for different purposes. The selection of a particular annealing treatment in lieu of another is often made to optimize particular properties such as fracture toughness, fatigue strength, or high temperature creep strength [107, 304, 305]. Titanium alloys are generally classified as α alloys, $\alpha + \beta$ alloys, or β alloys based on the resulting phases present in the alloy's microstructure at room temperature. The alloys relevant to the experiments reported in this thesis are in the $\alpha + \beta$ class of alloys and include Ti-6Al-4V, also known as Ti-6-4, and Ti-5Al-2Sn-2Zr-4Mo-4Cr, also known as Ti-17. In the nomenclature used to describe the alloys, the number before the alloying element signifies weight percentage. Table C.3 includes recommended heat treating cycles for these alloys. Special thermal treatments such as beta and recrystallization annealing are not included in Table C.3.

Ti-6Al-4V is the most widely used titanium alloy, accounting for approximately 60% of total titanium production. Ti-6-4 is designed for high strength at low to moderate temperatures, making it applicable for compressor and fan section components. The β transus temperature for Ti-6-4 is nominally $1000\text{ }^{\circ}\text{C} \pm 20\text{ }^{\circ}\text{C}$ ($1830\text{ }^{\circ}\text{F} \pm 30\text{ }^{\circ}\text{F}$) [107]. Other physical properties for the alloy include a density of 4.43g/cm^3 (0.16 lb/in^3) and

Table C.3: Recommended heat treatments for Ti-6-4 and Ti-17

Type of Heat Treatment	Alloy	Temp. ($^{\circ}\text{C}$)	Temp. ($^{\circ}\text{F}$)	Time (hr)	Cooling Method
Stress Relief Treatment	Ti-6-4	480-650	900-1200	1-4	Air/Furnace
	Ti-17	480-650	900-1200	1-4	Air/Furnace
Annealing Treatment	Ti-6-4	705-790	1300-1450	1-4	Air/Furnace
	Ti-17	Not normally supplied in annealed condition			
Solution Treatment	Ti-6-4	955-970	1750-1775	1	Water quench
	Ti-17 (1 st)	815-860	1500-1575	4	Rapid air
	Ti-17 (2 nd)	800	1475	1	Water quench
Aging Treatment	Ti-6-4	480-595	900-1100	4-8	
	Ti-17	620-650	1150-1200	8	

melting range of $1609\text{-}1660\text{ }^{\circ}\text{C}$ ($2929\text{-}3020\text{ }^{\circ}\text{F}$) [306]. The high solubility of the interstitial elements oxygen and nitrogen make Ti-alloys unique among metals and creates problems that are not of concern in other metallic alloys. Figure C.4(a) shows an example of one particular problem, the formation of an “alpha case”, which is a surface-hardened zone caused as a result of the inward diffusion of oxygen into titanium upon heating [307]. The alpha case layer is usually removed by machining, as in Figure C.4(b), or chemical milling prior to placing a part in service, because its presence reduces fatigue strength and ductility [305]. Ti-6-4 is relatively low in stabilizers, and thus has poor hardenability, requiring rapid quenching to achieve significant strengthening. For Ti-6Al-4V, the cooling rate of a water quench is not rapid enough to cause significant hardening in sections thicker than about 25mm (1.0 inch) [107, 304, 305]. This is a limiting factor for Ti-6-4, and the reason the Ti-17 alloy was developed for strength in heavy section components such as fan and compressor disks. For $\alpha + \beta$ alloys such as Ti-6-4 and Ti-17, solution treating and aging can increase strength by 50% or more over the annealed or overage condition [107, 305]. Ti-17 alloy typically undergoes a double solution treatment which results in higher tensile and creep strength than Ti-6-4, as well

as excellent forge-ability and hot work-ability [308]. Distortion of the alloy can occur during solution treatment, and fixtures typically are required. Sagging or distortion of the alloy adds another level of component variability, and for parts made from Ti-6Al-4V sagging during solution heat treating above 955 °C (1750 °F) is a known issue [107, 304-306]. The beta transus temperature for Ti-17 is around 890 °C (1635 °F). A limitation of Ti-17 is that the alloy may be susceptible to stress corrosion attack because of its high chromium content.

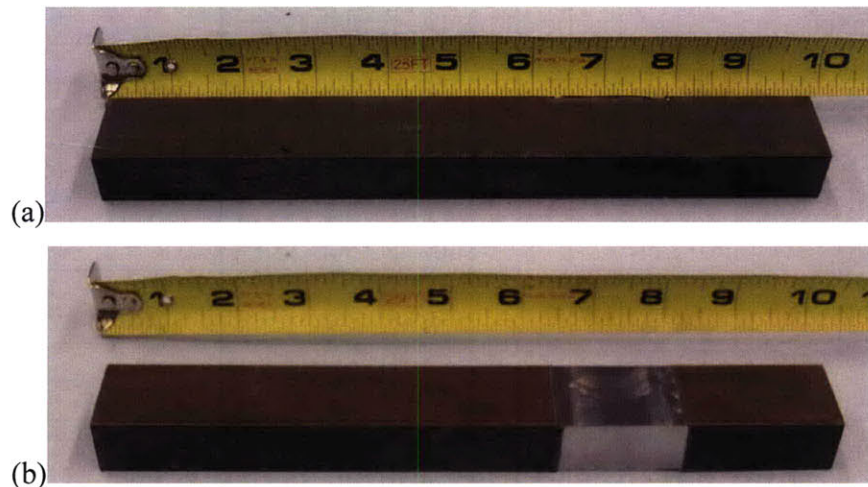


Figure C.4: (a) Alpha case layer on surface of Ti-6-4 after heat treating
(b) Removal of a section of alpha case layer via machining

There are three principal defects associated with titanium alloys. The first is a “High Aluminum Defect” (HAD or Type II defect), defined as an aluminum-rich alpha stabilized region which may extend across a large number of beta grains [4, 304]. The second is a “High Interstitial Defect” (HID or Type I defect), which is an alpha phase region of substantially higher hardness than the surrounding material. The higher hardness often results in a brittle alpha phase, and is caused from very high localized nitrogen, oxygen, or carbon concentrations that increase the beta transus [4]. This type of defect is also known as a low-density inclusion (LDI) or a hard-alpha (HA) inclusion, and is often associated with voids and cracks in the alloy. The third prominent defect associated with premium titanium-alloy material is a “High Density Inclusion” (HDI). This is a region with a high concentration of refractory elements having a higher density than the matrix [4, 304]. Typical refractory elements that cause this type of inclusion are tungsten, molybdenum, or columbium. The manufacture of Ti-alloy forged rotating

components can introduce component life-limiting anomalies at all stages of material processing, from sponge-processing, through melting, billet conversion, component forging, and finally to inspection of the finished component. The FAA has provided guidance to the manufacture of these components in [4], and recommends the use of newer technologies such as triple VAR and cold hearth melting (CHM), which has been shown to virtually eliminate the risk of having HDI's survive through the melting cycle.

Despite the best efforts of the FAA and industry to improve the manufacturing practices related to premium quality titanium-alloy engine components, it is extremely difficult to eliminate or even minimize the occurrence of these defects through process changes. The reason is because these defects are so infrequent, measuring success in the QA/QC methodology for processing and manufacturing would require massive sample sizes over long time spans [41]. This is neither cost-effective nor feasible for industry. An example is the occurrence rate of hard alpha (HA) inclusions. It is known HA defects can reduce fatigue life by an order of magnitude; however it has been reported that this type of defect only appears once for every 2-3 million pounds of premium quality billet [41]. The NTSB determined the catastrophe in Sioux City, Iowa resulted from an HA anomaly that was formed during the manufacture of a Ti-6-4 stage 1 fan disk and remained undetected through ultrasonic, macroetch, and multiple fluorescent penetrant (FPI) inspections performed during manufacture and service. Additionally, FPI missed a detectable in-service fatigue crack initiated by the HA anomaly during a routine inspection less than 1,000 cycles before failure [110, 117, 119, 120]. Heavy reliance on improved NDT techniques on a part-by-part basis has the potential to detect these rare events where there is the existence of an anomaly.

Even when rare anomalies are not present in a finished Ti-alloy component, inherent variability on a part-by-part basis is inevitable due to the many opportunities for variance in the heat treating and aging processes. An example of this inherent variability is in Ti-alloys that undergo stress-relief during processing. The uniformity of cooling is particularly critical in the temperature range from 480-315 °C (900-600 °F) [304], and non-uniform cooling can result in local regions rich in β stabilizers. Figure C.5(a-d) shows the significant microstructural variations that can occur within different locations of the same part and from sample to sample of the same alloy. The micrographs are from

two Ti-6Al-4V tensile samples that had the same lamellar beta annealing procedure specified, but were manufactured at different facilities. Islands of β transformed grains are evident in Fig. C.5(b), while Fig. C.5(c) shows a colony of acicular- α grains surrounding an α -rich grain whose basket-weave appearance is typical of a Widmanstätten structure.

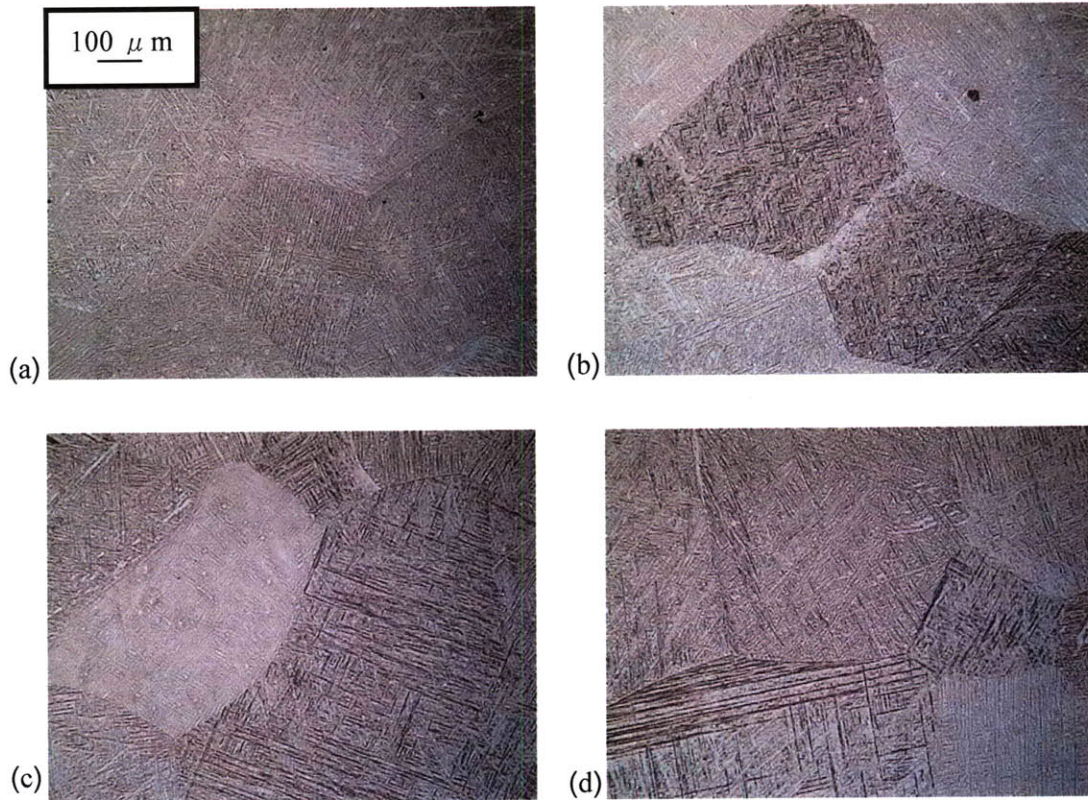


Figure C.5: (a-b) Micrographs from two different locations within the same Ti-6Al-4V tensile specimen. Micrographs in (c-d) from two locations in a Ti-6Al-4V tensile specimen different from (a-b) showing microstructural variation despite identical heat treatment. All micrographs taken on Olympus VANOX-T optical microscope at 50x magnification. Scale bar in (a) applicable to (a-d). Keller's reagent used as etchant in (a-d).

It has been reported in literature [104, 266, 267] as well as in patents [77] that both the size and orientation of clustered colonies is the fatigue-critical microstructural feature in Ti-alloys. Fatigue cracks tend to initiate in locations where the local microstructure promotes the accumulation of irreversible slip [104], and in $\alpha + \beta$ Ti-alloys fatigue damage typically accumulate in the HCP α phase because of the limited number of slip systems available [267]. Whittaker [266] notes that out of six Ti-6-4 microstructures

evaluated the worst resistance to fatigue crack initiation was shown by the Widmanstätten microstructure, whereas this may be the best for resistance to fatigue crack growth.

In addition to variables attributed to the thermo-mechanical processing steps, such as primary α grain size, primary α volume fraction, morphology of transformed product, and crystallographic texture, macroscopic textures are also known to influence average fatigue-life properties [104, 266]. Fretting fatigue in the dovetail region of compressor blades manufactured from Ti-alloys, resulting from the combination of elevated temperature and oscillatory motion from engine vibration, is a damage mode that is especially sensitive to these macroscopic textural differences [239, 309-311]. Cadario and Alfredsson [310] discussed the influence on fretting fatigue crack growth from shot peening, and found the improvement in fatigue life was explained by slower crack growth rates in the shallow surface layer containing compressive residual stresses. Other researchers [309, 312, 313] have discussed the dramatic benefits over traditional shot-peening of newer technologies such as laser shock peening (LSP) on HCF. Shepard [313] noted that the microstructural characteristics between LSP-treated and untreated regions were essentially indistinguishable except for minor elongation of grains in the transverse direction of the most intensely laser shock peened specimens. It has been reported that surface crack initiation generally leads to the shortest lifetimes, and competition between surface and sub-surface crack initiation in $\alpha + \beta$ alloys is attributed to the presence of these compressive residual surface stresses, as well as the specimen surface to volume ratio and environmental effects [104]. This is one of the reasons Ti-alloys do not follow the traditional Paris-Erdogan equation for fatigue crack growth rate [314, 315], described by the following equation:

$$\frac{da}{dN} = C \cdot (\Delta K)^n \quad (C.3)$$

where $\frac{da}{dN}$ is the fatigue crack propagation rate, ΔK is the stress intensity factor range, and C and n are empirical scaling constants for a log-log plot. Chan and Enright [178] highlighted this deficiency in traditional empirical fatigue crack models based on curve fitting of physical tests, and proposed a probabilistic micromechanical code for predicting fatigue life variability that includes initial crack size and intrinsic microstructural material properties as inputs to the code. Table C.4 contains values of deterministic material

values for Ti-6Al-4V at 24°C used in the microstructure based fatigue crack initiation and growth models of Chan and Enright. A comparison of the predicted and observed probability density functions (PDF) for the range of crack-initiation life values in [178] shows good agreement. Current life prediction methodologies are inadequate due to their reliance on empirical models that assume unique values for material parameters which can significantly vary based on microstructural features. The use of probabilistic models that incorporate Monte Carlo (MC) type simulations to account for the inherent randomness and variability of these features shows promise. An additional limitation of current life prediction models stems from not crediting the benefit of surface treatments in the analysis. This is a challenge because traditional nondestructive testing procedures are incapable of quantifying the benefit to fatigue life of such surface treatments.

Table C.4: Deterministic material values used as inputs in microstructural based FCI and FCG models (adapted from [178])

Variable	Description	Value
E	Young's modulus	1.61×10^5 MPa
n_1	Stage I exponent	23.0
n_2	Stage II exponent	3.87
s	Dislocation cell size	0.25 μm
d_o	Reference dislocation barrier spacing	1.0 μm
D_o	Reference grain size	1.0 μm
R	Stress ratio	0.1
K_C	Fracture toughness	66.7 MPa $\sqrt{\text{m}}$
ΔK_{th}	Fatigue threshold	2.0 MPa $\sqrt{\text{m}}$
D	Grain size	11.7 μm
σN_y	Cyclic yield stress	909.33 MPa
ϵN_f	Fatigue ductility coefficient	0.0389
γ	Dislocation barrier spacing exponent	1.0
M	Taylor factor	2
μ	Shear Modulus	4.4×10^4 MPa
ν	Poisson's ratio	0.333
λ	Universal constant	0.005
α	Fatigue imitation life exponent	0.5
σ_e	Fatigue limit (Mk)	272.5 MPa
h	Slipband width	5×10^{-8} m

As the damage tolerance element of the safe life methodology has grown more accepted in the aerospace industry, a greater emphasis has been placed on probabilistic risk assessments that incorporate flaw size and fracture mechanics. The Aerospace Industries Association (AIA) Rotor Integrity Sub-Committee [36, 72], in conjunction with the FAA developed hard alpha anomaly distributions for aircraft engine titanium disk alloys. These distributions were used as benchmarks to measure engine and component “Design Target Risk” (DTR) values. The DTR is the metric that determines the acceptability of new designs and the appropriateness of proposed field actions [72]. It should be noted the initial distributions estimated needed to be adjusted based on diverging commercial engine service experience from some of the industry committee members [122]. The explanation from the AIA was that, “...*the analytical process involved a set of difficult to evaluate assumptions leading to multiple potential solutions [72].*” A probabilistic, damage tolerance code called DARWIN (**D**esign **A**ssessment of **R**eliability **W**ith **I**nspection) [94, 220], was developed that integrated finite element stress analysis, fracture mechanics analysis, nondestructive inspection simulation, and probabilistic analysis to assess the risk of rotor fracture. Since all of the inputs to the code are not known, a probabilistic Monte Carlo analysis [94, 316] was needed. As MC simulations and the use of DT code such as DARWIN are increasingly incorporated into engine design and certification programs in lieu of costly experimentation, the need for state-of-the-art NDT programs becomes even more imperative. Only in-service NDT can ensure that design assumptions, which are intrinsic to all models and simulations, do not contain flawed logic that could result in catastrophic failure. Another caveat, symbolized in [72], is the need to continually update models as more service experience on particular engine components is gained.

C.3 Other Structural Materials

The previous two sections have thoroughly explained the properties and processing effect variations applicable to nickel-base superalloys and titanium alloys that comprise the raw materials for both compressor and turbine section disks and blades. This section will briefly touch on other structural materials that are being considered for critical components in new engine designs, as knowledge of these components has

relevance to future certification issues and engine compatibility issues discussed in Sections 6.4 and 6.5. Before that, aluminum alloys that comprise airframe structural components will be discussed, due to the similarities in NDT procedures for airframe and engine structural components. Current aircraft structures are mostly built using metallic aluminum or polymer composite materials, with metal-matrix composites (MMC) seeing use in rare instances [21]. It is expected that cracks will develop in the aluminum airframe as a result of the cyclic stresses imposed. Similar to engine components, the load history of the airframe has an important effect on crack growth rates and remnant life. Newman [317] proposed a crack closure model, based on a modified Dugdale strip-yield model, for prediction of fatigue crack growth under variable amplitude and spectrum loading in aluminum alloys. The model accounts for different effective and threshold stress intensity factors for both large and small cracks, but, like many models for Ni-base superalloys and Ti-alloys, it relies on empirical constants that do not fully account for the unique loading history [317]. This results in significant standard deviations in predicted to experimental fatigue lives. Another similarity between aluminum structural airframes and turbine engines is the use of visual inspection often followed by traditional eddy current or ultrasonic NDE during field inspections [46]. Bar-Cohen [46] notes that rapid inspection of large structures is an ongoing challenge to the NDE community, and generally metallic airframe structures are susceptible to corrosion and fatigue cracking while composites are sensitive to impact damage. For both large airframe and critical engine components, effective field inspection requires a portable, user friendly system that can rapidly scan large areas of complex structures. This is a necessity that will be addressed in the proposed methodology. A 6061 Al-alloy “wedding cake” probability of detection (POD) specimen was machined for some of the NDT and image analysis experiments described in Chapters 3-5.

It has previously been mentioned that the first jet engines relied on steel alloys for their hot-section components, before processing improvements in Ni-base superalloys in the 1950’s enabled their entry into the turbine engine arena. In 1990, Koul, Bellinger, and Gould [18, 19] proposed both a deterministic and probabilistic based damage tolerance life prediction approach for aero-engine compressor disks. The program was carried out on AM-355 martensitic stainless steel compressor disks. Results for the

probabilistic approach indicated it may be possible to obtain cost-effective safe inspection intervals (SII) if sensitive eddy current and automated ultrasonic leaky surface wave techniques were used to inspect the disks [19]. It was noted in this paper that the behavior of short cracks would need to be characterized prior to obtaining usable probabilistic fracture mechanics based data. Murakami and Endo [318] analyzed the effects of defects, inclusions, and inhomogeneities on the fatigue strength of steels. They observed that the threshold stress intensity factor range, ΔK_{th} , is useful for determining the maximum allowable stress when cracks or defects are detected in machined parts and structures under service load. However, they discovered this value is dependent on and decreased with decreasing crack size [318]. Figure C.6 graphically displays this dependence of ΔK_{th} on crack size for various steel alloys. In ultrasonic NDT

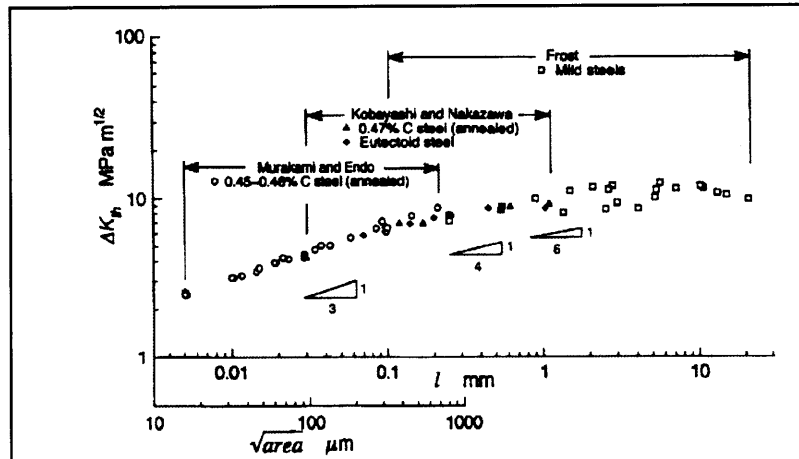


Figure C.6: Dependence of ΔK_{th} on crack size for various steel alloys (reprinted from [318])

experiments, Ruiz-Reyes [82] concluded that steel is a strongly scattering material, and detection of near-surface flaws in steel is very difficult because the ultrasonic grain noise is higher than flaw echoes that issue a back-scattered ultrasonic signal from the flaws. A POD wedding cake specimen machined from mild steel alloy 8620, as well as another steel wedding cake sample containing an embedded flaw were tested with advanced phased array and computed tomography techniques in Chapters 3-4.

The desire to increase turbine inlet temperatures beyond their current capabilities has spurred the development of new material classes developed specifically for incorporation into turbine engine components. Ceramic matrix composites (CMC) are being developed for high temperature commercial applications, including use in

advanced gas turbine engines [319]. These CMC materials are attractive for turbine engine applications due to their high strength/toughness ratio, relatively low density, and resistance to chemical attack at high temperature. As with nickel-base superalloys and titanium-alloys, the complex microstructures and multiple processing steps involved during the fabrication of CMC components may result in defect introduction of variable size and morphology [319]. Delamination defects and large voids associated with processing upsets, and also cracks or voids within the CMC matrix are examples of prevalent defects. As Eagar [320, 321] pointed out, issues such as cost, weldability, and the intricate joining requirements of sub-assemblies in the engine structure must be addressed if novel materials such as CMCs are to be realistically implemented into such a complex structural system. Sun [319] discussed the limitations of individual NDT processes in achieving 100% inspection of CMC-based components. He pointed out that ultrasonic methods are more sensitive to cracks and delamination detection, but they are not very reliable for imaging material property distributions. Another issue was the problems posed for CMCs that may have some porosity, but required coupling liquids or full immersion for UTI [319]. This is contrasted with X-ray computed tomography (CT) of CMCs, which is highly sensitive to material or volumetric composition but not suitable to detect tight cracks or delaminations [319]. These statements underscore a major theme: *no single NDT method is capable of detecting every material defect, so use of multiple NDT techniques in concert is necessary to achieve 100% component inspection, add redundancy to the design, and mitigate the possibility of missed flaw detection during inspection.*

Appendix D: Traditional UTI Data from Alloy Block Experiments at UMass Dartmouth

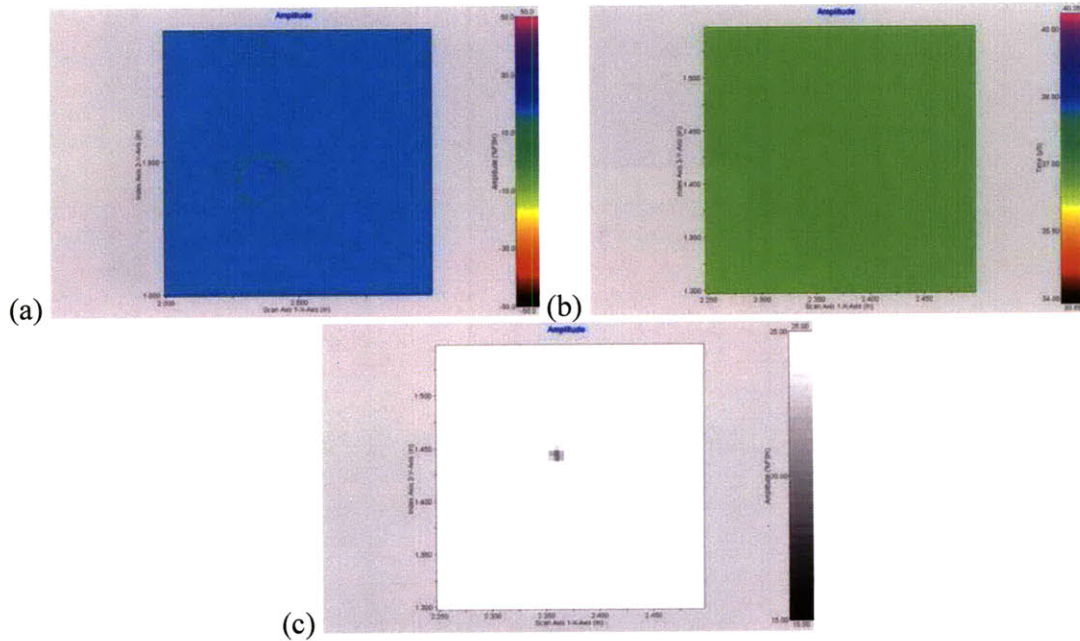


Figure D.1: Calibration test #1 for traditional ultrasonic C-scan system. (a) Gated amplitude (b) Lift-off (c) Grayscale pixel resolution for #1FBH

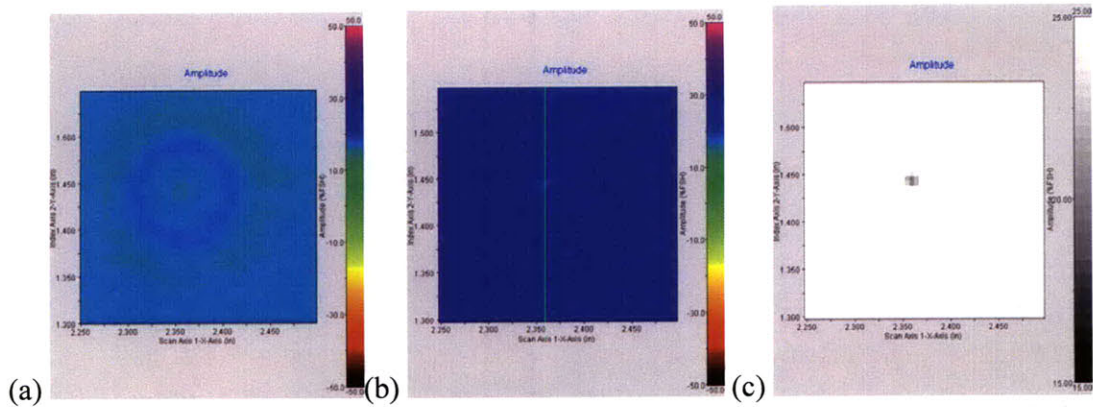


Figure D.2: Calibration test #2 for traditional ultrasonic C-scan system. (a) Gated amplitude (b) Focused gated amplitude (c) Grayscale pixel resolution for #1FBH

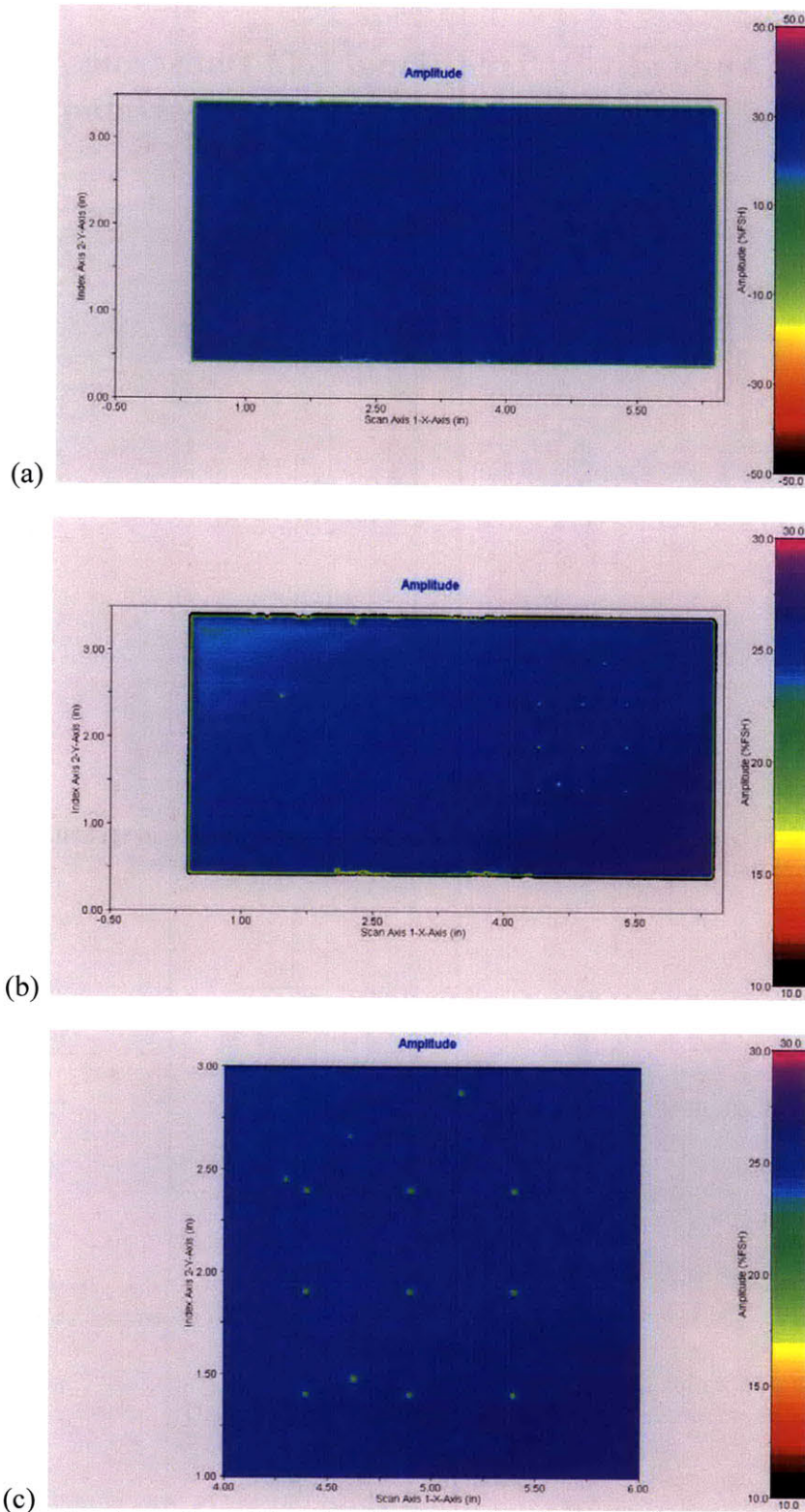


Figure D.3: Top surface inspection of Sample R88. Color Amplitude test data. (a) Full range (b) Manually optimized limited range (c) FBH-array ROI at manually optimized limited range

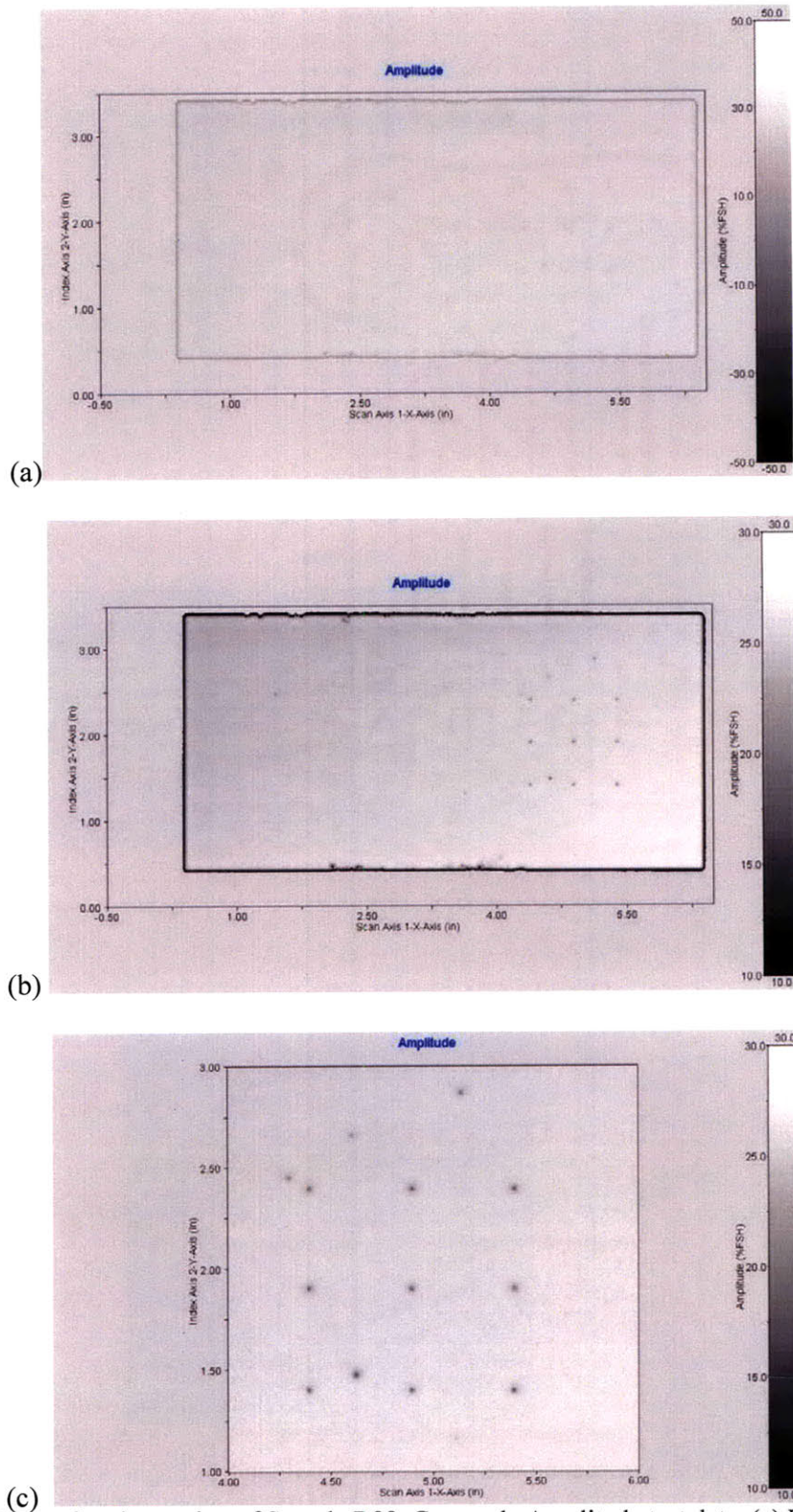


Figure D.4: Top surface inspection of Sample R88. Grayscale Amplitude test data. (a) Full range (b) Manually optimized limited range (c) FBH-array ROI at manually optimized limited range

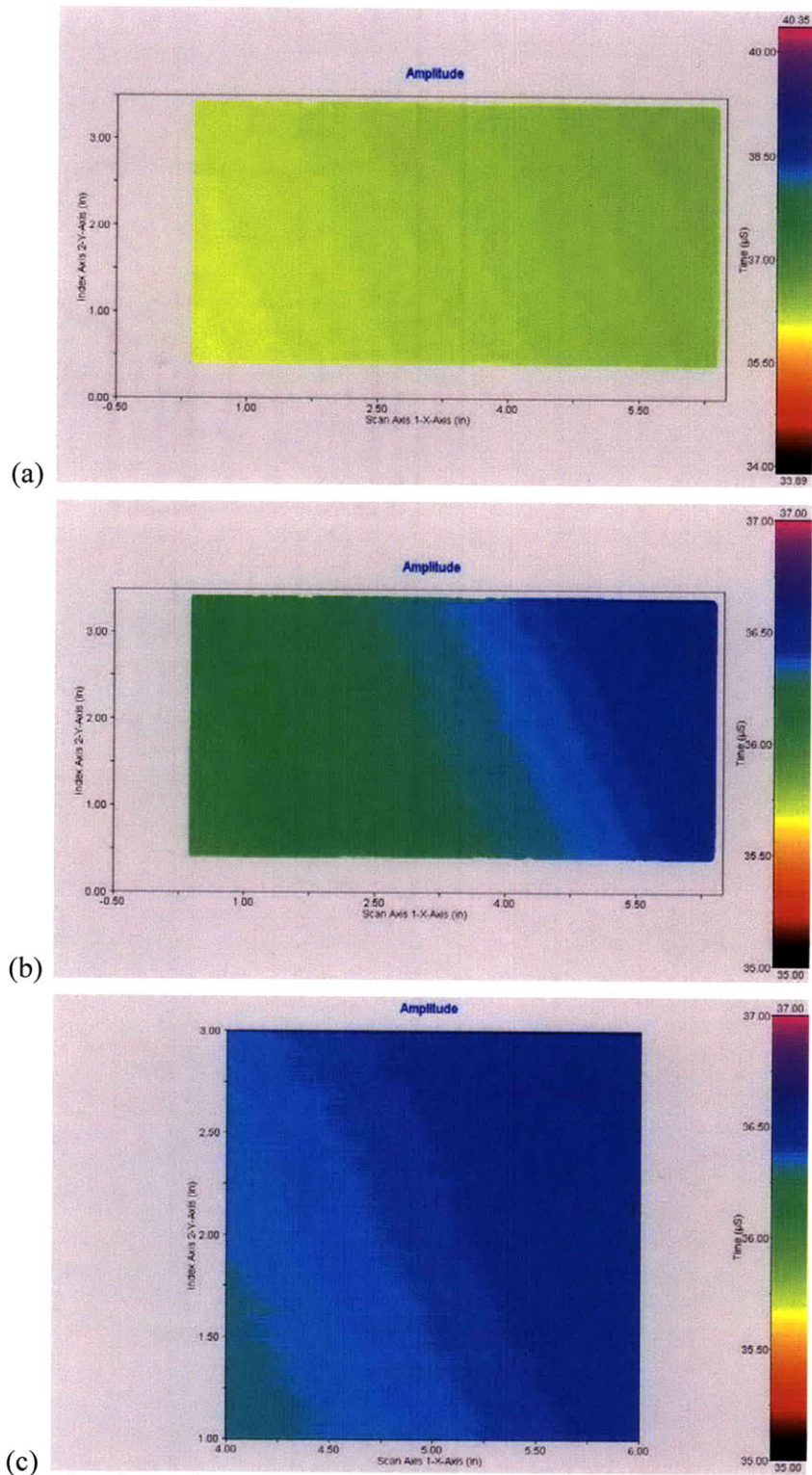


Figure D.5: Top surface inspection of Sample R88. Color Time of Flight test data. (a) Full range (b) Manually optimized limited range (c) FBH-array ROI at manually optimized limited range

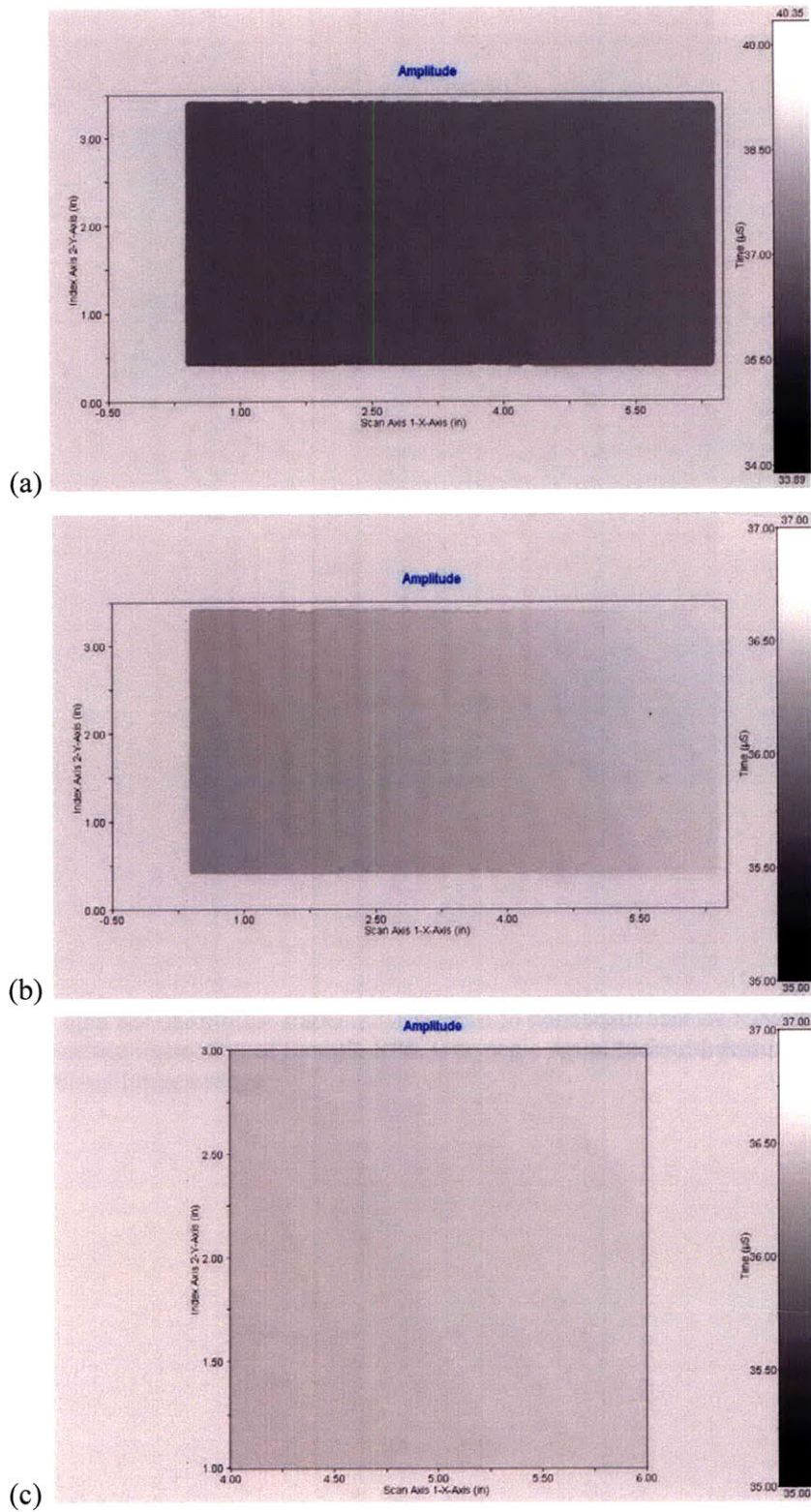


Figure D.6: Top surface inspection of Sample R88. Grayscale TOF test data. (a) Full range (b) Manually optimized limited range (c) FBH-array ROI at manually optimized limited range

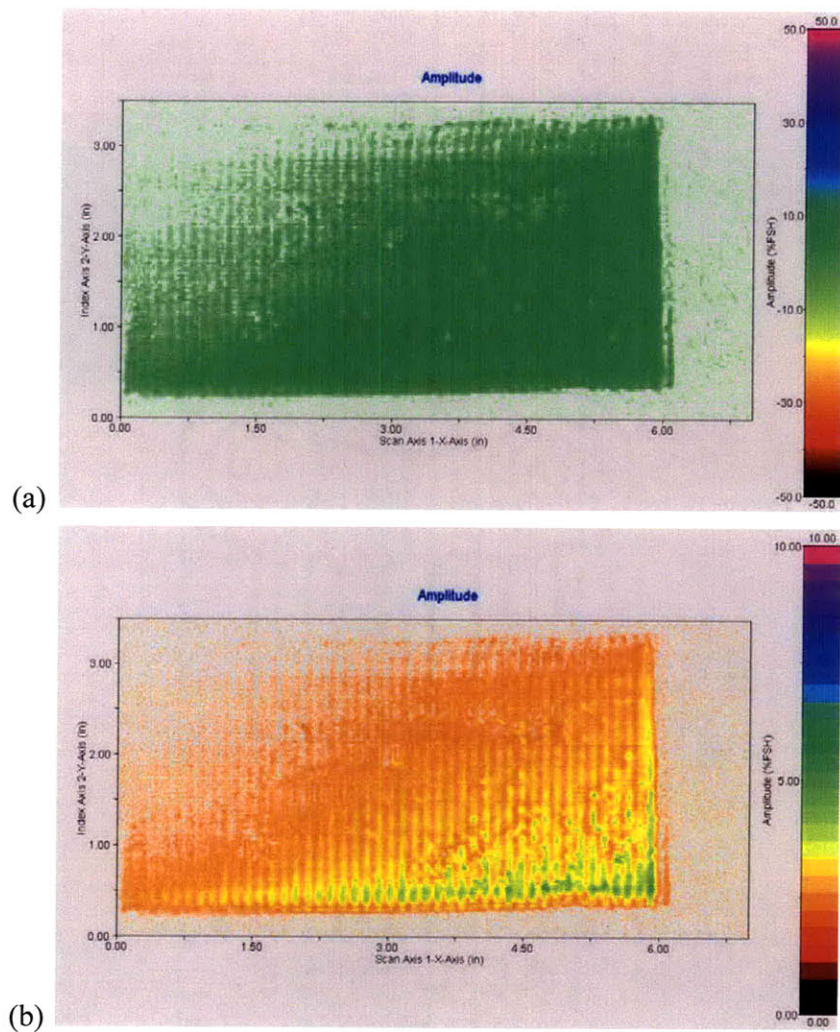


Figure D.7: Back surface inspection of Sample R88. Color Amplitude test data. (a) Full range (b) Manually optimized limited range

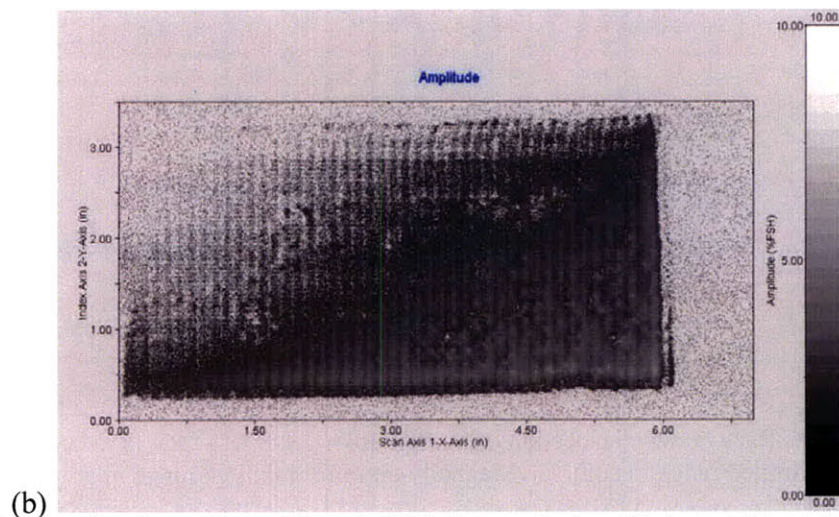
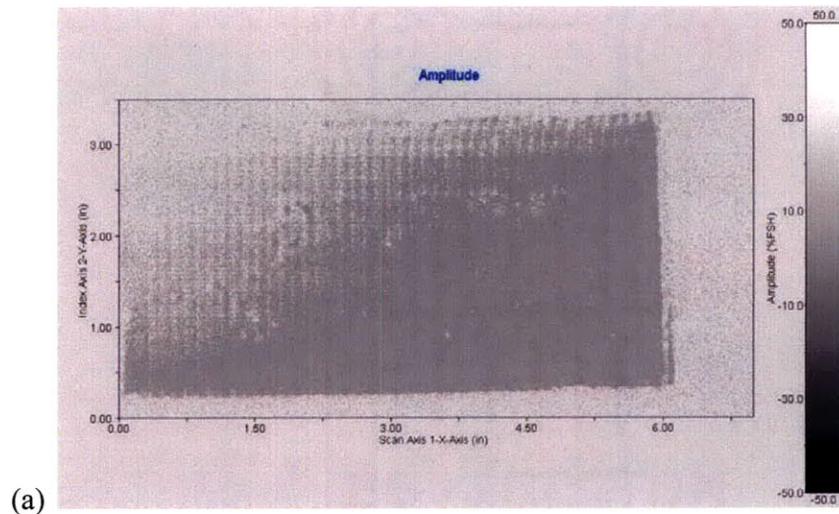


Figure D.8: Back surface inspection of Sample R88. Grayscale Amplitude test data. (a) Full range
(b) Manually optimized limited range

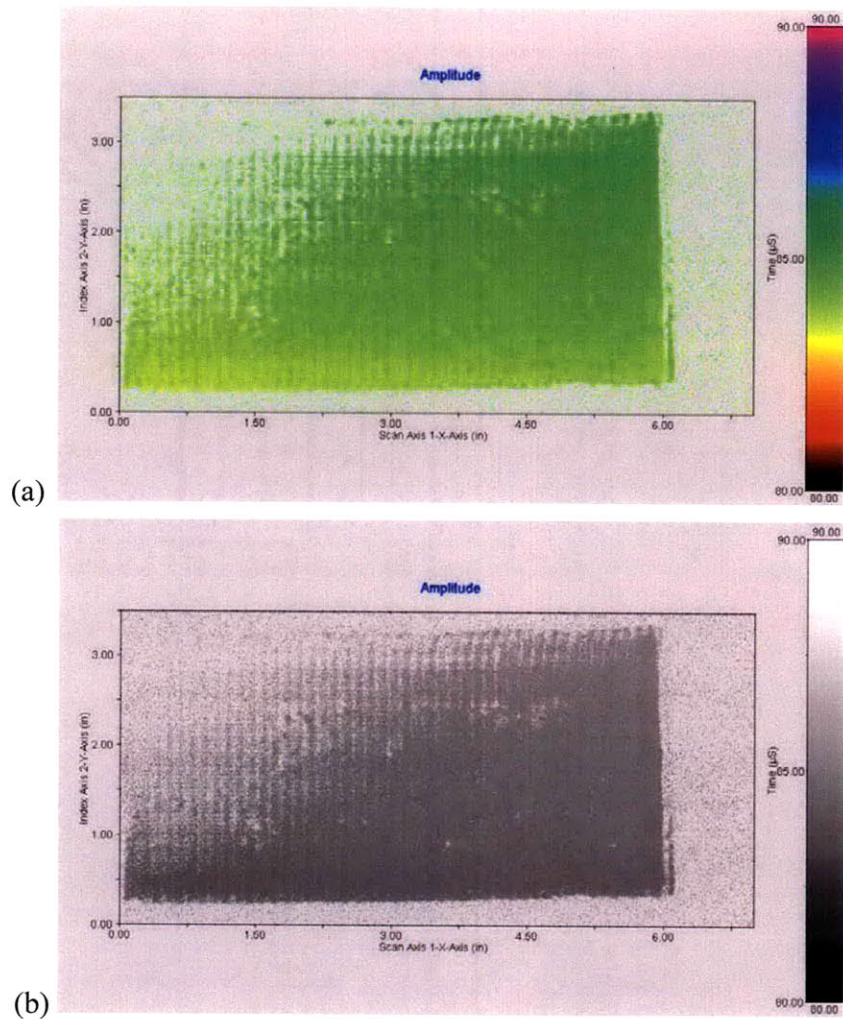


Figure D.9: Back surface inspection of Sample R88. TOF test data. (a) Manually optimized limited range in color (b) Manually optimized limited range in grayscale

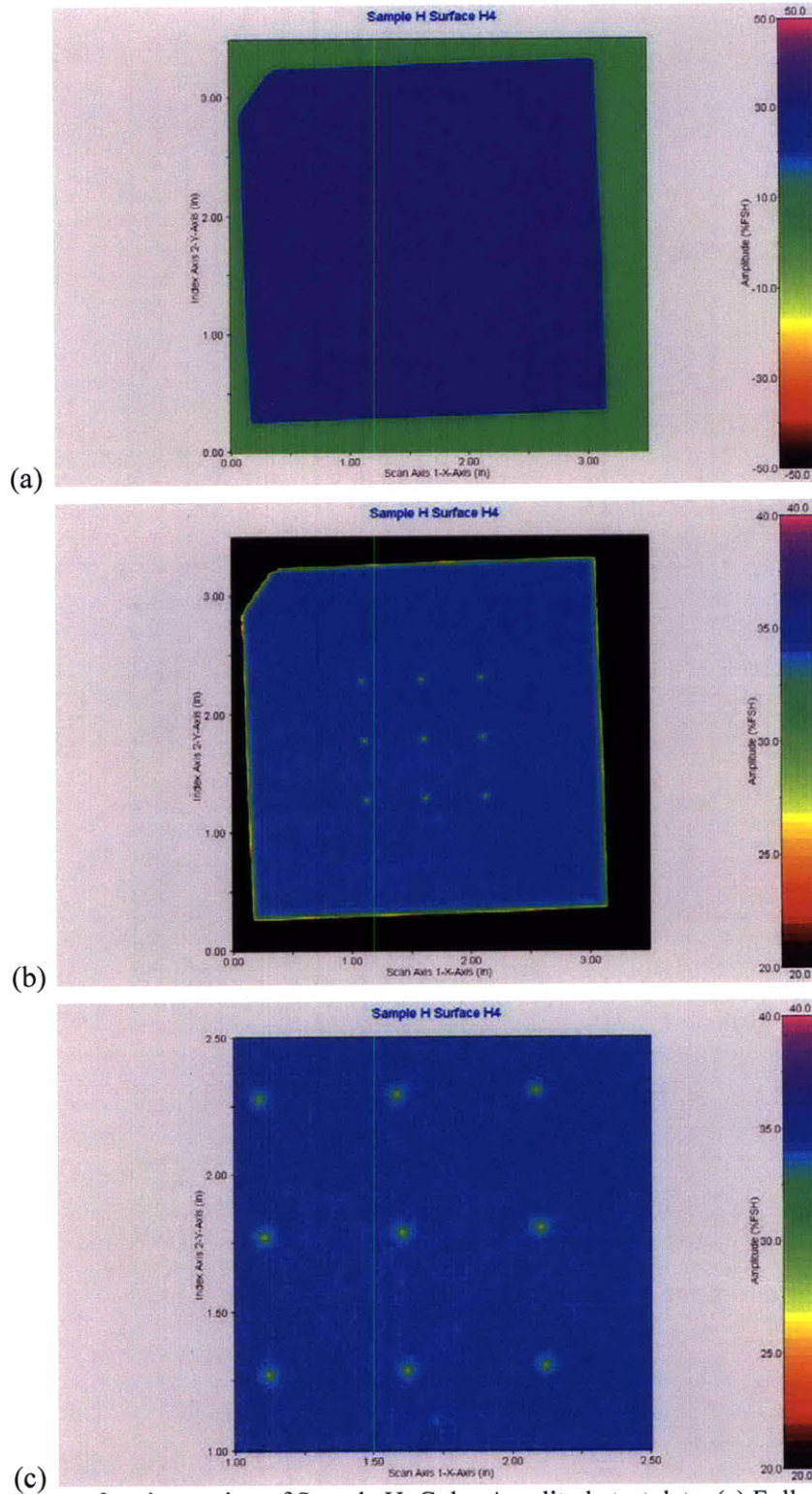


Figure D.10: Top surface inspection of Sample H. Color Amplitude test data. (a) Full range (b) Manually optimized limited range (c) FBH-array ROI at manually optimized limited range

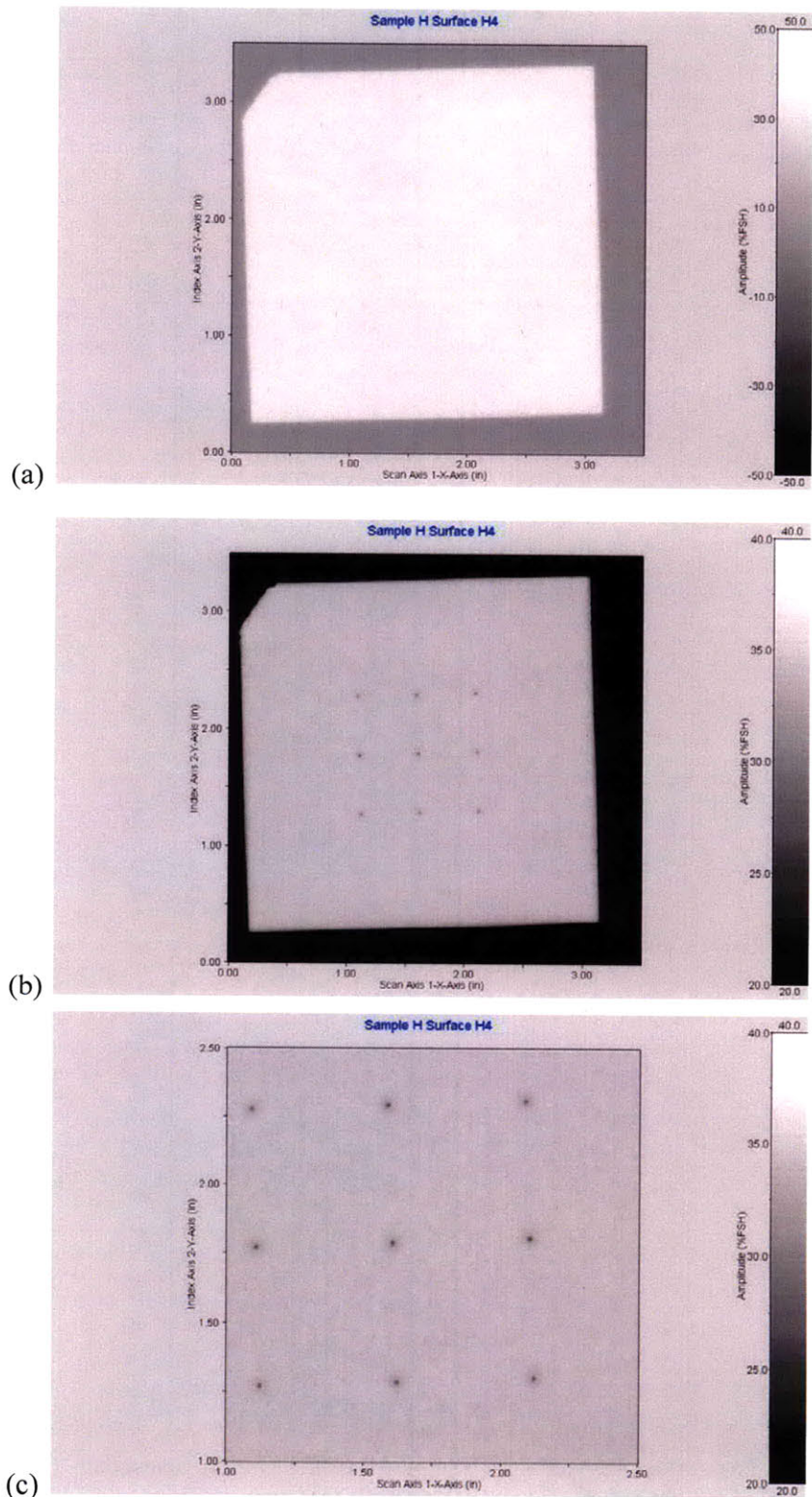


Figure D.11: Top surface inspection of Sample H. Grayscale Amplitude test data. (a) Full range (b) Manually optimized limited range (c) FBH-array ROI at manually optimized limited range

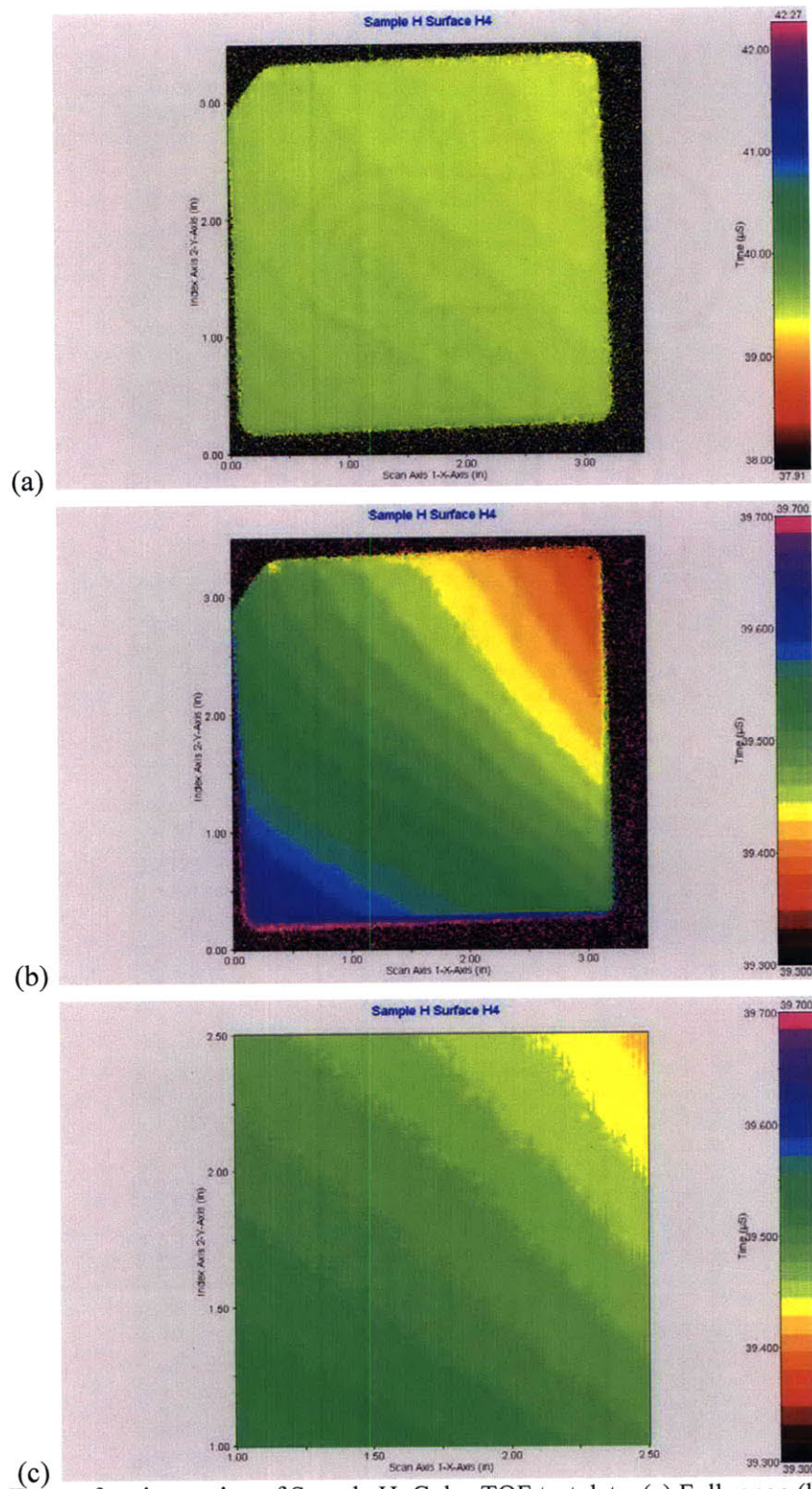


Figure D.12: Top surface inspection of Sample H. Color TOF test data. (a) Full range (b) Manually optimized limited range (c) FBH-array ROI at manually optimized limited range

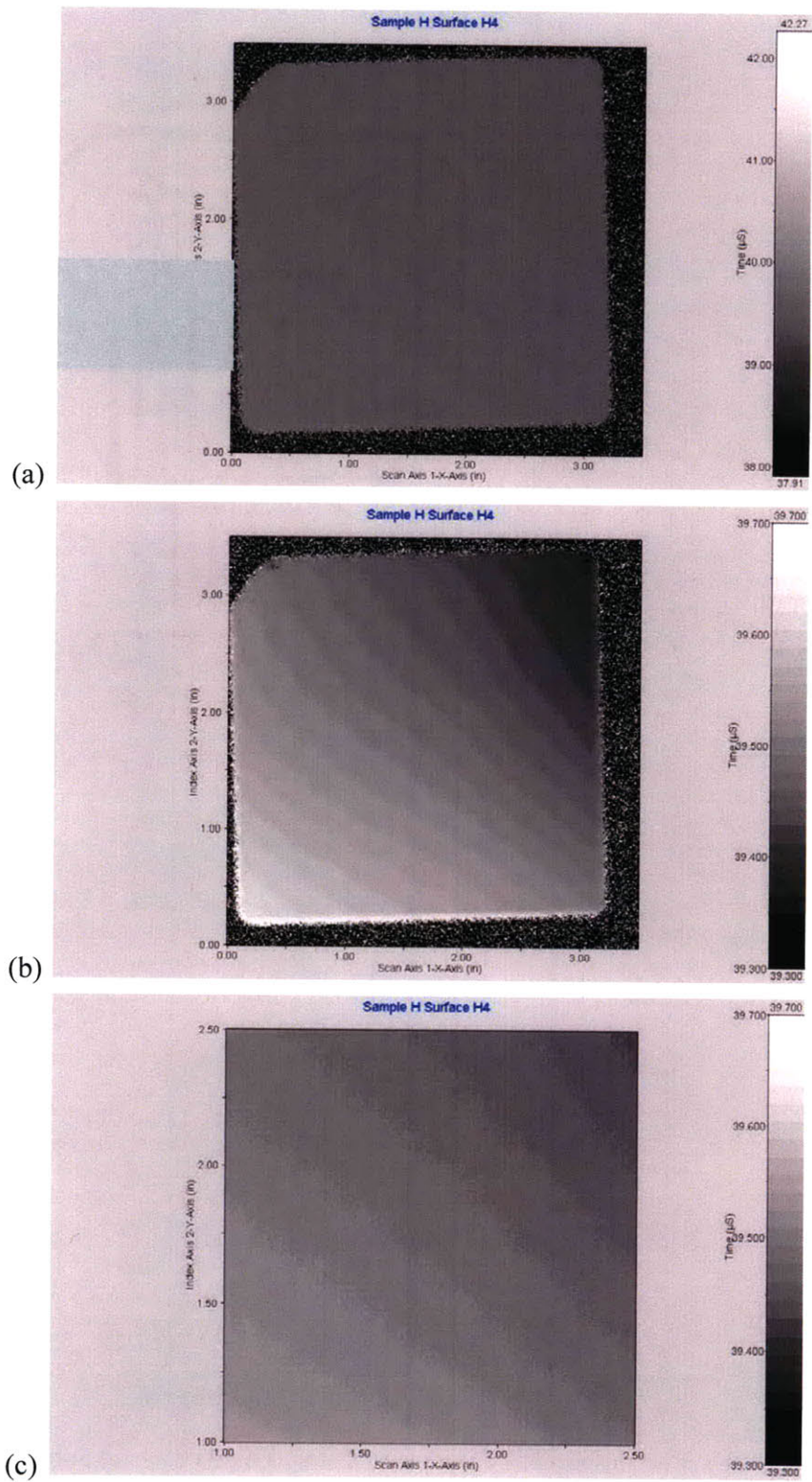


Figure D.13: Top surface inspection of Sample H. Grayscale TOF test data. (a) Full range (b) Manually optimized limited range (c) FBH-array ROI at manually optimized limited range

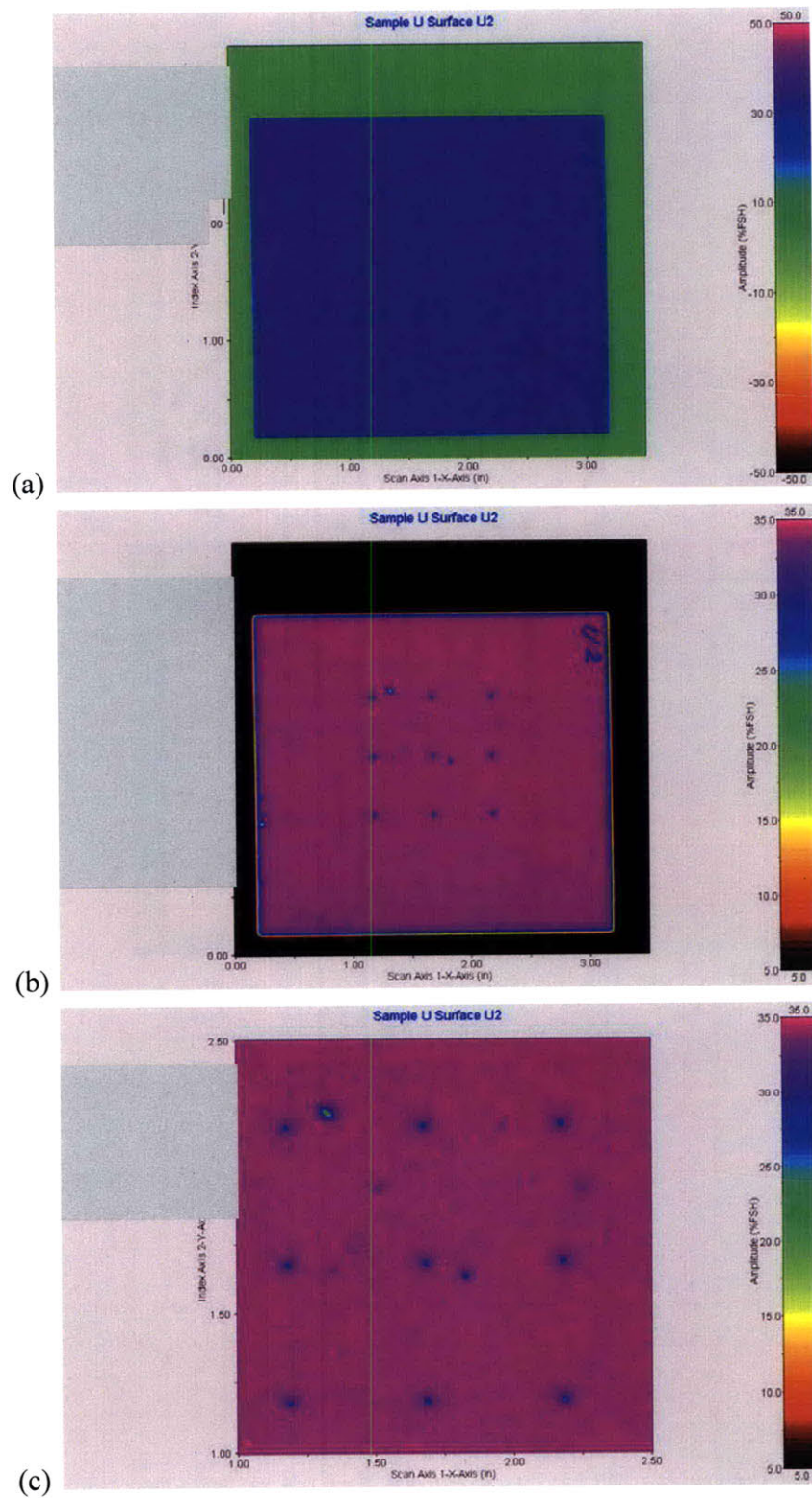


Figure D.14: Top surface inspection of Sample U. Color Amplitude test data. (a) Full range (b) Manually optimized limited range (c) FBH-array ROI at manually optimized limited range

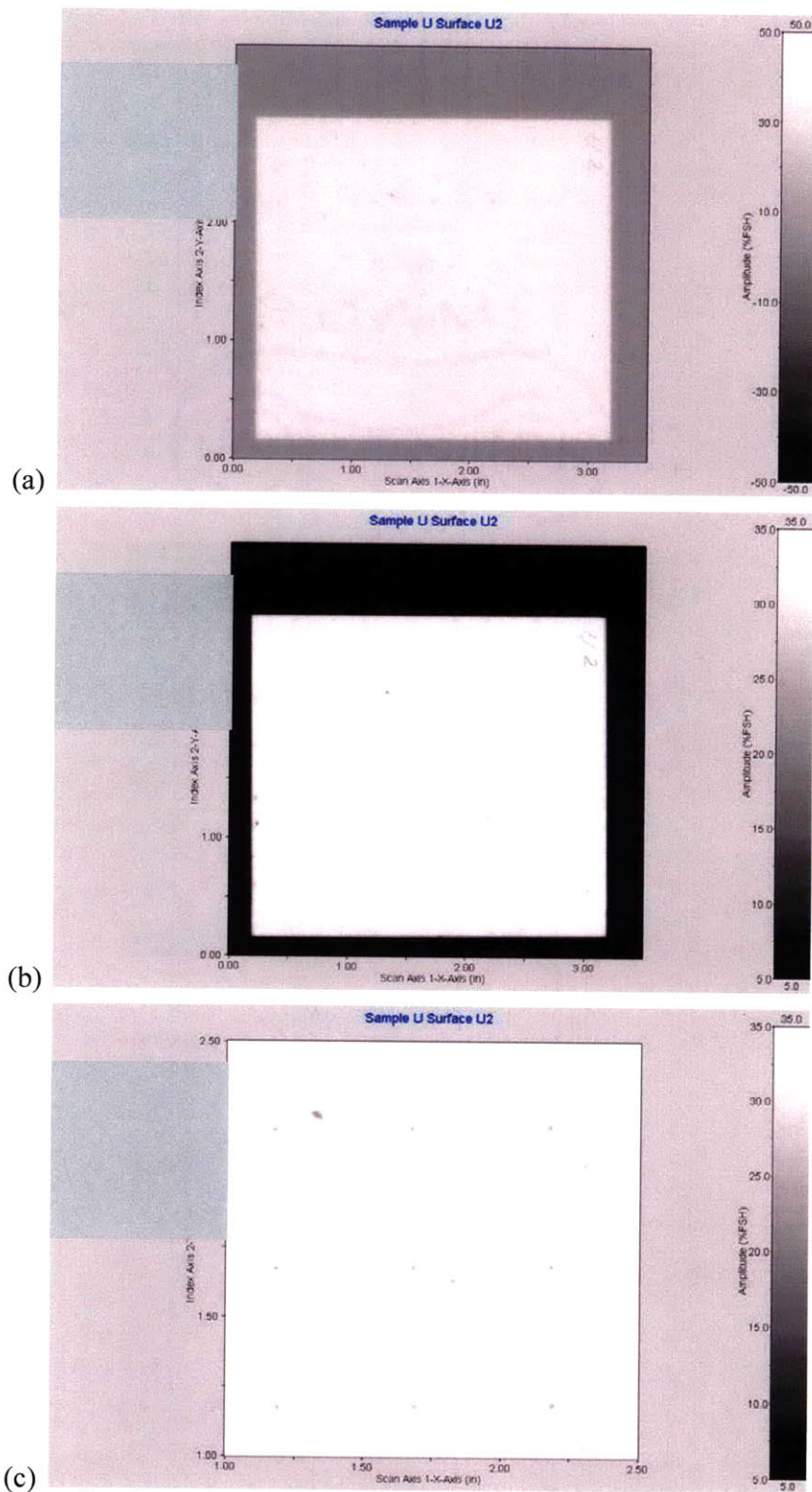


Figure D.15: Top surface inspection of Sample U. Grayscale Amplitude test data. (a) Full range (b) Manually optimized limited range (c) FBH-array ROI at manually optimized limited range

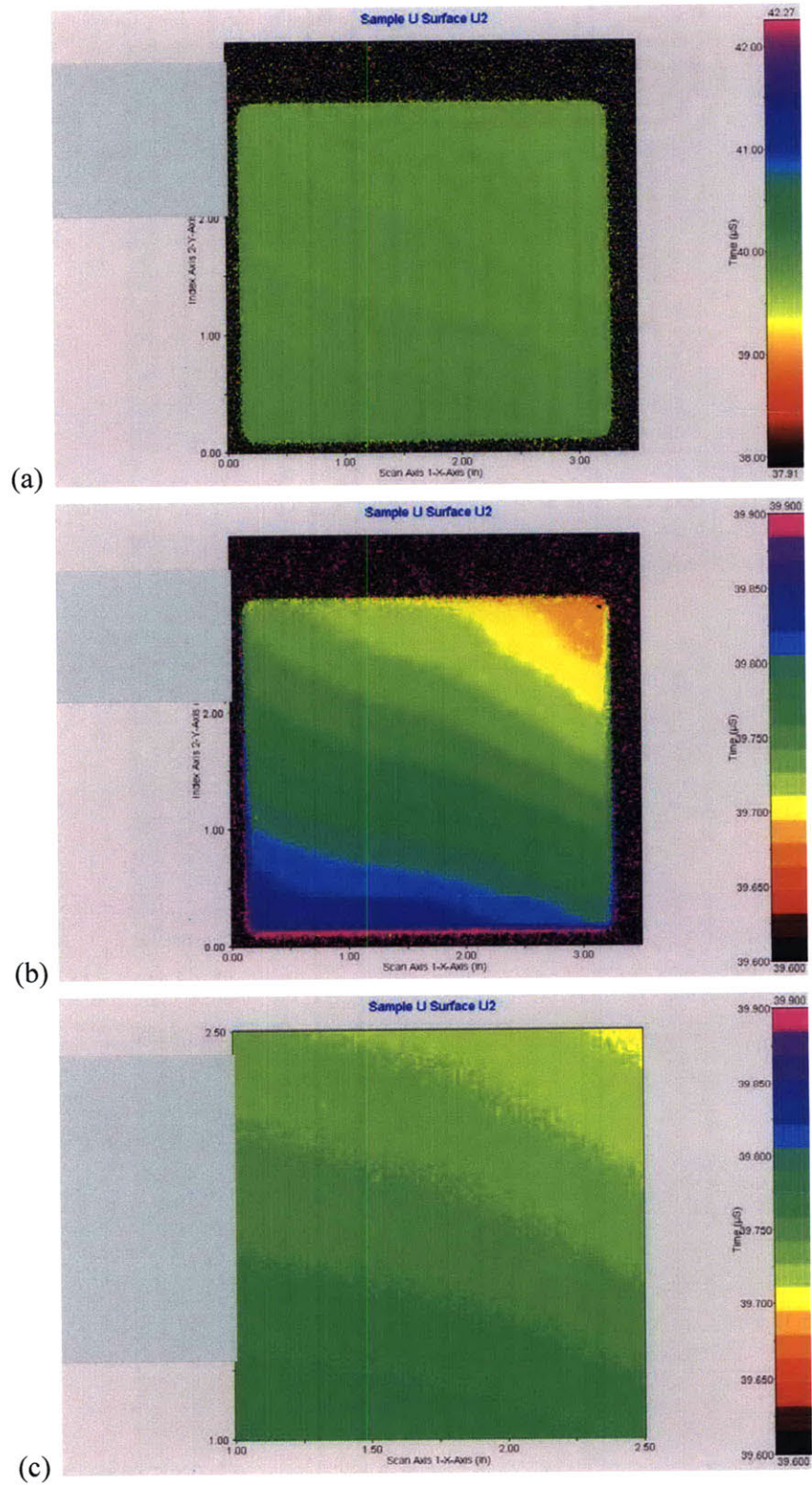


Figure D.16: Top surface inspection of Sample U. Color TOF test data. (a) Full range (b) Manually optimized limited range (c) FBH-array ROI at manually optimized limited range

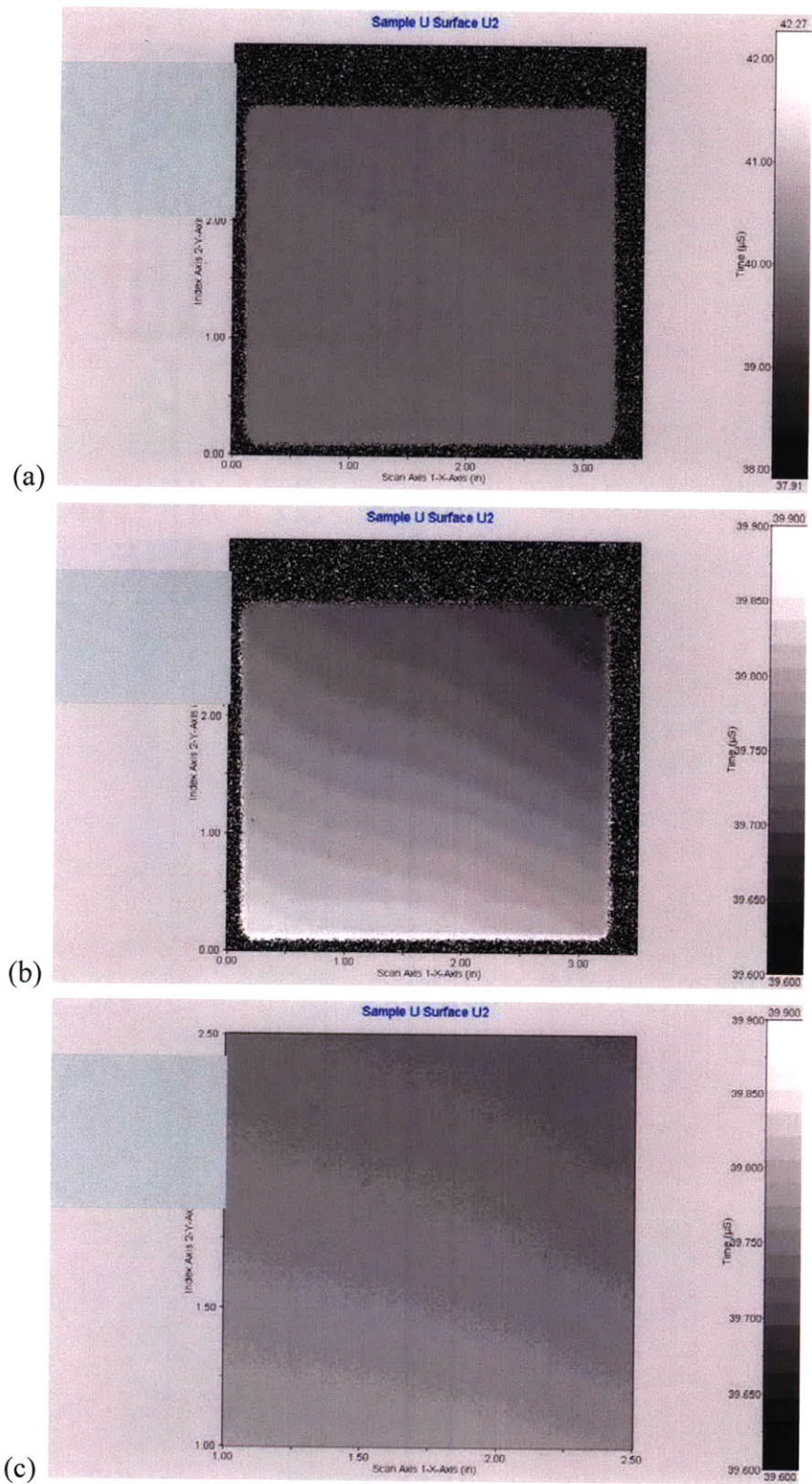


Figure D.17: Top surface inspection of Sample U. Grayscale TOF test data. (a) Full range (b) Manually optimized limited range (c) FBH-array ROI at manually optimized limited range

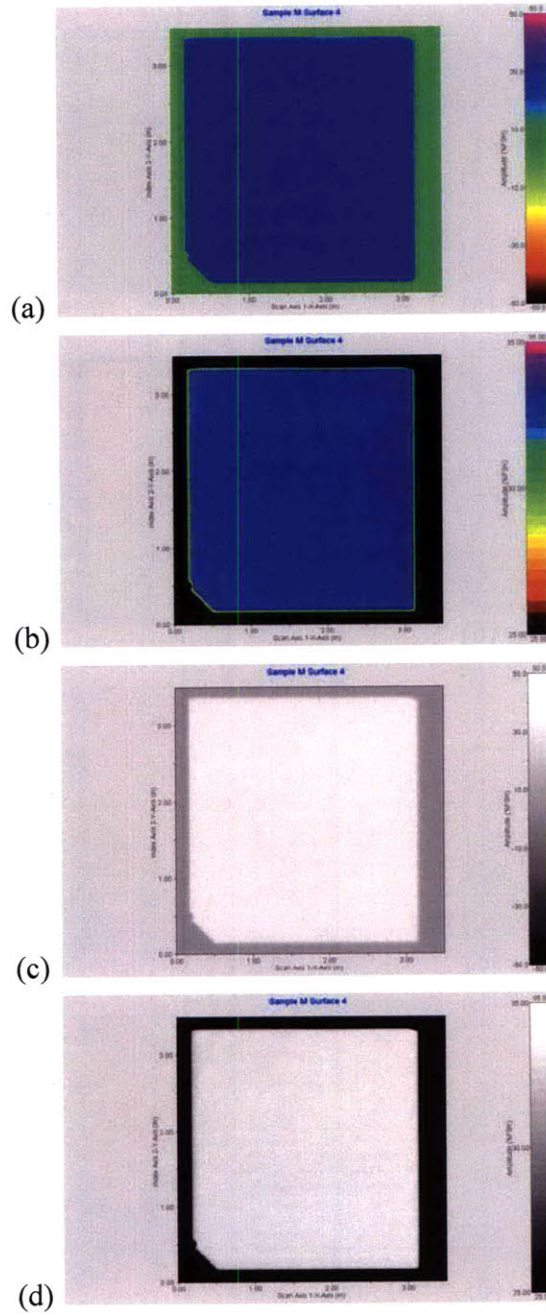


Figure D.18: Top surface inspection of Sample M. Amplitude test data. (a) Color full range (b) Color manually optimized limited range (c) Grayscale full range (d) Grayscale manually optimized limited range

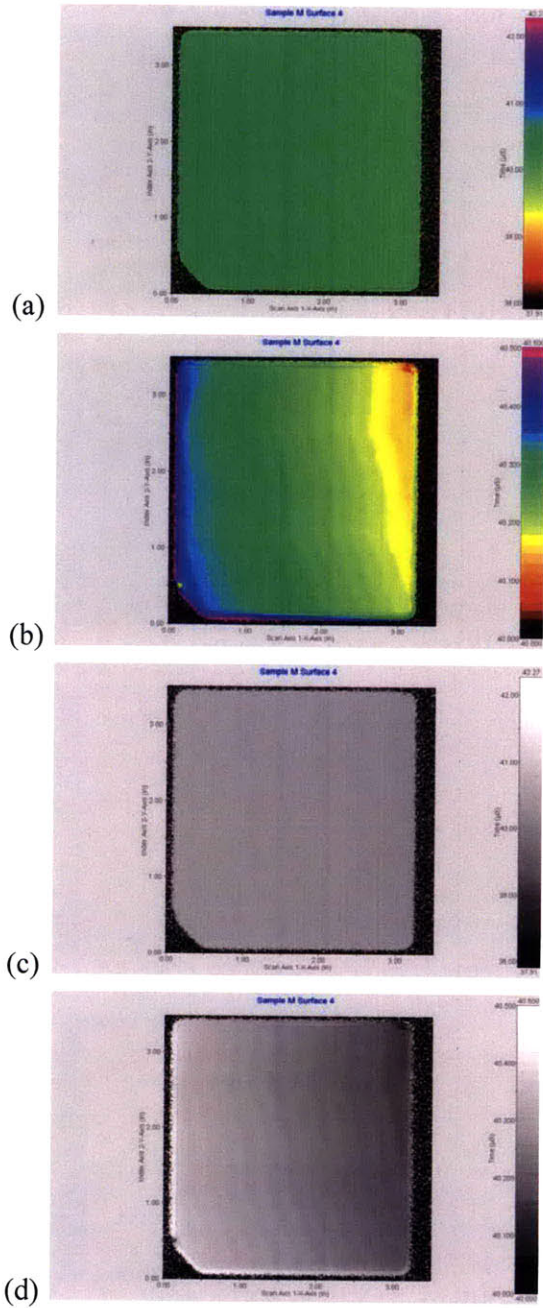


Figure D.19: Top surface inspection of Sample M. Time of flight test data. (a) Color full range (b) Color manually optimized limited range (c) Grayscale full range (d) Grayscale manually optimized limited range

Appendix E: Digital Radiographic Images

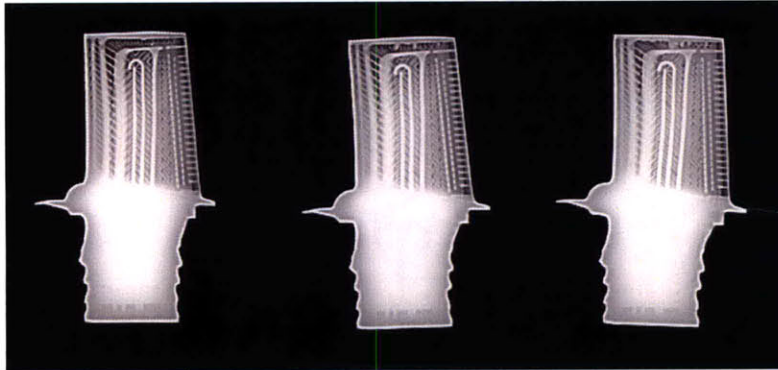


Figure E.1: Image #1 from Table 4.2

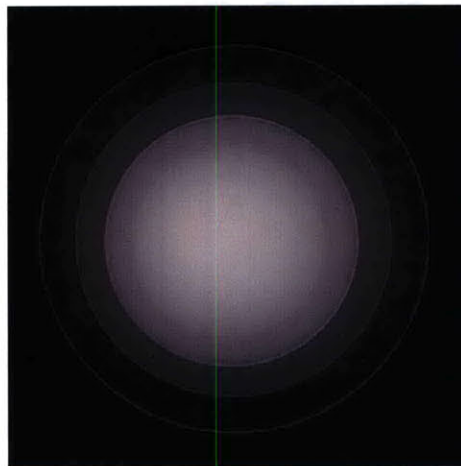


Figure E.2: Image #2 from Table 4.2

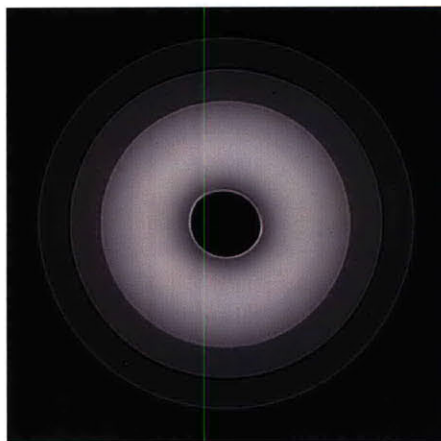


Figure E.3: Image #3 from Table 4.2

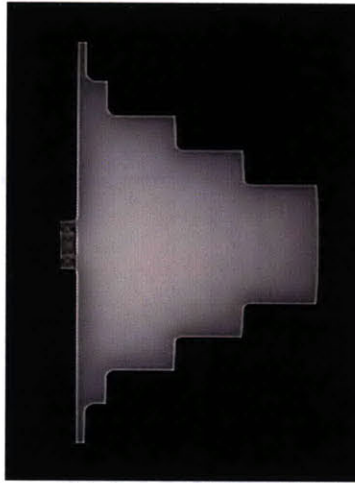


Figure E.4: Image #4 from Table 4.2

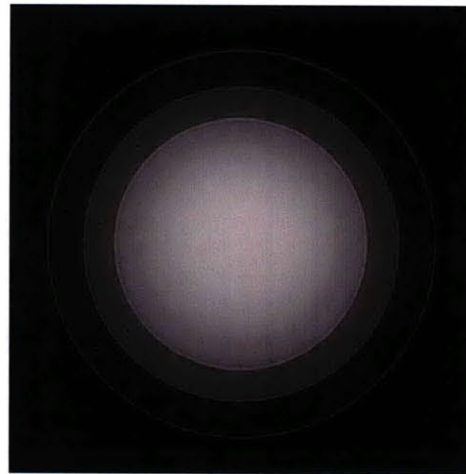


Figure E.5: Image #5 from Table 4.2

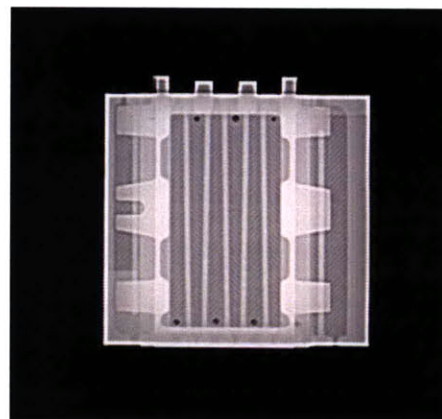


Figure E.6: Image #6 from Table 4.2

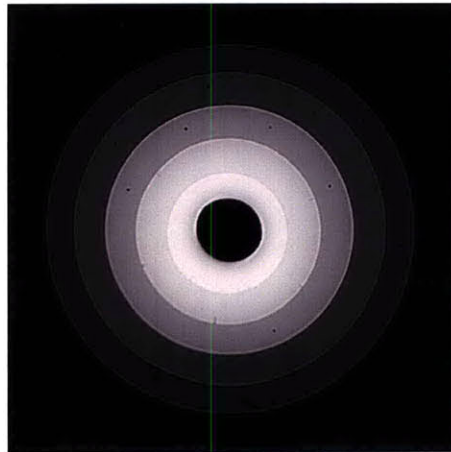


Figure E.7: Image #7 from Table 4.2

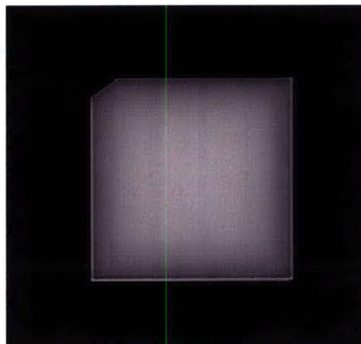


Figure E.8: Image #8 from Table 4.2

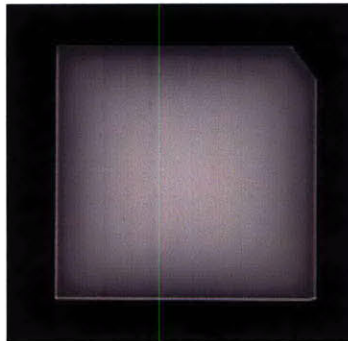


Figure E.9: Image #9 from Table 4.2



Figure E.10: Image #10 from Table 4.2

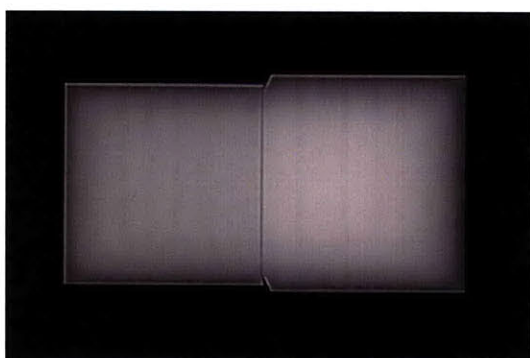


Figure E.11: Image #11 from Table 4.2

References

1. FAA, *Memorandum: Policy for Continued Airworthiness Assessment Methodology for Turbine Engine Rotating Life-Limited Parts Life Shortfall*, US Department of Transportation, Editor. Jan. 2009. p. 1-5.
2. FAA AC No. 33.4-2, *Instructions for Continued Airworthiness: In-service Inspection of Safety Critical Turbine Engine Parts at Piece-Part Opportunity*, U.S. Department of Transportation, Editor. 3/8/01. p. 1-9.
3. FAA AC No. 33.14-1, *Damage Tolerance for High Energy Turbine Engine Rotors*, U.S. Department of Transportation, Editor. 1/8/2001. p. 1-6.
4. FAA AC No. 33.15-1, *Manufacturing Process of Premium Quality Titanium Alloy Rotating Engine Components*, U.S. Department of Transportation, Editor. 9/22/98.
5. FAA AC No. 33.15-X, *Manufacturing Processes for Premium Quality Nickel Alloy for Engine Rotating Parts*, US Department of Transportation, Editor. 2007 (DRAFT). p. 1-17.
6. FAA AC No. 33.70-1, *Guidance Material for Aircraft Engine Life-Limited Parts Requirements*, US Department of Transportation, Editor. 7/31/09. p. 1-23.
7. FAA AC No. 33.70-2, *Damage Tolerance of Hole Features in High-Energy Turbine Engine Rotors*, US Department of Transportation, Editor. 8/28/09. p. 1-40.
8. FAA AC No. 33.70-X, *Damage Tolerance of Hole Features in High-Energy Turbine Engine Rotors*, US Department of Transportation, Editor. 2008 (DRAFT). p. 1-47.
9. FAA AC No. 33.70-Y, *ENGINE LIFE-LIMITED PARTS REQUIREMENTS*, US Department of Transportation, Editor. 2007 (DRAFT). p. 1-21.
10. FAA AC No. 33-X, *Comparative Analysis and Test Methods for Parts Manufacturer Approval of Turbine Engine and Auxiliary Power Unit Parts*, US Department of Transportation, Editor. 2007 (DRAFT). p. 1-13.
11. FAA AC No. 91-XX, *FATIGUE MANAGEMENT PROGRAMS FOR AIRPLANES WITH DEMONSTRATED RISK OF CATASTROPHIC FAILURE DUE TO FATIGUE*, US Department of Transportation, Editor. 2008 (DRAFT). p. 1-26.
12. Federal Aviation Administration ORDER 8110.42C, *Parts Manufacturer Approval Procedures*, US Department of Transportation, Editor. 2005 (DRAFT). p. 1-27.
13. Federal Register, *Airworthiness Standards; Aircraft Engine Standards for Engine Life-Limited Parts; Proposed Rule 14 CFR Part 33*, US Department of Transportation, Editor. 2/2/06. p. 5770-5775.
14. Federal Register, *Airworthiness Standards; Aircraft Engine Standards for Engine Life-Limited Parts; Final Rule 14 CFR Part 33*, US Department of Transportation, Editor. 9/4/07. p. 50856-50861.
15. Christodoulou, L. and J.M. Larsen, *Materials Damage Prognosis: A Revolution In Asset Management*, in *Materials Damage Prognosis*, J.M. Larsen, et al., Editors. Sept 26-30, 2004, TMS: New Orleans, LA. p. 3-9.

16. K.K. Brahma, *Damage Tolerance Approach for Life Management of Commercial Aircraft Engine*. 2005, CADES. p. 1-6.
17. Gallagher, J., C. Babish, and J. Malas, *Damage Tolerant Risk Analysis Techniques for Evaluating the Structural Integrity of Aircraft Structures*, in *The 11th International Conference on Fracture*. 2005. p. 3581-3587.
18. Koul, A.K., N.C. Bellinger, and A. Fahr, *Damage-tolerance-based life prediction of aeroengine compressor discs: I. A deterministic fracture mechanics approach*. International Journal of Fatigue, 1990. **12**(5): p. 379-387.
19. Koul, A.K., N.C. Bellinger, and G. Gould, *Damage-tolerance-based life prediction of aeroengine compressor discs: II. A probabilistic fracture mechanics approach*. International Journal of Fatigue, 1990. **12**(5): p. 388-396.
20. Hoppe, W.C., *Personal Communication RE: TESI Ultrasonic Inspection*, B. Hohmann, Editor. 10/29/2008. p. 5.
21. Boller, C. and W.J. Staszewski, *Ch. 2: Aircraft Structural Health and Usage Monitoring*, in *Health Monitoring of Aerospace Structures: Smart Sensor Technologies and Signal Processing*, W.J. Staszewski, C. Boller, and G.R. Tomlinson, Editors. 2004, John Wiley & Sons: London. p. 27-73.
22. Hudak, S.J., et al., *The Influence of Uncertainty in Usage and Fatigue Damage Sensing on Turbine Engine Prognosis*, in *Materials Damage Prognosis*, JM Larsen et al, Editor. Sept 26-30, 2004, TMS: New Orleans, LA. p. 157-166.
23. Iyyer, N., et al., *Management of Aging Aircraft using Deterministic and Probabilistic Metrics*, in *11th Joint NASA/FAA/DOD Conference on Aging Aircraft*. 2008: Phoenix.
24. Rummel, W. *Challenges in NDI Engineering*. in *ASNT Spring Conference*. 3/24/2010. Williamsburg, VA.
25. Rummel, W. *Overview of Nondestructive Evaluation (NDE) Capabilities Assessments and Probability of Detection (POD) Concepts*. in *World conference of NDT (WCNDT '96)*. 1996. New Delhi.
26. Rummel, W.D., *Low cost method of significantly improving the reliability of instrumented NDT procedures*, Presented to ASNT-Colorado Section, Editor. 9/14/2004: Denver.
27. *Nondestructive Evaluation and Quality Control: Volume 17*. 9th Edition ed. ASM Handbook. 1989: ASM International. 795 pgs.
28. Burkel, R.H., et al., *DOT/FAA/AR-01/96, A Methodology for the Assessment of the Capability of Inspection Systems for Detection of Subsurface Flaws in Aircraft Turbine Engine Components*, US DOT/FAA/Office of Aviation Research, Editor. 2002: Washington, D.C. p. 138.
29. Department of Defense, *DRAFT MIL-HDBK-1823: Nondestructive Evaluation System Reliability Assessment*. Feb. 28, 2007.
30. Smith, K., B. Thompson, and L. Brasche, *Model-Based POD: Successes and Opportunities*. 9/23/2004.
31. Thompson, R.B. and W.Q. Meeker. *Confidence Bounds on Model-Based Data*. in *Model-Assisted POD Working Group*. 11/16/2007.
32. Anderson, T.L., *Fracture Mechanics Fundamentals and Applications*. 2005, Boca Raton: CRC Press. 621 pgs.

33. Barsom, J.M. and S.T. Rolfe, *Fracture and fatigue control in structures : applications of fracture mechanics*. 2nd ed. Prentice-Hall international series in civil engineering and engineering mechanics. 1987, Englewood Cliffs, N.J.: Prentice-Hall. xx, 628 p.
34. Liu, A.F., *Structural Life Assessment Methods*. 1998: ASM International. 419 pgs.
35. Suresh, S., *Fatigue of Materials*. Second ed. 1998, Cambridge: Cambridge University Press. 679.
36. AIA Rotor Manufacturing Project Team, *DOT/FAA/AR-06/3, Guidelines to Minimize Manufacturing Induced Anomalies in Critical Rotating Parts*. 2006, DOT/FAA/Office of Aviation Research, Washington, D.C. p. 82.
37. Thompson, R.B. *Steps Required to Validate New POD Approaches*. in *Model-Assisted POD Working Group*. 11/16/2007.
38. Harlow, D.G., *Probability Versus Statistical Modeling: Examples From Fatigue Life Prediction*. International Journal of Reliability, Quality and Safety Engineering, 2005. **12**(6): p. 535-550.
39. Harlow, D.G. and R.P. Wei, *Linkage Between Safe-Life and Crack Growth Approaches For Fatigue Life Prediction*, in *Materials Lifetime Science & Engineering*. 2003, TMS. p. 3-8.
40. Zhang, R. and S. Mahadevan, *Reliability-based reassessment of corrosion fatigue life*. Structural Safety, 2001. **23**: p. 77-91.
41. Chang, D., R. Schafrik, *Nickel-based alloys in GE aircraft turbines: past, present & future*. Acta Metallurgica Sinica, 2005. **18**(5): p. 561-574.
42. *Personal Communication with the FAA on the cost of test cell experiments*, B. Hohmann and T. Eagar, Editors. 2008: Atlanta, GA.
43. Rosenberg, B., *Taking measure of the machine*, in *Aerospace engineering & manufacturing*. April 2008. p. 38-41.
44. Cartz, L., *Nondestructive Testing*. 1995: ASM International. 229 pgs.
45. Matzkanin, G., *Selecting a Nondestructive Testing Method, Part 2: Visual Inspection*, in *AMMTIAC Quarterly*. 2006. p. 7-10.
46. Bar-Cohen, Y., *In-service NDE of Aerospace Structures--Emerging Technologies and Challenges at the End of the 2nd Millennium*, in *NDT.net*. Sept. 1999. p. 1-26.
47. Matzkanin, G.A. and H.T. Yolken, *A Review of Techniques for Nondestructively Characterizing Residual Stress in Metals*, in *Residual Stress Measurement and General Nondestructive Evaluation*, D.E. Bray, Editor. 2001, The American Society of Mechanical Engineers: New York. p. 1-8.
48. Rice, R.C., ed. *SAE Fatigue Design Handbook, 3rd Edition, AE-22*. 1997, SAE International: Warrendale, PA. 470 pgs.
49. Markanich, J.A., *An Overview of Traditional and Unique Eddy Current Wire Testing Solutions*, Foerster Instruments, Inc. p. 1-9.
50. Nelligan, T. and C. Calderwood. *Introduction to Eddy Current Testing*. 2009 [cited 10/5/2009]; Available from: <http://www.olympus-ims.com/en/eddycurrenttesting/>.
51. *Maxwell's equations*. 2010 [cited 7/3/2010]; Available from: http://en.wikipedia.org/wiki/Maxwell%27s_equations.
52. Goldfine, N., et al., *Rapid, Nonlinear "System" Identification for NDT, Using Sensor Response Databases*. Materials Evaluation, 7/2008. **66**(7).

53. Goldfine, N., et al., *Eddy current sensor networks for aircraft fatigue monitoring*. Materials Evaluation, 2003. **61**(7): p. 852-859.
54. Grundy, D., Andrew Washabaugh, Darrell Schlicker, Ian Shay, Neil Goldfine, *Health Monitoring Using MWM-Array and IDED-Array Sensor Networks*, in *SPIE Symposium*. 2005: San Diego, CA.
55. JC Aldrin et al AFRL-RX-WP-TP-2008-4037, *Reliability Demonstration for an Eddy Current NDE Technique Using a Computational Electromagnetic Model-Assisted Approach*, A.F.R. Lab, Editor. 2006. p. 12.
56. Ingold, B., *Selecting a Nondestructive Testing Method, Part 4: Radiography*, in *AMMTIAC Quarterly*. 2007. p. 7-10.
57. Metris Corporation, *Advanced CT Training Presentation*, A. Ramsey, Editor. 2008.
58. Metris Corporation, *X6 Technology*, G. Dermody, Editor. 2008: Presentation at ROW08 Conference.
59. Tavares, S.M.O., B.P. Hohmann, and T.W. Eagar, *Advances in nondestructive techniques for aerospace structures: In Preparation*. 2010.
60. Levkun, G. and C. Mahendra, *Computed Radiography in the Pacific Northwest: Benefits, Drawbacks, and Requirements*, in *AMMTIAC Quarterly*. 2007. p. 11-14.
61. *Personal communication with David Bate of Nikon Metrology*, B. Hohmann, Editor. 11/9/2009: Cambridge, MA.
62. *ASTM Standard E1742-06, "Standard Practice for Radiographic Examination"*, ASTM, Editor. 2006, ASTM International.
63. GE Healthcare. *Intensifying screen*. 2010 [cited 7/26/2010; Available from: http://www.medcyclopaedia.com/library/topics/volume_i/i/intensifying_screen.aspx].
64. Nelligan, T. *An Introduction to Ultrasonic Flaw Detection*. 2009 [cited 10/5/2009]; Available from: <http://www.olympus-ims.com/en/applications-and-solutions/introductory-ultrasonics/introduction-flaw-detection/>.
65. Olympus Corporation, *Equipment Brochure: Panametrics-NDT (TM) Ultrasonic Transducers*. 2010. p. 49.
66. Matzkanin, G., *Selecting a Nondestructive Testing Method, Part 5: Ultrasonic Testing*, in *AMMTIAC Quarterly*. 2007. p. 9-13.
67. Nelligan, T. *An Introduction to Ultrasonic Material Analysis*. 2009 [cited 10/5/2009]; Available from: <http://www.olympus-ims.com/en/applications-and-solutions/introductory-ultrasonics/introduction-material-analysis/>.
68. Giurgiutiu, V. and A. Cuc, *Embedded Non-destructive Evaluation for Structural Health Monitoring, Damage Detection, and Failure Prevention*. The Shock and Vibration Digest, 2005. **37**(2): p. 83-105.
69. Chen, C., ed. *Ultrasonic and Advanced Methods for Nondestructive Testing and Material Characterization*. 2007, World Scientific Publishing Co.: Hackensack, NJ. 665 pgs.
70. Olympus Corporation, *Equipment Brochure: OmniScan MX*. Multitechnology Flaw Dector: UT, PA, EC, ECA. 2008. 11.
71. Olympus Corporation, *Equipment Brochure: Scanners and Accessories*. Industrial Scanners. 2009. 23.

72. Aerospace Industries Association Rotor Integrity Sub-Committee, *The Development of Anomaly Distributions for Aircraft Engine Titanium Disk Alloys*. 1997. p. 1-11.
73. Ciorau, P. and L. Pullia, *Phased Array Ultrasonic Inspection: A Reliable Tool for Life-Assessment of Low-Pressure Turbine Components*. *IMS Experience 2001-2005*, in *9th EPRI Steam/Turbine Generator Workshop*. 2005: Denver, CI.
74. Edmund Optics. *Electronic Imaging Resource Guide*. [cited November 7, 2007]; Available from:
<http://www.edmundoptics.com/TechSupport/DisplayArticle.cfm?articleid=286>.
75. Brockman, R.A., M.A. Huelsman, and R. John, *Simulation of Deformation Modes for Damage Detection in Turbine Engine Disks*, in *Materials Damage Prognosis*, JM Larsen et al, Editor. Sept 26-30, 2004, TMS: New Orleans, LA. p. 197-201.
76. Cobb, A.C., J.E. Michaels, and T.E. Michaels, *Experimental verification of a Kalman filter approach for estimating the size of fastener hole fatigue cracks*. 2008, Georgia Institute of Technology,. p. 1-12.
77. Bewlay, B.P., et al., *Patent # 6387197 B1: Titanium Processing Methods for Ultrasonic Noise Reduction*, USPTO, Editor. 5/14/2002, GE Company, Ladish Company: USA.
78. Gigliotti, M.F.X., et al., *Microstructure-Ultrasonic Inspectability Relationships in Ti6242: Signal-to-Noise in Fine-Grain-Processed Ti6242*. *Metallurgical and Materials Transactions*, Sept 2000. **31A**(9): p. 2119-2125.
79. Gigliotti, M.F.X., et al., *Patent #7,575,418 B2: Erosion and Wear Resistant Protective Structures for Turbine Components*, USPTO, Editor. 2009: United States.
80. Blodgett, M., *Anisotropic grain noise in eddy current inspection of noncubic polycrystalline metals*. *Applied Physics Letters*, 1998. **72**(9): p. 1045-1047.
81. Giakos, G.C., et al., *A Sensitive Optical Polarimetric Imaging Technique for Surface Defects Detection of Aircraft Turbine Engines*. *IEEE Transactions On Instrumentation And Measurement*, 2004. **63**(1): p. 216-222.
82. Ruiz-Reyes, N., et al., *High-resolution pursuit for detecting flaw echoes close to the material surface in ultrasonic NDT*. *NDT&E International*, 2006. **39**: p. 487-492.
83. Thompson, R.B., *Influence of texture on backscattered ultrasonic noise*. *Materials Science Forum*, 1994. **157-162**: p. 221-226.
84. Rummel, W., G. Hardy, and T. Cooper, *Applications of NDE Reliability to Systems*, in *ASM Vol. 17: Nondestructive Evaluation and Quality Control*, J.R. Davis, et al., Editors. 1989, ASM International. p. 674-688.
85. Makeev, A., Y. Nikishkov, and E. Armanios, *A concept for quantifying equivalent initial flaw size distribution in fracture mechanics based life prediction models*. *International Journal of Fatigue*, 2007. **29**: p. 141-145.
86. Cross, R., A. Makeev, and E. Armanios, *Simultaneous uncertainty quantification of fracture mechanics based life prediction model parameters*. *International Journal of Fatigue*, 2007. **29**: p. 1510-1515.
87. Gandossi, L. and K. Simola, *Bayesian analysis of flaw sizing data of the NESC III exercise*. *International Journal of Pressure Vessels and Piping*, 2006. **83**: p. 654-662.

88. Hasanzadeh, R.P.R., *Optimal signal-adaptive maximum likelihood filter for enhancement of defects in eddy current C-scan images*. NDT&E International, 2008. **41**: p. 371-381.
89. Lo, C.C.H., et al., *Self-Consistent Swept Frequency Eddy Current Measurements for Characterization of Near Surface Material Conditions*. Proceedings of the American Institute of Physics, 2009: p. 1363-1370.
90. Blodgett, M.P., F. Yu, and P.B. Nagy, *Eddy Current Nondestructive Residual Stress Assessment in Shot-Peened Nickel-Base Superalloys*, in *Review of Quantitative Nondestructive Evaluation*. 2005, American Institute of Physics. p. 1347-1354.
91. Goldfine, N. and D. Damm, *Material Condition and Usage Monitoring Sensors and Algorithms for Adaptive Management of Legacy and New Platforms*.
92. Kramb, V., *Probability of Detection For Embedded Defects: Needs For Ultrasonic Inspection of Aerospace Turbine Engine Components*, in *Advanced Topics in Phased Array Ultrasonics*. 2007, Olympus NDT.
93. Kramb, V.A., ed. *Linear Array Ultrasonic Transducers: Sensitivity and Resolution Study*. Review of Quantitative Nondestructive Evaluation, ed. D.O. Thompson and D.E. Chimenti. Vol. 24. 2005.
94. Srivatsa, S., *Effect of Forging on Defect Morphology Phase II Report*. 2002, GE Aircraft Engines. p. 1-46.
95. Kramb, V., *Design, Commissioning and Production Performance of an Automated Phased Array System for Jet Engine Disk Inspection*, in *Advanced Topics in Phased Array Ultrasonics*. 2007, Olympus NDT.
96. Stubbs, D.A. *Overview of the USAF Automated Ultrasonic Inspection System for Detecting Internal Defects in Aging Turbine Engine Components*. in *8th Joint NASA/FAA/DOD Conference on Aging Aircraft*. 2/2/2005. Palm Springs, CA.
97. Kramb, V., *Defect Detection and Classification in Aerospace Materials Using Phased Array Ultrasonics*, in *16th World Conference on Nondestructive Testing*. 2004: Montreal, Canada.
98. Kramb, V.A. *Use of Phased Array Ultrasonics in Aerospace Engine Component Inspections*. in *8th Joint NASA/FAA/DOD Conference on Aging Aircraft*. 2/2/2005. Palm Springs, CA.
99. Kramb, V.A., *Use of Phased Array Ultrasonics for Automated Aerospace Testing Applications*. Materials Evaluation, January 2007. **65**(1): p. 67-77.
100. Stubbs, D., et al., *An automated ultrasonic system for inspection of aircraft turbine engine components*. Insight, March 2005. **47**(3).
101. Kramb, V., *Assessment of Coverage and Sensitivity for Embedded Defect Detection In Preparation*, University of Dayton Research Institute. p. 1-14.
102. Kramb, V., *Use of Phased Array Ultrasonics in Aerospace Engine Component Inspections: Transition From Conventional Transducers*, in *16th World Conference on Nondestructive Testing*. 2004: Montreal, Canada.
103. Deyber, S., et al., *Probabilistic Life of DA718 For Aircraft Engine Disks*, in *Superalloys 718, 625, 706, and Derivatives*, E.A. Loria, Editor. Oct. 2-5,2005, TMS. p. 97-110.

104. Szczepanski, C.J., et al., *Microstructural Influences on Very-High-Cycle Fatigue-Crack Initiation in Ti-6246*. Metallurgical and Materials Transactions A, 2008. **39A**(December): p. 2841-2851.
105. Xie, X., et al., *Micro-Mechanical Behavior Study Of Non-Metallic Inclusions In P/M Disk Superalloy Rene '95*, in *Tenth International Symposium on Superalloys*. 2004, The Minerals, Metals & Materials Society: Champion, Pennsylvania.
106. Cooke, L., W. Miglietti, and D. Nagy. *Basic Gas Turbine Metallurgy and Repair Technology Workshop*. 2009: ASME International Gas Turbine Institute.
107. *Metals Handbook Volume 4: Heat Treating*. 9th Edition ed. 1981: ASM.
108. Kramb, V.A., et al., eds. *Considerations for Using Phased Array Ultrasonics in a Fully Automated Inspection System*. Review of Quantitative Nondestructive Evaluation, ed. D.O. Thompson and D.E. Chimenti. Vol. 23. 2004, American Institute of Physics. 817-825.
109. Patankar, M.S. and J.C. Taylor, *Risk Management and Error Reduction in Aviation Maintenance*. 2004, Hampshire, England: Ashgate Publishing Co.
110. SAE International SP-1270, *Uncontained Turbine Engine Rotor Events*. 1998, SAE: Warrendale, PA.
111. Goldfine, N., et al., *Damage and Usage Monitoring for Vertical Flight Vehicles*, in *American Helicopter Society (AHS)*. 2007: Virginia Beach, VA.
112. Goldfine, N., M. Windoloski, and V. Zilberstein, *Mapping and Tracking of Damage in Titanium Components for Adaptive Life Management*, in *10th Joint NASA/FAA Conference on Aging Aircraft*. 2007: Palm Springs, CA.
113. Olympus Corporation, *Equipment Brochure: Phased Array Probes and Wedges*. Phased Array Inspections. 2009. 23.
114. NTSB AAR-96-06, *In-flight Loss of Propeller Blade Forced Landing, and Collision with Terrain Atlantic Southeast Airlines, Inc., Flight 529 Embraer EMB-120RT, N256AS, Carrollton, Georgia, August 21, 1995*. 11/26/1996.
115. *NTSB Aviation Accident Statistics: Accidents Involving Passenger Fatalities, U.S. Airlines (Part 121) 1982-Present*. 2010 [cited 4/9/2010; Available from: <http://www.nts.gov/AVIATION/Stats.html>].
116. SAE International, *AIR 4003, Report on Aircraft Engine Containment* 1987: Warrendale, PA.
117. SAE International, *AIR 1537A, Report on Aircraft Engine Containment*. 1996: Warrendale, PA.
118. *FAA Accident & Incident Data*. 2010 [cited 2/11/2010; Available from: http://www.faa.gov/data_research/accident_incident/preliminary_data/].
119. National Transportation Safety Board, *Aircraft Accident Report--United Airlines Flight 232, McDonnell Douglas DC-10-10, Sioux Gateway Airport, Sioux City, Iowa, July 19, 1989*, NTSB, Editor. 1990. p. 1-129.
120. *United Airlines Flight 232*. [cited 11/1/2006]; Available from: http://en.wikipedia.org/wiki/United_Airlines_Flight_232.
121. McEvily, A.J., *Failures in inspection procedures: case studies*. Engineering Failure Analysis, 2003. **11**: p. 167-176.
122. Thompson, R.B., et al., *DOT/FAA/AR-07/63, Update of Default Probability of Detection Curves for the Ultrasonic Detection of Hard Alpha Inclusions in*

- Titanium Alloy Billets*. 2008, DOT/FAA/ Office of Aviation Research and Development: Washington,D.C. p. 152.
123. Wald, M.L. *Air Fatalities Drop Sharply Over Decade*. 2007 [cited November 2, 2007]; Available from: http://news.aol.com/story/ar/_a/air-fatalities-drop-sharply-over-decade/20071001092109990002.
 124. *ASN Aircraft accident McDonnell Douglas MD-88 N927DA Pensacola Regional Airport, FL (PNS)*. [cited 3/31/2008]; Available from: <http://aviation-safety.net/database/record.php?id=19960706-0>.
 125. National Transportation Safety Board, *Aircraft Accident Report 98-01, Delta Airlines Flight 1288, MD-88 N927DA, Pensacola,Florida*. 1996, FAA: Washington, D.C. p. 1-137.
 126. Melcher, J.R., *US Patent No. 5,015,951: Apparatus and Methods for Measuring Permeability and Conductivity in Materials Using Multiple Wavenumber Magnetic Interrogations*, USPTO, Editor. May 1991.
 127. Goldfine, N. and J. Melcher, *U.S. Patent No. 6,433,542B2: Apparatus and method for obtaining increased sensitivity, selectivity and dynamic range in property measurement using magnetometers*, USPTO, Editor. August 13,2002.
 128. Goldfine, N. and J. Melcher, *U.S. Patent No. 5,453,689: Magnetometer having a periodic winding structure and material property estimator*, USPTO, Editor. Sept. 26, 1995.
 129. Goldfine, N., D.C. Clark, and H.D. Eckhardt, *US Patent Number 5,793,206: Meandering Winding Test Circuit*, USPTO, Editor. August 11, 1998.
 130. Goldfine, N. and J. Melcher, *Magnetometers for Improved Materials Characterization in Aerospace Applications*. Materials Evaluation March 1993. **51**(3): p. 396-405.
 131. Sheiretov, Y. and M. Zahn, *Design and modeling of shaped-field magnetoquasistatic sensors*. Ieee Transactions on Magnetics, 2006. **42**(3): p. 411-421.
 132. Goldfine, N., David Grundy, Andrew Washabaugh, Chris Craven, Volker Weiss, Vladimir Zilberstein, *Fatigue and Stress Monitoring with Magnetic Sensor Arrays*, in *Society for Experimental Mechanics* 2006: St. Louis, MI.
 133. Goldfine, N., et al., *Enhancements in MWM-Array Hidden Corrosion Imaging*, in *Tri-Service Corrosion Conference*. 2003: Las Vegas, NV.
 134. Sheiretov, Y., et al., *TBC Characterization Using Magnetic Electric Field Sensors*, in *ASME Turbo Expo*. 2007: Montreal, Canada.
 135. Goldfine, N., et al., *MWM-Array Eddy Current Sensors for Detection of Cracks in Regions with Fretting Damage*. Materials Evaluation, 2002. **60**(7): p. 1-14.
 136. Goldfine, N. and J. Melcher, *US Patent No. 5,629,621: Apparatus and methods for obtaining increased sensitivity, selectivity, and dynamic range in property measurements using magnetometers*, USPTO, Editor. May 13,1997.
 137. Nelligan, T. and D. Koos. *An Introduction to Ultrasonic Phased Array Technology*. 2009 [cited 10/5/2009]; Available from: <http://www.olympus-ims.com/en/ultrasonics/intro-to-pa/>.
 138. Vidyasankar, S. *Phased Array Ultrasonics: Is it the future of ultrasonic nondestructive testing (NDT)?-Part 1*. 6/30/2006 [cited 6/25/08]; Available

- from: <http://www.frost.com/prod/servlet/market-insight-print.pag?docid=73772253>.
139. Vidyasankar, S. *Phased Array Ultrasonics: Is it the Future of Ultrasonic Nondestructive Testing (NDT)?-Part 2*. 9/62006 [cited 5/24/2010]; Available from: <http://www.frost.com/prod/servlet/market-insight-top.pag?docid=80759372>.
 140. University of Dayton Research Institute. *It's Not a Fish Tank*. 2003 [cited August 11, 2008]; Available from: <http://www.udri.udayton.edu/NR/exeres/CB55F482-2E2E-4C24-AA1E-B83678865F35.htm>.
 141. Raimondi, R., *Personal Communication RE: Olympus Omniscan rental*, B. Hohmann, Editor. 4/23/2010. p. 11.
 142. Drinkwater, B.W. and P.D. Wilcox, *Ultrasonic arrays for non-destructive evaluation: A review*. NDT&E International, 2006. **39**: p. 525-541.
 143. Moles, M. and A. Lamarre, *Ultrasonic Phased Arrays*, in *Advanced Materials & Processes*. March 2007. p. 37-40.
 144. Department of Defense, *Militarily Critical Technologies List*. 2004.
 145. Wende, R., *CT Technology*. 10/4/2007, Yxlon International. p. 1-45.
 146. Wheeler, E., *Air Force Manufacturing Technology NDE Programs Supporting Manufacturing and Maintenance*. 1989, Wright Research and Development Center (WRDC/MTM): Wright-Patterson Air Force Base, OH. p. 1539-1545.
 147. *X-ray computed tomography*. 2010 [cited 7/13/10; Available from: http://en.wikipedia.org/wiki/X-ray_computed_tomography.
 148. Azevedo, S.G., H.E. Martz, and D.J. Schneberk, *Potential of Computed Tomography for Inspection of Aircraft Components*, in *SPIE International Symposium on Optics, Imaging, and Instrumentation*. 1993: San Diego, CA.
 149. Noel, J., *Computed Tomography- 3D Scanning of Industrial Parts*, in *NDT Marketplace*. 5/2010. p. 27-31.
 150. Lecklider, T., *3-D X-ray Inspection Looks Into the Void*, in *Evaluation Engineering*. Dec. 2009. p. 1-6.
 151. Metris Corporation, *Metris Case Study: Reverse Engineering of Turbine Blades*. 8/1/2004.
 152. Pick, L. and O. Kleinberger, *Going Digital*, in *Materials Evaluation*. Oct. 2009. p. 1111-1116.
 153. U. Ewert et al., *New Compensation Principles for Enhanced Image Quality in Industrial Radiology with Digital Detector Arrays*, in *Materials Evaluation*. 2/2010. p. 163-168.
 154. Mounsey, S., *AI can see clearly now*, in *Imaging and Machine Vision Europe*. Aug/Sept 2009. p. 18-20.
 155. Metris Corporation, *Metris Case Study: Aircraft component inspection programs subcontracted as part of turnkey service*. 2009.
 156. Heuseveldt, J.W., *Metris Case Study: GE Advanced Materials uses a 3D laser scanner for enhanced application development support*. 2009.
 157. *ATOS-Advanced Topometric Sensor Overview*. [cited 7/15/10; Available from: http://www.3dscan-xpress.com.au/atos/atos_overview.html.

158. Bileschi, S. and L. Wolf, *A unified system for object detection, texture recognition, and context analysis based on the standard model feature set*. 2005, Massachusetts Institute of Technology: Cambridge, MA. p. 1-11.
159. Chandler, D., *MIT helps develops new image-recognition software*, in *TechTalk*. 2008: Cambridge, MA. p. 1, 3.
160. Chandler, J.G. *Future Inspection Technologies*. Overhaul and Maintenance February 2008 [cited 2/29/2008]; Available from: http://www.aviationweek.com/aw/generic/story_generic.jsp?channel=om&id=news/om208cvr.xml&headline=Future+Inspection+Technologies.
161. R. Tumbare and D.J. Brady, *Sensor plane processing for multiplex imaging*. IEEE, 2000: p. 1-6.
162. Wu, W., *Patent # 7,382,507, Image quality defect detection from image quality database*, USPTO, Editor. 2008, Xerox Corporation: United States.
163. Carpenter, A., et al., *Cellprofiler: image analysis software for identifying and quantifying cell phenotypes*. *Genome Biology*, 2006. 7(10): p. R.100.1-R.100.11.
164. Jones, T.R., *Personal Communication: Cellprofiler follow up*, B. Hohmann, Editor. 5/19/2010. p. 2.
165. Lamprecht, M.R., D.M. Sabatini, and A.E. Carpenter, *Cellprofiler(TM): free, versatile software for automated biological image analysis*. *BioTechniques*, 2007. 42(1): p. 71-75.
166. *Cellprofiler: Cell Image Analysis Software*. [cited 7/31/10]; Available from: <http://www.cellprofiler.org/>.
167. Jones, T.R., et al., *Scoring diverse cellular morphologies in image-based screens with iterative feedback and machine learning* *Proceedings of the National Academy of Sciences of the USA*, Feb. 2009. 106(6): p. 1826-1831.
168. The Medical News. *Advanced imaging algorithm makes for clearer ultrasound images*. 2007 [cited June 25, 2009]; Available from: <http://www.news-medical.net/news/2007/07/17/27671.aspx>.
169. The Associated Press. *Computers as good at reading mammograms as second eyes*. 2008 [cited October 2, 2008]; Available from: <http://www.cnn.com/2008/HEALTH/conditions/10/01/computer.mammogram.hel.p.ap/index.html>.
170. American Gastroenterological Association. *New Techniques Improve Imaging Quality, Not Diagnosis of Barrett's Esophagus*. 2008 [cited; Available from: <http://www.sciencedaily.com/releases/2008/03/080311140133.htm>.
171. Jobst, M., et al. *Developing New Information Object Definitions for DICONDE*. 4th European-American Workshop on Reliability of NDE 2009 [cited 7/31/10]; Available from: <http://www.ndt.net/article/reliability2009/Inhalt/th5b4.pdf>.
172. *ASTM Standard E 2339, "Standard Practice for Digital Imaging and Communication in Nondestructive Evaluation (DICONDE)"*, ASTM, Editor. 2006, ASTM International.
173. Samari, C. *Dealing with non-DICONDE Assets in a DICONDE World*. in *Digital Imaging XIII Conference*. 7/19-7/21, 2010. Foxwoods Resort, CT: ASNT.
174. Chati, M., J. Laflen, and K. Wright, *Cumulative Damage Models For Single Crystal Nickel-Based Superalloy*, in *Materials Damage Prognosis*, JM Larson et al, Editor. Sept 26-30, 2004, TMS: New Orleans, LA. p. 55-63.

175. Koul, A.K., et al., *Improving Component Life Prediction Accuracy and Reliability Through Physics Based Prognosis - A Probabilistic Turbine Blade Case Study*, ASME, Editor. 2008, Life Prediction Technologies: Ottawa. p. 1-7.
176. Wei, R.P. and D.G. Harlow, *Mechanistically based probability modelling, life prediction and reliability assessment*. Modelling and Simulation in Materials Science and Engineering, 2005. **13**: p. R33-R51.
177. Chan, K.S., et al., *Life Prediction Strategies For Land-Based Gas Turbine Blades*, in *Materials Lifetime Science & Engineering*. 2003, TMS. p. 191-209.
178. Chan, K.S. and M.P. Enright, *A Probabilistic Micromechanical Code for Predicting Fatigue Life Variability: Model Development and Application*. Journal of Engineering for Gas Turbines and Power, 2006. **128**(October): p. 889-895.
179. Mattingly, J.D., W.H. Heiser, and D.T. Pratt, *Aircraft Engine Design 2nd Edition*. 2002, Reston, VA: American Institute of Aeronautics and Astronautics. 692 pgs.
180. Campbell, J.E., W.W. Gerberich, and J.H. Underwood, *Application of Fracture Mechanics for Selection of Metallic Structural Materials*. 1982, Metals Park: American Society For Metals. 365 pgs.
181. Anderson, T.L. and D.A. Osage, *API 579: a comprehensive fitness-for-service guide*. International Journal of Pressure Vessels and Piping, 2000. **77**: p. 953-963.
182. Janssen, M., J. Zuidema, and R.J.H. Wanhill, *Fracture Mechanics*. Second ed. 2006, Delft: VSSD. 365 pgs.
183. Bonacuse, P. *Retirement for Cause as an Alternate Means of Managing Component Lives*. 1997 [cited 7/17/10; Available from: www.grc.nasa.gov/WWW/RT/RT1996/5000/5220b01.htm].
184. Margetan, F., et al., *DOT/FAA/AR-02/114: Fundamental Studies: Inspection Properties for Engine Titanium Alloys*, DOT/FAA/ Office of Aviation Research, Editor. Dec. 2002. p. 158.
185. Goldfine, N., et al., *Damage and Usage Monitoring for Vertical Flight Vehicles*, in *American Helicopter Society (AHS) 63rd Annual Forum*. 5/1-5/3, 2007: Virginia Beach, VA.
186. Goldfine, N., V. Zilberstein, and T. Lovett. *Pipeline & pipeline damage mapping and tracking using high-resolution imaging MWM-arrays*. in *ASNT international Chemical and Petroleum Industry Inspection Technology (ICPIIT) X Conference*. 6/20-6/23, 2007. Houston, TX: ASNT.
187. JENTEK Sensors Inc., *DRAFT: User's Guide-General Use*. 6/7/04. p. 40.
188. Zilberstein, V. and D. Grundy, *JENTEK Technology & Applications*. 8/29/07.
189. Goldfine, N., et al. *Automated Engine Disk Inspection for Detecting Cracks in Regions with Fretting Damage*. in *ASNT Fall Conference and Quality Testing Show 2005*. 10/17-10/19, 2005. Columbus, OH: ASNT.
190. Hohmann, B.P. and T.W. Eagar, *Advanced NDT processes for remnant life prediction of aerospace engine components*, in *Digital Imaging XIII*. 7/21/2010, ASNT: Foxwoods Resort, Mashantucket, CT. p. 66-76.
191. Kramb, V., *Personal Communication RE: Notched samples*, B. Hohmann, Editor. 5/17/2010. p. 4.
192. Olympus Corporation, *TomoView*. UT Data Acquisition and Analysis Software. 2010. 7.

193. Kramb, V., *Personal communication RE: Tomoview questions-- Can TESI system be used to accurately size FBH defects?*, B. Hohmann, Editor. 6/11/10.
194. Bar-Cohen, Y. and A. Mal, *Ultrasonic Inspection*, in *ASM Handbook: Volume 17, Nondestructive Evaluation and Quality Control*, J.R. Davis, et al., Editors. 1989, ASM International. p. 231-277.
195. Chen, C., *Personal Communication on Wedding cake samples*, B. Hohmann, Editor. 1/29/2010. p. 1.
196. Smith, A., *Personal Communication: Pricing Yxlon 600/800KV system*, B. Hohmann, Editor. 5/6/2010. p. 1.
197. Smith, A., *Personal Communication: follow up on CT*, B. Hohmann, Editor. 6/3/2010. p. 1.
198. Alfieri, R., *Personal Communication Re: X-ray sharpness of Wedding cake images*, B. Hohmann, Editor. 12/14/2009. p. 3.
199. Dennis, M., *Industrial Computed Tomography*, in *ASM Vol. 17: Nondestructive Evaluation and Quality Control*, J.R. Davis, et al., Editors. 1989, ASM International. p. 358-386.
200. Reinhart, C., et al., *How Industrial Computer Tomography Accelerates Product Development in the Light Metals Casting and Injection Moulding Industry*, in *Digital Imaging XIII*. 7/19-7/21, 2010, ASNT: Foxwoods Resort, Ct.
201. Annis, C., *Personal Communication RE: Mil-HDBK-1823 POD files*, B. Hohmann, Editor. 3/17/2009. p. 1.
202. Berens, A., *NDE Reliability Data Analysis*, in *ASM Vol. 17: Nondestructive Evaluation and Quality Control*, J.R. Davis, et al., Editors. 1989, ASM International. p. 689-701.
203. Enright, M.P. and L. Huyse, *Methodology for Probabilistic Life Prediction of Multiple-Anomaly Materials*. AIAA Journal, 2006. **44**(4): p. 787-793.
204. Hohmann, B., *Class Notes for "3.577: Engineering Risk Benefit Analysis"*, Instructor: George Apostolakis, Editor. Spring 2009: Massachusetts Institute of Technology.
205. Meel, A., et al., *Frequency and Consequence Modeling of Rare Events Using Accident Databases in 8th Process Plant Safety Symposium, 2006 Spring National Meeting*, 4/24-4/26, 2006, American Institute of Chemical Engineers: Orlando, FL. p. 19.
206. McMorro, D., *Rare Events*. 10/2009, JASON - The MITRE Corp.: McLean, VA. p. 104.
207. Gumbel, E.J., *Statistics of Extremes*. 1958, New York: Columbia University Press. 375.
208. NTSB, *AAR-96-06: In-flight Loss of Propeller Blade Forced Landing, and Collision with Terrain Atlantic Southeast Airlines, Inc., Flight 529 Embraer EMB-120RT, N256AS, Carrollton, Georgia, August 21, 1995*. 11/26/1996, FAA.
209. NTSB, *AAR96-03: Uncontained Engine Failure/Fire, ValuJet Airline Flight 597, Douglas DC-9-32, N908VJ, Atlanta, GA, June, 8, 1995*. 1996, FAA. p. 139.
210. NTSB, *AAR-97-06: In-Flight Fire and Impact with Terrain, ValuJet Airlines, Flight 592, DC-9-32, N904VJ, Everglades, near Miami, FL, May, 11, 1996*. 1997, FAA. p. 271.

211. NTSB, AAR-97-03: *Descent below visual glidepath and collision with terrain, Delta Airline Flight 554, MD-88, N914DL, Lagaurdia airport, NY, October, 19, 1996.* 1997, FAA. p. 180.
212. NTSB, AAR-10-03: *Loss of thrust in Both engines After Encountering a Flock of Birds and Subsequent Ditching on the Hudson river, US Airways Flight 1549, Airbus A320-214,N106US, Weehawken, NJ, January,15,2009.* 2010, FAA. p. 213.
213. *FAA certifies Pratt & Whitney CFM56-3 Engine Life Limited Parts*, in *Associated Press*. 3/19/2008.
214. *Flying Cheap*, in *Frontline*. 5/30/2010, PBS: USA. p. 1 hr.
215. *Event Details - Uncontained engine failure, Boeing B737-300, September 12,1999.* 2007 [cited 6/22/2007]; Available from: www.fss.aero/accident-reports/look.php?report_key=950.
216. Alabama & Northwest Florida Flight Standards District Office. *Human Error in Maintenance*. [Powerpoint presentation] 8/11/10 [cited; Available from: <http://www.avhf.com/html/Publications/FAA/FAA%20PowerPoint%20Files/HEI M.ppt>].
217. Bayha, T., et al., *The Metals Affordability Initiative Consortium*. Advanced Materials & Processes, 2002(May): p. 1-3.
218. Burchell, B., *PMA Debate*, in *Aviation Week*. Nov 2007. p. 48-50.
219. *Inflation rates in the US*. 2010 [cited 8/15/10; Available from: http://inflationdata.com/Inflation/Inflation_Rate/HistoricalInflation.aspx].
220. Leverant, G.R., et al., *DOT/FAA/AR-00/64, Turbine Rotor Material Design*, DOT/FAA/ Office of Aviation Research, Editor. Dec. 2000: Washington, D.C. p. 1-355.
221. Martin, R. and D. Evans, *Reducing Costs in Aircraft: The Metals Affordability Initiative Consortium*. JOM, 2000. **52**(3): p. 24-28.
222. Tegtmeier, L.A., *Balancing Competition in MRO*, in *Aviation Week*. 4/20/2009. p. 58-60.
223. Epstein, A., *Personal Communication: Pratt & Whitney MRO vs OEM sales for 2007*, B. Hohmann, Editor. 2008.
224. Backman, D., *Accelerated Insertion of Metallic Structural Materials*. Aircraft Engineering and Aerospace Technology, 2004. **76**(1).
225. Committee on Integrated Computational Materials Engineering, N.R.C., *Integrated Computational Materials Engineering: A Transformational Discipline for Improved Competitiveness and National Security*. 2008, National Academies Press: Washington. p. 152.
226. Derriso, M.M., J.R. Calcaterra, and S.E. Olson, *Integrated Systems Health Management: Enabling Technology for Effective Utilization of Air Vehicle Systems*, in *Materials Damage Prognosis*, JM Larson et al, Editor. Sept 26-30, 2004, TMA: New Orleans, LA. p. 47-51.
227. Machine Design. *Engineering PM Parts Without Pricey Alloys*. 9/8/2008 [cited 12/1/2008]; Available from: <http://machinedesign.com/print/69698>.
228. Hohmann, B., *Class Notes for "16.511: Aircraft Turbine Engine Design"*, Instructor: Choon Tan, Editor. Fall 2008: Massachusetts Institute of Technology.
229. Kerrebrock, J.L., *Aircraft Engines and Gas Turbines*. Second ed. 1992, Cambridge: The MIT Press. 478 pgs.

230. *Gas turbine engine*. [cited 3/09/08]; Available from: <http://ocw.mit.edu/ans7870/16/16.unified/propulsionS04/turbofan2.jpg>.
231. *Temperature and pressure demands in gas turbine engine sections*. [cited 3/1/2008]; Available from: http://www.msm.cam.ac.uk/phase-trans/2003/Superalloys/coatings/images/jet_engine_small.jpg.
232. Balsone, S.J., 4.4.1 - Buckets and Nozzles, in *The Gas Turbine Handbook*. 2006, NETL. p. 411-418.
233. Donachie, M.J. and S.J. Donachie, *Superalloys A Technical Guide*. Second ed. 2002, Materials Park: ASM International. 439 pgs.
234. Pollock, T.M. and S. Tin, *Nickel-Based Superalloys for Advanced Turbine Engines: Chemistry, Microstructure, and Properties*. Journal of Propulsion and Power, 2006. **22**(2): p. 361-374.
235. Wen, M., E.H. Jordan, and M. Gell, *Remaining Life Prediction of Thermal Barrier Coatings Based on Photoluminescence Piezospectroscopy Measurements*. Transactions of the ASME, 2006. **128**: p. 610-616.
236. Matz, J.E. and Massachusetts Institute of Technology. Dept. of Materials Science and Engineering., *Carbide formation in a nickel-based superalloy during electron beam solid freeform fabrication*. 1999. p. 94 leaves.
237. Akers, D.W. and C.A. Rideout, *Physically-Based Health Management Tool for Improved Prognostics and Diagnostics of Turbine Engines*, in *Materials Damage Prognosis*, J.L.e. al, Editor. Sept 26-30, 2004, TMS: New Orleans, LA. p. 287-293.
238. Witek, L., *Failure analysis of turbine disk of an aero engine*. Engineering Failure Analysis, 2006. **13**: p. 9-17.
239. Sahan, O., *Fretting Fatigue Behavior of a Titanium Alloy Ti-6Al-4V at Elevated Temperature*, in *Department of the Air Force Air University*. 2002, Air Force Institute of Technology: Wright-Patterson Air Force Base. p. 101.
240. Bhaumik, S.K., et al., *Failure of turbine rotor blisk of an aircraft engine*. Engineering Failure Analysis, 2002. **9**(3): p. 287-301.
241. Klotz, U.E., et al., *Manufacture and microstructural characterisation of bimetallic gas turbine discs*. Materials Science and Engineering, 2005. **21**(2): p. 218-224.
242. Krueger, D.D., et al., *Patent # 5,161,950, Dual Alloy Turbine Disk*, USPTO, Editor. 1992, General Electric Company: United States. p. 1-9.
243. Fecht, H. and D. Furrer, *Processing of nickel-base superalloys for turbine engine disc applications*. Advanced Engineering Materials, 2000. **2**(12): p. 777-787.
244. Furrer, D.U., R. Shankar, and C. White, *Optimizing the Heat Treatment of Ni-Based Superalloy Turbine Discs*. JOM, 2003(March): p. 32-34.
245. Kermanpur, A., et al., *Integrated model for tracking defects through full manufacturing route of aerospace discs*. Materials Science and Engineering, 2005. **21**(4): p. 437-444.
246. Kissinger, R.D., et al., *Patent #5,413,752, Method For Making Fatigue Crack Growth-Resistant Nickel-Base Article*, USPTO, Editor. 1995, General Electric Company: United States. p. 1-8.

247. Kumar, S. and A.K. Jha, *Present Status and Future Potential of Sinter-Forging Technology*, in *Powder Materials: Current Research and Industrial Applications III*, F.D.S. Marquis, Editor. 2003, TMS. p. 93-105.
248. Silva, J.M., et al., *Characterization of Powder Metallurgy (PM) Nickel Base Superalloys for Aeronautical Applications*. Materials Science Forum, 2006. **514-16**: p. 495-499.
249. Kantzos, P., et al., *Effect Of Powder Cleanliness On The Fatigue Behavior Of Powder Metallurgy Ni-Disk Alloy Udimet 720*, in *Tenth International Symposium on Superalloys*. 2004, The Minerals, Metals & Materials Society: Champion, Pennsylvania.
250. Huron, E., et al., *Development of high temperature capability P/M disk alloys*, in *Superalloys 2008*. 2008, TMS: Seven Springs, PA.
251. Hardy, M.C., et al., *Developing Damage Tolerance and Creep Resistance in a High Strength Nickel Alloy For Disc Applications*, in *Tenth International Symposium on Superalloys*. 2004, The Minerals, Metals & Materials Society: Champion, Pennsylvania.
252. Gabb, T., et al., *The effects of heat treatment and microstructure variations on disk superalloy properties at high temperature*, in *Superalloys 2008*. 2008, TMS: Seven Springs, PA.
253. Gabb, T.P., et al., *Effects Of High Temperature Exposures On Fatigue Life Of Disk Superalloys*, in *Tenth International Symposium on Superalloys*. 2004, TMS: Champion, Pennsylvania. p. 269-274.
254. A. Abdul-Aziz et al, *Health Monitoring of a Rotating Disk Using a Combined Analytical-Experimental Approach*, in *Materials Evaluation*. 3/2010. p. 353-359.
255. Littles, J.W. and M.B. Buczek, *Engine System Prognosis*, in *Materials Damage Prognosis*, J. Larsen, et al., Editors. Sept 26-30, 2004, TMS: New Orleans, LA. p. 23-28.
256. Littles, J.W., et al., *Demonstration of an Advanced Prognostic Health Management Approach for Gas Turbine Engines*, in *Materials Damage Prognosis*, J. Larsen, Editor. Sept 26-30, 2004, TMS: New Orleans, LA. p. 191-196.
257. Tamarin, Y., *Protective Coatings for Turbine Blades*. 2002, Materials Park: ASM International. 245.
258. Ham, W.D. and Massachusetts Institute of Technology. Dept. of Materials Science and Engineering., *Nickel-Based Superalloy Operating Temperature Determination via Analysis of Gamma/Gamma' Microstructure and Coating/Base Material Interdiffusion*. 2005, Massachusetts Institute Of Technology: Cambridge. p. 25 leaves.
259. Walston, W.S., *Coating And Surface Technologies For Turbine Airfoils*, in *Tenth International Symposium on Superalloys*. 2004, The Minerals, Metals & Materials Society: Champion, Pennsylvania.
260. Okazaki, M. and H. Yamano, *Mechanisms and mechanics of early growth of debonding crack in an APSed Ni-base superalloy TBCs under cyclic load*. International Journal of Fatigue, 2005. **27**: p. 1613-1622.
261. Al-Jarba, K.A. and G.E. Fuchs, *Effect of carbon additions on the as-cast microstructure and defect formation of a single crystal Ni-based superalloy*. Materials Science and Engineering A, 2004(373): p. 255-267.

262. Al-Jarba, K.A. and G.E. Fuchs, *Carbon-Containing Single-Crystal Nickel-Based Superalloys: Segregation Behavior and Carbide Formation*. JOM, 2004(March): p. 50-55.
263. Feng, Q., L.J. Carroll, and T.M. Pollock, *Solidification Segregation in Ruthenium-Containing Nickel-Base Superalloys*. Metallurgical and Materials Transactions A, 2006. **37A**(June): p. 1949-1962.
264. Kunz, L., P. Lukáš, and R. Mintách, *Effect of Vibrations on Lifetime of Ni Base Single Crystals Subjected to Tensile Stress*. Materials Science Forum, 2008. **567-568**: p. 293-296.
265. Mylaraswamy, D., E. Nwadiogbu, and Y. Mohamad, *Patent #7,254,491, Clustering system and method for blade erosion detection*, USPTO, Editor. 2007, Honeywell International: United States.
266. Whittaker, M.T., *The effect of microstructure and texture on mechanical properties of Ti6-4*. International Journal of Fatigue, 2009. **31**: p. 2022-2030.
267. Nalla, R.K., *Influence of microstructure on high cycle fatigue of Ti-6Al-4V: Bimodal vs. Lamellar Structures*. Metallurgical and Materials Transactions, 2002. **33A**(3): p. 899-918.
268. Koul, A.K., et al., *Residual Life Assessment and Life Cycle Management of Design Life Expired Discs*, ASME, Editor. 2008, Life Prediction Technologies: Ottawa. p. 1-7.
269. Koul, A.K. and W. Wallace, *Importance of Physics-based Prognosis for Improving Turbine Reliability Part 2: A Turbine Disc Case Study in a Fleet Environment*, Life Prediction Technologies: Ottawa. p. 1-8.
270. Koul, A.K. and W. Wallace, *Importance of Physics-based Prognosis for Improving Turbine Reliability Part 1: A Turbine Blade Case Study*, Life Prediction Technologies: Ottawa. p. 1-6.
271. Xie, X., et al., *The Effect of Nb, Ti, Al on Precipitation and Strengthening Behavior of 718 Type Superalloys*, in *Superalloys 718, 625, 706, and Derivatives*, E.A. Loria, Editor. Oct 2-5, 2005, TMS. p. 287-298.
272. Huron, E.S., et al., *The Influence of Grain Boundary Elements on Properties and Microstructures of P/M Nickel Base Superalloys*, in *Tenth International Symposium on Superalloys*. 2004, The Minerals, Metals & Materials Society: Champion, Pennsylvania.
273. Kountras, A. and Massachusetts Institute of Technology. Dept. of Materials Science and Engineering., *Metallographic study of gamma - gamma prime structure in the Ni-based superalloy GTD111*. 2004. p. 73 leaves.
274. Lavigne, O., et al., *Relationships Between Microstructural Instabilities And Mechanical Behaviour In New Generation Nickel-Based Single Crystal Superalloys*, in *Tenth International Symposium on Superalloys*. 2004, The Minerals, Metals & Materials Society: Champion, Pennsylvania.
275. Epishin, A. and T. Link, *Mechanisms of High Temperature Creep of Nickel-Base Superalloys Under Low Applied Stress*, in *Tenth International Symposium on Superalloys*. 2004, The Minerals, Metals & Materials Society: Champion, Pennsylvania.
276. *Superalloys 2004*. in *Tenth International Symposium on Superalloys*. 2004. Champion, Pennsylvania: The Minerals, Metals & Materials Society.

277. Couturier, R., et al., *Process Development And Mechanical Properties Of Alloy U720LI For High Temperature Turbine Disks*, in *Tenth International Symposium on Superalloys*. 2004, The Minerals, Metals & Materials Society: Champion, Pennsylvania.
278. Gayda, J., T.P. Gabb, and P.T. Kantzos, *The Effect Of Dual Microstructure Heat Treatment On An Advanced Nickel-Base Disk Alloy*, in *Tenth International Symposium on Superalloys*. 2004, The Minerals, Metals & Materials Society: Champion, Pennsylvania.
279. Mourer, D.P. and J.L. Williams, *Dual Heat Treat Process Development For Advanced Disk Applications*, in *Tenth International Symposium on Superalloys*. 2004, The Minerals, Metals & Materials Society: Champion, Pennsylvania.
280. Huang, Z.W., et al., *Thermomechanical fatigue behavior and life prediction of a cast nickel-based superalloy*. *Materials Science and Engineering A*, 2006. **432**: p. 308-316.
281. Ellison, K.A., J.A. Daleo, and K. Hussain, *A New Method Of Metal Temperature Estimation For Service-Run Blades And Vanes*, in *Tenth International Symposium on Superalloys*. 2004, The Minerals, Metals & Materials Society: Champion, Pennsylvania.
282. Evans, D.G. and M. Fahrmann, *A Study Of The Effect Of Electro-Slag Re-Melting Parameters On The Structural Integrity Of Large Diameter Alloy 718 ESR Ingot*, in *Tenth International Symposium on Superalloys*. 2004, The Minerals, Metals & Materials Society: Champion, Pennsylvania.
283. Caldwell, E.C., F.J. Fela, and G.E. Fuchs, *Segregation Of Elements In High Refractory Content Single Crystal Nickel Based Superalloys*, in *Tenth International Symposium on Superalloys*. 2004, The Minerals, Metals & Materials Society: Champion, Pennsylvania.
284. Tin, S. and T.M. Pollock, *Predicting freckle formation in single crystal Ni-base superalloys*. *Journal of Materials Science*, 2004. **39**: p. 7199-7205.
285. Mueller, E., et al., *Failure analysis of weld-repaired B-1900 turbine blade shrouds*, in *Superalloys 2008*. 2008, TMS: Seven Springs, PA. p. 469-477.
286. Kim, I.S., et al., *Mechanical Behavior of As-cast and High Temperature Exposed Ni-Base Superalloy B1900*. *Materials Science Forum*, 2004. **449-52**: p. 541-544.
287. Morrissey, R.J., *Fatigue variability of a single crystal superalloy at elevated temperature*. *International Journal of Fatigue*, 2009. **31**: p. 1758-1763.
288. Guo, Z., et al., *Quantification of High Temperature Strength of Nickel-based Superalloys*. *Materials Science Forum*, 2007. **546-49**: p. 1319-1326.
289. Jha, S., M. Caton, and J. Larsen, *Mean vs. Life-limiting fatigue behavior of a nickel-based superalloy*, in *Superalloys 2008*, Roger Reed et al, Editor. 2008, TMS: Seven Springs, PA. p. 565-572.
290. Jha, S.K., et al., *Superimposing Mechanisms and Their Effect on the Variability in Fatigue Lives of a Nickel-Based Superalloy*, in *Materials Damage Prognosis*, J.L.e. al, Editor. Sept 26-30,2004, TMS: New Orleans, LA. p. 343-350.
291. Lu, Y.L., et al., *Elevated-Temperature Crack-Growth Behavior of Nickel-Base Hastelloy X Alloy*, in *Materials Lifetime Science & Engineering*. 2003, TMS. p. 33-42.

292. Wright, P.K., M. Jain, and D. Cameron, *High Cycle Fatigue In A Single Crystal Superalloy: Time Dependence At Elevated Temperature*, in *Tenth International Symposium on Superalloys*. 2004, The Minerals, Metals & Materials Society: Champion, Pennsylvania.
293. Shyam, A., et al., *Development Of Ultrasonic Fatigue For Rapid, High Temperature Fatigue Studies In Turbine Engine Materials*, in *Tenth International Symposium on Superalloys*. 2004, The Minerals, Metals & Materials Society: Champion, Pennsylvania.
294. Shyam, A., et al., *Ultrasonic Fatigue of a Nickel-Base Turbine Disk Alloy at Room and Elevated Temperatures*, in *Materials Damage Prognosis*, J.L.e. al, Editor. Sept 26-30, 2004, TMS: New Orleans, LA. p. 247-252.
295. Krueger, D.D., et al., *Patent # 4,957,567, Fatigue Crack Growth Resistant Nickel-Base Article and Alloy and Method For Making*, USPTO, Editor. 1990, General Electric Company: United States. p. 1-12.
296. Caton, M.J., et al., *Divergence Of Mechanisms And The Effect On The Fatigue Life Variability Of Rene` 88 DT*, in *Tenth International Symposium on Superalloys*. 2004, The Minerals, Metals & Materials Society: Champion, Pennsylvania.
297. Antolovich, S.D. and B.F. Antolovich, *A Mechanistic Based Study of Fatigue Crack Propagation In The Single Crystal Nickel Base Superalloy CMSX-2*, in *Materials Lifetime Science & Engineering*. 2003, TMS. p. 9-10.
298. Chen, Q., et al., *Small crack behavior and fracture of nickel-based superalloy under ultrasonic fatigue*. *International Journal of Fatigue*, 2005. **27**: p. 1227-1232.
299. Marx, M. and H. Vehoff, *Propagation of microcracks in single crystalline nickel-based superalloys: size effects on the crack opening*. *Materials Science and Engineering A*, 2004(387-389): p. 511-515.
300. Stoschka, M., et al., *Assessments of lifetime calculation of forged IN718 aerospace components based on a multi-parametric microstructural evolution*, in *Superalloys 2008*. 2008, TMS: Seven Springs, PA. p. 573-582.
301. Ranjan, S. and N.K. Arakere, *A Fracture-Mechanics-Based Methodology for Fatigue Life Prediction of Single Crystal Nickel-Based Superalloys*. *Journal of Engineering for Gas Turbines and Power*, 2008. **130**: p. 032501-1 - 032501-11.
302. Abu-Nabah, B.A. and P.B. Nagy, *High-frequency eddy current conductivity spectroscopy for residual stress profiling in surface-treated nickel-base superalloys*. *NDT&E International*, 2007. **40**: p. 405-418.
303. Buchanan, D.J., et al., *A coupled creep plasticity model for residual stress relaxation of a shot peened nickel-base superalloy*, in *Superalloys 2008*. 2008, TMS: Seven Springs, PA. p. 965-974.
304. *Metals Handbook Volume 9: Metallography and Microstructures*. 9th Edition ed. 1985: ASM.
305. Beal, J., R. Boyer, and D. Sanders, *Forming of Titanium and Titanium alloys*, in *ASM Handbook, Volume 14B: Metalworking: Sheet Forming*, S.L. Semiantin, Editor. 2006, ASM. p. 656-669.
306. Rolled Alloys Corp., *Titanium 6Al-4V Alloy Data Sheet*. 2003.

307. Gurrappa, I., *An oxidation model for predicting the life of titanium alloy components in gas turbine engines*. Journal of Alloys and Compounds, 2005. **389**: p. 190-197.
308. ATI Allvac, *Ti-17 Technical Data Sheet*. 2008.
309. Ashbaugh, N.E., et al., *Life Prediction Methodologies for Aerospace Materials*. 2001, University of Dayton Research Institute. p. 1-152.
310. Cadario, A. and B. Alfredsson, *Influence of residual stresses from shot peening on fretting fatigue crack growth*. Fatigue & Fracture of Engineering Materials & Structures, 2007. **30**: p. 947-963.
311. Garcia, D.B. and A.F. Grandt, *Application of a total life prediction model for fretting fatigue in Ti-6Al-4V*. International Journal of Fatigue, 2007. **29**: p. 1311-1318.
312. Brar, N.S., A. Hopkins, and M.W. Laber, *Laser Shock Peening of Titanium 6-4 Alloy*, in *Shock Compression of Condensed Matter*. 1999. p. 435-438.
313. Shepard, M.J., P.R. Smith, and M.S. Amer, *Introduction of Compressive Residual Stresses in Ti-6Al-4V Simulated Airfoils via Laser Shock Processing*. Journal of Materials Engineering and Performance, 2001. **10**(6): p. 670-678.
314. Mohanty, J.R., B.B. Verma, and P.K. Ray, *Prediction of fatigue crack growth and residual life using an exponential model: Part I (constant amplitude loading)*. International Journal of Fatigue, 2009. **31**: p. 418-424.
315. Mohanty, J.R., B.B. Verma, and P.K. Ray, *Prediction of fatigue crack growth and residual life using an exponential model: Part II (mode-I overload induced retardation)*. International Journal of Fatigue, 2009. **31**: p. 425-432.
316. Dizikes, P. (5/17/2010) *Explained: Monte Carlo simulations*. MIT News Office **Volume**,
317. Newman, J.C., *Prediction of Fatigue Crack Growth under Variable-Amplitude and Spectrum Loading Using a Closure Model*, in *Design of Fatigue and Fracture Resistant Structures*. 1982. p. 255-277.
318. Murakami, Y. and M. Endo, *Effects of defects, inclusions and inhomogeneities on fatigue strength*. International Journal of Fatigue, 1993. **16**: p. 163-182.
319. Sun, J., *Evaluation of Ceramic Matrix Composites by Thermal Diffusivity Imaging*. International Journal of Applied Ceramic Technology, 2007. **4**(1): p. 75-87.
320. Eagar, T.W., *Chapter 16: Processes of Joining Materials*, in *MIT Course 3.37 Class Notes: Welding and Joining Processes*: Cambridge, MA. p. 16.1-47.
321. Eagar, T.W., *The only constant is change*. Welding Journal, December 1995: p. 63-68.